



UNIVERSITA' DEGLI STUDI DI NAPOLI
FEDERICO II

**DOTTORATO DI RICERCA IN
INGEGNERIA GEOTECNICA XXII CICLO**

Coordinatore
Prof. Carlo Viggiani

**SEISMIC SOIL PILE INTERACTION:
EXPERIMENTAL EVIDENCE**

Flaviana Moccia

Ottobre 2009

RELATORI
Prof. Armando L. Simonelli
Prof. George Mylonakis

Abstract

The comprehension of the real behaviour of pile foundations under earthquake loading is very important, since it can significantly affect the performance of the superstructure.

As a matter of fact the experience of recent earthquake has confirmed that piles can suffer extreme damage and failure under earthquake loading.

The case histories from Kobe earthquake (1995) indicate that not only the inertial actions but also the kinematic ones, due to ground movements, which was overlooked in design specifications at that time, had significant effects on pile damage.

The purpose of this work is to examine the complex soil-structure interaction problem, on the basis of the results of an original experimental activity on shaking table, particularly devoted to the evaluation of kinematic interaction effects in layered soil configurations.

A great amount of data has been collected during the experimental study, relative to around 400 shaking events on a single pile. The test focused on three different subsoil configurations, a monolayer and two layered deposits, with the aim of highlighting the influence of soil stiffness contrast on kinematic interaction.

The effects of different pile head conditions, including the presence a single degree of freedom superstructure, have been investigated.

The pile response has been evaluated mainly in terms of bending moments induced by both kinematic interaction and coupled kinematic and inertial effects. The seismic motions at the foundation level, due to kinematic interaction, has been investigated and compared with the free field response.

To my lovely family

1. Introduction	
1.1 The study of piles in civil engineering	1
1.2 Observed damage during earthquake	2
1.2.1 Introduction	2
1.2.2 Observed pile response during earthquake	5
1.3 Scope of research	10
1.4 Organization of dissertation	10
2. Background	
2.1 Introduction	12
2.2 Seismic soil pile superstructure interaction (SPPSI)	12
2.3 Kinematic interaction	16
2.3.1 Winkler foundation approach (BWF)	21
2.3.1.1 P-y curve	21
2.3.1.2 Dynamic beam on Winkler foundation (BDWF)	23
2.3.2 Continuum approach (BEM and FEM)	29
2.4 Inertial interaction	30
2.5 Piles group	38
2.6 Recent research on SPPSI (numerical analyses)	44
2.7 Recent research on SPPSI (experimental analyses)	61
2.8 Building code provisions	61
2.8.1 NEHRP: National Earthquake Hazard Reduction Program (USA code)	74
2.8.2 EUROCODE (EC8)	75
2.8.3 ASCE (Workshop)	75
2.8.4 Norme tecniche per le costruzioni (NTC 2008)	76
3. One-g scale modelling and experimental set up	
3.1 Introduction	77
3.2 Aim of shaking table test and prototype	77
3.3 Scale modelling similitude	79
3.4 Definition of scaling law	80
3.4.1 Scaling law for pile stiffness (pile thickness)	82
3.4.2 Scaling law for mass of superstructure	86
3.5 Experimental set up	90
3.5.1 Shaking table at BLADE laboratory	90
3.5.2 Digital Spectrum	92
3.5.3 Soil container: “shear stack”	92
3.5.4 Accelerometer	94
3.5.5 Linearly variable differential transformer (LVDT)	94
3.5.6 Displacement transducer	96
3.5.7 Strain gauges	97
3.5.8 Earthquake input motion	98

4. Experimental testing on materials	
4.1 Testing plan	111
4.2 Model pile	112
4.2.1 Bending test	118
4.2.2 Push test	121
4.2.3 Experimental evaluation of bending moment on the pile	124
4.3 Materials for physical soil modelling	126
4.3.1 Leighton Buzzard sand mixer fraction E and Fraction B	128
4.3.2 Proprieties of mixer LB fraction E and fraction B	130
4.4 Soil test	134
4.4.1 Pluviaton test	134
4.4.2 Modal test	139
4.4.3 Results of modal test: Monolayer Leighton Buzzard fraction E	142
4.4.4 Results of modal test: Monolayer Leighton Buzzard fraction BE	146
4.4.5 Results of modal test: Rubber CT0515(R)	153
4.4.6 Conclusion of the Modal tests	154
4.5 Physical and mechanical proprieties of soil configurations	155
4.5.1 Monolayer Leighton Buzzard fraction E	155
4.5.2 Layered soil: Leighton Buzzard fraction BE and Leighton Buzzard fraction E	159
4.5.3 Layered soil: Leighton Buzzard fraction E and Rubber	162
4.5.4 Stiffness during dynamic test	164
5. Shaking table test results	
5.1 Introduction	167
5.2 Matching and repeatability of test	168
5.3 Soil column response	171
5.3.1 Example: test _BE+E_STU2_FH pile	171
5.3.2 Example: test _BE+E_STU12_FH pile	176
5.3.3 Conclusion on free field response	180
5.4 Kinematic interaction: free head pile (FH)	186
5.4.1 Effects of stiffness contrast	187
5.4.2 Effects of scaling factors	191
5.4.3 Some reflections on kinematic phenomenon	195
5.5 Pile head condition: no rotation head pile (NRH)	197
5.5.1 Bending moment: monolayer configuration (E)	199
5.5.2 Bending moment: layered soil configuration (BE+E)	209
5.5.3 Bending moment: layered soil configuration (E+R)	217
5.5.4 Motion on the pile head	222
5.5.5 Bending pile: effects of stiffness contrast	223
5.6 Kinematic interaction: effects of superstructure (SDOF))	225
5.6.1 NRH+SDOF bending moment: layered configuration (BE+E)	228
5.6.1.1 BE+E_STU 12 and 2 scale: simultaneous effects of inertial and kinematic interaction	237
5.6.1.2 BE+E_TMZ 12 and 2 scale: simultaneous effects of inertial and kinematic interaction	240
5.6.1.3 Conclusion on the simultaneous effects of inertial and kinematic interaction in layered soil BE+E	242

5.6.2	NRH+SDOF bending moment: layered configuration (E+R)	245
5.6.2.1	E+R_STU 12 and 2 scale: simultaneous effects of inertial and kinematic interaction	251
5.7	Soil shear strain and bending strain on pile	253
5.7.1	test: BE+E_TMZ2_NRH	255
5.7.2	test: BE+E_TMZ2_NRH +SDOF	257
5.7.3	test: BE+E_TMZ12_NRH	258
5.7.4	test: BE+E_TMZ12_NRH +SDOF	259

6. Analysis and Discussion

6.1	Introduction	260
6.2	Free field analyses	260
6.2.1	EERA code analyses: earthquake scaled 2 times	263
6.2.2	EERA code analyses: earthquake scaled 12 times	264
6.2.3	Soil shear strain: EERA LE and experimental values	271
6.2.4	General observation on free field comparison with EERA code and experimental data	273
6.3	Literature Vs Experimental results	274
6.4	Numerical analysis Vs Experimental results	276

7. Summary and Conclusion

References

Acknowledgments

APPENDIX I: list of tests

APPENDIX II: mass of oscillator

APPENDIX III: raw data

1. Introduction

1.1 The study of piles in civil engineering

The study and use of bearing piles as support structures was one of the first achievements in the history of civil engineering. The first examples of such use, in fact, date back to the prehistoric era.

Piles are columnar elements in the soil (deep foundation) deep lying soil which have the function of transferring load from the superstructure through weak compressible strata or through water to more compact and less compressible soil or onto rock. Among other things, piles are used in civil engineering to carry uplift loads in order to support tall superstructures subjected to overturning forces from winds or waves (Tomlinson, 1994)

The study of the load – carry capacity of piles has long been investigated; at the present time, its calculation is based only in part on theoretical concepts derived from the sciences of soil and rock mechanics, but mainly on empirical methods based on experience.

A lot of progress has been made in recent decades towards the development of engineering methods for the static and pseudodynamic analysis of pile foundations and different approaches can be adopted in solving the problem. The static behaviour of piles is well known and it is an active field of research.

The same cannot be said for the study and our understanding of the dynamic behaviour of piles. Predicting the behaviour of pile foundations in soil under earthquake loading is a complex problem, involving consideration of design motions, freefield site response, superstructure response, and soil-pile-superstructure interaction. Evaluating pile foundation behaviour requires a deep analysis of the loads imposed on the piles and of their pile-cap connections, of the transient or permanent deformations of the foundation, and of the influence of the pile foundations on the dynamic response of the superstructure.

The real behaviour of pile foundations under earthquake loading is an important factor, which affects the performance of many essential structures.

Historically, it has been common seismic design practice to ignore or simplify the influence of pile foundations on the ground motions applied to the structure. This is generally accepted as a conservative design assumption for a spectral analysis approach, as the flexible

pile foundation results in period lengthening and increased damping, and consequent decreased structural forces relative to a fixed base case.

In many cases, the possible resonance effects of longer period soft soil sites, which may amplify ground motions, and large structures can exacerbate the problem, the liquefaction effects and/or strain-softening potential in these soft soils can impose additional demands on pile foundation systems.

However, from the observation of pile performance during earthquakes it emerges that the piles can suffer extreme damage and failure under earthquake loading.

The field case histories from the Kobe earthquake (1995) strongly suggest that not only the inertial force but also the kinematic force due to ground displacement, which was overlooked in the design specification at that time, might have significant effects on pile damage.

The purpose of this work is to examine the complex soil-structure interaction problem, using the results of shaking table tests, with particular attention to layered soil and kinematic interaction effects. The results from experimental studies, used in conjunction with lessons from case histories and numerical analyses, are an essential tool for the study of this complex matter. The centrifuge or 1-g shaking table studies of the seismic behaviour of pile foundations are the mean tools for understanding the fundamental mechanisms of soil-pile-superstructure interaction, in particular for evaluating the reliability of current design procedures and for the development of improved design procedures.

The obvious advantage of centrifuge or 1-g shaking table studies is the ability to obtain detailed measurements of response in a series of tests designed to physically evaluate the importance of varying the characteristics of the earthquake (e.g. level of shaking, frequency content, waveforms), of the soil profile and/or of the pile-superstructure.

1.2 Observed damage during earthquakes

1.2.1 Introduction

The recent (April 2009) Italian earthquake in the Apennine Abruzzo region (and in particular in the city of l' Aquila) is estimated to have generated damages for more than 2-3 billion Euros for civil building alone (CNR- consiglio nazionale delle ricerche) but, more important, has caused more than 300 victims, most of whom died in collapsed structures, making this the deadliest earthquake in Italy since the 1980 Irpinia earthquake.

Collapsed and damaged structures in l' Aquila and its surroundings included both older masonry buildings and relatively modern reinforced concrete structures.

Usually, the failure of structures during earthquakes is the result of structural inadequacies or foundation failures, or a combination of both. In Figures 1.1 (a) to (c), typical damage due to structural inadequacies of a building is shown.

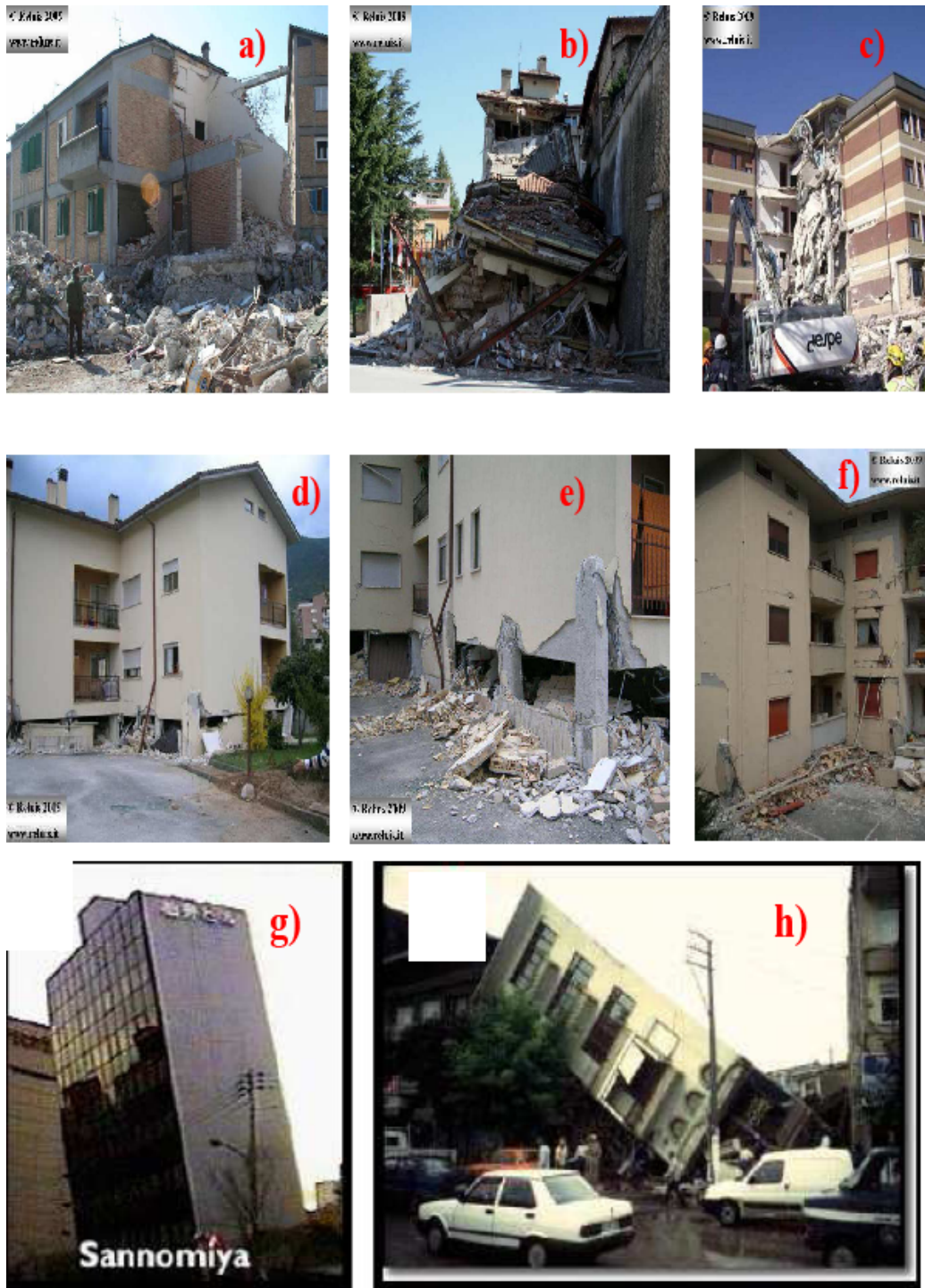


Figure 1.1: (a) Collapse of a reinforced concrete (R.C.) building; (b) Hotel Duca degli Abruzzi – L’Aquila; (c) Casa dello studente – L’Aquila; (d) – (e) Soft storey mechanism on a three-storey R.C. building – Pettino (AQ); (f) Soft storey mechanism on a four-storey R.C. building – Pettino (AQ); photo by RELUIS 2009: I. Iervolino, P. Ricci and G.M. Verderame, A. Occhiuzzi, N. Caterino and G. Maddaloni; (g) a highrise building during the 1995 Kobe earthquake, after U.C. Berkeley (1995); (h): Tilting of a building during the 1999 Koceli earthquake (Turkey), after EERI (1999)

In particular, Figure 1.1(a) shows the collapse of a reinforced concrete (R.C.) building construction realized in the 60s in adhesion with a pre-existing building; Figure 1.1 (b) shows the collapsed division of a building; Figure 1.1 (c) shows the collapsed portion of a building: the failure mechanism involved all of the storeys; the beams show a high plastic rotation.

Figures 1.1 (d-e-f) shows the soft storey mechanism on a three-storey R.C. building in Pettino (near l'Aquila). It is worth noting the absence of stirrups in the beam-column joint, whereas the displacement demand is concentrated at the ground level.

These photos show the failure of residential buildings predominantly due to structural inadequacies, such as poor ductility and improper beam column detailing. On the other hand, in Figure 1.1 (g-h) the failures shown are not due to any structural inadequacies but due to foundation failure. In such failures the soil supporting the foundation plays an important role.

Forecasting the exact time of an earthquake can at best reduce casualties. Therefore, structures need to be designed to withstand the impact of an earthquake and prevent collapse, as "it is buildings that kill people, not earthquakes".

Earthquakes in the past have shown the shortcomings of current design methodologies and construction practices, which produced structural failures and loss of lives. Post earthquake investigations have led to improvements in design engineering analysis, design and construction practices.

A brief historical development of earthquake engineering practice showing how earthquake engineers have learned from failures in the past is outlined in Table 1.1. There is no doubt that future events will continue to advance the state of knowledge.

Table 1.1: Historical development of earthquake engineering practice

Earthquake	Remarks	Post earthquake developments
1908 Messina (Italy). Reitherman (2000)	120,000 fatalities. A committee of nine practising engineers and five professors were appointed by the Italian government to study the failures and to set design guidelines.	Base shear equation evolved i.e. the lateral force exerted on the structure is some percentage of the dead weight of the structure (typically 5 to 15%).
1923 Kanto (Japan) Kawashima (2002)	Destruction of bridges, buildings. Foundations settled, tilted and moved.	Seismic coefficient method (equivalent static force method using a seismic coefficient of 0.1 - 0.3) was first incorporated in design of highway bridges in Japan (MI 1927).
1933 Long Beach (USA) Fatemi and James (1997)	Destruction of buildings, especially school buildings.	UBC (1927) revised. This is the first earthquake for which acceleration records were obtained from the recently developed strong motion accelerograph.
1964 Niigata (Japan)	Soil can also be a major contributor of damage.	Soil liquefaction studies started.
1971 San Fernando (USA)	Bridges collapsed, dams failed causing flood. Soil effects observed.	Liquefaction studies intensified. Bridge retrofit studies started.
1994 Northridge (USA)	Steel connections failed in bridges.	Importance of ductility in construction realised.
1995 Kobe (Japan) Kawashima (2000)	Massive foundation failure. Soil effects were the main cause of failure. Liquefaction phenomena: collapse bridges and numerous harbour side structures	Downward movement of a slope (lateral spreading) is said to be one of the main causes. JRA (1996) code modified (based on lateral spreading mechanism) for design of bridges.
2003 Molise (Italy)	Massive foundation failure. Soil effects were the main cause of failure.	National code modified (based on EC8 prescriptions - soil amplification factor s etc.).
2009 Abruzzo (Italy)	Near-field effect: combination of vertical and horizontal component of earthquake	Starts to study near -field phenomena?

1.2.2 Observed pile response during earthquakes

Pile distress and failure during seismic shaking, although difficult to observe in post-earthquake site investigations, have been well documented.

In Mizuno (1987), for example, 28 cases involving seismic pile failures in Japan have been reported, EEFIT (1986) has described the case of pile failure in Japan, CNEL-ENEL (1976) has documented pile ruptures under two bridges in the Friuli (Italy) 1976 earthquake. Mizuno (1987), in summarizing the Japanese experience with regard to the likely causes and different types of pile failure, underlines inertial effects, liquefaction effects and kinematic effects.

Mizuno (1996) has reported the case of a civil building, twelve floors high, on rc piles and demolished after the earthquake. This real case shows a direct case of the pile head's failure mechanism. Four different mechanisms of failure have been identified: compression failure,

shear compression, the combination of shear and compression failure; displacement of soil and pile fix in his position. In his PhD Thesis (1998) Meymand describes all typical mechanisms of collapse from the observations of pile response during an earthquake. Many cases of damage to piles and pile-supported structures have been examined from the San Francisco earthquake (1903) to the Kobe earthquake (1995). Meymand shows that each individual earthquake has imparted specific lessons about SSPSI. From observed pile damage during earthquakes, the following failure modes can be discerned, where failure is defined as the loss of structural capacity of the pile and/or degradation of the pile-soil load carrying capacity.

Figure 1.2 and figure 1.3 show some examples of inertial effects on the structures during earthquake. The failure arises from the transmission of the structural inertial forces transferred to the pile foundation from the superstructure (forces are created by the superstructure vibration). They impose lateral loads which are concentrated near the pile head.

Figure 1.2 shows a typical failure mode observed in the San Francisco, Alaska, Niigata, Loma Prieta, and Kobe earthquakes. It consists in a loss of lateral soil support due to the liquefaction of cohesionless soils or the strain softening of cohesive soils near the pile head. When it is combined with large structural inertial loads, excessive displacements and bending strains concentrated near the pile head develop and result in pile damage, frequently at the pile to cap connection. Structural distortions may also be a consequence.

Figure 1.3 shows one particular failure which consisted in the loss of pile bearing capacity delete which is typical at the Anchorage City Dock and of a number of observed failures in Mexico City. It may occur, that, when soil along the length of the pile softens due to liquefaction or strain softening, the pile may experience a loss of bearing capacity. When combined with a rocking mode induced by superstructure inertia forces, the piles frequently undergo settlement, punching failure, and/or tensile pull-out failure.

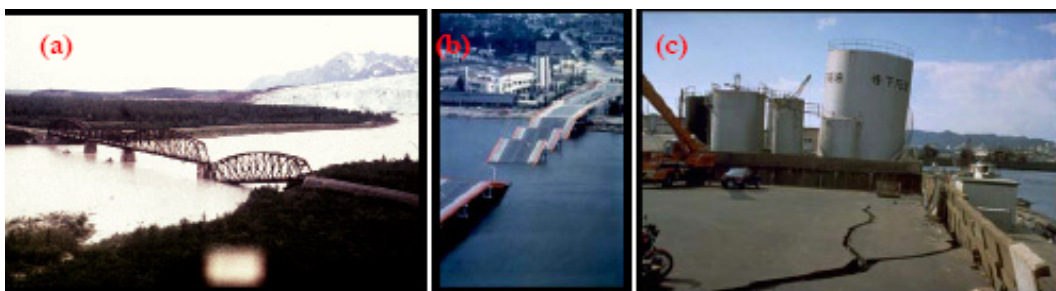


Figure 1.2: (a) Piled “Million Dollar” bridge after 1964 Alaska earthquake (USA); (b) Piled “Showa Bridge” after 1964 Niigata earthquake (JAPAN); (c) Piled tanks after 1995 Kobe earthquake (JAPAN), photo courtesy NISEE

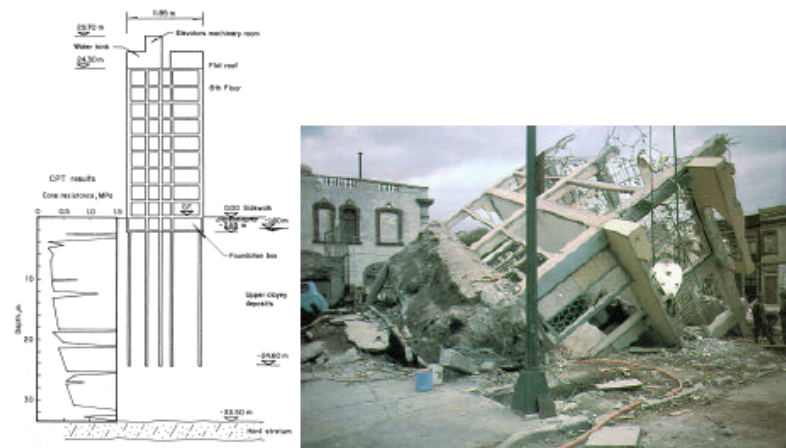


Figure 1.3 Ten storey pile supported building built on soft soils during the 1985 Mexico City Earthquake: a) elevation including geotechnical conditions; b) overturned structure (after Mendoza and Auvinet, 1988)

Figure 1.4 and figure 1.5 show some examples from liquefaction effects: induced failures have also been frequent and stunning. Figure 1.5 shows the liquefaction ground failure mechanism.

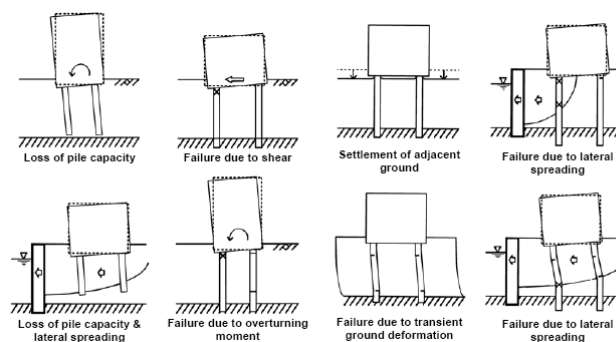


Figure 1.4 Schematics of pile damage mechanisms in liquefied ground (modified from Tokimatsu et al. 1996)

The failures at Moss Landing in 1906, the Showa Bridge in Niigata, the collapsed bridges in Alaska and Costa Rica, and numerous harbour side structures in Kobe are all illustrative of the liquefaction phenomena. A common liquefaction hazard arises from the large loads and displacements that a laterally spreading soil deposit exerts on piles, which often results in pile damage.

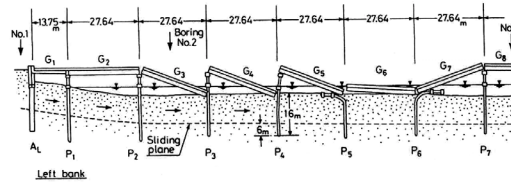


Figure 1.5: (a) Liquefaction induced collapse of the Showa bridge during the 1964 Niigata earthquake (after Iwasaki, 1972); (b) schematic diagram of the fall-off of the girders in Showa bridge (Takata et al., 1965)

Figure 1.6 describes a typical case of the kinematic effects on pile collapse in the Niigata earthquake, 1964. Piles may be subject to damaging bending strains at interfaces between soil layers of strong impedance contrast. This contrast may be provided by soft and stiff soil layers or by soil layers that undergo liquefaction or strain softening under earthquake loading. This is best evidenced by the foundations that have been excavated subsequent to the Niigata earthquake. This mode of deformation and potential failure has not received proper attention in engineering practice

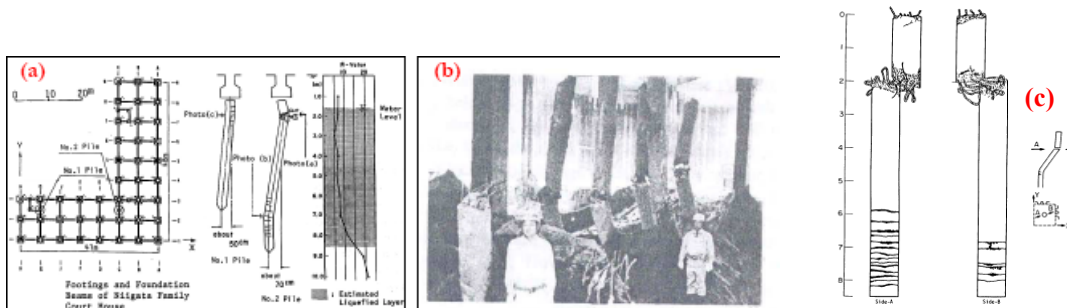


Figure 1.6: (a): pile failure of Niigata Family Court House building during the 1964 Niigata earthquake, Hamada (1992a); (b) pile failure observed during the excavation of the NHK building after the 1964 Niigata earthquake, Hamada (1992a); (c) damage pattern to foundation piles supporting the Niigata Family Courthouse during the 1964 Niigata Earthquake (after Hamada, 1991)

Some case histories, during the San Fernando (1971), Loma Prieta (1989), and Kobe (1995) earthquakes, show that in some cases the inadequate (or nonexistent) structural connections of pile to cap connections is an elementary design deficiency. The result is a shear failure in the pile.

Batter piles are designed to accommodate large lateral loads, but they often attract forces that the pile heads and/or pile cap cannot sustain. Considerable damage at the Port of Oakland during the Loma Prieta earthquake provides evidence of this failure mechanism. In summarizing (Tokimatsu, 2003a) there were significant differences in the damage pattern of

piles among non-liquefied, liquefied, and laterally spreading areas. This is considered to be due mainly to the following:

1. the non-liquefied surface soil amplifies ground motions significantly, leading to extensive damage to buildings or otherwise e shear failure at the pile heads.
2. soil liquefaction de-amplified the ground motions particularly in the period range less than 1s, reducing the damage to superstructure in the liquefied and laterally spreading areas.
3. soil liquefaction and lateral spreading increased ground displacement and thus kinematic effects, leading to the damage to pile foundations, which were concentrated not only at the pile head but also near the boundary between liquefied and non-liquefied layers.
4. the spatial variation of ground displacement in the laterally spreading area had a significant effect on the differences in failure modes of piles within a building.

Thanks to these case histories a qualitative understanding of the superstructure-pile-soil interaction (SSPSI) has been achieved. The field case histories from the Kobe earthquake strongly suggest that not only the inertial force but also the kinematic force due to ground displacement, which was overlooked in the design specification at that time, might have significant effects on pile behaviour.

An important support can be given studying instrumented cases, which can provide quantitative valuation of SSPSI. From the instrumented cases, it can be seen that SSPSI often results in spectral deamplification of pile cap motions relative to free-field motions. This deamplification was generally seen to occur at periods less than the period of the composite soil-pile-structure system, and varies greatly in amplitude. This phenomenon was observed in a number of case histories of building structures in Japan subjected to low intensity shaking, and several case histories (though not all) of buildings and bridge structures in the U.S. subjected to moderate to high levels of ground shaking.

At low levels of shaking, kinematic interaction generally dominates the system response; period lengthening and increased radiation damping of the system are responsible for dissipating energy and deamplifying motions up to the resonant period.

At higher levels of shaking, soil modulus degradation and soil-pile gapping can inhibit radiation damping, and structural inertial forces predominate, decreasing the overall effects of spectral deamplification. When system components yield, the system period further lengthens and radiation damping may be effectively suppressed; such period lengthening may be towards or away from resonant response.

The fact that SPSSI effects do not operate on a strict continuum additional reinforces the notion that a fully coupled analysis technique is desirable to properly capture the range of system response from linear to nonlinear behaviour. Analytical methods for SSPSI will be examined in the following chapter, with a review of building code provisions. The aim of this research is to gain an insight into the failure mechanism of kinematic interaction and superstructure- pile-soil interaction in a dry cohesionless soil during earthquakes.

1.3 Scope of research

This dissertation describes the results of a study on the dynamic response of pile foundations in dry sand and in layered subsoil during strong shaking.

Referring to kinematic interaction, within the framework provided by the NTC 2008 (Italian code “Norme tecniche per le costruzioni”), two main issues should be addressed by a building code: when has kinematic interaction to be considered ?(or, conversely, when can it be neglected?); how has kinematic interaction to be analysed.? Moving to the latter issue, the experimental work described in this thesis has been programmed in order to focus on some crucial aspects that affect kinematic interaction phenomena:

- soil stiffness contrast;
- subsoil deformability;
- wave form input motion;
- pile head condition: free head pile and no rotation pile head;
- correlation between inertail and kinematic bending moment.

The research consisted of four phases: (1) a critical study of analytical techniques and limitations; (2) a series of dynamic shaking table tests of pile supported structures in monolayer and in two different layered subsoils performed using the recently completed shaking table at the BLADE laboratory of University of Bristol; (3) improve understanding of pile-soil interaction during earthquake in the light of the experimental results; (4) back-calculation of behaviour from recordings of pile bending moment, pile head and superstructure accelerations, and soil profile accelerations.

1.4 Organization of dissertation

A great amount of data has been collected in the experimental activity of this research. Data from a total of around 400 shaking events on a single-pile have been obtained. The test focused their attention on three different subsoil configurations: a monolayer and two layered deposits with the peculiarity that each layer has different stiffness. These different materials have been chosen to emphasize the effects of layer stiffness contrast on the kinematic interaction. The experimental tests focus on the data from single pile considering five different pile head conditions including the structures during selected shaking events. All of the tests done in this experimental work are listed in table 4.1 (Chapter 4).

The dissertation is divided into seven chapters, whose content is stated below:

Chapter 1 Introduction - includes a brief discussion on the importance of understanding soil-pile-structure interaction and an organizational summary of the dissertation.

Chapter 2 Theoretical background - includes a brief overview of published knowledge on soil-pile-structure interaction that (1) provides a general introduction to the theoretical problem; (2) specifically discusses the approach to study delete seismic soil-pile-

superstructure interaction; (3) summarizes recent research on this topic; (4) discusses experimental procedures of direct relevance to the present study.

Chapter 3 One-g modelling and experimental set up –presents the shaking table scaling law for modelling the prototype, the derivation and application of which is discussed. The shaking table modelling equipment and techniques are critically evaluated.

Chapter 4 Shaking table experimental testing –discusses the characteristics of the materials used in the shaking table test and the model pile. The results of the “*modal test*” are set out to define the materials’ stiffness values.

Chapter 5 Shaking table test results - presents the results of the shaking table tests. It includes a discussion of the shaking table performance and the model container response. Soil pile and structure accelerations, pile head displacements, and maximum bending moment along the pile are determined for different physical model configurations. Soil shear stains and bending strain on pile are also discussed.

Chapter 6 Analysis and discussion of experimental results – the soil container system performance is observed and compared with the free field response analysed by EERA code. The soil-structure interaction is examined by BDWF tools. The observed behaviour is found to be consistent with the expected behaviours of the different soil types used.

Chapter 7 Summary and conclusion - includes a summary of the dissertation and its findings.

2. Background

2.1 Introduction

The performance of pile-supported structures (such as bridges) during recent devastating earthquakes (e.g. Bhuj Earthquake of 2001, Chi-Chi Earthquake of 1999, and Kocaeli Earthquake of 1999) has come under scrutiny. The damage caused to pile foundations during these earthquakes has emphasized the importance of understanding seismic soil-pile structure interaction (SSPSI). Moreover, the advances in computer technology justify the use of rigorous soil-pile-structure interaction analysis in many important practical engineering structures and rigorous dynamic analyses, including (SPSI), for the design of such complex structures. Substantial research efforts have been carried out to investigate the kinematic seismic behavior of single piles and pile groups. Further, several studies by Mylonakis and Gazetas (1997), Guin and Banerjee (1998) have focused on SPSI analyses. In the following sections the main findings from the lecturature on this topic are highlighted.-Techniques for the analysis of single piles and pile groups under dynamic loading have also been described. A review of building code requirements has been proposed.

2.2 Seismic soil-pile-superstructure interaction (SSPSI)

The complex dynamic interaction between soil-pile-structure is governed by two phenomena referred in the technical literature as inertial and kinematic phenomena. As we know, earthquake design loads applied to the foundation arise from inertia forces, which develop in the superstructure, and from soil deformation, caused by the passage of seismic waves, imposed on the foundation (Nikolau, 2001; Pecker and Pender, 2000).

In Figure 2.02 the principal characteristics of seismic soil-pile-superstructure interaction (SSPSI) are illustrated schematically (Gazetas-Mylonakis, 1998): the system components include the superstructure, the pile cap, the pile (s), the soil and the seismic energy source (a_r).

The first step in the study of SSPSI focuses on the knowledge of seismic motion through the soil deposit. Before seismic wave propagation, pile installation and loading, soil

displacement, and load transfer, are in a unique stress state in the pile and surrounding soil. With seismic motion numerous incident waves, shear waves (S waves), dilatational waves (P wave), and surface waves (R or L waves), travel on soil layers moving the structure. The particular seismologic conditions affect the nature of incoming waves, and the geometry and the physical characteristics of soil deposits (stiffness and damping) modify this motion (free field motion at the site of the foundation). The origin of the SSPS interaction is delete seismically soil deformation. Hence, the mechanism of SSPSI is compounded by two phenomena:

- kinematic interaction defined as the seismic response of the soil profile transmitted to the pile foundation. Seismic soil deformation forces the pile to move, the different levels of stiffness between soil, pile, and foundation generates a seismic modified motion of the foundation which is different from free field motion. Incident waves are reflected and scattered by foundation and piles, which, are subsequently stressed developing curvatures and bending moments.
- inertial interaction consists of structural inertial forces being transferred to the pile foundation. The motion induced at the foundation level generates oscillations in the superstructure, which develop inertia forces and overturning moments at its base. These forces impose lateral loads which are concentrated near the pile head, and axial loads, if a rocking mode of the structure is present.

The modes of system interaction include kinematic-inertial effects and physical interaction, and radiation damping. The radiation damping which occurs due to the stiffness contrast between the soil and pile, is an important aspect. Piles vibrate at much higher frequencies than the surrounding soil, but soil-pile contact forces the soil to vibrate at these high frequencies, resulting in the transmission of high frequency energy away from the pile into the surrounding soil. Radiation damping is most pronounced at high frequencies and low levels of soil damping, and cannot propagate through “gaps” opened between the pile and soil. The pile cap can also be an important source of radiation damping. During seismic loading, gaps may also open between the soil and the pile near the ground surface; in cohesionless soils, the gap may fill in and be compacted; however in cohesive soils, the gap may stay open, resulting in a reduction of soil-pile lateral stiffness. The methods usually adopted to analyze the SSPS interaction are:

- **Substructuring method-** Multistep Method: this consists in breaking down the problem into three tasks (site response analysis, kinematic interaction, inertial interaction). It is convenient for highlighting the various contributions of each to the results, and implies that the steps must be performed separately. The radiation of energy is considered at pile-soil interface, by a correlation with force and displacement (Figure 2.01);
- **Direct analysis-** Direct Method (Wolf, 1991): this consists in a complete interaction analysis (usually with the finite element method). The radiation condition is defined on an artificial boundary (Figure 2.02).

Generally the computation of the foundation's seismic loads follows the multi-steps delete approach. A direct (or complete) interaction analysis is laborious and not well suited for design, especially in 3D analysis. For systems with strong nonlinear response, a complete analysis technique may be desirable. The multistep approach is not only attractive for illustrating the fundamental aspects of soil structure interaction, it is also of great mathematical use which relates, in linear systems, to the superposition theorem (Kausel and Roesset, 1974). This theorem states that the seismic response of the complete system of figure 2.2 can be computed in two steps:

1. the **kinematic interaction** involving the response to base acceleration of a system which differs from the actual system in that the mass of the superstructure is equal to zero;
2. the **inertial interaction** referring to the response of the complete soil-structure system to forces associated with accelerations equal to the sum of the base acceleration plus those accelerations arising from the kinematic interaction. The latter system is further divided into two consecutive steps: computation of the dynamic impedances at the foundation level and analysis of the dynamic response of the superstructure supported on the dynamic impedances and subjected to the kinematic motion, also called effective foundation input motion.

The multistep approach breaks down the problem into more agreeable stages and does not necessarily require that the whole solution be repeated again if changes occur in the superstructure. In addition, it has the advantage that some of the intermediate steps can be ignored—providing that each step described above is performed rigorously and under the restriction that the system remains linear. For a mathematical description of the superposition theorem, the reader is referred to Kausel and Roesset (1974) or Gazetas and Mylonakis (1998)

Obviously kinematic interaction is exactly zero for shallow foundations in a seismic environment consisting exclusively of vertically propagating shear waves or dilatational waves. Gazetas (1984) has demonstrated that when the piles are flexible with respect to the surrounding soil, kinematic interaction is significant for small to medium frequencies.

During the last decade, numerous solutions for the dynamic impedances of any foundation shape and of piles have been published (Gazetas, 1990). They are available for homogeneous soil deposits but also for moderately heterogeneous ones. For some situations, kinematic interaction can be ignored and the second step of the multistep approach can be bypassed. The kinematic analysis is relevant in presence of piles with a big diameter, in layered soil or in very soft soil deposits. However, more often, design engineers refer to inertial loading as SSI, ignoring the kinematic component. Kinematic deformations and bending moments of piles have been studied by Tazoh et al. (1987), Gazetas et al. (1992), Poulos & Tabesh (1996), Mylonakis (2001), Nikolaou et al. (2001).

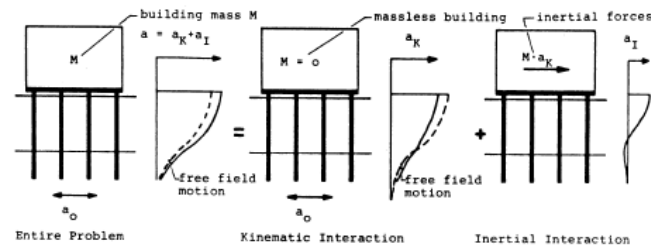


Figure 2.01 Substructuring method for seismic soil-pile-superstructure interaction (after Gazetas et al., 1993)

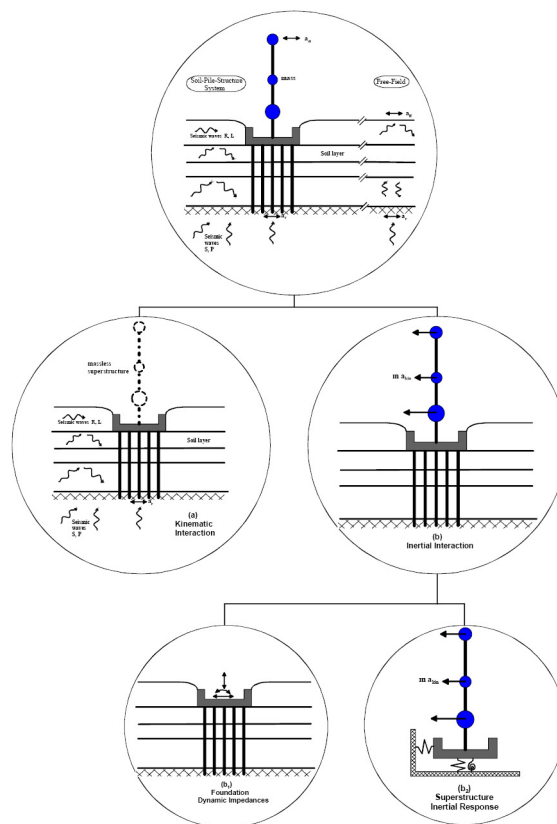


Figure 2.02: Generalized pile head/free field transfer function for kinematic interaction (after Fan and Gazetas, 1991)

Kinematic bending moments depend mainly on:

- the stiffness contrast between two consecutive soil layers;
- the boundary conditions at the head of the piles;
- the proximity of the excitation frequency to the fundamental natural frequency of the soil deposit;
- the depth of the interface of the layers with stiffness contrast, in relation to the active length of the pile.

In addition, simplified methods are available in the case of pile foundations to account for the group effect (Dobry and Gazetas, 1988). Therefore, provided all the aspects listed above are properly covered, seismic soil structure interaction can be covered at a minimal cost and reduces to the last step of the multistep approach: dynamic response of the structure connected to the impedance functions and subjected to the free field motion (equal to the kinematic interaction motion). However to be fully efficient, and to allow for the use of conventional dynamic computer codes, the impedance functions which are frequency dependent must be represented by frequency independent values. The simplest version of frequency independent parameters are the so-called springs and dashpots. From the published results, it appears that only under very restrictive soil conditions (homogeneous half-space, regular foundations) can dynamic impedances be represented by constant springs and dashpots. Nevertheless, structural engineers still proceed using these values, which, more often than not, are evaluated as the static component (zero frequency) of the impedance functions. The following sections will present a brief overview of SSPSI analyses; these generally fall into the discrete and continuum classes of models.

2.3 Kinematic interaction

The different types of seismic response from soil and pile-give a different displacement profile for soil and for piles. Many authors have studied this phenomenon. Seismically induced kinematic interaction of piles has been studied by various researchers: Margason (1975), Kagawa & Kraft (1980), Flores-Berrones & Whitman (1982), Dente (1983), Sheppard (1983), Dobry & O'Rourke (1983), Tazoh et al. (1987), Mineiro (1990), Kavvadas & Gazetas (1993), Kaynia (1996), Poulos & Tabesh (1996), Mylonakis (2001), Cairo (2005), Saitoh (2005) and others.

Reviews of the subject have been presented by Novak (1991), Pender (1993) and Gazetas & Mylonakis (1998).

Kinematic interaction is usually expressed in terms of a transfer function, defined as the frequency domain, between each component of the foundation input motion and the free-field motion. Theoretical studies have been performed by Mamoon & Ahmad (1990), Fan et al. (1991), Gazetas et al. (1992), and others. The results show that, for a soil deposit containing a thin upper soft layer, the kinematic transfer function tends to fluctuate with frequency at an increasing rate, as the top layer becomes relatively softer. At certain frequencies, pile head deflection may be greater than free-field surface displacement.

Generally speaking, to study the kinematic interaction the theoretical assumption is founded on linear elastic behaviour of piles. Closed form expressions have been derived for computing the maximum steady-state bending moment at the interface between two consecutive soil layers (Margason, 1975; Dobry & O'Rourke, 1983; Nikolaou et al. 2001;

Mylonakis 2001) (see paragraph n. 2.3.1). Winkler methods are also used to analyze kinematic interaction.

To describe pile-soil behaviour Gazetas (1984) and Fan et al (1991) defined two dimensionless factors of kinematic interaction: I_u and I_ϕ , expressed as follows

$$\begin{cases} I_u = \frac{|u_p|}{u_{ff}} \\ I_\phi = \frac{|\phi_p| d}{2 u_{ff}} \end{cases} \quad [2.1] \text{ and } [2.2]$$

where u_{ff} and u_p are the amplitude of horizontal displacement at soil surface (free-field) and the pile head, respectively; ϕ_p is the amplitude of rotation at pile head; d is the diameter of pile (Figure 2.1.a). The u_p e ϕ_p are the parameters of effective motion of foundation. Actually without kinematic interaction u_{ff} is equal to u_p , also ϕ_p is equal to zero.

The trend of I_u function trends/rates are shown in Figure 2.1 b), I_u is plotted in relation to dimensionless frequency $a_o = \frac{d \omega}{V_s}$ where ω is the pulse of input motion and V_s is the shear velocity of soil.

From the plot three different regions are identified:

- for $a_o < a_{o1}$: low frequency range, I_u is around 1, the pile head follows soil deformation;
- for $a_{o1} < a_o < a_{o2}$: mean frequency range; I_u decrease rapidly with the increase in frequency. In this case the seismic motion of the foundation is different from the soil due to different levels of soil and the pile foundation rigidity;
- for $a_o > a_{o2}$ high frequency range; I_u decreases very quickly, the value is between 0.2 and 0.4.

The a_{o1} and a_{o2} values depends on soil profiles: relative soil-pile stiffness, the condition of the pile head boundary. So that for low and middle frequency, the pile group interaction is influential. In this frequency range the value of I_u does not change with the number of piles, kinematic effects on pile group is not so important (Gazetas, 1993).

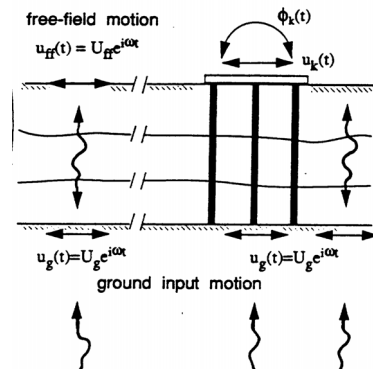


Figure 2.1.a) Substructuring method for seismic soil-pile-superstructure interaction analysis: kinematic interaction (after Gazetas et al., 1993)

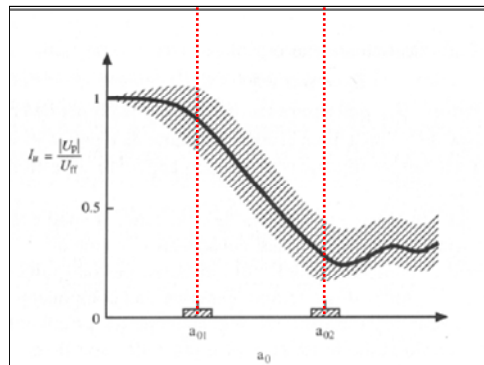


Figure 2.1.b): Generalized pile head/free field transfer function for kinematic interaction (after Fan and Gazetas, 1991)

For near field earthquakes or for earthquakes with a high frequency content, the ratio between the two displacements is around 0.6. The high frequency is filtered by kinematic interaction (acceleration at pile head is smaller than free field conditions). Using a dynamic Winkler model, the authors found pile group effects to be more pronounced for inertial than kinematic loading. The results obtained by Fan (1991) are important for evaluating the displacement and rotation of a single pile or pile groups. Knowing the free field input motion, the effective input motion has also been calculated. Mylonakis et al. (1997) applied this substructuring approach based on an equivalent linear method to analyze pile supported bridge piers. The importance of non-homogeneity of soil is analyzed by Kaynia and Kausel (1991). They observe that for single piles and for pile groups, with heterogeneity of soil filter and high frequency of input motion, as shown in Figure 2.2, the value of I_u function rapidly decreases.

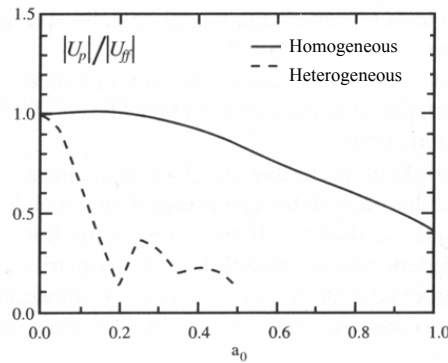


Figure 2.2: Horizontal displacement factor for single piles ($L/d=20$, $E_p/E_s=100$) (Kaynia and Kausel, 1991)

Figure 2.3 shows I_u trends for different levels of shear velocity contrast between layers. Considering a thin soft upper layer, ($h/d < 5$; $V_a/V_b < 1/3$), the I_u trend changes. It fluctuates and, for some high frequencies, the pile head displacement is bigger than free field displacement. The importance of stiffness contrast is underlined.

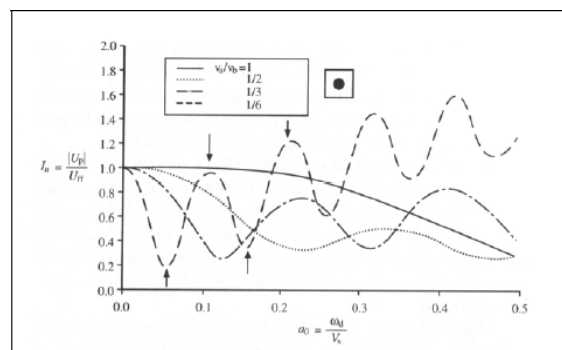


Figure 2.3 Kinematic response no rotation pile head: effect of an upper layer thin and soft (Gazetas et al, 1992)

The kinematic effects on the bending moment of piles during an earthquake has been closely examined by Kavaddas and Gazetas (1992) and Gazetas and Nikolaou (1996). As we have already explained, the kinematic stress on piles depends on many factors: soil-pile stiffness; ratio L/d of pile, the condition of the pile head; the thickness and the stiffness of different soil layers, and the propriety of input motion. Kinematic effects are present at pile head and length. The displacement profile of free field and pile displacement profiles are different as shown in Figure 2.4 (Kavvadas and Gazetas, 1992): it is plotted the I_u trend/ratio

with depth, four different harmonic excitation so that for different value of a_0 (0.05, 0.11, 0.16, 0.21). Different displacement rates means pile bending moment and curvature

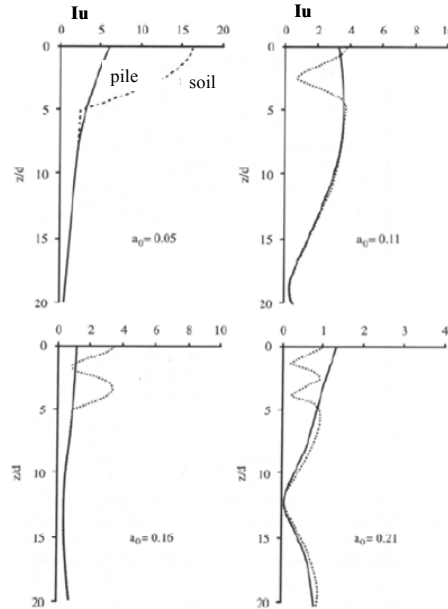


Figure 2.4: Rates of soil displacement and pile displacement with depth (Gazetas et al, 1992)

These Authors apply the Winkler method to carry out a parametric study on kinematic bending moment, for different shear wave and L/d ratios. In this study, the importance of kinematic effects is underlined. Figure 2.5 shows the kinematic bending moment along the pile length for two different subsoil conditions: subsoil A and subsoil D. The input motion is an harmonic motion characterized by fundamental resonant frequency ω_1 . The continuum line; represents the amplitude of normalized bending moment for subsoil A and subsoil B, and the dash line is the amplitude of normalized bending moment produced by the coincident of pile head displacement with free-field displacement. As shown in figure 2.5 pile behaviour is influenced by kinematic effects.

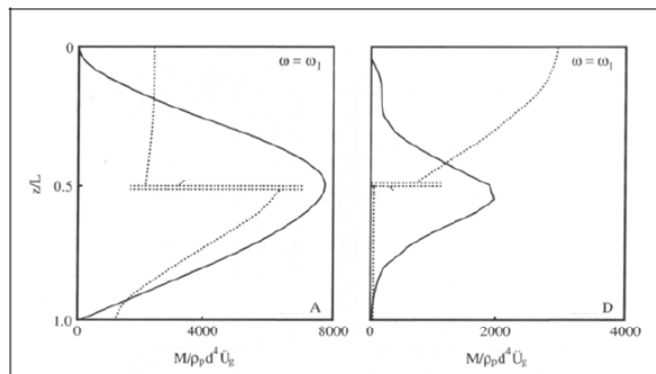


Figure 2.5: Bending moment trend (after Kavvadas and Gazetas, 1992)

For homogeneous soil, the maximum kinematic bending moment (free head pile) is around at $L/2$ depth, while in the case of fixed head piles, it is located-at the pile head.

For layered subsoil the bending moment tendency is different. At the interface, the stiffness contrast causes large deflections, which correspond to a maximum bending moment for free head piles and a big moment for fixed pile heads. If the stiffness contrast is very high, the value of the kinematic bending moment at the interface may be higher than the bending moment at pile head. The amplitude of normalized bending moment for frequencies applied, corresponding to the fundamental frequency of subsoil, gives the biggest kinematic bending moment at the interface (or very close to it). Increasing the value of frequency, the location of maximum bending moment changes. Kavaddas et Gazetas (1993) find that, in a real earthquake, where different frequencies are present, the maximum bending moment is near interface, close to $2d$. Nikolaou et Gazetas (1996) compare the kinematic bending moment obtained from different levels of input motion (real and artificial) which is smaller than the kinematic bending moment obtained in stationary conditions with frequencies corresponding to fundamental subsoil frequency -

In the following paragraphs, the results of the main study on kinematic effects are reported to valuate the kinematic bending moment.

2.3.1 Winkler foundation approach (BWF)

By accepting Winkler's foundation assumption (1876) that each layer of soil responds independently to adjacent layers, a beam and discrete spring system may be adopted to model pile lateral loading. However, this assumption ignores the shear transfer between layers of soil. These soil-pile springs may be linear elastic or nonlinear; p - y curves typically used to model nonlinear soil-pile stiffness have been empirically derived from field tests.

2.3.1.1 P - y curves

The simplified numerical approach is based on the idea of coupling and evaluating the effects due to the applied load at the pile head and lateral movements along the pile length by a series of independent " p - y curves", relating soil reaction and soil - pile movements.

Since these relations are nonlinear, the equivalent linear procedure using secant modulus is normally used to establish a law relating a set of discrete interaction forces at the soil/pile interfaces to a corresponding set of discrete relative motions between piles and *free-field* soil. The implementation of the method involves imposing a known *free-field* soil movement profile. When the expected *free-field* movement is large enough to cause the ultimate pressure of laterally spreading soils to be fully mobilized, the ultimate pressure, instead of *free-field* soil movement, may be used.

Piles surrounded by moving soil are relevant for many engineering applications. This soil movement will in turn displace the pile by a certain amount depending on the relative stiffness between the pile and the soil. The soil loading must be considered by taking into account the

relative movement between the soil and the pile. If the soil mass moves and the pile movement y_p is less than the soil movement y_s , the soil exerts a driving force on the pile. However, if the pile movement y_p is greater than the soil movement y_s , the soil provides the resistance force p_{lim} to the pile. The response of the pile can then be obtained by solving the following governing differential equation:

$$EI \frac{d^4 y}{dz^4} - p(y_p - y_s) = 0 \quad [2.3]$$

where EI = pile stiffness, p = soil reaction per unit pile length and z = depth. This equation can be solved by a numerical procedure based on a pile finite-element discretization, in which the pile load (force per unit area [FL^{-2}]) due to relative pile-soil movement ($y_p - y_s$), can be represented by a series of p - y curves on both sides of the pile shaft along its length. Taking into account that the lateral pile response to static or dynamic loading is non linear, the following p - y relationship can be written:

$$p(z) = \frac{[y_p(z) - y_s(z)]}{\frac{I}{E_{si}(z)} + \frac{|y_p(z) - y_s(z)|}{p_{lim}(z)}} \quad [2.4]$$

According to the proposed approach, when an individual pile of a group is taken into consideration, in equation (2.4) the empirical reduction factors f_m and ζ_m may be adopted.

It must be borne in mind that the p -multipliers reported in the literature were developed from the analysis of static or cyclic load tests on single piles and pile groups. These tests, however, do not represent the dynamic loading conditions during an earthquake event; therefore, it is necessary to check the validity of the p -multiplier concept under dynamic loading conditions and develop, if possible, p -multipliers from dynamic loading events.

Nevertheless, it can be noted (NCHRP, 2001) that the main factors that affect the dynamic p -multipliers are the spacing ratio, s/D , and the pile-head displacement ratio, y/D . The p -multipliers increase as s/D increases, meaning that the group effect decreases. The p -multipliers also increase as the y/D increases. This means that during a dynamic loading event, which is characterized by large pile head displacement, the pile-soil-pile interaction decreases, and the piles tend to behave as individual piles.

It can be seen that the p -multipliers are less dependent on frequency than on pile deformation (NCHRP, 2001). Thus, the same p -multipliers could be adopted for the pseudo-static loading at the pile head (inertial effect) and for the kinematic loading induced by the ground movements that occur during an earthquake. It must be emphasized, however, that these considerations are based on limited results and further investigations should be carried out before these observations can be asserted.

2.3.1.2 Dynamic Beam on Winkler Foundation (BDWF)

Various approaches have been developed for the dynamic response analysis of single piles. One such method is the Dynamic Beam on Winkler Foundation (BDWF) model, which is a decouple method to evaluate the effects of kinematic interaction on piles.

The Winkler-model assumes (Dobry et al., 1982; Gazetas & Dobry, 1984; Dobry & Gazetas, 1988; Makris & Gazetas, 1992; Gazetas et al., 1992; Kavvadas & Gazetas, 1993) that the soil-pile contact is discretized to a number of points where combinations of springs (linear or non linear) and dashpots represent the soil-pile stiffness and damping at each particular layer (Figure 2.6).

The mechanical parameters are the stiffness and the damping of soil (elastic constant of spring and damping of dashpot). They are a function of frequency ω . They are calculated by rigorous analytical solutions. After the evaluation of free field motion u_{ff} , the seismic response of pile $u(z)$, at interface, is obtained solving the following dynamic equilibrium equation:

$$\frac{d^4 u(z)}{dz^4} + \lambda^4 u(z) = \varsigma u_{ff}(z) \quad [2.5]$$

where

$$\lambda = \sqrt[4]{\frac{k_x + i\omega c_x - m_p \omega^2}{E_p I_p}} \quad [2.6] \text{ and } [2.7]$$

$$\varsigma = \frac{k_x + i\omega c_x}{E_p I_p}$$

where m_p is the mass for unit length of pile. The dynamic equation is solved numerically for layered soil; the pile is discretized by finite elements. The bending moment is obtained from the equation 2.8.

$$M(z) = E_p I_p \frac{d^2 u(z)}{dz^2} \quad [2.8]$$

The seismic motion for inertial analysis is obtained from two times the $u(z)$ value.

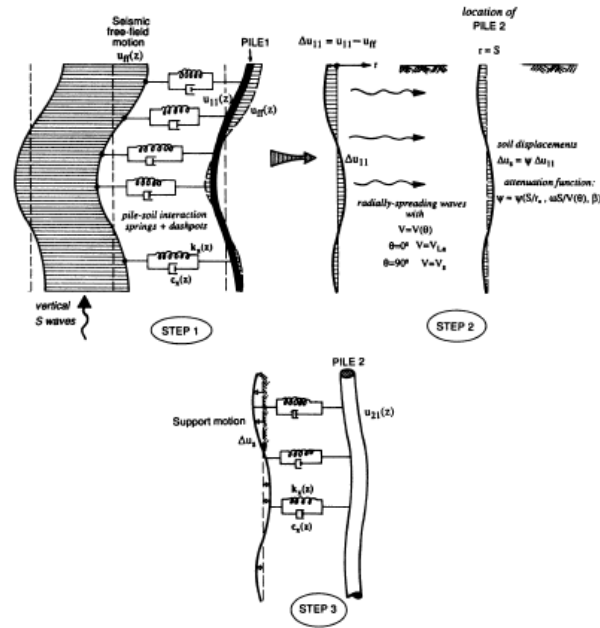


Figure 2.6: Illustration of three-step procedure for computing pile-soil-pile interaction (after Makris and Gazetas. 1992)

Simplified approaches

Analyses based on simplified approaches have been mainly performed to define approximate analytical solutions capable to reproduce kinematic bending moments at the interface between two layers characterized by different shear modulus. The simplest method of analysis for kinematic interaction is to assume that the pile follows the free-field soil motion, thus ignoring the interaction between pile and soil. Pile bending moments are then computed from the curvature of the horizontal displacements of the soil along a vertical line. This approach has been suggested by Margason and Holloway (1977) and is also recommended in some code provisions (NEHRP-2003). The bending moment at any depth z and time t , can be computed as:

$$M(z, t) = E_p I_p \frac{1}{R(z, t)} \quad [2.9]$$

where $E_p I_p$ is the pile flexural rigidity, and $1/R$ is the curvature of the vertical line. In the particular case of a homogeneous visco-elastic layer subjected to the passage of SH-propagating waves the maximum curvature, according to Margason and Holloway (1977), is a function of the free-field soil acceleration, $a_{ff} = a_{ff}(z, t)$, and of the shear wave velocity V_s :

$$\frac{1}{R(z,t)} = \frac{a_{ff}}{V_s^2} \quad [2.10]$$

In the case of layered soil, eq. [2.10] is inapplicable at interfaces between layers of different stiffness as the soil shear strain at these depths is discontinuous and, consequently, the soil curvature is infinity. Soils are rarely homogeneous, thus the *free-field method* is not suitable in the majority of engineering problems. A number of closed form expressions for a preliminary assessment of kinematic pile bending at the interface between two layers is available (Dobry and O'Rourke 1983; Nikolaou and Gazetas 1997; Nikolaou et al. 2001; Mylonakis 2001). The accuracy of these simplified criteria has been checked against some experimental evidence (Nikolaou et al. 2001) and benchmark solutions (Kanyia 1997; Mylonakis 2001) and, at the present time, such methods are commonly thought of as the most suitable for engineering purposes. However, there are still significant limitations about their applicability and particularly under circumstances where the subsoil conditions do not meet the hypotheses on which the methods are based.

Dobry and O'Rourke (1983) developed a simple method for determining kinematic pile bending moments at the interface of two layers, modelling the pile as a beam on a Winkler foundation (BWF) and assuming that:

- (i) the soil in each layer is homogeneous, isotropic, and linearly elastic characterized by their shear modulus G_1 and G_2 ;
- (ii) both layers are thick enough so boundary effects outside the layers do not influence the response at the interface;
- (iii) the pile is long, vertical, and linearly elastic;
- (iv) perfect contact exists between pile and soil;
- (v) each layer is subjected to uniform static stress field, τ , which generates constant shear strains ($\gamma_1 = \tau/G_1$, $\gamma_2 = \tau/G_2$);
- (vi) displacements are small.

The explicit expression for the pile bending moment at the interface is:

$$M = 1.86 (E_p I_p)^{3/4} \cdot (G_1)^{1/4} \cdot \gamma_1 \cdot F \quad [2.11]$$

where

$$F = \frac{(1 - c^{-4})(1 + c^3)}{(1 + c)(c^{-1} + 1 + c + c^2)} \quad [2.12]$$

c is a dimensionless function of the ratio of the shear moduli of the two layers and:

$$c = \left(\frac{G_2}{G_1} \right)^{1/4} \quad [2.13]$$

The Authors suggested computing the peak shear strain γ_1 in the first layer from a free-field response analysis. Alternatively, if the maximum acceleration $a_{\max,s}$ is specified at the soil surface, as is usual the case when a seismic area is already available, the maximum shear strain may be evaluated by the approximate expression suggested by Seed and Idriss (1982):

$$\gamma_1 = \frac{r_d \rho_1 H_1 a_{\max,s}}{G_1} \quad [2.14]$$

where ρ_1 and H_1 are the density and the thickness of the upper layer respectively, and $r_d = r_d(z)$ is the well-known depth factor (Seed and Idriss, 1982), which for preliminary design purposes can be assumed as:

$$r_d = 1 - 0.015 \cdot z \quad [2.15]$$

in which z is the depth in meters from the ground surface. It should be pointed out that eq. [2.15] is not reliable for depth in excess of approximately 15 m.

The method can predict the kinematic effects at any interface of a multi-layered soil profile, provided that the confining layers are thick enough.

Nikolaou et al. (2001) derived a simplified expression for kinematic pile bending moments at the interface of two soil layers underlain by a rigid base. The pile is modelled as a beam on a dynamic Winkler foundation (BDWF) and the soil in each layer is assumed to be homogeneous, isotropic and linearly elastic, with a constant soil damping ratio. The expression for the interface bending moment has been derived by means of the non-linear regression of numerical data computed from a comprehensive parametric study carried out for a two layer soil profile subjected to harmonic steady-state excitation.

This can be briefly set out as:

$$M = 0.042 \cdot \tau_c d^3 \left(\frac{L}{d} \right)^{0.30} \left(\frac{E_p}{E_1} \right)^{0.65} \left(\frac{V_{s2}}{V_{s1}} \right)^{0.50} \quad [2.16]$$

where τ_c is a characteristic shear stress which is proportional to the actual shear stress that is likely to develop at the interface, L/d the pile slenderness, E_p/E_1 the relative pile-soil stiffness and V_{s2}/V_{s1} the ratio of the shear wave velocities of the two layers. Nikolaou et al. (2001) suggest expressing τ_c as a function of the maximum free-field acceleration at the soil surface:

$$\tau_c = a_{\max,s} \rho_1 H_1 \quad [2.17]$$

Even though the method has been developed for harmonic excitations, it can be directly used in the time domain with the maximum acceleration $a_{\max,s}$ of the soil surface obtained from a free-field response analysis.

The method does not consider any particular condition about the thickness of the two layers and is therefore applicable for any depth of the interface. Even though the Authors recognize the importance of soil damping, all the analyses were performed using a prefixed value of $D=10\%$ and no sensitivity study was performed.

Another simplified method for predicting the kinematic bending moment at the interface between two layers was developed by Mylonakis (2001). The method is fundamentally different from the one used by Nikolaou et al. (2001) as it is not based on a curve fitting of numerical data but on the response analysis of a mechanistic model. The basic assumptions are the same as those of the Dobry and O'Rourke method. The improvements with reference to the Dobry and O'Rourke method are: (i) the seismic excitation is a harmonic horizontal displacement imposed at the bedrock; (ii) both radiation and material damping are accounted for; (iii) soil layers are thick but not unbounded. The maximum bending moment can be compactly expressed as:

$$M = \frac{(E_p I_p) \cdot (\varepsilon_p / \gamma_1) \phi}{r} \gamma_1 \quad [2.18]$$

where γ_1 is the peak shear strain in the upper layer at the interface depth, r is the pile radius and ε_p / γ_1 is the static strain transfer function that can be expressed according to the theoretical solution:

$$\frac{\varepsilon_p}{\gamma_1} = \frac{1}{2c^4} (c^2 - c + 1) \left(\frac{H_1}{d} \right)^{-1} \left\{ \left[3 \left(\frac{k_1}{E_p} \right)^{1/4} \left(\frac{H_1}{d} \right) - 1 \right] c(c-1) - 1 \right\} \quad [2.19]$$

with k_1 being the soil-spring stiffness according to Kavvadas and Gazetas (1993):

$$k_1 = \delta E_1 \quad [2.20]$$

where:

$$\delta = \frac{3}{1-\nu^2} \left(\frac{E_p}{E_1} \right)^{-1/8} \left(\frac{L}{d} \right)^{1/8} \left(\frac{H_1}{H_2} \right)^{1/12} \left(\frac{G_1}{G_2} \right)^{-1/30} \quad [2.21]$$

where H_2 is the thickness of lower layer, while the other symbols have already been defined. The coefficient ϕ in equation [2.18] is an amplification factor accounting for the effect of the

dynamic nature of the excitation on the strain transfer function. As highlighted by Mylonakis this coefficient is usually less than 1.25. At a preliminary stage of the study on the kinematic response of a piled foundation it can be therefore ignored ($\phi = 1$) without any particular implication.

If the seismic excitation is specified at an elevation below the interface, Mylonakis suggests performing a free-field analysis to estimate the peak shear strain γ_1 . Alternatively, it is suggested to use the expression [2.8] by Seed and Idriss (1982), which, however, is valid for relatively shallow depths, as it focuses on liquefaction phenomena more than soil foundation interaction.

The ratio, ϵ_p/γ_1 , is regarded by Mylonakis (2001) as a “strain transmissibility” function depending on the layer stiffness contrast G_2/G_1 , pile-soil relative stiffness E_p/E_1 , and embedment ratio h_1/d (Figure 2.6). The effect of frequency on strain transmissibility can be incorporated through an amplification factor ϕ that multiplies the strain transmissibility ϵ_p/γ_1 . Parameter analyses showed that ϕ tends to increase with frequency and may exceed the value of 2, especially for stiff piles and deep interfaces.

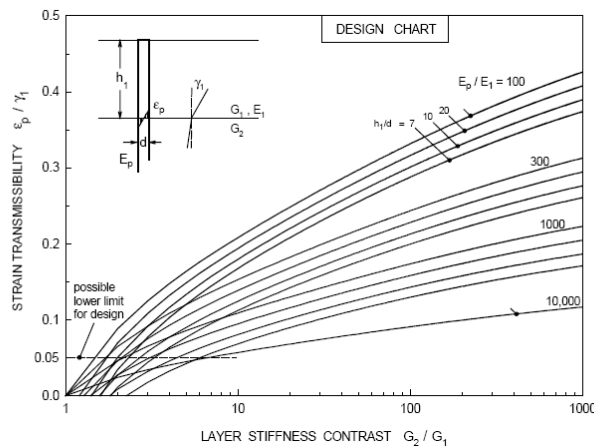


Figure 2.7: Strain transmissibility E_p/E_1 at a soil layer interface as function of layer stiffness contrast G_2/G_1 , pile-soil relative stiffness E_p/E_1 , and embedment ratio h_1/d (after Mylonakis, 2001).

2.3.2 Continuum approach (BEM and FEM)

The continuum approach model considers the soil, pile and superstructure as a whole. The soil-pile geometry typically is modelled in 3-D and discretized by F.E.M. or B.E.M. techniques (Kaynia 1996, Kimura e Zhang, 2000; Zhang et al. 2000; Zhang e Kimura 2002; Wu e Finn, 1997; Bentley & El Naggar, 2000; Finn e Fujita, 2002;(Cairo et al., 2005) (Cairo & Dente, 2007a, 2007b). Soil is usually modelled by elasto-plastic models. In the following paragraph some aspects of the recent research on this topic are explained in detail.

Worth mentioning is the simplified continuum approach developed by Wu & Finn (1997) in which vertically propagating shear waves are modelled disregarding seismic induced deformations in the vertical direction and normal in relation to the direction of shaking (quasi 3-D approach). In this way, bending of the pile occurs only in the direction of shaking. Soil non linearity is modelled by an equivalent linear approach.

However, fairly simple rheological models can be used to properly account for the frequency dependence of the impedance functions. These models can be developed using curve fitting techniques, or with physical insight, such as the series of cone models developed by Wolf (1994). With such models, which are most conveniently used in time history analyses, the actual dynamic action of the soil can be properly accounted for; even "negative stiffness", which are frequently encountered in layered soil profiles, can be apprehended with those models. An illustrative example presents the application of model to an actual bridge pier foundation, which is a large circular caisson, 90 m in diameter, resting on a highly heterogeneous soft soil profile. The "exact" impedances were computed using a frequency domain finite element analysis. Note the very good fit achieved by the model (square symbols) even for the negative stiffness of the rocking component. Clearly, implementation of such simple rheological models does not impose a heavy burden on the analyst and is a significant improvement upon the lengthy and tedious iteration process in which springs and dashpots are updated to become compatible with the SSI frequencies.

All these models consider a pile modelled using the ordinary Eulerian beam theory. Bending of the piles occurs only in the direction of shaking. Dynamic soil-pile interaction is maintained by enforcing displacement compatibility between the pile and soils. The theory focuses on the solution of the dynamic equilibrium equation which is set out as follows.

The global dynamic equilibrium equations is written as:

$$[M]\{\ddot{v}\} + [C]\{\dot{v}\} + [K]\{v\} = -[M]\{I\}\ddot{v}_o(t) \quad [2.22]$$

in which $\{\ddot{v}_o\}$ is the base acceleration, $\{I\}$ is a unit column vector; $\{\ddot{v}\}$, $\{\dot{v}\}$ and $\{v\}$ are the related nodal acceleration, velocity and displacement respectively. $[M]$, $[C]$, and $[K]$ are the mass, damping and stiffness matrices respectively. Direct step-by-step integration is employed to solve the equations of motion in eq. [2.22].

2.4 Inertial interaction

The main phenomena that characterized the inertial interaction may be summarized in two different steps:

1. definition of all stresses on the superstructure generated by the seismic wave propagation at foundation level;
2. determination of the inertial forces on the foundation and caused by the weight of superstructure.

The transmission stress mechanism is strongly influenced by soil-foundation related stiffness. This stiffness has to be calculated for each freedom degree of the foundation. The evaluation of the dynamic impedance is one of the main problems in solving the inertial interaction problem. The dynamic impedance is a function of the system frequency and it is obtained from the sum of a real and an imaginary part, as shown in equation 2.20, which is set out as follows:

$$K = k + i\omega c \quad [2.23]$$

where the real part k is the dynamic stiffness of soil-structure and this term takes into account the inertia of the soil. The imaginary term, $c\omega$ is the damping factor and it takes into account the *geometric damping*, damping at soil-pile interface, and the *material damping*, hysteretic soil damping. It is a function of the frequency of the system.

All analytical solutions used to calculate the impedance function are founded on the evaluation of displacement and stress at a particular point soil, due to a unitary force applied to another point of the soil (Green function). The same procedure is the equation of Mindlin (1936) in static domains. In dynamic domains numerical solutions for semispace and for layered semispace are used to obtain the dynamic impedance formula. Pile behaviour is studied considering horizontal forces on the pile head. Generally, the soil is modelled as a continuous material or a Winkler soil (Gazetas and Dobry, 1984; Dobry and Gazetas, 1988; Gazetas et al. 1992). Novak, 1987, has also done some field and laboratory tests to study the problem of impedance. There are many formulations to obtain the dynamic stiffness of piles when the length of pile, L , is bigger than active length L_a (Gazetas, 1991).

In the presence of heterogeneous soil, the main problem lies in defining different values of soil stiffness with depth ($G(z)$). *Gapping* (separation between soil and pile near a very soft soil surface) between the soil and pile head also has been taken into account. Gazetas (1991)

obtained some algebraic formulations of impedance function. Figure 2.8 shows the typical impedance functions. The value of all the three different dynamic impedances are:

- K_{hh} : dynamic impedance in horizontal direction;
- K_{mm} : dynamic impedance for rotation (bending);
- $K_{hm}=K_{mh}$: coupled rotation and translational impedance.

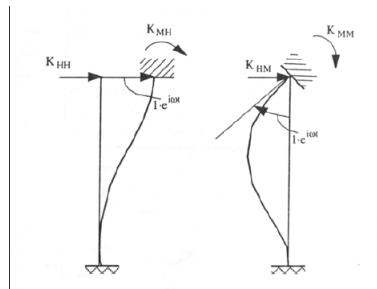


Figure 2.8: Definition of impedance function (after Mylonakis, 1997)

Impedance functions are defined as the amplitude of a harmonic input motion applied on pile head to obtain a unitary displacement in a particular direction.

Many authors have proposed solutions to obtain stiffness formulations. Cairo et al, 1999 extends Wolf et al. 1992 and Wolf and Meek 1994, applied the cone model. This method compared with the numerical method seems quite good—and it is very simple to use. From these studies the following observations have been pointed out:

- the dynamic stiffness of pile is quite close to the static one, for low frequencies;
- a reduction of stiffness and damping values is obtained, taken into account the variation of stiffness with depth;
- for frequencies lower than natural layer frequency pile damping is very limited because the geometric damping is around zero for these frequency values;
- the boundary effects on pile head influences the values of the dynamic function. In particular, free head piles compared with fixed head piles have—lower stiffness and damping values;
- floating piles on the vertical load have a significant damping value, but their stiffness is less than the bearing pile capacity.

All these considerations regard a single pile.

Maravas et al, 2007, present novel analytical solutions for single degree-of-freedom (SDOF) oscillators founded on footings and piles on compliant soil. They investigate a solution for determining the fundamental natural period and effective damping of a simple oscillator supported on a surface foundation.

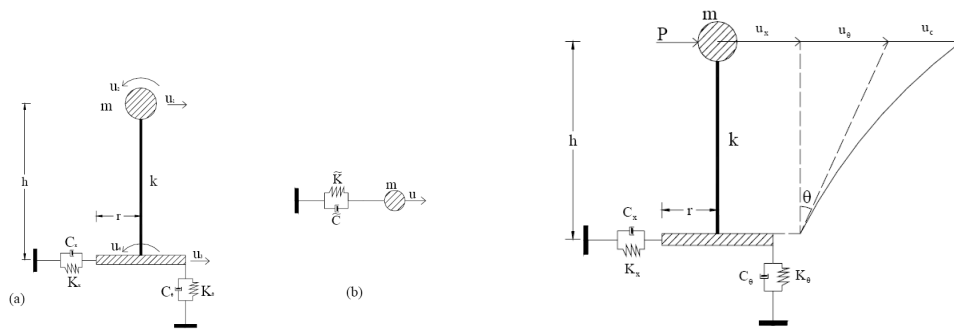


Figure 2.9: (a) Structure idealized by a stick model, (b) Reduced single degree-of-freedom model (c) Deflection diagram for soil-structure system

The response of the soil-pile-structure system depends on the properties of the pile, the supporting soil, the superstructure and the excitation. These properties are included in dimensionless parameters, as in the case of the structure supported on surface footing. In Figure 2.10, results obtained with the use of the proposed procedure are presented. Specifically, Figure 2.10(a) presents the influence of the slenderness ratio (h/d) on the natural period of the interacting system. Evidently, the behaviour is similar to the behaviour of the soil-footing-structure system presented earlier. The same observation holds for the effective damping, as shown in Figure 2.10 (b). The influence of pile-soil stiffness ratio E_p/E_s , on the properties of the system is significant, as shown in Figures 2.10 (c,d). For relatively flexible piles (low values of E_p/E_s), the soil-pile-structure system is more flexible and dissipates larger amounts of energy.

The concept of statically and geometrically equivalent interacting systems is also introduced, in an effort to compare the damping of systems in pile or surface footing foundations. To achieve this, the lateral stiffness of the two SSI systems should be comparable at the elevation of mass m . Accordingly, the two systems are geometrically equivalent, i.e., $h/d=h/2r$, the ratio of Young's modulus for the soil (Maravas,2006).

Using the proposed methodology, the influence of common assumptions on the computation of the mechanical properties of such systems was elucidated. Results are provided in ready-to-use graphs and charts that elucidate the salient features of the problem and can be directly implemented in design. By introducing the concept of statically and geometrically equivalent SSI systems, the amounts of radiation damping generated from a single pile and a footing have been compared. The main conclusions of the study are:

- (1) the proposed solution is simpler, more accurate, and more general than the classical methods by Parmelee, Veletsos, Bielak, Wolf and co-workers.
- (2) the common approximation of neglecting higher-order terms involving products of damping coefficients may be inaccurate for highly-damped SSI systems.
- (3) the proposed analysis can easily incorporate embedded foundations, by translating the reference system to the depth below the surface where the resultant soil reaction is applied. This ensures a diagonal foundation impedance matrix and greatly simplifies calculations.

(4) a structure founded on a pile may generate 100% more radiation damping than a similar structure on a spread footing. The difference becomes more pronounced with high-frequency, squatty structures on stiff soil.

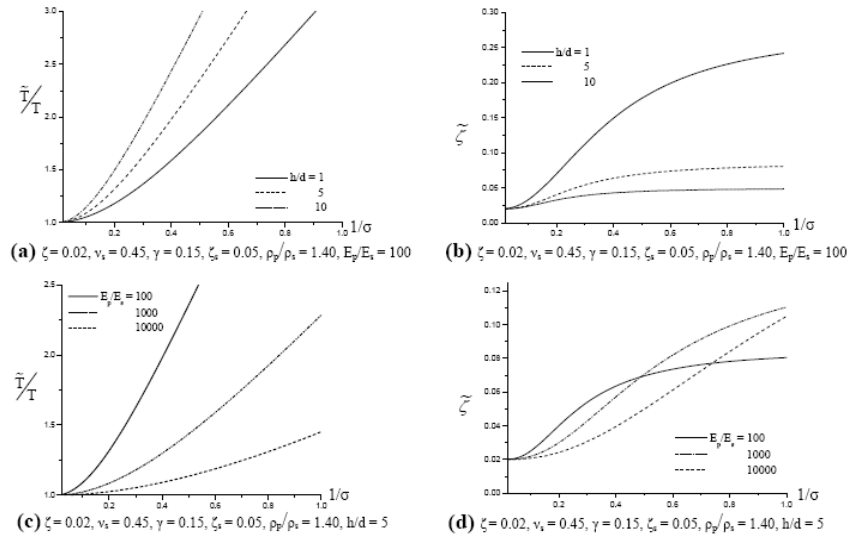


Figure 2.10: (a) System period as function of h/d , (b) System damping as function of h/d . (c) System period as function of E_p/E_s , (d) System damping as function of E_p/E_s

The p - y curve approach (load transfer method) is a widely accepted method for predicting pile response under static loads because of its simplicity and practical accuracy. To predict the response of pile-supported structures, the p - y method has been extensively used and several p - y curves for different soil-pile systems have been proposed. The p - y method can be extended to earthquake loading conditions if dynamic p - y curves are adopted (Kagawa & Kraft, 1980). The dynamic p - y curves, in fact, allow for the generation of different p - y relationships based on the frequency of loading and soil profile. Substituting dynamic p - y curves in place of traditional static p - y relationships for analysis should result in better estimates of the response of structures also to dynamic loading (Hajjalilue-Bonab *et al.*, 2007; Rovithis *et al.*, 2007a; 2007b).

The p - y approach for analyzing the response of laterally loaded piles is essentially a modification of the basic Winkler model, where p is the soil pressure per unit length of pile and y is the pile deflection. The soil is represented by a series of non linear p - y curves that vary with depth and soil type.

Researches based on results of field tests on full scale piles suggests employing a non linear p - y relationship (Reese *et al.*, 1974; Reese & Welch, 1975; Reese & Van Impe, 2001; Juirnarongrit & Ashford, 2006), thus a hyperbolic p - y relationship can be adopted:

$$p(z) = \frac{y_p(z)}{\frac{I}{E_{si}(z)} + \frac{y_p(z)}{p_{lim}(z)}} \quad [2.25]$$

where E_{si} [FL⁻²] is the initial modulus of horizontal sub-grade reaction, y_p [L] is the pile lateral deflection, p and p_{lim} [FL⁻²] are the mobilized and the ultimate horizontal soil resistance respectively.

To incorporate the dynamic effects in the framework of Winkler's approximation, a conventional and widely accepted method is to add a dashpot in parallel to the non linear spring governed by p - y curve, in order to account for the radiation damping effect. Thus the soil-pile contact is discretized at a number of points where combinations of springs and dashpots represent soil-pile stiffness and damping at each particular layer, through the development of a complex stiffness as a function of the frequency content. The complex stiffness has a real part k_1 and an imaginary part k_2 :

$$p_d = ky = (k_1 + ik_2)y \quad [2.26]$$

$p_d \leq p_{lim}$ at depth of p - y curve

where p_d is the dynamic value of the reaction p on the p - y curve at depth z [e.g., in N/m] and k the secant modulus to the static p - y curve at pile deflection y .

The real part k_1 represents the true stiffness k , the imaginary part of the complex stiffness k_2 , describes the out of phase component and represents the damping caused by the energy dissipation in the soil element. Because this damping component generally grows with frequency, it can also be defined in terms of the constant of equivalent viscous damping (the dashpot constant) given by $c = k_2/\omega$, where ω is the circular frequency of loading equal to $2\pi f$ and f the actual frequency of loading [rad/s].

The overall relationship between the dynamic soil resistance and loading frequency for each test can be established in the form of the generic equation:

$$p_d(z) = p_s(z) \left[\alpha + \beta a_o^2 + \kappa a_o \left(\frac{\omega y(z)}{D} \right)^n \right] \quad [2.27]$$

where p_d is the dynamic value of the reaction p on the p - y curve at depth z ; p_s is the corresponding reaction on the static p - y curve at depth z [N/m]; a_o is the frequency of loading, expressed in dimensionless terms $\omega r_o/v_s$; v_s is the propagation velocity of seismic shear waves; r_o is the pile radius equals; D is the pile diameter [m]; α , β , κ and n are dimensionless constants defining the dynamic p - y curves.

Values are given for various soil types (NCHRP, 2001). To generate dynamic p - y curves according to equation (2.26), the corresponding static reaction p_s given by equation (2.27) can be used. The constant α is taken to be equal to unity to ensure that $p_d = p_s$ for $\omega=0$. For large frequencies or displacements, the maximum soil resistance in dynamic conditions is limited to the ultimate static lateral resistance p_{lim} of the soil. The dynamic p - y curves are most accurate when $a_o > 0.02$.

Equation (2.27) can be used directly to represent the dynamic relationship between a soil reaction and a corresponding lateral pile deflection. Thus the total dynamic soil reaction at any depth is represented by a nonlinear spring whose stiffness is frequency dependent.

The approach proposed was employed and implemented in an original computer code. Such a code allows us to assess the lateral response of a single pile (lateral deflection, bending moment and shear force distribution). Using the p - y method the lateral secant stiffness of piles can be developed as functions of lateral deformations through the considered non linear p - y analysis.

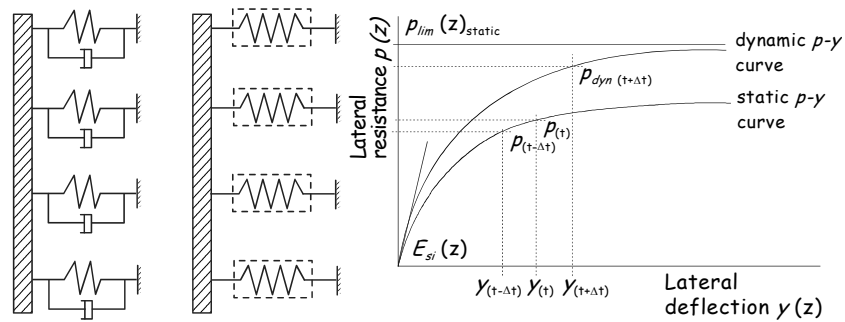


Figure 2.11a) and 2.11 b): Equivalent stiffness including damping and dynamic p - y curves

Generally speaking the available analytical approaches for the study of SSPIS the dynamic interaction can be roughly classified as the Winkler method and continuum approach, as explained before.

Koo et al, 2003 present a continuum model for the interaction analysis of a fully coupled soil–pile–structure system under seismic excitation which is presented in this paper. Only horizontal shaking induced by harmonic SH waves is considered so that the soil–pile–structure system is under anti-plane deformation. The soil mass, pile and superstructure were all considered as elastic with hysteretic damping, while geometrically both pile and structures were simplified as a beam model. Buildings of various heights in Hong Kong designed to resist wind load were analysed using the present model. It was discovered that the acceleration of the piled-structures at ground level can, in general, be larger than that of a free-field shaking of the soil site, depending on the excitation frequency. For typical piled-structures in Hong Kong, the amplification factor of shaking at the ground level does not show simple trends with the number of storeys of the superstructure, the thickness and the

stiffness of soil, and the stiffness of the superstructure if the number of storeys is fixed. The effect of pile stiffness on the amplification factor of shaking is, however, insignificant. Thus, simply increasing the pile size or the superstructure stiffness does not necessarily improve the seismic resistance of the soil–pile–structure system; on the contrary, it may lead to excessive amplification of shaking for the whole system. The soil is modelled as a linear visco-elastic layer containing a pile that is modelled as a beam and connecting to a superstructure through a rigid pile cap. Earthquake shaking is modelled as a harmonic SH wave propagating from the rock stratum to the ground surface. The main new feature of the present analysis is that the soil response, the pile response as well as the structural response were coupled and were solved simultaneously. Numerical results show that the ground level response (indicated by an amplification factor K_0) of a coupled soil–pile–structure system is usually larger than that of free field shaking. The values of K_0 do not show simple trends with changes in the height of the wind-resistant designed buildings, and the thickness and stiffness of the soil. The effect of the increase in the bending stiffness of the pile system is found to be insignificant. The main conclusion is that the soil–pile–structure interaction is highly non-linear and is not to be ignored. The increase in superstructure or pile stiffness does not necessarily reduce the seismic response of the soil–pile–structure system, but quite on the contrary may lead to larger seismic ground shaking. And the present approach should provide a simple analytical tool to carry out a preliminary assessment of seismic performance of a soil–pile–structure system before a time consuming finite element analysis is carried out.

A few works in the literature adopt models of the so-called Advanced Plasticity to properly reproduce soil response under cyclic loading conditions, and some works describe the possibility to simulate gaps at the pile-soil interface under strong motion events (Maheshwari et al., 2004).

B.K. Maheshwari et al, 2004 present the seismic response of structures constructed on pile foundations. The analysis is formulated in the time domain and the effects of the material nonlinearity of soil on the seismic response are investigated. A subsystem model consisting of a structure subsystem and a pile-foundation subsystem is used. Seismic response of the system is found using a successive coupling incremental solution scheme. Both subsystems are assumed to be coupled at each time step. Material nonlinearity is accounted for by incorporating an advanced plasticity-based soil model, HiSS, in the finite element formulation. Both single piles and pile groups are considered and the effects of kinematic and inertial interaction on seismic response are investigated while considering harmonic and transient excitations. It is seen that nonlinearity significantly affects seismic response of pile foundations as well as that of structures. Effects of nonlinearity on response are dependent on the frequency of excitation with nonlinearity causing an increase in response at low frequencies of excitation. The effects of soil plasticity on the seismic response of SPS systems are investigated using three-dimensional finite element analyses in the time domain. The analyses involve a subsystem model and a successive-coupling incremental scheme. The following conclusions can be drawn:

-
1. the effect of inertial interaction (for the range of foundations and structure parameters considered) is, generally speaking to increase the pile head response but to significantly decrease the response of the structure.
 2. for a harmonic excitation, soil nonlinearity increases pile head and structural responses at low frequencies. At high frequencies, both the pile head and the structural responses are slightly affected by soil nonlinearity.
 3. for transient excitation, soil nonlinearity increases both pile head and structural responses. Smoothed Fourier spectra show that generally nonlinearity increases the responses at low and moderate frequencies but its effect is negligible at high frequencies.
 4. the pile group effect decreases the peak values of the response for both harmonic and transient excitations (i.e. reduces the effect of soil nonlinearity).
- Based on the range of parameters considered in this study, soil nonlinearity increases the response at low frequencies which represent the range of interest for earthquake loading.

2.5 Piles Group

In the case of groups of piles the definition of dynamic impedance is very difficult. The impedance of pile groups is different from a simple sum of the dynamic impedance of each pile.

The results of single soil-pile interaction analyses must be extended to reflect the group configurations that piles are typically installed in for undertaking full SSPSI analyses. This is in contrast to substructuring or complete analysis methods which inherently consider the entire group response. If piles are arrayed in groups with large pile-to-pile spacing (greater than 6 - 8 pile diameters), pile group interaction effects are normally ignored for static loading (see Figure 2.12).

But this may be an inaccurate approach for dynamically loaded piles, as much of the pile group interaction effects arise from wave energy reflected between neighbouring piles, which does not attenuate as rapidly as static loading pile group interaction. Pile group dynamic response is also a function of load level; many of the group analysis methods that will be described address small strain elastic response, and few researchers have investigated nonlinear pile group interaction. There is evidence however to suggest that pile group effects lessen with increasing soil-pile nonlinearity, which inhibits wave energy transmission between piles. The behaviour of a pile group subjected to lateral loading and overturning moment is shown in Figure 2.12b, which illustrates the components of pile group response.

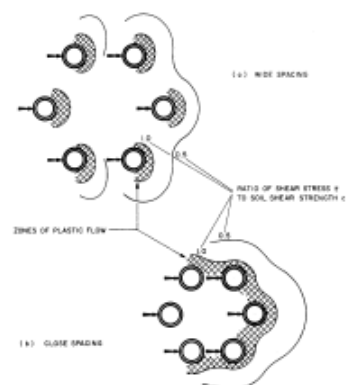


Figure 2.12 a): Pile group interaction as function of pile spacing (after Bogard and Matlock, 1983)

These components include: group rotation, inducing axial tensile/compressive forces, most severe at end piles; group translation and relative pile translations; individual pile head rotations at pile to cap connections, and individual pile deflections and consequent bending moments. The factors that influence the group response are:

- individual pile response: small strain elastic or nonlinear behaviour,
- loading: static, cyclic, or dynamic; transient or steady state,

- soil properties, particularly as modified by pile group installation,
- relative soil-pile stiffness; more flexible piles experiencing greater interaction,
- group geometry, including individual pile cross sections and group spacing,
- head fixity, idealized as a free head or fixed head, but actually lying between the two,
- tip condition, either floating or end-bearing,
- superstructure mass and flexibility, which impart inertial loads to the pile group,
- pile cap embedment depth, stiffness and damping characteristics.

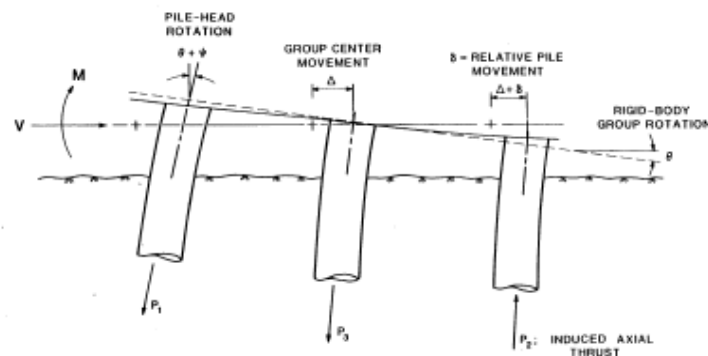


Figure 2.12b): Components of pile group response under lateral loading (after O'Neill and Dunnavant, 1985)

The objectives of conducting a pile group analysis are to determine the following: pile group and individual piles deflection; individual pile head shear forces and moment distributions and modifications to the input ground motion for superstructure analysis. The manner in which this is accomplished relates to the level of single pile analysis. Single pile kinematic response analyses can be modified to approximate group effects and superstructure influence. Single pile impedance functions can be assembled into group impedance functions with a group interaction theory. The group impedance function is then used in a global structural analysis, which produces forces and deflections acting on the pile group. These forces and deflections can then be distributed to the individual piles with group interaction theory, and individual pile head forces can be checked not to exceed the pile to cap connection capacity. Then the most critically loaded pile(s) in the group can be assessed in a single pile integrity analysis mode to determine whether pile moment distributions exceed capacity. To determine the effect of the pile group on modifying ground motion input to the superstructure, the analysis must be either conducted in a true substructuring fashion or alternatively, this effect can be captured in a complete SSPSI analysis.

In static analysis the presence of a pile group produces a reduction of stiffness compared to the single pile solution—an increase of in displacement and a not uniform distribution of pile load. Generally with regard to static problems an interaction static factor has been used. Poulos (1971) introduced the concept of pile group interaction factors. He used Mindlin's

elasticity equations to solve stresses and displacements between pairs of piles due to horizontal point loads applied in an elastic half space. Poulos described interaction factors as (eq. 2.28):

$$\alpha = \frac{\text{additional displacement (rotation) due to adjacent pile}}{\text{displacement (rotation) of pile due to its own loading}} \quad [2.28]$$

He presented charts of a factors for both fixed and free head piles subject to lateral and moment loadings as functions of pile flexibility K_r , pile spacing, pile diameter, pile length, and departure angle (angle between piles and direction of loading). The studies on the dynamic impedance of groups have shown that the dynamic characteristics of groups are very complex and they are strongly dependent on frequency, and different from the values obtained for single piles due to pile-soil-pile interaction.

For high and middle frequency values Novak (1991) and Gazetas et al (1993) suggest ignoring the interaction pile-soil-pile and to consider the static interaction factor.

Kaynia and Kausel (1982) derived dynamic interaction factors for floating pile group interaction analysis by combining a numerical integration for the evaluation of the influence coefficients with an analytical solution for the pile stiffness and flexibility matrices. This boundary element formulation computed Green's functions from imposed barrel and disk loads in a homogeneous soil medium, and used a consistent stiffness matrix to account for the far field. Their interaction factors were presented as complex-valued frequency dependent ratios of the dynamic displacement of pile i to the static displacement of pile j , due to a unit harmonic load on pile j . Vertical and horizontal interaction factors are shown in Figure 2.13, demonstrating positive and negative group efficiencies.

Dobry and Gazetas (1988) presented a simplified method for calculating dynamic pile interaction factors in homogeneous soil by assuming that cylindrical wave propagation governs vibration of source piles and displacement of neighbouring piles. Fan and Gazetas (1991) studied pile group kinematic interaction effects, and as shown in Figure 2.7, the generalized pile head to free-field transfer function illustrates the pile group effect in filtering out high frequency components of motion. They found that pile group configuration and spacing have little influence on kinematic response, as pile head fixity and relative soil-pile stiffness play a stronger role. Gazetas and Makris (1991) and Makris and Gazetas (1992) developed simplified methods of analysis for pile group axial and lateral dynamic response, respectively (see Figure 2.11). Using a dynamic Winkler model, they found pile group effects to be more pronounced for inertial than kinematic loading. The substructuring approach unifying the kinematic and inertial analyses is described in Gazetas et al. (1992), and is shown schematically in Figure 2.13. Mylonakis et al. (1997) applied this substructuring approach in an equivalent linear method to analyze pile supported bridge piers.

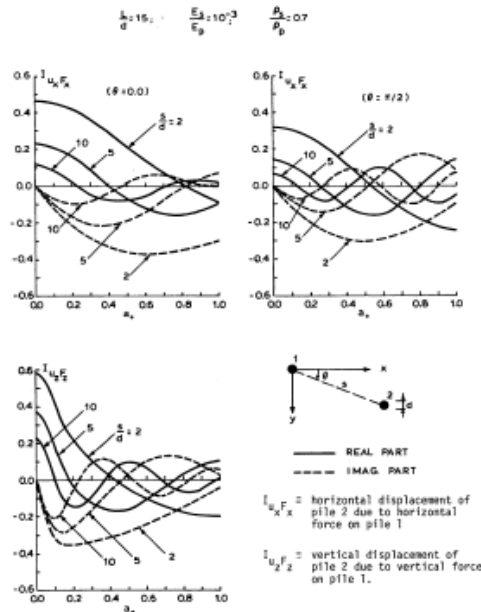


Figure 2.13: Vertical and horizontal dynamic pile interaction factor (after Kaynia and Kausel, 1982)

El-Marsafawi et al. (1992) derived pile group dynamic interaction factors from a boundary integral formulation for floating and end-bearing piles in homogeneous or non-homogeneous soil deposits. They also verified the applicability of the superposition approach for the conditions studied, with some limitations. A set of translation, rotation, translation rotation coupling, fixed head, and vertical interaction factors were described in terms of amplitude and phase angle, a more convenient form for interpolation than real and imaginary stiffness terms. The authors concluded that the superposition method worked well except for cases of vertical response of stiff end-bearing piles, and the high frequency range for heterogeneous soils.

Kaynia and Kausel (1991) consider a group of pile 3x3 with different values of interaxes (s) and Miura et al (1994) studied the influence of layered soil, for different pile groups 2x2 and 4x4, for three different $E(z)$ trends with depth. The conclusions of the studies are summarised in the following:

- the response of pile groups is more dependent on frequency compared with homogenous soil. The interaction effects are stronger in heterogeneous soil.
- the interaction effects are more important in soft soil than in stiff soil. Therefore the behaviour of pile groups under a horizontal load is governed by soil properties on the surface;
- in dynamic conditions not only boundary piles but also piles located in the central position are loaded from horizontal and vertical weights.

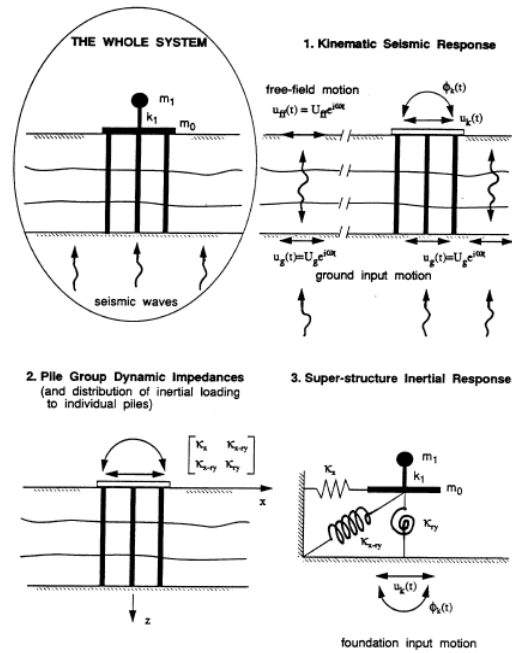


Figure 2.14: Substructuring method for seismic soil pile superstructure interaction analysis (after Gazetas et al., 1993)

Mitwally and Novak (1987) presented complex, frequency dependent interaction factors for dynamic pile group response of offshore structures, with the recommendation that the equivalent linear method be employed to simulate nonlinear soil-pile response. The authors evaluated the effects of including pile group interaction effects on the response of a pile-supported platform subjected to wave loading; the results shown in Figure 2.15 illustrate the frequency dependence of group interaction.

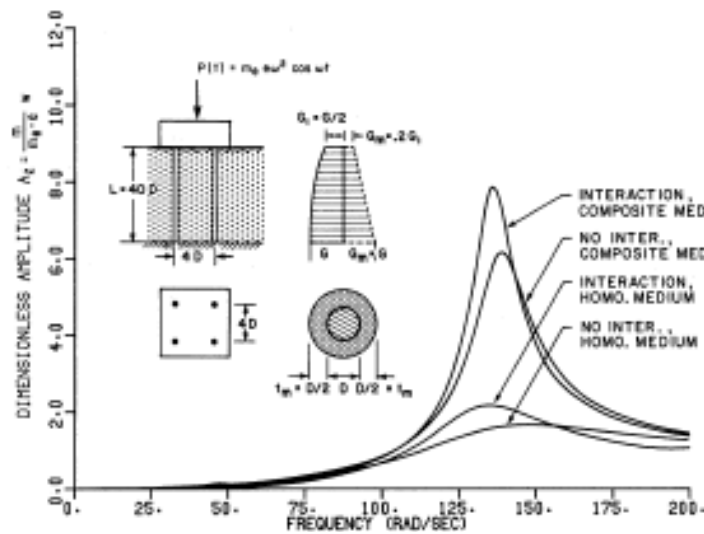


Figure 2.15: Vertical and horizontal dynamic pile interaction factor (after Kaynia and Kausel, 1982)

El Naggar and Novak (1994a) described a nonlinear model for dynamic axial pile response that consisted of a slip zone, inner field, and outer field that simulated a variety of field test results with great success. El Naggar and Novak (1994b) presented chart solutions for pile group interaction factors derived from this model. Most recently, El Naggar and Novak (1995) described a dynamic nonlinear time-domain Winkler soil-pile interaction model that allowed for both axial and lateral pile group response.

The axial model consisted of a linear outer region and a nonlinear inner field connected to the pile by a plastic slider allowing for soil-pile slip. The lateral response mode also consisted of inner and outer fields with formulations by Novak and Aboul-Ella (1978) and Novak and Sheta (1980) but with the addition of a directional gapping model. Interpile springs were used to model lateral and axial pile group effects. They found that nonlinear foundation response is more pronounced for non-homogeneous soil profiles than homogeneous ones, and that nonlinear foundation behaviour decreases the structural damping ratio, but this is more than offset by the increase in foundation damping. They also concluded that dynamic pile group effects increase foundation damping, significantly for linear conditions, but to a lesser extent for nonlinear conditions.

Nogami (1979) presented solutions for the dynamic axial response of pile groups in homogeneous soil profiles. Nogami and Konagi (1987) studied nonlinear pile group axial response by incorporating slips at the soil-pile interface in a dynamic Winkler model. They found this nonlinearity to reduce wave interference effects and suppress the frequency dependence of dynamic group response. Nogami et al. (1988) and Otani et al. (1991) extended the dynamic Winkler pile group model to lateral loading, and included slip, gapping and inelastic soil behaviour. Their nonlinear near field model was found to dull the peaks of computed pile head impedance functions. Unfortunately, Nogami has not presented his work in a form convenient for use by the profession, and it remains underused and not well validated.

In addition to studying pile group interaction under static loading, Banerjee has also researched pile group dynamic interaction effects. Banerjee and Davies (1980) compared the results of a boundary element formulation pile group analysis method with static loading field case histories. Banerjee and Sen (1987) reported on boundary element formulations for pile group dynamic response. They also investigated the effects of a ground contacting massless pile cap, and found a marginal increase in pile head impedance of small floating pile groups, most pronounced for the damping component.

Makris and Badoni (1995b) followed their earlier work with a simplified method for analysing pile groups subject to obliquely incident shear and Rayleigh waves, with spring and dashpot coefficients evaluated from the techniques described in Makris and Gazetas (1992). The method consisted of computing the difference between single “source” piles and free-field response, and propagating it to neighbouring “receiver” piles. By superposition, the pile

group displacement, rotation, and individual pile head forces were obtained, incorporating both kinematic and inertial sources of loading.

2.6 Recent research on SSPSI (numerical analyses)

Lu et al, (2005) propose a three-dimensional finite element analysis of the soil–pile–structure interaction system. The analysis is based on data from shaking table model tests made in the State Key Laboratory for Disaster Reduction in Civil Engineering, Tongji University, China. The general finite element program ANSYS is used in the analysis. The surface-to-surface contact element is taken into consideration for the nonlinearity state of the soil–pile interface, and an equivalent linear model is used for soil behaviour. A comparison of the results of the finite element analysis with the data from shaking table tests is used to validate the computational model. It shows that separation, closing, and sliding exist between the pile foundation and the soil. The lateral acceleration response at the top of the superstructure is determined by the rocking and swing of the foundation and the deformation of the structure of a SSI system has been conducted by combining the results of a general finite element program with the experimental results from shaking table tests. By comparing calculated and test results, it was verified that the modelling method is rational. The model is suitable for the numerical analysis of a SSI system under small and strong ground motions. Important conclusions that can be drawn from the computational analysis that are consistent with those that can be drawn from the test are as follows:

- the lateral displacement of the superstructure is composed of the deformation of the structure itself and that caused by the rocking and swing of the foundation. The deformation of the structure is the main component of the structural response, and the rocking and swing of the foundation take second place.
- with increasing input acceleration, the amplification factor of the acceleration peak value is reduced because of the nonlinearity of the soil.
- vertical excitation has little effect on the response of the dynamic SSI.
- the distribution of the strain amplitude along the pile shows that large strains occur at the top of the pile and small strains occur at the tip.
- the distribution of the contact pressure on the pile-soil interface shows that a high pressure is present at both ends of the pile and that low pressure is present at the middle of the pile.

Important results from the calculations that cannot be made from the test are as follows:

- the computational analysis shows that a significant error will occur in the calculation for soft soil if the nonlinearity of the soil and the nonlinearity of the soil structure interface are not taken into consideration.
- the phenomena of separation, closing, and sliding occur between the pile foundation and the soil under severe seismic input.

-
- the strain amplitude of the pile at the corner is bigger than that of the middle pile in the side row and that of the pile at the center.
 - the sliding at the pile in the side row is larger than that at the piles in the middle row along the vibrating direction.

Clouteau et al (2006) concentrated on a limited number of piles and present the dynamic behaviour of a large pile group. The influence of certain parameters of the cap foundation, such as the flexibility and soil-cap contact on the response of the building and the piles is analyzed. Finally, a simplified method for the seismic design of the building is proposed and compared with the exact solution. For embedded foundations, soil impedances show important frequency dependences when a wide range of frequencies is considered. The usual simplification proposes the replacement of the frequency dependences by a constant static stiffness. For a limited range of the frequency parameter a_0 , these formulae are satisfactory when applied to the study of a circular foundation. However, when used to solve dynamic soil-structure problems, the difference between the computed structural response and the rigorous solution is often significant, mostly due to added inertial effects of the foundation which modify the value of the stiffness around the natural frequency of the soil-structure system. Hence the key idea in this procedure is to retain for the frequency-independent impedances the values computed for fundamental frequency of the soil-structure system. The method requires knowledge of the fundamental frequency of the soil-structure system, which depends on the impedance. The dynamic behaviour of a reservoir resting on a pile group foundation with 380 piles is studied. The pile group has a cap with 1 m in thickness and 81m in diameter. The concrete piles are identical with 1 m in diameter and 4.2m in spacing. On a square grid, the gas reservoir is 80m in diameter and 38m in height. The concrete shell of this structure 80 cm thick. This study has been carried out with two conditions of the soil layers. The soil-pile group-reservoir system is divided into two parts, a so called near field and a far field. FEM (SDT models) and also the reservoir BEM (MISS3D) based on boundary integral equations is used for the infinite media of the soil. Then, using FE-BE coupling techniques, these two sub-domain are assembled. Soil between piles, cap foundation and the reservoir are modelled with solid elements. The solid elements have eight nodes with three degrees of freedom at each node. The piles are modelled with beam elements with degrees of freedom at each node. These piles have fixed heads in the cap foundation. The Craig- Bampton method is used to obtain the modes of pile group foundations and the superstructure and the effects of soil-cap contact, the flexibility of the cap in dynamic response of piles and the superstructure. Although ignoring the contact between soil and cap and the flexibility of cap has no influence in the response of the superstructure, the shear forces of the piles heads are strongly dependent on the cap condition, especially for soil-cap contact. A method for frequency-independent impedances ignoring kinematic interaction has been proposed for the soil-pile group-superstructure system. Results of this method and those of an exact numerical solution with frequency-dependent of impedances and with the kinematic interaction are presented in

forms of transfer function and time history response. Good agreement is found between the two solutions. From this case study it seems that the proposed method of analysis with frequency independent of impedance at the natural frequency of the coupled soil-structure system and ignoring the kinematic interaction, provides a sufficiently accurate technique for determining the response of buildings.

Dezi et al., (2007) propose a numerical procedure to evaluate the effects of kinematic and inertial interactions on pile groups by using a finite element approach. The method is used to calibrate Lumped Parameter Models (LPMs) which can be implemented in commercial finite elements programs to perform time domain analyses. The procedure is employed to study the spatial dynamic response of the railway bridge on the Tronto River (Marche region, Italy) which, due to the particular stiffness of substructures and deck, is an interesting case study. The seismic analysis is carried out in the time domain considering several real accelerograms. The results are compared with those obtained from the fixed base model by showing the importance of Soil-Structure Interaction (SSI) in the actual design of the bridge. The main conclusions are:

- foundation flexibility increases the fundamental periods of the system and alters the shape of the vibration modes with respect to the fixed base structure;
- the SSI analysis allows the design optimization of longitudinal seismic restraints;
- the 3D modelling of the bridge was found critical in accounting for the complex effects of the mutual interaction between the deck and the substructures and for considering their influences on transversal seismic response.

Padro'et al., (2009) presents a numerical study on the dynamic through-soil interaction between nearby pile supported structures in a viscoelastic half- space, under incident S and Rayleigh waves. To this end, a three-dimensional viscoelastic BEM-FEM formulation for the dynamic analysis of piles and pile groups in the frequency domain is used, where soil is modelled by BEM and piles are simulated by one-dimensional finite elements as Bernoulli beams. This formulation has been enhanced to include the presence of linear superstructures founded on pile groups, so that SSPSI can be investigated making use of a direct methodology with an affordable number of degrees of freedom. The influence of SSPSI on lateral spectral deformation, vertical and rotational response, and shear forces at pile heads, for several configurations of shear one-storey buildings, is addressed. Maximum response spectra are also presented. SSPSI effects on groups of structures with similar dynamic characteristics have been found to be important. The system response can be either amplified or attenuated according to the distance between adjacent buildings, which has been related to dynamic properties of the overall system. The system under investigation is composed of several neighbouring one-storey linear shear structures, three- dimensionally distributed, founded on 3 x 3 fixed-head pile groups embedded on a viscoelastic half-space. The three-dimensional BEM-FEM code previously developed by the authors for the dynamic analysis of pile groups has been enhanced to allow for one or more superstructures founded on pile groups. Stratified

soils are modelled by BEM, each stratum being considered as a continuum, semi-infinite, isotropic, zoned- homogeneous, linear, viscoelastic medium. The integral equation is written so that pile–soil interface tractions arising from the pile–soil interaction can be regarded as body forces acting within the soil. Fully bonded contact conditions are assumed between soil and piles, which are modelled as vertical Bernoulli beams using one-dimensional three-node FEM elements, and whose heads can be fixedly connected to a rigid non-ground-contacting cap.

Brendon A. Bradley, (2009) investigate the efficacy of various ground motion intensity measures for the seismic response of pile foundations embedded in liquefiable and non-liquefiable soils. A soil-pile-structure model consisting of a two-layer soil deposit with a single pile and a single degree -of-freedom superstructure is used in a parametric study to determine the salient features of the seismic response of the soil-pile-structure system. A suite of ground motion records scaled to various levels of intensity are used to investigate the full range of pile behaviour, from elastic response to failure. Various intensity measures are used to inspect their efficiency in predicting the seismic demands on the pile foundation for a given level of ground motion intensity. It is found that velocity-based intensity measures are the most efficient in predicting the pile response, which is measured in terms of maximum curvature or pile head displacement. In particular, velocity spectrum intensity (VSI), which represents the integral of the pseudo-velocity spectrum over a wide period range, is found to be the most efficient intensity measure in predicting the seismic demands on the pile foundation. VSI is also found to be a sufficient intensity measure with respect to earthquake magnitude, source-to-site distance and has a good predictability, thus making it a prime candidate for use in seismic response analysis of pile foundations.

Yang and Yan, (2009) present an analysis framework for accounting the nonlinear dynamic interaction effects in a practical yet rational way. It is shown that soil nonlinearity plays an important role in altering the response of the structure and the procedure commonly used in practice to account for soil nonlinearity may not be adequate. A hypothesized soil-structure system is considered. The site is assumed to comprise a surface soil layer of 30 m, which has the shear wave velocity of 180 m/s and an underlying rock half-space which has the shear wave velocity of 600 m/s. Using the site classification system of UBC (1997), the site is classified as a SD type. The structure is assumed to be a multi-story building with a circular surface, a foundation of 15 m in diameter and a damping ratio of 5%. The effective weight of the building is assumed to be 62177 MN. The natural period of the building is approximately estimated as $0.1N$ (s), where N is the number of storeys. By varying the natural period of the structure, the stiffness of the building is varied accordingly. The ground motion recording obtained at a rock station in California during the 1994 Northridge earthquake is used as input motion at the rock outcropping. The peak acceleration of the record is 0.316 g with the dominant frequency of 2.95 Hz. The dynamic stiffness of the foundation is calculated. Three cases are considered: Linear (dynamic stiffness is calculated using the initial shear modulus of the soil. No soil nonlinearity is accounted for); Nonlinear w/o SSI (dynamic

stiffness is calculated using the reduced modulus derived from site response analysis in the free field condition) and Nonlinear w/o SSI (additional soil nonlinearity due to dynamic interaction is allowed for). The real part of the dynamic stiffness under the linear condition is the greatest, whereas the stiffness calculated taking into account the nonlinear soil behaviour induced by dynamic soil-structure interaction is the smallest. The stiffness of the foundation calculated for the case (2) is in between. This is reasonable as the dynamic interaction will result in additional nonlinearity compared with the free field condition. Of more interest is the influence of soil nonlinearity on the response of the structure. The variations of the modulus and damping with the strain level are described using the expressions of the Ramberg-Osgood model (Darendeli 2001). It is noted that the influence of nonlinearity is significant. Generally, soil nonlinearity reduces the peak response of the structure, and in the mean time the periods corresponding to peak response tend to shift to the long period end. This paper presents a practical framework for an analysis of seismic soil-structure interaction problems taking into account the nonlinear soil behaviour and the layering conditions of natural soil deposits. The illustrative example shows that the influence of soil nonlinearity is significant on the response of structure and thus requires serious consideration. The method commonly used in practice to account for the nonlinear soil behaviour through the free-field site response analysis is not adequate as additional nonlinearity may arise from the dynamic interaction between the soil and the structure.

Lin et al, (2009) propose an efficient method to derive cyclic p-y curves from shaking table test results. The Fourier series function, satisfying the boundary conditions of a pile, is used to represent deflection behaviour of the pile-soil system at each instant of time during loading intervals. In order to obtain soil reaction along the pile shaft, convergence of the series after differentiation is guaranteed by applying the Cesaro sum technique. Results of two shaking table test results, conducted at the National Center for Research on Earthquake Engineering in Taiwan, are used to verify the feasibility of the proposed method. A detailed derivation of the proposed analytical method are described in this paper. Moreover, the feasibility of the developed method was further verified using results of two real case histories. Advantages of the proposed analytical method include: 1) only either inclinometer data or strain gage data is needed for deriving the deflection or the curvature function, respectively; 2) the derived deflection or curvature function can be used to describe lateral behaviour of a single pile system, such as p-y curves, satisfying various boundary conditions of the pile.

Maiorano et al, 2009 present a report-on kinematic pile-soil interaction analyses for single piles and pile groups using a quasi-3D finite element computer program (VERSAT P3D, Wu 2006) in order to study the influence of a number of factors, like the subsoil model and the soil properties, and to assess the applicability of simplified design methods available in literature. Simplified subsoil conditions are considered, consisting of a two layer profile, with different values of the stiffness contrast between the two soil layers, in terms of their respective S-waves velocities V_{s2}/V_{s1} . Italian real acceleration time histories are considered

(Scassera et al. 2006). Kinematic interaction analyses have been performed for pile groups and isolated piles embedded in an ideal subsoil consisting of two layers underlain by a rigid base. Such a base is located at a depth $H=30$ m while the interface between the layers (H_I) was located at variable depths (5, 10, 12, 15, 17, 19 m). The shear wave velocity V_{s1} of the upper layer was taken 50 m/s or 100 m/s, while the ratio of the two shear wave velocities was set to be equal to 2 and 4 for both values of V_{s1} . Finally a soil density ρ of 1.94 Mg/m^3 and a Poisson ratio $\nu=0.4$ have been assumed, in order to compare the results with those obtained by Nikolaou et al. (2001). Piles with a length $L=20\text{m}$, a diameter $d=0.6\text{m}$ and a Young's modulus $E_p=25 \text{ GPa}$ were considered. The pile head is fixed against rotation. A 3x3 or alternatively 5x5 pile group was considered. The pile spacing was taken to be equal to 4 diameters. In a few cases (G4-2 and G4-4) the pile spacing was also set to be equal to 2.5 d . A number of 144 analyses has been performed. Linear elastic analyses were performed in the time domain; a damping ratio $D=10\%$ was assumed for the soil layers, in order to compare the results with those of the simplified approaches (Nikolaou et al. 2001). From a comparison of the results the following conclusions are reached:

- (a) the simplified solutions do not significantly differ with each other and tend to be conservative;
- (b) there are significant discrepancies between the bending moments predicted by the finite element analyses (M_v) and those evaluated by the simplified expressions (M), especially for decreasing values of V_{s1} (or increasing E_p/E_1) and increasing values of H_I , with a maximum ratio of M_v/M of about 2.4.
- (c) the bending moments obtained by the simplified expressions increase for increasing values of the interface depth, while those computed by the finite element analyses exhibit a sort of "plateau". The simplified expressions could be applied within reasonable accuracy only for certain depths of the interface between the two layers ($H_I < 50\%L$) and moderate values of the pile-soil relative stiffness contrast. Considerable discrepancies are expected for higher values of H_I , i.e in the case of end-bearing piles which is quite frequent in engineering practice. A modified criterion to evaluate the maximum kinematic bending moments has been proposed. The closed form expression suggested by Mylonakis can be put in the form:

$$\frac{M}{a} = \alpha \gamma_s \quad [2.29]$$

where α is equal to 1 in the original Mylonakis approach and a is a coefficient independent of the seismic excitation according to the expression:

$$a = (E_p I_p) \left(\frac{\varepsilon_p}{\gamma_p} \right) \left(\frac{1}{r} \right) \quad [2.30]$$

Figure 2.18 illustrates the plot of the ratio M_V/a , where M_V is the bending moment computed by VERSAT, against the peak shear strain γ_{1ff} . The linear regression in this plane provides $\alpha = 1.3$. Even if there is an evident relationship between M_V and γ_{1ff} there are cases for which this linear correlation is not satisfactory. This can be attributed to the hypothesis of thick layers adopted by Mylonakis (2001) to develop the theoretical solution synthesised by eq. [2.29]. As a consequence of this hypothesis the method is intrinsically unable to provide accurate results when the interface between the two layers is in the vicinity of the pile base or the pile head. As shown in Figure 2.17, a very substantial improvement of the accuracy of the correlation between M_V and γ_{1ff} may be obtained considering only the points corresponding to cases with H_1 ranging between L_{a1} and $L-L_{a2}$, with L_{a1} and L_{a2} being respectively the “active pile length” in the upper and in the lower layer (as defined by Mylonakis 2001).

The same procedure has been applied for the closed form expression of Nikolaou et al. (2001). Indeed that equation has been put in the form:

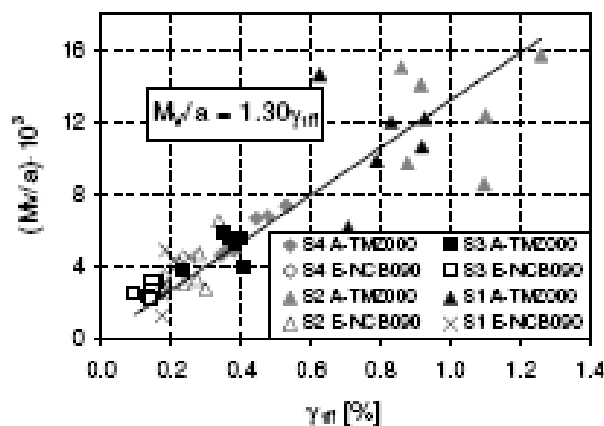


Figure 2.16: Plot of M_V/a against γ_{1ff} .

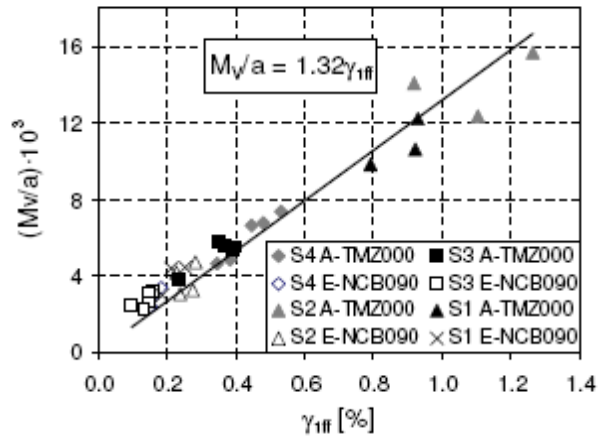


Figure 2.17: Plot of M_v/a vs. γ_{1ff} with the exception of the cases for which H_1 is within the active pile

$$\frac{M}{b} = \beta \tau_c \quad [2.31]$$

$$b = d^3 \left(\frac{L}{d} \right)^{0.3} \left(\frac{E_p}{E_1} \right)^{0.65} \left(\frac{v_{2v}}{v_1} \right)^{0.5} \quad [2.32]$$

where $\beta = 0.042$ in the original expression of Nikolaou et al. (2001), and b a coefficient independent of the earthquake excitation:

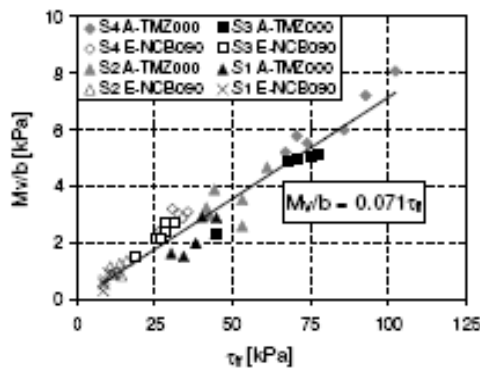


Figure 2.20: Plot of M_v/b vs. the maximum shear stress at the interface τ_{1ff} .

In Figure 2.20 the ratios M_v/b is plotted against the peak shear stress τ_{ff} . In this case all data can be fitted within satisfactory accuracy by the linear regression:

$$\frac{M_v}{b} = 0.071 \tau_{ff} \quad [2.33]$$

A modified criterion for assessment of the kinematic pile bending moments at the interface between two layer is therefore suggested. This involves the following steps:

1. Performing a preliminary analysis of the free-field response to evaluate τ_{ff} at the interface;
2. Evaluating the maximum bending moment at the interface with the following equation (adapted from Nikolaou et al. 2001):

$$M = 0.071 d^3 \left(\frac{L}{d}\right)^{0.3} \left(\frac{E_p}{E_1}\right)^{0.65} \left(\frac{\nu_2}{\nu_1}\right)^{0.5} \tau_{ff} \quad [2.34]$$

Despite these assumptions and the limited number of earthquake events employed in the analyses, the Maiorano et al, 2009 paper highlights a number of fundamental issues about the kinematic response of piles under transient earthquake excitations. Groups effects due to kinematic interaction have been found to be negligible, in agreement with analytical studies and field recordings published in the literature. The study has been therefore focused on the kinematic response of single piles. It has been shown that the simplified methods available in the literature may be not suitable for all subsoil conditions examined in the present paper. A modified criterion to evaluate the maximum kinematic bending moment at the interface between two layers has been then suggested. This is essentially based on a modified expression of the method proposed by Nikolaou et al (2001) in conjunction with the peak shear stress at the interface directly evaluated from a free-field response analysis.

Referring to the recent Italian building code - Norme Tecniche per le Costruzioni, (NTC) 2008, five operative units (Unisannio, Uniparthenope, Unicalabria, Unicatania, Unibasilicata) are involved in the Italian research program ReLUIIS line 6.4 “Deep Foundations” of the ReLUIIS Project.

The research group has made a considerable effort to analyse the effects of kinematic interaction (k.i) for schemes of both single piles and pile groups under several accelerograms selected from the Italian catalogue of recorded earthquakes (Scasserra et al., 2008) and to develop experimental procedures aimed at providing further insight in the phenomenon of kinematic interaction. Their efforts have also included a thorough review of the state-of-the-art on kinematic interaction and a check of the reliability of simplified procedures suggested for simple estimates of kinematic bending moments induced in piles. Moving in this direction, some preliminary indications have been obtained form this research group, and they are briefly summarised here:

(1) Simplified closed-form solutions:

(1A) The use of simplified closed form solutions to evaluate kinematic bending moments is appealing, but requires caution, since they feature several important limitations. In particular, these methods tend to be conservative especially when the stiffness contrast of the two soil layers is high and the embedded length of the pile in each layer is much lower than the so-called “active pile length”. For example, this occurs in the case of end-bearing piles. The simple procedure suggested by Cairo et al. (2009) partly overcomes these drawbacks.

(1B) For a better use of simplified closed-form solutions it is suggested to introduce the requirement to perform a preliminary free-field response analysis and to express the effects at the interface (maximum bending moment) as a function of the maximum effect (maximum shear stress or strain) of the free-field site analysis (Simonelli & Sica, 2008; Maiorano et al., 2009).

(1C) A new criterion to evaluate kinematic bending moment has been developed as an enhancement of the formula proposed by Nikolaou et al (2001). This criterion has a general applicability to engineering problems and can distinguish and handle cases where resonance occurs from those where it does not take place. The new criterion differs from the original approach essentially in that it requires a preliminary assessment of the peak shear strain at the interface to be performed by a free-field response analysis (de Sanctis and Maiorano, 2009; Maiorano et al., 2009). This additional step is relatively simple, due the widespread availability of reliable and friendly codes for free-field response analyses.

(2) Numerical approaches:

analyses based on the Beam-on-Dynamic-Winkler-Foundation approach (BDWF) seem to be adequate, since their results compare favourably with those obtained by means of more refined approaches (Moccia et al., 2009).

(3) Selection of the natural accelerograms for time-domain analyses: the dominant period of the recordings expected at a given site should be accounted for when selecting the accelerograms for time-domain analyses. The accelerograms characterized by dominant periods closer to that of the subsoil should be compulsorily taken into account, as they may induce the higher kinematic moments in the piles due resonance phenomena (Sica et al., 2009).

(4) Group effects:

the analysed performed have shown that group effects do not seem to play a major role, in agreement with other studies published in literature and with field recordings on a 12-storey building in Japan supplied by Nikolaou et al. (2001). It is thus suggested that kinematic effects can be analysed according to results obtained for a single pile.

(5) Subsoil category:

extensive numerical analyses indicated that kinematic effects in piles should be extended also to subsoil type C with *consecutive layers of sharply different stiffness* when the seismicity of the zone is high (Sica et al., 2007).

In this group Cairo et al, 2009 have presented three different approaches developed by Unical

RU. The first (SASP or Seismic Analysis of Single Pile) is based on a continuum formulation (Cairo et al., 2005) and permits soil layering effects to be reliably accounted for (Cairo & Dente, 2007a, 2007b).

The study is conducted in the frequency domain and is limited to linear, viscoelastic behaviour of the soil-pile system. The method originally developed by Conte & Dente (1988, 1989) for the seismic analysis of piles in layered soils has been reviewed (Cairo et al., 2008). It is based on the Winkler foundation model formulated in the time domain, which makes use of p-y curves described by the Ramberg-Osgood relationship (BNWF or Beam on Nonlinear Winkler Foundation). Finally, available analytical solutions (Dobry & O'Rourke, 1983; Mylonakis, 2001; Nikolaou et al., 2001) have been investigated and a simplified procedure for an approximated estimate of the maximum bending moment induced in the pile by the kinematic interaction has been proposed (Cairo et al., 2009).

From the numerical analyses carried out by Unical R.U., the following observations on the kinematic response of single piles emerged:

- At lower frequencies, the fixed-head piles follow the movement of the ground while, at higher frequencies, they experience considerably reduced deformations. For free-head piles a rotational motion arises. The stiffer piles filter out, to a greater extent, the high frequency components of the free-field motion.
- The passage of seismic waves through the surrounding soil imposes curvatures on the piles which generate bending moments even in the absence of the superstructure. These moments are concentrated in the vicinity of interfaces of alternating soft and stiff soil layers, and at the pile head in the case of a fixed-head pile. Kinematic bending moments depend mainly on: the stiffness contrast between two consecutive soil layers; the boundary conditions at the head of the piles; the proximity of the excitation frequency to the fundamental natural frequency of the soil deposit; the depth of the interface of the layers with stiffness contrast, respect to the active length of the pile.
- Under severe seismic excitation (related to its frequency content versus the fundamental frequency of the soil deposit) in the presence of a sharp stiffness contrast between two soil layers and soil type D, bending strain can exceed 0.1% which may induce damage to the pile. Moreover, nonlinear soil behavior can exert a strong influence on the pile's response.
- An approximate equivalent linear calculation, for instance based on the suggestions given by Eurocode, may be carried out with sufficient accuracy.
- On the basis of the available analytical solutions, an approximate procedure for the kinematic bending moment of a single pile at the interface of two soil layers has been proposed. From a practical point of view, this simplified approach (fully analytical) is very attractive as it needs only a few parameters (the peak ground acceleration and the mean period of the design motion) which can be easily assumed by the engineer.

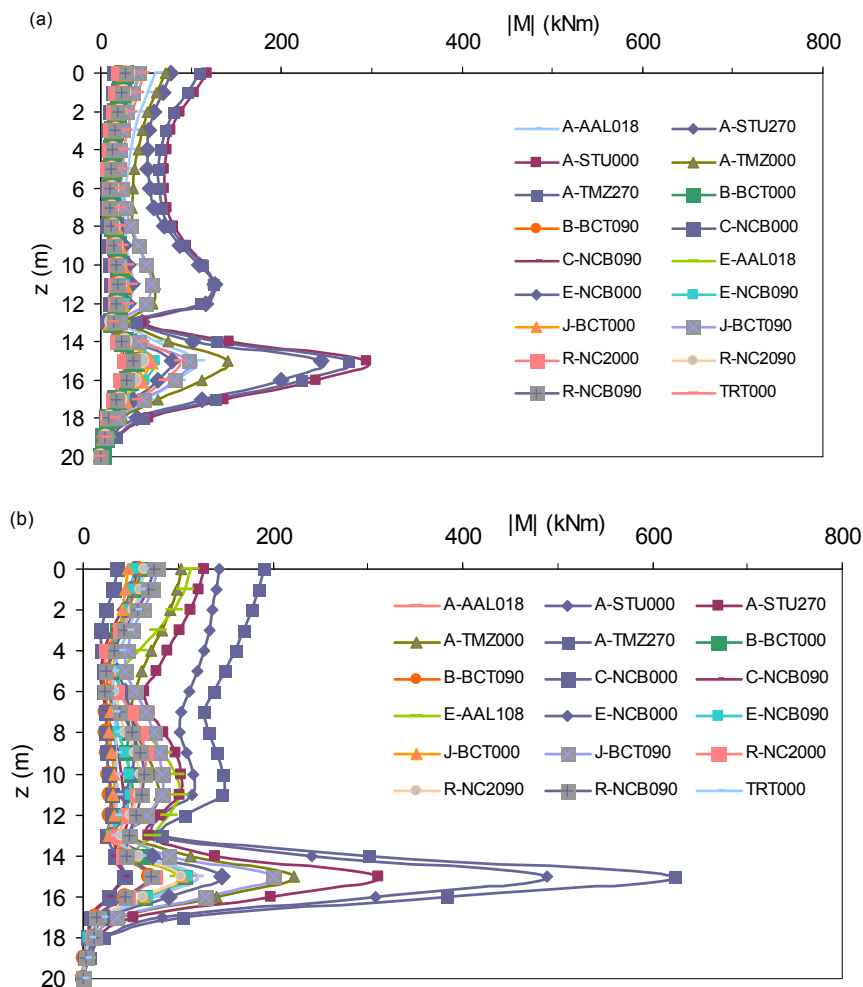
It should be noted that the influence of the nonlinear behaviour of the soil on kinematic pile bending needs to be well investigated owing to the scarcity of available solutions and especially experimental results. Moreover, both the proposed simplified approach and the

equivalent linear calculations resulting from preliminary analyses and a more in-depth study, will be performed in the future. In the follow figures selected results from Cairo et al, are set out.

The linear elastic behaviour of the soil is first examined. The pile response is presented in terms of the envelopes of the maximum bending moment along the pile, which has length $L=20$ m, diameter $d=0.6$ m, Young's modulus $E_p=2.5 \cdot 10^7$ kN/m², and mass density $\rho_p=2.5$ Mg/m³. Poisson's ratio, mass density and damping ratio of the soil are: $\nu_s=0.4$, $\rho_s=1.9$ Mg/m³, $\beta_s=0.10$. The shear wave velocity of the rock is 1200 m/s.

Figures 2.21 shows the results obtained by Cairo et al. (2007, 2008) through the BDWF approach and considering the 18 accelerograms selected from the database SISMA, assumed to consist solely of vertically propagating shear waves. As expected, the bending moment diagrams exhibit a pronounced peak at the interface between the two layers. The corresponding values can be greater than the bending moment at the pile head, depending on the stiffness contrast, the subsoil condition (soil type) and the seismic excitation considered.

Three accelerograms, labelled A-STU000, A-STU270, A-TMZ270, systematically induce the higher bending moments along the pile.



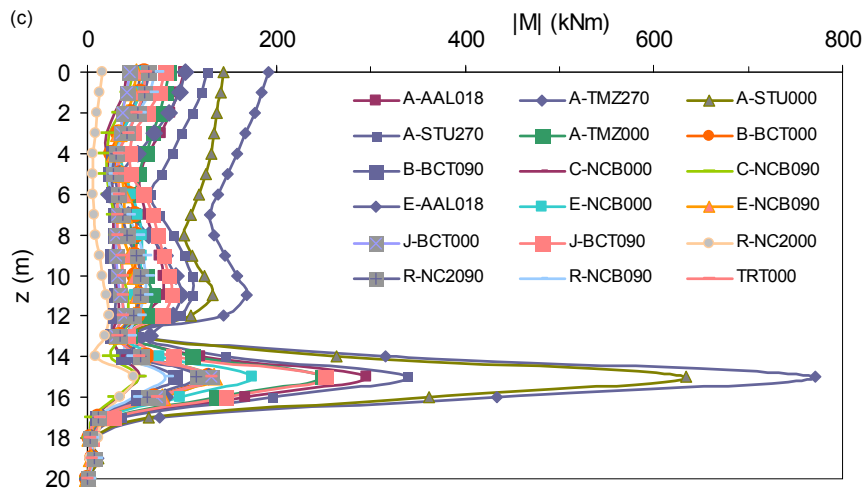


Figure 2.21. Bending moments along the pile for the two-layer soil profile S_1 , soil type D: (a) $V_{s2}/V_{s1}=2$; (b) $V_{s2}/V_{s1}=3$; (c) $V_{s2}/V_{s1}=4$ (Cairo et al. 2007, 2008)

Referring to the three seismic recordings comparisons between the more rigorous approach SASP and the BDWF developed at the University of Calabria are presented in Figures 2.22-2.24. These Figures validate the Winkler models with respect to the continuous approach SASP (with BEM spatial discretization), at least with regard to the linear elastic behaviour of the materials.

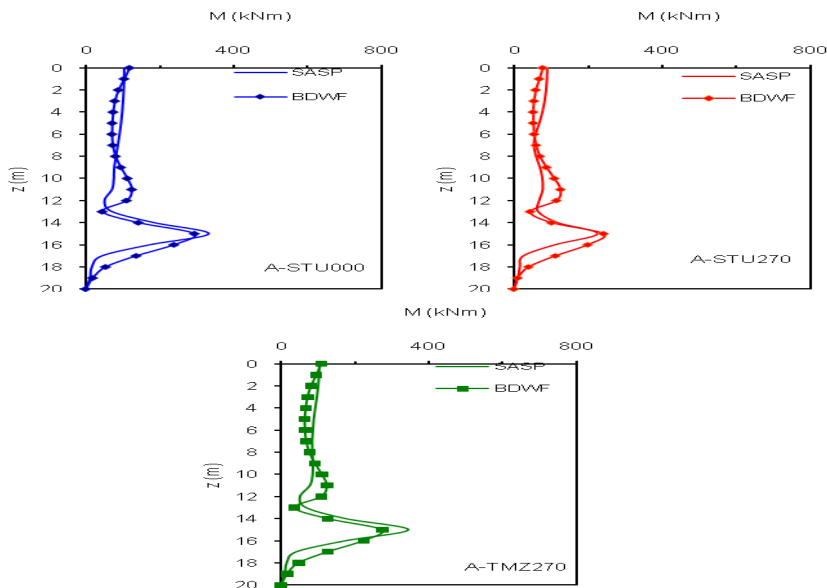


Figure 2.22. Comparison between SASP and the BDWF: scheme S_1 , soil type D, $V_{s2}/V_{s1}=2$. (Cairo et al. 2007, 2008)

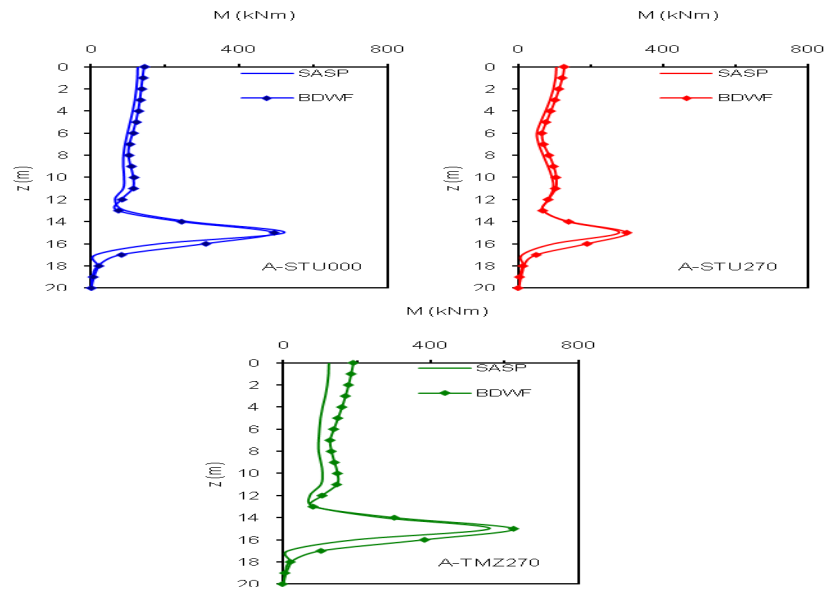


Figure 2.23. Comparison between SASP and the BDWF: scheme S_1 , soil type D, $V_{s2}/V_{s1}=3$. (Cairo et al. 2008)

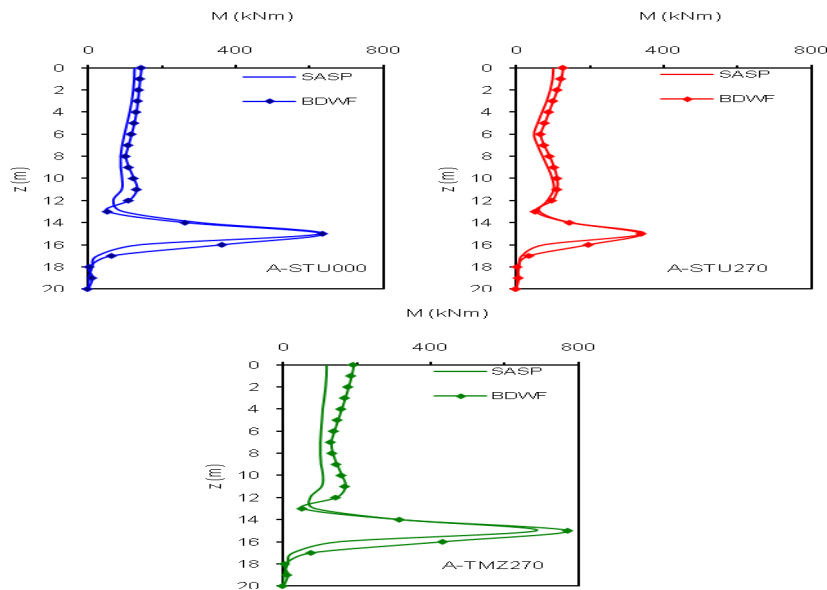


Figure 2.24. Comparison between SASP and the BDWF: scheme S_1 , soil type D, $V_{s2}/V_{s1}=4$. (Cairo et al. 2008)

Catania RU have developed three different approaches to analyze the kinematic interaction of single piles in layered soils: a) numerical, b) analytical and c) simplified p-y approaches. From a practical point of view, the simplified approaches are very attractive as they need few parameters which can be easily evaluated. The first step in a kinematic pile-soil interaction analysis should consist of a seismic soil response analysis for the soil profile specific to each pile location in the absence of the foundation structure (analysis of the free-field conditions).

Then, to evaluate the kinematic effects, the analysis of the seismic interaction of the pile with the adjacent soil should be performed.

For a more realistic approach to the phenomenon of the pile-soil dynamic pile-soil it is necessary to use simplified or complete dynamics analyses. In this last the latter case, the analysis consists of a global analysis of the whole soil-pile-superstructure system in one step.

All the analyses carried on show that kinematic effects tends to be amplified in the vicinity of interfaces between soft and stiff soil layers and kinematic interaction may induce strong bending moments on the piles. It should be noted that the stiffness contrast, more than the soil type, may play a significant role in the increasing of bending moment along the pile length.

Because the stiffness contrast may cause severe pile damages if located in the upper soil strata, it may be desirable to carry out a kinematic interaction analysis particularly under these conditions.

Unisannio RU have carried out with respect to numerical modelling, a broad parametric study to investigate the kinematic response of single piles by taking into account different seismic inputs, stratigraphic conditions, and mechanical properties of the subsoil. The theoretical approaches adopted by Unisannio may be classified in two categories:

- a Beam-on-Dynamic-Winkler-Foundation (hereafter called BDWF) approach by adopting a home-made code (Mylonakis et al., 1997);
- a continuum approach by the FEM codes VERSAT-P3D and ABAQUS.

The main conclusions of the extensive parametric study by the BDWF approach may be summarized as follows:

1. the maximum kinematic bending moment generally occurs along the soil layer interface;
2. at the soil layer interface, the kinematic bending moment dramatically increases when the shear wave velocity contrast between the bottom and top layer V_{s2}/V_{s1} increases from 2 to 4, for both subsoil types D and C (Sica et al., 2007).
3. For most of the subsoil profiles of class D and some cases of the subsoil profiles of class C (NTC, 2008), the computed kinematic bending moments may be well above the yielding moments of the pile cross section (Sica et al., 2007).
4. A huge dynamic interaction has been numerically detected between the input wave-forms (different accelerograms scaled to the same PGA) and the pile-soil system. A simple criterion may be provided to establish whether a specific subsoil, with associated natural accelerograms (at the present in Italy it is possible to know the peak ground acceleration on rock for any specific site; it is plausible that in a short period wave-forms may also be provided), is likely to cause major kinematic bending in piles. To To this end the predominant period of any signal expected at a given site should be compared to that of the subsoil in hand $S_1 (T_{soil})$. The predominant period of the recordings (T_{input}) may be computed both as the value, T_p , corresponding to the maximum spectral acceleration in an acceleration response spectrum, computed for 5% viscous damping, and as the mean period, T_m , as defined by Rathje et al. (1998) on the basis of the Fourier spectrum of the signal. Actually T_m should provide a better indication of the frequency content of the

recordings because it averages the spectrum over the whole period range of amplification. As shown in Figures 2.25 and 2.26, the accelerograms characterized by the ratio T_p/T_{soil} or T_m/T_{soil} within a critical band (close to one) provide the higher kinematic moments in Figure 2, due to the occurrence of a resonance phenomenon. It is worth pointing out that all accelerograms with T_p/T_{soil} and T_m/T_{soil} external to the critical band, induce lower kinematic moments along the pile. In such cases, kinematic interaction could be disregarded and only inertial effects taken into account. Furthermore, the above observations may help in selecting the recordings from databases which should be taken into account for time domain analyses.

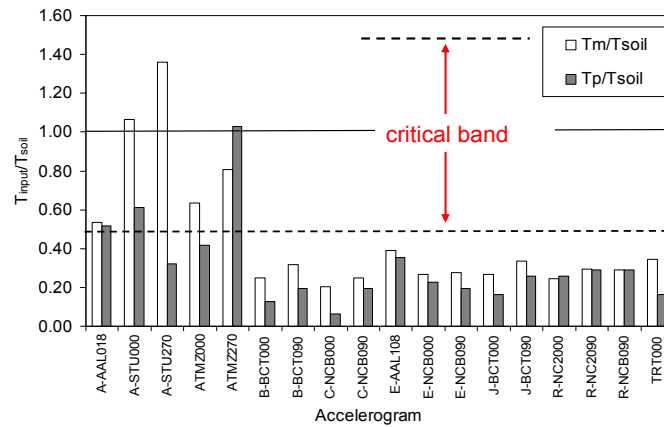


Figure 2.25. Ratios among the dominant period of the input signals and the fundamental period of the reference subsoil (Simonelli & Sica, 2008)

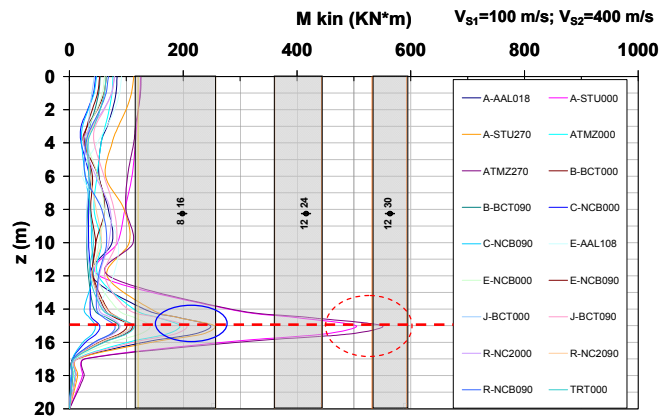


Figure 2.26. Kinematic bending moments for the two-layer soil profile S1 ($H1=15$ and $H2=15$ m) and soil type D of EC8. $V2/V1=4$. Soil damping $D=10\%$ (adapted from Sica et al., 2007)

5. If kinematic effects are to be taken into account, simplified formulation should be provided in a technical code. An extensive application of the simplified literature formulas of Dobry & O'Rourke (1983), Nikolaou et al. (2001) and Mylonakis (2001) have been carried out to compute the kinematic moments at the interface of the subsoil

configurations investigated numerically by the BDWF approach of Mylonakis et al. (1997). The formulas of Dobry&O'Rourke (1983) and Mylonakis (2001) have been applied by adopting both the shear strain at the bottom of the first layer γ_1 provided by the simplified formula of Seed & Idriss (1982) (Figure 2.27a) and the value of γ_1 directly computed with SHAKE or EERA for each selected accelerogram (Figure 2.27b). In the same way, the Nikolaou et al. (2001) equation has been applied by adopting both the shear stress at the interface provided by the authors $\tau_{int} \approx a_s \rho_1 h_1$ (Figure 2.27a) and the value directly provided by EERA (Figure 2.27 b). The formula of Nikolaou et al. (2001) has been applied without any corrective factor η .

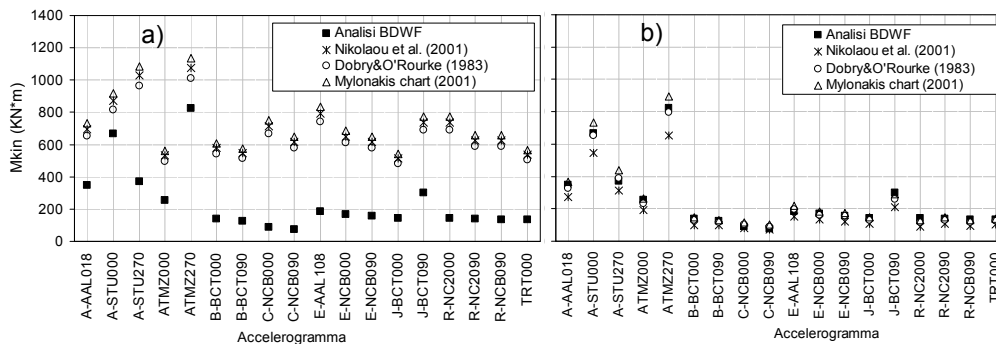


Figure 2.27 a) and b). Kinematic moments computed at the interface by the simplified literature formulas and numerical BDWF analyses

From Figures 2.27a and 2.27b, it emerges that if the literature formulas are adopted with the values of γ_1 and τ_{int} provided by the simplified approaches, all literature formulas - Nikolaou et al. (2001), Dobry&O'Rourke (1983) and Mylonakis (2001) - overestimate the kinematic moments with respect to the values computed numerically by BDWF analyses. Conversely, if γ_1 or τ_{int} are derived from a free-field analysis, carried out with Shake or EERA, the kinematic moments provided by the literature formulas are quite close to those computed numerically (Figure 2.24b). It seems more suitable to apply the literature formulas to obtain the pile's kinematic moment at the interface in combination with free-field analyses (with Shake or EERA) in order to obtain the proper value of γ_1 or τ_{int} .

In short, it is recommended to improve the following points in the technical code:

- Extending the evaluation of kinematic bending in piles for subsoil profiles of class C with layers of sharply differing stiffness.
- Providing a simple criterion to establish whether a specific subsoil, with associated representative natural accelerograms, is likely to cause major kinematic bending in piles.
- Applying the literature formulas of Dobry&O'Rourke (1983), Nikolaou et al. (2001) and Mylonakis (2001) in combination with free-field site response analyses (with Shake or EERA) to obtain the proper value of shear strain γ_1 or stress τ_{int} at the two-layer interface.

Moccia et al, 2009 perform an extensive parametric study on single fixed-head piles in two-layered soil deposits subjected to vertically propagating seismic waves. Analyses have been

performed by a FEM approach implemented in the VERSAT-P3D numerical code, for studying kinematic interaction effects. Italian accelerometric recordings have been used as input motion for numerical analyses. Maximum bending moment envelopes computed along the pile have been highlighted. Hence a significant comparison has been performed among VERSAT results and those obtained by extensive analyses performed by BDWF and BEM approaches in the same soil conditions. The results obtained by the different BWDF methods are in good agreement with those by the more refined and reliable BEM approach; this evidence encourages the use of BDWF simpler analysis as an effective tool for practical applications. Bending moments computed by the FEM approach (VERSAT code) are generally quite higher than those by BDWF and BEM approaches. This evidence suggests performing further analyses, possibly using other tools based on the FEM approach, in order to achieve a more extensive and effective comparison.

2.7 Recent research on SSPSI (experimental test)

A significant number of cases of damage to piles and pile-supported structures during earthquakes have been observed, but few instrumented recordings of the response and performance of such structures during earthquakes have been obtained. Much of the observed damage to piles during earthquakes has been due to the effects of liquefaction and lateral spreading, though some important cases of seismically-induced pile failures in clay have been observed in the Mexico City and Loma Prieta earthquakes.

A methodical review of field and laboratory experimental programs designed to investigate SSPSI has revealed that most efforts have focused on liquefaction problems, leaving a gap in our understanding of SSPSI in cohesive soils. Currently available analytical methods for SSPSI problems range from simple static analyses to derive pile head secant stiffness for input to dynamic structural models, to complete dynamic pile group interaction analyses. Many analytical tools consider visco-elastic response, and others model soil-pile nonlinearity with p-y curves, but nearly all have the common characteristic of disconnecting the site response, soil-pile interaction, and superstructure response elements of SSPSI.

In his PhD thesis at Berkley University 1998, Meymand conducted an extensive experimental study on the seismic soil-pile structure interaction with a shaking table using a large laminar container using a monolayer soft soil (clay). A logical review of the theoretical background and experimental work on SSPSI is reported. The state-of-the-art and current building code recommendations reflect the lack of consensus on how to evaluate SSPSI effects. An enormous data on pile performance during strong shaking have been obtained, a series of scale model shaking table tests of model piles in soft clay was performed. His research effort had the goals of providing insight into a variety of SSPSI topics, and generating a a series of data with which to calibrate an advanced SSPSI analysis tool being developed at U.C. Berkeley (Lok, 1999), as well as data suitable to evaluate other analytical tools and methods.

The principles of scale model similitude were used to derive a set of model scaling relationships that were used in a method of “implied prototypes” to relate model and prototype behaviour.

Consideration was given to the dynamic and nonlinear nature of soil pile interaction in developing the model soil and model piles for the testing program. A specialized flexible wall test container was designed to allow the soil to respond in the same fashion as the free-field, unencumbered by boundary effects. The performance of the shaking table was generally seen to be good, with reasonable reproduction of 1-D and 2-D input motions. Unwanted twist, pitch, and roll motions were present, however, and exerted unquantifiable influence on the model’s response. Qualitative analysis of the single pile and pile group response yielded a number of interesting results.

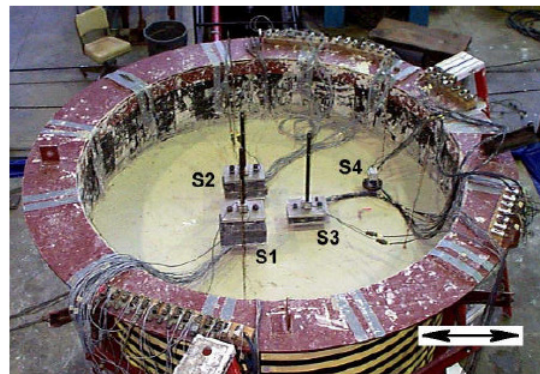
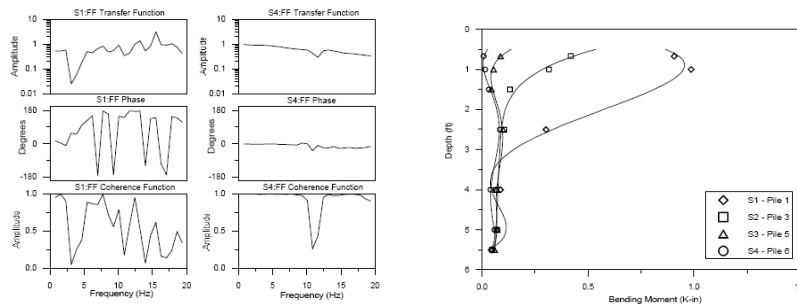


Figure 2.13 Test Series 1.1 Setup



Figures 2.28 a) Meymand’s test series 1.1 setup b) Test 1.15 pile head: free-field transfer functions c) test 1.15 pile bending moment envelopes

Here the main points of experimental findings in Meymand’s experimental work are set out Both the kinematic and inertial interaction elements of SSPSI were observed in the single pile model tests, and the inertial element of response dominated in most cases:

- For single piles with light axial loads kinematic effects did cause maximum bending moments; this result may vary for a pile embedded in a non-uniform soil profile with a strong interlayer stiffness contrast.

-
- Pile head fixity controlled pile bending moment patterns, with characteristic bending moment envelopes observed for the single pile (free-head) and pile group (fixed-head) tests.
 - The frequency response and resonant vibration characteristics of the model structures exerted a major influence on their response, which in turn drove foundation bending and axial force demands.
 - Resonance of the superstructure's natural period with the ground motion/site period stimulated a strong response, and the ability of pseudo-static analysis methods to adequately capture and predict such effects is questioned.
 - Wave scattering effects were observed for pile group foundations, indicating that free-field ground motions are not suitable inputs for pile cap motions. This necessitates the calculation of a "foundation input motion" for substructured analyses, or the use of a fully-coupled SSPSI model.
 - In one case, static lateral preloading of a pile group softened the foundation stiffness to the extent that it was partially base isolated and exhibited less response than the analogous group that had not been preloaded. The influence of pile cap embedment on dynamic response was tested with various cap configurations, and cap base-soil contact was found to be a greater contributor to lateral resistance than cap side-soil contact.
 - The dynamic rocking stiffness of the 3x3 pile cap alone may be computed from the pile raft foundation test results.
 - Experiments designed to evaluate the performance of pile raft foundations and the effect of "dynamic scour" were inconclusive. However these tests do offer the possibility of studying cyclic degradation of lateral resistance under medium term (60+ cycles) loading.

Thus, from his work the conclusions are:

- The single piles were seen to respond with elements of inertial and kinematic interaction, though the inertial elements produced upper bound bending moments. This result may suggest that developing pile demands by considering inertial loading only may be acceptable for cases where site stiffness contrasts or ground failure (lateral spreading) do not exert significant soil loads or deformations on the piles.
- The response of pile groups was highly frequency dependent, which calls into question the applicability of applying pseudo-static analyses to such problems. Pile cap and free field motion variations illustrated wave scattering effects and the necessity of developing modified foundation input motions for substructuring analyses. Moderate effects of pile cap embedment were observed, particularly in contributing to pile group rocking stiffness, though further study is warranted in this area.
- A group that had been first subjected to considerable deformation static lateral loading was seen to have lesser seismic response than an identical group that had not been pre-loaded, suggesting that pre-loading remolded the near-field soils and base-isolated the group. A 5x3 pile group and single pile with the same average load per pile were subjected to 2-D shaking, and the single pile was seen to have greater bending moment demands than the

group piles. This was attributable to long period motion and resulting lack of resonance of the pile group superstructure, which did not impart large inertial loads to the foundation.

- Finally, tests evaluating pile raft performance and the effects of impounded water scouring the soil-pile gap and degrading resistance were somewhat inconclusive, but can be revisited with improved test designs.
- Site characterization included laboratory and in-situ testing to establish undrained shear strength and shear wave velocity profiles. T-bars tests were adapted from centrifuge testing, and produced continuous profiles of strength versus depth. The strength determined in the T-bar tests was found to include a shearing velocity rate effect, which was quantified in relation to vane shear testing. Hammer blow tests were performed from the base and surface of the model container to determine the site shear wave velocity profile. The latter method was found to yield good results except near the surface, where surface wave interference obscured the shear waves, and at depth, where the wave energy attenuated and reflected. Piles in very close proximity to the accelerometer arrays were found to artificially increase the apparent wave velocity by proving alternate travel paths for the wave energy. Soil-specific dynamic modulus degradation and damping curves as a function of strain level were derived from testing with an advanced cyclic triaxial testing apparatus with internal strain and shear wave velocity measurements.
- SHAKE91 was successfully used to simulate a free-field response, vindicating that the model soil-container system adequately reproduced free-field site conditions. The small errors between the observed and predicted behaviour may be acceptable for pure site response analyses, but the propagation of these errors into the SSPSI analysis requires further study.

The data series generated in this research provides a rich information base for extensive study of SSPSI. Much work remains to be performed in the analysis of group interaction in both the static and seismic tests. The rocking response of pile raft foundation and cap contributions to dynamic group response may also be investigated. The procedures developed for the derivation of experimental p-y curves can be applied to the many single pile and group pile cases. The implications of response prediction with the range of pile head stiffness values observed can be studied. Nonlinear site response analyses may provide improved estimates of model soil site amplification. Most importantly, the single pile and pile group seismic response can be simulated with the wide range of existing and developing analytical tools.

Generally speaking, all the experimental regard liquefiable soil in centrifuge model tests. For example, a recent study (soil-pile interaction, only) is presented in Tomisawa and Miura 2007 (Thessaloniky) on the seismic response of single piles in improved ground through dynamic centrifuge model tests. This study presents a practical design method, in which ground improvements are made around the heads of pile foundations constructed in soft ground and ground subject to liquefaction by using deep mixing, sand compaction piling, preloading and other methods. In this design method, the strength of ground after improvement mainly causes an increase in horizontal resistance of pile foundations. The main

concerns of the proposed design method, however, are the shortening of the frequencies of pile foundation structure and related problems, since artificial ground that is not balanced with the original ground is formed around pile heads. The dynamic behaviour of piles installed in the improved ground, which depends on the ground's earthquake response, was therefore investigated using a series of centrifuge model tests. As a result, the shear strength of the ground was higher in the improved ground, and increased earthquake resistance, such as reductions in the horizontal displacement and bending moment of piles against earthquake motion, was verified.

The horizontal resistance of piles is determined by the coefficient of horizontal subgrade reaction k , which is calculated by Eq. (2.29) (Japan Road Association, 2002a) from the deformation modulus of ground E . Accordingly, the effect of the shear strength S enhanced by ground improvement is evaluated as the degree of increase in the modulus of deformation of ground E in the design of piles to be constructed in improved ground.

$$k = \frac{1}{0.3} \alpha E \cdot \left(\frac{\sqrt{D/\beta}}{0.3} \right)^{-3/4}$$

[2.35]

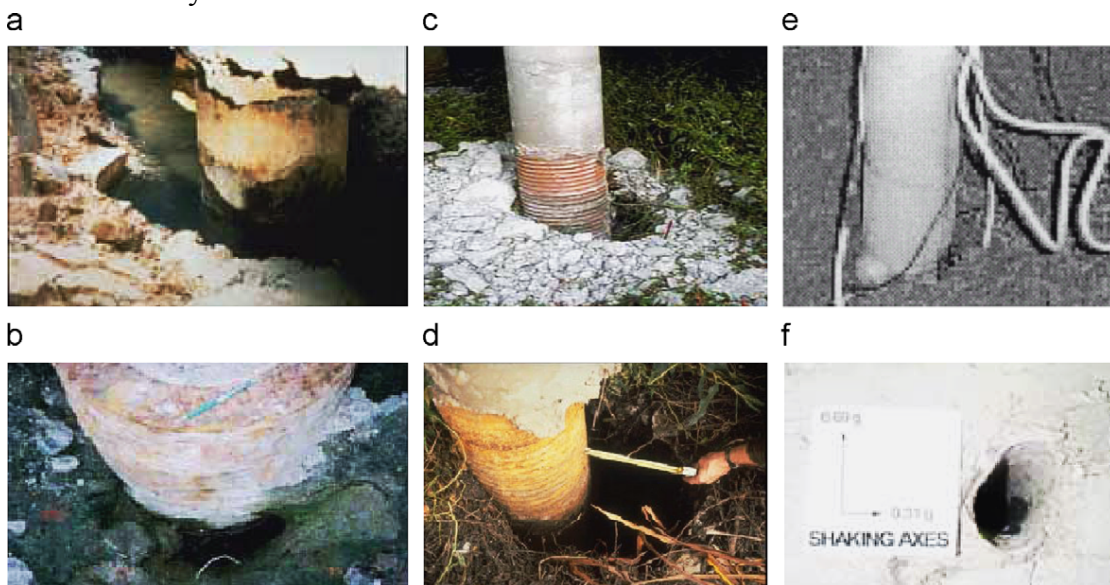
As a result of verification through dynamic centrifuge model tests, the following findings were obtained concerning the static and dynamic horizontal behaviour of piles in improved ground:

- 1) Static horizontal resistance of piles in improved ground is controlled by the material properties of the ground within the range of the characteristic depth of pile $1/\beta$, and pile displacement and bending moment converge within the range of improved ground. The static coefficient of subgrade reaction k of piles in the improved ground with Toyoura sand calculated from the results of static horizontal loading tests in this study was found to correspond with the ground strength ratio to the uniform ground of kaolin clay.
- 2) A series of centrifuge shaking tests showed that the improved ground using Toyoura sand and pile did not resonate as an integral structure and that dynamic behaviour differed depending on their respective deformability and response characteristics.
- 3) Owing to the increments of density and strength by ground improvement, the shortening of natural frequencies in pile foundations in improved ground need to be carefully noticed.
- 4) The dynamic centrifuge model tests also revealed that the displacement and bending moment of piles may be controlled depending on the strength of improved ground around pile heads, and that earthquake resistance may be enhanced due to ground improvement.

Through a series of dynamic centrifuge model tests, basic data were obtained for the establishment of a rational design method of piles in improved ground using deep mixing, sand compaction piling, preloading and other methods. The authors intend to do further study on this subject and clarify the dynamic behaviour of pile foundations under various conditions using numerical and experimental analyses

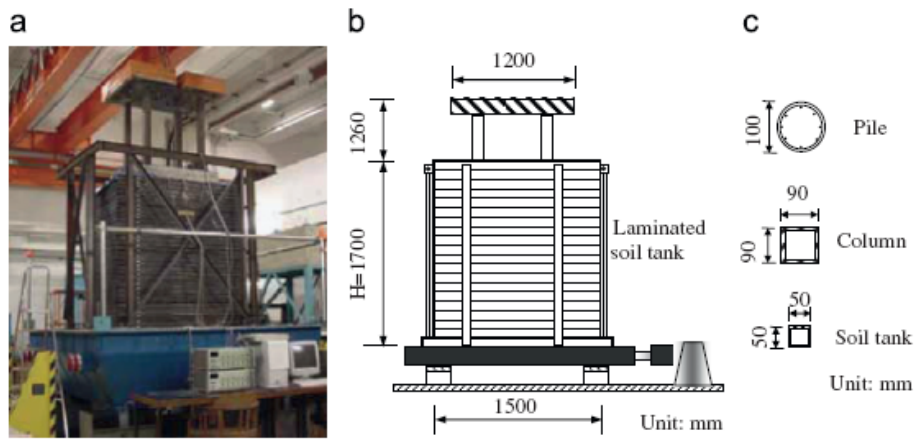
In **K.T. Chau 2009**, the soil–pile–structure model is tested on a shaking table subject to both a sinusoidal wave and the acceleration time history of the scaled 1940 El Centro earthquake.

The main focus of the present study is to report a newly observed phenomenon in our shaking table tests—pounding between soil and pile when a soil–pile–structure model is subjected to seismic excitations. When the soil–pile–structure model is subjected to seismic excitations, the soil surrounding the pile may be compressed laterally such that a soil–pile gap separation may develop. Consequently, pounding may appear between soils and piles due to the different dynamic responses of the pile–structure system and the soil. They show that this pounding may lead to a very large inertial force at the pile cap level, which may lead to cracking in the foundation piles. Finite element analysis is used to explain the unusually large acceleration suffered at the pile cap level. Although soil–pile gaps have been observed in the field after earthquakes and in shaking table tests after soil–pile–structure models are subjected to seismic excitations, the pounding between soil and pile has not been recognized and examined. Photographs in Fig. 2.26 a-f show soil–pile gap separations observed in the field and in the laboratory.



Figures 2.29 a)-f): Examples of soil-pile gap

Experiments on a model of a soil–pile–structure system were performed on an MTS uniaxial seismic shaking table of size 3mx3m. To simulate the shaking of soil in the free field, a rectangular laminated soil tank is constructed by stacking up 32 laminar rectangular steel frames made by welding four rectangular hollow sections of 50mmx50mmx2.8 mm together. The laminar rectangular frame has an internal size of 1.4mx0.9 m. The height of the soil tank is about 1.7m.



Figures 2.30 a)-b): Shear stack and shaking table

Four concrete piles are cast independently using a template of PVC pipe of 100mm in diameter. The piles are 1.7m long, which gives a slenderness ratio of the piles as 17. Young's modulus, Poisson ratio and the 28-day cube strength of the concrete are 21.8 GPa, 0.18, and 19.55 MPa, respectively. The reinforcement in the pile consists of eight vertical mild steel bars 6mm in diameter (or a steel ratio of 2.8%). Circular stirrups made of 9mm mild steel with a spacing of 20mm are fixed to the vertical bars. Eight strain gauges were attached to the vertical steel bars near the top of the piles.

The piles are fixed to the bottom steel plate by a wooden template 10 mm thick when soil is put into the laminated soil tank.

The soil used is poorly grade driver sand imported from the Mainland China. The D_{10} , D_{30} , D_{50} , and D_{60} of the sand are about 0.22, 0.34, 0.41, and 0.42mm, respectively, with all particles smaller than 1mm. The specific gravity of the sand is 2.662. It was found that when the system is subject to shaking with an acceleration less than 0.02g, all displacements are in phase; when the system is subject to shaking—with an acceleration more than 0.04g, out-of-phase motions are observed between the structure and the soil tanks. More importantly, the fundamental frequency recorded at the top of the soil tank increases from 4.6 to 11.6Hz, which agrees with the fundamental frequency of the soil and the laminated tank alone (without pile and structure) reported earlier. Therefore, it is clear that the soil and laminated tank vibrate independently of the pile–structure system. This again supports our earlier speculation that the soil has compressed laterally and a gap develops between soil and pile.

The FEM results suggest that one of the probable causes of pile damages is due to seismic pounding between the laterally compressed soil and the pile near the pile cap level.

The soil is medium-grade driver sand and is embedded into a 1.7m laminated tank made of steel sections covered with Teflon to reduce the sliding friction. A single-storey steel structure is placed on a concrete pile cap, which is supported by four end-bearing concrete piles. A very distinct but unexpected phenomenon is observed. After the system has been subjected to a number of sinusoidal waves of moderate magnitude (let us say peak acceleration more than

0.05g), the acceleration response at the pile cap level may increase to three times of that of the structural response. In addition, the acceleration response of the pile cap shows spikes of considerable acceleration response, which resembles that of nonlinear pounding between two systems. This observation seems to contradict the prediction by structural dynamics.

However, a closer look of the model after the test reveals that gaps develop between soil and piles, probably due to the lateral soil compression caused by the prolonged shaking of moderate earthquake waves input to the system. Finite element analyses were carried out using “SAP2000Nonlinear” incorporating a non-linear gap element installed along the top on one-third of the soil–pile interface.

Various levels of contact stiffness and gap separation have been assumed and as long as appropriate magnitudes of stiffness, depth of the gap, and initial gap separation are assumed, the spikes in the acceleration response of the pile cap can be modelled quite adequately. The results appear to be insensitive to the depth variation of stiffness of the gap element. In addition, when the magnitude of the input acceleration is 0.116g or above, strain gauge data show that cracking can occur at the pile near the pile cap level. This cracking is clearly caused by the notable inertia force experienced by the pile cap due to the pounding between soil and pile.

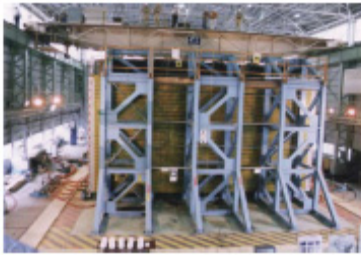
However, it remains to be seen whether such a pounding between soil and pile does occur in the field during strong earthquakes. If it does happen, pile damages reported in the field may be caused by soil–pile pounding instead of liquefaction. The shaking table tests by Lui and Chan showed that the maximum response of the pile foundation may appear before the onset of liquefaction. In addition, Luo and Muroso showed that severe pile damage did occur when no liquefaction was observed. Since the pounding phenomenon between soil and pile was observed in a scaled model, direct application to field situations may not be straightforward. Therefore, a brief discussion of the scaling model that we have adopted is given here.

When the shaking table model was designed, a 1:7 scale model was adopted. This scaling is based upon the scale laws for shaking table test for structures discussed by Harris and Sabnis 1995 and for soil–structure models proposed by Iai. More specifically, our soil–pile–structure system roughly is equal to a three-storey building with a natural period of 0.4 s resting on end-bearing piles 0.7 m in diameter and 12 m in length.

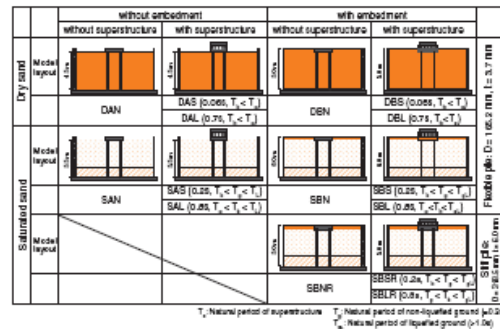
Therefore, the same pounding phenomenon between soil and pile is expected to occur in the field for a prototype of such scale. It should, however, be emphasized that this is only an approximation since a complete set of scaling for soil–pile–structure model is still not available in the literature. Nevertheless, the present study provides a new explanation for the observed damage-in piles during strong earthquakes. In particular, they speculate that one of the causes of pile damaging may be due to pounding between the laterally compressed soil and the pile near the pile cap level. However, much work remains to be done on this seismic pounding phenomenon between soil and pile, before conclusive statements can be made.

Tokimatzu et al, 2009 presents a study on shaking table tests conducted on soil-pile-structure models with dry and saturated sands for examining and quantifying the effects of inertial and kinematic forces and the effects of earth pressure acting on the embedded foundation and of horizontal subgrade reaction of piles. A pseudo-static analysis for estimating pile stress in liquefiable and non-liquefiable sand is presented in which inertial and kinematic effects observed in large shaking table tests are incorporated and the effectiveness of the method has been demonstrated through the comparison of observed and computed pile stresses in the shaking table tests. A sensitivity analysis is also made to differentiate crucial factors affecting pile stress in a liquefied soil.

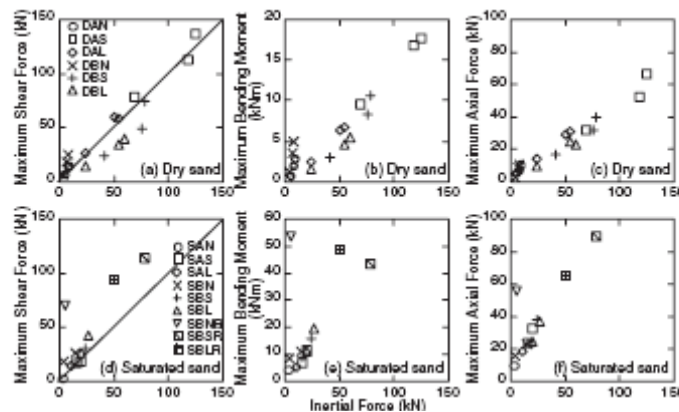
A field investigation of pile foundations that experienced the 1995 Hyogoken-Nambu earthquake has shown the significant effects of cyclic and permanent ground displacement in both liquefied and lateral spreading grounds on damage to pile foundations. In contrast, soil liquefaction that de-amplified ground motions particularly in the period range less than 1s lessened the damage to superstructure in the liquefied and laterally spreading areas, compared with the extensive superstructure damage in non-liquefied area.



Figures 2.31 a) Shear stack and shaking table



Figures 2.31b) Shear stack and shaking table



Figures 2.32 some results

The large shaking table tests conducted to estimate the effects of dynamic soil-pile-structure interaction in both dry and saturated sands have shown the following:

1. if the natural period of the structure is less than that of the ground, the kinematic force tends to be in phase with the inertial force, increasing the stress in piles. The maximum pile stress tends to occur when both inertial force and ground displacement take the peaks in the same direction.

2. if the natural period of the structure is greater than that of the ground, the kinematic and inertial forces tend to be out of phase, restraining pile stress. The maximum pile stress hardly occurs when both inertial force and ground displacement peak at the same time.

3. the above findings are valid for both dry and saturate liquefied deposits. The maximum pile stress may be estimated by applying both the inertial and kinematic forces on the pile at the same time, if the natural period of the structure is less than that of the ground. It may be estimated as the square root of the sum of the squares of the two moments estimated by applying the inertial and kinematic forces on the pile separately, if the natural period of the structure is greater than that of the ground. Effects of stress states in soil around piles on subgrade reaction development in liquefied and laterally spreading ground have been investigated through shaking table tests with both level ground and inclined ground. A discussions of the test results have shown the following:

1. In both liquefied level ground and laterally spreading ground, extension and compression stress states develop at the rear and front sides of a pile with increasing relative displacement between soil and pile. The pore water pressure on the extension side decreases due to the combined effects of extension and shear stresses, while that on the compression side maintains almost constant due to the adverse effects of compression and shear stresses.

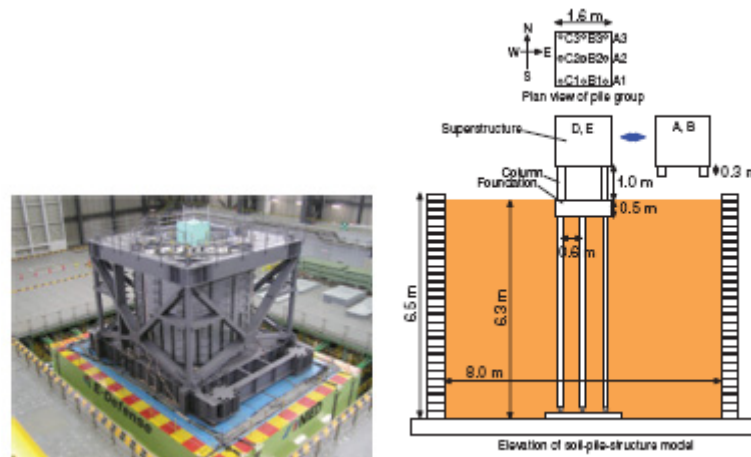
2. The increase in horizontal subgrade reaction of a pile in liquefied and laterally spreading ground is caused by the difference in pore water pressures on both sides of the pile. The pile may be pulled by the soil on the extension side. The mechanism of p-y behaviour in liquefied soil is different from that in dry sand where horizontal subgrade reaction is caused by the increase in soil pressure on the compression side of the pile.

3. In liquefied level ground, the extension and compression stress states alternately develop on both sides of a pile. As a result, the pile is pulled by the soil on the right and left sides alternately. In laterally spreading ground, the extension stress state develops on the downstream side of the pile only when the ground moves downstream. As a result, the pile is pulled only by the downstream soil when the ground moves downstream.

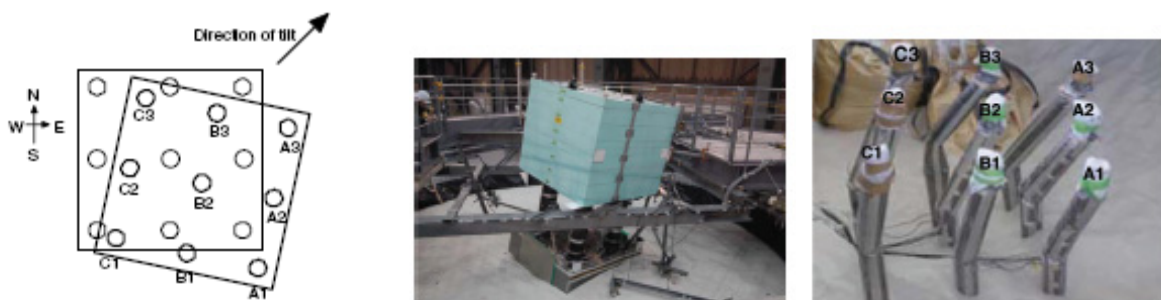
4. The subgrade reaction in laterally spreading ground consists of two elements. One is caused by the cyclic ground deformation, which increases in a stiff pile. The other is caused by permanent ground deformation, which increases in a flexible pile. This is because the stiff pile resists ground movement, while the flexible pile follows ground movement.

The authors show different tests. The facilities used are at the E-Defense shaking table platform 15 m long and 20 m wide was used. It is supported on fourteen vertical hydraulic jacks and connected to five hydraulic jacks each in the two orthogonal horizontal directions. Figures 32 and 33 show the shaking table with a cylindrical laminar box, with a height of 6.5 m and a radius of 8.0 m, made especially for geotechnical-related studies (Tokimatsu et al.,

2007a, 2007b). The cylindrical laminar box consists of forty one stacked ring flanges, enabling shear deformation of the inside soil during two-dimensional horizontal shaking. The first soil pile structure interaction studies using the facilities were made with dry sand in FY2005. Preparation of the soil pile foundation model in the laminar box was made in the preparation building next to the main building that accommodates the large shaking table. A 3×3 steel pile group was used for the test. The piles are labelled A1 to C3 according to their locations within the pile group, as shown in Figure 14. Each pile had a diameter of 152.4 mm and a wall thickness of 2.0 mm. The piles were set up with a horizontal space of four-pile diameters center to center. Their tips were joined to the laminar box base with pins and their heads were fixed to the foundation that weighed 10 tons. After setting the pile group in the laminar box, the sand was air-pluviated and compacted to a relative density of about 70% to form a uniform sand deposit. The results of the shaking table tests performed at E-Defense –show that:



Figures 2.32 Test model on E-Defense large shaking table and Soil-pile-structure model.



Figures 2.33 Inclined structure after test with high input motion. And Damage to piles.

in the E-Defense shaking table test with a 3×3 pile group and a pile spacing of 3.75 in dry sand, the bending strain is larger in the leading piles than in the trailing piles probably due to pile group effects; the depth at which the inflection of bending strains occurs is shallower in the leading piles than in the trailing piles.

The piles failed, accompanied by tilting of the superstructure under high input motion. The piles not only suffered local buckling at their heads but also in the ground. The depth of the

later failure varied from 0.7 to 1.0 m below the pile heads, probably due to pile group effects and the redistribution of pile stress following the preceding failure of the leading piles. The direction of permanent pile deformation is equal to that of the strong axis of inertial force and ground displacement. In the E-Defense shaking table test with a 3×3 pile group and a pile spacing of 3.75 in liquefiable sand, the bending strain also becomes the largest in the leading pile. Its variation within the pile group, however, is quite small, compared to the test with dry sand. All the pile heads yielded under the highest input acceleration, causing residual deformation and settlement of the foundation along the strong axis of the inertial force and ground displacement. The axial strain in piles decreases with depth in non-liquefied ground but is almost constant or even increases with depth in liquefied ground, probably due to the reduction in positive frictional resistance of the pile during soil liquefaction.

The results of the E-defense shaking table tests confirm the centrifuge shaking table tests regarding pile group effects and have shown the following:

1. In the non-liquefied ground, the shear forces at the pile heads tend to become larger in the leading row than in the trailing rows with decreasing pile spacing. This is because the subgrade reaction in non-liquefied ground is caused by an increase in normal stress on the compression side of a pile and such an increase is largest in the leading piles due to the shadowing effects of pile group. Such pile group effects are apparent at a pile spacing of about 4.
2. In liquefied ground, shear forces at the pile heads tend to become larger in the outside piles than in the inside piles as the pile spacing decreases. This is probably because, in the liquefied ground, the subgrade reaction is caused by a difference in pore water pressure changes between the compression and extension sides of a pile. This condition is well developed in perimeter piles but this may not be the case in inside piles. This may lead to a decrease in the difference in pore water pressures on both sides of the inside piles as well as the smaller subgrade reaction in the inside piles. Such pile group effects are apparent only at a pile spacing less than about 3.
3. The critical pile spacing beyond which pile group effects become notable appears to be smaller in dry sand than in liquefied sand, probably due to the difference in strain level between the two.
4. The estimated bending moment based on a pseudo static analysis is in fairly good agreement with the observed values both in dry and saturated liquefied sands for both single piles and pile groups. This suggests that pseudo-static analyses are promising for estimating pile stress with a reasonable degree of accuracy. A pseudo-static analysis for estimating pile stress in liquefiable and non-liquefiable sand has been presented in which inertial and kinematic effects observed in large shaking table tests are incorporated, and its effectiveness has been demonstrated through the comparison of observed and computed pile stresses in the shaking table tests. A sensitivity analysis has been made to differentiate between crucial and less crucial factors affecting pile stress in liquefied soil.

The following conclusions may be made based on the test results, analytical results, and their discussions:

1. pseudo-static analyses can estimate the pile stresses in large shaking table tests with a reasonable degree of accuracy, regardless of the pile stiffness, the presence of foundation embedment and the occurrence of soil liquefaction.
2. pseudo-static analyses can also reproduce qualitatively the significant features of pile damage in the field as well as in laterally spreading ground.
3. the difference in deformation modes observed within the pile foundation in dry sand was caused by pile group effects, whereas that in the laterally spreading zone was presumably caused by the difference in spatial variations of lateral spreading.
4. the pile stress in liquefied soil with low stiffness is governed by inertial force from the superstructure, while that with high stiffness is governed by ground displacement. The effects of inertial force on pile stress become less significant when the foundation is embedded in a non-liquefiable crust overlying a liquefiable/soft layer.
5. the bending moment at the pile head without embedment is sensitive to the scaling factor for p-y spring but becomes insensitive when the foundation is embedded in a non-liquefiable crust.
6. the bending moment and axial force in piles caused by two-dimensional shaking can be estimated by the sum of those obtained by applying the two orthogonal components separately. The bending moment depends only on the magnitude of combined external (inertial and kinematic) forces in the two-dimensional horizontal plane, regardless of the direction of its strong axis, resulting in almost the same value within the pile group. In contrast, the axial force depends not only on the magnitude of combined external forces but also on the direction of its strong axis, producing different axial forces within the pile group.
7. in dry sand, the soil near the foundation tends to act against the inertial force from the superstructure. The axial force is almost controlled by the overturning moment that is induced by the inertial force in the horizontal plane, with its rotational axis near the bottom of the foundation. In liquefied sand, in contrast, the kinematic force arising from the ground displacement tends to act with the inertial force. The axial force is controlled by the overturning moment that is induced by the combined inertial and kinematic force in the horizontal plane, with its rotational axis near the bottom of the liquefied layer.

2.8 BUILDING CODE PROVISIONS

This section will examine the building code recommendations for conducting soil-structure interaction design and analyses, and provisions for dealing with the seismic performance of pile foundations. Although many of these codes incorporate simplified soil structure interaction analysis methods, they acknowledge the need for site-specific studies for structures on soft soils subject to strong levels of shaking. The kinematic phenomenon has

been taken into account in some recent codes and recommendations (e.g. EC8) and these oblige engineers to consider it in design.

2.8.1 NEHRP: National Earthquake Hazard Reductions Program (USA code)

The 1997 NEHRP Recommended Provisions for Seismic Regulations for New Buildings and Other Structures (BSSC, 1997) includes detailed procedures for incorporating the effects of soil-structure interaction in the determination of design earthquake forces in the structure. Incorporating these effects has the direct result of reducing the base shear applied to the structure, and consequently the lateral forces and overturning moments, but may increase lateral displacements (due to rocking). The maximum permissible base shear reduction factor is 30 %, and it is computed as a function of flexible base period and damping factors. The flexible base period is a composite of fixed base, flexible rocking, and flexible translational periods, the latter two computed from foundation stiffness. The accompanying Commentary presents a procedure for deriving the foundation stiffness factors from a simple model of a rigid mat bonded to an elastic half-space. The model can take into account foundation shape, embedment, and soft soil over stiff layers, but the Commentary acknowledges that its application to pile foundations is more tenuous. This is the type of model that Stewart investigated (see chapter 2), and his findings echoed this conclusion. The Commentary states that individual pile stiffness factors may be determined from field tests or beam-on-elastic-subgrade analyses, but provides scant details. Perhaps not conservatively, the Commentary recommends summing individual pile stiffness factors to compute pile group stiffness, without reduction factors. The 1997 NEHRP Guidelines for the Seismic Rehabilitation of Buildings (BSSC, 1997) provides simplified expressions for pile axial and rocking stiffness and the influence of pile caps on pile group seismic response. For cases where the piles may significantly contribute to lateral stiffness (i.e., soft soils, battered piles), the Provisions recommend that a beam-column analysis be performed. In promoting an elastic model of soil-structure interaction, the NEHRP Provisions do not directly incorporate nonlinear effects, but attempt to overcome this limitation by recommending that foundation stiffness factors be selected based on anticipated strain levels in the soil response. The NEHRP foundation design requirements primarily focus on assuring adequate pile cap connections, transverse reinforcement, and the ability to withstand maximum imposed curvatures resulting from seismic loading. These curvatures are observed to potentially arise from: 1) soil settlement beneath the pile cap, leaving an unsupported pile length in the zone of maximum inertial forces; 2) large deformations and/or reduction in soil strength as a result of liquefaction; and 3) large deformations in soft soils, particularly at soft/stiff soil interfaces.

2.8.2 EUROCODE (EC8)

BS EN 1998 applies to the design and construction of buildings and civil engineering works in seismic regions. The aim of BS EN 1998 is to protect people and limit damage during earthquakes. BS EN 1998 Eurocode 8 is in six parts:

- Part 1 covers general rules, seismic actions and rules for buildings.
- Part 2 covers bridges.
- Part 3 covers the strengthening and repair of buildings.
- Part 4 deals with silos, tanks and pipelines.
- Part 5 deals with foundations, retaining structures and pipelines.
- Part 6 covers towers, masts and chimneys.

It is unlikely that BS EN 1998 needs to be used in the UK, except for special structures (e.g. nuclear structures, long span bridges and tall buildings). The tendency in Eurocode 8 is for nonlinear analysis, static (Pushover) or dynamic, to become the reference method for the direct design of new buildings. These recent seismic codes prescribe taking into account kinematic interaction in pile design, e.g. “piles have to be designed for soil deformations arising from the passage of seismic waves which impose curvatures and thereby lateral strains on the piles along their whole length”, Eurocode 8, Part 5 (EN1998-5, 2003). The Eurocode advises designers to design piles against bending due to inertia and kinematic forces arising from the deformation of the surrounding soil. It goes on to say: “*Piles shall be designed to remain elastic. When this is not feasible, the sections of the potential plastic hinging must be designed according to the rules of Part 1-3 of Eurocode 8*”.

Eurocode 8 (Part 5) says: “*Potential plastic hinging shall be assumed for: a region of $2d$ from the pile cap; a region of $2d$ from any interface between two layers with markedly different shear stiffness (ratio of shear moduli > 6) where d denotes the pile diameter. Such a region shall be ductile, using proper confining reinforcements*”.

In part 5 it is further written: *Analyses to determine the internal forces along the pile, as well as the deflection and rotation at the pile head, shall be based on discrete or continuum models that can realistically (even if approximately) be reproduced;*

The bending moments that develop due to kinematic interaction shall be computed only when all of the following conditions occur simultaneously:

- the ground profile is of type D, S1 or S2, and contains consecutive layers of sharply differing stiffness;
- the zone is of moderate or high seismicity, i.e. the product $ag \cdot S$ exceeds 0,10 g
- the supported structure is of importance class III or IV.

Piles should in principle be designed to remain elastic, but may under certain conditions be allowed to develop a plastic hinge at their heads.

2.8.3 *ASCE Workshop*

At an ASCE Technical Workshop on the Lateral Response of Pile Foundations conducted in San Francisco in 1994, representatives from major geotechnical engineering firms gave presentations indicative of the local state of the art. A variety of methods for analysing lateral loading of single piles were presented ranging from simplified chart solutions to the advanced computer code PAR (Bea, 1988). Group effects were treated with Poulos' elastic/static interaction factors and empirical results from Reese (1990). Finally, the lateral response of piles in liquefaction susceptible soils was addressed with a method for degrading the p-y curve based on soil index properties. To analyze earthquake and liquefaction-induced pile curvatures, two methods were outlined: the first, using a site response analysis (i.e. SHAKE91) to determine the soil response with depth, and imposing that on the pile to generate moment and shear distribution along the pile; the second, using a nonlinear dynamic 2-D or 3-D finite element analysis (i.e. SASSI) that models both piles and soil. The first approach is conservative in that it does not account for soil-pile interaction, and the second approach is complex, costly to implement, and does not capture important soil-pile interface nonlinearities.

2.8.4 *Norme tecniche per le costruzioni (NTC, 2008)*

The recent seismic Italian code “Norme Tecniche per le Costruzioni” (NTC, 14.01.2008) also specifies that kinematic effects should be taken into account when seismicity of the area is moderate or high ($a_g > 0,25g$), subsoil type is D or worse, and consecutive soil layers with sharply different shear moduli are present. In the application of the new provisions, the difficulty of putting theory into engineering practice emerged.

Some of its features should be recalled:

- NTC requires that analyses of the overall behaviour of structures, aimed at obtaining internal actions on the structural elements (including foundations), have to be performed assuming that the foundations of the building are restrained from movement;
- NTC considers modal analysis with response spectra as the “reference analysis” for the behaviour under seismic loading, i.e. it is likely that most design analyses will be performed in the frequency domain rather than in the time domain;
- in line with point one, kinematic interaction is considered only as an additional source of actions on piles, but it is not required for evaluating its effects on the overall behaviour of the structure.

3. One-g scale modelling and experimental set up

3.1 Introduction

The role of physical modelling in earthquake geotechnical engineering cannot be over-emphasised. Physical model not only plays a key role in understanding failure mechanism or physical processes but also helps to validate theoretical or empirical or simplified method of analysis. For other investigations (e.g., seismic soil-pile interaction), scale model tests allow the possibility of simulating phenomena that cannot be achieved “at-will” in the prototype.

Scaling law are pivotal in the success of designing experiments. Scaling laws fro dynamic testing of structure can be found in Shabnis (Edited book of ASCE) and others.

For dynamic testing in centrifuge in Shofield (1984 paper), Wood et al.(2002), 1-g testing in Muir Wood (2004)., Tobita and Iai (2006, 2007). This chapter concerns the scaling laws for 1.g dynamic soil-pile-structure interaciton.

This chapter discusses the principles of shaking table modelling scaling law. It will first describe theories of scale model similitude, and elucidate the development of scale modeling criteria for the shaking table test program. The application of these criteria to and design of the model soil and model piles used in the test program will then be described.

3.2 Aim of shaking table tests and prototype

This PhD thesis focuses it attention on a experimental work on shaking table. This study is a part of a large italian research project ReLUIS Project, line 6.4 “Deep Foundations”. In it five operative units have been involved and they have provided considerable efforts:

- a) to analyse the effects of kinematic interaction for schemes of both single piles and pile groups under several accelerograms selected from the Italian catalogue of recorded earthquakes (Scasserra et al., 2008);
- b) to develop experimental procedures aimed at providing further insight in the phenomenon of kinematic interaction.

Their efforts have also included a thorough review of the state-of-the-art on kinematic interaction and a check of the reliability of simplified procedures suggested for simple estimates of kinematic bending moments induced in piles..

Referring to the recent Italian building code - Norme Tecniche per le Costruzioni, (NTC) 2008 - some of its peculiarities must be recalled:

- NTC requires that analyses of the overall behaviour of structures, aimed at obtaining internal actions on the structural elements (including foundations), have to be performed assuming that the foundations of the building are restrained from movement;
- NTC considers modal analysis with response spectra as the “reference analysis” for the behaviour under seismic loading, i.e. it is likely that most design analyses will be performed in the frequency domain rather than in the time domain;
- consistently with (a), kinematic interaction is considered only as an additional source of actions on piles, but it is not required to evaluate its effects on the overall behaviour of the structure.

Hence to improve the Italian code, referring to kinematic interaction, within the framework provided by the NTC 2008, two main questions have to find answer:

- (2) when has kinematic interaction to be considered (or, conversely, when can it be neglected?);
- (3) how has kinematic interaction to be analysed?

At present, the evidence collected is far from providing answer to the former question, but is adequate to indicate what has still to be done for this issue. In order to compare the theoretical evidence derived from the analysis an extensive experimental work has been performed.

Moving to the latter issue, this PhD thesis has been programmed to try to respond to some crucial questions affected the kinematic interaction phenomena:

- wave form input motion effect;
- subsoil deformability effects;
- stiffness contrast effects;
- pile head condition: no rotation head; free head pile ecc..
- correlation between inertial and kinematic bending moment;
- influence of the non linear behavior of soil.

Hence the physical model employed in this study was based on a reference numerical prototype (Fig 3.1) employed in previous parametric studies Mylonakis *et al* (1997), Nikolaou *et al* (2001), Sica *et al* (2007), Maiorano *et al*, (2008).

The pile prototype is a concrete pile of Young's modulus $E_p=25$ GPa, diameter $d=600$ mm and length $l=20$ m. The pile is embedded in a two-layer soil deposit. Each soil layer is characterised by its thickness h , density ρ , shear wave velocity v_s , Poisson's ratio ν , and damping ratio β . The prototype shear wave velocities are $v_{s1}=100$ m/s and $v_{s2}=400$ m/s. The Poisson's ratio and the thickness of the soil were considered the same for the two layers ($\nu_1=\nu_2=0.4$, respectively $h_1=h_2=15$ m).

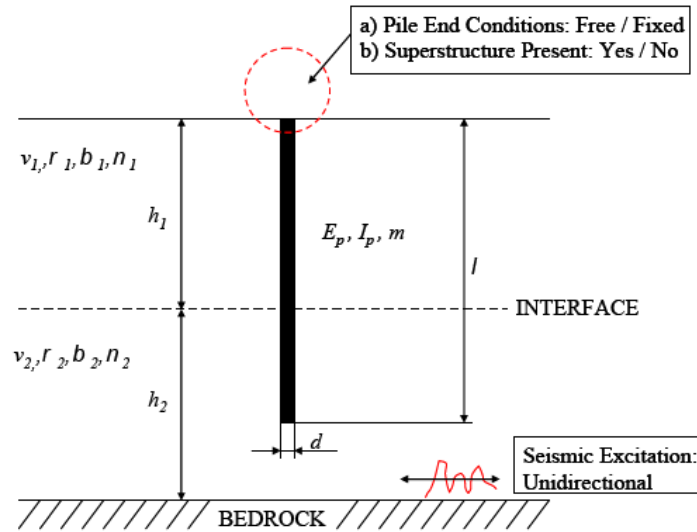


Figure 3.1: Reference prototype for the physical model

This prototype has been a reference for physical model. The scaling law have been applied on the prototype to obtpn the physical model.

3.3 Scale model similitude

Dynamic centrifuge testing is often considered as one of the best possible ways to study foundation related problems as 1:N model is subjected to Ng creating compatiblr stress fields. This particularly creates realistic stress-strain behaviour of soil. However, studying SSPI problem in a centrifuge can be challenging due to potncial errors such as: radial distortion; angular distortion; gravitational distortion; Coriolis distortion;

Radial and angular distortions are caused by model sizes in relation to the siradius of the centrifuge. Gravitational distortion acts due to earth's gravitational force acting on the soil. The body force acts at N-g radially outwards and 1-g vertically downwards or a resultants at an inclination

This can be particularly challenging during the swing up of the model to the required g-level. In contrast, the advantagees in using 1-g modelling rather than N-g (as in a centrifuge) to study are based on that it is difficult to study a complex SFSSPSI in a centrifuge due to the 1-g gravitational distortion of the superstructure. An example of this can be found in Bhattacharya et al (2004), where the pile instability was studied in a centrifuge. Also the 1-g test gives the opportunity to have more space for placing equipments, sensors and loading actuators. As well know the particle size problems can be reduced and boundary condition can be well defined as well controlled.

Shaking table tests of model piles have provided another important means for understanding and validating SSPSI effects. The principal features of shaking table tests are that they are conducted in a 1-g environment.

Similar to centrifuge tests, shaking table model tests are sensitive to boundary effects imposed by the test container, and hinged, laminar, and shear boxes have been employed to overcome these effects. Shaking table model pile tests do not require special in-flight procedures for pile installation or verification of in-situ soil properties. Scale model similitude is more complex in shaking table testing than in centrifuge testing.

The relationship between a scale model and the corresponding prototype behaviour is described by a theory of scale model similitude. In Meymand 1998 the overview on all scaling method is reported.

Every physical phenomena and mechanism can be expressed in terms of non-dimension groups. Therefore the steps are:

1. find out the non -dimensional group. This can be achieved by thinking of the hypothesis that governs the particular behaviour under interest both at model scale and at prototype scale; at micro and macro scale;
2. it is then necessary to ensure that crucial dimensionless group are simultaneously conserved between model and full scale ;
3. often there can be conflicting scaling laws that are required to be dealt with.

3.4 Definition of scaling laws

The present study considers the problem of modelling the pile in layered soils. The physical model is located in a laminar box, the shear stack, and in figure 3.2 are reported the sizes. Therefore with the aim of modelling the prototype (30 m) a deep of 0.814 m has been considered.

The problem with the small scale modelling resides in its limited ability to satisfy the laws of physical and geometrical similarity between the model and the prototype. Its effectiveness depends on whether all the relevant factors that influence the behaviour of the prototype have been captured in the model. Muir Wood *et al* (2002) derived a number of scaling factors for single gravity soil models from four fundamental scaling factors (length, density, stiffness and acceleration). These are presented in Table 3.1. From the scale factor for length, all others can be derived. From the scale factor for length, all others can be derived. In this study, the ratio between the prototype soil depth (30 m) and the shear stack height (0.8 m) gave the fundamental scale factor for length ($n=37.5$). The scaling laws, shown in Table 3.1, have been used to obtain:

- input motion frequency and duration;
- target shear wave velocities for the physical model;
- pile length;
- soil stiffness.

3.4.1 Scaling law for pile stiffness (pile thickness)

As for the model soil, the model pile was subject to competing scale modelling criteria. By addressing the principal governing factors of pile response, a successful model pile design was attained. The theoretical model employed for pile modelling is described in Muir Wood (2004). The pile was assumed to behave as an Euler-Bernoulli beam in pure bending (fig. 3.3) for which the horizontal deflection is governed by equation [3.1]. For bending of piles governed by small deflection theory (almost all practical cases with exception of buckling instability in extremely soft soil or liquefiable soils) the governing law is Eulerian –Bernoulli moment-curvature.

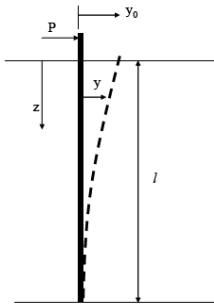


Figure 3.3: Eulerian – Bernoulli pile

$$E_p I_p \frac{d^4 y}{dz^4} = -k_s y \quad [3.1]$$

where EI is the pile flexural rigidity, y is the horizontal deflection of the pile, z is the distance measured down the pile and k_s is the coefficient proportional to soil shear modulus G . Rearrangement of equation [3.1] gives:

$$\frac{d^4 y}{dz^4} + \frac{k_s}{E_p I_p} y = 0 \quad [3.2]$$

Using the normalisation technique of normalising the depth of the pile by the diameter, it has been obtained $\bar{z} (=z/d)$.

Also it has been hypnotized that the length of pile (beam) is bigger than the active length of pile L_a (active length is typically 10-15 d)(Randolph 1980). Therefore the derivate of z is expressed in equation [3.3]:

$$d\bar{z} \cdot d = dz \quad [3.3]$$

where d is the pile's diameter. Consequently equation [3.2] gets transformed to equation [3.4]:

$$\frac{d^4 y}{dz^4} + \frac{k_s d^4}{E_p I_p} y = 0 \quad [3.4]$$

Equating real parts and focusing on relatively low frequencies, where the inertia term ($m \times \omega^2$) is small, it is a simple matter to show that the above equations yield the simple result (Novak 1974). Basic to pass from prototype and model it is to conserve a non-dimensional group. The non-dimensional group to study this problem is given from equation [3.5] from Eulerian beam theory. This non-dimensional group must be conserved in both model and prototype scale.

$$\left(\frac{k_s d^4}{E_p I_p} \right) \quad [3.5]$$

Noting that k_s can be related to relative pile-soil stiffness ratio (E_p/E_s) through Winkler factor (δ) given by equation [3.6] (Dobry et al.,1982). Figure 3.4 plots the variation of the Winkler factor for various pile-soil stiffness ratios.

$$k_s = \delta E_s = 1.67 \left(\frac{E_p}{E_s} \right)^{-0.053} \quad [3.6]$$

We can further simplify equation [3.6] by expressing k_s and I (inertia of pile) in terms of diameter shown by equation [3.7].

$$\left(\frac{k_s d^4}{E_p I_p} \right) = \left(\frac{\delta E_s d^4 64}{E_p \pi d^4} \right) = \frac{64 \delta}{\pi} \left(\frac{E_s}{E_p} \right) \quad [3.7]$$

Given the minor dependence of δ on frequency (Novak 1974, Blaney et al 1976, Roesset 1980) and considering other contributing factors (e.g., Poisson's ratios) as approximately equal in the model and the prototype, the above equation can further simplify to the general similitude relationship given by equation [3.8], following reported:

$$\left(\frac{E_s}{E_p} \right)_{Model} = \left(\frac{E_s}{E_p} \right)_{Prototype} \quad [3.8]$$

This remarkably simple expression suggests a pile-soil stiffness contrast similarity between model and prototype. From equation [3.7] and equation [3.8] the following equation can be written:

$$\left(\frac{E_s d^4}{E_p I_p} \right)_{prototype} = \left(\frac{E_s d^4}{E_p I_p} \right)_{model} \quad [3.9]$$

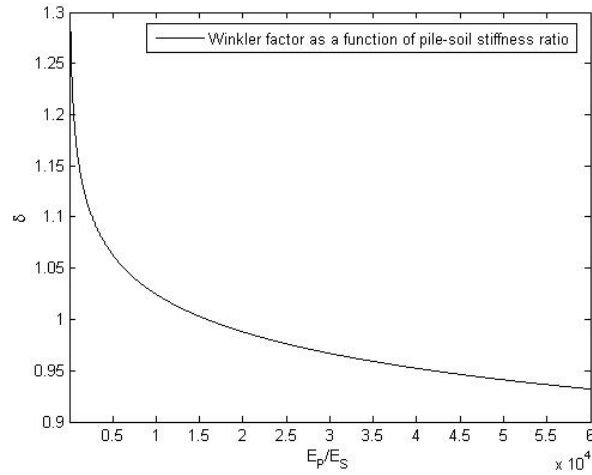


Figure 3.4: Winkler parameter for various pile soil stiffness ratio

The pile model is an aluminium tube (Meymand, 1998; Hoe I. Ling, 2003, Suzuki 2003). From the prototype the diameter of the solid concrete pile is equal to 600 mm and Young's modulus is 25 GPa.

By adopting an aluminium alloy model pile ($E_{Al} = 70$ GPa) and applying the geometry scaling law (see table 3.1) the outside diameter and the length of pile has been obtained as shown in figure 3.5 and in equation [3.10].

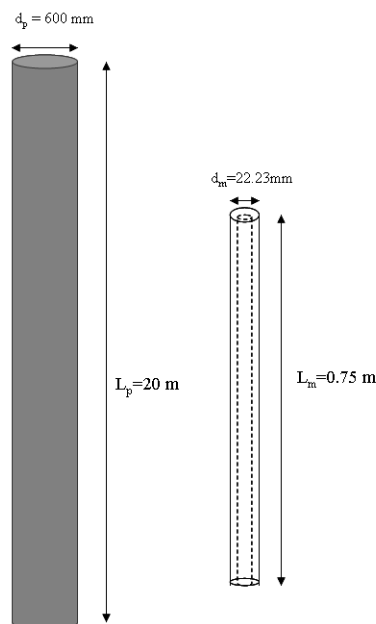


Figure 3.5 Pile: model and prototype

$$\left\{ \begin{array}{l} L_m = \frac{L_p}{n} = \frac{20}{37.5} = 0.53 \text{ m} \\ d_{o_m} = \frac{d_p}{n} = \frac{600}{37.5} = 16 \text{ mm} \end{array} \right\} \quad [3.10]$$

It should be noted that in this experimental work a different length of pile and different outside diameter have been chosen.

It has been considered a longer pile, L is 75 cm, to have a hinged pile on a flexible support (Chap. 4, figure 4.3 b) to avoid any settlement of pile during the shaking motion.

For problem of scale it is assumed a different outside diameter for the pile. The original value of diameter obtained from scaling law was too small. So that it has been chosen an outside diameter equal to 20 mm, the easier to realized.

The ratio between the model and prototype Young modulus is given by equation [3.11], from table 3.1, where the value of the scale factor is $n = 37.5$ and therefore the ratio between the soil modulus are followed reported:

$$\frac{(E_s)_{model}}{(E_s)_{prototype}} = \frac{1}{\sqrt{37.5}} \quad [3.11]$$

The ratio of the second moment of area of model pile and prototype pile is given by equation [3.12] following reported:

$$\frac{(I)_{model}}{(I)_{prototype}} = \frac{(E_s)_{model}}{(E_s)_{prototype}} \frac{(d)_{model}}{(d)_{prototype}} \frac{(E_p)_{model}}{(E_p)_{prototype}} = \frac{1}{\sqrt{37.5}} \frac{1}{37.5} \frac{25}{70} = 2.95 \cdot 10^{-8} \quad [3.12]$$

$$(I)_{model} = 2.95 \cdot 10^{-8} * (I)_{prototype} = 187.6 \text{ mm}^4 \quad [3.13]$$

The outside diameter of model pile is 20 mm, in this hypothesis the inside diameter (d_i) is obtained as shown below in equation [3.14]:

$$\frac{\pi}{64} (20^4 - d_i^4) = 187.6 \text{ mm}^4 \quad [3.14]$$

Therefore the inside diameter is 19.66 mm and the thickness of model pile is 0.06 mm. The smallest thickness aluminium tube that was commercially available at the time of testing was the 6063-T6 HE9TF aluminium alloy tube of thickness $t = 0.71$ mm and outer diameter $D_o = 22.23$ mm. This tube has been adopted for the model pile. In Chapter 4 (table 1 and figure 1) are reported the properties of pile used in dynamic test.

3.4.2 Scaling law for mass of superstructure (SDOF)

The classical approach for elastic-dynamic analysis of soil-structure interaction aims at replacing the actual structure by an equivalent simple oscillator supported on a set of frequency-dependent springs and dashpots accounting for the stiffness and damping of the soil medium. This model has been adopted by several researchers, including Parmelee (1967), Veletsos et al (1974, 1975, 1977), Jennings & Bielak (1973), Wolf (1985) and more recently Aviles et al (1996, 1998).

The classical solution for a standard system is shown in figure 3.6. It involves a simple oscillator on flexible base representing a single storey structure, or a multi storey structure after a pertinent reduction of its degrees-of-freedom (e.g., considering that the mass is concentrated at the point where the resultant inertial force acts).

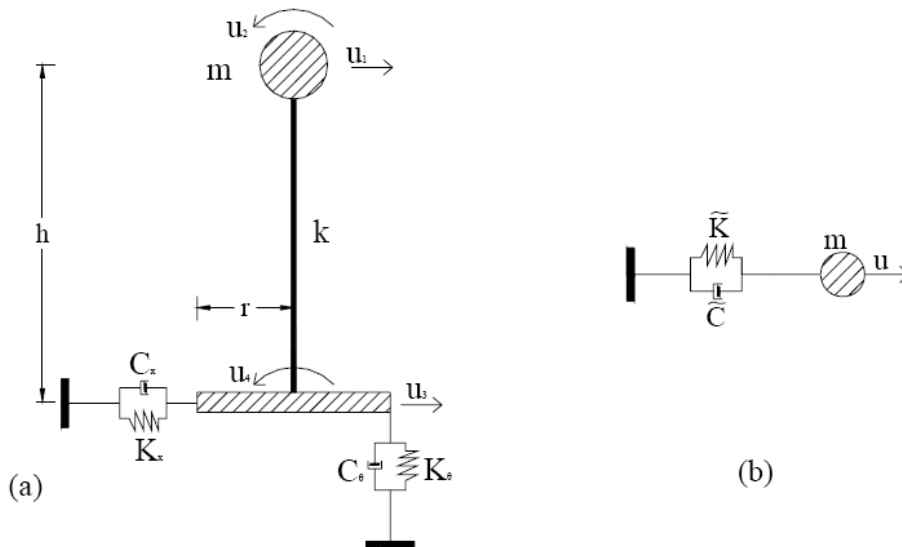


Figure 3.6) Structure idealized by a stick model, (b) reduced single degree-of-freedom model

On this theory the scaling laws for oscillator mass are presented. With the aim to analyse the behaviour of pile with different pile head condition and the inertial effects with influence of the oscillator, five different pile head conditions are tested, chapter 4 . In case of an oscillator (SDOF) (figure 3.7) structure is attached to a pile, it have to computed a value of the mass of oscillator.

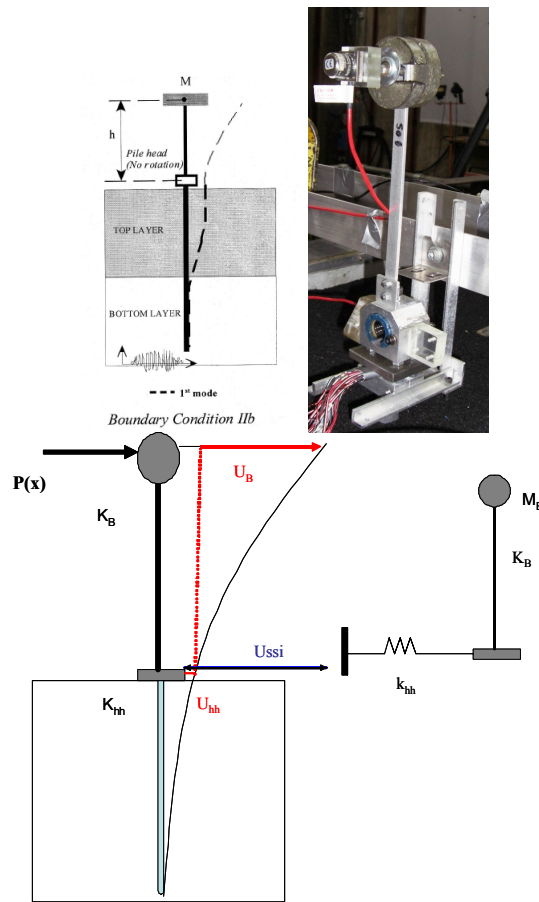


Figure 3.7: Pile head condition: no rotation head + oscillator

The calculation of weight of oscillator has been done, taken some reference work on scaling factor. In figure 3.6 the oscillator typically use in the experimental work is shown.

The scheme shows in figure 3.7 it references to a single degree of freedom system (SDOF) fixed to an no rotation pile head support.

During the motion it has been considered only translational dynamic impedance, as shown in figure 3.7.

The response of the soil-structure system depends on the mechanical properties of the foundation, the soil, the superstructure and the characteristics of the excitation.

The total displacement of the soil –structural-system is equal to u_{ssi} :

$$u_{SSI} = u_B + u_{hh} \quad [3.15]$$

The displacement is also defined by equation [3.16] following reported:

$$u_{SSI} = \frac{P}{k_{ssi}} \quad [3.16]$$

Hence equation [3.15] is equivalent to equation [3.17], following reported.

$$\frac{P}{k_{SSI}} = \frac{P}{k_B} + \frac{P}{k_{hh}} \quad \text{or} \quad \frac{1}{k_{SSI}} = \frac{1}{k_B} + \frac{1}{k_{hh}} \quad [3.17]$$

The fundamental quantities are K_{ssi} , the stiffness of soil-pile-structure system, K_B is stiffness of the building, in this case is the stiffness of the oscillator and K_{hh} is the dynamic impedance in lateral direction (pile-soil stiffness in lateral direction). Hence multiplied equation 3.17 for the value of mass of the oscillator, M_B , equation [3.18] has been obtained:

$$\frac{M_B}{k_{SSI}} = \frac{M_B}{k_B} + \frac{M_B}{k_{hh}} \quad [3.18]$$

In general the stiffness of soil-pile-structure system K_{ssi} , is obtain as a function of the all stiffness present (equation 3.19):

$$K_{ssi} = \frac{K_B K_{hh}}{K_B + K_{hh}} \quad [3.19]$$

The other fundamental parameters are: ω_{ssi} , the natural frequency of superstructure-pile-soil; ω_{hh} swaying oscillations of the base and ω_B oscillations of the superstructure (foundation assumed rigid). Equations [3.20], [3.21], [3.22] show the expression of fundamental quantities.

$$\omega_{ss} = \sqrt{\frac{K_{SSI}}{M_B}} \quad [3.20]$$

$$\omega_B = \sqrt{\frac{K_b}{M_B}} \quad [3.21]$$

$$\omega_{hh} = \sqrt{\frac{K_{hh}}{M_0}} \quad [3.22]$$

From equation [3.18], the natural frequency of superstructure-pile-soil ω_{ssi} is reported:

$$\omega_{SSI}^{-2} = \frac{M_B}{k_B} \left(1 + \frac{k_B}{k_{hh}} \right) \quad [3.23]$$

Known the characteristic of the soil-structure system, from equation [3.23], it is possible to obtain the value of M_B weight of the oscillator.

The non-dimensional group to study the inertial interaction is the normalised first natural frequency denoted by β , the frequency ratio, given by the following expression [3.24]:

$$\beta = \frac{\bar{\omega}}{\omega_n} \quad [3.24]$$

Where $\bar{\omega}$ is the natural frequency of superstructure-pile-soil, and ω_n is the natural frequency of the input motion.

The above frequency ratio represents the key dimensionless group that should be preserved between the model and the prototype if the SSI effect has to be replicated (Veletsos 1977; Mylonakis & Gazetas 2000)

The requirement for scaling it to conserve this dimensionless group to study the inertial interaction is following shown by equation [3.25]:

$$\left(\frac{\bar{\omega}}{\omega_n} \right)_{model} = \left(\frac{\bar{\omega}}{\omega_n} \right)_{prototype} \quad [3.25]$$

From this assumption and from equation [3.23] the formulation of mass it has been obtained. The equation obtained the superstructure mass is given by equation [3.26]:

$$M_B = \frac{\beta \cdot k_B}{\left[1 + \frac{k_B}{k_{hh}} \right] \cdot \left(\frac{\omega_{nm}}{\omega_{np}} \right) \cdot \omega_{np}^2} \quad [3.26]$$

where ω_{nm} and ω_{np} are the natural frequencies of the input motion in the model and in prototype, respectively. The all stiffness value and formulation are following reported:

- K_{hh} is the dynamic impedance in lateral direction. In equation [3.27] is reported the expression:

$$K_{hh} = 4 E_p I_p \lambda^3 \quad [3.27]$$

where the λ expression is following reported (equation 3.28):

$$\lambda = \left[\frac{\delta E_s}{4 E_p I_p} \right] \quad [3.28]$$

Noting that K_s can be related to relative pile-soil stiffness ratio (E_p/E_s) through Winkler factor (δ) given by equation 3. 29) following Dobry et al.(1982).

$$\delta = 1.67 \left[\frac{E_p}{E_s} \right]^{-0.053} \quad [3.29]$$

The estimation of K_{hh} is obtained for Push test (Chapetr 4, section 4.3) on the pile. The value of K_{hh} depends from the first layer of the deposit: for Rubber is 66 N/mm and for LB fraction E is 153 N/mm. ω_p is frequency of input motion in rad/sec

- K_B is the stiffness of superstructure. It has been chosen an aluminium bar with two different heights, and rectangular cross section. In equation 18) is reported the expression of the stiffness of superstructure:

$$K_B = \frac{3E_{bar} \left(\frac{a_{bar} b_{bar}^3}{12} \right)}{h_{bar}^3} \quad [3.30]$$

where E_{bar} is the value of Young's modulus of bar used for the oscillator.

Dimension of Bar				
E_{bar}	a_{bar}	b_{bar}	I_{bar}	h_{bar}
MPa	mm	mm	mm ⁴	mm
70000	12	3	27	200/400

So that different values of weight of oscillator are estimated. The scaling factor laws apply to the weight mass; have been only a reference to have an idea of the weight of the mass to use for the test. Any prototype has been simulated.

3.5 Experimental set up

The Bristol Laboratory for Advanced Dynamic Engineering (BLADE) shaking table is the main facility for experimental research into earthquake engineering at the University of Bristol.

3.5.1 Shaking table at BLADE laboratory

The Earquake simulator consists of a 3 m x 3 m cast aluminium platform weighing 3.8 tonnes and capable of carrying a maximum payload of 15 tonnes. The platform has the shape of an inverted pyramid made from four sections and has a honeycomb-like network of stiffening diaphragms giving it high strength and bending stiffness.

The platform surface is an arrangement of 5 aluminium plates with a regular grid of M12 bolt holes for attaching to the platform body and for mounting of specimens.

The platform sits inside a reinforced concrete seismic block that has a mass of 300 tonnes. The block is located in a pit in the Earthquake Engineering Laboratory and is isolated from the rest of the laboratory by a 20 mm cork filled gap running between the block and the rest of the laboratory. Hydraulic power for the ES is provided by a set of 6 shared variable volume hydraulic pumps providing up to 900 litres/min at a working pressure of 205 bar. The maximum flow capacity can be increased to around 1200 litres/min for up to 16 seconds at times of peak demand with the addition of extra hydraulic accumulators. The platform is attached to the block by eight hydraulic actuators arranged so as to make best use of the space available. The horizontal actuators are attached to the block by concrete filled steel box sections and to the platform by smaller closed triangular brackets. The vertical actuators are connected directly to the block and platform. Each actuator has a dynamic capacity of 70 kN and has a maximum stroke of 300 mm. The four vertical actuators each have a static section to carry the static loads of the platform plus specimen. The table has an operating frequency range of 0-100Hz, the maximum operative frequency is 60Hz.

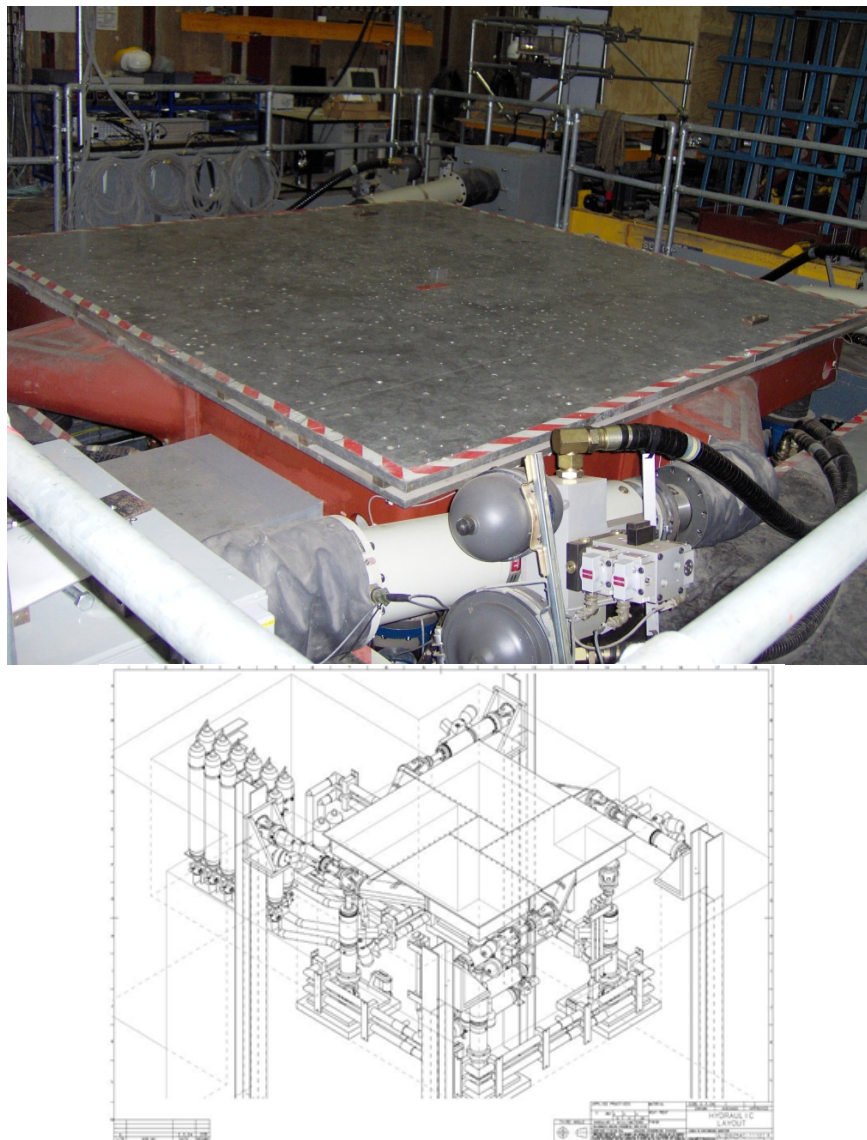


Figure 3.8: Shaking table at Bristol University (BLADE laboratory)

3.5.2 *Digital Spectrum Analyser*

A digital spectrum analyzer (Advantest 9211C) have been employed in the dynamic measurements (shape modes, natural frequency of vibration, damping). The analyzer computes the frequency response function (FRF) function between the input and the output signals of interest. The frequency response function is applied to the product between the signal data and a window function (rectangular). The rectangular window function is zero valued outside a chosen frequency interval. The rectangular window function has been proved to work well in the low dynamic range, when the signals have comparable strengths and frequencies. The FRF measurements have been processed using curve-fitting algorithms that take the experimentally measured FRFs and fit them to an analytical function using a least squared error technique. The poles of the transfer function have been used to compute the viscous damping for various modes of vibration.

3.5.3 *Soil container: “Shear stack”*

Shaking table soil containers are commonly used to investigate a wide variety of earthquake engineering problems.

A number of different designs have been presented, they generally consist of hollow boxes secured at their base to a shaking table and filled with a test soil. Boundary effects induced by the container walls must be minimized according to the modeling application. To model liquefaction, for example, the large lateral displacements associated with a liquefied soil must be unimpeded. Thus, the ‘laminar box’ was devised (e.g. Hushmand et al., 1988, Ueng et al., 2006). These containers are constructed from a stack of stiff rings each capable of independent and unrestrained lateral displacement giving the box negligible shear stiffness. Internal walls of the rings are made smooth to restrict boundary shear stresses.

When liquefaction is not of interest boundaries must be both frictional and flexible. For instance, Zeng & Schofield’s (1996) Equivalent Shear Beam (ESB) centrifuge container, has roughened internal walls to enable shear stress transmission. It was constructed from an alternating stack of aluminium alloy and rubber rings for flexibility. The composite shear stiffness of the ESB was tuned to the dynamic stiffness of a test soil by careful detailing of the rubber layer thickness. This design specification is rather restrictive since soil-stiffness degradation ensures it can be achieved at only a single level of seismic excitation. For other soils and other levels of excitation the ESB malfunctions by either constraining or enhancing the dynamic lateral soil displacements. The term ‘shear stack’ refers to those containers designed and built to enable geotechnical modelling in conjunction with the shaking table at the University of Bristol. The latest incarnation is a direct descendant of the ‘large flexible shear stack’ described by Crewe et al. 1995.

However, the new stack is closer in size to Dar’s 1993 original: 1.2m long as opposed to 5m, 0.55m wide as opposed to 1m, and 0.8m deep as opposed to 1.2m, significantly reducing

the costs and time scales associated with testing. The apparatus consists of eight aluminium rings, rectangular in plan, which are stacked alternately with rubber sections to create a hollow yet flexible box which can be filled with the test soil. The rings are constructed from aluminium box section to minimise inertia while providing sufficient constraint for the K_0 condition. It is intended that the composite shear stiffness of the stack be significantly less than the shear stiffness of an included soil deposit. In this way the deposit drives the response, not the stack. The stack is secured to the shaking table by its base and shaken horizontally lengthways (in the y direction). Its floor is roughened by sand-grain adhesion to aid the transmission of shear waves; the internal end walls are similarly treated to enable complementary shear stresses. Internal side walls are lubricated to make easier shaking on Y direction. The inside surface of longitudinal walls of the stack has been covered with silicone grease and a new latex membrane has been fitted (Figure 3.10).

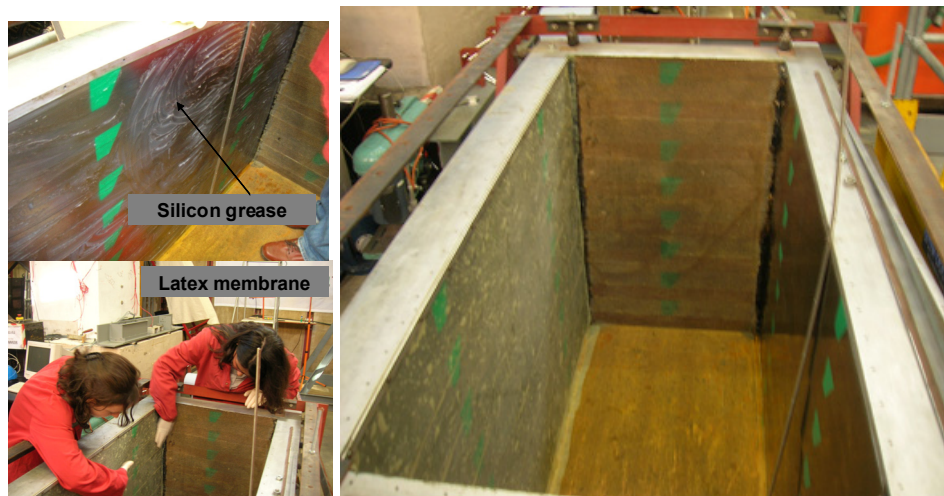


Figure 3.9: Shear stack

Figures 3.2 and figure 3.9 show the rigid steel restraining frame and the system of bearings used to prevent unwanted motion in the x and z-directions (red structure). The performance of the shear stack is of major importance to the SSI seismic test series.

The shear stack model is normally prepared on the shaking table. The instruments that are used are listed.

1. Accelerometers SETRA: to measure accelerations in dynamic tests;
2. LVDT (Linearly varying differential transformers):to measure displacements (contact device);
3. Displacement transducer CELESCO: to measure displacements (device) of the shear stack;
4. Strain Gauges: to measure strain in model structure.

3.5.4 Accelerometers

Accelerator type SETRA 141A were used to measure the accelerations in the model. Fifteen accelerometers are used to record the lateral acceleration response in the y-direction, one in z-direction. The accelerometers are high output capacitance type with inbuilt pre-amplifiers which operate over a frequency range of 0 to 3000Hz (Calibrated range: +/-8g).

As depicted by circles in figure 3.10, six sensors are secured at different z-ordinates to the external walls of the stack. Four sensors are encased within an aluminium box with roughened external faces and embedded during sample deposition within the deposit. The box dimensions are designed to give an average mass density equivalent to that of the sand deposit. Two sensors are positioned on sand surface, in two different position. Also there are one located on the pile head and one on the structure (on the oscillator). The SETRA accelerometer signals have been amplified by a set of Fylde 245G miniampifiers. These have multiple gain, variable sensitivity and offset options. The amplified signal have been supplied to a FERN EF6 multi-channel programmable filter that have been set at a common cut-off frequency on all channels (80 Hz)(Dietz et al.,2007).

3.5.5 Linearly Varying Differential Transformer (LVDT)

LVDT's were used to measure the displacements of the pile-cap in the vertical direction. They were powered by 10V AC supply. They had a maximum stroke length of 22mm and were calibrated against a micrometer. This is an electromagnetic device that produces an electrical voltage proportional to the displacement of a movable magnetic core. The calibration constant is typically 1.5 mm/volt to 3.5 mm /volt. Figure 3.11 (a) shows a typical LVDT and Figure 3.11(b) shows the working principle. In the Figure 3.11(b) P denotes primary coil and S the secondary coil. When the magnetic core is displaced from null position, an electromagnetic imbalance occurs. This imbalance generates a differential AC output voltage across the secondary coils, which is linearly proportional to the direction and magnitude of the displacement.

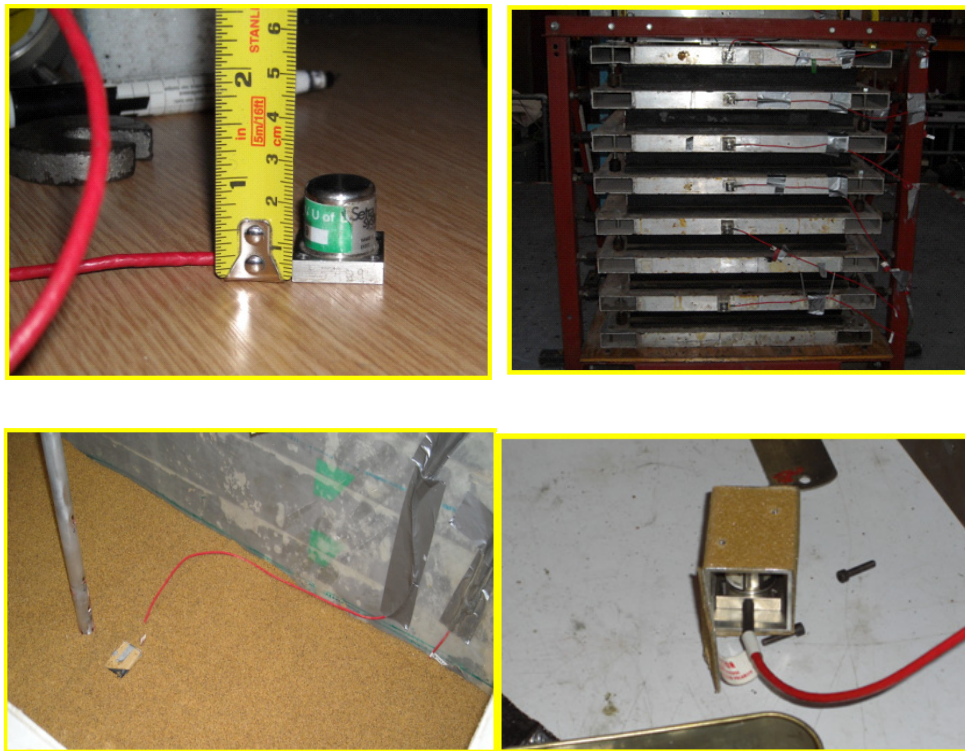


Figure 3.10: (a) Accelerometer Setra 141 A (b) accelerometer outside shear stack (c) accelerometer inside shear stack (d) accelerometer in an aluminium box with roughened external faces

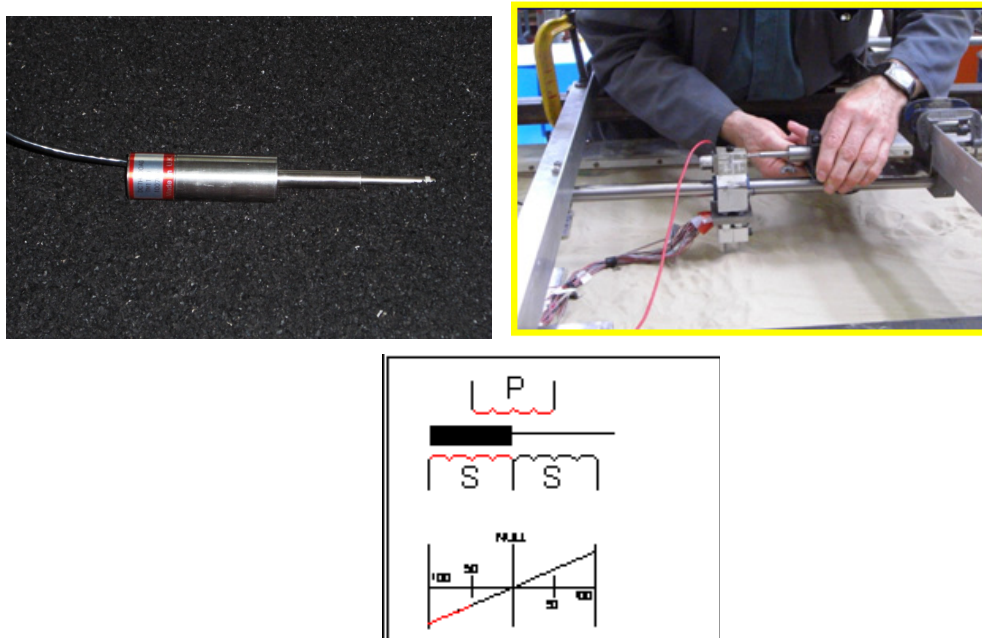


Figure 3.11: (a) LVDT; (b): LVDT at top head pile; (c) Working principle of LVDT

3.5.6 Displacement Transducer (CELESCO)

The CELESCO transducer, type PT101 have been used to measure the displacements of the shear stack. They are used to monitor the displacement in Y direction, they are positioned on the rings 1, 2, 4, 8. They are a potentiometer displacement transducers, and the Range: 0-300 mm. They have been calibrated. An RDP 600-type modular electronics system has been supplied the excitation voltage for the displacement transducers and the strain gauges. The completion of the bridge and the excitation voltage for the strain gauges have been made via RDP 628-type strain gauge amplifier modules installed in the RDP 600 rack.

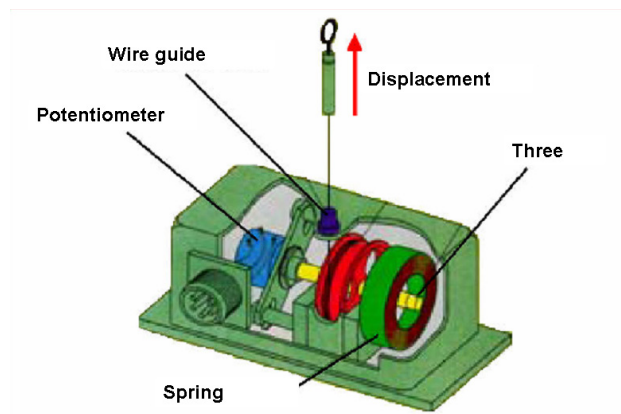
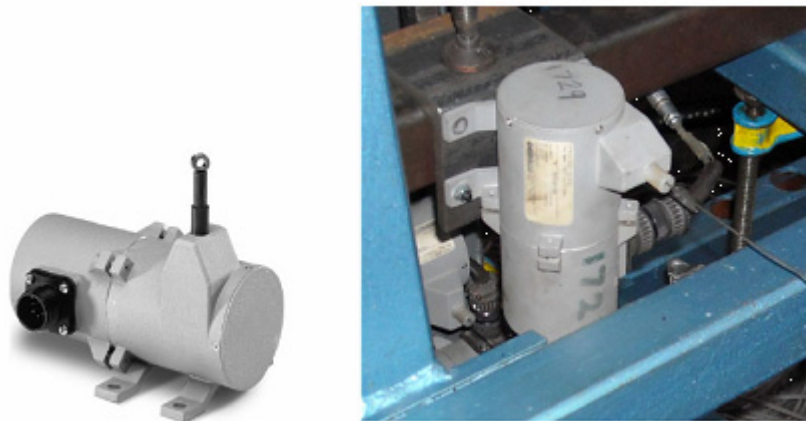


Figure 3.12: (a) CELESCO Transducer

3.5.7 Strain gauges

On the external pile surface, eighteen strain gauges are located at eight different elevations. They are used to monitor the bending strain of pile embendend in sand, on y-direction

The strain gauges are EA13-120LZ-120 (vishay ltd), they are linear strain gauges and their length is 3 mm. At interface beetwen two layer, in corrispondence of the half hight of shear stack, two strain gauges on x-direction are positioned. They are usefull to valuete possible torsional effects on pile. Figure 3.12 b-d.

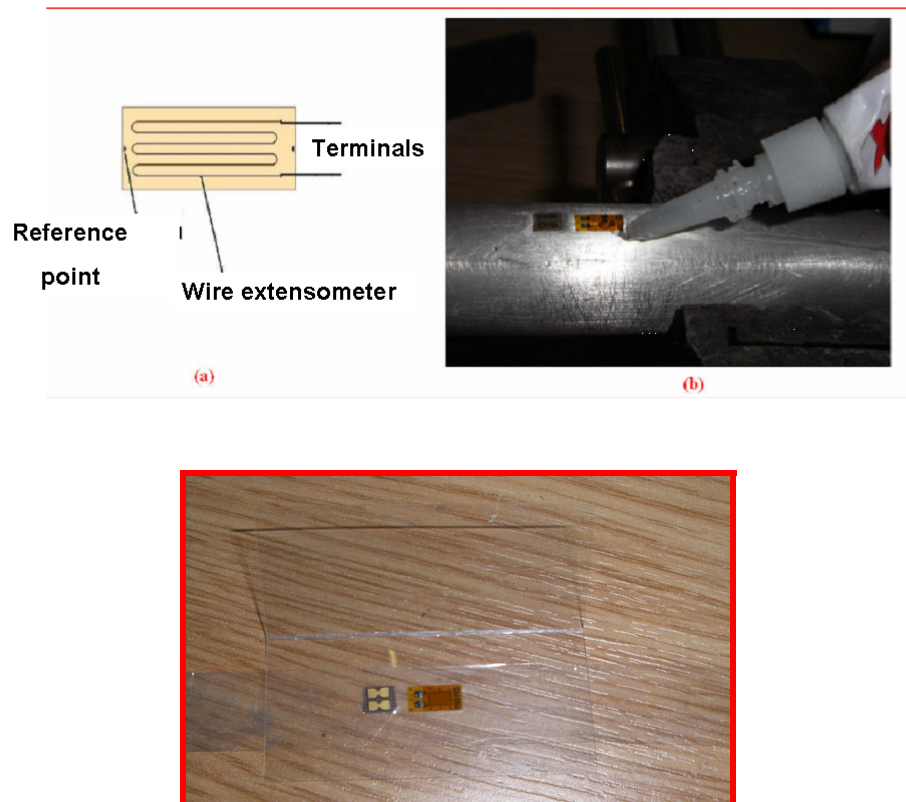


Figure 3.12: (b) strain gauge schema; (c):paste strain gauge;(d) strain gauges used in the test

3.5.8 Earthquake input motions

Real acceleration records of three Italian earth-quakes (Friuli (1976), Irpinia (1980) and Norcia (1998)) were employed in testing. The following real accelerograms were selected: Tolmezzo-A270, Sturmo-A000, and Norcia-R090. Italian recordings from the database SISMA (Scasserra et al. 2008; <http://sisma.dsg.uniroma1.it>) have been used as input motions in the numerical analyses. The accelerograms have been chosen in such a way that their original peak ground accelerations are as close as possible to the reference maximum peak acceleration on soil type A of the selected seismic zone.

Table 3.2 shows the characteristic of input motion, the predominant frequency is defined as the frequency of the vibration corresponding to the maximum value of the Fourier amplitude spectrum (Kramer, 1990).

Table 3.2: Input motion

Input Motion	ID	PGA	ΔT	Duration	Arias Intensity	Frequency Band	Frequency predominant	Frequency mean(*)
		g	s	s	m/s	Hz	Hz	Hz
Sturmo 000	A-STU 000	0.226	0.0024	18	1.102	2-3	2.34	1.47
Tolmezzo 270	A-TMZ 270	0.315	0.005	37	1.202	1-3	1.49	1.96
Norcia Umbra 090	R-NCB 090	0.311	0.005	23	0.209	4-6	5.98	5.56

The mean frequency is defined by Rathje et al. (1998) (*) formulation following reported:

$$T_m = \left[\frac{\sum_i C_i^2 \left(\frac{1}{f_i}\right)}{\sum_i C_i^2} \right] \quad [3.31]$$

where C_i is the Fourier amplitudes of the entire acceleration time history; f_i is a discrete Fourier transform frequencies between 0.25 and 20 Hz. The Fourier amplitude is defined as the square root of the sum of the squares of the real and imaginary parts of the Fourier coefficient. T_m is similar to the mean square frequency.

In figures 3.13, 3.14 and 3.15 the time histories and the FFT of the three input motion are shown.

From table 3.1 (scaling factor law), the required scaling factor for seismic amplitude is one, (one-g scale modelling), but all input motion are scaled to 0.3 g to compare with prototype

analysis. From Table 3.1 (scaling factor law), the required scaling factor for seismic input frequency is $n^{0.75} = 15.25$, where $n=37.5$ is the scaling factor for length.

The maximum Fourier amplitude regions are (1-3) Hz for Tolmezzo-A270, (2-3) Hz for Sturmo-A000 and (4-6) Hz for Norcia Umbra-R090. Scaling up the frequency by a factor of 15, would bring the maximum energy regions to frequencies with maxima lying around the 60Hz region.

The earthquake simulator at Bristol operates well in the (0-50) Hz range, therefore a small reduction of the scaling factor for frequency was needed.

A scaling factor of 12 was considered achievable for the matching of the given acceleration histories. The 12 times scaled acceleration histories were fed into the time wave replication software associated with the shaking table. the shaking table were generated.

The iterative process of matching involved calculation of FFTs of the scaled input time histories followed by the calculation of test response spectra from the table output time histories.

By adjusting the required magnitude of response for each frequency, command signals (displacement time histories) for the shaking table were generated.

Scaling factors of 2 and 5 were also employed in order to understand the pile response at different input magnitudes.

Figures 3.15 a,b show the matched time histories for the un-scaled and the 12 times scaled input for Sturmo-A000.

Table 3.3 shows the characteristic of input motion scaled. For different scaling factor are reported the values of: predominant frequency, Arias intensity, duration and PGA.

The Figures 3.16 a,b, c-Figures 3.17a b, Figures 3.1208 a, b,c are shown the Fourier transform and time histories for each input motion, for different scaling factor .

Table 3.3 : Earthquakes scaled

Input Motion	Scaling factor	PGA scaled	Duration	Arias Intensity	Frequency Band	Frequency predominant
		g	s	m/s	Hz	Hz
STU 000	12	0.3	2	0.209	24-50	43.99
STU 000	5	0.3	4	0.266	2-12	11.76
STU 000	2	0.3	9	0.94	0.7-6	4.712
TMZ 270	12	0.3	3	0.173	24-50	47.92
TMZ 270	2	0.3	19	0.583	3-4	2.979
NCB 090 (E)	12	0.3	2	0.209	24-70	47
NCB 090 (E+R)	12	0.1	2	0.047	25-45	47
NCB 090	5	0.3	5	0.051	25-45	29.9
NCB 090	2	0.3	12	0.133	8-12	11

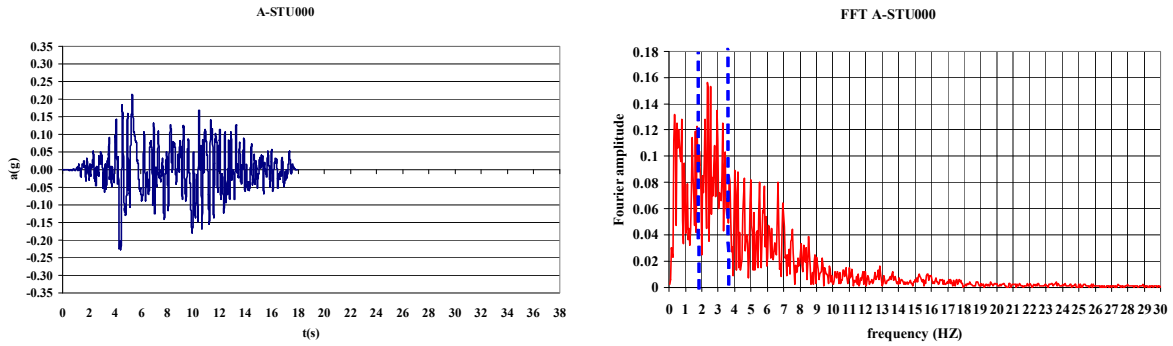


Figure 3.13: original A-STU000(a) acceleration time history (b)FFT

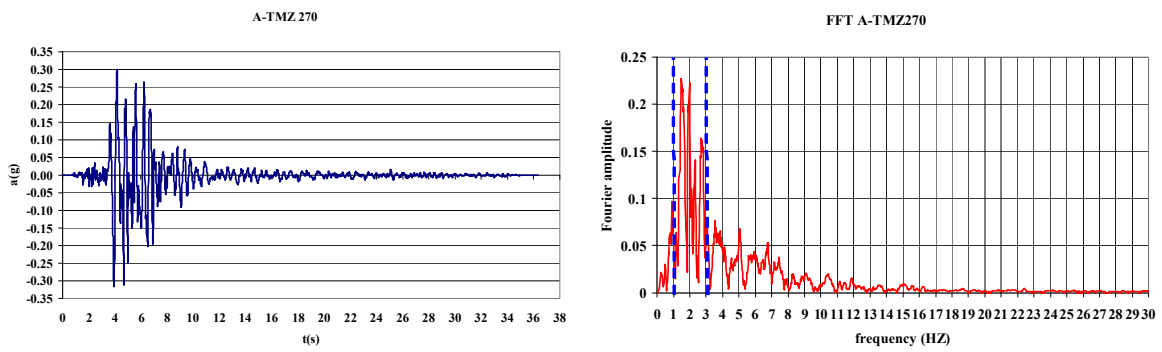


Figure 3.14: original A-TMZ 270:(a) acceleration time history (b)FFT

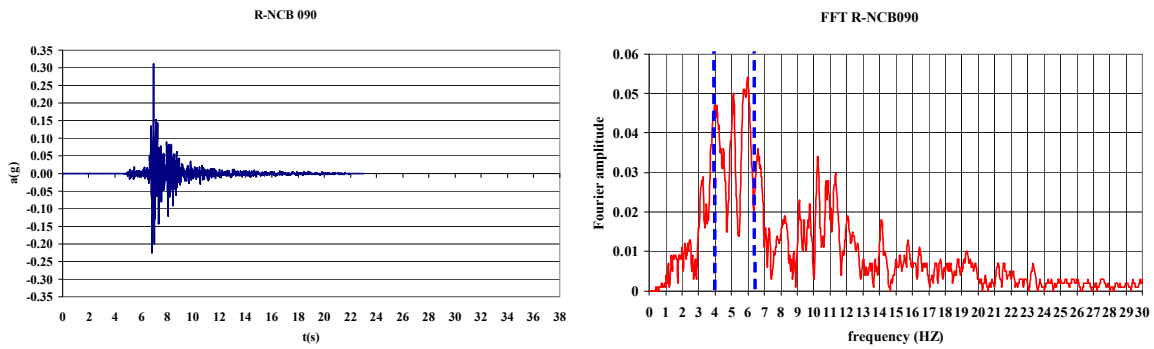


Figure 3.14: original R-NCB 090(a) acceleration time history (b)FFT

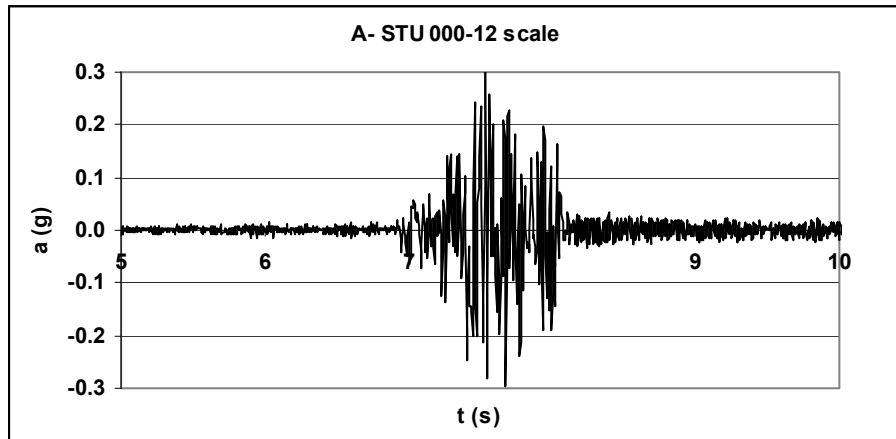


Figure 3.15: A SU000 (a) 12 scale acceleration time history

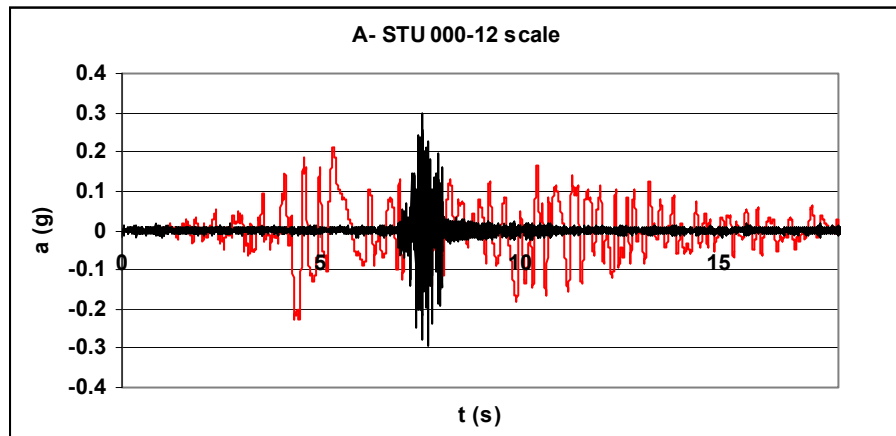


Figure 3.15: A SU000 (b) un-scaled and scaled STU000

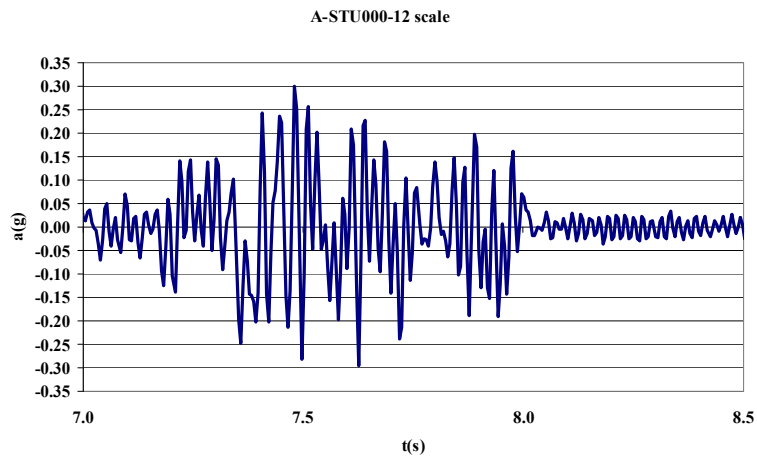


Figure 3.16: A-STU 000 12 scale (a) acceleration time history

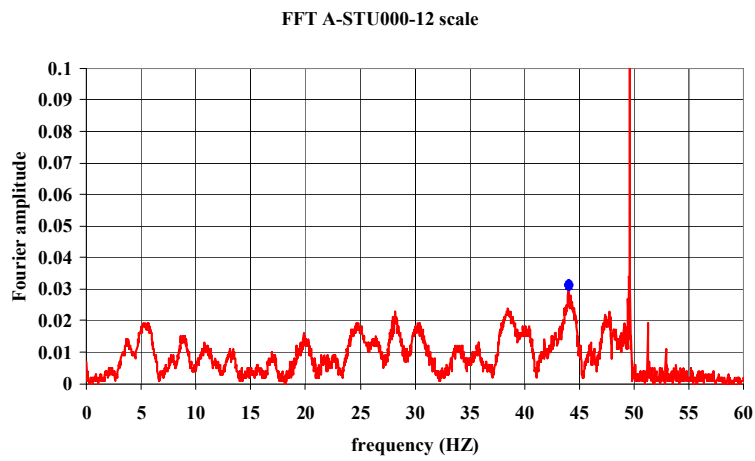


Figure 3.16 A-STU 000 12 scale (b) Fourier Spectrum

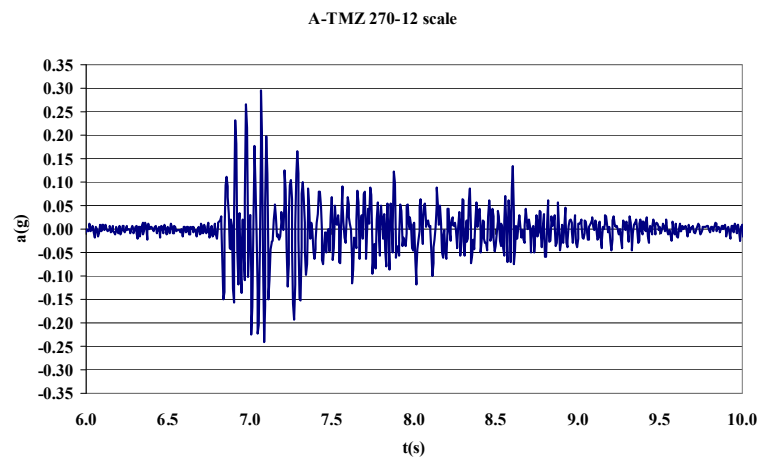


Figure 3.17: 12 scale A-TMZ 270 (a) acceleration time histories

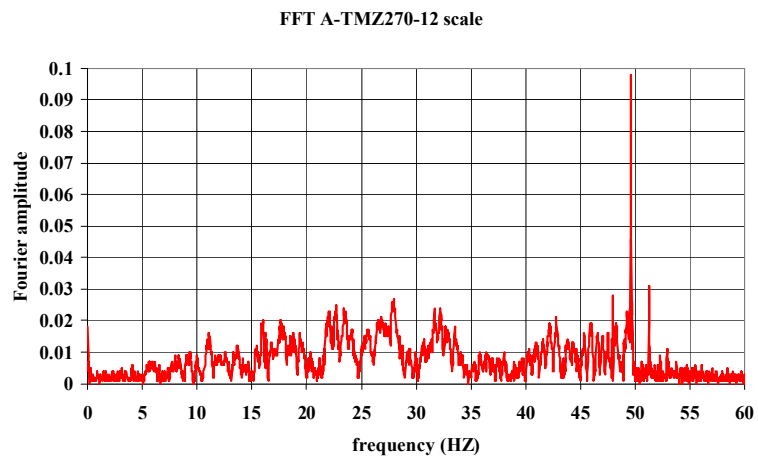


Figure 3.17: 12 scale A-TMZ 270 (b) Fourier spectrum

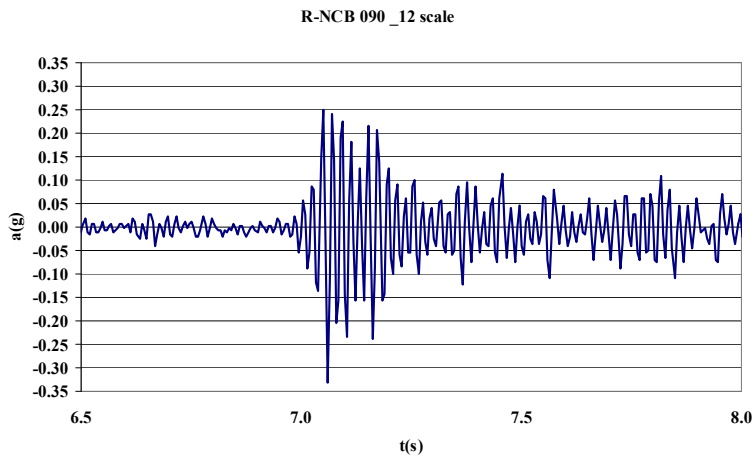


Figure 3.18: 12 scale R NCB090 (a) acceleration time history (E)

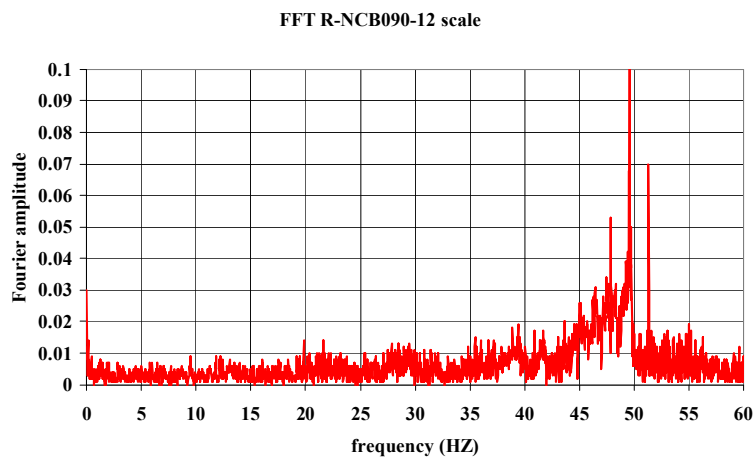


Figure 3.18: 12 scale R NCB090 (b) Fourier spectrum (E)

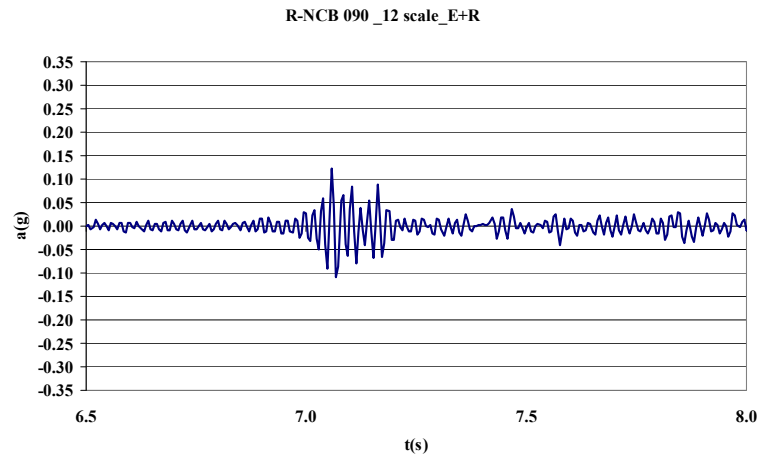


Figure 3.19: 12 scale R NCB090 (a) acceleration time history

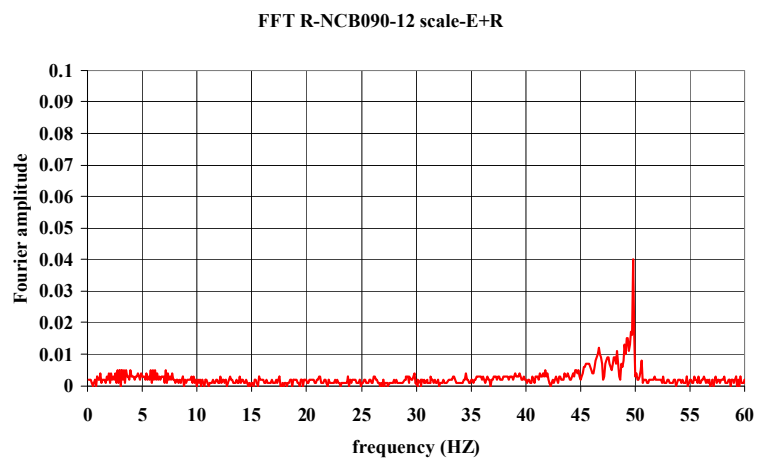


Figure 3.19: 12 scale R NCB090 (b) Fourier spectrum (E+R)

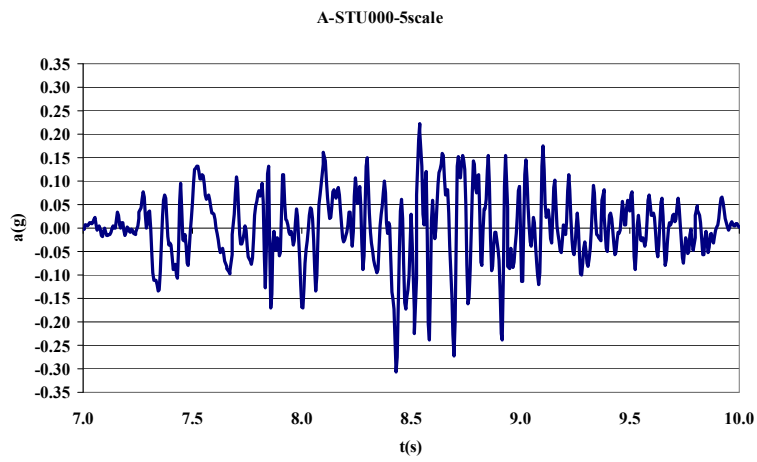


Figure 3.20 5 scale ASTU000 (a) acceleration time history

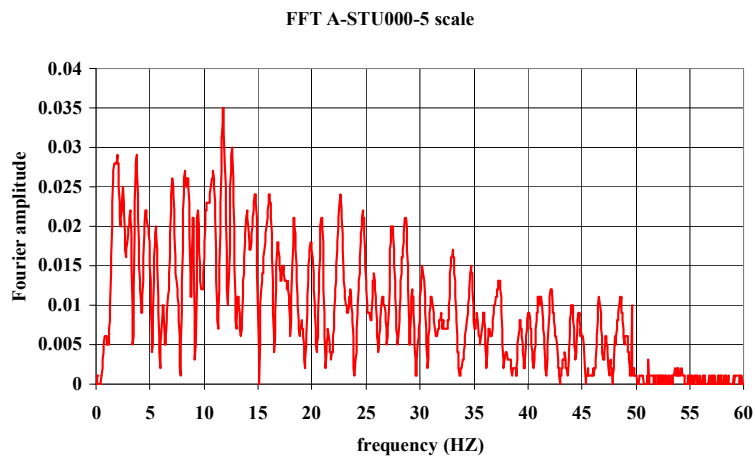


Figure 3.20 5 scale ASTU000 (b) Fourier spectrum

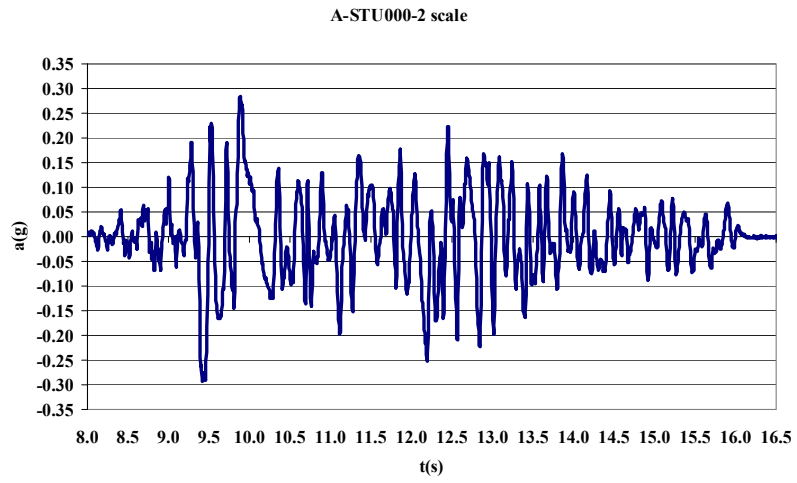


Figure 3.21:2 scale A STU000 (a) acceleration time history

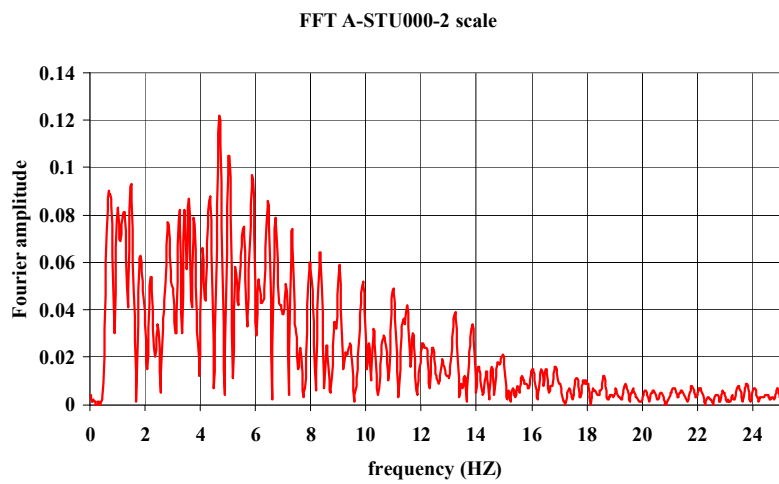


Figure 3.21:2 scale A STU000 (b) Fourier spectrum

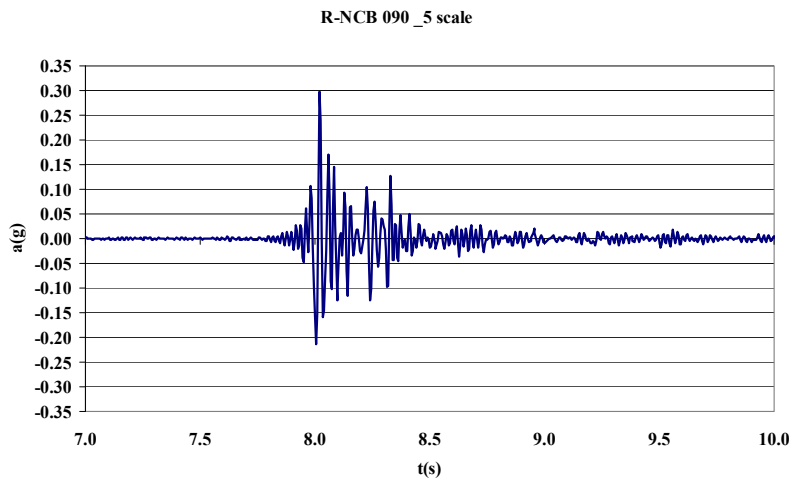


Figure 3.21: 5 scale R NCB090 (a) acceleration time history

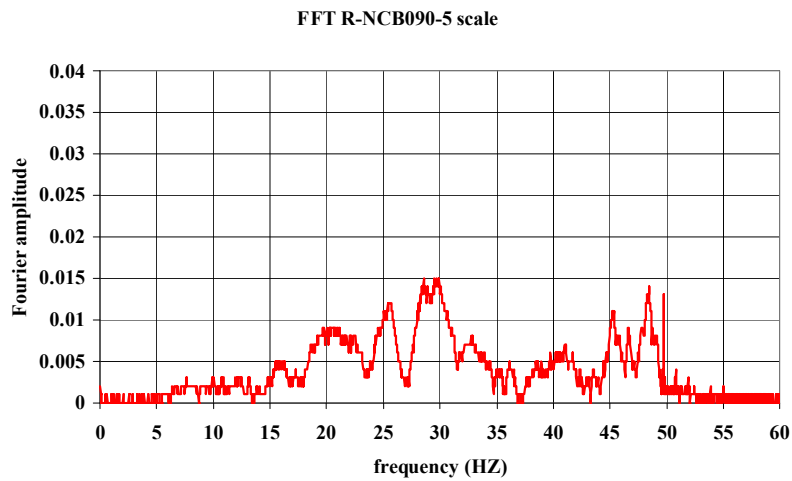


Figure 3.21: 5 scale R NCB090 (b) Fourier spectrum

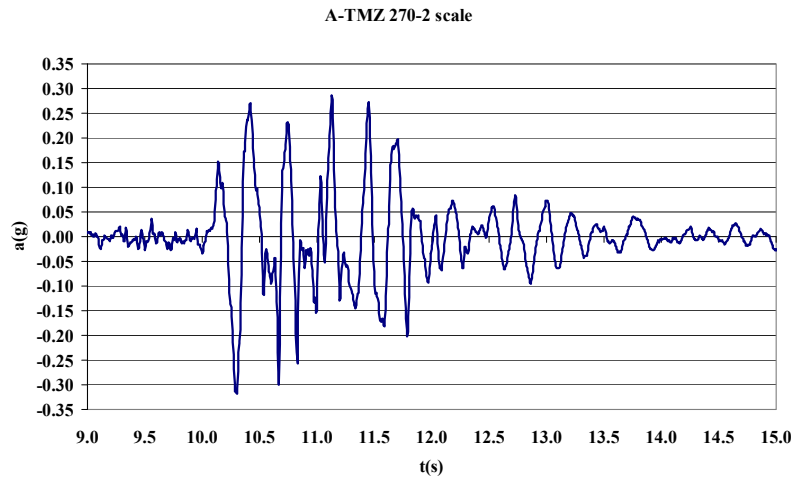


Figure 3.22:2 scale ATMZ 270 (a) acceleration time history

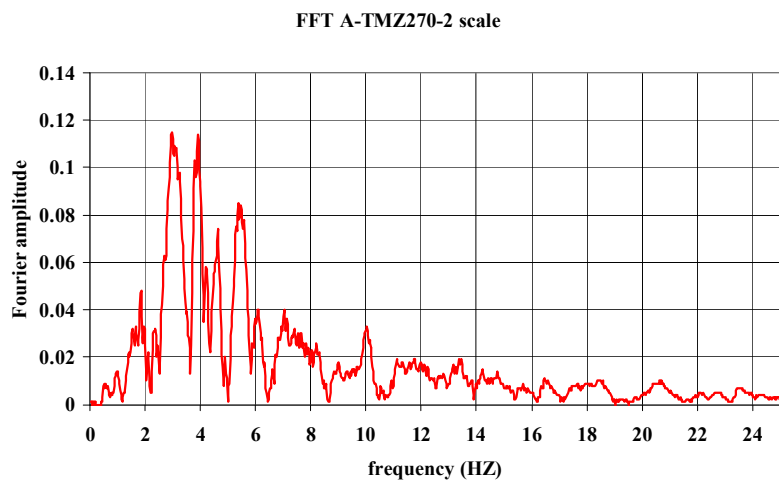


Figure 3.22:2 scale ATMZ 270 (b) Fourier spectrum

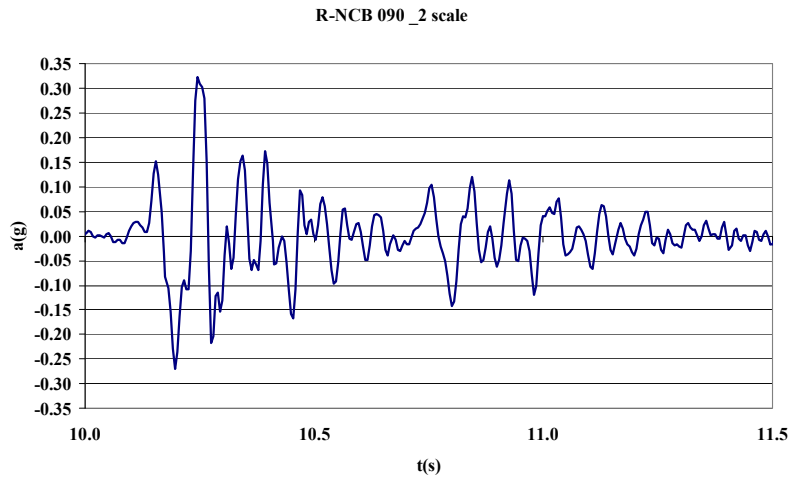


Figure 3.23: 2 scale R NCB090 (a) acceleration time history

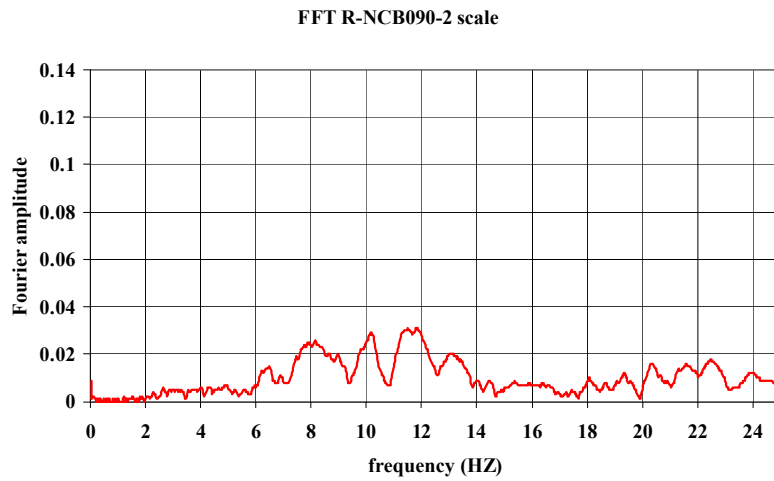


Figure 3.23: 2 scale R NCB090 (b) Fourier spectrum

4. Experimental testing on materials

4.1 Testing plan

Around forty hundred shaking table tests were carried out in soil model, in order to study the effects of dynamic load on piles and to understand the importance of kinematic effects in the dynamic response of soil-pile system.

The test program involves the combinations of different: soil configurations, pile head conditions and input motions. For all tests, the model of pile is an aluminium alloy pile (Tube). Table 4.1 summarises the test program. Three different soil configurations are tested in shear stack, they are characterized by different values of shear wave velocity contrast between lower (V_{s2}) and upper (V_{s1}) layer. In particular they are: a monolayer configuration (E); a layered sand deposit BE+E ($V_{s2}/V_{s1} \sim 1.6$); a layered deposit with the biggest stiffness contrast value ($V_{s2}/V_{s1} \sim 8$). (Figure 4.1).

The development of the model piles and the different pile condition analyzed, are discussed in detail in section 4.6. In Annex I there is a list of all tests with each peculiarity.

In this chapter the proprieties of model of pile used in the tests are illustrated and the results of soil tests have been reported.

Table 4.1: Test program

	V_{s2}/V_{s1}	Materials	Earthquake	Scaling factor	N° TEST	Type tests
DYNAMIC TESTS	1	E: LB fraction E	A-STU000; A-TMZ270; R-NCB090	1:12; 1:5; 1:2	113	Dynamic test and Pulse test for different five pile head conditions
	1.6	BE+ E: Bottom layer: LB fraction B+E; Upper layer: LB fraction E	A-STU000; A-TMZ270;	1:12; 1:2	93	
	8	E+R Bottom layer: LB fraction E; Upper layer: Rubber	A-STU000; A-TMZ270; R-NCB090	1:12; 1:5; 1:2	98	

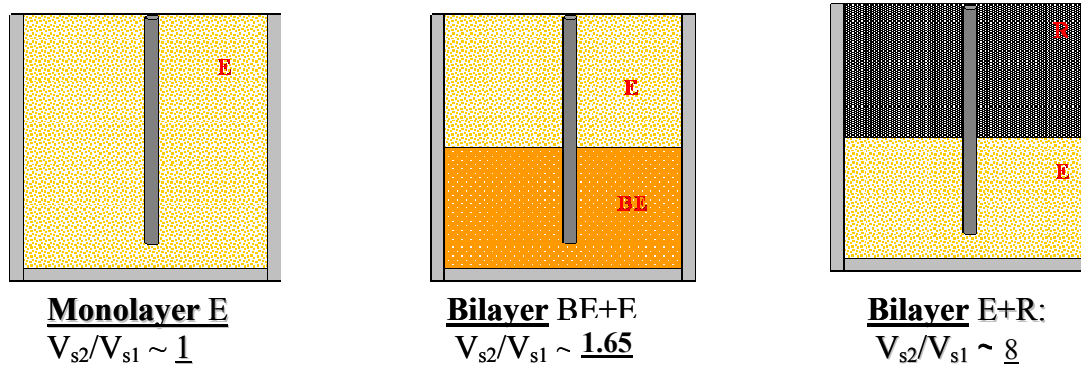


Figure 4.1 Soil configurations tested: (a) Monolayer configuration; (b) – (c) layered configuration

4.2 Model pile proprieties

As explained in Chapter 3, the theoretical model employed for pile modelling is in Muir Wood (2004). The pile was assumed to behave as an Euler-Bernoulli beam in pure bending for which the horizontal deflection by equation 3.1.

From the physical model an aluminium pipe alloy has been chosen, this material is widely used for experimental work on the shaking table or centrifuge machine (Meymand, 1998; Hoe I. Ling, 2003, Suzukii 2003). From the prototype the diameter of the solid concrete pile is equal to 600 mm and Young's modulus is 25 GPa. By adopting an aluminium alloy model pile ($E_{Al} = 70$ GPa) and applying the geometry scaling law (see Table 3.1) the outside diameter and the length of pile has been obtained as shown in figure 3.5 and in equation 3.10. The smallest thickness aluminium tube that was commercially available at the time of testing was the 6063-T6 HE9TF aluminium alloy tube of thickness $t = 0.71$ mm and outer diameter $D_o = 22.23$ mm. This tube has been adopted for the model pile. In table 4.2 and in figure 4.1 are shown the proprieties of the model pile tested.

Table 4.2 Proprieties of model pile used in test

Material	Length	Outside Diameter	Thickness	Inside Diameter	Young Modulus	Yield Stress
	L	Do	t	Di	E	σ_{yield}
	[mm]	[mm]	[mm]	[mm]	[GPa]	[MPa]
6063T6HE9TF Aluminium alloy	750	22.23	0.71	20.83	70	260



Figure 4.2: Aluminium alloy pile

On the external pile surface, eighteen strain gauges are located at eight different elevations. Four holes at different elevations on pile are made. These holes became necessary to allow the passage of the wires from internal to external surface of the pile. The wires are utilized to connect the strain gauges to the amplifier; they are located inside the pile to reduce the contact with the sand during the dynamic test. Figure 4.3 shows the scheme with strain gauges position and holes position. In section 3.3 the proprieties of the strain gauges are explained.

The bottom of pile is hinged on a flexible support (figure 4.4 b)) to avoid displacement of pile during the dynamic test. Before start the pluviation procedure, the pile is positioned in the shear stack as shown in figure 4.4.c). A metal hold has been used to fix the position of pile during filling of the shear stack (figure 4.4 c) d)).

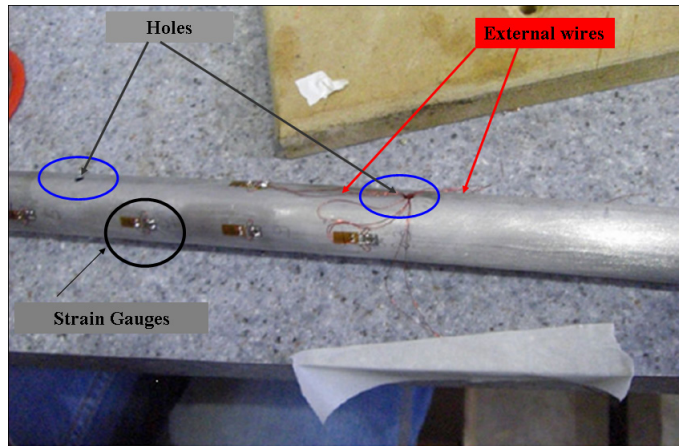


Figure 4.3 (a) Strain gauges on aluminium alloy pile

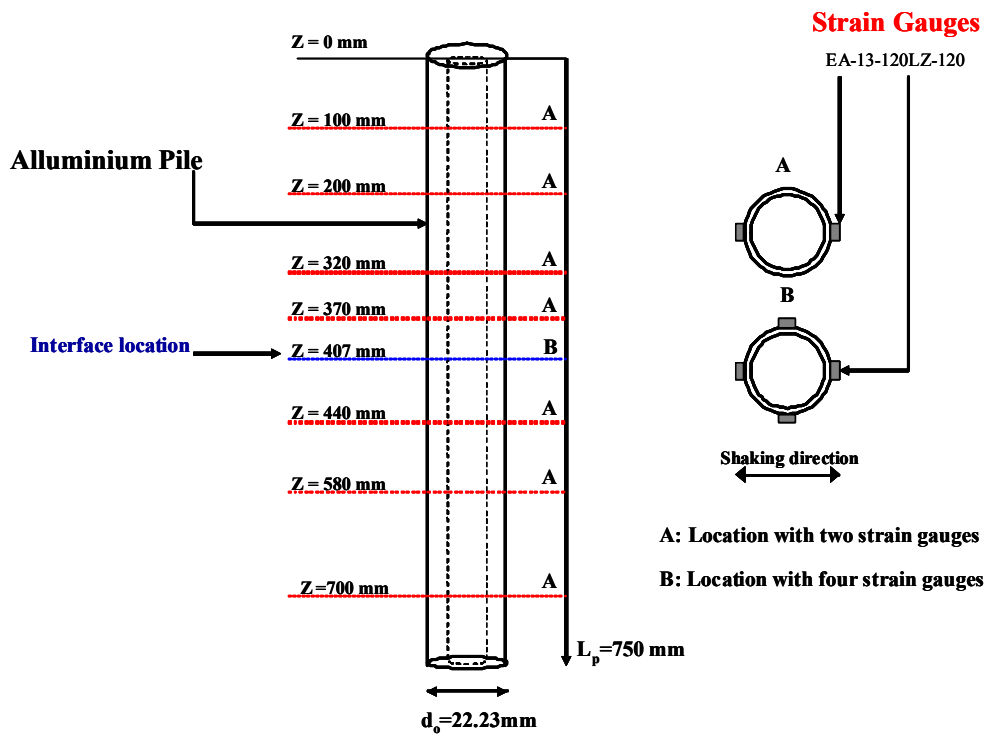


Figure 4.3 (b) locations of strain gauges along pile



Figure 4.4:(a) View of the strain gauged pile in shear stack (b) flexible support for the pile on the bottom of shear stack



Figure 4.4:(c) Pile in shear stack before pluviation (d) pile during pluviation

With the aim to analysed the behaviour of pile with different pile head condition, five different pile head conditions are tested. As shown in figure 4.5 and figure 4.6 two basic pile head conditions have been tested:

1) Boundary condition I: free head pile (FH pile). For this configuration three types of pile head condition have been done: a simply free head pile (FH); a free head with in addition a mass on pile head (FH+M) and free head pile in addition mass on the pile head and an oscillator (FH+M+SDOF) (figure 4.5).

2) Boundary condition II: no rotation pile head (NRH pile). For this configuration two types of pile head conditions have been done: a simply no rotation pile head (NRH pile) and a no rotation pile head with an oscillator located on the top (NRH+SDOF) (figure 4.6).

The structure of the oscillator (SDOF) consists in aluminium flat bar 12 x 3 mm (rectangular section) and a steel mass on the top of the bar. Two different highs of the flat bar have been chosen (400mm and 200mm). The weight of mass of the oscillator depends on frequency of input motion and of the stiffness of the global system: soil-pile-superstructure. The formulation uses to obtain the value of the mass for each test has been explained in Chapter 3, also all values of mass of superstructure for each test is reported in the Annex II. In figure 4.7 are reported the two different types of oscillator tested.

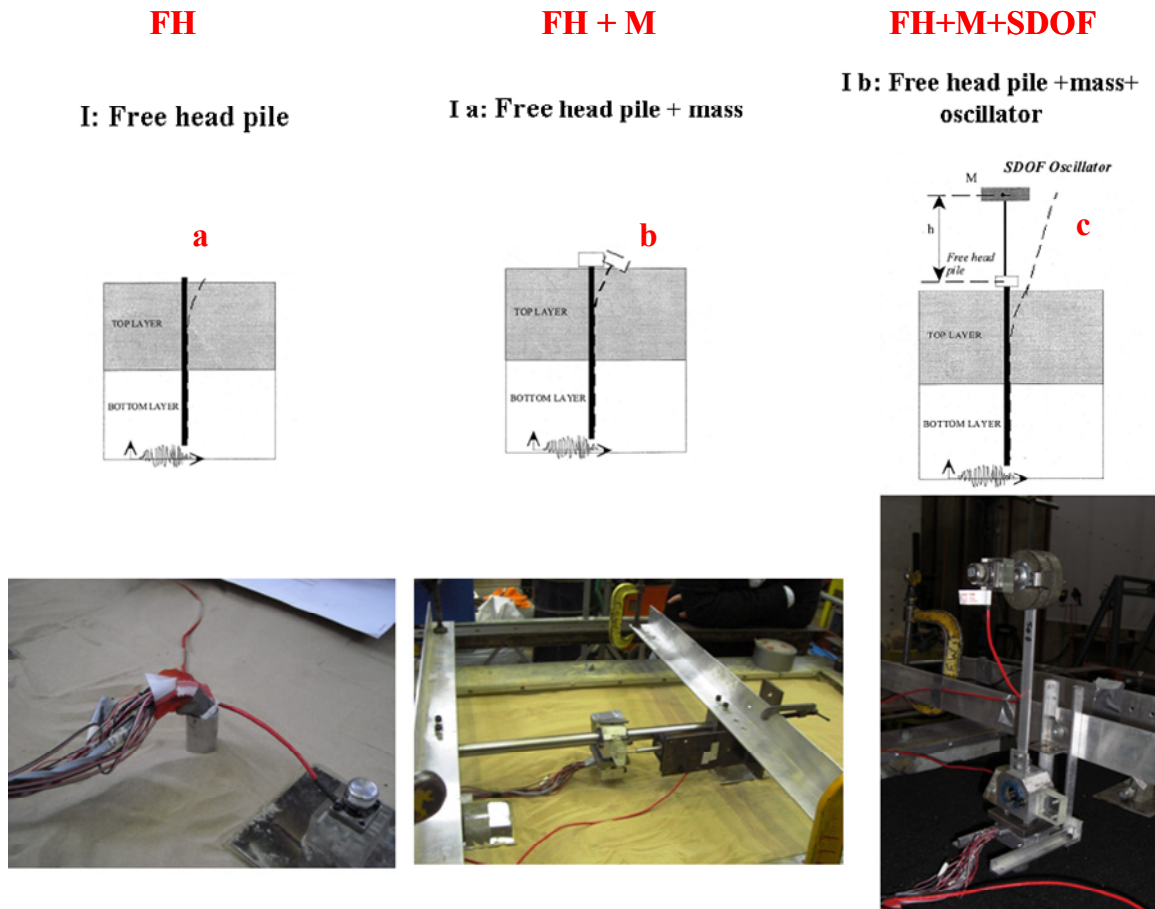
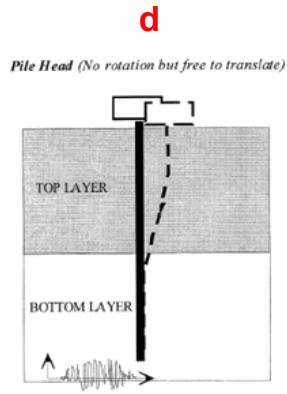


Figure 4.5:(a) FH pile (b) FH pile + mass(c) FH pile+mass+SDOF

NRH

IIa: No rotation pile head



NRH+SDOF

IIb: No rotation pile head + oscillator (SDOF)

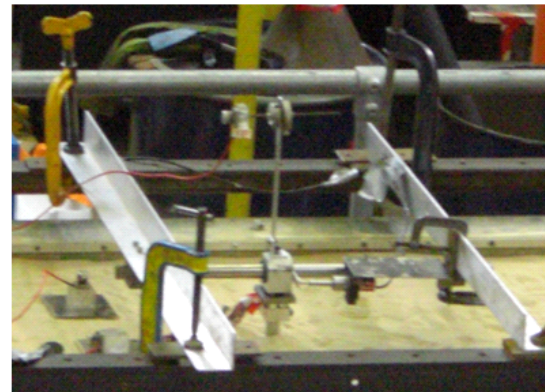
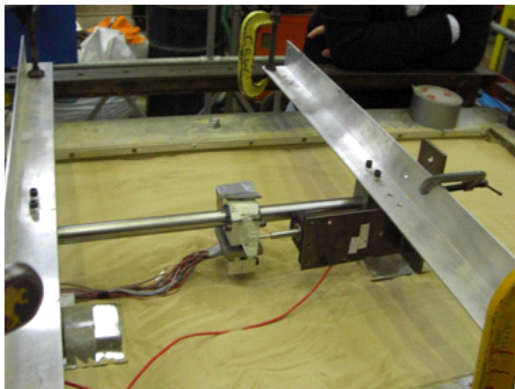
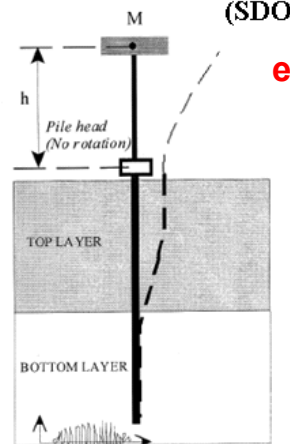


Figure 4.6:(d) NRH pile (e)NRH pile+ oscillator

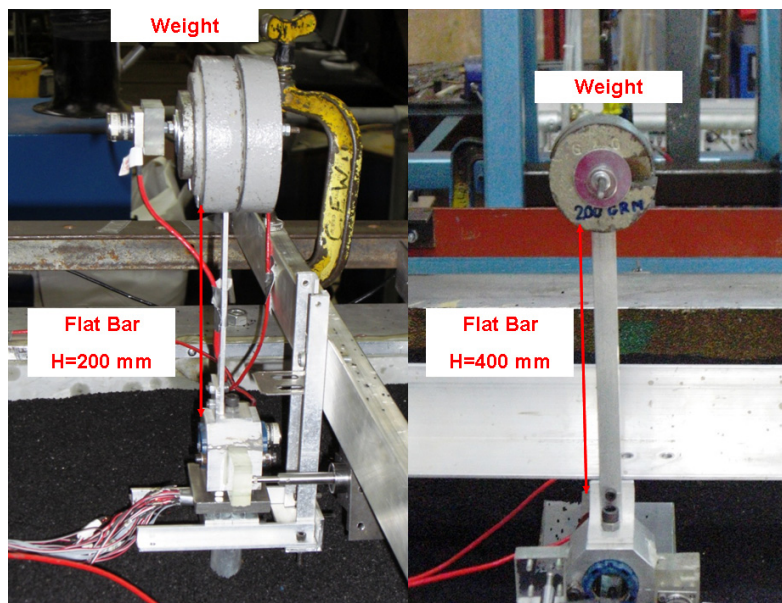


Figure 4.7 View of SDOF on the pile head: H=200mm and H=400 m

4.2.1 Bending test

The relation between the bending moment and the pile curvature has been determined experimentally. The bending test has been conducted to find the plastic moment capacity of the pile section.

The bending capacity of the pile have been measured and compared with the theoretical plastic moment capacity. A layout of the bending testing rig is shown in Figure 4.8 a)

The experimental set up of a 4-point bending test is shown in Figure 4.8 b). The load has been applied in two positions and a displacement gauge measures the central deflection. The central portion of the beam has a constant bending moment and no shear force, hence this test is often termed as *pure bending* by structural engineers. The test is load-controlled and the load is increased gradually manually until the section form is near a plastic hinge. The estimation of curvature comes out from the central deflection.

The beam (pile) is loaded in 4-point bending as shown in Fig 4.8. The beam is loaded from the top, so that the lower bearing support bar moves downwards. The result is an uniform curvature over the central portion of the beam. Since the curvature is uniform the central section can be consider a part of an arc of a circle with a radius r . One half of the central section is shown in figure 4.8 (d). The radius of curvature is related to the measured central deflection and may be determined from equation 4.1:

$$r^2 = (r - \delta)^2 + (b / 2)^2 \quad [4.1]$$

where δ is the measured deflection. This may be simplified by neglecting δ^2 terms since δ is so small compared with r , yielding, and b is the distance between the deflection gauge feet. The curvature is $1/r$ and the moment is expressed respectively in equation 4.2 and 4.3:

$$\frac{1}{r} = \left(\frac{b^2}{8\delta} \right) \quad [4.2]$$

$$M_f = \left(\frac{P}{2} \right) a \quad [4.3]$$

Hence for each load the relative deflection and curvature have been expressed. In figure 4.9 a) two load-deflection curves are shown: the blue line and the red line respectively refer to the test done on pile with and without holes. Figure 4.9 b) shows the plot of moment versus curvature. Based on the test data the measured plastic moment capacity of the section is 90000 N x mm or 0.09 KN m.

This value has been compared with the theoretical yielding moment obtains by equation 4.4, (Bhattacharya, 2003) following reported:

$$M_{theoretical} = \left(\frac{d_{out}^3}{6} - \frac{d_{in}^3}{6} \right) \sigma_y \quad [4.4]$$

The theoretical moment is equal to 0.085 KN m. This is the yielding moment value used in the test. Figures 4.9 c) e d) show the pile before and after the bending test.

Table 4.3 Yielding moment of model pile used in test

Material	I	EI	ϵ_y	ϵ_y	My	My
	[mm ⁴]	[KNxmm]		%	[Nxmm]	[KN x m]
6063T6HE9TF Aluminium alloy	2780	194624	0.003714	0.37	84000	0.085

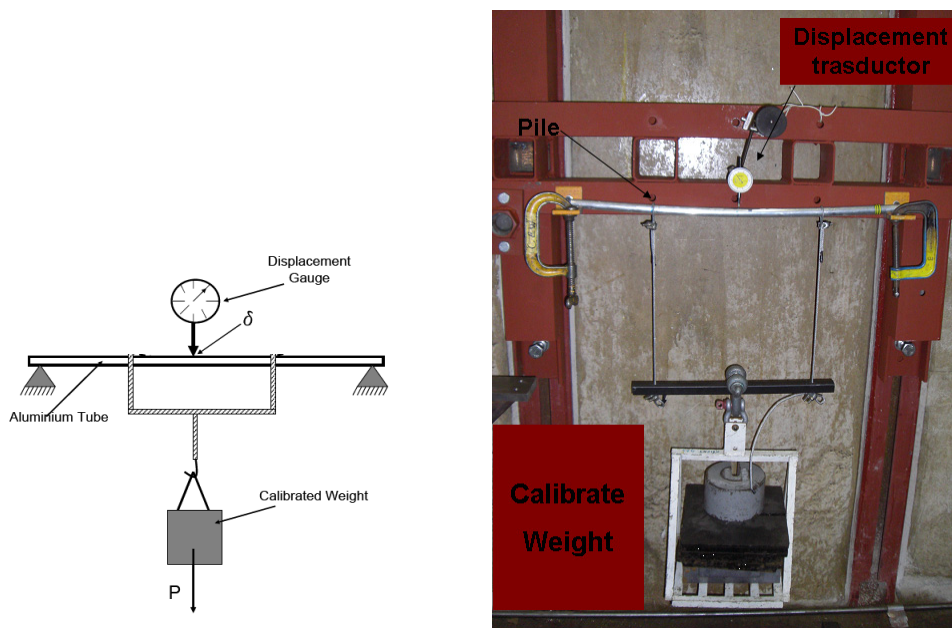


Figure 4.8: (a) scheme of bending test (b) instrumentations for bending test

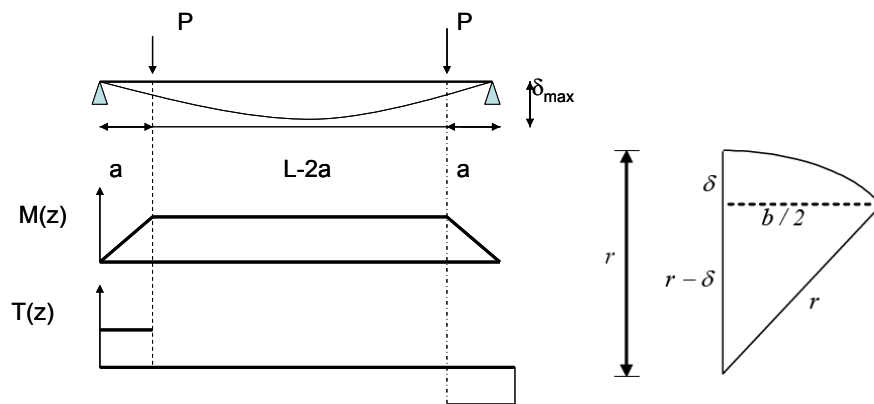


Figure 4.8: (c) representation of moment and shear force on the pile (d) deflected shape of beam

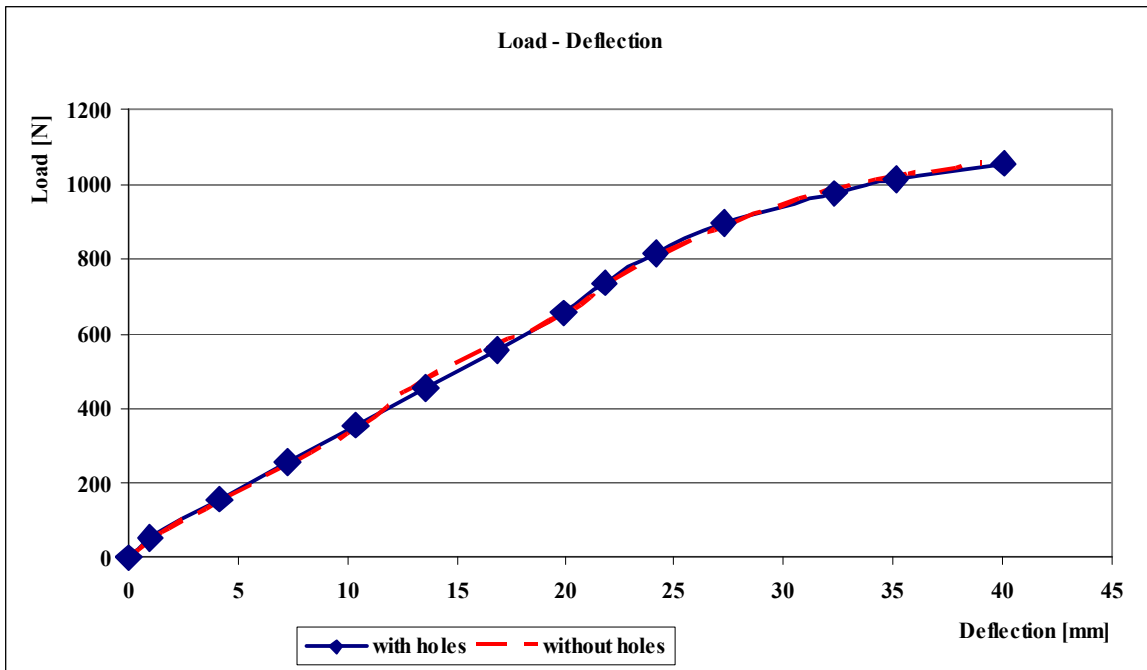


Figure 4.9 a) bending test results: Load – Deflection

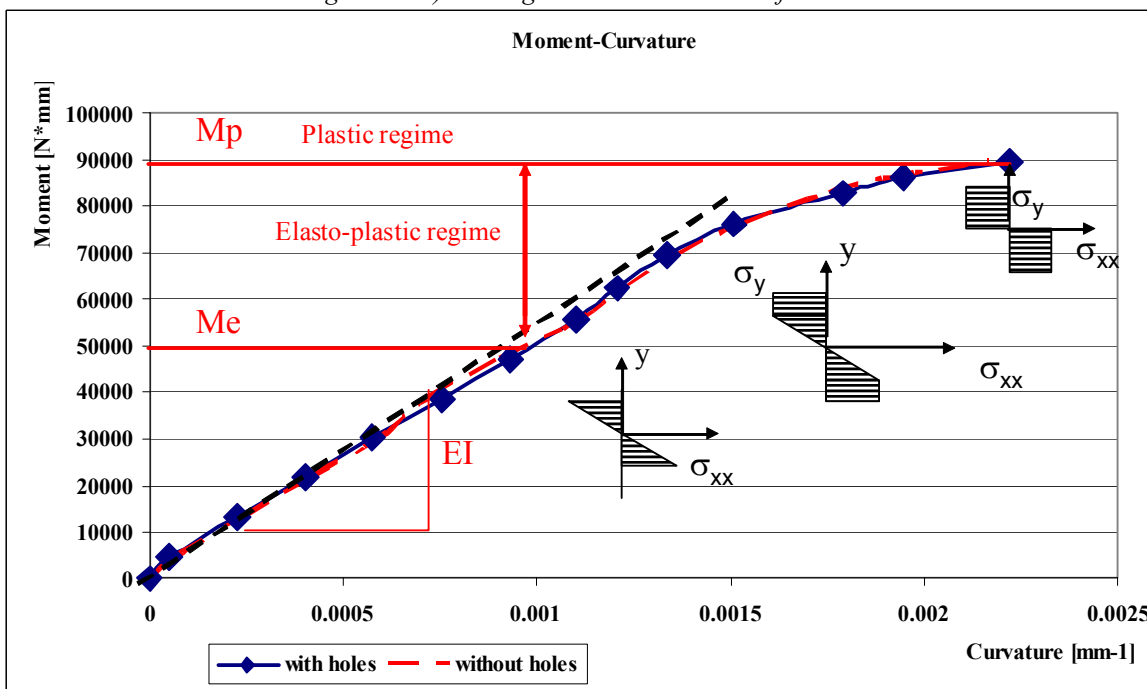


Figure 4.9 b) bending test results: Moment – Curvature

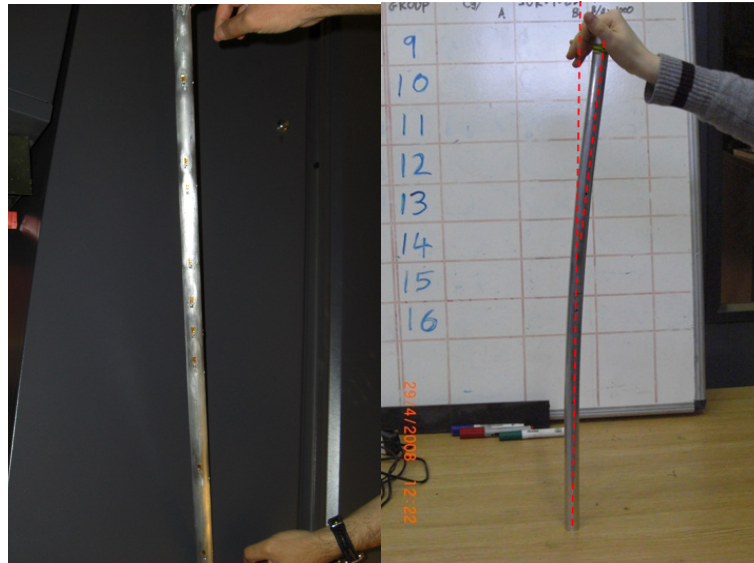


Figure 4.9 c) pile before the bending test d) pile after the bending test

4.2.2 Push test

To evaluate the soil-pile relative stiffness a spreading loading (Push test) test has been done. A layout of the push testing is shown in Figure 4.10 b). The experimental set up of push test is shown in Figure 4.10 a). The load is applied on the pile head and the displacement is measured by a displacement gauge or LVDT. The test is load-controlled and the load is increased gradually manually.

The value of relative stiffness K_{xx} is calculated from the load-deflection curve, the formulation is following reported:

$$K_{xx} = \left(\frac{\Delta P}{\Delta \delta} \right) \quad [4.5]$$

where ΔP is the first incremental load and $\Delta \delta$ is the incremental displacement at head pile.

For the two different soil configurations, E+R (Leighton Buzzard fraction E+ Rubber) and E (Leighton Buzzard fraction E) the load - deflection diagrams are plotted in Figures 4.11 and 4.12.

The values of relative stiffness K_{xx} are 66 N/mm, for E+R configuration, and 153 N/mm for monolayer configuration E. The K_{xx} value is influenced from the top layer in the soil deposit, therefore the same value of K_{xx} is obtained for monolayer configuration (E) and for layered configuration BE+E (top layer Leighton Buzzard fraction E and bottom layer mixer of two types of Leighton Buzzard sand).

4.5.1

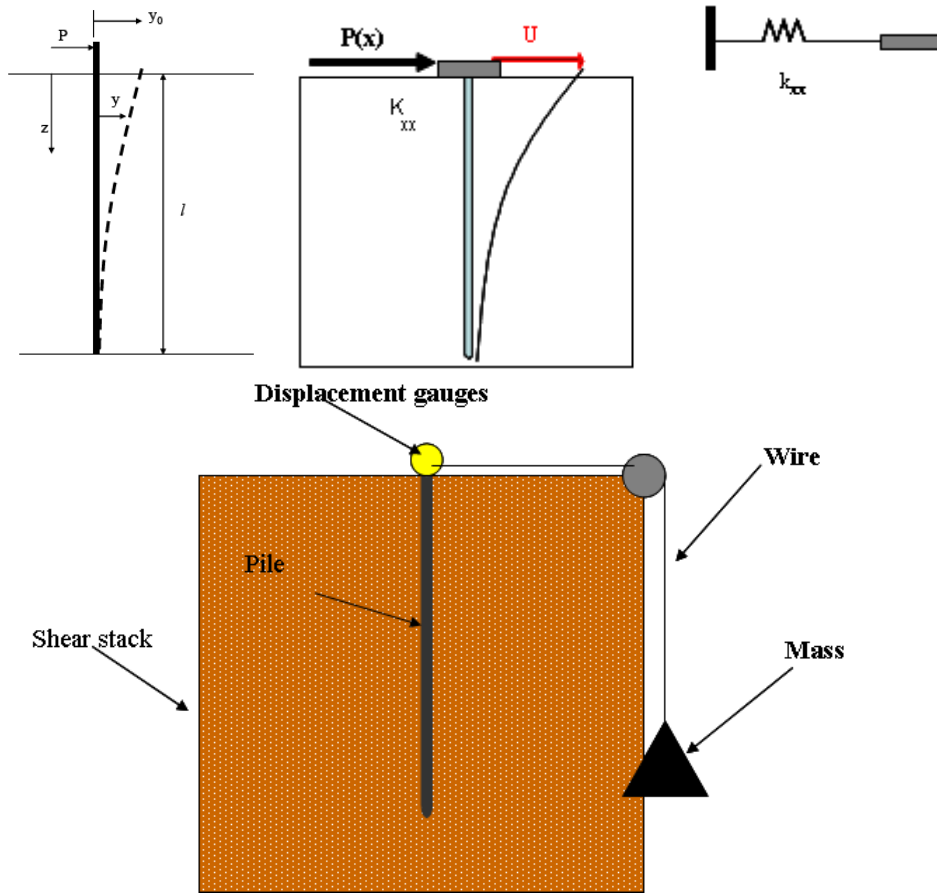


Figure 4.10 a) schema of push test

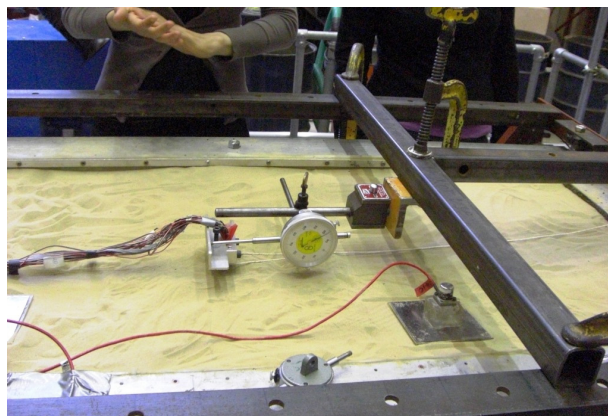


Figure 4.10 b) layout of push test in the shear stack

Rubber + LB fraction E
(E+R)

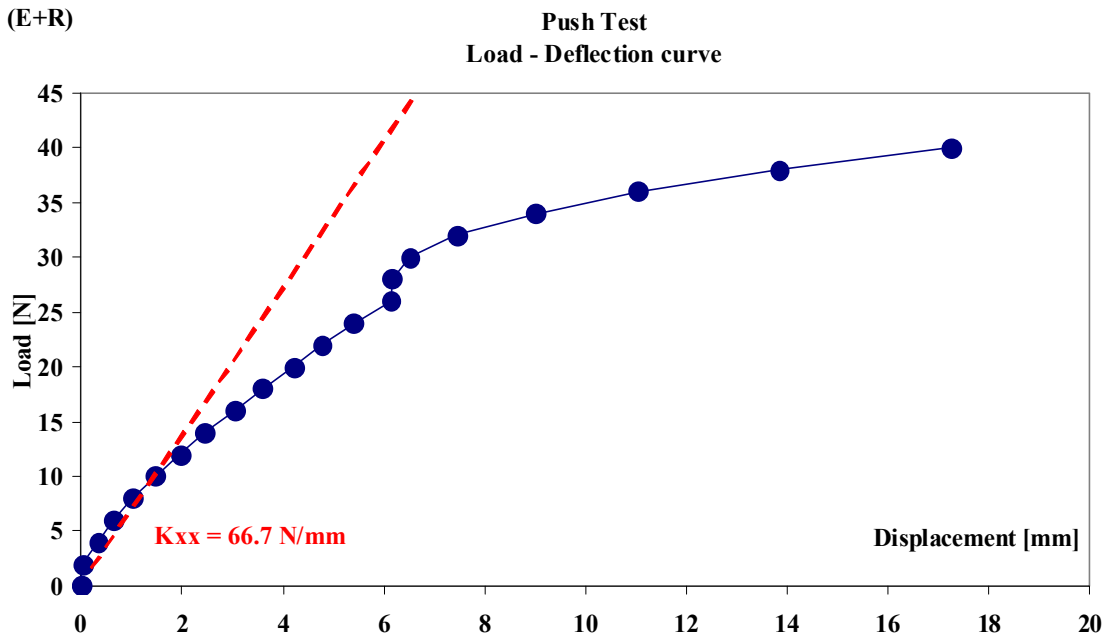


Figure 4.11 Push test: load–deflection curve for LB fraction E and Rubber configuration (E+R)

LB fraction E (E)

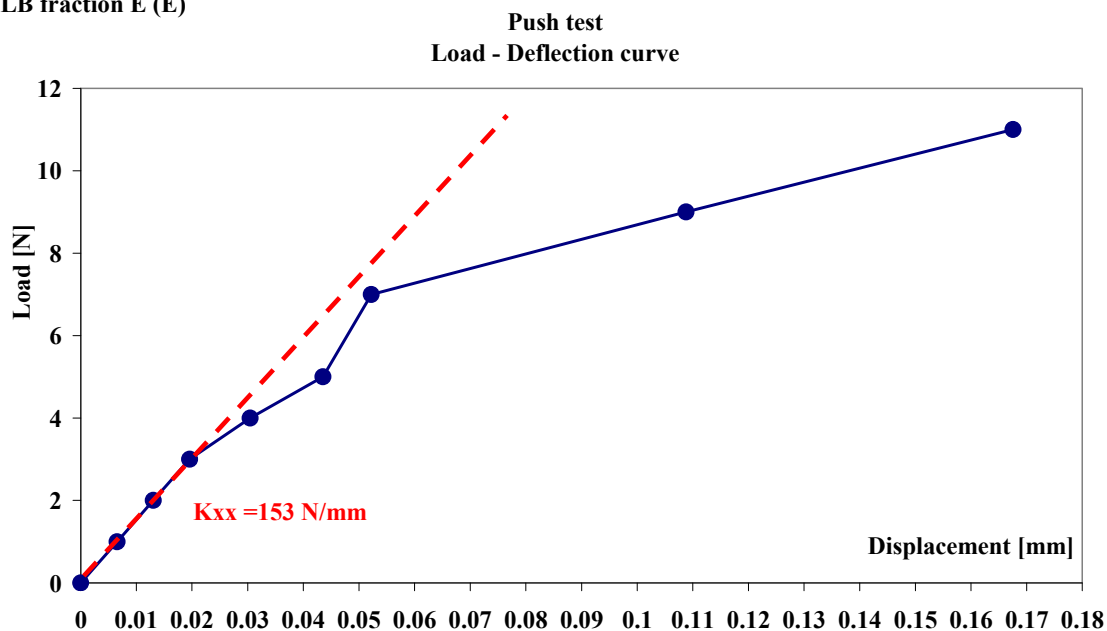


Figure 4.12 Push test: load–deflection curve for LB fraction E (E)

4.2.3 Experimental evaluation of bending moment on the pile

The raw strain gauges data are processing applying an offset procedure using Matlab “*dtrend*” command. In figure 4.13 there is an example of procedure, Figure 4.13 a) shows the raw strain gauge measurement for the two strain gauges located on the left and on the right of the pile section at 200 mm elevation. Figure 4.13 b) shows the same measurements purify by

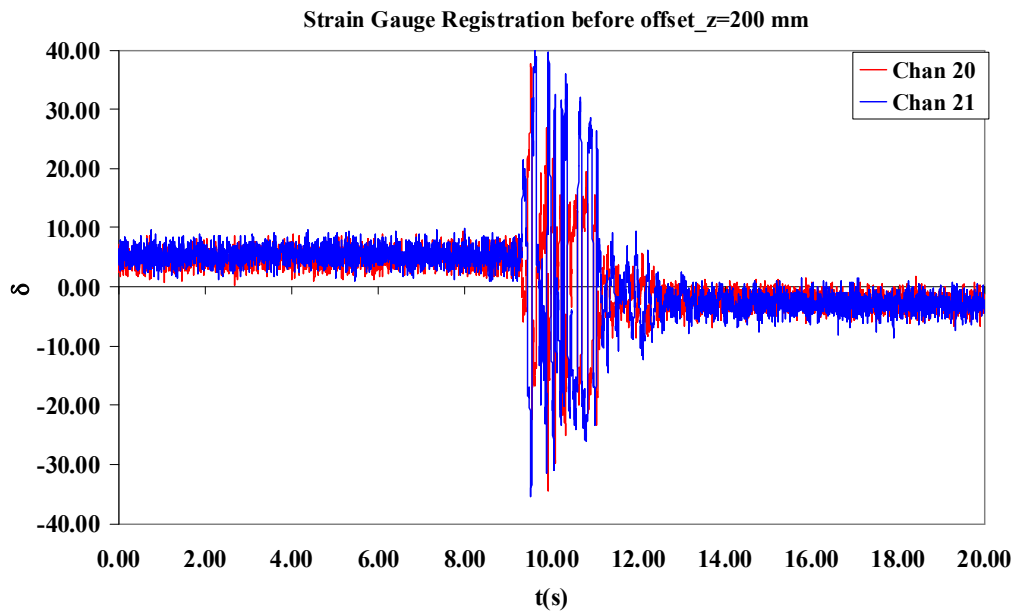


Figure 4.13: a) strain gauges time history before offset delete: z=200 mm

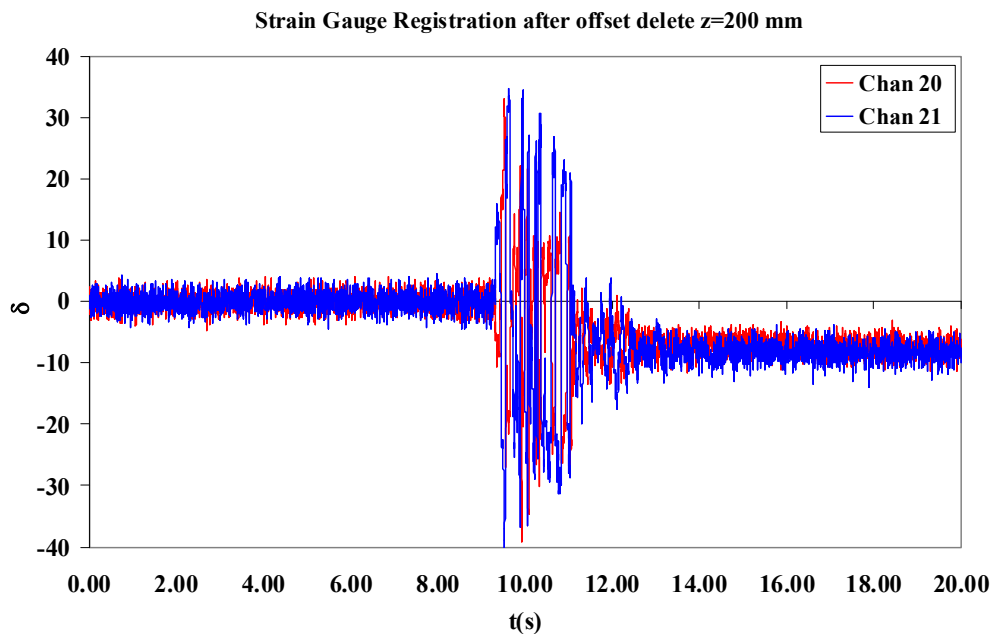
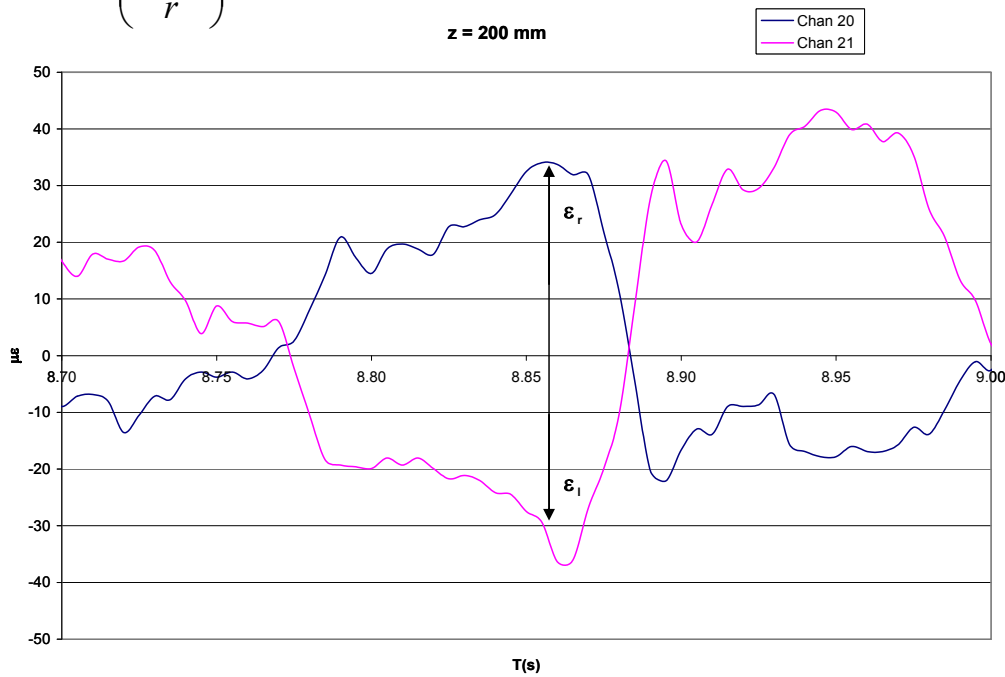


Figure 4.13: b) strain gauges time history before offset delete: z=200 mm

the offset. *Dtrend* command removes a linear trend from a vector, In this example it removes just the mean value from the column of the measurement from zero second to eight second. With the finality to obtain the pure bending strain, for each elevation, the measure of the strain gauges has been purified from normal stress on pile with the formulation reported in equation 4.6. The formulation to obtain the bending moment is reported in equation 4.7.

$$\varepsilon_{bending} = \left(\frac{\varepsilon_{right} - \varepsilon_{left}}{2} \right) \quad [4.6]$$

$$M_b = \left(\frac{E_p I_p}{r} \right) \cdot \varepsilon_b \quad [4.7]$$



Bending strain: $\varepsilon_f = \frac{(\varepsilon_r - \varepsilon_l)}{2}$ **Normal strain:** $\varepsilon_n = \frac{(\varepsilon_r + \varepsilon_l)}{2}$

Figure 4.14 a) strain gauges zoom time history z=200 mm

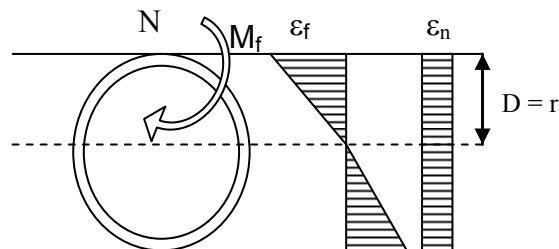


Figure 4.14 b) General strains on the pile section

4.3 Materials for physical soil modelling

With the finality of study different soil configurations, to achieve the effects of stiffness contrast on kinematic phenomena, three different deposits have been tested. Two different kinds of Leighton Buzzard have been chosen: Fraction E silica sand and Fraction B silica sand. Besides a mixture of LB-Fraction B and LB-Fraction E sands has been used to model the bottom layer, the stiffest layer. The mixture sand has been employed with the aim to obtain a big stiffness contrast in a layered soil. The peculiarity of the mixture is to increase the density of bottom layer with the results to obtain a relevant different of stiffness between the bottom and top layer. Furthermore, an artificial material, rubber type Charles Lawrence CT0515B, has been chosen to model behaviour of a very soft layer in the layered deposit, for the top layer. The physical proprieties of materials have been employed in table 4.3.

In figure 4.16 a) the technical proprieties of rubber CT 0515 are shown.

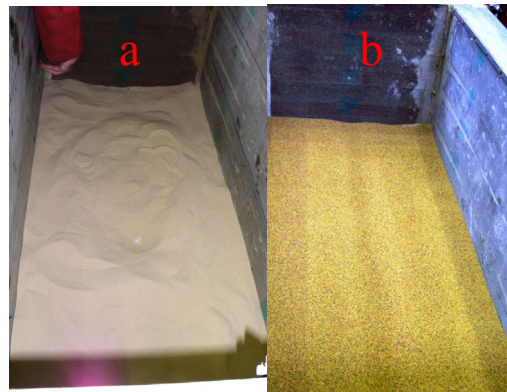


Figure 4.15: Soil model material: (a) Leighton Buzzard fraction E (b) Leighton Buzzard fraction B



Figure 4.16 Soil model material: (c) Leighton Buzzard mixer fraction E(15%) and B(85%) and (d)Rubber

n

Table 4.3: Physical proprieties of materials tested

Physical Proprieties									
Materials	Type	G_s [t/m ³]	e_{min}	e_{max}	D_{10}	D_{50}	D_{60}	ϕ_{crit}	
LB fraction E	sand BS 881-131	2.647	0.613	1.014	0.095	0.14	0.15	32°	Tan (1990)
LB fraction B	sand BS 881-132	2.647	0.486	0.78		0.82			Lings & Dietz (2004)
LB fraction E+B	-	2.647	0.289	0.614					Laboratory test
Rubber	type Charles Lawrence CT0515B	1.15	1.6	2.3	0.5	1			Hydo, Yamada

Product Code: CT0515

Description: Tyre rubber granulate 0.5-1.5mm

Total polymer content (natural and synthetic rubbers): 56% minimum

Acetone extract: 5-20%

Carbon black: 25-35%

Ash at 550°C: 15% maximum

Sulphur: 1-3%

Hardness: 60-79 IRHD

Bulk density (uncompacted): 432 kg/m³

Charles Lawrence International Ltd
 14 Long Way Newark, Nottinghamshire, NG24 2BN, England
 Tel: 01634 612254
 Fax: 01634 612254
 E-mail: international@clgplc.co.uk
www.clgplc.co.uk

CT0515 Sieve analysis

Sieve Size (mm)	Min Retention (%)	Max Retention (%)
0.075	0.00	2.00
0.15	0.00	35.00
0.3	30.00	60.00
0.6	50.00	65.00
1.18	60.00	65.00
2.0	65.00	100.00

Applications:

	Sports Surfaces	Playgrounds	Equestrian	Rubber Mouldings
	✓✓✓	✗	✗	✓

✓✓✓ = Preferred use ✓ = Occasional use ✗ = Unavailable

IMPORTANT NOTES:
 Material fully conforms to the European standard CEN Workshop Agreement CWA 14243:2002. For safety information covering this and other grades of tyre derived granules, see details on our site.

This material specification is given in good faith. However, the basic material is a waste stream product and its composition cannot be guaranteed. Customers should carry out tests to ensure the material meets their application and, where necessary, is compatible with their particular chemical binders.

The Company maintains a policy of continuous research and development to improve products and reserves the right to alter specifications without notice. Customers should check with the Company that they have the latest information.

All measurements on this data sheet are nominal.

Charles Lawrence International Ltd

Product Code: **CT0515**

Size: **0.5-1.5mm**

Figure 4.16 a) proprieties of Rubber CT0515

4.3.1 Leighton Buzzard sand mixer fraction E and fraction B

A finer fraction of particles (LB fraction E) has been mixed with the LB fraction B sand in order to increase its packing density. To define the rate of LB fraction E has been carried out:

- 1) a pluviation tests in a graduated cylinder (d=30 mm) for each combination of volume fraction of two sand to have theoretical valuation of shear wave velocity;
- 2) a theoretical valuation by R.M. German of optimum ratio to define the weight composition of the mixture (Particle Packing Characteristics', Metal Powder Industries Federation, Princeton, NJ, USA, 1989).

The mean diameter ratio between the two fractions of sands (D50, Fraction B : D50, Fraction E =5.77) has been considered beneficial for an increase of packing when the two types of particles have been mixed together. The fine particles have been expected to fill in efficiently the voids in the large particle matrix.

The mass composition corresponding to the theoretical maximum packing density of the mixture was calculated according to the German (1989) model of packing, resulting in XFraction B: XFraction E = 85:15.

The German's procedure is following reported. The theoretical association starts from the equation 4.8, or rather, from the definition of the rate of max, f , function of the particles density ($\rho_{a_{\max}}$) and it is the theoretical density (G_s) as following define:

$$f = \frac{\rho_{a_{\max}}}{G_s} \quad [4.8]$$

The particle density is defined by equation 4.9:

$$\rho_{a_{\max}} = \frac{G_s}{e_{\min} + 1} \quad [4.9]$$

Hence the value of rate of max is equal to f_L (first material, 1, LB fraction B) and f_s (second material, 2, LB fraction E) respectively:

$$f_L = \frac{\rho_{a_{\max 1}}}{G_s} \quad [4.10]$$

$$f_s = \frac{\rho_{a_{\max 2}}}{G_s} \quad [4.11]$$

The theoretical increase of density has been defined by Δf , expressed in equation 4.12:

$$\Delta f = 0.23 \left[1 - 2.35 \frac{D_s}{D_L} + 1.35 \left(\frac{D_s}{D_L} \right)^2 \right] \quad [4.12]$$

where D_S and D_L are expressed in [μm] and they are the D_{50} value for each sand. The theoretical increase of density Δf is expressed by equation 4.13 :

$$f_{\text{mixture}}^{\text{theoretical}} = f_l + \Delta f \quad [4.13]$$

German expresses the mass compositions X in function of the ratio of mass f and the ratio of on maximum mass f_{max} , as expressed in equation 4.14 and 4.15:

$$X_L = \frac{f_L}{f_{\text{max}}} \quad [4.14]$$

$$X_S = \frac{f_S}{f_{\text{max}}} \quad [4.15]$$

where f_{max} is equal to

$$f_{\text{max}} = f_l + \left(1 - \frac{D_L}{D_S}\right) + 1.35 \left(\frac{D_S}{D_L}\right)^2 \quad [4.16]$$

Table 4.4 shows the values of mass composition for LB fraction B (index l) and LB fraction E (index s).

Table 4.4: Mass ratio LB fraction B (L) and LB fraction E (s)

	Gs	e_{min}	γ_a	D_L	D_s	f_L	f_s	f_{max}	X_L	X_S
	Kg/m3		kg/m3	mm						
1		0.486	1776	820	142	0.58	0.67	0.79	0.85	0.15
2		0.613	1636	-						

To obtain the mixer a Mixer machine has been used (Figure 4.17.)



Figure 4.17: Sand dried in the oven

4.3.2 Proprieties of fraction E and B Leighton Buzzard sand mixer

For this sand-mixture the laboratory tests have employed in the Bristol Laboratory of “Soil Mechanics”. A British Standard procedure has been followed(BS 1377-4, 1990) to valuate e_{\min} and e_{\max} of mixer Leighton Buzzard fraction B (85%) and Leighton Buzzard fraction E (15%).

As well known in the case of sand the *density index* (I_D) is used to express the relationship between the *in-situ* void ratio (e), or the void ratio of a sample, and the limiting values e_{\max} and e_{\min} . The density index (the term ‘relative density’ is also used) is defined by equation 4.17:

$$I_D = \frac{e_{\max} - e}{e_{\max} - e_{\min}} \quad [4.17]$$

Thus, the density index of a soil in its densest possible state ($e = e_{\min}$) is 1 (or 100%) and the density index in its loosest possible state ($e = e_{\max}$) is 0.

The maximum density is determined compact a sample underwater in a mould, using a circular steel tamper attached to a vibrating hammer: a 1–L mould is used for sands and a 2.3–L mould for gravels. The soil from the mould is then dried in an oven, enabling the dry density to be determined.

The minimum dry density can be determined by following procedures. In the case of sands, a 1–L measuring cylinder is partially filled with a dry sample of mass 1000g and the top of the cylinder closed with a rubber stopper. The minimum density is achieved by shaking and inverting the cylinder several times, the resulting volume being read from the graduations on the cylinder. All full details of the above tests are given in BS 1377 (Part 4). Before start its test 8kg of sand have been dried in the oven. Then the mass was divided in 2 samples:

- To obtain e_{\max} have been considered 2 specimen of 1 kg each;
- To obtain e_{\min} have been considered 2 specimen of 3 kg each

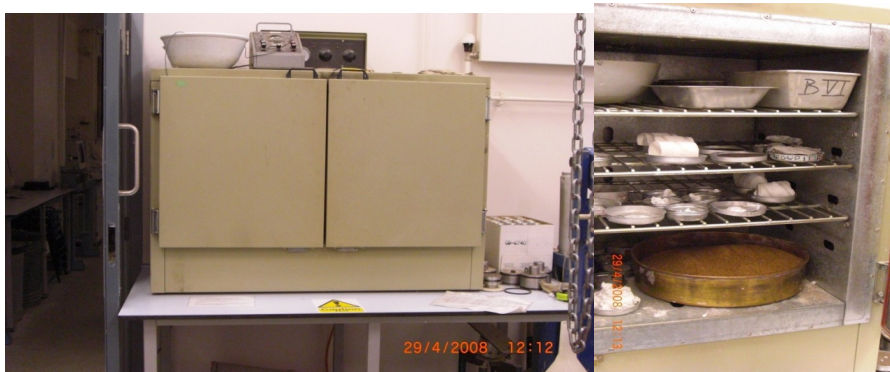


Figure 4.18: Sand dried in the oven

- ***“Determination of minimum dry densities of sand***

This test covers the determination of minimum density which a clean, dry sand can sustain. This does not necessarily relate to a state attainable in the field. The method is suitable for sands containing up to about 10% of fine material passing the 63µm test sieve and with no material retained on the 2mm tests sieve. The dry sand is shaken in a glass cylinder and it is allowed to fall freely, thereby entrapping air and forming a grain structure enclosing the maximum possible volume of voids. Calculation and expression of results:

Minimum dry density of sand $\rho_{d \min}$ (in Mg/m³) has been obtained from equation:

$$\rho_{d \min} = 1000/V \quad [4.18]$$

where V is the greatest of the 10 or more volume readings recorded in (mL). The values of the tests are reported in Table 4.5.



Figure 4.19: Sieves for soil and graduated glass cylinder

Table 4.5: Volume read for each test

1 Mould times	1000 g Volume read	2 Mould times	1000 g Volume read
1	620 ml	1	600ml
2	625 ml	2	590 ml
3	615 ml	3	590 ml
4	620 ml	4	600 ml
5	630 ml	5	600 ml
6	630 ml	6	610 ml
7	630 ml	7	600 ml
8	630 ml	8	610 ml
9	620 ml	9	590 ml
10	620 ml	10	600 ml

Hence the values of minimum density are:

Table 4.6 Minimum density

	ρ_{dmin}	ρ_{dmin}	Gs	e_{max}
	g/m ³	Mg/m ³	Mg/m ³	
1 moul	1587.302	1.587301587	2.647	0.66761
2 moul	1663.894	1.639344262	2.647	0.61467

The greatest value has been chosen. Consequently, the value of minimum void ratio for the mixture (85% of Leighton Buzzard fraction B and 15% of Leighton Buzzard fraction E) is 0.67.

- ***Determination of maximum dry densities of sand and minimum void***

Each sample of 3 kg is poured into warm water in a bucket and stirred thoroughly to remove air bubbles and allowed to stand for several hours overnight, to cool. After several hours, the soil is compacted into a 1L mould under water using an air hammer. It has been added a portion of the soil-water mixture to the mould with the scoop, placing it carefully under the water surface. The quantity of sample should be such that the mould is about one-third filled when compacted. It has been added water to the surrounding container up to the same level as in the mould. Place the circular tamper on the soil and compact with the vibrating hammer at least 2 min until there is no further decrease in sample height. This operation has been repeated twice more, ensuring that the surface of the sample is always under water.

Remove the mould containing the soil from the container; extract the compact soil from the mould into the small weighed metal tray. Dry the soil in an oven at 105° C to 110° C, weigh when cool and determine the mass of soil. Figure 4.20 a) to e) show the different steps of the procedure. Minimum void ratios e_{min} is 0.289.



Figure 4.20 a)-b) sand poured in a warm water and portion of soil-water mixture in the mould



Figure 4.20 c)-d) air hammer



Figure 4.20: e) dry sample

4.4 Soil tests

Before start the dynamic tests, different soil tests are made, in order to obtain the target stiffness contrast and to individuate the stiffness of all materials used. In table 4.7 the peculiarity of each soil tests are shown. The soil test can be clustered:

- Pluviation tests;
- Modal test: White noise tests; Pulse tests; Hammer tests;
- Exploratory tests.

Table 4.7 Peculiarity of soil tests (before dynamic tests)

Soil tests		Aim	Valuation of Vs or G
Pluviation test		Measure of packing density	Theoretical valuation of stiffness by Hardin and Drnevich formula's
Modal test	Pulse test	Definition of shear wave velocity Vs	Measurement of time delay of signal between two accelerometer located in sand at two different elevations
	White noise test	Measure of natural frequency of soil f_n	The shear wave velocity is obtained from the natural frequency of the deposit as $4 H f_n$, where H is the high of the deposit.
	Hammer test	Measure of natural frequency of soil f_n	The shear wave velocity is obtained from the natural frequency of the deposit as $4 H f_n$ where H is the high of the deposit
Exploratory test	Dynamic test with pile	Check all the instrumentations	

4.4.1 Pluviation test

The density, the stress level in the shear wave polarization plane and the particle characteristics, determines the shear wave velocity of a soil deposit.

The main control parameter for tailoring the shear wave velocity and the stiffness for each layer is density. To control the density value of sand many pluviation procedures have been designed, with the aim of obtain a layered soil with a strong stiffness contrast.

The dry pluviation technique consists in a deposition of sand in the shear stack. A 300 kg drum of the test material is inverted 1.2 m above the base of the shear stack. On releasing a valve, the sand flows through a funnel attached to the underside of the suspended drum. The flow is constricted by an adjustable aperture (valve) at the tip of the funnel. This aperture provides the primary control on the resulting sample density (Miura & Toki, 1982). On leaving the funnel, the sand flows into a flexible tube 1 m in length and 50 mm diameter allowing the flow to be directed. It takes around three hours to deposit the 800 mm depth (nearly 900 kg mass) of sand required to fill the shear stack. The tube is manually operated. Its purpose is to allow an uniform deposition

over the cross-section of the shear stack. In general, the packing density resulted from pluviation is determined by the particle characteristics, the height of fall and the size of the pluviation nozzle. In principle, for the same material, the density increases with the increase of the height of fall and the decrease of the nozzle diameter. Layers of 100 mm depth are poured, the flow is stopped, and the drum is raised by 100 mm. The packing density have been determined from the sand deposit mass and the inside volume of the shear stack.

Table 4.8 summarizes all pluviation tests done before the dynamic tests for the materials chosen.

Table 4.8 List of pluviation tests done before dynamic tests

Soil test	Code	Materials	Diameter nozzle	Soil configuration in shear stack	High of material in shear stack	Pile
Pluviation test	PT1	LB B	d= 15 mm	monolayer	500 mm	NO
	PT2	LB E	d= 15mm	monolayer	Full (814 mm)	NO
	PT3	LB E	d= 40mm	monolayer	Full (814 mm)	NO
	PT4	LB B+E	d= 15 mm	monolayer	500 mm	NO
Pluviation for Modal test	PT5a/b	LB B+E	d= 15 mm	monolayer	500 mm	NO
	PT6	LB E	d= 40 mm	monolayer	Full (814 mm)	NO
	PT7	Rubber CT005	d= 40 mm	monolayer	Full (814 mm)	NO
	PT8	Rubber CT0515	d= 40 mm	monolayer	Full (814 mm)	NO

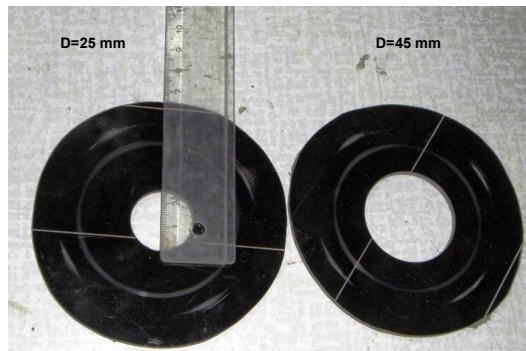


Figure 4.21 a) nozzle attached to the underside of the suspended drum.



Figure 4.21 b) pluviation: flexible tube, drum and funnel with an adjustable outlet

The first pluviations have been done only for LB fraction B (PT1), and LB fraction E (PT2 and PT3). The smaller diameter of nozzle (15 mm) (PT1) has been used for depositing the bottom layer of sand, in order to target higher densification values. Preliminary test on LB fraction B reveals that an aperture of 15 mm produces a void ratio of 0.7 and density 1.69 tonne/m³.

A 25 mm and 40 mm aperture have been used for the top layer, the softer one. In table the results for two different Pluviation on LB fraction E (PT2-PT3) are shown. Preliminary tests on LB fraction E reveal that an aperture of 40 mm produces a void ratio of 0.891 and density 1.40 tonne/m³. Table 4.9 shows the results of the Pluviation PT1, PT2 and PT3.

Table 4.9 Preliminary Pluviation Test on LB fraction E and LB fraction B

PT1: Pluviation Test for Leighton Buzzard Fraction B (nozzle 15 mm)									
H[mm]	M _{drum} [kg]		M _{ss} [kg]	V[m ³]	γ _d [t/m ³]	Void ratio(e)	Dr	Go[MPa]	V _s [m/s]
500	856		546	0.323	1.691	0.565	0.73	86.7	226
		Half Volume	M_{ss}[kg]	V[m³]	γ_d [t/m³]	Void ratio(e)	Dr	Go[MPa]	V_s [m/s]
			440	0.26	1.691	0.565	0.73	24	119
PT2: Pluviation Test for Leighton Buzzard fraction E (nozzle D=25 mm)									
H[mm]	M _{drum} [kg]		M _{ss} [kg]	V[m ³]	γ _d [t/m ³]	Void ratio(e)	Dr	Go[MPa]	V _s [m/s]
814	1008		734	0.52	1.421	0.863	0.38	20.7	121
		Half Volume	M_{ss}[kg]	V[m³]	γ_d [t/m³]	Void ratio(e)	Dr	Go[MPa]	V_s [m/s]
			369	0.26	1.421	0.863	0.38	14.2	100
PT3: Pluviation Test for Leighton Buzzard fraction E (nozzle D=40 mm)									
H[mm]	M _{drum} [kg]		M _{ss} [kg]	V[m ³]	γ _d [t/m ³]	Void ratio(e)	Dr	Go[MPa]	V _s [m/s]
814	886		736	0.52	1.400	0.891	0.31	19.7	119
		Half Volume	M_{ss}[kg]	V[m³]	γ_d [t/m³]	Void ratio(e)	Dr	Go[MPa]	V_s [m/s]
			364	0.26	1.400	0.891	0.31	13.6	98

The theoretical valuation of shear modulus for sand have been calculated using Hardin & Drnevich's (1972), an empirically derived relationship for sands (equation 4.19):

$$G(d_0) = \frac{3230 \times (2.973 - e)^2}{1 + e} \sqrt{\sigma'_m} \quad [4.19]$$

where, σ'_m is the mean effective confining stress. Stroud (1971) measured K_0 values of 0.445 and 0.46 for dense and loose LB 14-25 sand whilst developing the Cambridge Simple Shear Apparatus. At the base of the shear stack, taking K_0 as 0.45 (the average of Stroud's measurements).

However, the pluviations tests have not lead to satisfactory results, in terms of sands' stiffness contrast. LB fraction E and LB fraction B are quite similar in terms of stiffness. The ratio between the shear wave velocity contrast obtained was around 1.2 ($V_{s2}=119$ m/s and $V_{s1}=98$ m/s). According to the prototype, the target of velocity should be 4, as explained in chapter 3.

Therefore, different solutions have been chosen to increase the stiffness contrast of layered model (as explained in section 4.3.1):

- to increase the sand packing density for the bottom layer, a finer fraction of particles (fraction E), in different proportions, has been mixed with the LB Fraction B;

- to decrease the packing density of the top layer, an artificial soft material has been used (Rubber-CT050).

The results of Pluviation test for mixer Leighton Buzzard fraction E and fraction B (PT4 - d=15 mm) is shown in table 4.10

Table 4.10 Preliminary Pluviation Test on mixture LB fraction E and LB fraction B

PT4: Pluviation Test for Leighton Buzzard fraction B and Leighton Buzzard fraction E (nozzle D=15 mm)									
H[mm]	M_{drum}[kg]	Half Volume	M_{ss}[kg]	V[m³]	γ_d [t/m³]	Void ratio (e)	D_r	Go[MPa]	Vs [m/s]
414.5	504			466	0.26	1.791	0.478	0.420	28

The fine fraction of LB fraction E mixed with the Leighton Buzzard fraction B has the effect to increase the packing density as expected, but it's not enough to obtain a target V_{s2} equal to approximately 160 m/s (shear velocity's contrast equal to 1.3).

To further increase the packing density of the bottom layer in the layered soil configuration a mechanical densification of sand has been obtained shaking the table after the pluviation, by tapping technique.

The tapping technique consists in shaking the table up and down by means of a vertical input motion. The packing density has been calculated by the measured displacement of the deposit surface. The vertical displacement of the surface is obtained as average value of 18 settlements measured at 11 points along the border and 7 internal points.

To maximize the tapping effects several tests have been performed with different amplitude and number of cycles. After 10000 cycles of vertical sine vibrations of 10 Hz frequency and 0.35 g amplitude, a 5% density gain has been achieved. In figure 4.22 b) the effects of tapping procedure are illustrated.

Table 4.11 shows the value of void ratio and relative density for the mixture sand between LB fraction E and fraction B. The best result obtained is relative to a packing density produces a void ratio of 0.375 and packing density 1.925 tonne/m³

Table 4.11 Pluviation Test results after tapping procedure on mixture LB fraction E and LB fraction B

PT5b	Pluviation's results for LB fraction E (15%) and LB fraction B (85%)						
	V [m³]	γ_d [kg/m³]	Void ratio (e)	Dr (%)	σ_m [kN/m²]	Go [MPa]	Vs [m/s]
Half volume after tapping	0.26	1925	0.375	73.5	4.87	34.99	135

Therefore for the sandy layered configuration the effect of the mixer LB fraction B+E and the effect of tapping procedure have a good results to achieve the implementation of stiffness contrast between the soft layer (LB fraction E) and the stiffer layer (LB fraction BE).

The results of pluviation for Rubber CT005 (fine particle) and Rubber CT0515 (course particle) are shown in table 4.12 and in table 4.13.



Figure 4.22: a) location of accelerometer on the surface before Tapping procedure

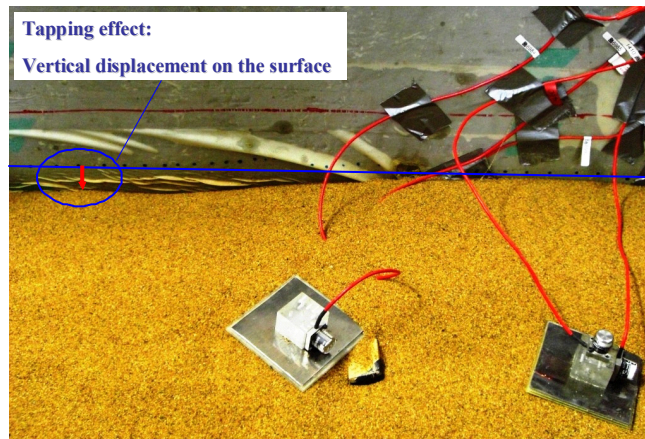


Figure 4.22: b) location of accelerometer on the surface after Tapping procedure

Table 4.12 Pluviation test results for rubber CT005

PT7	Pluviation's results for Rubber CT005						
	V [m ³]	ρ_d [kg/m ³]	Void ratio (e)	Dr (%)	σ_m [kN/m ²]	Go [MPa]	Vs [m/s]
Half volume	0.26	545.40	1.11	1.68	1.40	-	-

Table 4.13 Pluviation test results for rubber CT0515

PT8	Pluviation's results for Rubber CT0515						
	V [m ³]	γ_d [kg/m ³]	Void ratio (e)	Dr (%)	σ_m [kN/m ²]	Go [MPa]	Vs [m/s]
Half volume	0.26	504.306	1.28		1.208	-	-

4.4.2 Modal test

The stiffness design of the model soils assumed that soils behave elastically at low strain amplitudes (less than 10^{-3} %). This allowed the theory of wave propagation through elastic media to be applied. The shear modulus at low strain amplitude has been obtained from the shear wave velocity V_s and the soil mass density ρ as:

$$G_{\max} = \rho V_s^2 \quad [4.20]$$

Three modal testing techniques have been employed in the measurement of small shear stiffness of the test materials: a) pulse testing, b) white noise testing and c) hammer testing.

Pulse Test

Pulse testing employed 10 Hz, half-sine pulses that have been generated by the shaking table in the horizontal direction. The shear wave velocity has been inferred by measuring the vertical shear wave travel time between accelerometers located at certain ordinates in the deposit. In figure 4.22 The layout of instrumentation is shown.

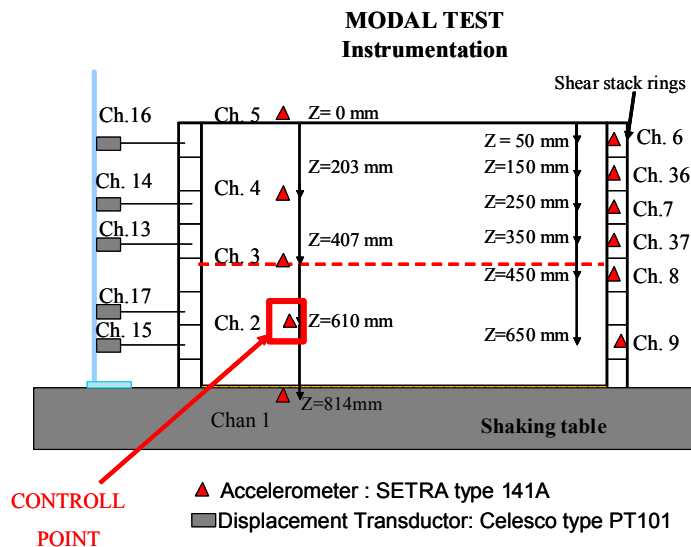


Figure 4.22 layout of instrumentation in sand and outside

The pulse technique presents the advantage of being least disturbing, having thus the ability to capture the stiffness at very small strains. However, the measurements have been found to be influenced by the position of the accelerometer receiver and by the pulse amplitude.

In figure 4.23 are reported some examples of the pulse test done on the mixture LB fraction E+B. The measured shear wave travel time between accelerometers a1 and a4 increases as the magnitude of input increases from a) to b) in figure 4.23. The same increasing trend is noticed for the time of travel between accelerometers a₁ and a₄ when the pulse input increases. At low magnitudes of strain, shear wave travel times are small.

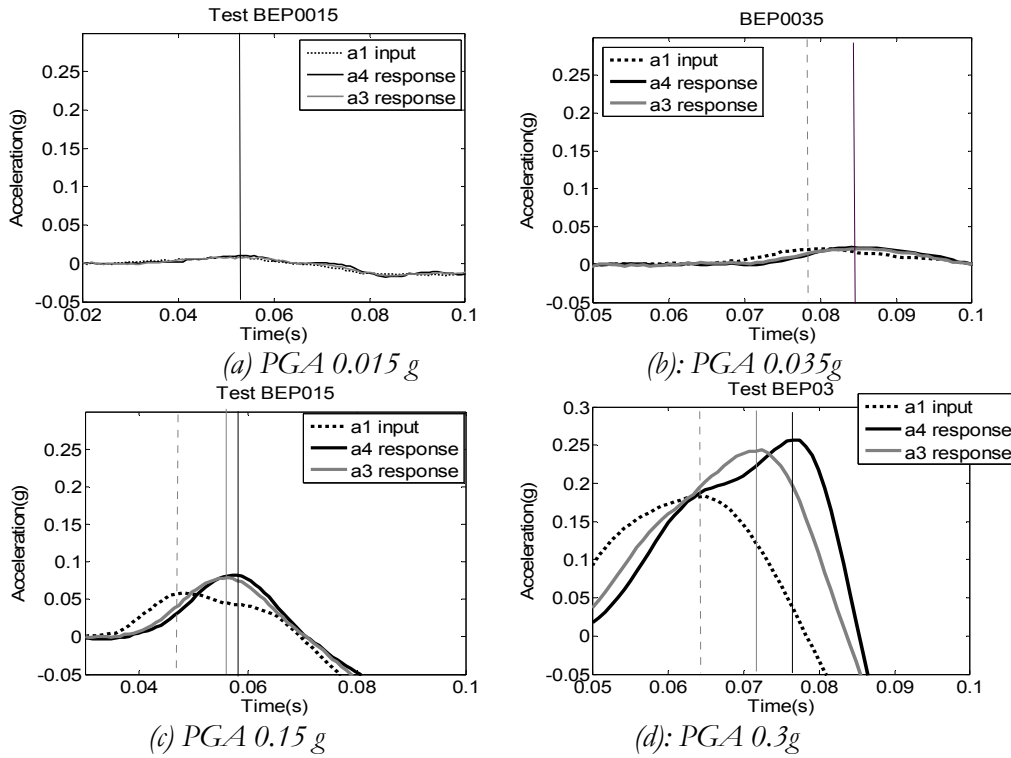


Figure 4.23: pulse tests on the mixture BE for different value of PGA

The travel time t of a shear wave propagating vertically through the shear stack can be determined using a pulse type excitation and subtracting the time of peak base response from the time of peak surface response. For homogeneous soil deposits of density ρ and depth H , travel times can be converted to shear moduli with the following relationship:

$$G H^2 t_{trav} = \rho \quad [4.21]$$

White noise or Broad band test

White noise testing used a random noise signal of bandwidth 1-50 Hz and $RMS=50$ mV. Frequency response functions (FRFs) have been computed by normalising the output of accelerometer a_4 by the output of accelerometer a_1 in the frequency domain (Figure 4.22). A digital spectrum analyzer (of type Advantest series R9211) is used to measure the resonant properties of the test sand within the shear stack. A random signal of bandwidth 1-50 Hz from the analyser's inbuilt signal generator excites the shaking table in the y -direction. Noise effects are minimized by analyzing 32 four second data segments and averaging the results. A Hanning window is used. FRFs are dominated by a single resonant peak corresponding to the first shear mode of the soil layer response. The peak reduces in height, increases in width and migrates to lower frequencies with increases in excitation indicating reduced amplification, increased damping and a softening of response at increased strain levels. No other modes of soil response exist within the 1-50Hz frequency band. FRFs display a second resonant peak at 20Hz smaller in magnitude and comparatively insusceptible to changes in excitation. It represents a table (oil column) resonance and is not representative of the test soil response.

Resonant frequencies f are obtained, noting that the first mode of response corresponds to a shear wave of length $4H$, where H is the high of the deposit ($\lambda = V_s * T$). The resonant frequencies can be converted in shear velocity.

Hammer test

The hammer testing involved a different source of excitation (batch of instrumented hammer impulses). However, the extraction of dynamic soil properties has been based on the same FRF computation technique.



Figure 4.24: Hammer test

Methodology of soil test

The material is poured in the shear stack for its total high. During the pluviation tests the accelerometers are located in the shear: one at a quarter from the bottom (chan 2); one in the middle (chan 3); one at a quarter from the top (chan 4); two accelerometers have been positioned in the top of the shear stack (at surface) (chan 9 and chan 5) and one accelerometer has been located on the shaking table (chan 1) (Figure 4.22). Once that packing density (average density of deposit) of materials is known, the modal tests can start.

To reduce noise, data signals from the instruments are passed through a low pass Butterworth filter set to 80Hz. Data are acquired at 1000 Hz (pulse excitation). To aid data processing, acquisition is initiated a few seconds prior to the start of any movement of the shaking table and ends a similar amount of time afterward. The input used are:

- Pulse test: sine pulse, 10 Hz , various amplitudes;
- White noise, (0-50) Hz, various amplitudes;
- Instrumented hammer tests.

The channel corresponds to the accelerometer are:

- a_1 = accelerometer on the shaking table ($Z=814$ mm measured from the uppermost surface of shear stack);
- a_4 = accelerometer embedded in sand ($Z=203$ mm);
- a_3 =accelerometer embedded in sand ($Z=407$ mm);
- a_5 or a_9 =accelerometer at surface ($Z=0$ mm).

4.4.3 Results of Modal Tests: Monolayer Leighton Buzzard fraction E (E)

Eleven modal tests have been made for the monolayer Leighton Buzzard fraction E deposit. The total high of the shear stack has been filled with LB fraction E sand (814 mm). Table 4.14 shows the list of the all modal tests, while the results of these tests are reported in Table 4.15.

Table 4.14 list of modal test on LB fraction E

Modal test	
LB fraction E	
1	Pulse 3mm - 10Hz sine
2	Pulse 1 mm - 5 Hz sine
3	Pulse 4 mm - 10 Hz sine
4	Pulse 2 mm - 10 Hz sine
5	Pulse 3mm - 10Hz 3 cycle
6	Broad Band test 005g-50m
7	Broad Band test 005g-50m-Half Depth
8	Broad Band test 005g-50m-Damping
9	Hammer 1
10	Hammer 2
11	Hammer 3

Table 4.15: Results of Modal test on LB fraction E

LB fraction E								
Total number of tests: 11		Displacement command signal for Shaking table	$\Delta z(1-4)$	t1	t4	$\Delta t14$	v14	G14
TIME DOMAIN		mm	Mm	s	s	s	m/s	(MPa)
1	Pulse 3mm - 10Hz sine	3	610	4.0709	4.0808	0.0099	61.6	5.46
2	Pulse 1 mm - 5 Hz sine	1	610	-	-	-	-	-
3	Pulse 4 mm - 10 Hz sine	4	610	4.0709	4.0808	0.0074	82.3	9.73
4	Pulse 2 mm - 10 Hz sine	2	610	8.1194	8.1234	0.0040	152.5	33.42
5	Pulse 3mm - 10Hz 3 cycle	3	610	8.9630	9.0118	0.0488	12.5	0.22
FREQUENCY DOMAIN		transfer function	Hz	fn (Hz)	Vs(m/s)	G(MPa)	D(%)	
1	Broad Band test 005g-50m	chan 1- chan 4 ($\Delta z = 610$ mm)	0-50	23.94	76.61	8.40		
2	Broad Band test 005g-50m-Half Depth	chan 1- chan 3 ($\Delta z = 407$ mm)	0-50	23.56	75.39	8.14		
3	Broad Band test 005g-50m-Damping	chan 1- chan 4 ($\Delta z = 610$ mm)	0-50	20.18	64.58	5.97	15%	
1	Hammer 1	chan 1- chan 4($\Delta z = 610$ mm)	0-200	24	76.80	8.45		
2	Hammer 2	chan 1- chan 4($\Delta z = 610$ mm)	0-100	23.75	76.00	8.27		
3	Hammer 3	chan 1- chan 4($\Delta z = 610$ mm)	0-100	24	76.80	8.45		

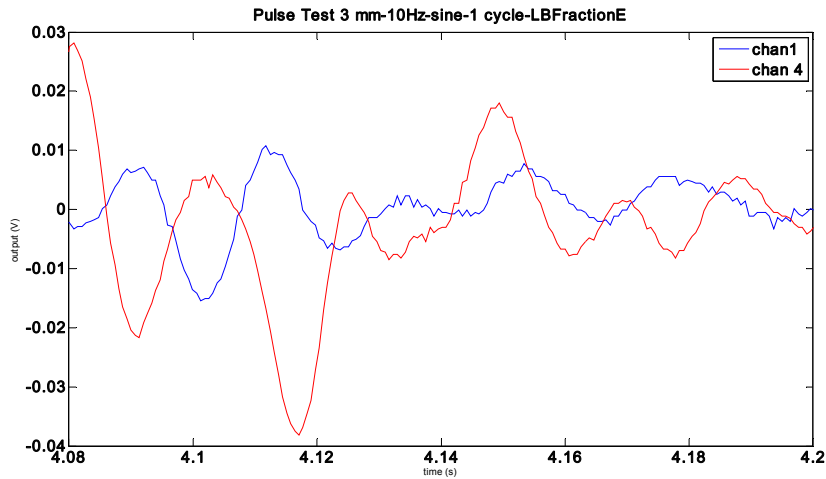


Figure 4.25: Example of time delay in the pulse test

In figure 4.25 an example of pulse test (3mm) made on the LB fraction E is plotted. As explain in the previous paragraph the shear wave velocity has been calculated from the measure of the time delay of the input motion from sensor a_1 to sensor a_4 . It is a visual analysis.

The frequency domain analysis of the random excitation tests are in a good agreement. The test soil void ratio decreases resulting in an increased sample density. Strictly, these variations should be reflected in the calculations for shear stress and stiffness.

For the test soil in question, measured contractions had negligible influence on other parameters and volumetric change has been disregarded.

Nevertheless, if substantial settlement does occur, any derived dynamic soil properties should be related to average soil properties over the test. The amount of settlement is dependent on the magnitude and duration of the shear strain. For tests of equivalent shear strain magnitude, the prolonged duration of the random excitation test maximizes settlement while the short duration of the pulse test minimizes settlement. In figure 4.26 two examples of FRFs function relative to Hammer Test 1 and Broad Band test 2 have been reported.

To ensure a soils behave elastically at low strain amplitudes (less than 10^{-3} %), the tests with a low magnitude have been considered more reliable. In particular in table 4.16 the reference value for LB fraction E has been chosen.

Table 4.16: Results of Modal test on LB fraction E

Results of Modal test in LB fraction E			
γ	V_s	G	f_n
kg/m ³	m/s	MPa	Hz
1437	76.61	8.40	23.94

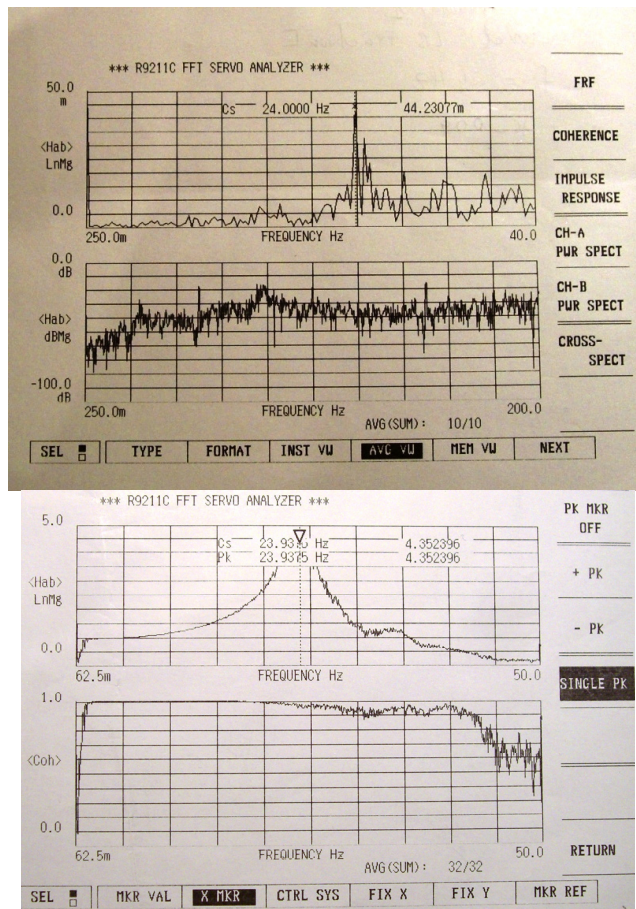


Figure 4.26: Examples of broad band and hammer tests output: FRFs (Hammer 1 and Broad band 2)

4.4.4 Results of Modal Tests: Leighton Buzzard Mixer fraction B (85%) and E (15%)

Thirteen modal tests have been made for the monolayer deposit of mixer fraction B (85%) and E (15%), before tapping procedure, and twelve after it. The total high of the deposit in the shear stack is 579 mm, due to technical problems we were not able to fill in the all whole shear stack. Table 4.17 shows the list of the all modal tests made, while the results of the tests before tapping are reported in Table 4.18 a), b), c). The results of test after tapping procedure are shown in table 4.22.

Table 4.17 list of modal test on mixture LB fraction E and fraction B

1	BEP001g.m	P= Pulse test
2	BEP0015g.m	N= White noise test
3	BEP002g.m	H= Hammer test
4	BEP0035g.m	T= Tapping
5	BEP0065g.m	AT= after Tapping
6	BEP0015gbis.m	BE= Mixer Sand
7	BEP015g	
8	BEN001g.m	
9	BEN0015g.m	
10	BEN003g.m	
11	BEN01g.m	
12	BEN02g.m	
13	BEH1	
14	T035g.m	
15	T09g.m	
16	T032g.m	
17	T2g.m	
18	T2g.m	
19	ATBEP0015g.m	
20	ATBEP002g.m	
21	ATBEP0035g.m	
22	ATBEP0065g.m	
23	ATBEP01g.m	
24	ATBEP013g.m	
25	ATBEP017g.m	
26	ATBEN001g.m	
27	ATBEN0015g.m	
28	ATBEN003g.m	
29	ATBEN01g.m	
30	ATBEN015g.m	

Table 4.18 a) results of Pulse test for LB fraction E and fraction B, before tapping

INPUT	shape	f_{input} (Hz)	Accelerometer consider			Sand
			a_1 (on shaking table)	a_3 (in sand at middle)	a_4 (in sand)	γ (Kg/m ³)
Pulse	sine	10	$z=814$ mm	$Z=407$ mm	$Z=203$ mm	1842
Name tests	Displacement in command signal for Shaking table	Amplitude Pulse PGA	Shear velocity V_{14}	Stiffness G_{14}	Shear velocity V_{13}	Stiffness G_{13}
	mm	g	m/s	MPa	m/s	MPa
BEP001g.m	0.2	0.01	91.19	15.32	70.17	9.07
BEP0015g.m	0.3	0.015	138.86	35.52	68.98	8.77
BEP002g.m	0.4	0.035	127.29	29.85	101.75	19.07
BEP0035g.m	0.5	0.02	107.19	21.17	84.79	13.24
BEP0065g.m	0.8	0.065	91.19	15.32	81.40	12.21
BEP0015gbis.m	0.3	0.015	-	-	70.17	9.07
BEP015g	1.5	0.15	89.85	14.87	79.80	11.73

Table 4.18 b) Results of White noise test on mixture LB fraction E and fraction B, before tapping

White Noise	Input	Channel 1-4				Channel 1-3			
Test Name	A(g)	f_{n14}	H	v_{s1-4}	G_{1-4}	f_{n13}	H	v_{s13}	G_{13}
	g	Hz	mm	m/s	MPa	Hz	Mm	m/s	MPa
BEN001g.m	0.01	35.7	579	82.68	12.59	34.75	579	80.48	11.93
BEN0015g.m	0.015	34.5	579	84.32	13.1				
BEN003g.m	0.03	34.75	579	84.93	13.29	34.5	579	79.90	11.76
BEN01g.m	0.1	33.25	579	81.26	12.16				
BEN02g.m	0.2	26.5	579	64.77	7.73				

Table 4.18 c) Results of Hammer test on mixture LB fraction E and fraction B, before tapping

Hammer Test	frequency range	Peak of FRF	H	v_{s1-9}	Stiffness
Name Test	Hz	f_n (Hz)	mm	m/s	G(MPa)
BEHI	0-200	34.75	579	80.48	12.16

From the pulse tests (P) and the broad band tests done (N) some observations are reported:

- The signal to noise ration in test P0015g has been too low to distinguish the maximum peak of the response. Therefore the Test P002g has been considered the first to yield the small- strain stiffness measurement. For half the shear stack the stiffness value is 18.3 MPa.
- As the input amplitude increases, the damping increase and the shear wave velocity decreases.

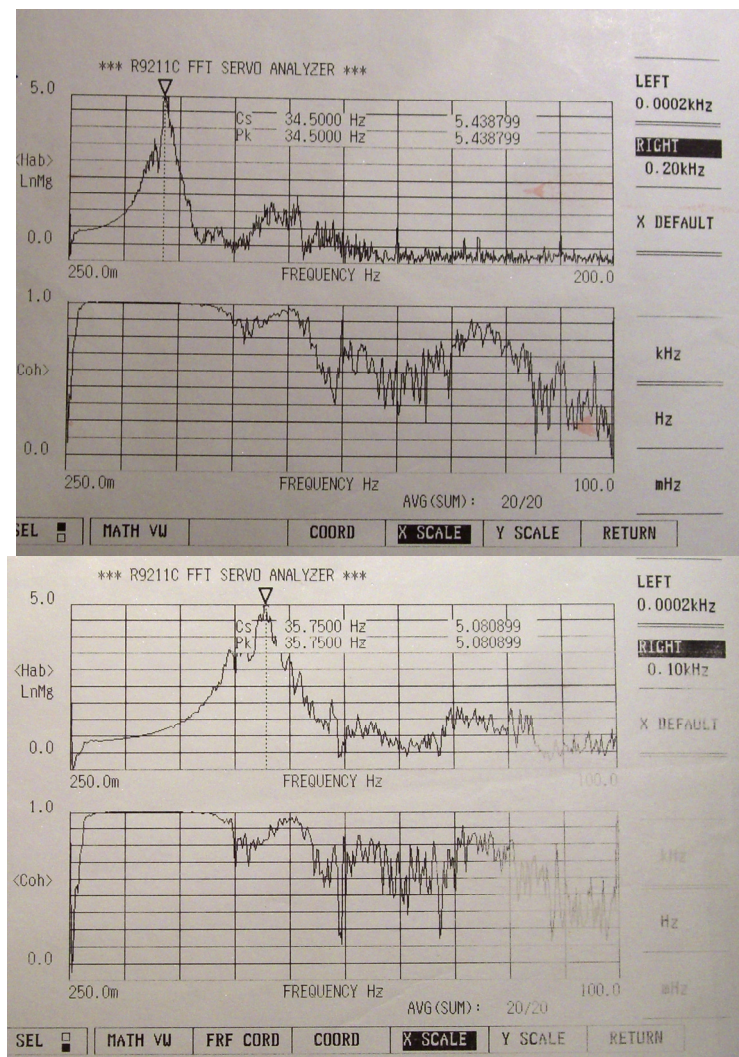


Figure 4.27: Examples of broad band outputs: FRFs BEN003g and BEN001g

In Figure 4.27 two examples of FRFs function relative to Broad Band test (BEN001 g and BEN003g) have been reported. As shown in the tables the results obtained in time and in frequency domain are quite dissimilar.

Hence, to take in account the stress condition of soil in the shear stack, it has been used the theoretical formulation to estimate the value of the stiffness. As explain in equation 4.19 the Hardin and Drnevich's formulation considers the value of σ'_m , mean effective confining stress and the void ratio of the materials in the shear stack. Table 4.19 shows the value of the stiffness from the application of the Hardin and Drnevich's formula.

To increase the packing density of the mixture several tapping procedures with different value of amplitude of vertical motion have been made. As shown in table 4.20 the tapping procedure is useful to achieve the packing density, a 7% density gain has been achieved (from 1825 to 1951 Kg/m³).

Table 4.19 Theoretical estimation of stiffness for LB fraction B+E, before tapping

Pluviation Test Leighton Buzzard Fraction E -B (nozzle D=15 mm)								
Mdrum[kg]	Mss[kg]	V[m3]	γ_d [t/m3]	void ratio (e)	Dr	σ_m [kN/m2]	Go[MPa]	Vs [m/s]
850	558	0.3029	1.842	0.437	0.55	5.3681	33.70	134.85

Table 4.20 Results of tapping procedures in the deposit

Name test	A	H _Z	Cycle	A	Displacement	total H from Top	Volume deposit	Mss[kg]	γ_d	H deposit
	mm		n°	g	mm	mm	m3	Kg	[kg/m ³]	mm
T035g.m	4	6	10000	0.35	0	255	0.361	659	1825.40	559
T09g.m	4	10	10000	0.9	8	263	0.356	659	1851.91	551
T032g.m	2	10	10000	0.32	9	264	0.355	659	1855.27	550
T2g.m	6	10	10000	2.0	32	287	0.340	659	1936.24	527
T2g.m	6	10	10000	2.0	36	291	0.338	659	1951.05	523

Table 4.21 shows the value of theoretical estimation of stiffness applying the Hardin and Drnevich formula.

Table 4.21 Theoretical estimation of Stiffness fro mixture LB fraction E and B

Theoretical Stiffness for Leighton Buzzard Fraction E -B after tapping (nozzle D=15 mm)									
H layers	Mss[kg]	V[m3]	γ_d [t/m3]	void ratio (e)	Dr	σ_m [kN/m ²]	Go[MPa]	Vs [m/s]	
523	659	0.34	1.951	0.357	0.79	6.34	41.03	145.02	
407	659	0.26	1.951	0.357	0.79	4.93	36.19	136.21	

From the tapping the last value of packing density is 1951 Kg /m³. The application of Hardin and Drnevich's formulation give the valuation of stiffness and shear velocity for mixer LB fraction B+E (G= 36 MPa and Vs=136 m/s).

After tapping procedure, the results of modal test are shown in table 4.22 and in table 4.23. The high of the deposit after mechanical densification is 523 mm. Figure 4.28 shows some particular examples of the outputs of the broad band test after tapping.

Table 4.22 Pulse tests results after tapping for LB fraction E and fraction B mixer

Pulse tests results					Chan 1-4			Chan 1-3		
Name tests	Displacement Shaking table	Input	Dz1-3	Dz1-4	Dt14	v14	G14	Dt13	v13	G13
	mm	g	mm	mm	s	m/s	MPa	s	m/s	MPa
BEP0015gat.m	0.3	0.015	407	611	0.0039	156.67	48.81	0.0039	104.36	21.25
BEP002gat.m	0.4	0.02	407	611	0.0044	138.86	38.35	0.0059	68.98	9.28
ATBEP0015g.m	0.3	0.015	407	611	0.0037	165.14	54.23	0.0032	127.19	31.56
ATBEP002g.m	0.4	0.002	407	611	0.0046	132.83	35.09	0.004	101.75	20.20
ATBEP0035g.m	0.5	0.0035	407	611	0.0066	92.58	17.04	0.004	101.75	20.20
ATBEP0065g.m	0.8	0.0065	407	611	0.0027	226.30	101.85	0.002	203.50	80.80
ATBEP01g.m	1	0.1	407	611	0.0032	190.94	72.51	0.0025	162.80	51.71
ATBEP013g.m	1.2	0.13	407	611	0.0052	117.50	27.46	0.0038	107.11	22.38
ATBEP015g.m	1.5	0.17	407	611	0.0053	115.28	26.43	0.006	67.83	8.98

Table 4.23 Broad Band tests results after tapping for LB fraction E and fraction B mixer

White Noise	Input t		Chanel 4				Chanel 3			
Name Test	A	A(g)	f _{n14}	H	v _{s1-4}	G ₁₋₄	f _{n13}	H	v _{s13}	G ₁₃
	mm/V	g	Hz	mm	m/s	MPa	Hz	mm	m/s	MPa
ATBEN001g.m	0.5	0.01	40.25	523	84.20	13.65	40.75	523	85.25	13.99
ATBEN0015g.m	0.7	0.015	41.5	523	86.82	14.51	39.5	523	82.63	13.14
ATBEN003g.m	1.2	0.03	40.75	523	85.25	13.99	41.00	523	85.772	14.16
ATBEN01g.m	2.5	0.1	40.75	523	85.25	13.99	40.75	523	85.249	13.99
ATBEN015g.m	3	0.15	35.5	523	74.27	10.62	34.5	523	72.174	10.03
ATBEN02g.m	4	0.2	35	523	73.22	10.32	34.5	523	72.174	10.03
				average	79.50	12.23		average	78.84	12.05

The three methodologies used to obtain the shear wave velocity and stiffness provide different velocity values.

In figures 4.29 and 4.30 a comparison of pulse test results, broad band results and Hardin and Drnevich's formulation is illustrated. Very low input motion amplitudes for the pulse and white noise tests have been chosen in order to guarantee small shear strains in the soil. Broad band tests, in general, underestimate velocity and stiffness values. The soil frequency is affected by the height of the deposit; in these cases the shear stack is not totally filled in with the LB BE sand.

Hence the theoretical results and the pulse tests are in good agreement. For the LB BE the average value of shear wave velocity from the pulse tests is 146 m/s (G= 45 MPa). This value is in agreement with the theoretical formulation.

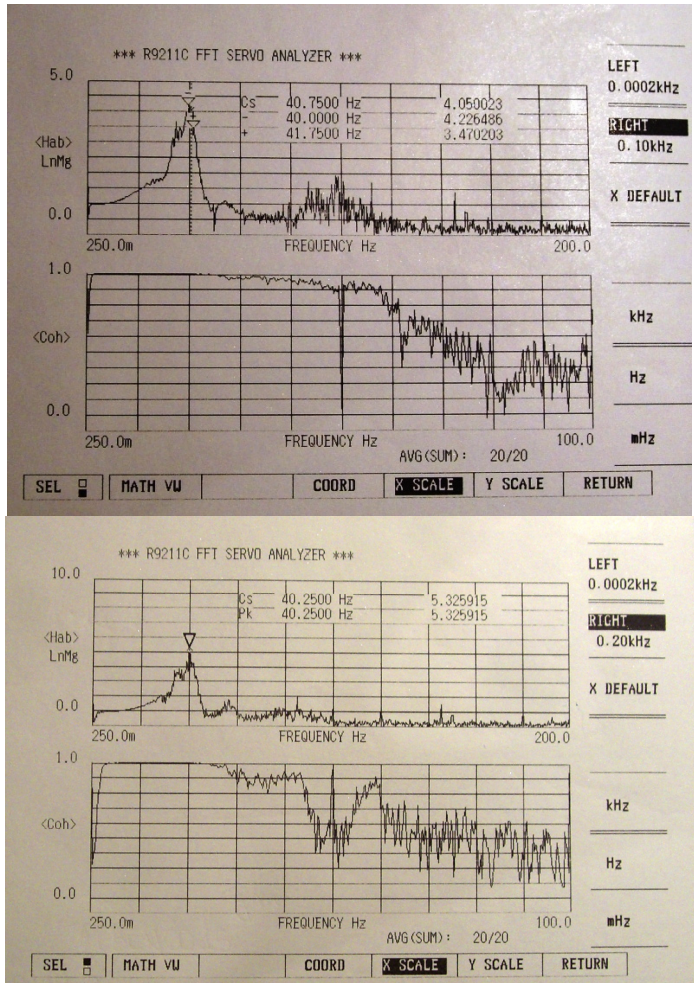


Figure 4.28: Examples of broad band outputs after tapping: FRFs ATBEN01g and ATBEN001g

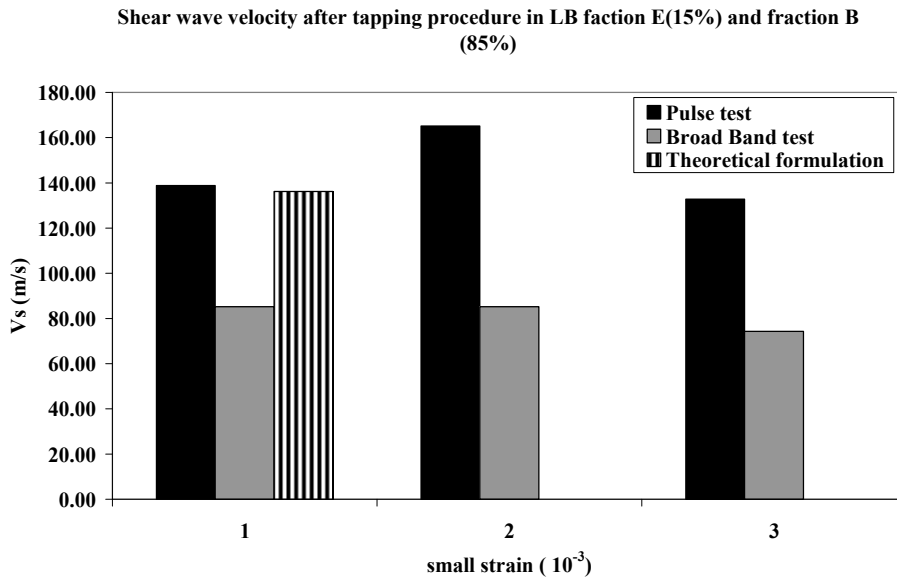


Figure 4.29: Comparison between Pulse tests, Broad Band tests and theoretical estimation of shear wave velocity

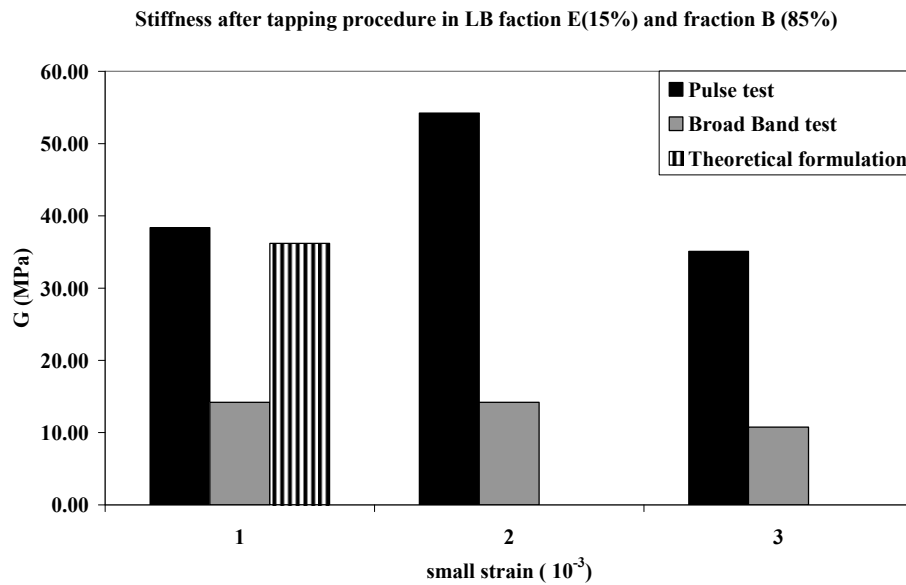


Figure 4.30: Comparison between Pulse tests, Broad Band tests and theoretical estimation of stiffness

4.4.5 Results of Modal Tests: monolayer Rubber CT0515 (R)

After pluviation the packing density of the rubber has been found (0.504 t/m^3). Five modal tests have been made for the monolayer deposit of Rubber CT 0515. All the shear stack has been filled in with Rubber (814 mm). In figure 4.31 the set up of the test have been shown.

Table 4.23 shows the list of the all modal tests made, while the results of the tests before tapping are reported in table 4.24 an table 4.25.



Figure 4.31: set up for modal test in Rubber

Table 4.23 List of modal test done on the results Rubber

Exploratory test	
Rubber CT0515	
1	Exp-01g (Broad Band)
2	Exp-01g-2 (Broad Band)
3	Exp-02g ch 4 (Broad Band)
4	Pulse 3 mm - 10 Hz sine 1 cycle
5	Pulse 3 mm - 10 Hz sine 2 cycle

The Broad Band tests for Rubber are not able to find the resonance frequency. Shear stack natural frequency is a 7 Hz, an extra peak visible at 17.68 Hz, it could be representative of a table (oil column) resonance and is not representative of the test soil response. The shear stack drives the response, the rubber stiffness is very small, and hence the frequency could not be measured. The results of pulse test are more reliable. Therefore the shear wave velocity of Rubber measured from pulse test is 13 m/s and the relative stiffness G is around 0.1 MPa.

Table 4.24 Results of pulse test on Rubber

PULSE TEST	Channel 4					
	Name tests	A	Dz ₁₋₄	Dt ₁₄	Shear velocity v ₁₄	Stiffness G ₁₄
		mm	mm	s	m/s	MPa
Pulse 3mm 10 hz sine 1 cycle	3	611	0.047	13.00	0.09	
Pulse 3mm 10 hz sine 2 cycle	3	611	0.04	15.28	0.12	
Pulse 3mm 10 hz sine 2 cycle	3	611	0.06	10.18	0.05	

Table 4.25 Results of broad band test on Rubber

Broad Band	Input Test	Channel 4				
		A(g)	f _{n14}	d	v _{s 1-11}	G ₁₋₁₁
		g	Hz	mm	m/s	MPa
Exp-01g	0.1					
Exp-01g-chan 4	0.1	17.68	611	43.21	-	
Exp-02g-chan 4	0.1	17.68	611	43.21	-	

4.4.6 Conclusion on the Modal Test results

Among the three methodologies, Pulse test requires the least effort. Signal processing is comparatively simple and test durations are short.

The frequency domain analysis of the random excitation tests is easier, particularly if a spectrum analyzer is available. On grounds of practicality, it is this test methodology, which must be suggested. There are occasions when random excitation tests may not be proper. As explained in the previous paragraphs, when the shear stack was not completely filled, an underestimated value of stiffness has been obtained. In the case of Rubber, it is not possible to read the resonant frequency of the material too soft to drive the response of the system (shear stack and deposit).

To evaluate material stiffness the theoretical formulation by Hardin and Drnevich's has been applied, which takes into account the effects of void ratio and soil mean stress in the deposit. In conclusion, material proprieties are shown in table 4.26.

Table 4.26 Proprieties of material

Results of Modal test of all materials				
	γ	Vs	G	fn
	kg/m ³	m/s	MPa	Hz
LB fraction E	1437	76.61	8.4	23.94
Mixture LB fraction E(15%) and B(85%)	1951	146	42	
Rubber	504	13	0.1	

4.5 Physical and mechanical proprieties of soil configurations

In this paragraph, the stiffness proprieties of the deposit configurations tested in the shaking table are examined. Three different deposit configurations have been tested: monolayer LB fraction E configuration (code “E”); a layered configuration of LB fraction E (top layer) and mixer of LB fraction B (85%) and E (15%) (bottom layer) (code “BE+E”); a layered configuration of Rubber CT0515 (top layer) and LB fraction E (bottom layer) (code “E+R”).

With the exceptions of E+R configuration, before the dynamic tests, some pulse tests have been performed in order to measure the shear velocity of soil deposit in the shear stack.

In order to check material stiffness variations induced by the shaking, pulse tests have been performed randomly. Unfortunately these tests have often been ineffective, because of the unfavourable coupling between the signal sample frequency (1000 Hz) and the distance between the receivers (200mm). However, it must be noted that a 1000 Hz frequency is much higher than those usually employed in earthquake engineering tests (around 200 Hz). Only an analysis in the frequency domain it is possible as reported following.

4.5.1 *Monolayer Leighton Buzzard fraction E (E)*

Table 4.27 shows the results of pluviation test done for the dynamic test on monolayer LB fraction E configuration.

Before start the shaking table test, it has been done five pulse tests. In the following table are shown results for all five different pulse tests. The pulse tests have been done with different amplitude of acceleration.

Table 4.28 shows the list of the all modal tests made, while the results of the pulse tests are reported in Table 4.29. To measure the shear wave travel time it is considered time delay between accelerometers a_1 and a_4 (0.610 m distance) and between accelerometers a_2 and a_4 (0.407 m distance).

Table 4.27 Pluviation test for monolayer configuration (E)

Pluviation Test Leighton Buzzard Fraction E (nozzle D=40 mm)

Shear stack			
Length[mm]	Width [mm]	Area [mm ²]	H [mm]
1185	545	645825	814

Physical Properties (Leighton Buzzard)			
Gs [t/m ³]	Gs [kg/m ³]	e _{min}	e _{max}
2.647	2647	0.613	1.014

Tan 1980

LB fraction E : void ratio and Dr for single layer										
layer	H[mm]	M _{drum} [kg]	M _{ss} [kg]	V [m ³]	γ _d [kg/m ³]	γ _d [t/m ³]	void ratio (e)	Dr	σ _m [N/m ²]	
	First drum	336								
1(Bottom)	139	220	116	0.090	1292.20	1.292	1.048	-0.086	1115.949	
2	110	118	102	0.071	1435.80	1.436	0.844	0.425	981.266	
	Second drum	270								
3	111	212	104	0.072	1450.76	1.451	0.825	0.472	1000.506	
4	109	112	100	0.070	1420.56	1.421	0.863	0.376	962.025	
	Third drum	302								
5	110	270	104	0.071	1463.95	1.464	0.808	0.513	1000.506	
6	95	180	90	0.061	1466.91	1.467	0.804	0.523	865.823	
7(top)	140	96	84	0.090	929.04	0.929	1.849	-2.083	808.101	
									0.000	
				M _{ss} [kg]	V [m ³]	γ _d [kg/m ³]	γ _d [t/m ³]	void ratio (e)	Dr	σ _m [N/m ²]
Total Weight				700	0.526	1331.6	1.3316	0.988	0.0651	6734.177

Table 4.28 list of pulse test done before the dynamic test on LB fraction E

Sequential time	Id test	Peculiarity
Test 2	EP015g.m	Peack:0.15 g No_Channels = 40; Buffer_Size = 10; Points = 10162; Frequency = 1016.26 Hz Filter = 80;
Test 3	EP002g.m	Peack:0.2 g No_Channels = 40; Buffer_Size = 10; Points = 10162; Frequency = 1016.26 Hz Filter = 80;
Test 4	EP035g.m	Peack:0.35 g No_Channels = 40; Buffer_Size = 10; Points = 10162; Frequency = 1016.26 Hz Filter = 80;
Test 5	EP04g.m	Peack:0.4 g No_Channels = 40; Buffer_Size = 10; Points = 10162; Frequency = 1016.26 Hz Filter = 80;
Test 6	EP06g.m	Peack:0.5 g No_Channels = 40; Buffer_Size = 10; Points = 10162; Frequency = 1016.26 Hz, Filter =80;

Table 4.29 results of pulse tests on monolayer configuration E, before start the dynamic test

E Pulse 2 name:EP015g							
LB E	t1	t4	Δt	s1-s4	v14	$\gamma_d(\text{Kg/m}^3)$	G(MPa)
	6.6981000	6.7010000	0.0029000	0.610	210	1331	58.9
LB E	t2	t4	Δt	s2-s4	v24	$\gamma_d(\text{Kg/m}^3)$	G(MPa)
	6.6646320	6.6666000	0.00197	0.407	207	1331.00	56.9
E Pulse3 name:EP002g							
LB E	t2	t4	Δt	s2-s4	v24	$\gamma_d(\text{Kg/m}^3)$	G(MPa)
	5.8981000	5.9030000	0.0049	0.407	83	1331	9.2
E Pulse 4 name:EP035g							
LB E	t2	t4	Δt	s2-s4	v24	$\gamma_d(\text{Kg/m}^3)$	G(MPa)
	-	-	-	-		1331.00	-
E Pulse5 name:EP04g							
LB E	t2	t4	Δt	s2-s4	v24	$\gamma_d(\text{Kg/m}^3)$	G(MPa)
	6.2090000	6.2120000	0.0030	0.407	136	1331.00	24.50
E pulse 6 EP06g							
LB E	t2	t4	Δt	s2-s4	v24	$\gamma_d(\text{Kg/m}^3)$	G(MPa)
	6.1765700	6.1814900	0.0049	0.407	83	1331	9.11

The results reported are quite questionable. The sample frequency is not at all appropriate for a small distance between the accelerometer in sand (internal array).

The signal are quite noise and it is very difficult to read the time delay. From the visual analysis, the EP002g and EP06 g are the most reliable. In figure 4.32 the typical measured shear wave travel time between accelerometers a_2 and a_4 has been plotted for EP002 g test. In figure 4.33 the time histories of the accelerometers a_2 and a_4 has been plotted for EP06 g.

Just in these two last cases, the results are comparable with the modal test results. Hence we can assume that the initial value of stiffness for Monolayer configuration E is 9 MPa, which corresponds to a shear velocity of 83 m/s. The theoretical estimation of natural frequency, f_n , of the deposit is done in function of height and shear velocity of the soil deposit. It is 25 Hz.

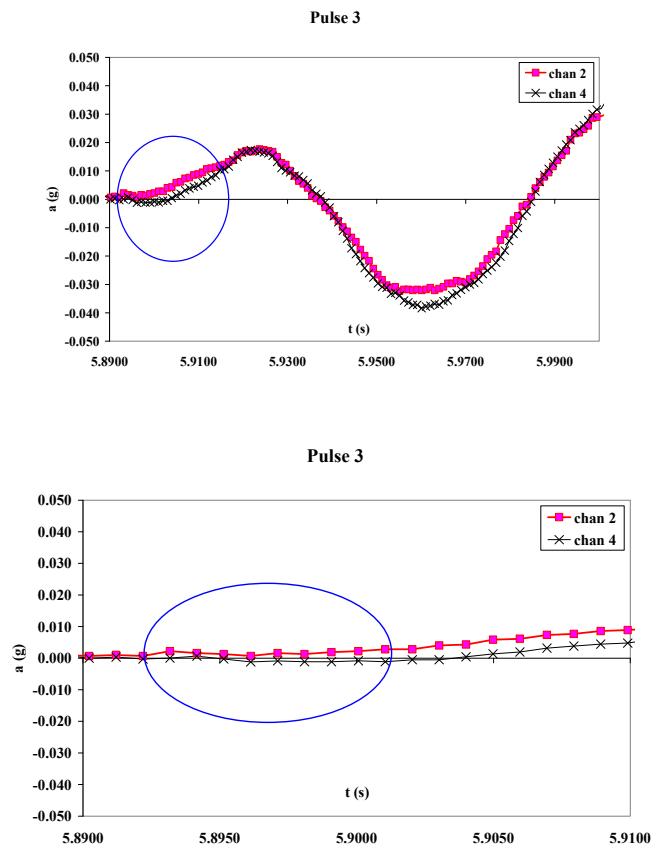


Figure 4.32: Pulse test 3(EP002g) LB fraction E, acceleration time histories for sensors a2 and a4

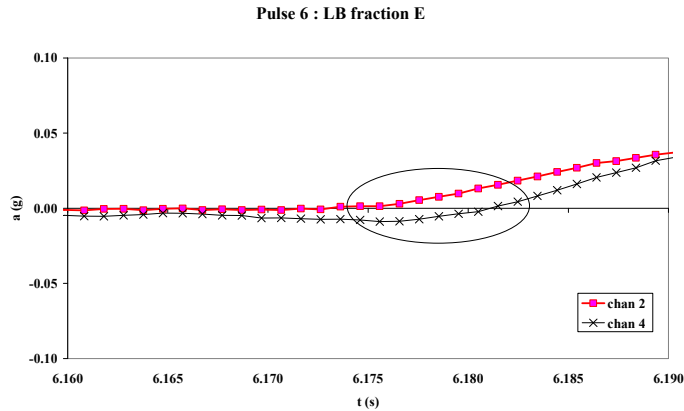


Figure 4.33: Pulse test 6(EP06g) LB fraction E, acceleration time histories for sensors a_2 and a_4

4.5.2 Layered soil: Leighton Buzzard fraction BE and LB fraction E (BE+E)

Table 4.30 shows the result of pluviation test done before the dynamic test in a layered soil configuration BE+E: upper layer LB fraction E and bottom layer LB fraction E (15%) and fraction B (85%).

Table 4.31 shows the proprieties of the upper layer E ($\gamma_d = 1324 \text{ Kg/m}^3$; $e = 0.98$, $Dr = 4\%$) and of the bottom layer BE (γ_d is 1923 Kg/m^3 ; the void ratio is 0.38 and the relative density is equal to $Dr = 73\%$).

Before starting the dynamic test, just one pulse test has been made. It should be useful to measure the shear wave velocity of the upper and bottom layer.

Due to the small distance of the accelerometer in sand (Figure 4.22) around 200 mm, the test is unable to give a reasonable value of shear velocity.

Figure 4.34 a) shows the comparison between the acceleration time histories of a_2 sensor and a_3 sensor (Figure 4.22), the respectively signals travel together in the time. Therefore the shear wave arrival times is equal to zero.

Figure 4.34 b) shows the comparison between the acceleration time histories of a_3 sensor and a_4 sensor (Figure 4.22), the shear wave arrival times is established by the manual comparison of time histories, the peaks are simultaneous.

The initial value stiffness for these configurations are chosen plausibly with the experimental data available.

For the top layer, LB fraction E, it has been chosen the same value of shear wave velocity obtained for the monolayer configuration (pulse test EP002g), shown in the previous paragraph. The deposition of LB fraction E in monolayer configuration and in this layered soil

configuration are very close, the variation of packing density is around 1%, also the measure of shear wave velocity is relative to a layer high 400 mm.

For the bottom layer, LB fraction BE, it has been chosen the value of shear wave velocity obtained for the Hardin and Drnevich's formulation, as reported in table 4.31

Table 4.32 Layered soil BE+E: proprieties

	γ_d [kg/m ³]	void ratio (e)	Dr %	σ_m [Kg/m ²]	Go [MPa]	Vs [m/s]	Vs2/Vs1 [m/s]
Bottom layer LB fraction B+E	1923	0.376	73%	5374	36.68	136.78	1.65
Upper layer LB fraction E	1324	0.999	4%	3348	9	83	

Pulse test: bottom layer LB fraction B+ E

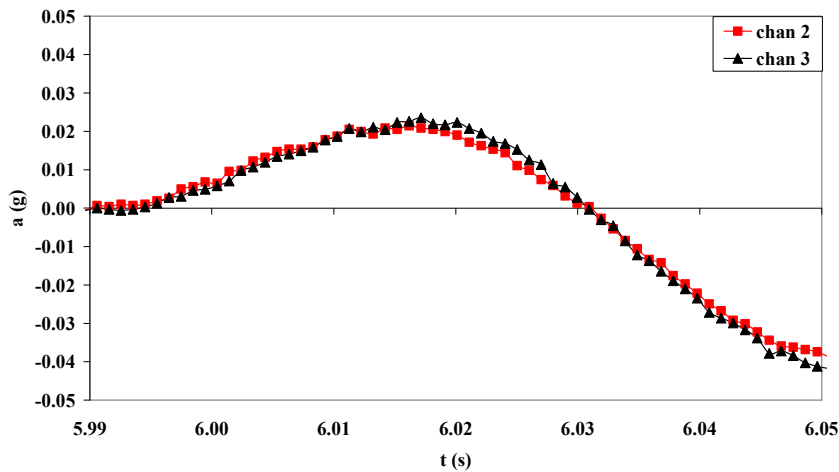


Figure 4.34a Pulse test: comparison signal a2 and a3 in the bottom layer of LB fraction BE

Pulse test: bottom layer LB fraction E

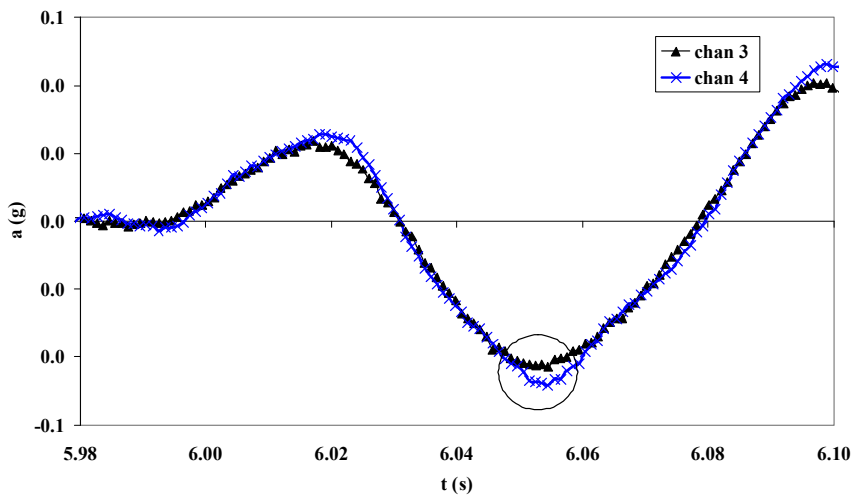


Figure 4.34b Pulse test comparison signal a4 and a3 top layer of LB fraction E

Table 4.30 Pluviation test for LB fraction E and LB fraction B (85%)+E(15%)

BOTTOM LAYER: LB fraction E+B (nozzle 15 mm)								
Layer	H[mm]	M _{drum} [kg]	M _{ss} [kg]	V[m ³]	γ _d [kg/m ³]	γ _d [t/m ³]	void ratio (e)	Dr
	First drum	388						
1(Bottom)	139	242	148	0.090	1648.66	1.649	0.606	0.026
2	110	114	129	0.071	1815.86	1.816	0.458	0.481
3	111	80	38					
	Second drum	414						
3	111	333	119	0.072	1660.00	1.660	0.595	0.060
4(109)	54	272	73	0.035	2093.22	2.093	0.265	1.075
TOP LAYER: LB fraction E (nozzle 40mm)								
	L.B.fraction E	354						
4	55	310	44	0.036	1238.73	1.239	1.137	-0.306
5	110	224	86	0.071	1210.57	1.211	1.187	-0.430
6	95	128	96	0.061	1564.71	1.565	0.692	0.804
7	140	90	38					
	Second drum	346						
7	140	268	116	0.090	1282.97	1.283	1.063	-0.123

Table 4.31 Theoretical valuation of stiffness by Hardin and Drnevich formula

	H [mm]	M _{ss} [kg]	V [m ³]	γ _d [kg/m ³]	void ratio (e)	Dr %	σ _m [Kg/m ²]	Go [MPa]	V _s [m/s]
Bottom layer LB BE	407	500	0.26	1923	0.376	73%	5374.53	36.68	136.78
Upper layer LB E	407	342	0.26	1324	0.999	4%	3347.99	11.52	92.37

The fundamental period of layered soil profiles has been calculate by the A. H. Hadjian, 2002 formulation (equation 4.22), it is an simpler alternative to the Rayleigh method for shear beams or soil columns.

$$\frac{T_2}{T_1} > 0.1$$

$$T = \left\{ T_1 \left[1 + b \left(\frac{T_2}{T_1} \right)^{2.2} \right] \left[1 + 2 \left(\frac{H_1}{H_2} \right)^{2.2} \right]^{\frac{1}{2.2}} \right\} \quad [4.22]$$

where H_1 is the high of the first layer and H_2 is the high of the second layer, and b is the ratio between equal to $1-0.2(H_1/H_2)^2$

The fundamental period of layered soil configuration BE+E is 0.037 s and the theoreticàò fundamental frequency is 27 Hz.

4.5.3 Layered soil: Leighton Buzzard fraction E and Rubber (E+R)

Table 4.33 shows the result of pluviation test done before the dynamic test in a layered soil configuration E+R: upper layer Rubber and bottom layer LB fraction E.

Table 4.34 shows the proprieties of the upper layer R ($\gamma_d = 479 \text{ Kg/m}^3$; $e = 1.40$) and of the bottom layer E (γ_d is 1594 Kg/m^3 ; the void ratio is 0.66 and the relative density is equal to $D_r = 88\%$).

The initial value stiffness for these configurations are chosen reasonably with the theoretical prediction, for LB fraction E, and by experimental results of modal test, for Rubber.

Table 4.35 Layered soil E+R: proprieties

	γ_d [kg/m ³]	void ratio (e)	D_r %	σ_m [Kg/m ²]	G_o [MPa]	V_s [m/s]	V_{s2}/V_{s1} [m/s]
Bottom layer LB fraction E	1594	0.66	88%	4060	20	114	8.8
Upper layer Rubber	47	1.40	-	-	0.1	13	

The fundamental period of layered profiles E+R has been calculate by the A. H. Hadjian, 2002 formulation (equation 4.22), the fundamental frequency is 8 Hz and the fundamental period is 0.129s.

Table 4.33 Pluviation test for LB fraction E and Rubber

LB fraction E + Rubber : void ratio and Dr for sigle layer													
layer	H[mm]	Mdrum[kg]	Mss[kg]	V[m3]	γ_d [kg/m3]	γ_d [t/m3]	void ratio (e)	Dr	σ_m [N/m2]	σ_m [kN/m2]	Go [kN/ m2]	Go[Mpa]	Vs [m/s]
LB fraction E	first drum	360											
1(Bottom)	139	234	126	0.090	1403.592	1.404	0.886	0.320	1385.841	1.386	12444.626	12.445	94.161
2	110	120	114	0.071	1604.713	1.605	0.650	0.909	286.008	0.286	1510.947	1.511	30.685
3	111	90	30	0.072	418.488	0.418	5.325						
	second drum	262											
3	111	144	148	0.072	2064.543	2.065	0.282	1.825	726.137	0.726	2330.671	2.331	33.599
4	50	110	34	0.032	1052.917	1.053	1.514	-1.247	301.954	0.302	1018.005	1.018	31.094
Rubber	third drum	174											
4	59	152	22	0.038	577.3721	0.577	0.992						
5	110	122	30	0.071	422.293	0.422	1.723						
6	95	88	34	0.061	554.167	0.554	1.075						
7(top)	140	82	6	0.090	66.360	0.066							
	fourth drum	158											
7(top)	140	125	39	0.090	431.342	0.431	1.666						

Table 4.34 Proprieties of LB fraction E and Rubber

	H [mm]	Mss [kg]	V [m3]	γ_d [kg/m3]	void ratio (e)	Dr	σ_m [t/m2]	Go [MPa]	Vs [m/s]
LB fraction E	407	422	0.26	1594	0.66	88%	4.060	20.95	114.65
Rubber	407	125	0.26	479	1.40				

4.5.4 Stiffness during dynamic tests

As explained before the pulse tests done during the shaking table test are not so accurate.

In order to check material stiffness variations induced by the shaking, pulse tests have been performed randomly. Unfortunately these tests have often been ineffective, because of the unfavourable coupling between the signal sample frequency (1000 Hz) and the distance between the receivers (200mm). However, it must be noted that a 1000 Hz frequency is much higher than those usually employed in earthquake engineering tests (around 200 Hz). Only an analysis in the frequency domain it is possible as reported following.

In order to try to interpret the results also a Cross Correlation of the acceleration signal after filtering has been done. This procedure is useful to appreciate the values of time delay of recorded signal which travelling in the soil from two different positioned accelerometer. In signal processing, cross-correlation is a measure of similarity of two waveform as a function of a time-lag applied to one of them. It is commonly used to search a long duration signal for a shorter, known feature. For continuous functions, f and g , the cross-correlation is defined as:

$$(f \bullet g)(t) = \int_{-\infty}^{+\infty} f^*(\tau)g(t + \tau)d\tau \quad [4.23]$$

where f^* denotes the complex conjugate of f . Similarly, for discrete functions, the cross-correlation is defined as:

$$(f \star g)[n] \stackrel{\text{def}}{=} \sum_{m=-\infty}^{\infty} f^*[m] g[n + m]. \quad [4.24]$$

In an autocorrelation, which is the cross-correlation of a signal with itself, there will always be a peak at a lag of zero. If X and Y are two independent random variables with probability distribution f and g , respectively, then the probability distribution of the difference $X - Y$ is given by the cross-correlation $f \star g$.

Hence, after filtering pulse test signals, they are cross correlated. The MATLAB command *Xcorr* has been used. As shown in figure 4.35 a) and b) the Cross Correlation give a delay equal to zero. It can not appreciate the time delay. It seems that sample frequency of pulse tests are too small to obtain a significant value of time delay.

From the all the pulse tests done during the test just an analysis in frequency domain it is possible. From the valuation of the transfer function between the input motion, at bottom of the shear stack (a1, accelerometer), to the surface of the deposit (a5 accelerometer), the fundamental frequency of deposit may be computed.

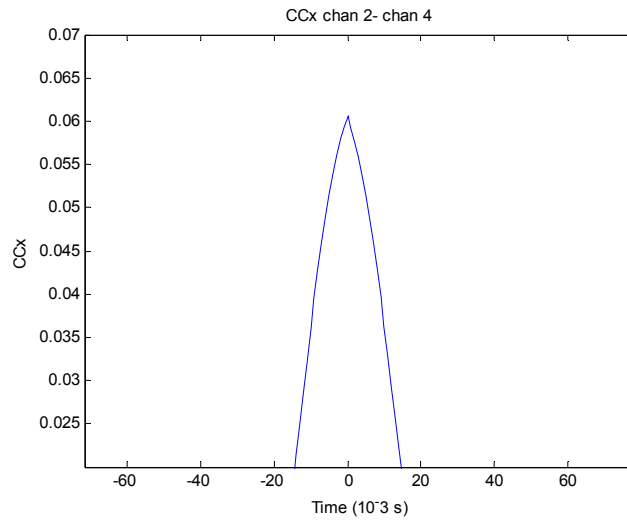


Figure 4.35a Cross correlation chan 2-chan 4, pulse test for LB fraction E (EP004g)

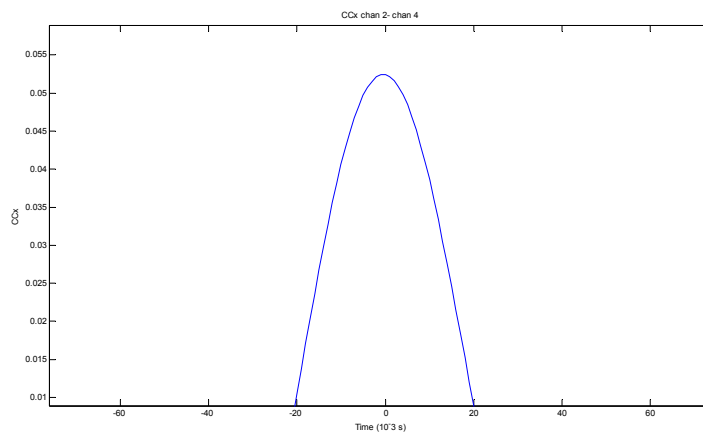


Figure 4.35b Pulse test comparison signal a4 and a3 top layer of LB fraction E

Table 4.35 shows the results in frequency domain for the successive pulse tests every ten runs done in the monolayer configuration E.

Table 4.35 LB fraction E: fundamental frequency variation in time (pulse test during dynamic test)

TFFT	fn	v15(m/s)	γ_d (Kg/m3)	ρ (Kg*s2/m4)	G(MPa)
Ch.5-1	Hz	m/s			
Test 2	26.7	86.94	1331	136	10.2
test 21	27.0	87.91	1331	136	10.4
test 33	29.7	96.70	1331	136	12.6
test 47	30.0	97.55	1331	136	12.9
test 110	30.0	97.55	1331	136	12.9

With the aim of estimating the stiffness variation the average shear wave velocity is simply multiplied by the average density of the whole deposit.

Table 4.36 shows the results in frequency domain for the successive pulse tests every ten runs done in the layered soil configuration BE+E.

Table 4.36 BE+E soil configuration: fundamental frequency variation in time (pulse test during dynamic test)

BE+E	Frequency	V _s	γ _{average}	ρ _d	G
Ch.5-Ch.1	Hz	m/s	Kg/m ³	kg/m ³	MPa
test 1	29.2	94.99	1625	166	14.95
test21	30.3	98.56	1625	166	16.09
test 41	32.1	104.53	1625	166	18.10
test 51	30.0	97.77	1625	166	15.84
test 54	31.7	103.22	1625	166	17.65
test 68	31.1	101.35	1625	166	17.02
test 71	28.9	94.2	1625.0	166	14.70
test 98	31.25	101.75	1625	166	17.15

5. Shaking table tests results

5.1 Introduction

This chapter presents the results of dynamic tests on shaking table. As previously described, the shaking table tests were designed so that each test setup provided different conditions of subsoil and pile head. In this way, the effect of superstructure inertial forces, pile cap embedment, stiffness contrast could be analyzed.

The physical model is located in the laminar box called Shear Stack (specifically designed at BLADE in Bristol). Three different soil configurations have been pluviated inside the box: a monolayer subsoil and two deposits constituted by two soil layers, with stiffness increasing with depth. The shear wave velocity ratio at the interface V_{s2}/V_{s1} (between lower and upper layer) is equal to about 1.7 and 8 respectively.

Due to the great number of acquired data, in the present dissertation the most significant experimental results have been illustrated referring to free head (FH) and no rotation head pile conditions (NRH). The effect of the single degree of freedom structure (NRH+SDOF) located on pile head has been enhanced too.

Three earthquakes have been utilised as input motion, properly scaled by three different factors (12, 5, 2 times). The proprieties of each earthquake are shown in table 3.3, chapter 3.

The peculiarity of each tests are presented in the form of acceleration (and bending strain) time histories, and fast Fourier transforms (FFTs).

The pile response has been evaluated mainly in terms of bending moments induced by both kinematic interaction and coupled kinematic and inertial effects. They are defined by the absolute peak strain at each gauge during the excitation.

To reduce noise, data signals from the instruments have been passed through a low pass Butterworth filter set to 80Hz. Data were acquired at a rate of 200 Hz. Data processing has consisted exclusively on the remove the trend (dtrend command), the acceleration has been filtered before the procedure used to estimate the soil shear strains. In Appendix III all accelerations, displacements, strain gauges time histories are plotted for tests analyzed in this chapter.

5.2 Matching and repeatability of tests

A crucial component of high quality experimental results is the performance of the shaking table.

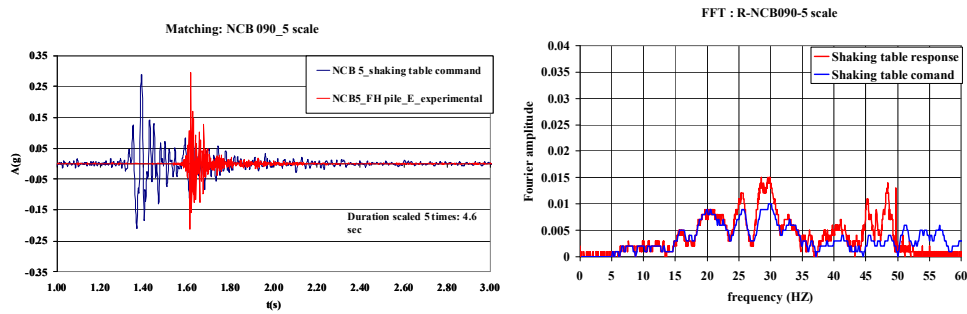


Figure 5.1 a) Shaking table response: acceleration time histories for Norcia 5 scale and FFT

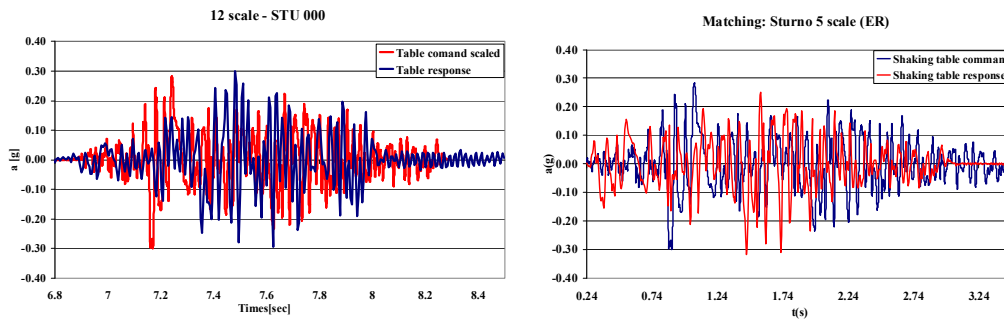


Figure 5.1 Matching: b) Sturno 12 scale and c) Sturno 5 acceleration time histories comparison

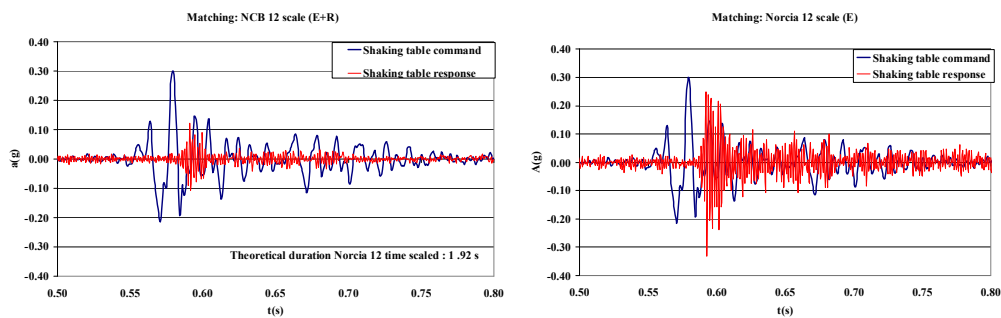


Figure 5.1 Matching: d) Norcia12 scale for E+R configuration and e) Norcia 12 scale acceleration time histories

Figure 5.1 plots the acceleration time histories of command signal response with the shaking table response.

The table response match to the command signal is good. The theoretical scaled input motion (shaking table command) time history is compared with the experimental input motion (shaking table response) one. In figure 5.1 *a)* and *b)* the time histories and the FFT for the two input motion are shown for Norcia 5 scale. They are in good agreement. It has been noted that during the matching the high frequency are amplified.

In figures 5.1 *b)* and *c)* the shaking table response and the theoretical shaking table command are plotted together. From the comparison, the results are very good. Just for Norcia 12 times scaled some different from input motion give to shaking table and the input motion recorded on the shaking table surface occurs. In case of Norcia 12 scale in E+R configuration also the PGA are very different (0.1 g), as shown in figure 5.0 e). For the test done in E+R configuration for Norcia 12 scale the matching is not coherent with the original input motion scaled theoretically. For the other test small different in PGA values are noted, but they are obviously normal, and they depend on the shaking table hydraulic system. The shaking table is an analogical controlled servo-hydraulic system that is sensitive to such factors as atmospheric conditions, “warm-up” procedures, test-specific table balance settings, etc.

In this experimental work, three or two different runs have been performed for each dynamic test. This choice has been very important to verify the extendibility and trustworthiness of tests, to be sure about the results. In figures 5.2 *a)*, *b)* and *c)* are shown three different examples of repeatability of test in terms of time histories of input motion, time histories of strain at elevation 200 mm, and maximum bending moment along the pile. The outputs obtained from three different runs are equivalent. The shaking table tests have the ability to reproduce signals from one test to the next.

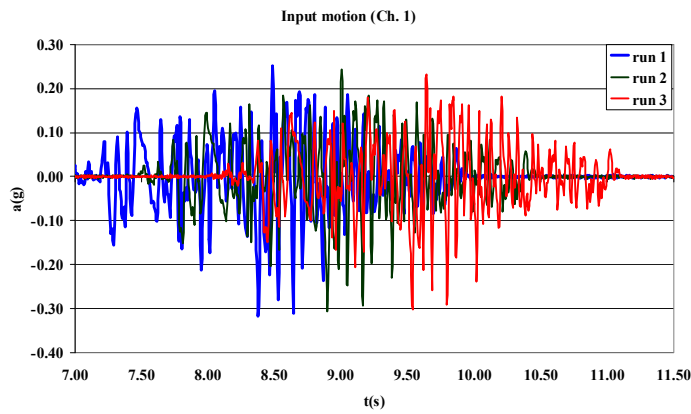


Figure 5.2 a) input motion time histories comparison for three different runs-Sturno 5 scale (E+R)

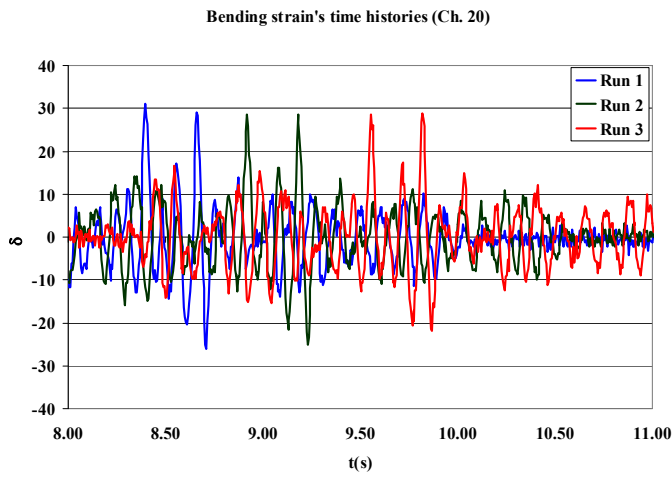


Figure 5.2.b) bending strain time histories comparison for three runs -Sturno 5 scale (E+R)

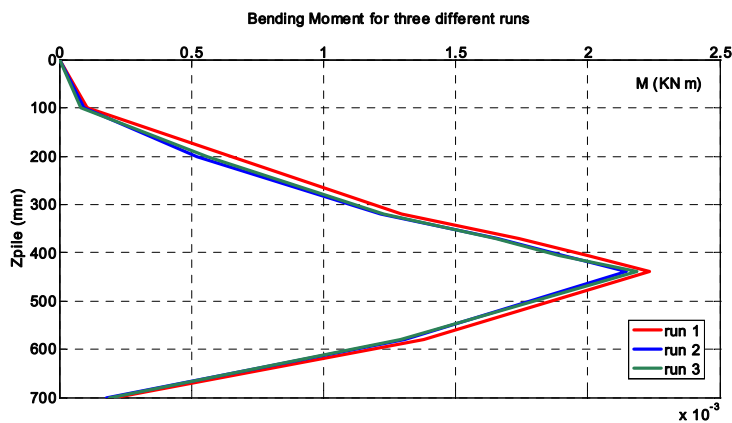


Figure 5.2.c) maximum bending moment along the pile comparison between three runs- Sturno 5 scale (E+R)

5.3 Soil column response

The recorded soil column response will be compared with analytical site response models in Chapter 6, whereas this section considers trends of experimental site response. Site response amplification in a dense accelerometer array is examined for two vertical arrays: “inside” or “array in sand”, the accelerometers are located inside shear stack, and “outside” the accelerometers are fixed on the shear stack rings (Figure 5.3). The issue of vertical accelerations has been studied by the two arrays.

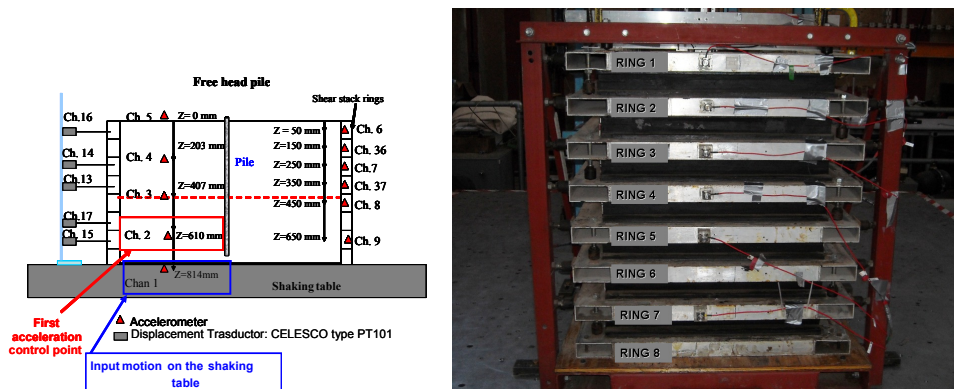


Figure 5.3 Layout instrumentations: accelerometers in the shear stack and outside on the external ring

The two arrays consist in four accelerometers located in shear stack at four different elevations: 0 mm (Ch.5); 203 mm (Ch.4); 407 mm (Ch.3); 610 mm (Ch.2), “inside” or “in sand”; and six accelerometers on the shear stack rings at six different elevations (“outside”): 50 mm; 150 mm; 250 mm; 350 mm; 450 mm; 650 mm. One accelerometer (Ch.1) is positioned on the shaking table (814 mm), it is a control point for the input motion give to shaking table. Also the Celesco transducer are used to measure the displacement of shear stack. However, these measurements should be taken cautiously in consideration, since these transducers are not doing very well in the dynamic range. For rigorous assessments of the displacement profiles inside and outside the shear stack, only the accelerometer measurements have been considered.

5.3.1 Example 1: Test- BE+E_STU 2_FH pile

The time histories and FFTs for acceleration array in sand are shown in figure 5.4 a)-b). In figure 5.5 the amplification function between the FFT of superficial accelerometer (Ch.5) and the input motion at base of shear stack, on the shaking table (Ch. 1) is also shown. The trend

of amplification from the bottom of shear stack (0.2 g) to the surface of deposit (0.31 g) is realistic. The FFT energy concentration at 4-6 Hz in deeper instruments (Ch. 2) directly correlates to the 4-6 Hz acceleration relative to the input motion (Ch 1). From the bottom of shear stack to the surface, the frequency band changes. As shown in figure 5.5 a change of energy is present at surface. The predominant frequency reflects the fundamental site frequency (25-38 Hz). It should be noted that the first record of acceleration in sand (Ch. 2) is very different from the input motion recorder on the shaking table (Ch.1). There is an attenuation of signal in the passage through shear stack. Since the model soil container is intended to approximate one-dimensional site response, which requires that ground motions be identical at all points on any horizontal plane, a comparison between two arrays has been done. In figure 5.6, the external array time histories are reported. In figure 5.7 a), the comparison between the time histories of acceleration for two different arrays is shown. The waveform and the amplitude of acceleration are very close. In figure 5.7 b), the comparison between the peak acceleration values with depth obtained from the two recorder arrays is illustrated. Again, the peak values and the waveform are very similar.

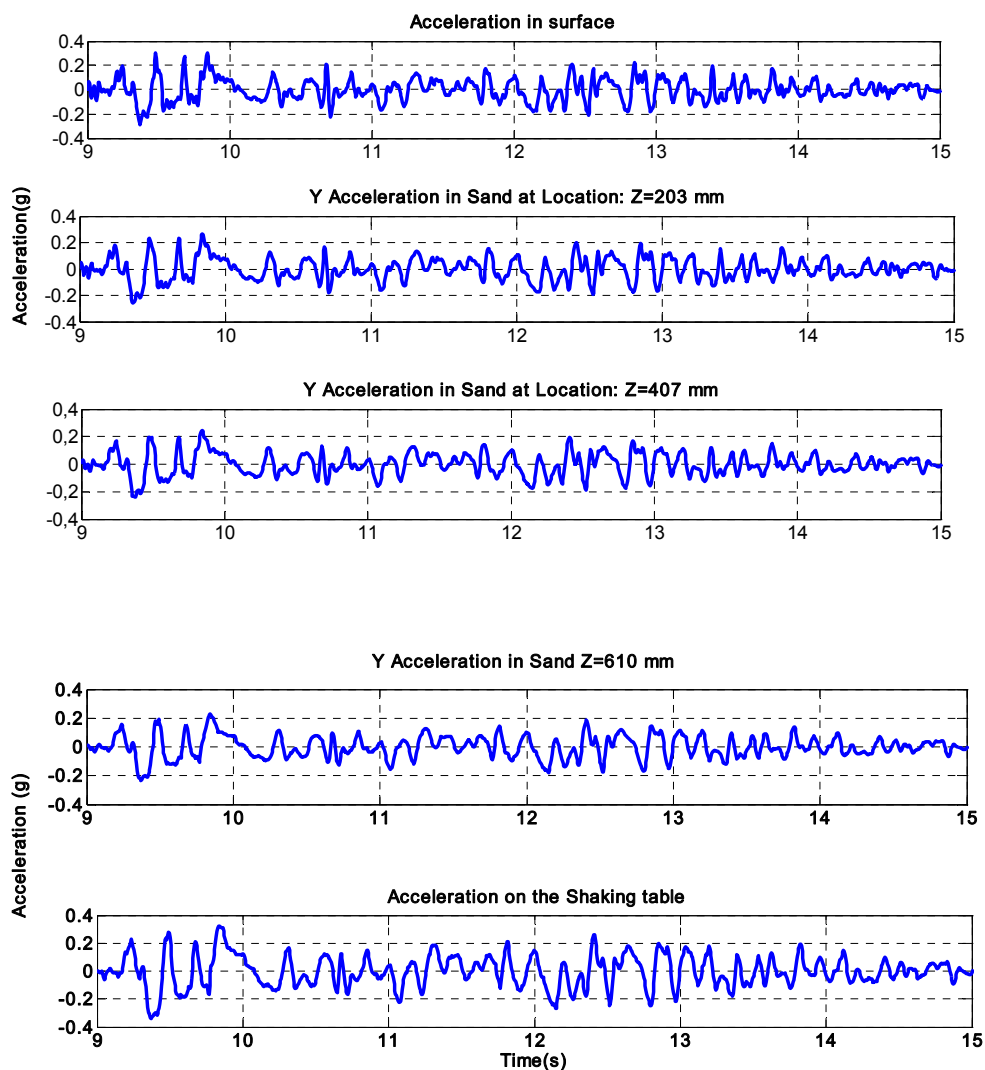


Figure 5.4 a) acceleration time histories of inside array

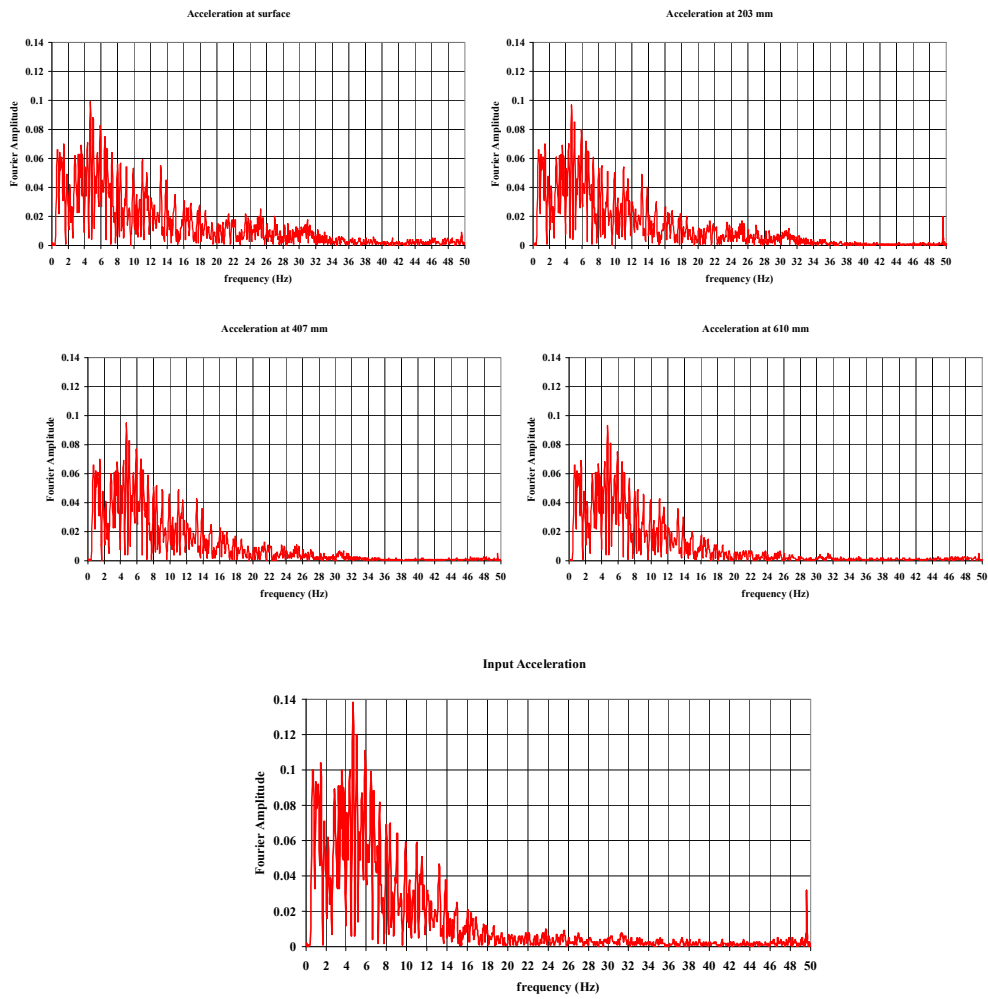


Figure 5.4 b) FFT of array inside deposit

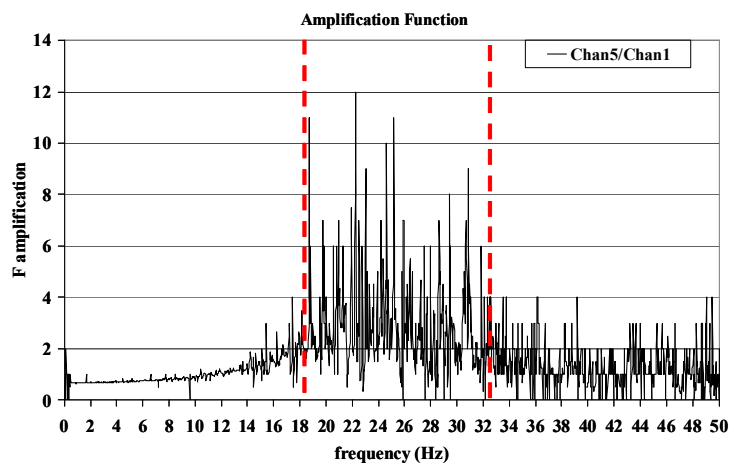


Figure 5.5: Transfer function between surface and input motion

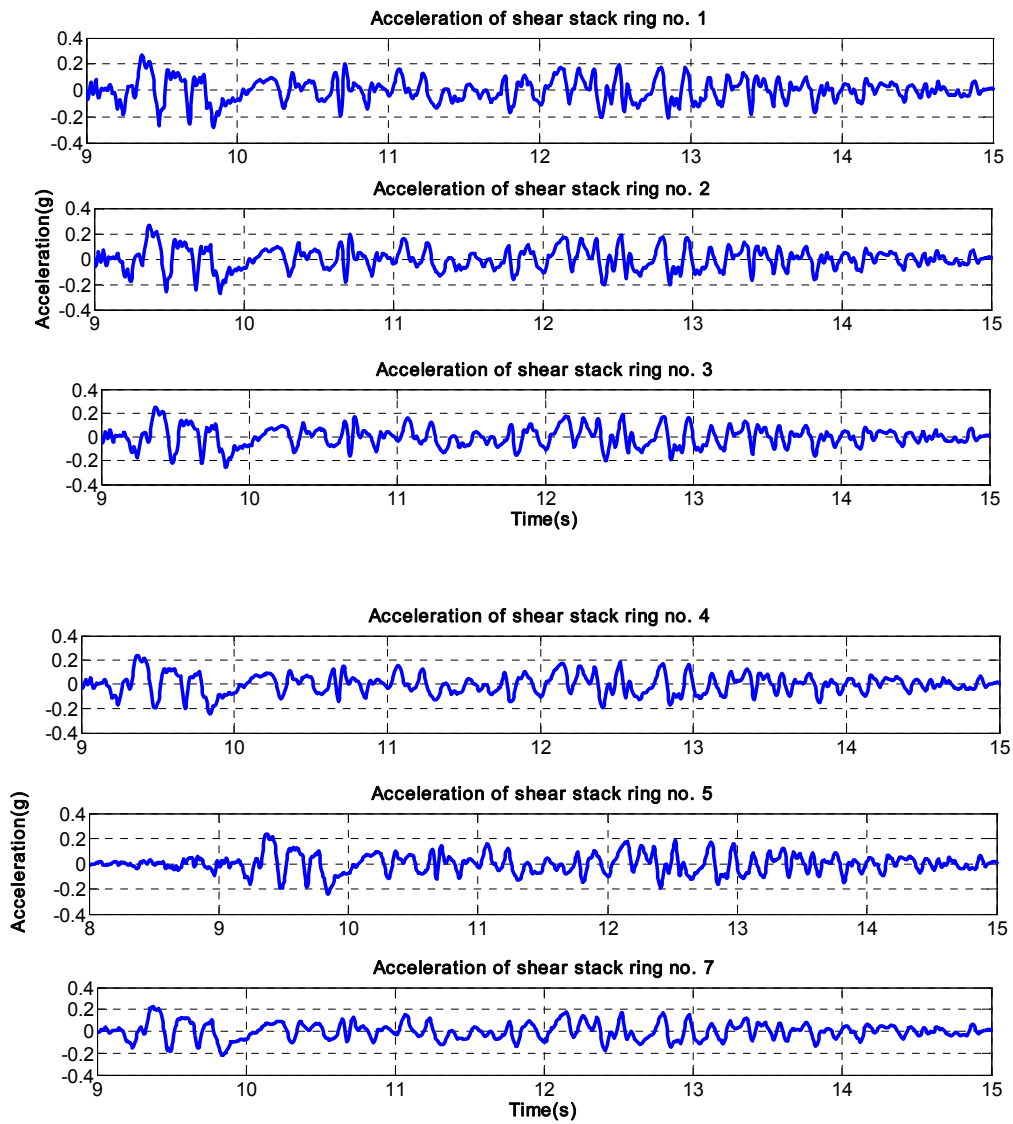


Figure 5.6 acceleration time histories : external array

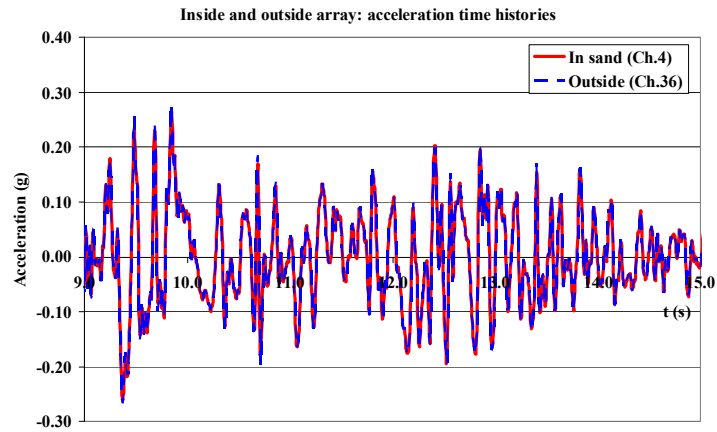


Figure 5.7a) Comparison between acceleration time histories of arrays in sand and external

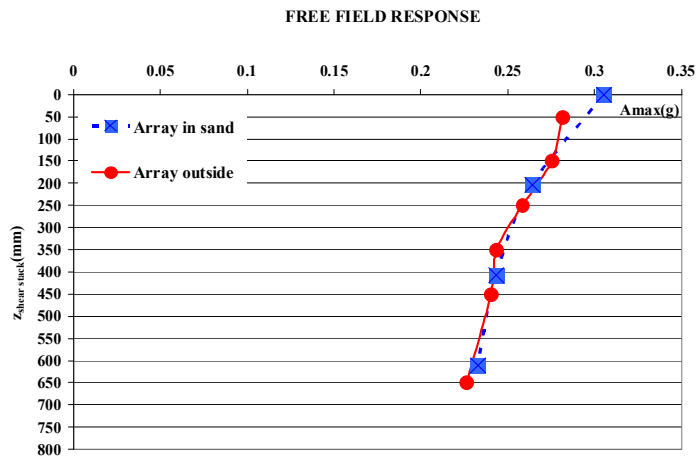


Figure 5.7b) Peak acceleration with depth: in sand and external array

5.3.2 Example: Test- BE+E_STU 12_ FH pile

Here a different kind of input motion is reported. The original accelerometer is always Sturmo 000, but 12 times scaled. The fundamental frequency of input motion is 48 Hz (band frequency: 25-48 Hz).

In figure 5.8 a-b) are shown the time histories and FFTs for array in sand. In figure 5.9 the amplification function between the FFTs of superficial accelerometer (Ch. 5) and the input motion on shaking table (Ch.1) are also plotted.

The trend of amplification from the base of the shear stack (0.06 g) to surface of deposit (0.25 g) is expectable. As in the previous cases, a transformation of energy content is associated with depth of deposit. The FFT energy concentration at 48 Hz in deeper instruments directly correlates to the 48 Hz acceleration relative to the input motion. The transfer function between the recorder on the bottom of the shear stack and the surface, underlines the fundamental site frequency (25Hz and 32 Hz) (figure 5.9).

It should be noted that the acceleration recorder in sand, at 200 mm from the bottom of the shear stack (Ch. 2), are very different from the input motion on the shaking table (Ch. 1). The attenuation of signal amplitude is bigger than the previous cases. The peak acceleration change from 0.3g (input motion on shaking table) to 0.08 g (Ch.2). The signal lost all high frequency.

In figure 5.10 the time histories of acceleration for one accelerometer located in sand at 200 mm and one external at elevation 150 mm are plotted. The results are satisfactory in terms of amplitude and waveform of acceleration. In particular, figure 5.11 a comparison between the peak acceleration values obtained from the two arrays recorder in the shear stack depth is depicts. The comparison confirms the very good agreement between acceleration recorder in sand and outside of deposit.

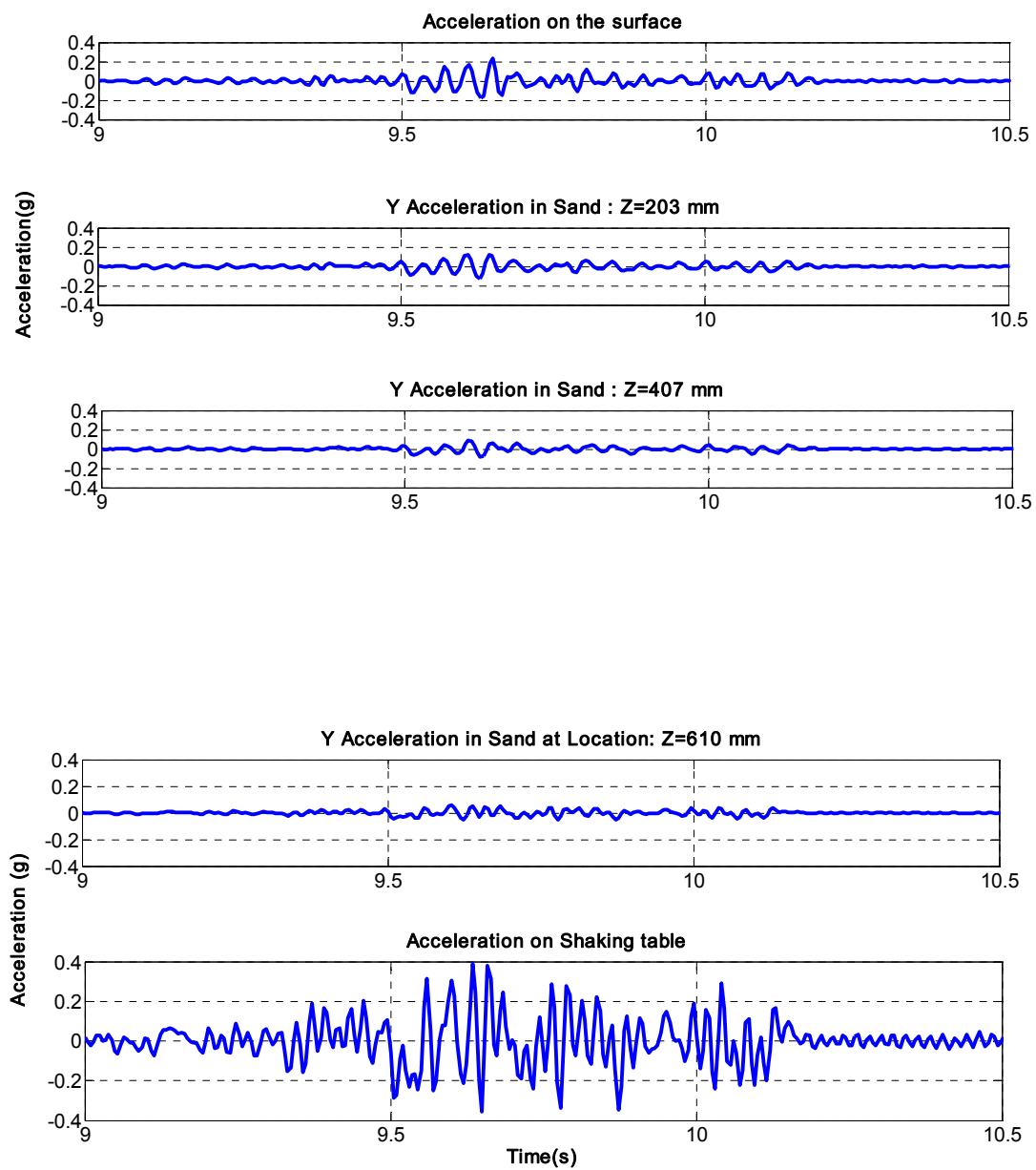


Figure 5.8 a) Time histories of inside acceleration array

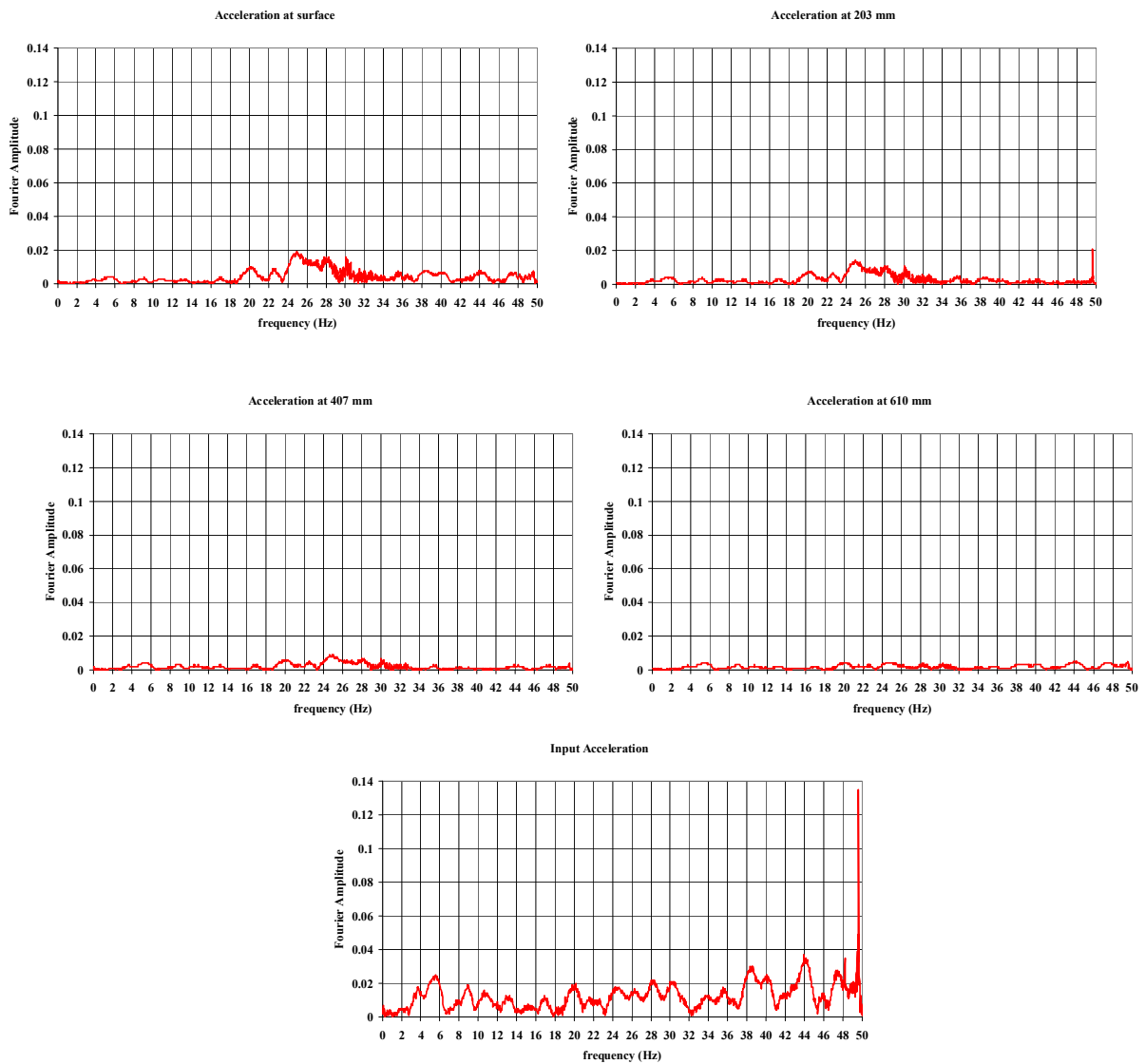


Figure 5.8 b) FFT of array inside the deposit

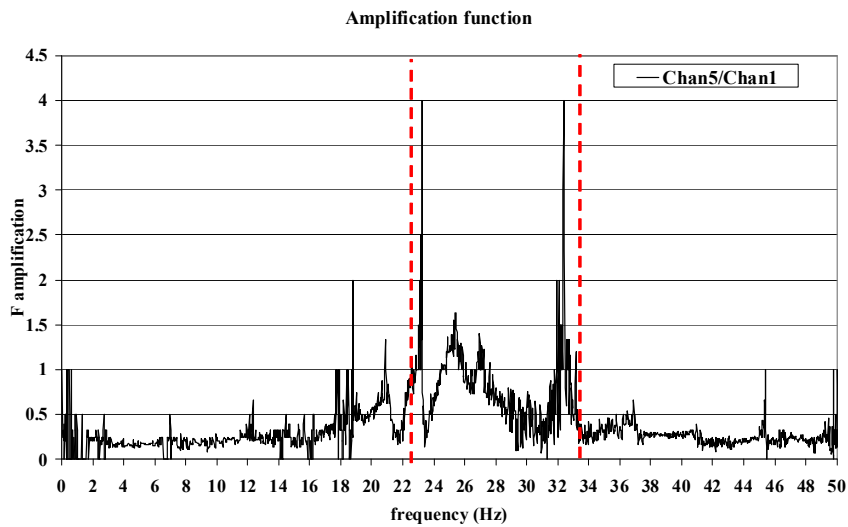


Figure 5.9-Amplification function between surface and input motion

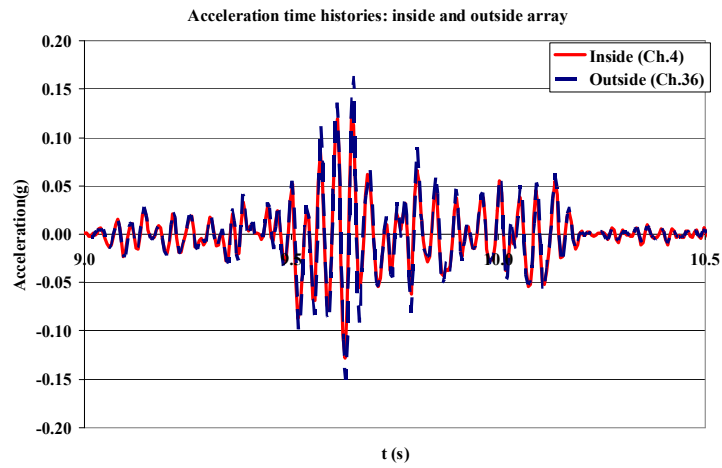


Figure 5.10 - Time histories of acceleration: inside and outside ($z \sim 200\text{mm}$)

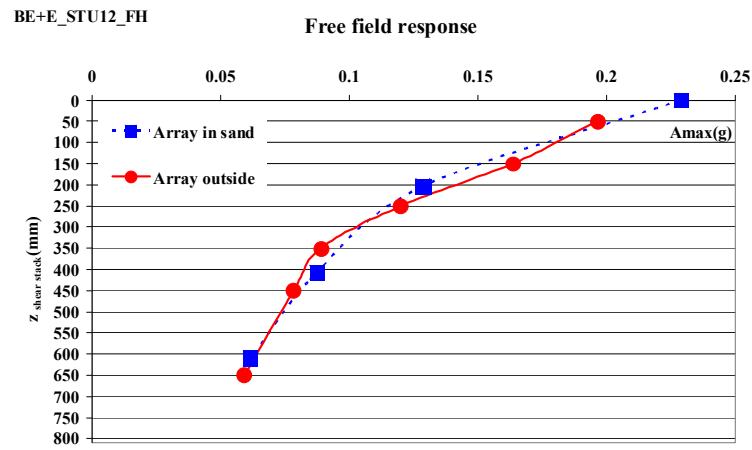


Figure 5.11 Peak acceleration with depth: array in sand and outside

5.3.3 Conclusion on free field response

From observation of free field response some considerations are following reported. In figure 5.0 a sketch of the shear stack is shown, the two input motion control points, Ch. 1 ($z=814$ mm) on the shaking table, and Ch. 2 in the shear stack at 610 mm from the surface are indicated.

In general, all the earthquakes have been scaled to a 0.3g, peak ground acceleration value, therefore the input motion PGA is around 0.3 g (Ch.1). From a detailed analyses it have been discovered that the PGA of accelerometer registrations near the shear stack bottom, in sand (Ch. 2), are difference. As well, it is confirmed by the recorder acceleration on the shear stack ring (Ch. 9, ring number 7).

When the earthquakes are rich in high frequency content (12 times scaled) this discrepancy is not negligible.

In figures 5.01 a); 5.02 a); 5.03 a); 5.04 a); 5.05 a), the acceleration time histories for Ch.1 and Ch.2 points control are shown, in particular while for Ch.1 the peak ground acceleration is around 0.3g for Ch.2 it is generally smaller than 0.1 g.

Moreover, for the input motion scaled 2 times the situation is rather different, the de-amplification effects on the acceleration recorder in sand are not so drastic.

As shown in figure 5.01 b) for Sturno 2, the PGA for Ch. 1 is around 0.3 g and for Ch. 2 is around 0.25 g, even for Norcia 2, the PGA for Ch. 1 and for Ch. 2 are fairly close to the same value (figure 5.05 b).

In the case of Tolmezzo 2 time scaled this discrepancy disappears. As shown in figure 5.02 b); 5.03 b); 5.04 b); for the same soil configuration and for different pile head conditions the different between acceleration time histories of Ch.1 and Ch. 2 vanished at all.

The foregoing results are similar for all the tests. Usually this variation of PGA between the input motion on the shaking table (Ch. 1) and the acceleration recording in the sand at 203 mm from the bottom of the shear stack (Ch.2) increases with the high frequency content of input motion.

This discrepancy could be due to the decay of the amplitude of these high frequency signals in the soil, or could be caused by the connection system among the table surface, the shear stack iron frame and its wooden base.

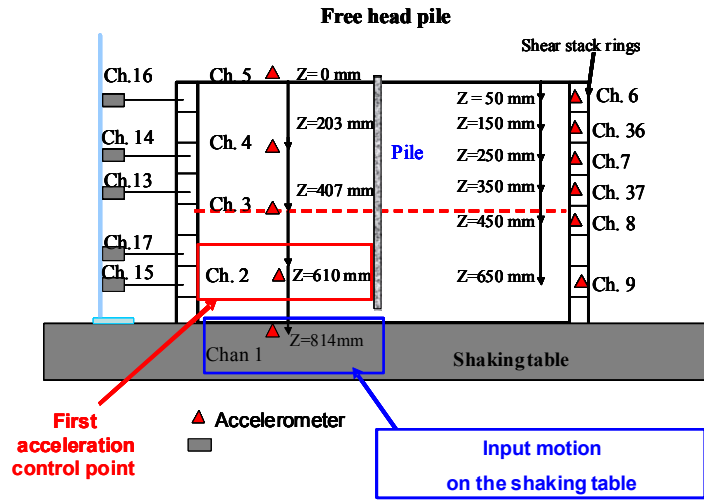


Figure 5.0 input motion: acceleration control point

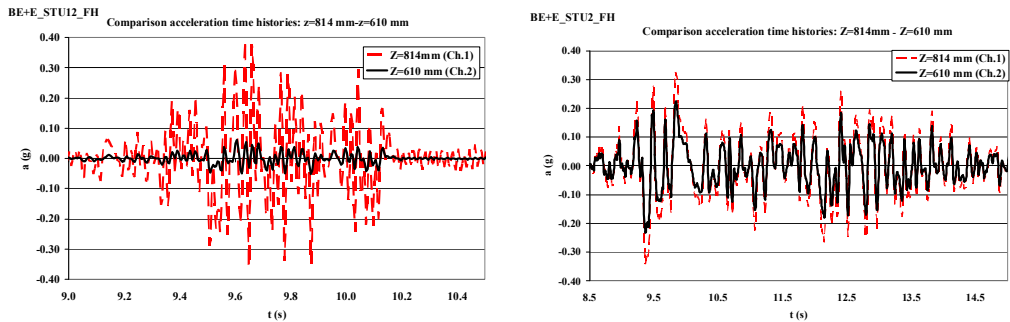


Figure 5.01: Acceleration time histories comparison between input motion ($z=814$ mm): and first measurement in sand ($z=610$ mm): a) STU 12 and b) STU 2

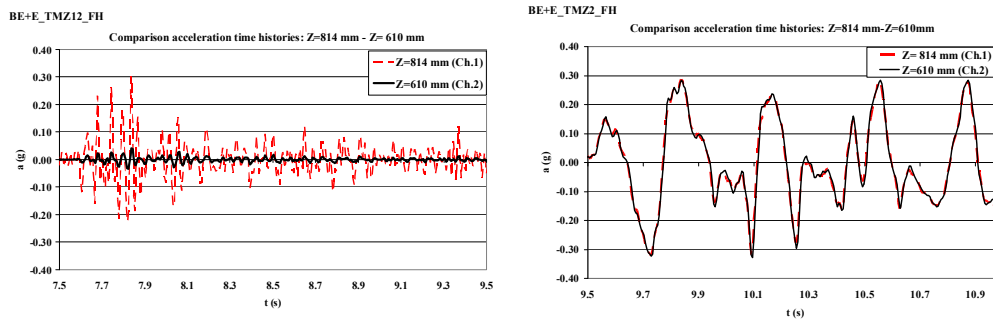


Figure 5.02: Acceleration time histories comparison between input motion ($z=814$ mm) and first measurement in sand ($z=610$ mm): a) TMZ 12 and b) TMZ 2_free head pile

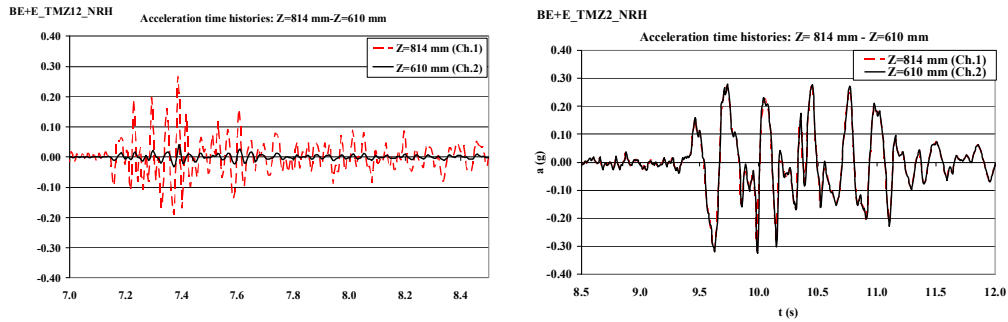


Figure 5.03: Acceleration time histories comparison between input motion ($z=814$ mm) and first measurement in sand ($z=610$ mm): a) TMZ 12 and b) TMZ 2 No rotation head pile

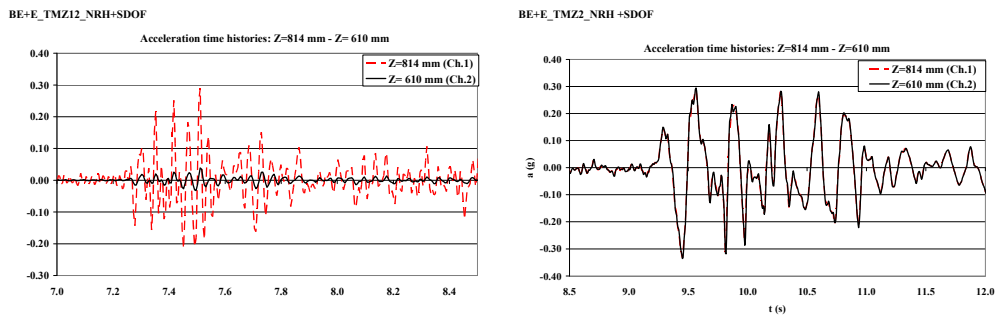


Figure 5.04: Acceleration time histories comparison between input motion ($z=814$ mm) and first measurement in sand ($z=610$ mm): a) TMZ 12 and b) TMZ 2 _no rotation head pile + oscillator

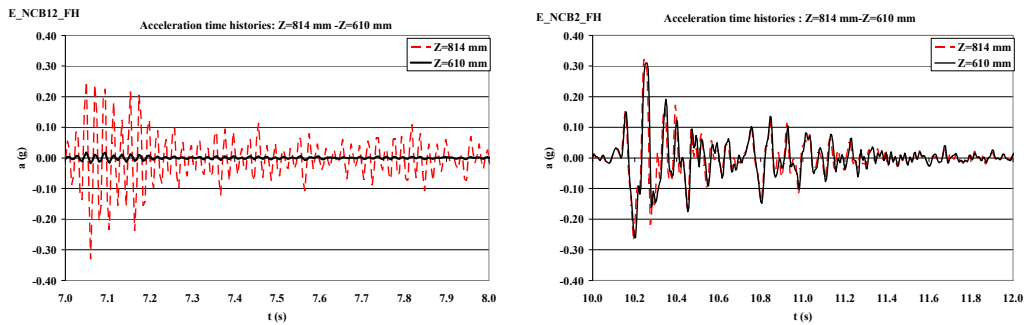


Figure 5.05: Acceleration time histories comparison between input motion ($z=814$ mm) and measurement in sand ($z=610$ mm): a) NCB 12 and b) NCB 2 free head pile

In general, for all tests, there is a good agreement between the acceleration values recorded in the sand and outside of the shear stack as shown in figures 5.12 and 5.13 for soil configuration E and BE+E respectively, in case of free head pile configuration.

Obviously, the pile head condition does not affect the free field response inside the shear stack and outside of it (figures 5.14 a-b).

These excellent results validate the hypothesis that the dynamic response of the physical model is governed by the soil and not by the container. So that the shear stack does not interfere with the dynamic propagation.

The model soil container has been designed specifically to allow the model soil deposit to respond in the same manner as a free-field soil deposit, characterized by a simple shear deformation mode (Crewe, 1999).

It should be noted that in case of soil configuration E+R, the acceleration value on the surface is always bigger than the others. The amplification site response is very high. The Rubber behaviour is typically of soft soil.

The free field response in soil configuration E+R is in agreement with outside accelerometer until 400 mm from the bottom of the shear stack. In the upper part the two free field responses are not comparable, in particular the rubber layers decoupled from the shear stack, due to the very low stiffness ratio between the two, the rubber is more deformable. (Figure 5.15 a) to d)).

In general accelerations amplify through the soil column toward the surface, as expected, depending on the coupling between the input motion and soil stiffness.

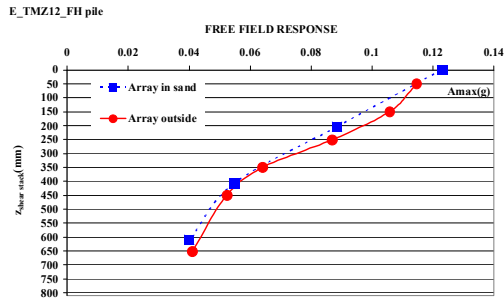
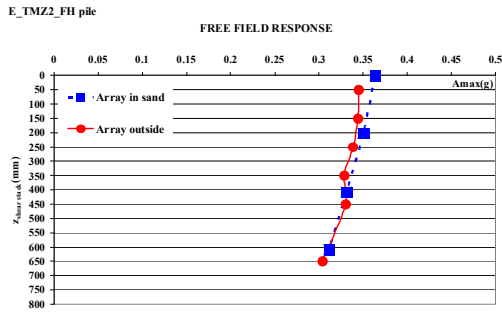


Figure 5.12 Peak acceleration with depth: array in sand and external for a) E_TMZ 2 and b) E_TMZ12_FH pile

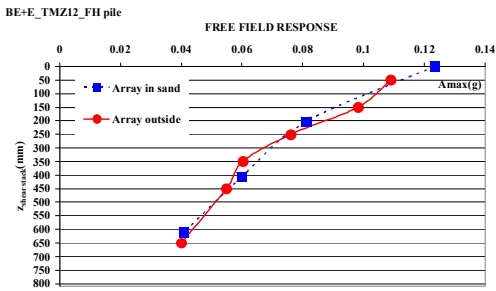
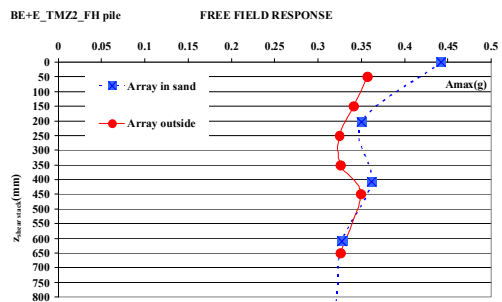


Figure 5.13: Peak acceleration with depth: array in sand and external for BE+E_a) TMZ 2 and b) TMZ12_FH pile

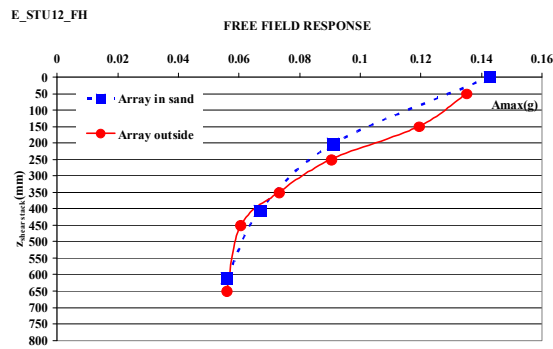


Figure 5.13: Peak acceleration with depth: array inside and external for c) E_STU 12

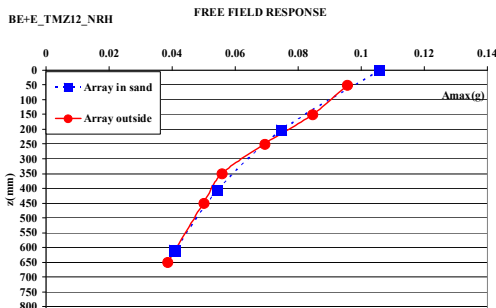
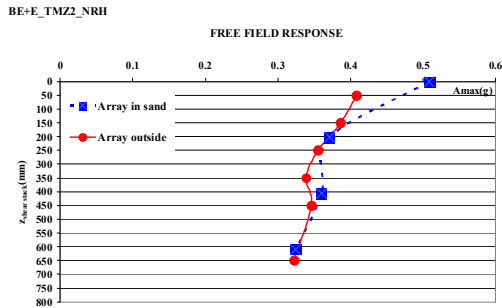


Figure 5.14a) Peak acceleration with depth: array in sand and external for BE+E_TMZ 2 and b) TMZ12_NRH pile

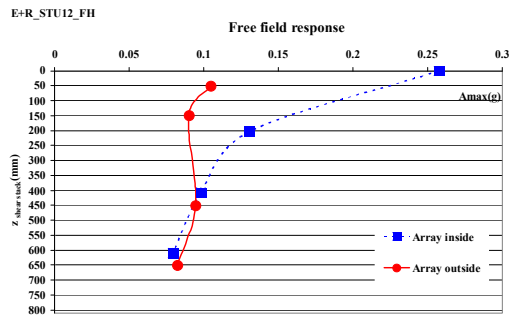
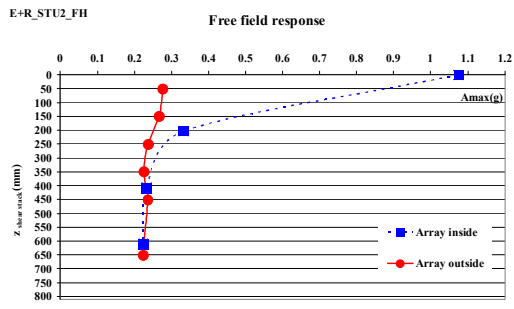


Figure 5.15 Peak acceleration with depth: array in sand and external for E+R_a)STU 2 and b)STU 1
2_NRHpile

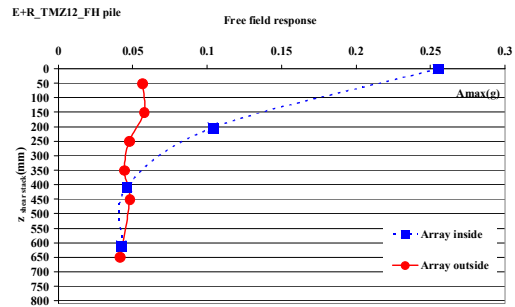
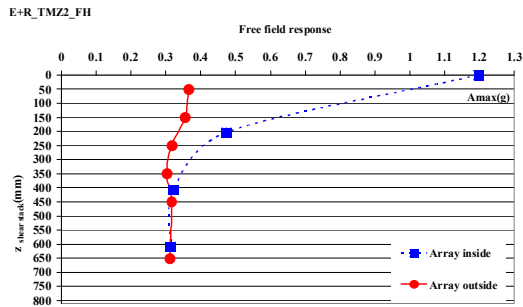


Figure 5.15: Peak acceleration with depth: array inside and external for c) E+R_TMZ 2 and d) E+R
TMZ12_FHpile

5.4 Kinematic interaction: free head pile (FH pile)

As know in Mylonakis et al. 1997, the kinematic interaction between pile and soil has, in general, two consequences: (i) it filters out low-period components. It filters out low-period components of the motion while at the same time it induces a rotational component at the pile head (ii) it induces axial, bending, and shear deformations on piles. Bending is significant at two locations: at the top of fixed-head piles and at the interfaces of soil layers with sharply different stiffness.

In the following section the effects of soil stiffness contrast is underline. It has been chosen a free head pile configuration to analyze the kinematic phenomena, with the aim to understand the relative importance of it on bending moment on pile during a seismic events.

As explained in detail in Chapter 4, the external surface of pile coated with strain gauges at different elevation (around each 100 mm) and the bending moment are obtained from a strain gauges registrations, purified by possible normal force on the pile. Figure 5.16 shows the model setup for tests on free head pile.

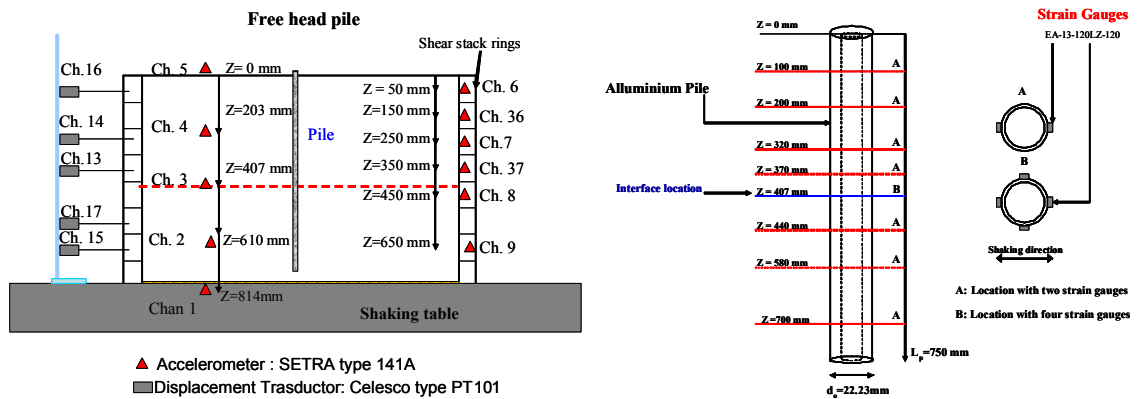
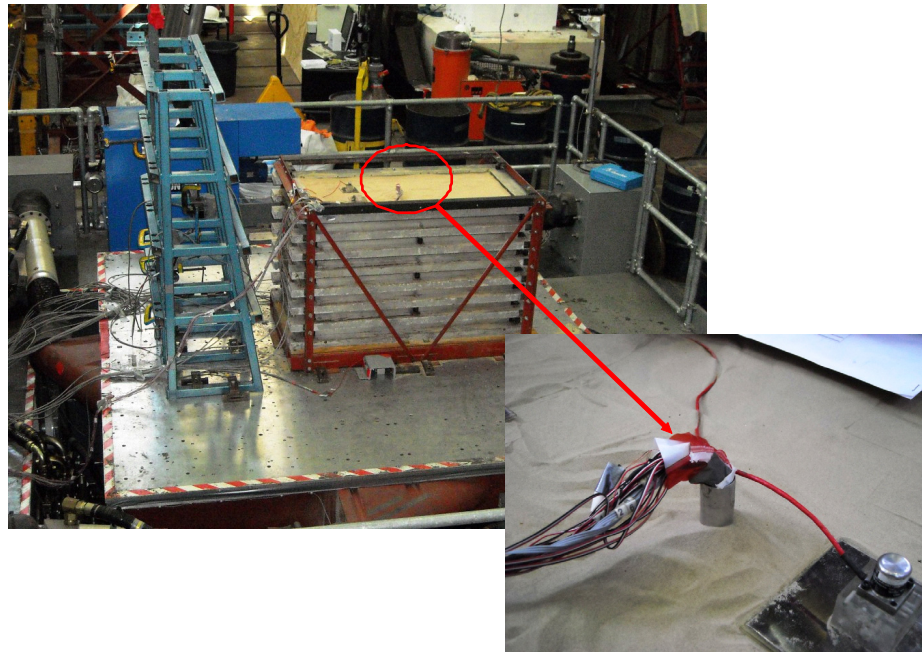


Figure 5.16: Layout of shear stack with free head pile configuration and strain gauged aluminium pile

5.4.1 Effects of stiffness contrast

The value of maximum kinematic bending moments, normalized by the yielding moment of the pile ($M_y=0.085$ KN m), for the three subsoil configuration tested, characterized by a shear wave velocity contrast (V_{s2}/V_{s1}) equal to 1 (E), 1.7 (BE+E) and 8 (E+R) are shown (figure 5.17).

The experimental evidences generally confirm the main knowledge provide by theoretical studies.

In homogeneous soil the kinematic bending strain for a free-head pile increases with depth, reaching its maximum at approximately the mid-length of the pile (Gazetas et al.1992).

The moments are characterized by a raise trend with increase of stiffness contrast, the presence of softer layer on the top, produces a significant increment of bending on pile. (Gazetas et al.,1993). In case of soil configuration E+R the presence of the rubber at top layer increase too much the amplitude of moment at interface.

The maximum kinematic bending moment normalized by yielding moment of pile (M_y), for each scaling factors (12 times, 5 times and 2 times) are reported in detail in figures 5.18, 5.19, 5.20. The plots show clearly that the pile is always in elastic region during each tests.

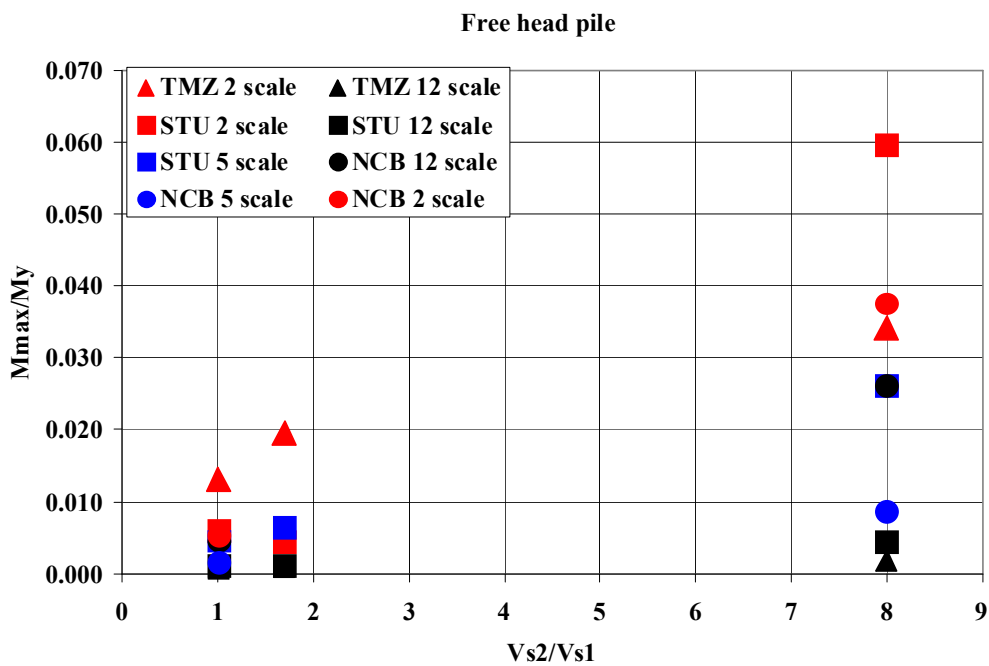


Figure 5.17: Maximum kinematic bending moment normalized by M_y for different soil configuration

It should be noted that in case of input motion scaled 12 times (high frequency content and low energy, figure 5.17b, c, d), the bending strain on pile are very small, around 5 - 10 $\mu\epsilon$. Hence the bending moment associated are less than around 10^{-5} KN m (figure 5.18). The effects of scaling factor are analyzed in the following section.

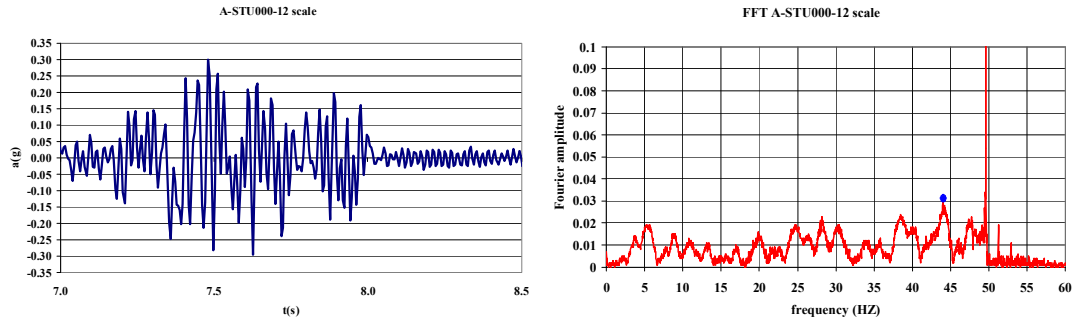


Figure 5.17b) STU 12: Time histories acceleration and FFT

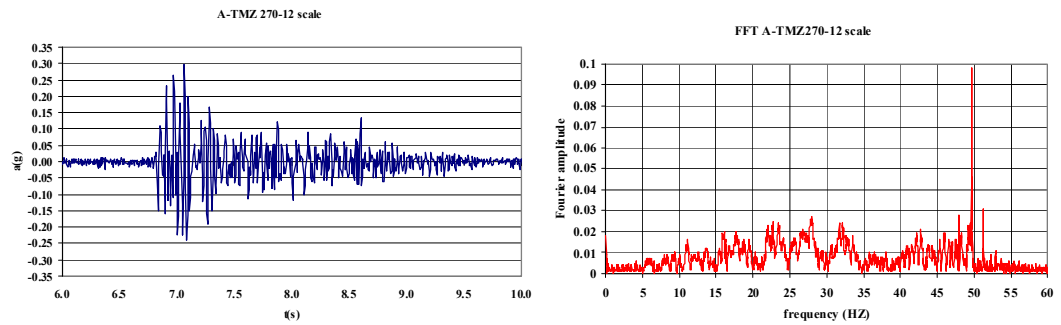


Figure 5.17c) TMZ 12: Time histories acceleration and FFT

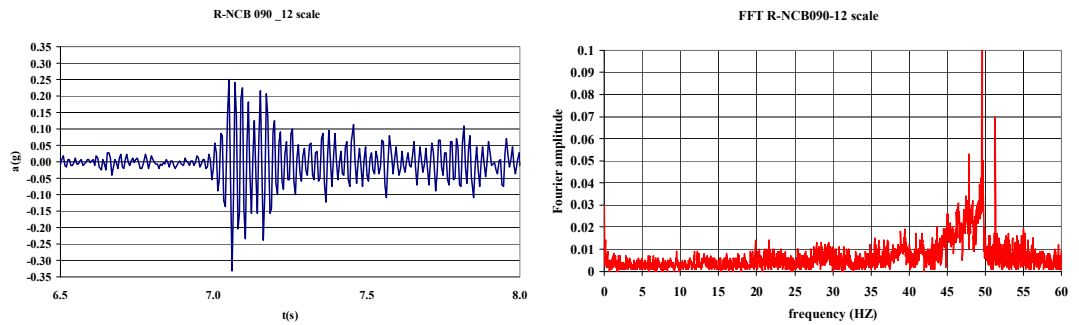


Figure 5.17d) NCB 12: Time histories acceleration and FFT(E)

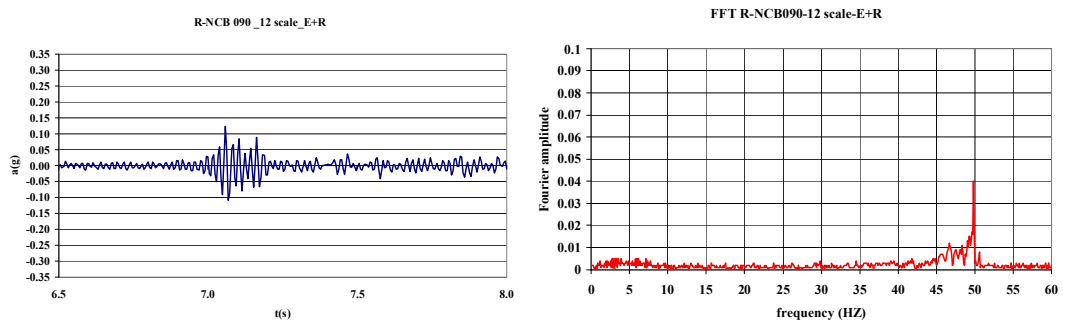


Figure 5.17e) NCB 12: Time histories acceleration and FFT(E+R)

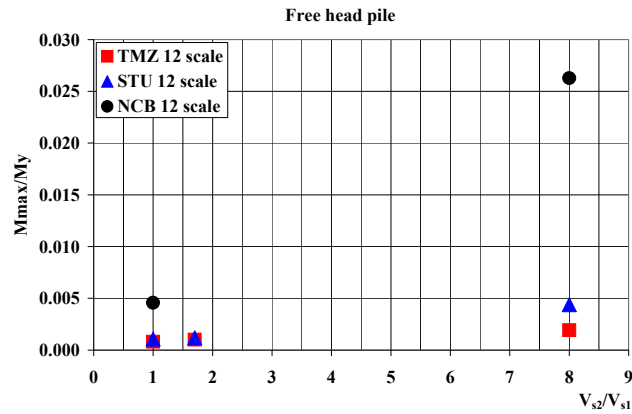
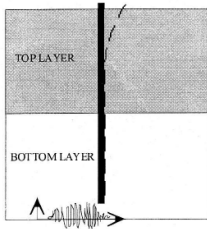


Figure 5.18: Maximum kinematic bending moment normalized by M_y for different soil configurations 12 scale

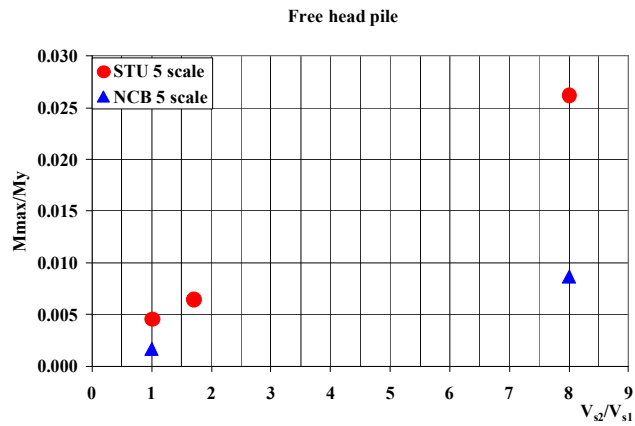


Figure 5.19: Maximum kinematic bending moment normalized by M_y for different soil configurations 5 scale

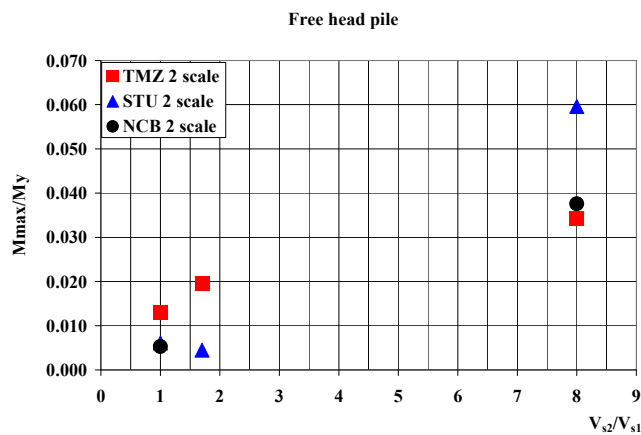


Figure 5.20: Maximum kinematic bending moment normalized by M_y for different soil configurations 2 scale

5.4.2 *Effects of scaling factor*

In the previous paragraph the stiffness contrast effects on kinematic phenomenon has been emphasized, in case of free head pile.

The scaling factor of input motion is an important factor to consider for the valuation of the amplitude of kinematic bending moment. Different scaling factor means different value of arias intensity and frequency content. These two last parameters are very important to do a good valuation of the dynamic phenomenon (resonance effects etc..).

The envelopes of maximum bending moment along pile for monolayer configuration (E), layered sand configuration (BE+E) and layered configuration (E+R) respectively are shown in figures 5.21, 5.22, 5.23.

As expected the maximum bending moment is located near the interface. In case of soil configuration E+R the presence of the rubber at top layer increase very much the amplitude of moment at interface. The soil pile relative stiffness changes. The presence of rubber, a very soft material, induces the pile to move freely in the deposit.

In double-layered deposits (configurations BE+E and E+R), the maximum bending moment was recorded close to the $z = 440$ mm position, just below the initial layer interface ($z = 407$ mm). Note in this regards that soil settlement during shaking may have changed the position of the interface to lower ordinates. The bending moment magnitude increased significantly when the stiffness contrast between the second and the first layer V_{s2} / V_{s1} increased from 1.7 to 8. For configuration BE+E (sand double layer), the bending moment presents two local maxima: one situated close to the 200 mm ordinate down the pile and the second one near the interface. The local maximum close to the 200 mm position is not recorded for configuration E+R. In this latter case, the moment increases steadily from top to the interface.

In particular Figures 5.24, 5.25, 5.26 show for the three soil configurations the bending moment profile along the pile for scaling factor 12. As before mentioned, this kind of input motion are very peculiar. All the input motion scaled twelve times have the same PGA (0.3g) value, also the same frequency band predominant (24-49 Hz). It is very difficult to individuate a predominant frequency. For input motions scaled 12 times the values of moment are extremely low. The value of moments are neglected for value smaller then around $3 \cdot 10^{-5}$ KN m.

Figures 5.26, 5.27, 5.29 show, for the three soil configurations, the bending moment profile along the pile for scaling factor 2.

For all the three configurations it should be noted that with the reduction of input motion high frequency content (going from 12 to 2 earthquake scaling factor) the kinematic bending moment along the pile amplifies.

A comparison of bending moment along pile for the same input motion (TMZ2) for the three soil configuration is shown in figure 5.29 b)

Just for BE+E configuration, the moment at interface obtained for STU 5 is bigger than STU 2. It is acceptable because the predominant frequency of STU 5 (11 Hz) is closer than STU 2 (5Hz) to the natural frequency of deposit (28Hz).

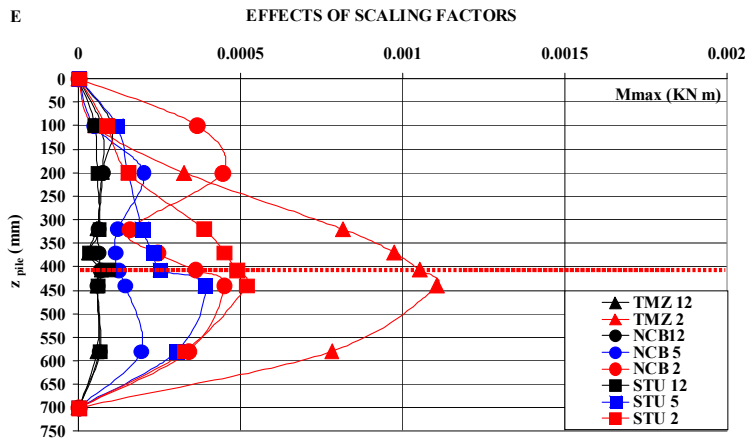


Figure 5.21 Maximum Kinematic bending moment along pile_E_FH pile BE+E

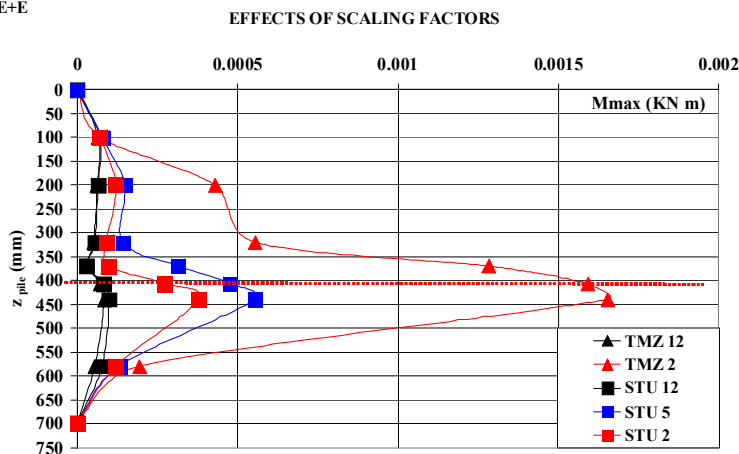


Figure 5.22 Maximum kinematic bending moment along pile_BE+E_FH pile

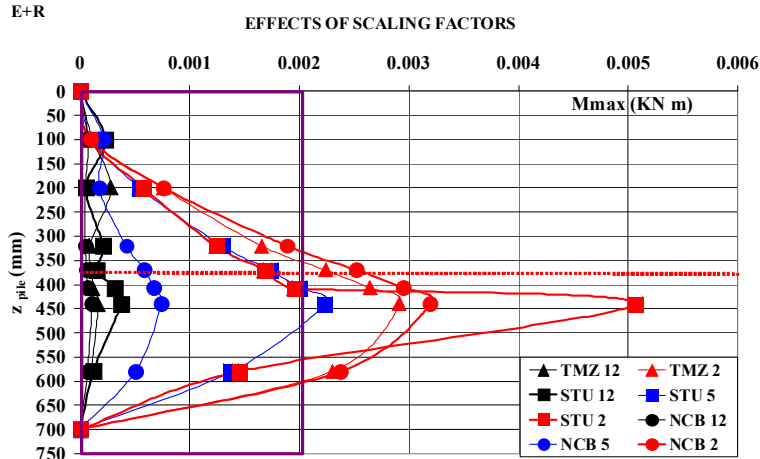


Figure 5.23 Maximum kinematic bending moment along pile_E+R_FH pile

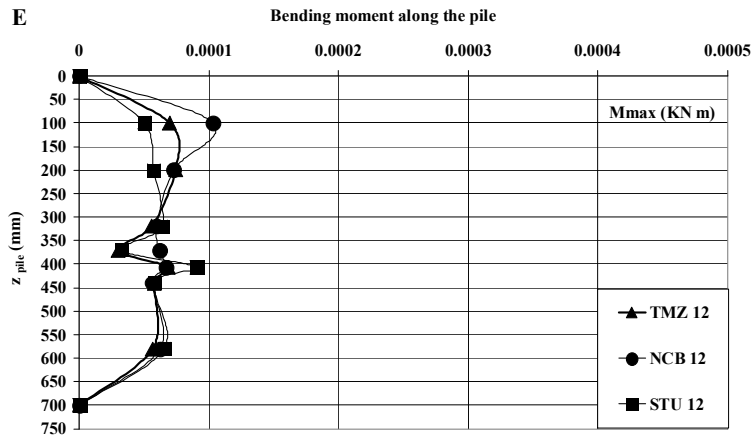


Figure 5.24: Maximum kinematic bending moment along pile (E-12 scale)

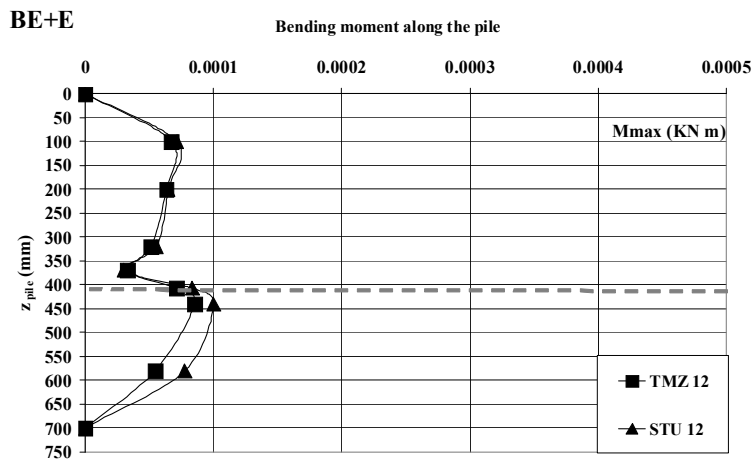


Figure 5.25: Maximum kinematic bending moment along pile (BE+E-12 scale)

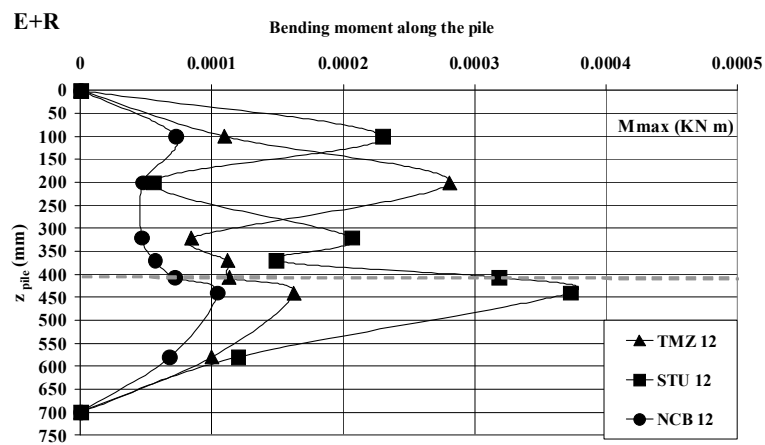


Figure 5.26: Maximum kinematic bending moment along pile (E+R-12 scale)

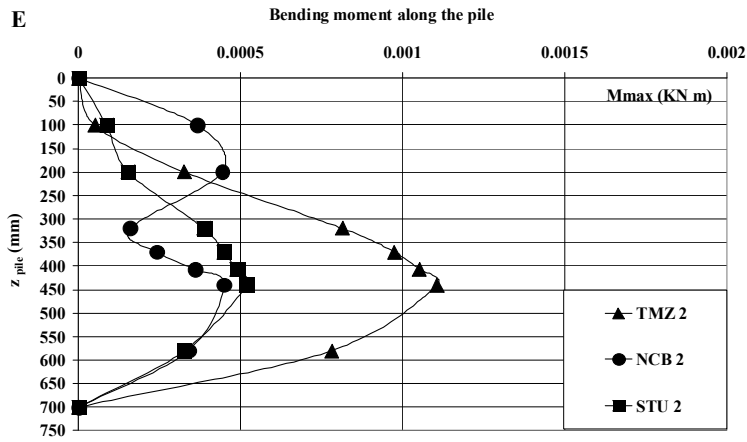


Figure 5.27: Maximum kinematic bending moment along the pile -2 scale_E

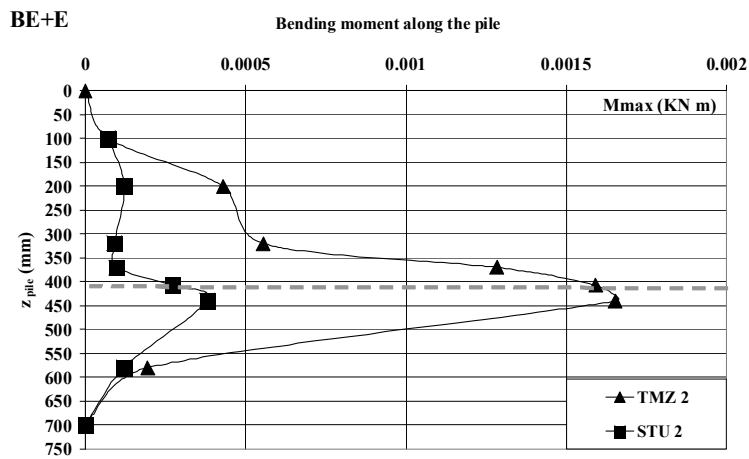


Figure 5.28: Maximum kinematic bending moment along the pile -2 scale_BE+E

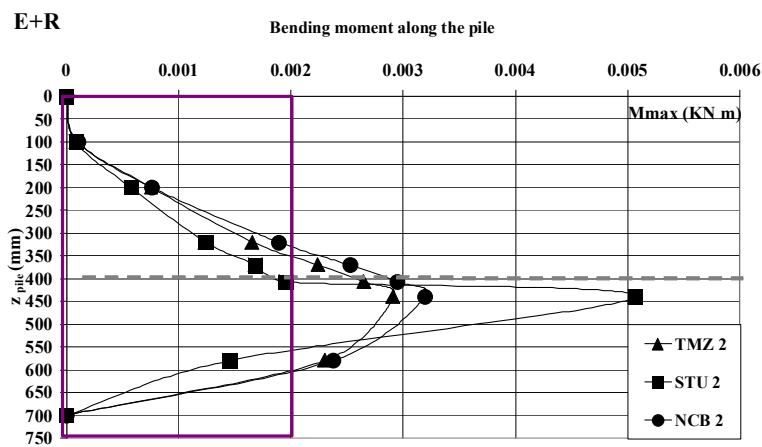


Figure 5.29: Maximum kinematic bending moment along the pile -2 scale_E+R

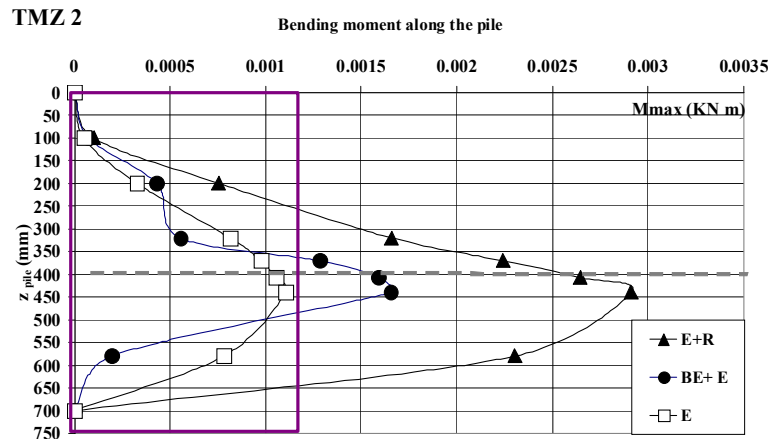


Figure 5.29a) Maximum kinematic bending moment along the pile –TMZ 2 for all deposits

5.4.3 Some reflections on kinematic phenomenon

In this section the pure kinematic effects, generated by the passage of seismic waves through the soil surrounding a pile, are studied. The passage of seismic waves imposes lateral displacements and curvatures on the pile, thereby generating 'kinematic' bending moments even in the absence of a superstructure. These moments are concentrated in proximity of alternate interfaces of soft and stiff soil layers (Gazetas et al.1992).

The experimental test led to the following observations:

1. The kinematic bending strain in a free-head pile in homogeneous soil (figure 5.21-5.24-5.25) increases with depth, reaching its maximum at approximately the mid length of the pile (375 mm) (Gazetas et al.1992). For layered soils, the maximum kinematic bending moment is concentrated at interface (figures 5.27, 5.28, 5.29a)).
2. The bending moments are characterized by a raise trend with the increase of stiffness contrast; the same results have been obtained by theoretical studies by Gazetas et al.,1993.
3. In presence of the sharpest stiffness contrast the value of the maximum bending moment increase too much. Comparing the results for V_{s2}/V_{s1} equal around 1.7 (BE+E soil configuration) and 8 (E+R soil configuration) in general the kinematic bending moment increases about two times (figure 5.29.b and figure 5.17).
4. The pile is always in elastic region (figures 5.18-19-29).
5. Generally, for all the three configurations it should be noted that with the reduction of input motion high frequency content (going from 12 to 2 earthquake scaling factor) the kinematic bending moment along the pile amplifies.

-
6. Some combined effects with frequency, Arias intensity and waveform are remarked. Just for BE+E the value of moment at interface obtained for STU 5 is bigger than STU 2. It is acceptable because the predominant frequency of STU 5 (11 Hz) is closer than STU 2 (5Hz) to the natural frequency of deposit (28Hz).

5.5 Pile head condition: no rotation head (NRH pile)

As previously established, SSPSI consists of components relating to superstructure inertial forces and kinematic forces exerted by the soil on the pile. As detailed in Chapter 2, it is common practice to decouple these factors and separately analyze inertial and kinematic interaction for their relative contributions to SSPSI. An important question is whether the relative proportions of inertial and kinematic interaction are magnitude dependent.

The single pile test offers the best opportunity for isolating this mechanism of SSPSI.

In the following section the behaviour of no rotation pile head (NRH pile) condition of single pile is discussed. These tests reproduce the pile-foundation system.

Figure 5.30 shows the model setup for no rotation pile head tests (NRH pile), with the primary shaking axis indicated by the arrow. In figure 5.31 b the layout of the instruments to measure accelerations and displacements are shown. At top pile it is located a LVDT transducer. In this pile configuration for understand the effective motion in foundation an accelerometer is located on the pile head (Ch.38).

The no rotation pile head condition has been realized by using of a bar connected to two aluminium frames (L section). These frames are fixed to the steel frame of shear stack, their motion is simultaneous with shear stack during the shaking. In this way the weight of the bar does not overweight the pile. In figure 5.31 a) detail of pile head condition is exposed. The connection between the pile head and the bar is realized by an aluminium interconnection device positioned on the pile head (figure 5.32 a). This particular connection forbidden a translational motion of pile head in direction of shaking (y-direction), deleting any rotational movement. The structural sketch is illustrated in figure 5.32 b).

This cave aluminium section is connected on the pile head and it models the presence of a foundation on the pile. The total mass on the pile head is provided by the weight of connection (516 g) and the weight of the accelerometer (126 g). The total pile head weight is 642 g. Due to the particular constrain, the weight on the pile head (figure 5.32a) does not affect the soil pile system by inertial force ($M_{inertial}$, Inertial moment on pile head is neglected). Hence this configuration has been supposed as kinematic system ($M=0$).

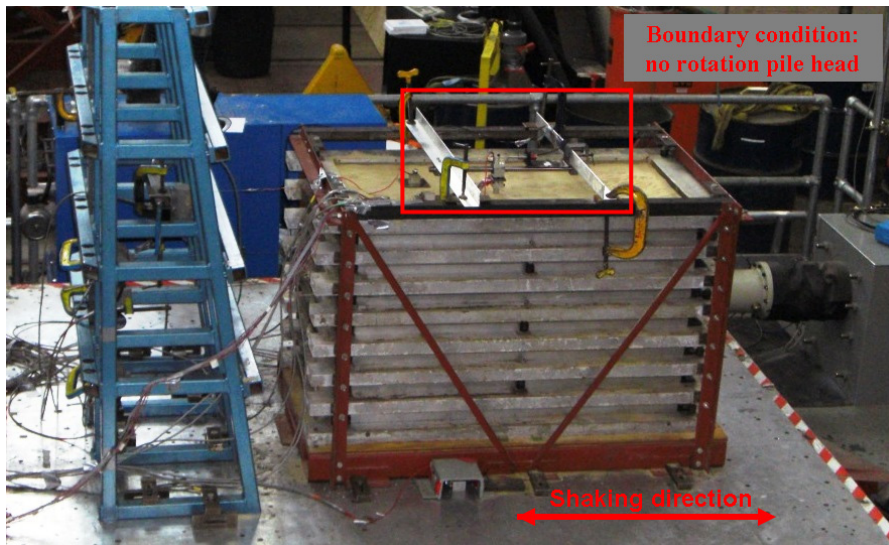


Figure 5.30 Shear stack layout: boundary condition no rotation head pile

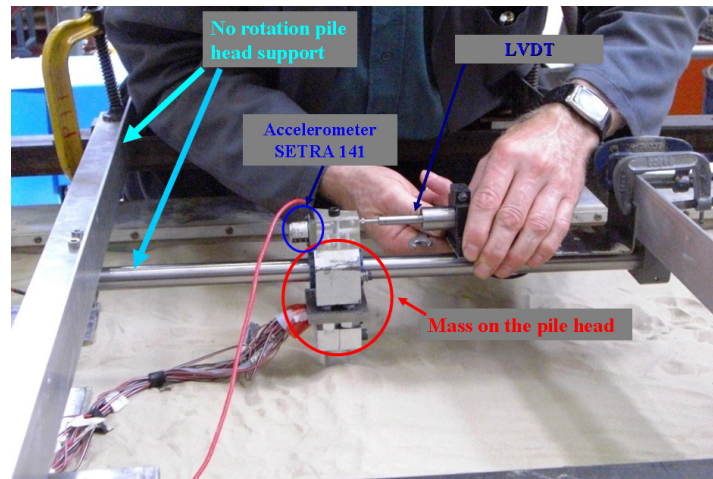


Figure 5.31:(a) Detail of no rotation pile head condition

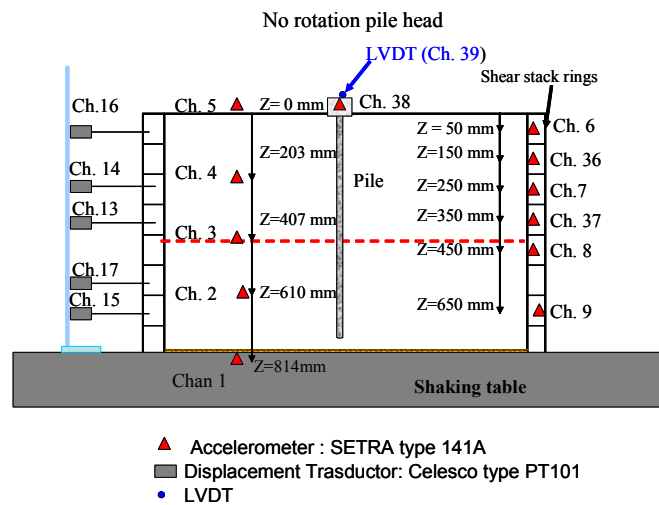


Figure 5.31:(b) layout instrumentation

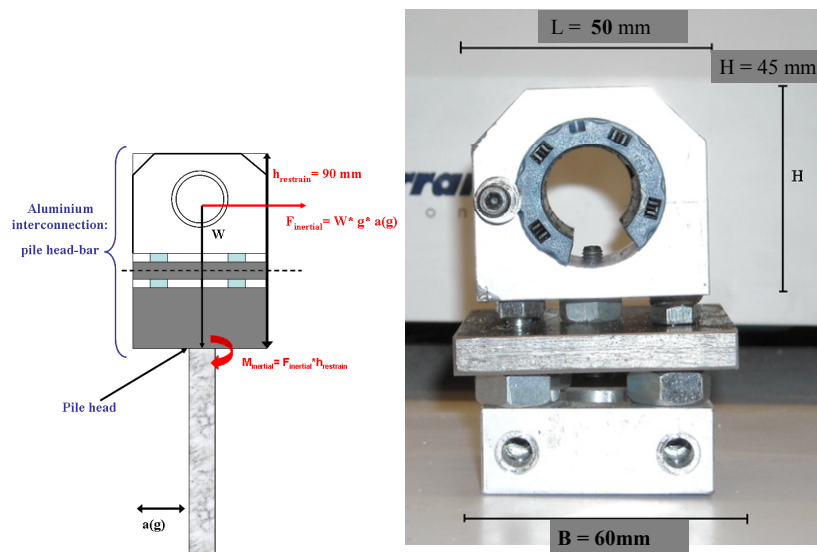


Figure 5.32(a) pile head-bar connection: aluminium interconnection

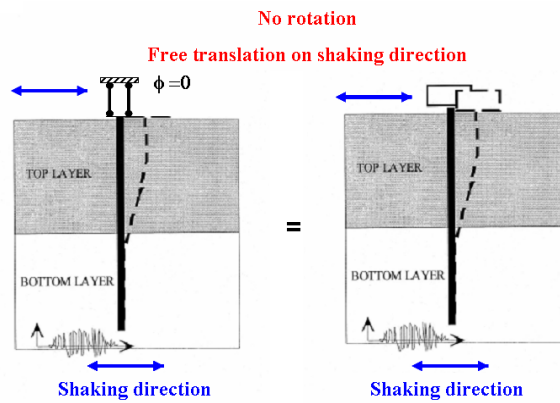


Figure 5.32(b) structural sketch for no rotation pile

5.5.1 Bending moment: monolayer configuration (E)

In these section the bending moment of monolayer configuration are analyzed each soil layer is quite homogeneous and the pile behaves is linear-elastic.

The embedded length of the pile in each layer is greater than the so-called “active length”. This latter is usually expressed by the equation 5.1 (Randolph, 1980):

$$L_a = 1.5d \left(\frac{E_p}{E_s} \right)^{0.25} \quad [5.1]$$

where d is the outside diameter of pile, E_p and E_s are respectively the Young modulus of pile and of the first layer of the subsoil. Usually the value of active length is around 10-15 d .

The model pile is a hollow aluminium tube, an equivalent solid pile as a Young's modulus is:

$$\bar{E}_p = \left[E_p \left(1 - \frac{2t}{d} \right)^4 \right] \quad [5.2]$$

where t denotes the thickness of tube. With the above-modified Young's modulus \bar{E}_p the "replacement" solid cylinder has flexural rigidity ($E_p I_p$) as the original hollow pile. (Mylonakis, 2001). The modified Young's modulus \bar{E}_p is equal to 16244 MPa.

In particular, considering the first value of stiffness G_0 (9 MPa), E_s is equal to 23 MPa, and the active length is 171 mm.

The active length is an important parameter for the reason that the maximum kinematic bending moment does not depend on the pile length, provided this is beyond the characteristic pile length as defined by Randolph (1981) or Pender (1993). The kinematical restraint acting on the pile when it is embedded in the lower layer does not exert any particular influence on the maximum bending moment at the pile-head.

Considering the variation of stiffness during the shaking table test, the active length reduces. In particular, at the end of dynamic test the value of stiffness is equal to 12.9 MPa, so that the L_a value corresponds to 156 mm.

The results of eight different tests are illustrated ($E_{STU12_NRHpile}$, $E_{STU5_NRHpile}$, $E_{STU2_NRHpile}$, $E_{TMZ12_NRHpile}$, $E_{TMZ2_NRHpile}$, $E_{NCB12_NRHpile}$, $E_{NCB5_NRHpile}$, $E_{NCB2_NRHpile}$) in figure 5.33.

The values shown in the plots represent the envelopes of bending moment along the pile, which involve different excitation periods.

These tests subjected the model to the input motion 0.3 g (on the shaking table), resulting in a free-field of 0.35 g (2 scale) or 0.2g (12 scale).

Clearly, the increase of amplitude of shaking emphasizes the action of restrain condition. It makes a large bending moments near the pile head. The second peak of bending moment is located along the pile in depth. However, occurred at a depth of 400 mm (L_a is 156 mm), it indicates that soil movement produce the largest stresses in pile.

The bending moments along the pile are shown for the three different input motion scaled with the same factor in Figures 5.34a) b) c).

The different in terms of bending moment amplitude between 2 scale and 5 scale input motion is not so evident. In particular, STU 2 produces bending strain on pile surface smaller than STU5, as in the previous case (FH pile). It is acceptable because the predominant frequency of STU 5 (11 Hz) is closer than STU 2 (5 Hz) to the natural frequency of soil deposit (30 Hz).

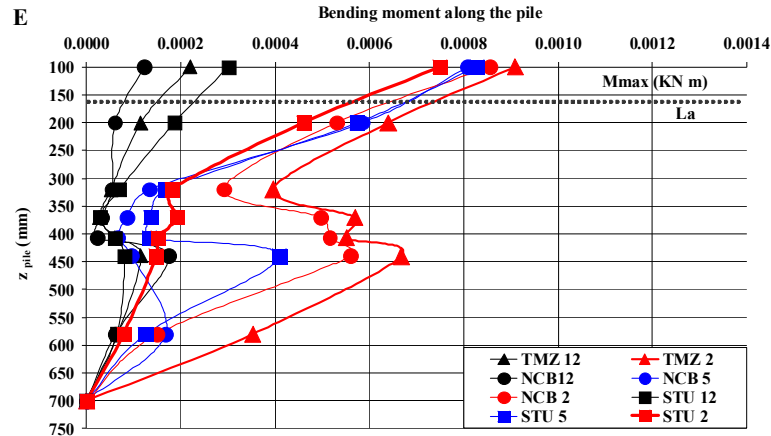


Figure 5.33 Envelop of maximum bending moment along the pile for all input motions ($E_{NRHpile}$)

Figures 5.35 shows a comparison between the bending moments along the pile obtained for the two different pile head configurations, for three different input motions scaled.

It has been noted that the influence of scaling factor manifests efficiently on the kinematic bending moment (moment around at mid of length of pile).

In order that the perceptual variation of the bending moment at middle of the soil deposit from the case of input motion scaled 2 times to 5 times is bigger that the variation of on the bending moment on the pile head.

The free head and no rotation pile head configurations are shown in figures 5.36 a-f. Several interesting points are worthy of note:

1. The biggest moments are concentrated approximately on the pile head; a second peak of moment is present around the mid length of the pile (375 mm). Considering that the active length is equal to 171 mm, this secondary peak is a kinematic effect in homogeneous soil (figure 5.34a) b) c)).
2. The effects of scaling factors occur in the amplitude of bending moment with depth.
3. The bending moment diagrams of free-head and no rotation head piles converge with depth and become practically identical beyond a certain distance from the surface, as shown in figure 5.35 a) to d). This depth coincides with the 'active pile length', beyond which a head-loaded pile behaves as in infinitely long beam. Not for all cases this tendency is discovered (figure 5.35 e)-f))

Further, validate kinematic interaction effects the characteristic of motion in surface and at pile head are shown in the following plots.

The Fourier Fast transform and a spectra response (5% damping) are shown for each signal. These functions are important to estimate the modified motion in foundation (at pile head).

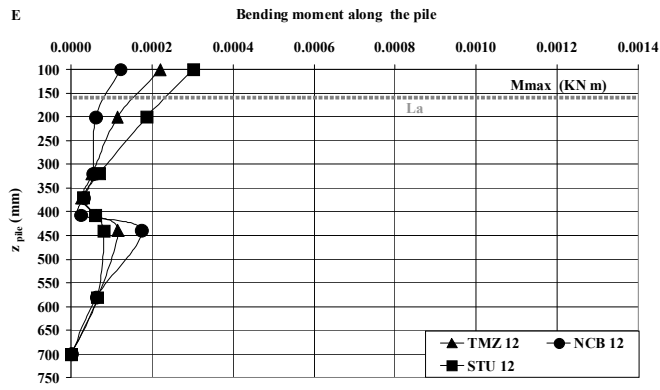


Figure5.34 a) Envelop of maximum bending moment along the pile for 12 scale input motion ($E_{NRHpile}$)

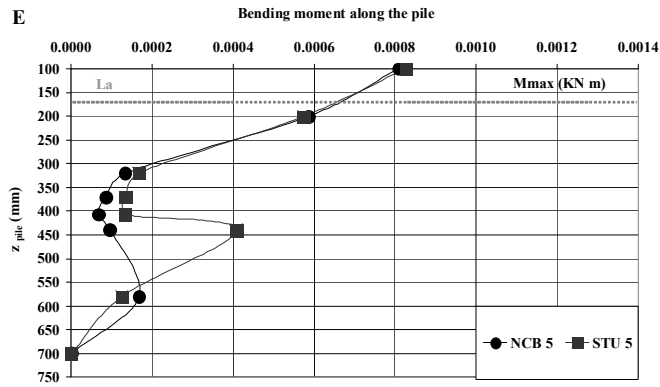


Figure5.34 b) Envelop of maximum bending moment along the pile for 5 scale input motion ($E_{NRHpile}$)

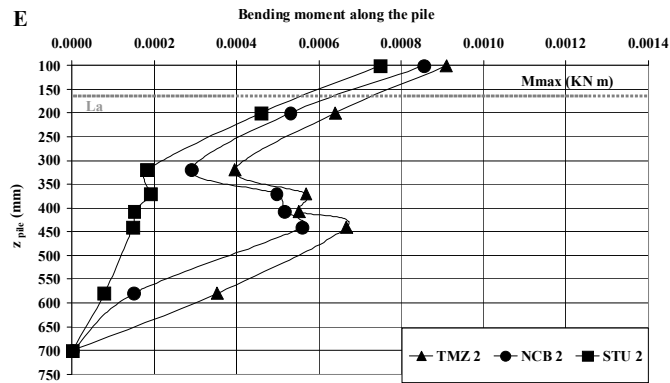


Figure5.34 c) Envelop of maximum bending moment along the pile for 2 scale input motion ($E_{NRHpile}$)

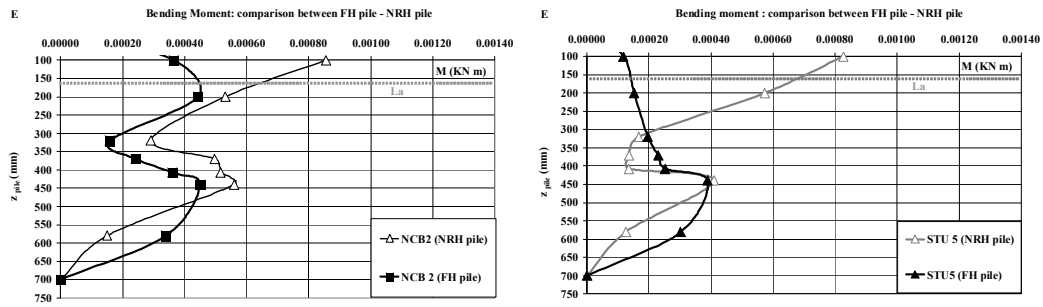


Figure 5.35 a) Comparison FH – NRH pile NCB 2 scale b) Comparison FH- NRH pile STU 5 scale

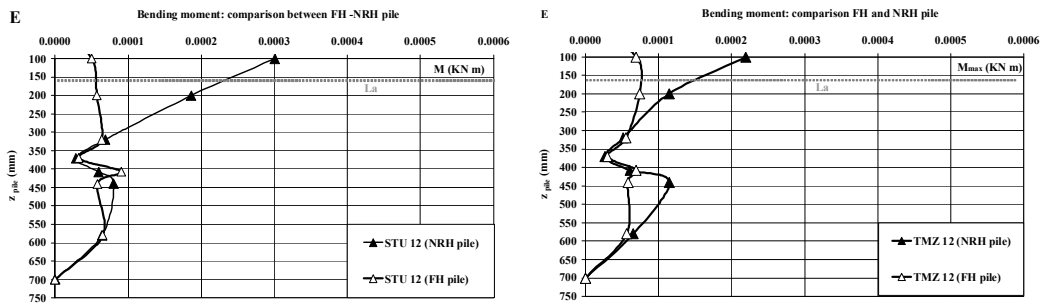


Figure 5.35 c) Comparison FH – NRH pile STU 12 scale, d) Comparison FH- NRH pile TMZ 12 scale

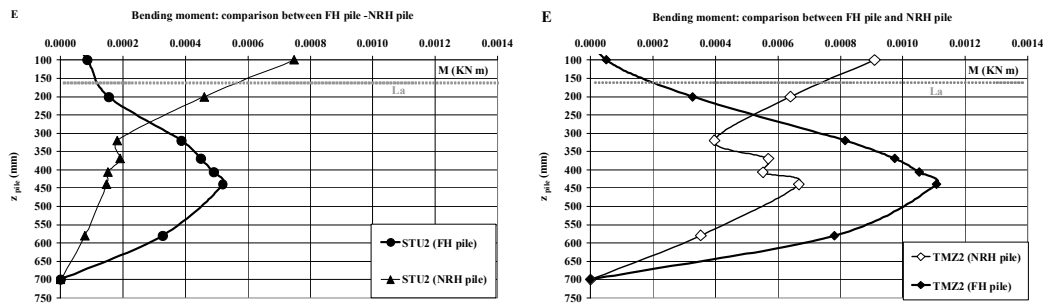


Figure 5.35 e) Comparison FH – NRH pile STU 2 scale, f) Comparison FH- NRH pile TMZ 2 scale

Figures 5.36 for E_TMZ2_NRH pile, it is very interesting to note that for this, the foundation input motion is very big comparing ($PGA = 0.9\text{ g}$) to the free-field ground motion (0.35g). Therefore the motion on the pile head is amplified. The spectra response shows that pile head response is different from free field response for high frequency, until 14 Hz .

The spectra response shapes is similar after 10 Hz . The maximum displacement on the top pile is around 6 mm , as shown in figure 5.36 d).

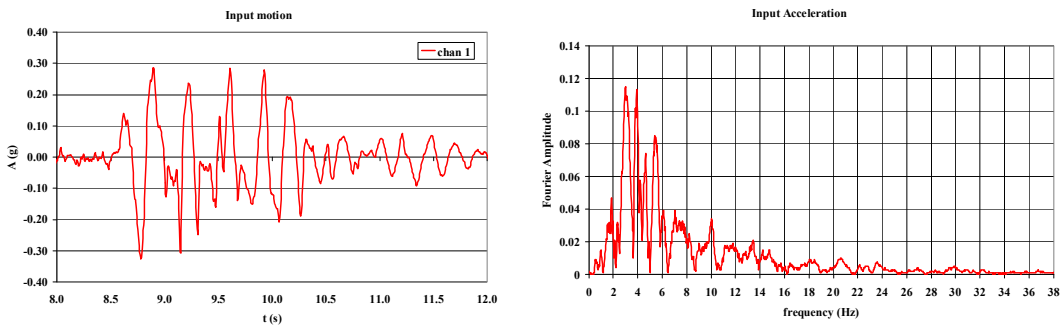


Figure 5.36 a) input motion time histories and FFT (E_TMZ2_NRH)

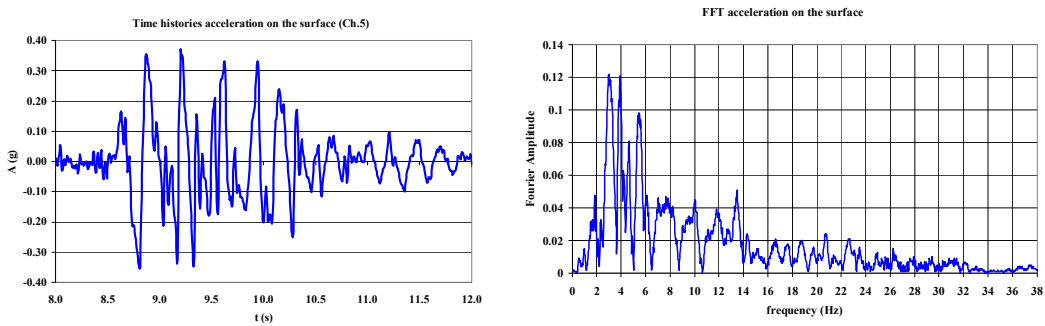


Figure 5.36 b) surface acceleration time histories and FFT (E_TMZ2_NRH)

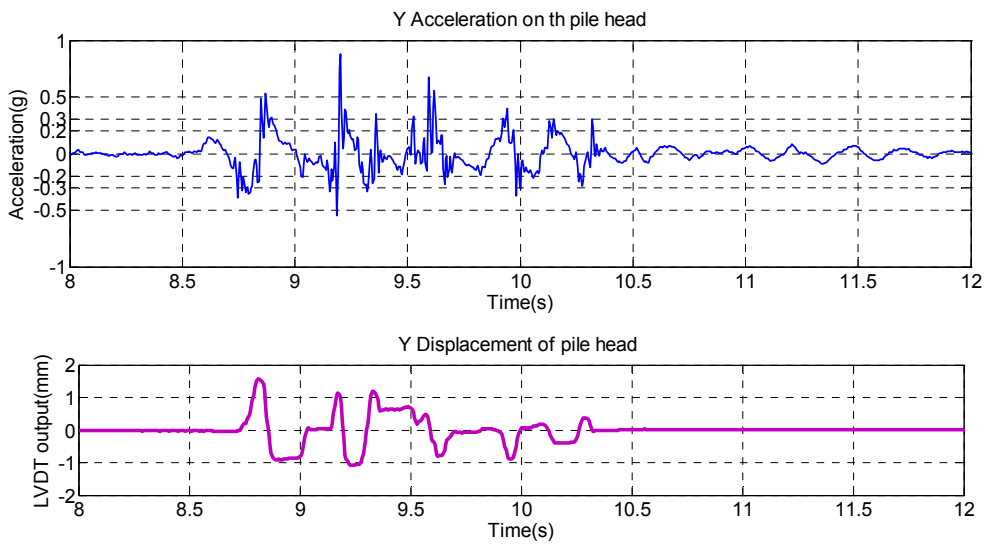


Figure 5.36 c) acceleration time histories and d) displacement at pile head (E_TMZ2_NRH)

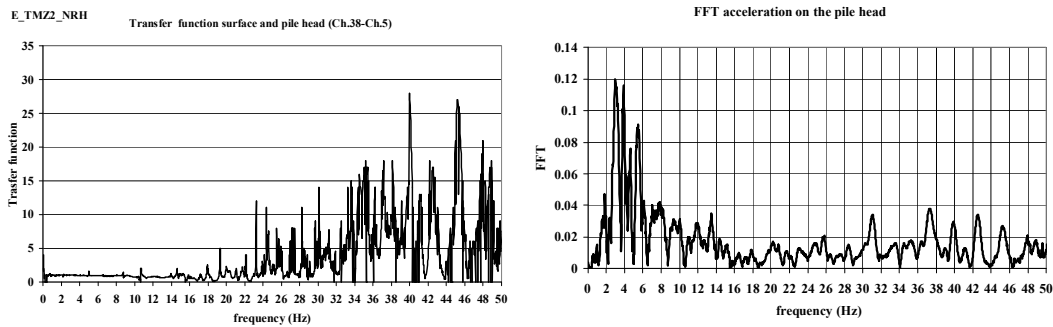


Figure 5.36e) Transfer function and f) FFT at pile head (E_TMZ2_NRH)

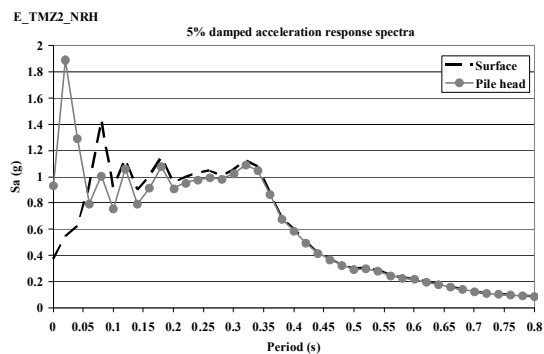


Figure 5.36 g) Spectra response (E_TMZ2_NRH)

In Figure 5.37a), b), c) for the E_STU2_NRH accelerations time histories for input motion, surface, pile head cap are plotted. As in the previous case, there is an amplification of input motion at foundation level (PGA 0.6 g), in particular for high frequency the pile head acceleration is predominant as shown in figure 5.37 f). Figure 5.38 plots transfer function estimates, for the E_STU12_NRH pile accelerations to the free - field soil response.

These tests are examples of general trend of transfer between input motion and the bottom to the pile head(foundation).

For monolayer configuration (E), in general, the free-field transfer functions are strongly in phase.

In these cases, with the increase of Arias Intensity, the seismic motion recorded at the top of the pile increases, even though it is always smaller than the one recorded in free field condition.

It is therefore very interesting to note that for no rotation head single pile, wave scattering effects are negligible and the foundation input motion is nearly equivalent to the free-field ground motion.

For 12 times scaled input motions, the motion in foundation is smaller than surface one. The presence of pile filters the high frequency component of input motion (Kanya and Kausel, 1991)

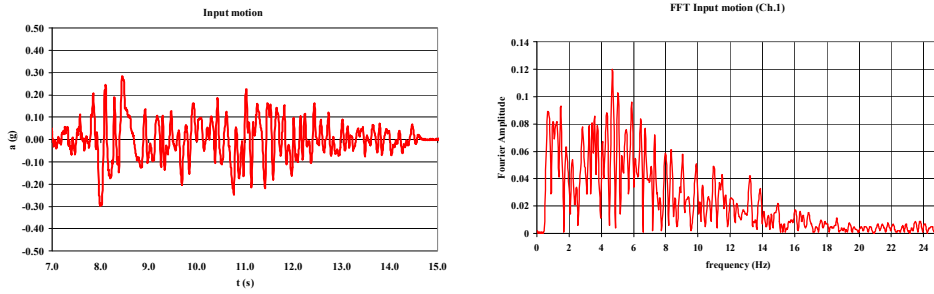


Figure 5.37 a) input motion time histories and FFT (E_STU2_NRH)

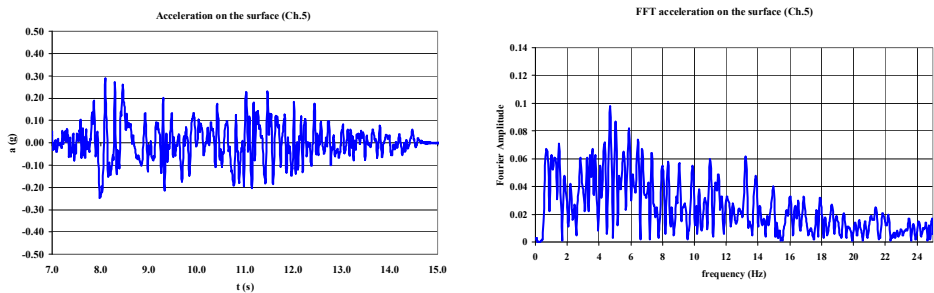


Figure 5.37 b) surface acceleration time histories and FFT (E_STU2_NRH)

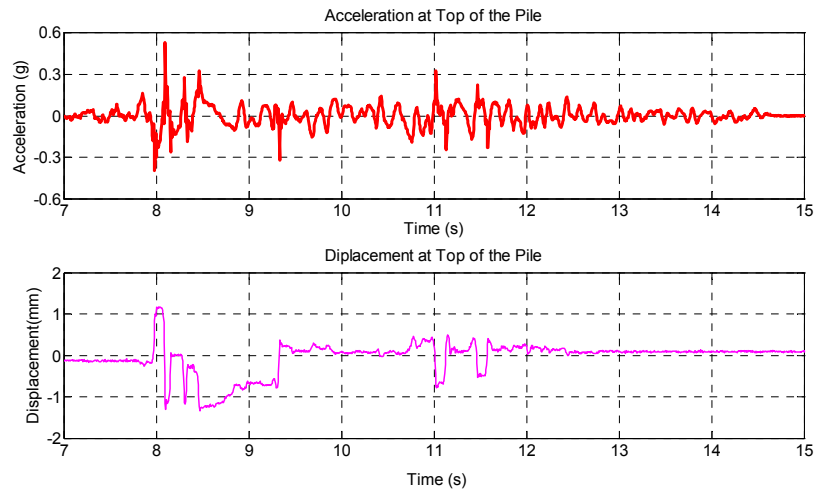


Figure 5.37 c) acceleration time histories and FFT at pile head d) and displacement (E_STU2_NRH)

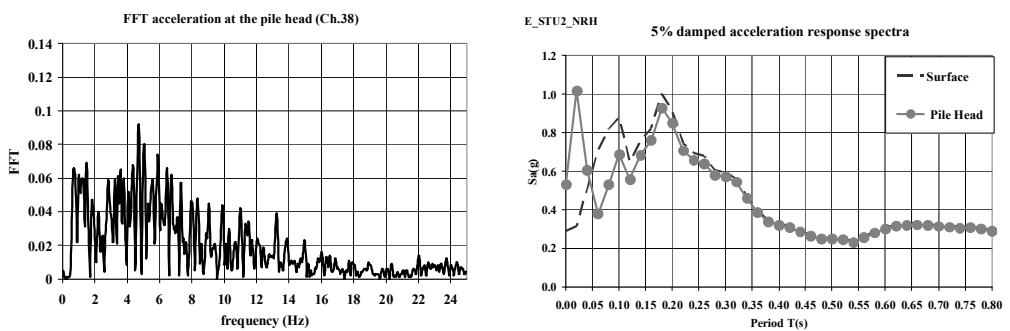


Figure 5.37 e) FFT at pile head and f) Spectra response (E_STU2_NRH)

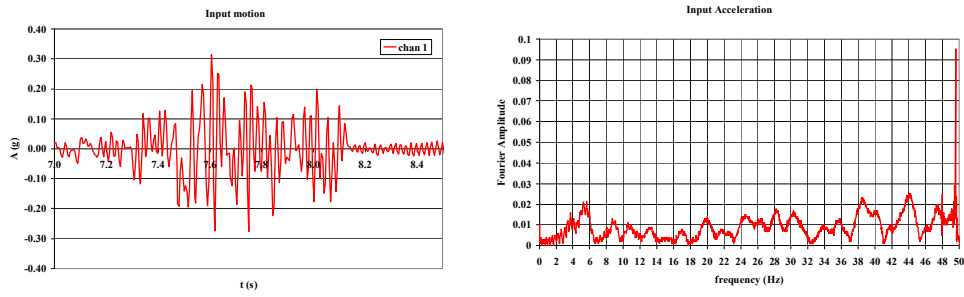


Figure 5.38a) input motion time histories and FFT (E_STU12_NRH)

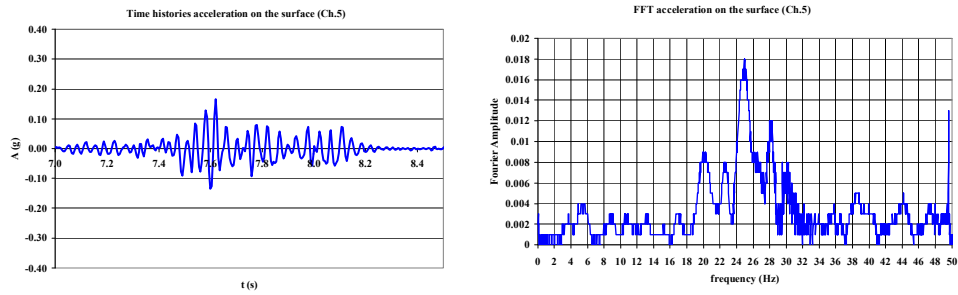


Figure 5.38b) surface acceleration time histories and FFT (E_STU12_NRH)

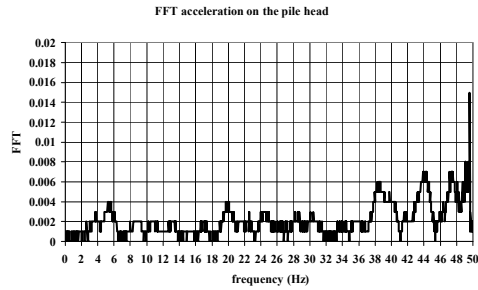


Figure 5.38c) acceleration time histories and FFT at pile head (E_STU12_NRH)

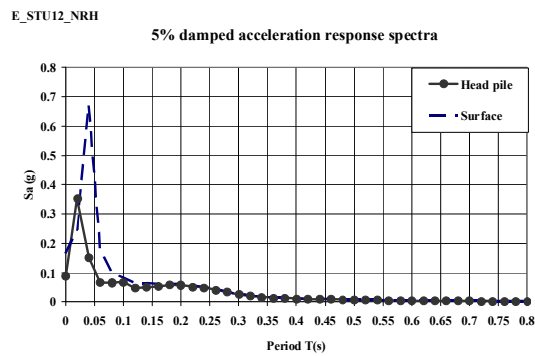


Figure 5.38d) Response spectra (E_STU12_NRH)

5.5.2 Bending moment : layered soil configuration BE+E

In this section the bending moments of layered configuration (BE+E) are analyzed. Each soil layers are homogeneous and the pile behaves is linear-elastic. In following plot, Figure 5.39, the bending moment envelop, for five different excitation periods are illustrated (BE+E_STU12_NRHpile, BE+E_STU5_NRHpile, BE+E_STU2_NRHpile, BE+E_TMZ12_NRHpile, BE+E_TMZ2_NRHpile). The active length of pile is 171 mm.

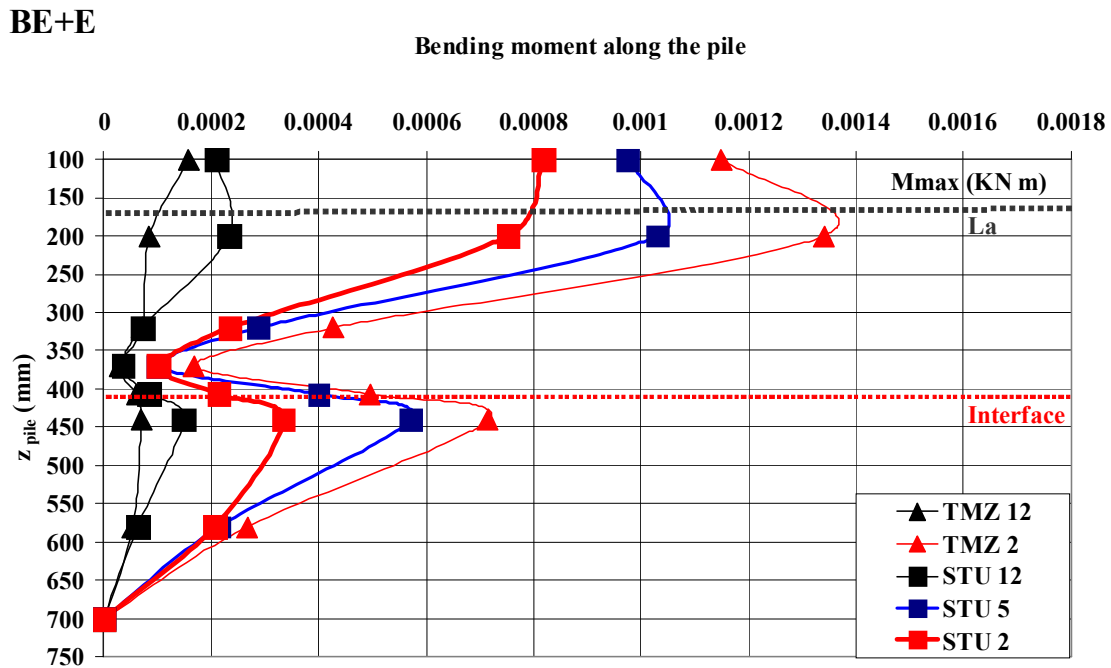
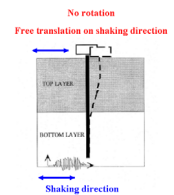


Figure 5.39 Envelop of maximum bending moment along the pile for all input motion (BE+E_NRHpile)

Tests carried out for different seismic inputs and at different frequency scales show that the bending moment magnitude is affected by both the frequency and the energy content of the seismic input.

The pile bending moment response of test for BE+E configuration, depicted in Figure 5.39, have a similar trends of monolayer configuration. Restraint condition on pile head induces large bending moments in the upper sections of pile, for all input motions.

Otherwise, for this layered soil configuration the maximum bending moment is concentrated in a section lower than the pile head. The maximum bending moment is located around at 200-100 mm.

In correspondence of interface the second bending moment peak occurs ($2d = 4.4\text{cm}$ from interface; Kavaddas and Gazetas, 1993).

A comparison between the bending moments along the pile obtained for the two different pile configurations are reported for the three different input motion scaled with the factor (figures 5.39 (a-e)).

It should be noted that as the input motion high frequency content reduces (going from 12 to 2 earthquake scaling factor) the kinematic bending moment along the pile amplifies at interface.

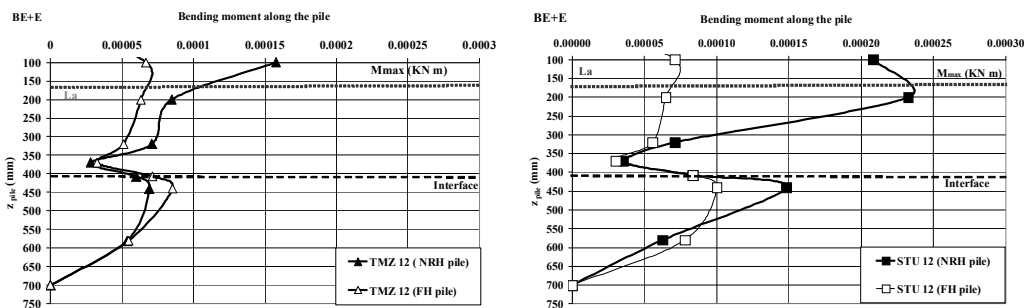


Figure 5.39 Comparison FH – NRH pile a) TMZ 12- b) STU 12 scale

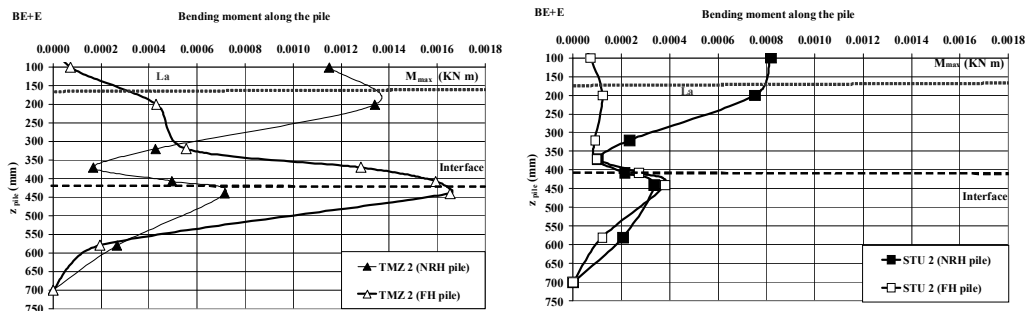


Figure 5.39 Comparison FH – NRH pile c) TMZ 2- d) STU 2 scale

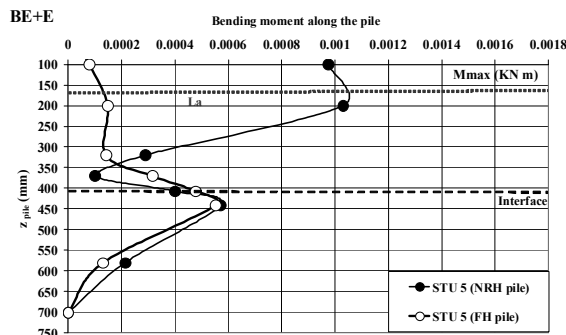


Figure 5.39 Comparison FH – NRH pile e) STU 5scale

The influence of scaling factor affects the kinematic bending moment value more than total moment on the pile head.

Finally, Figures 5.40-5.41-5.42-5.43-5.44 present a time histories acceleration and FFT for surface, input motion, pile head and the LVDT measurement on pile head for five different tests: BE+E_TMZ 2_NRH pile, BE+E_STU 2_NRH pile, BE+E_STU12_NRH pile, BE+E_TMZ 12_NRH pile, BE+E_STU 5_NRH pile

Further validate kinematic interaction effects, for the BE+E_TMZ 2_NRH Figures 5.40 a)-b)-c)-d)-e)-f) plot input motion, surface, pile head accelerometer time histories and FFT respectively associated. The pile head motion (PGA = 0.31 g) is smaller than free field motion on the surface (PGA= 0.5 g). The time histories are strongly in phase.

On the pile head the high frequency are reduced. In figure 5.40 e), for the BE+E_TMZ 2_NRH the transfer function is plotted. Also, the spectra responses are very similar (figure 5.40 d)).

Figure 5.41 shows transfer function estimates, for the BE+E_STU 2_NRH pile. Figures 5.42 a)-b)-c) d) –e) show the properties of motion for BE+E_STU12_NRH pile.

From the compare between the acceleration time histories, it is clear that the pile response and the soil response are very different.

The PGA values are dissimilar: in surface the peak is 0.22 g, at pile head is smaller (0.1 g).

Generally, for 12 times scaled input motion the de-amplification of motion occurs.

Figures 5.43 a)-b) c) shown the same plot for BE+E_TMZ12_NRH pile. In this case the de-amplification of motion in foundation is noted, the PGA on the surface is 0.1 g and on the pile head is equal to 0.05 g. The high frequency of input motion are filtered from pile presence.

The wave scattering effects are evident and the foundation motion is quite different to the free-field ground motion.

The tendency of motion on the pile head is influenced by the frequency content of input motion, the amplitude of de-amplification increases with the high frequency content of motion.

In general the presence of pile seems to filter the high frequency (low period). This result is typical for layered soil configuration BE+E.

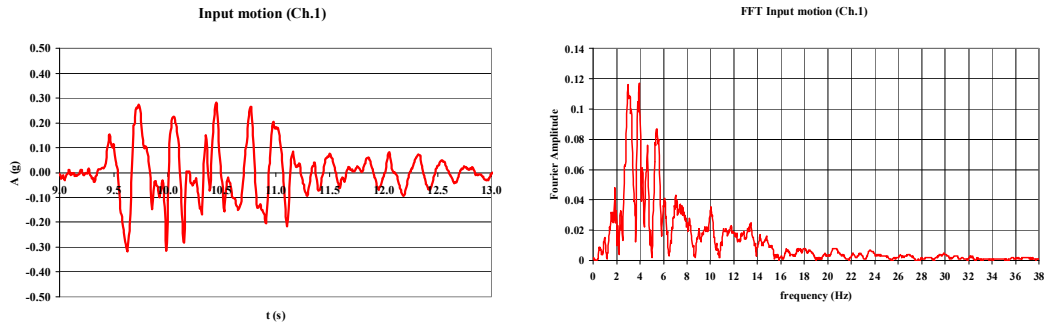


Figure 5.40 a) input motion time histories and FFT BE+E_TMZ 2_NRH pile

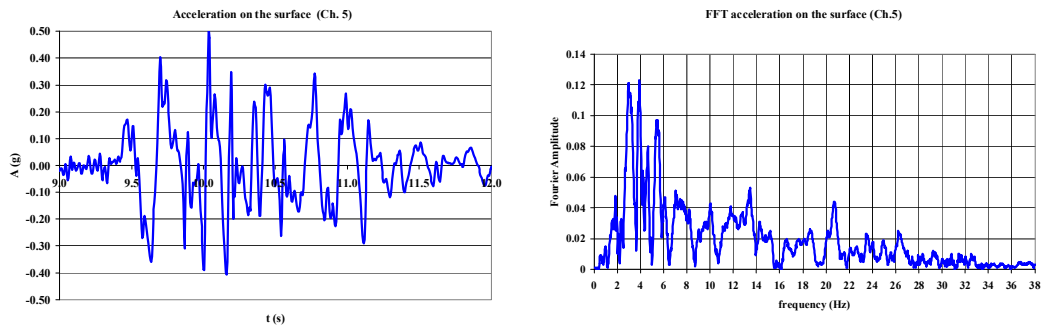


Figure 5.40 b) time histories acceleration and FFT on the surface BE+E_TMZ 2_NRH pile

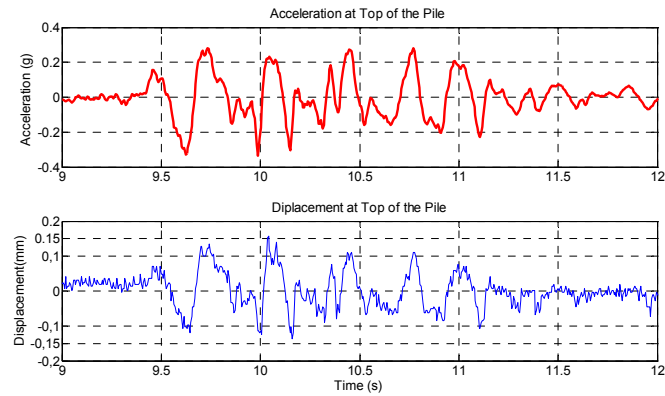


Figure 5.40 c) time histories acceleration on the pile head and d) LVDT measure BE+E_TMZ 2_NRH pile

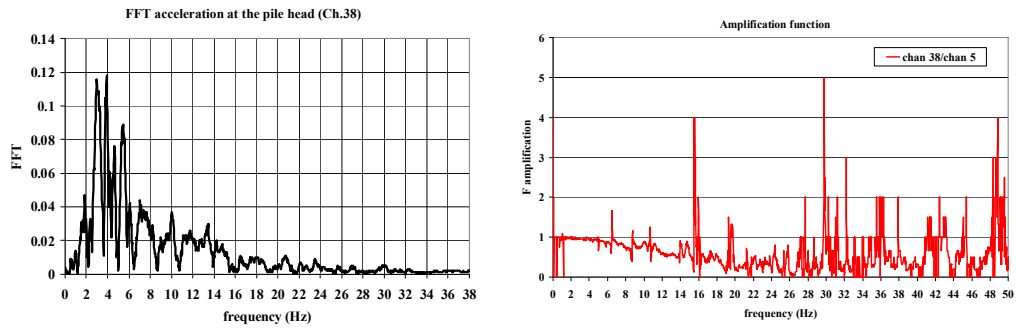


Figure 5.40 e) FFT on the pile head f) transfer function BE+E_TMZ 2_NRH pile

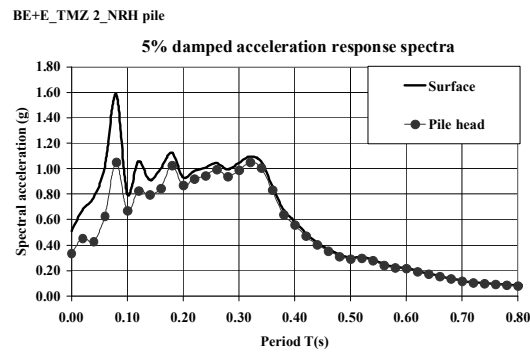


Figure 5.40 g) Spectra response BE+E_TMZ 2_NRH pile

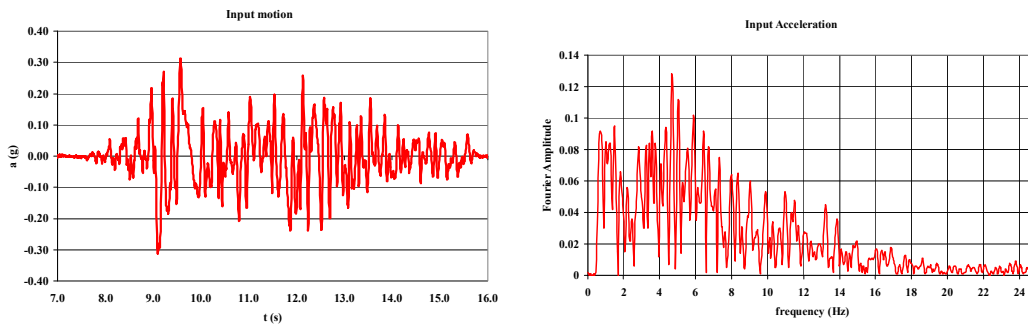


Figure 5.41 a) input motion time histories and FFT BE+E_STU 2_NRH pile

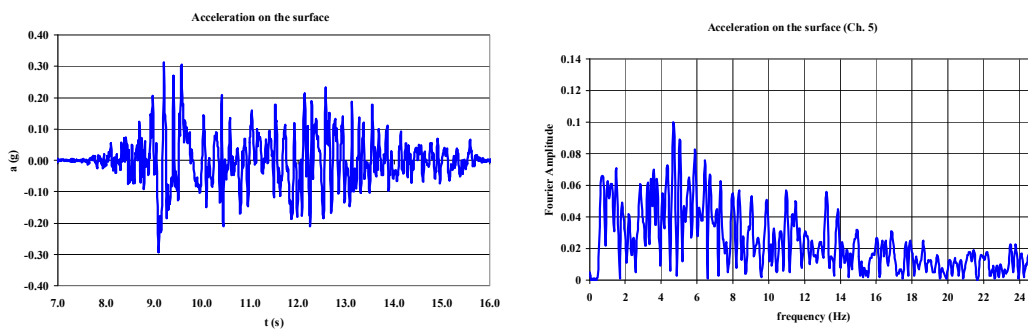


Figure 5.41 b) time histories acceleration and FFT on the surface BE+E_STU 2_NRH pile

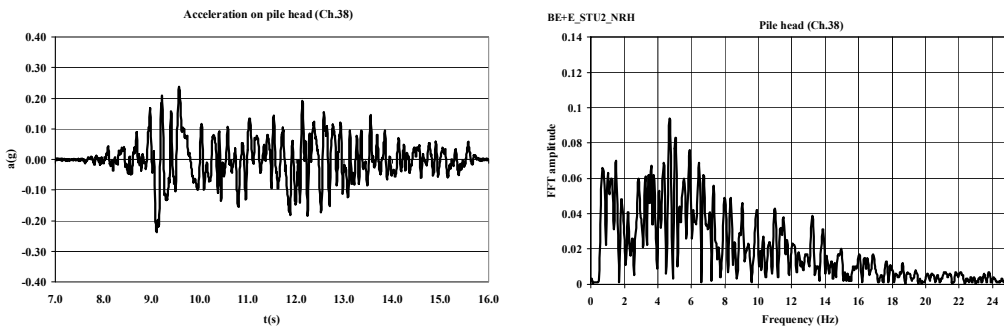


Figure 5.41 c) time histories acceleration and FFT on the pile head BE+E_STU 2_NRH pile

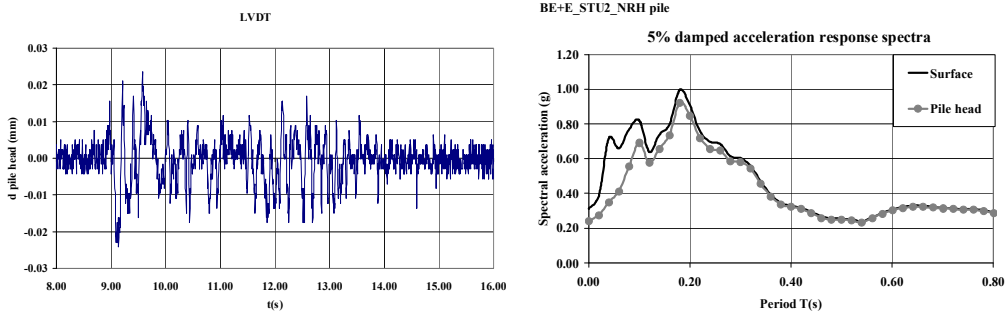


Figure 5.41 d) LVDT on the pile head and e) spectra response BE+E_STU 2_NRH pile

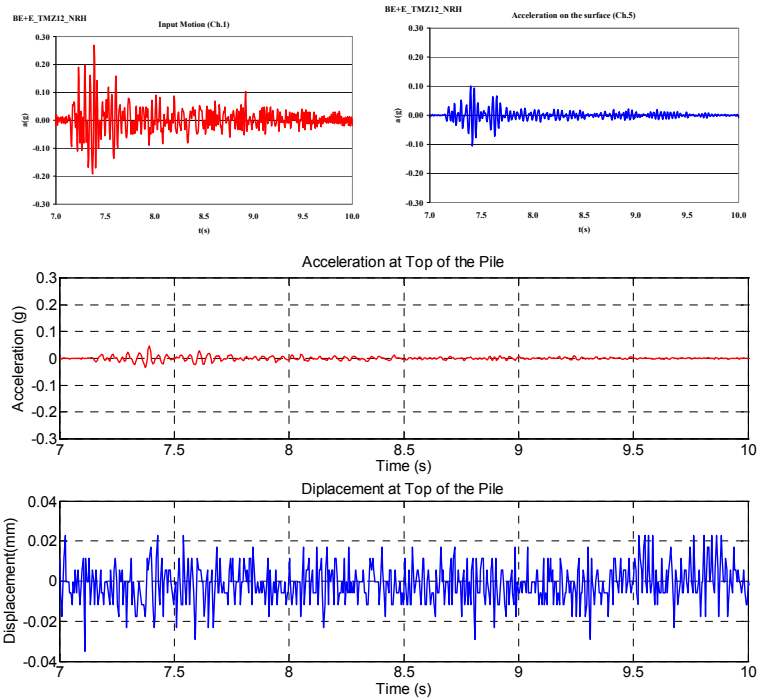


Figure 5.43 a) : Time histories of acceleration for BE+E_TMZ12_NRH

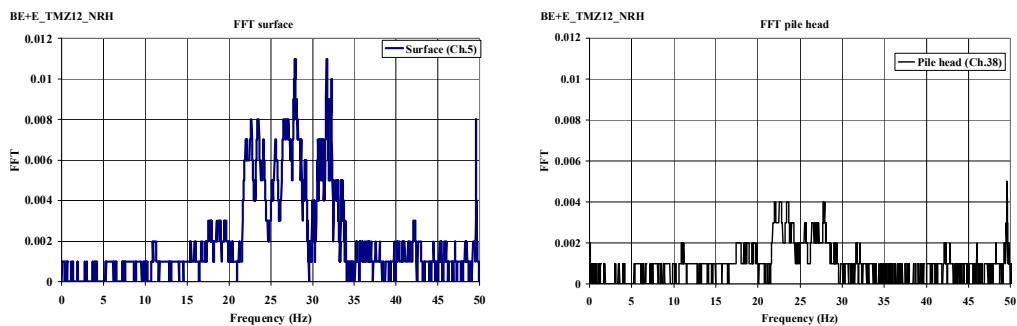


Figure 5.43 b) FFT- BE+E_TMZ12_NRH

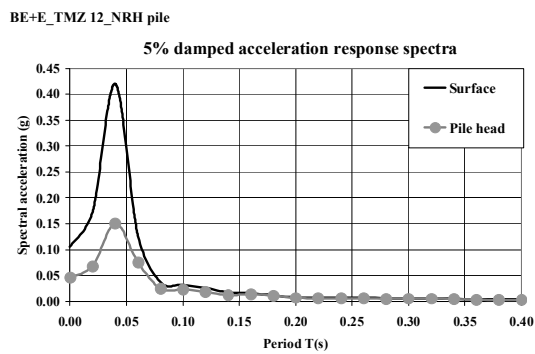


Figure 5.43 c): FFT - BE+E_STU 12_NRH

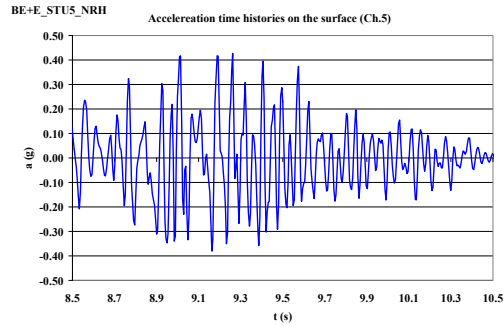


Figure5.44a) Spectra response - BE+E_STU5_NRH

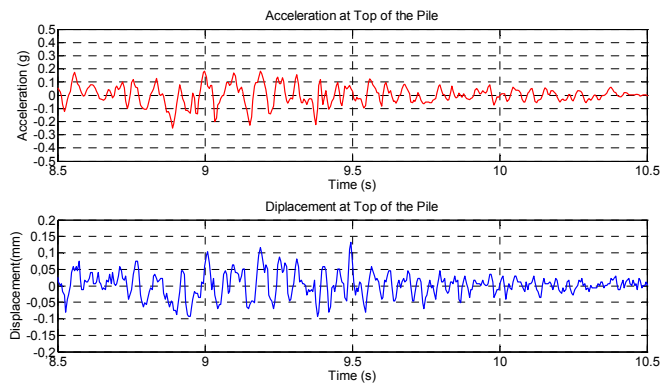


Figure5.44 a) Acceleration on the pile head and b) LVDT on the pile head - BE+E_STU5_NRH

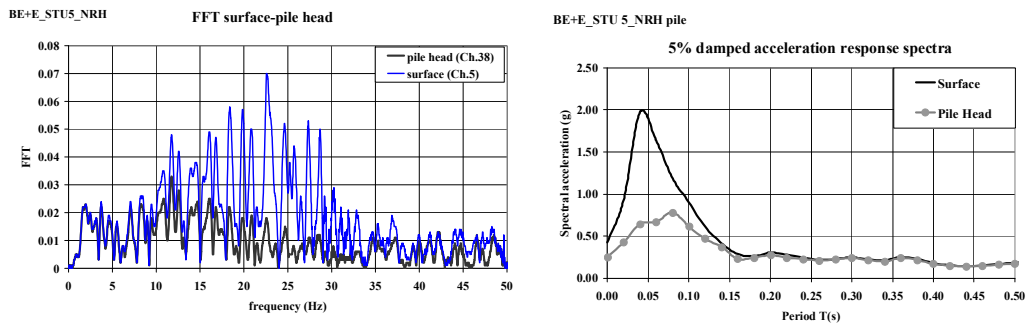


Figure5.44 c) Spectra response - BE+E_STU5_NRH

5.5.3 Bending moment: layered configuration E+R

In following plots, Figure 5.45, the envelopes of bending moment for eight different earthquakes are illustrated (E+R_STU12_NRHpile, E+R_STU5_NRHpile, E+R_STU2_NRHpile, E+R_TMZ12_NRHpile, E+R_TMZ2_NRHpile, E+R_NCB12_NRH pile) for E+R configuration ($v_{s2}/v_{s1}=8$).

The presence of a very soft layer (upper layer) increases the bending strain on pile, they are in amplitude bigger than BE+E soil configuration ($V_{s2}/V_{s1}=1.7$).

At interface the effects of stiffness contrast is always the same: the moment increase with the stiffness contrast.

In addition, the influence of constraint conditions on the pile head are highlighted by the peculiar shape of bending moment along the pile. The maximum bending moment is not perfectly at pile head, but around at 200 mm from the top. In compare with the BE+E configuration the peak of maximum bending moments happen in a section lower. It is justified, because, in this case, the active length of pile is bigger than the interface depth. For Rubber the active length is 527 mm (the stiffness value is G_1 is 0.1 MPa, the Young modulus E is 0.3 MPa).

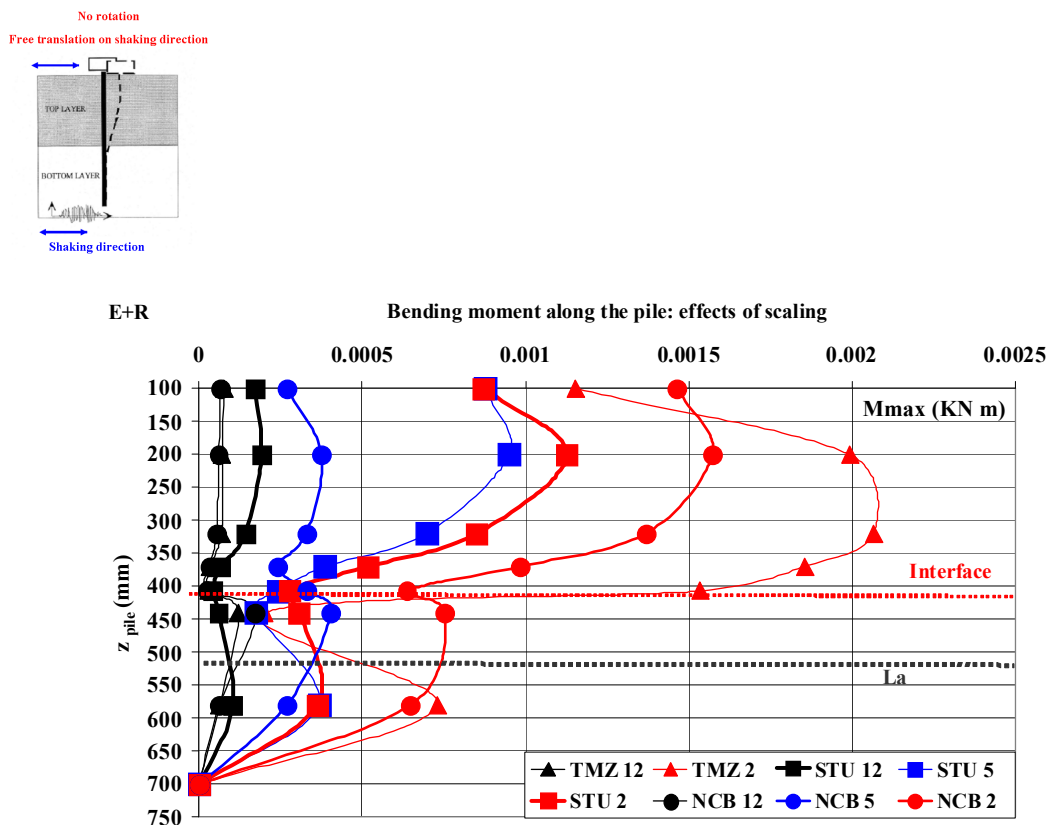


Figure 5.45: Envelop of maximum bending moment along the pile for all input motion (E+R_NRH pile)

The experimental results show that the soil-pile kinematic interaction is strongly influenced by the soil deposit configuration, in particular by the stiffness ratio between the layers.

Figures 5.45 (a-e) show a comparison between the bending moments along the pile obtained for the two different pile configurations FH and NRH pile. It has been noted that the influence of scaling factor manifests efficiently on the kinematic bending moment (moment around at mid of length of pile).

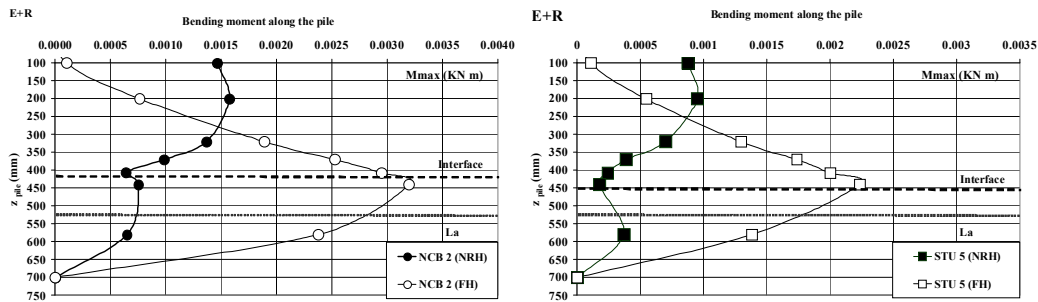


Figure 5.45 a)- Comparison FH – NRH pile NCB 2 scale b) Comparison FH- NRH pile STU 5 scale

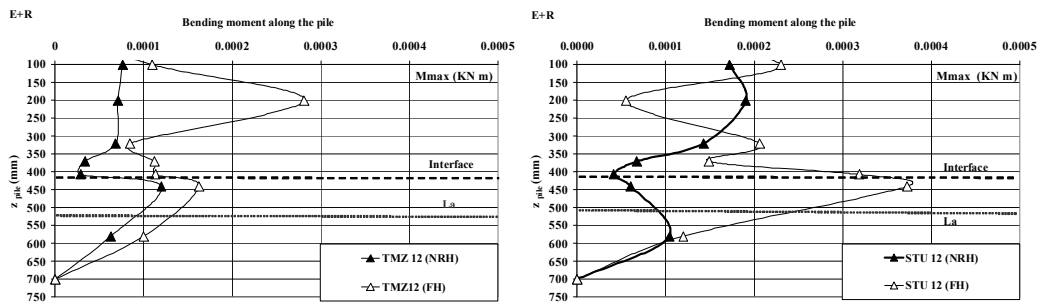


Figure 5.45 c)- Comparison FH – NRH pile STU 12 scale d) Comparison FH- NRH pile TMZ 12 scale

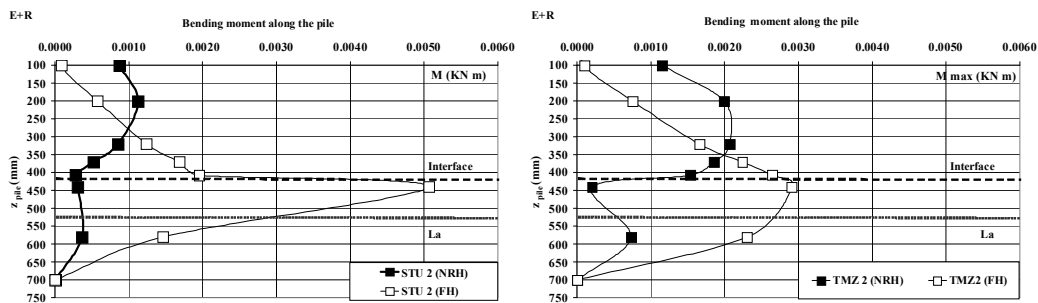


Figure 5.45 e) Comparison FH – NRH pile STU 2 scale f) Comparison FH- NRH pile TMZ 2 scale

In the following figures are plotted the values of acceleration spectral response and FFT between pile head, input motion, and interface elevation.

The results of analysis in frequency domain for Norcia: from 12 scale to 2 scale are shown in figures 5.46-5.47.-5.48.

The frequency content of acceleration on the pile head migrates to the input motion one. The increase of Arias intensity of input motion (for 5 scale and 2 scale) determinates an amplification of acceleration in foundation, but they are always smaller that free-field one. The motion in foundation and in the surface are different in terms of amplitude and in frequency content, but the acceleration spectra response are similar in shape.

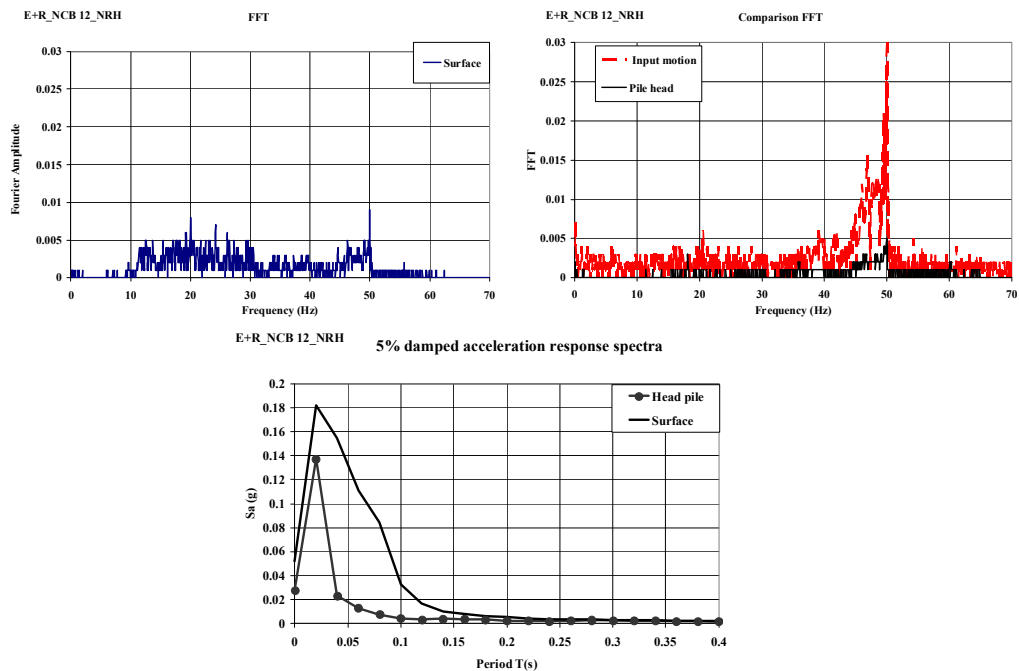


Figure 5.46. Spectra response and FFT (input motion-surface-pile head) for NCB 12 (E+R_NRH pile)

The results for Sturmo 12 scale and 2 scale are shown in figures 5.49-5.50. In addition, for this input motion, the frequency content of pile head recorder moves to compare the input motion one.

The increase of Arias intensity of input motion, from 12 scale to 2 scale, determinates an amplification of acceleration in foundation.

As well, the spectra responses for pile head signal is very close to interface one.

The results for Tolmezzo: 12 scale and 2 scale are shown in figures 5.51-5.52. The tendency is the same before explained.

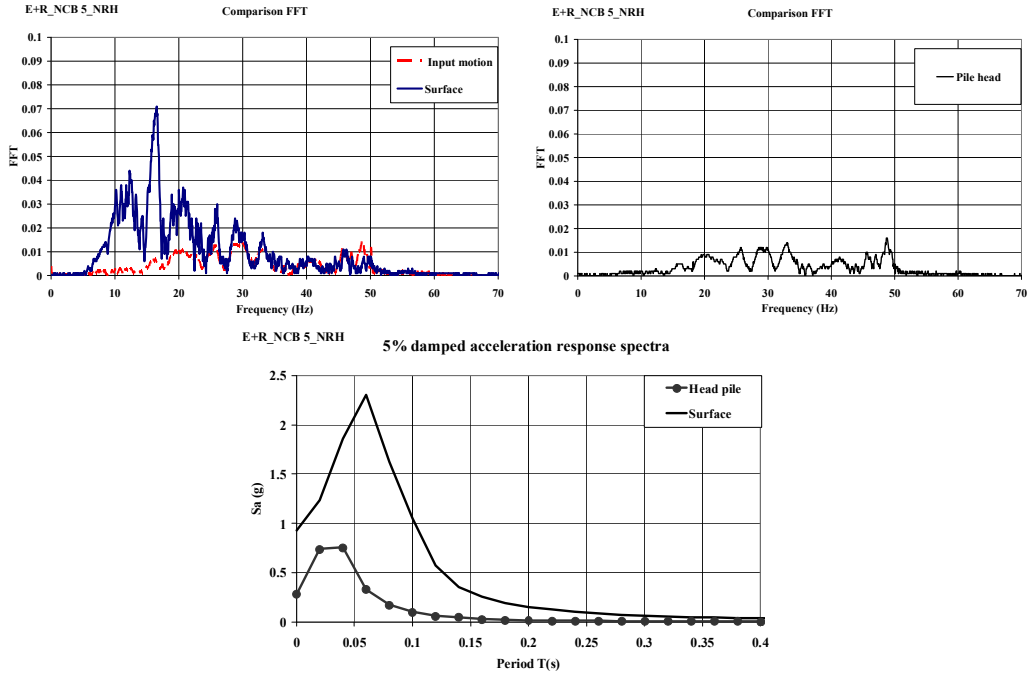


Figure 5.47: FFTs Spectra response and (input motion-surface-pile head) for NCB 5 (E+R_NRHpile)

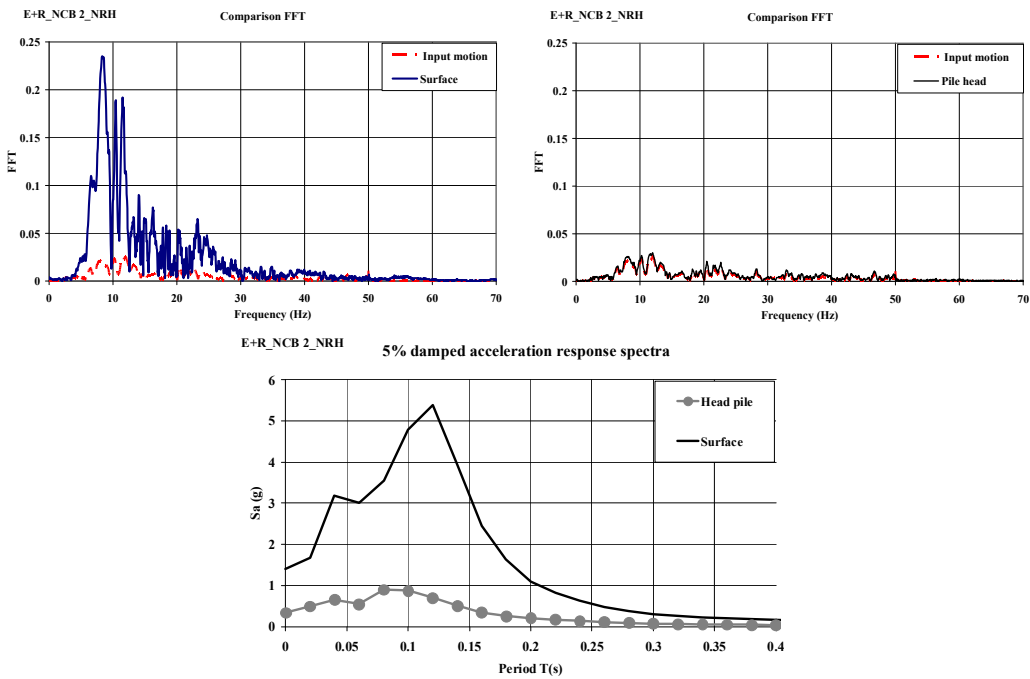


Figure 5.48. Spectra response and FFT (input motion-surface-pile head) for NCB 2:(E+R_NRHpile)

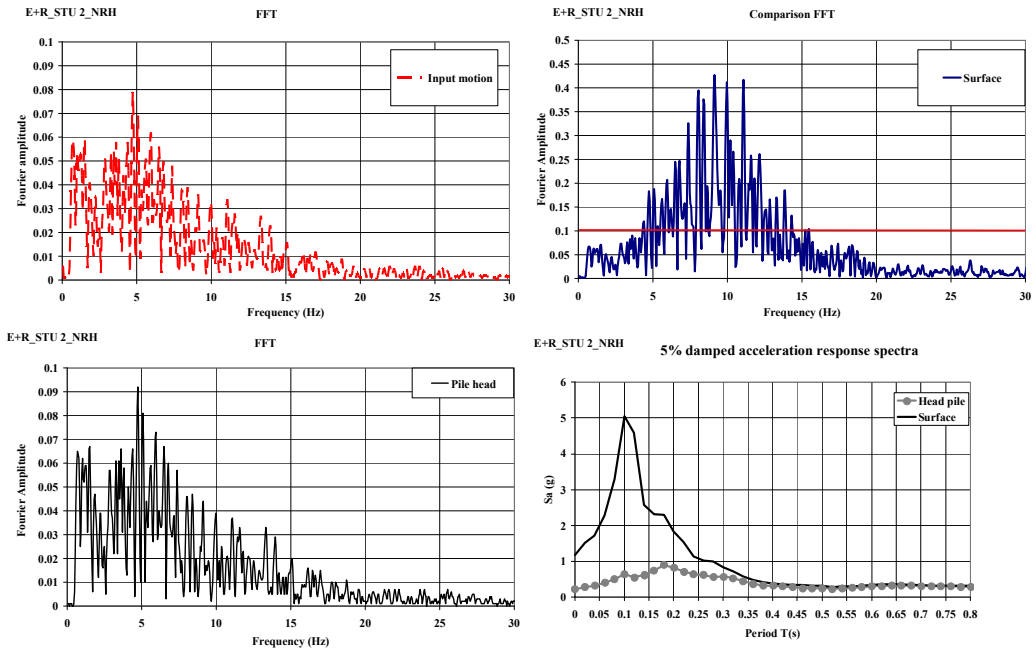


Figure 5.50. Spectra response and FFT (input motion-surface-pile head) for STU 2(E+R_NRHpile)

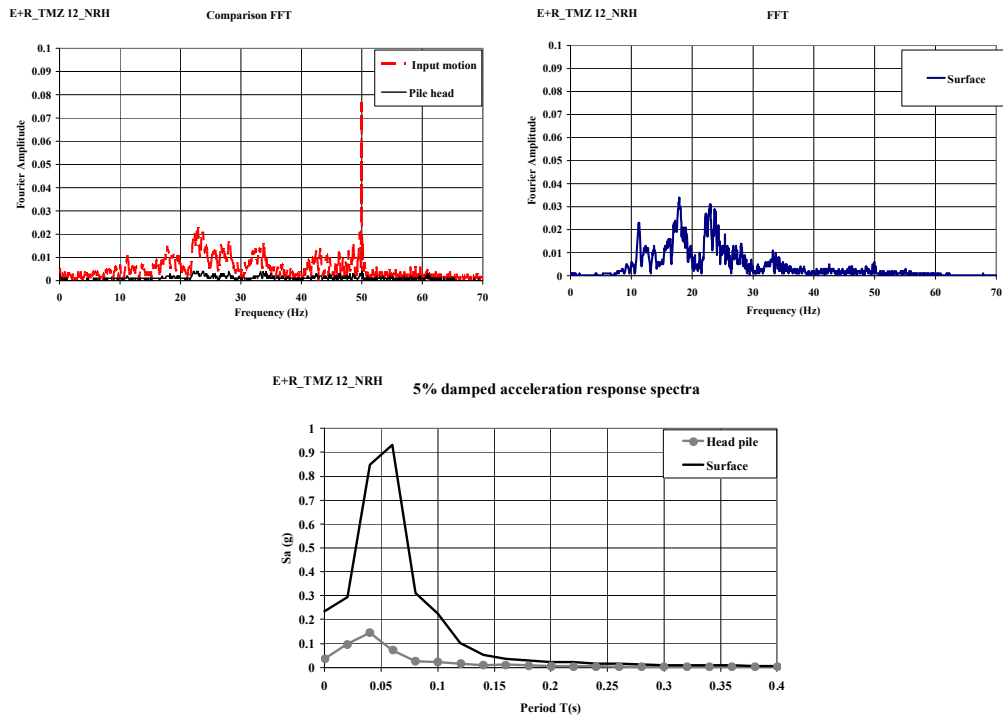


Figure 5.51. Spectra response and FFT (input motion-surface-pile head) for TMZ12(E+R_NRHpile)

5.5.4 Motion on the pile head

In most cases the free field pile head acceleration are strongly in phase. Only for the monolayer configuration it is therefore very interesting to note that with stronger input motion, 2 times scale, the wave scattering effects are negligible and the foundation input motion is bigger than the free-field ground motion.

In these cases, with the increase of Arias Intensity, the seismic motion recorded at the top of the pile increases, even though it is always smaller than the one recorded in free field condition.

Further it has been proved that the pile filters the high frequency components of the input motion (see Kanya and Kausel, 1991).

The pile head displacements are always smaller than the free field one. Different displacement means bending moment and curvature on the pile. From the valuation of adimensional factors of kinematic interaction, $I_u = \frac{|u_p|}{u_{ff}}$ (expressed in chapter 2) it is possible to describe the pile-soil behaviour Gazetas (1984) and Fan et al.(1991).

The amplitude of horizontal displacement on the soil surface (free-field), u_{ff} , and the amplitude of horizontal displacement at pile head, u_p , are obtained from velocity. Velocities data are integrated with respect to time using the trapezoidal method to produce displacement, as explain in the following paragraph 5.9.

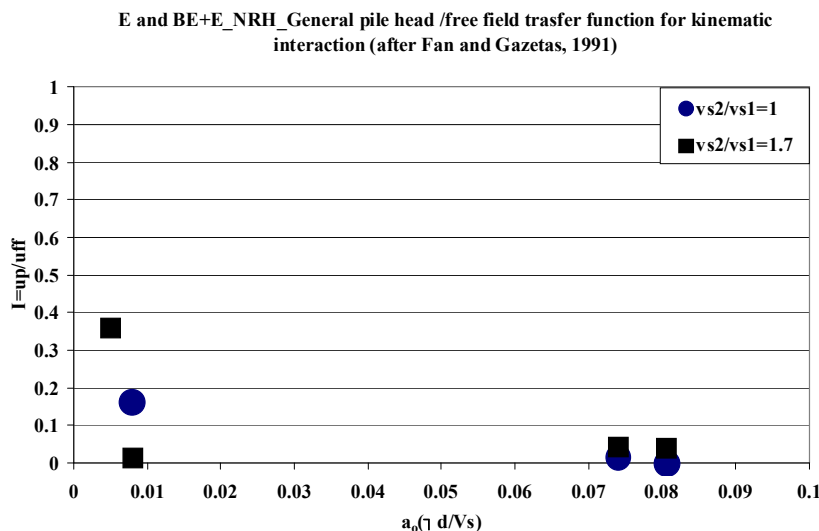


Figure 5.51 a): Pile Head/Free Field Transfer Function for Kinematic Interaction for Experimental data

The trend of I_u is plotted in function of a-dimensional frequency $a_0=d\omega/V_s$. Where ω is the pulse of input motion, it depends from the value of scaling factor of the input motion, and V_s is the shear velocity of sub-soil.

In figure 5.51a) are reported the value of adimensional factor I_u for different input motion for all three soil deposits.

In our case for soil configuration the terms of a dimensional kinematic interaction, I_u is smaller than unit.

5.5.5 Bending pile: effects of stiffness contrast

Figure 5.53 a) and b) show the ratio between the maximum bending moment, respectively near interface and at pile head, normalized by yield moment of pile

The experimental results show that the present of a very soft layer at top (rubber) of deposit increase the bending strain on pile, the moments of E+R soil configuration are in amplitude bigger than the BE+E soil configuration.

It is interesting to note that the effects of stiffness contrast at the interface are significant both for the free head pile condition and the no rotation one

Figures 5.54 a)- b)- c) show the normalized value of maximum bending moment near interface and on the pile head by yield moment of pile, for the three different configurations.

The most important conclusions that emerged from these analyses are (see also Nikolaou et al., 1995):

- (a) The kinematic bending strain depends mainly on the stiffness contrast (V_{s2}/V_{s1}) between any two consecutive soil layers in the deposit;
- (b) The constraint conditions at the pile head change the tendency of moment: in the monolayer configuration the maximum bending moment occur at pile head (in a section very close to it); for the layered soil configuration the maximum bending moment happens in a section lower that 100 mm from the top of pile. The migration of the maximum bending moment from the top to a lower section depends on the reduction of stiffness of the top layer (soft soil).
- (c) The effects of scaling factors are more evident on the kinematic bending moment value instead of the maximum bending moment at top of pile.
- (d) The bending moment diagrams of free-head and no rotation head piles converge with depth and become practically identical beyond a certain distance from the surface. This depth coincides with the 'active pile length', beyond which a head-loaded pile behaves as in infinitely long beam. Not all cases show this tendency (figure 5.35 e)- f)figure 5.45d-f).

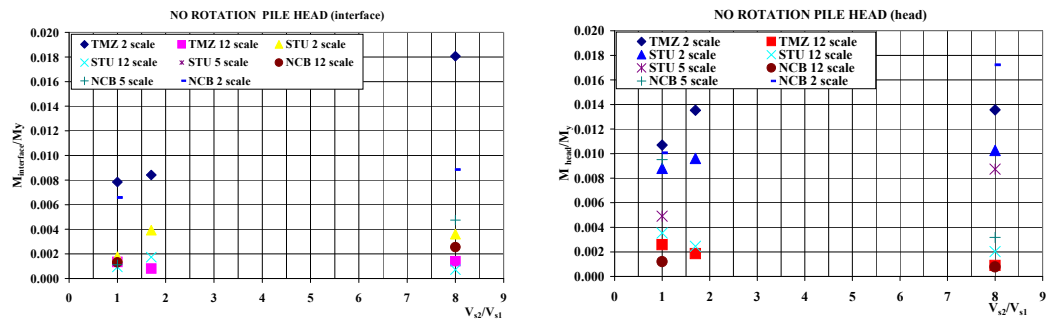


Figure 5.53 Maximum kinematic bending moment normalized by M_y for different soil configuration-

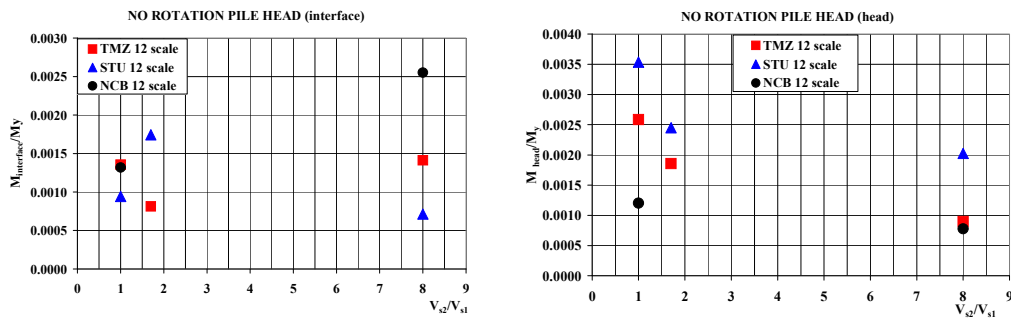


Figure 5.54.a-b) Maximum kinematic bending moment normalized by M_y for different soil configuration 12 scale

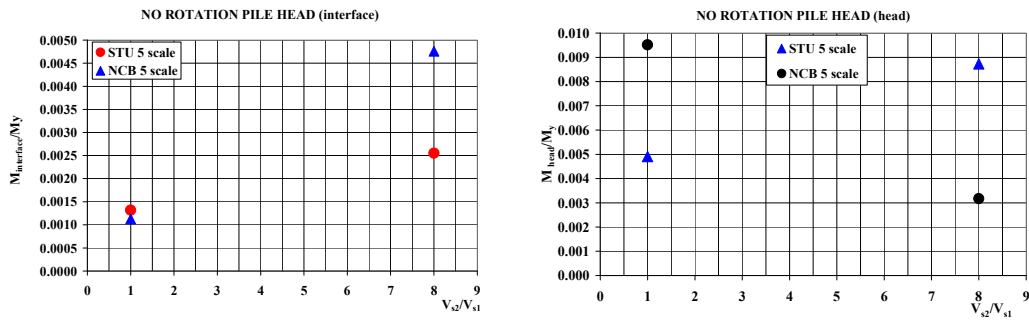


Figure 5.55a-b) Maximum kinematic bending moment normalized by M_y for different soil configuration 5 scale

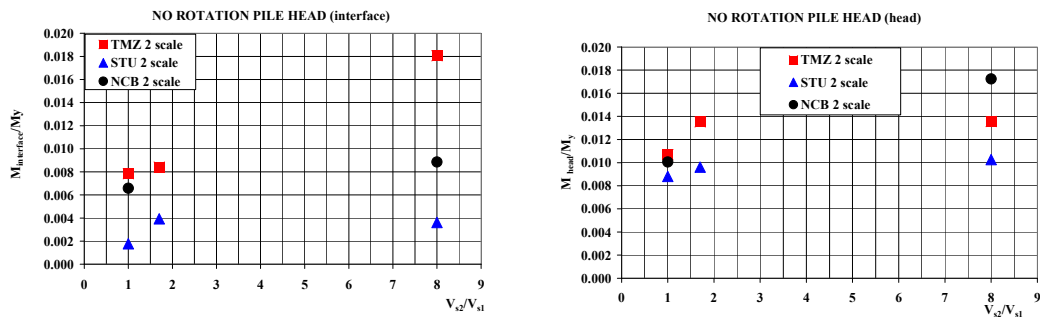


Figure 5.56.a-b) Maximum kinematic bending moment normalized by M_y for different soil configuration 2 scale

5.6 Kinematic interaction: effects of superstructure (SDOF)

To simulate the presence of the superstructure and investigate on the inertial effects an oscillator on the pile head is located. As explained in chapter 3, the weight of the oscillator has been chosen taking in account the frequency of input motion and the Young modulus of the first layer of the deposit.

Therefore, each test is characterized by the different values of the weight of the oscillator, which increases with the energy of the input motion. The layered soil configuration BE+E and E+R are investigated with this particular constraint (no rotation pile head) and the oscillator.

This configuration has been chosen to study the inertial effects respect to the kinematic effects. This particular configuration, pile constrain at top against rotation and the oscillator, (NRH+SDOF), simulates the behavior of the complete system (soil-pile-structure).

The oscillator generates inertial force consist in a structural inertial forces being transferred to the pile foundation. The motion induced at the foundation level generates oscillations in the superstructure which develop inertia forces and overturning moments at its base. For the peculiarity of restraint at pile head, the rocking mode is neglected.

The interesting aim is focused on relation between kinematic and inertial interaction in time during an earthquake. From the actual engineering practise, (code prescription) the combination of maximum effects, kinematic and inertial, is an usual procedure.

In reality it is very frequent that the motion of the superstructure is in phase opposite to the foundation, in this case the sum of the two maximum effects thus resulting in an over-conservative design. In the following tests the simultaneity of the two phenomena is investigated.

The soil-pile-structure response (NRH+SDOF) has been compared with a no rotation pile head configuration, massless building configuration (kinematic interaction).

Figure 5.57 a) shows the model setup for no rotation pile head + oscillator tests (NRH+SDOF).

In figure 5.57 b) the layout of the instruments to measure accelerations and displacements are shown. On the pile head it is located a LVDT transducer and an accelerometer to know the pile –foundation proprieties.

Besides, to investigate on the effective motion on the superstructure an accelerometer is located on the mass of the oscillator (Ch.40).

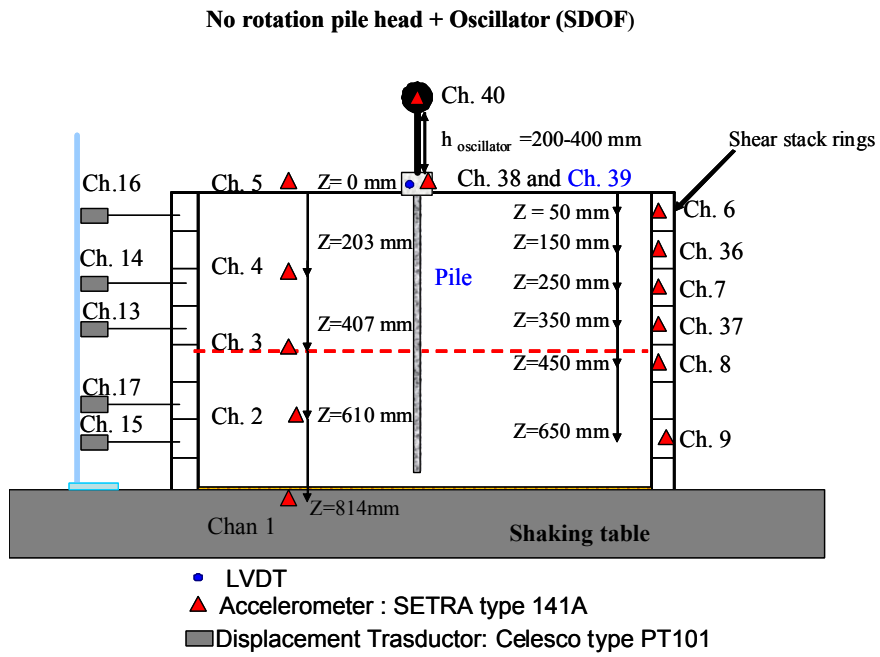


Figure 5.57a) Layout instrumentations no rotation head and oscillator (NRH+SDOF)

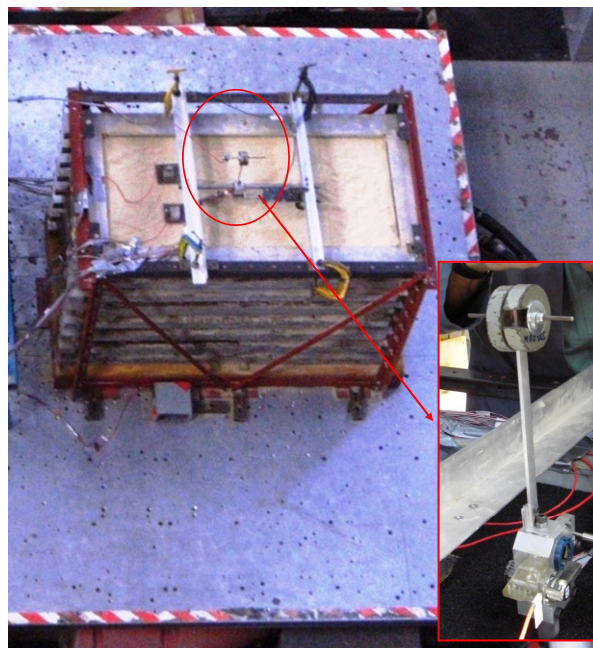


Figure 5.57 b) Set up shear stack for no rotation head and oscillator (NRH+SDOF)

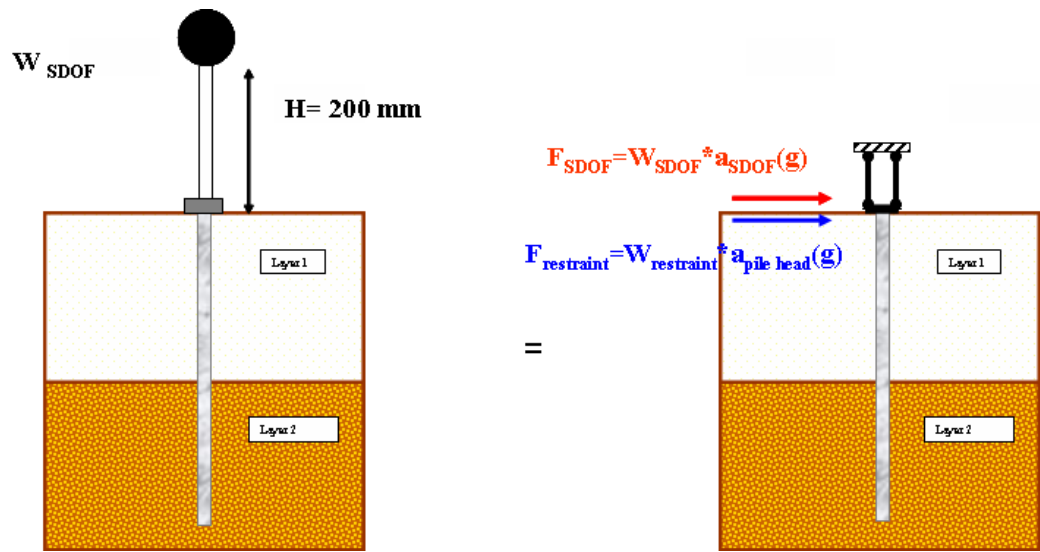


Figure 5.57c) structural check of no rotation head and oscillator (NRH+SDOF)

It has been noted that at the pile head location there are no strain gauges, so the experimental valuation of the moment cannot be made directly.

Considering the peculiarity of the restraint on the pile head, the presence of bar, avoid rotation on the pile head. The action of the oscillator on pile head is explain by a horizontal inertial force, F_{SDOF} , obtained by the weight of the oscillator multiplied by the acceleration on the top of the oscillator.

Inertial moment generated from this inertial force for the arm (distance from the base to the oscillator -h=200mm) is absorbed by the constraint on the pile head (bar connected to two aluminium frames fixed to the steel frame of shear stack, their motion is simultaneous with shear stack during the shaking). Therefore the value of the maximum inertial moment on the pile head could be obtained from a theoretical formulation of the moment, as following reported:

$$M_{Theoretical} = W_{SDOF} g a_{SDOF} d + W_{Restraint} g a_{Restraint} d \quad [5.3]$$

The second term of the sum can be neglected.

5.6.1 NRH+SDOF bending moment: layered configuration BE+E

In this section, the effects of superstructure on the layered sand configurations are investigated. In Table 5.1 the values of weight of SDOF are shown. The height of superstructure is 200 mm. In addition, the total weight on the pile head is specified. The presence of superstructure induces an additional weight on the pile head.

Table 5.1: Total weight on pile head: NRH +SDOF configuration

Soil Configuration BE+E					
LB fraction E + LB fraction BE					
Sturmo 000		SDOF (h=200 mm)	Accelerometer	Pile head support	Total weight on pile head
ω_p	ω_m/ω_p				
rad/sec		gr	gr	gr	gr
18.84	12	150	260	646	906
	5	400	510	646	1156
	2	1000	1110	646	1756
Tolmezzo 270		SDOF (h=200mm)	Accelerometer	Pile head support	Total weight on pile head
ω_p	ω_m/ω_p				
rad/sec		gr	gr	gr	gr
12.56	12	400	510	646	1156
	2	2200	2310	646	2956

The maximum bending moment along pile in presence of the oscillator are shown for BE+E soil configuration (figure 5.58). The horizontal blue line indicates the depth of the active length (171 mm).

As expected the effect of the single degree of freedom structure induce a large bending moments in the upper sections of pile. The second peak of moment is located at interface.

As observed before, the maximum bending moment along pile in general increase with the energy of input motion (means also with the weight of oscillator), for 12 times to 2 times input motion, the amplitude of moment increase.

As described for NRH pile configuration, just in case of STU5 (PGA=0.3 g and predominant frequency is around 11.7 Hz) the bending moment obtain is bigger that the bending moment obtained for STU 2 (PGA=0.3 g and predominant frequency is around 4.7 Hz). The relation between the natural frequency of soil (around 30 Hz) and the input motion frequency emphasizes the amplitude of bending moment.

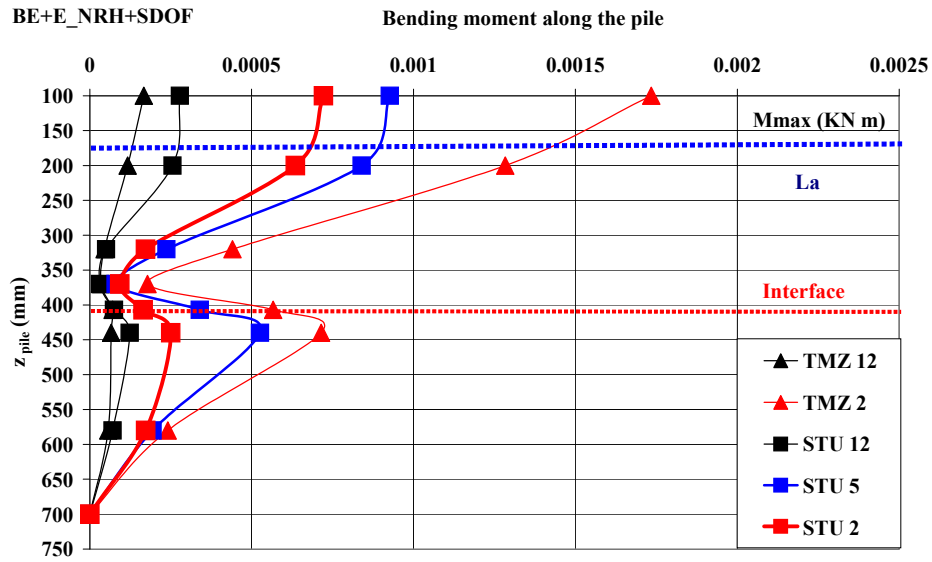
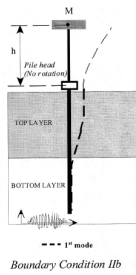


Figure 5.58 Envelop of maximum bending moment along the pile BE+E_NRH+SDOF

In figure 5.59 a comparison between NRH pile configuration and NRH +SDOF pile configuration for two different input motion is plotted in case of Tolmezzo and Sturno input motion 12 times scaled.

It is clear that the effects of oscillator are not so incisive: there are some differences on the pile head due to the additional mass on pile cap, but at interface location the bending moment are almost the same. The constraint effect influences the amplitude of bending moment until 200 mm from the top of the pile (“active length”).

The same comparison is shown for TMZ and STU 2 scale (figures 5.60 a-b).

A peculiar behaviour has been noted for STU2: the value of moment on the pile head for STU 2 NHR pile slightly higher than NRH+SDOF pile configuration. The maximum bending moment of the complete system (pile+soil+superstructure) is smaller than the maximum kinematic bending moment relative to the kinematic system.

The relative bending moments are comparable or smaller than one in absence of this added mass.

The percentage variation of bending moment is syntheses in the table 5.2.

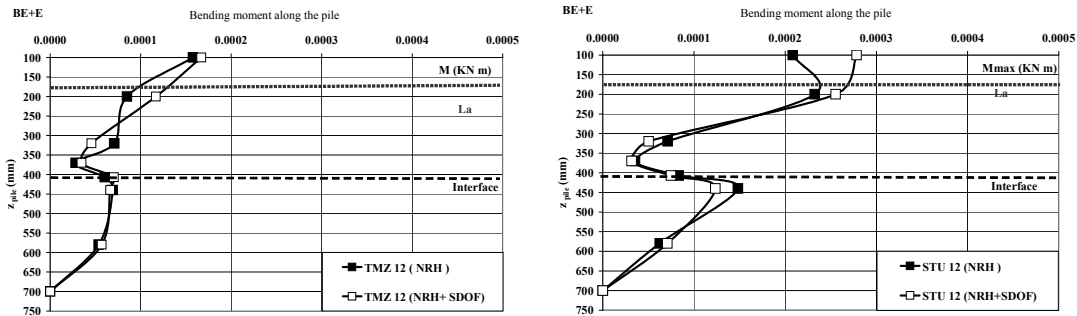


Figure 5.59 BE+E comparison between NRH and NRH + SDOF pile configuration a) TMZ 12- b) STU 12

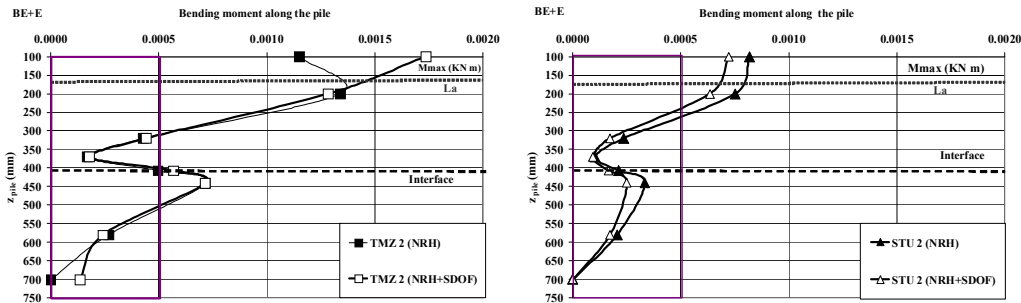


Figure 5.60 BE+E comparison between NRH and NRH + SDOF pile configuration: a) TMZ 2-b) STU 2

Table 5.2: Percentage variation of bending moment in absence of superstructure

BE+E	HEAD	INTERFACE
Input motion	NRH/SDOF	NRH/SDOF
STU12	-34%	10%
STU 5	5%	15%
STU2	26%	59%
TMZ 12	-6%	-17%
TMZ 2	-51%	-14%

Finally, figures 5.61 - 5.62 - 5.63 - 5.64 present a time histories acceleration and FFTs relative of different location: on the bottom of shear stack (input motion), on the surface, on the pile head for four different tests (BE+E_TMZ 2_NRH +SDOF, BE+E_STU 2_NRH+SDOF, BE+E_STU12_ NRH+SDOF, BE+E_TMZ 12_ NRH+SDOF).

Furthermore, in this case, the de-amplification of motion in foundation is very common, the PGA on the surface is 0.6 g and on the pile head is equal to 0.4 g (TMZ2). As known the high frequency of input motion are filtered from pile as explain in Mylonakis et al, 1997. This phenomena is more evident for input motion rich in high frequency (12 times scaled)

Comparing the input motion with the free field time histories acceleration the PGA amplification of signal is around of 70 % (PGA=0.5g). In figure 5.61 c) a comparison between the acceleration time histories on the pile head (black line) and oscillator time histories (green line) are reported. The value of the peak acceleration for the oscillator is equal to 1.4 g.

In figure 5.61 d) a comparison between the FFTs of the signal on the pile head, on the top of the oscillator is plotted.

Also the transfer function of this two signal is shown. The main frequency of the oscillator is 3 Hz, which corresponds to a mean period of 0.33 s. In Figure 5.61 e) the acceleration spectra response of the pile head are plotted for different values of damping.

Values of damping ξ_m for common materials of construction are outlined in Table 5.6 for the elastic range. These are expressed as ratios of the critical damping. It is observed that ξ_m increases with the amplitude of action or deformation. The values in Table 5.3 are, however, approximate estimates of damping for different construction materials.

Table 5.3. - Damping for different construction materials in the elastic range (after Bachmann et.al., 1995).

MATERIAL	DAMPING ξ_m (%)
Reinforced concrete	
Small amplitudes (un-cracked)	0.7 - 1.0
Medium amplitudes (fully cracked)	1.0 - 4.0
High amplitudes (fully cracked) but no yielding of reinforcement	5.0 - 8.0
Pre-stressed concrete (un-cracked)	0.4 - 0.7
Partially stressed concrete (slightly cracked)	0.8 - 1.2
Composite	0.2 - 0.3
Steel	0.1 - 0.2

Comparing the acceleration spectra responses with the experimental response of the oscillator (red point), the appropriate value of the damping is around 2%. This value is peculiar for an aluminium and steel structure as explained in table 5.3.

In figure 5.61 f) the pile head and surface spectra response are plotted for a damping values equal to 5%.

The damping values has been confirmed also for all the earthquakes (figure 5.62f, 5.63b).

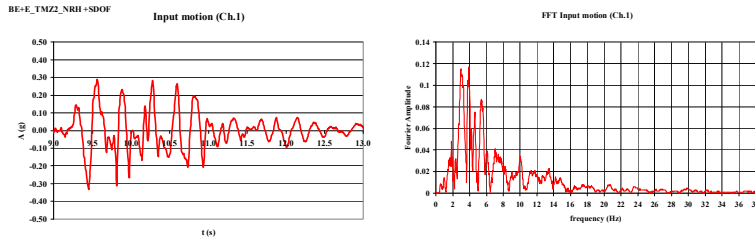


Figure 5.61 a) Input motion _acceleration and FFT _TMZ 2 scale (BE+E)_NRH+SDOF

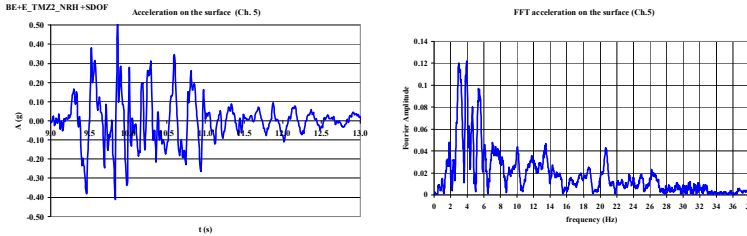


Figure 5.61 b) Surface _acceleration and FFT TMZ 2 scale (BE+E)_NRH+SDOF

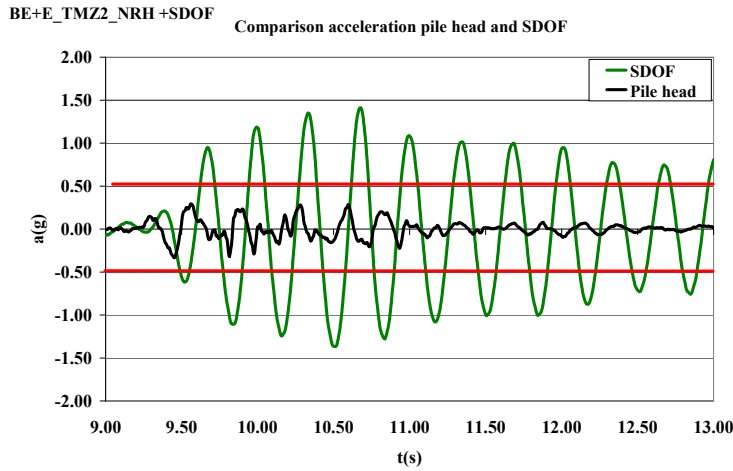


Figure 5.61 c) pile head and SDOF acceleration _TMZ 2scale (BE+E)_NRH+SDOF

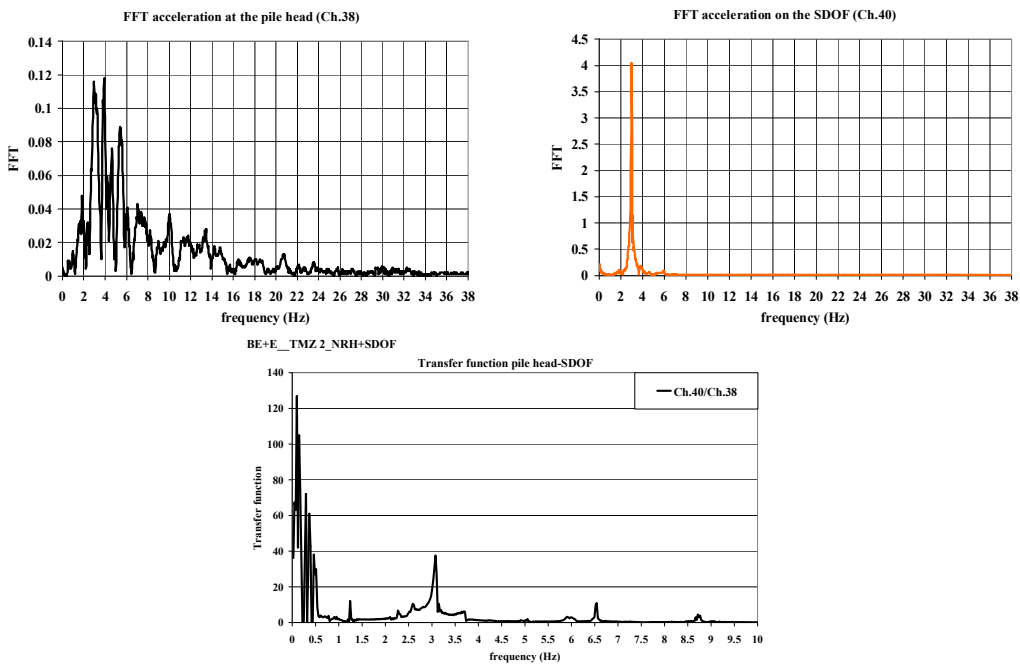


Figure 5.61 d) pile head and SDOF _TMZ 2scale (BE+E)_NRH+SDOF

BE+E_TMZ2_NRH+SDOF

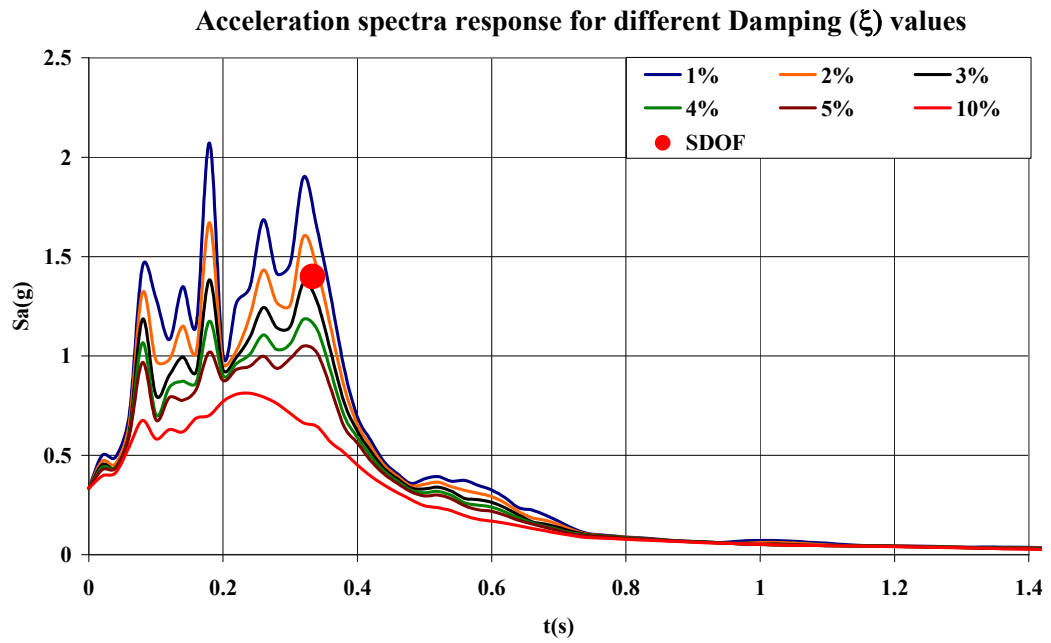


Figure 5.61 e) Pile head acceleration spectra response for different values of damping

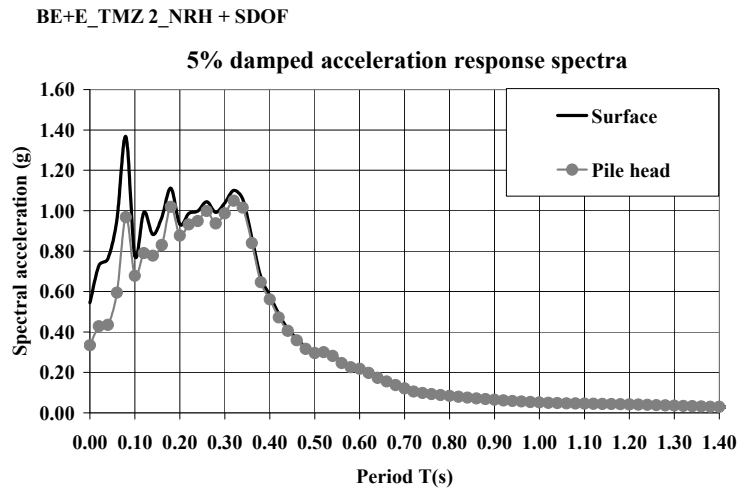


Figure 5.61 f) Pile head and surface acceleration spectra response for 5% damping value

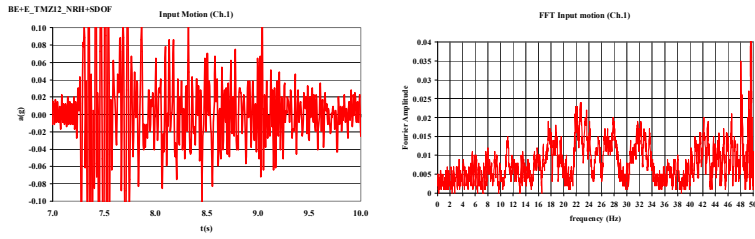


Figure 5.62 a) input motion and surface acceleration $_TMZ12scale (BE+E)_NRH+SDOF$

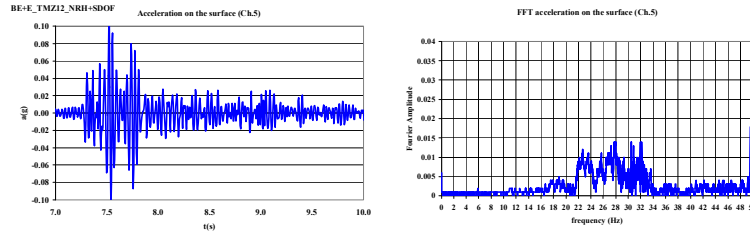


Figure 5.62 b) input motion and surface FFT $_TMZ12_ (BE+E)_NRH+SDOF$

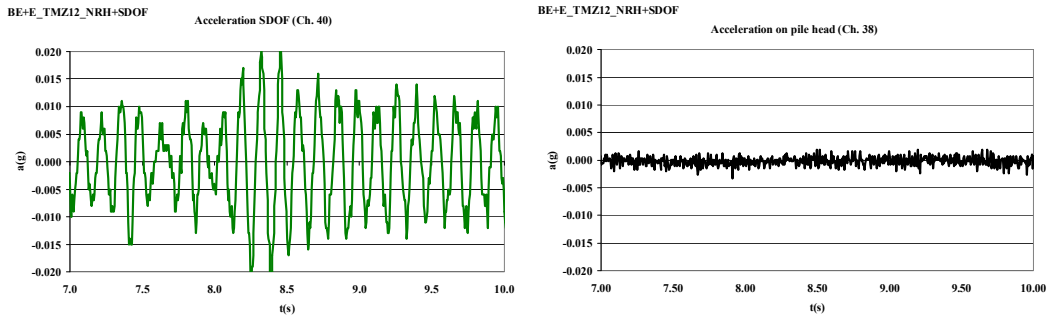


Figure 5.62 c) pile head and SDOF $_TMZ12scale (BE+E)_NRH+SDOF$

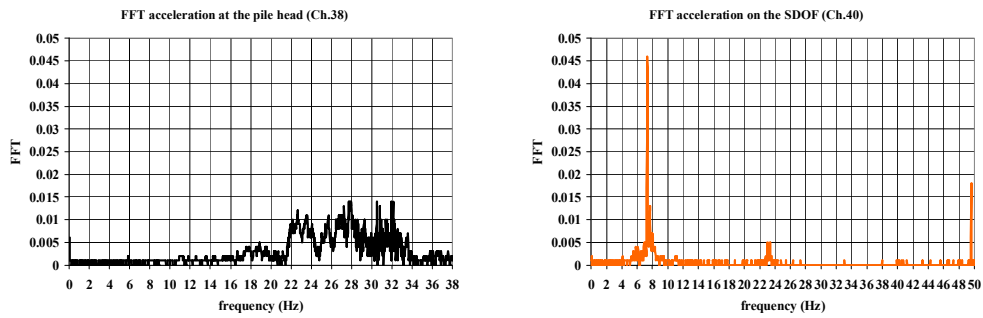


Figure 5.62 d) FFT pile head and SDOF $_TMZ12scale (BE+E)_NRH+SDOF$

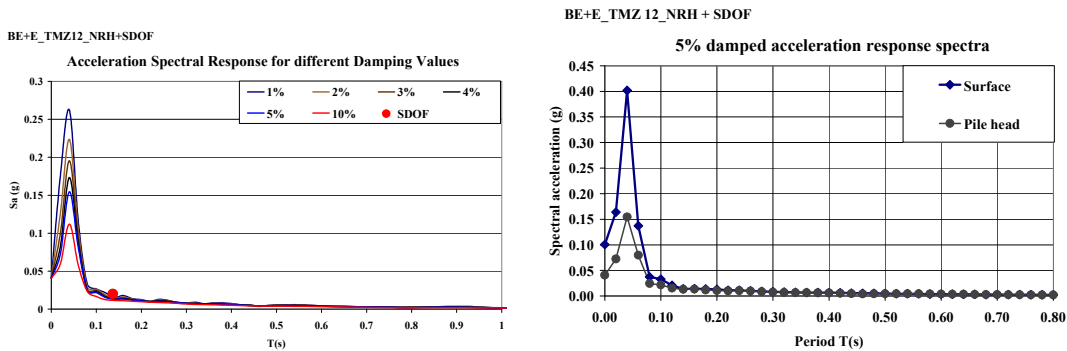


Figure 5.62 f) Spectra response $_TMZ12scale (BE+E)_NRH+SDOF$

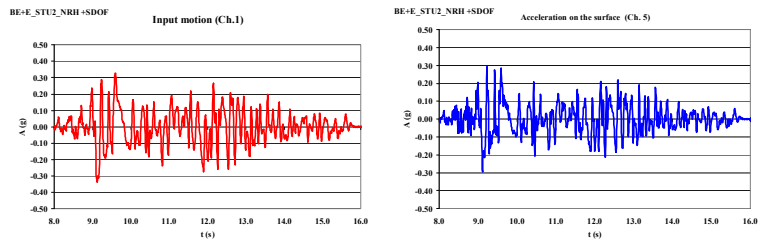


Figure 5.63a) Input motion-surface *_STU 2scale (BE+E)_NRH+SDOF*

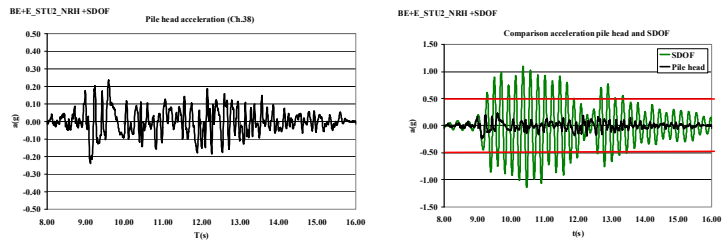


Figure 5.63b) Pile head-SDOF acceleration *_STU 2scale (BE+E)_NRH+SDOF*

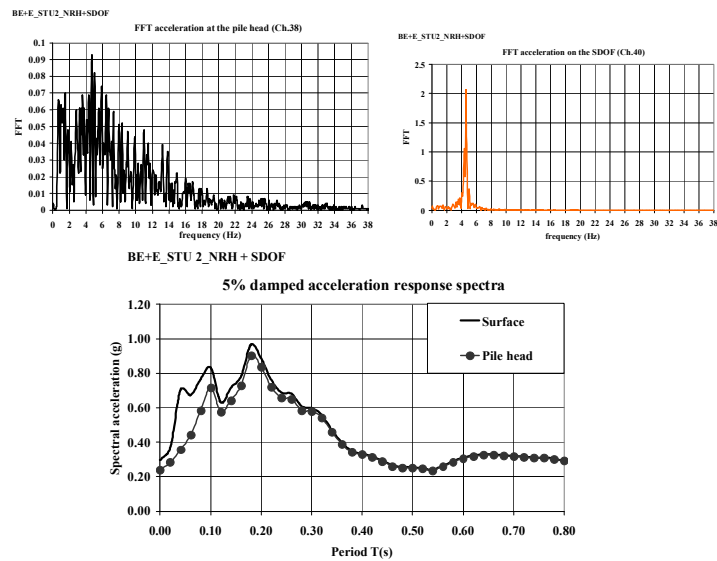


Figure 5.63 c) Surface-pile head-SDOF FFT *_STU 2scale (BE+E)_NRH+SDOF*

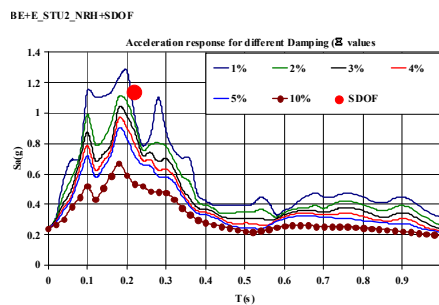


Figure 5.63 d) Pile head acceleration spectra response for different values of damping TMZ 12scale *(BE+E) NRH+SDOF*

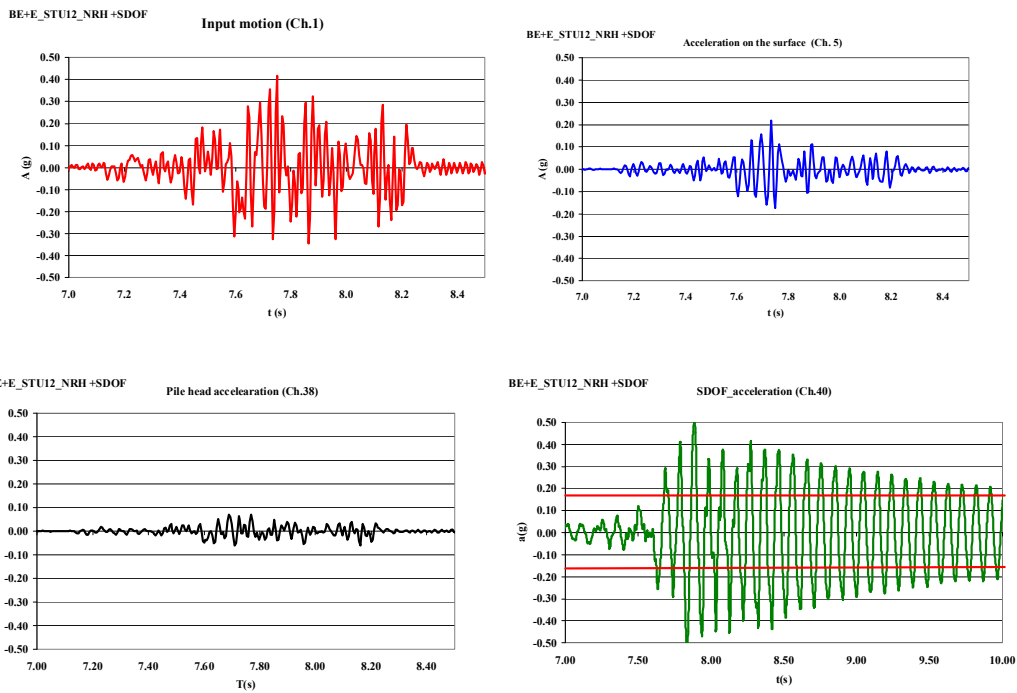


Figure 5.64 a) Input motion-surface-pile head-SDOF acceleration *STU 12scale (BE+E)_NRH+SDOF*

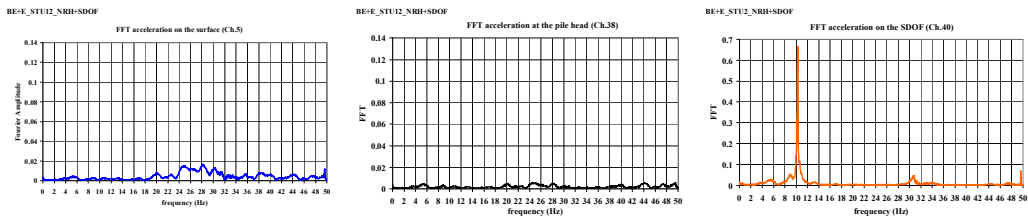


Figure 5.64) Surface-pile head-SDOF FFT *STU 12scale (BE+E)_NRH+SDOF*

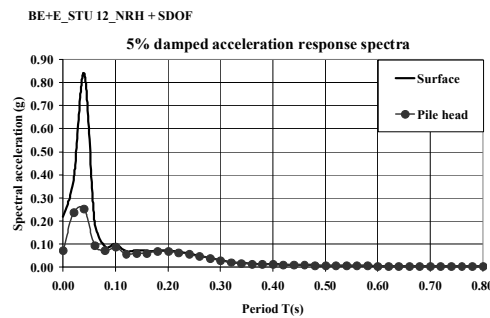


Figure 5.64) Surface-pile head-SDOF Spectral response *STU 12scale (BE+E)_NRH+SDOF*

5.6.1.1 *BE+E_TMZ 12 and 2 scale: simultaneous effects of inertial and kinematic interaction*

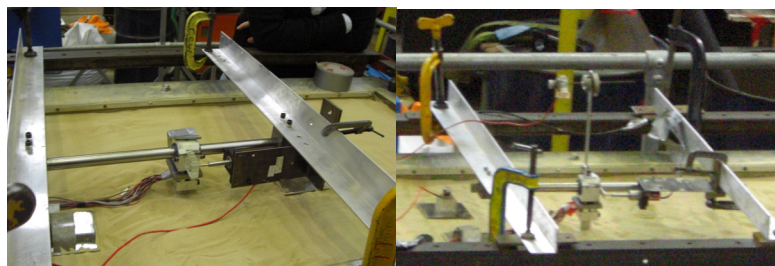
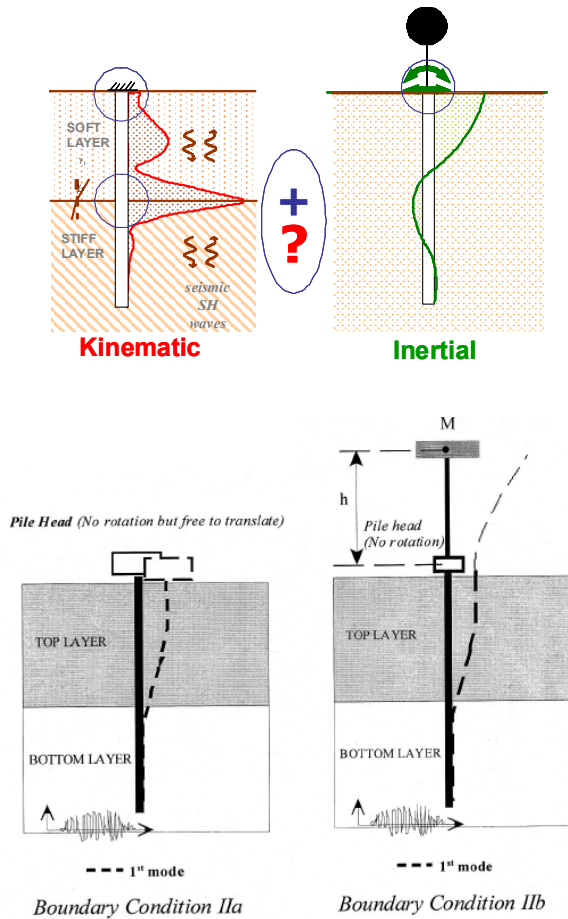


Figure 5.65) Surface-pile head-SDOF Spectral response _STU 12scale (BE+E)_NRH+SDOF

In order to investigate on the correlation between kinematic and inertial effects, the bending moment time histories at pile head, in the two no rotation configurations without the mass and in presence of the SDOF system have been compared.

In this section the chronological occur of inertial and kinematic moment is investigated. In the following figures the time histories of moment on pile head for NRH configuration (no rotation head) and NRH +SDOF pile configuration are compared. The NRH corresponds with

the kinematic situation, in absence of superstructure. The moments are computed at 100 mm elevation from the measurement of bending strain on pile.

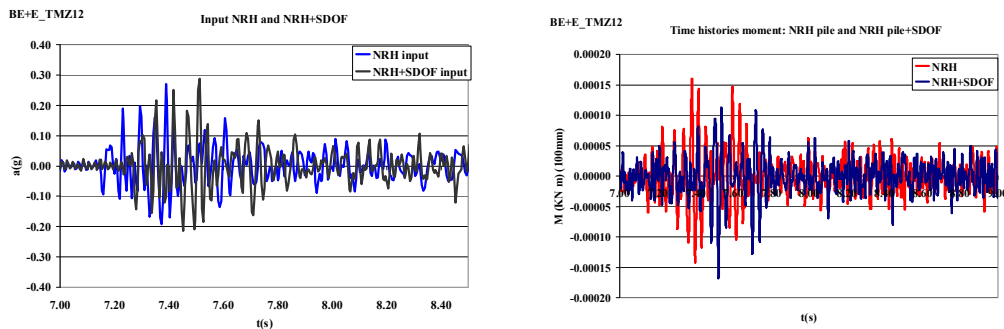


Figure 5.66 a) input motion for NRH-NRH+SDOF b) bending moment on the NRH-NRH+SDOF_TMZ 12scale

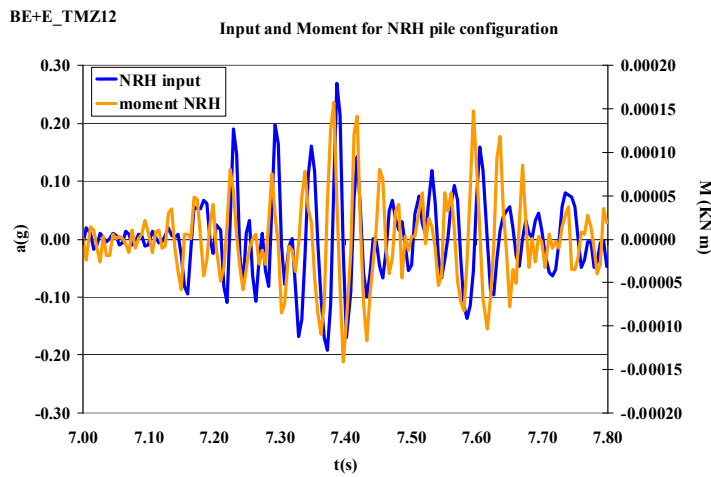


Figure 5.66 c) bending moment on the NRH compares with input motion NRH TMZ 12scale

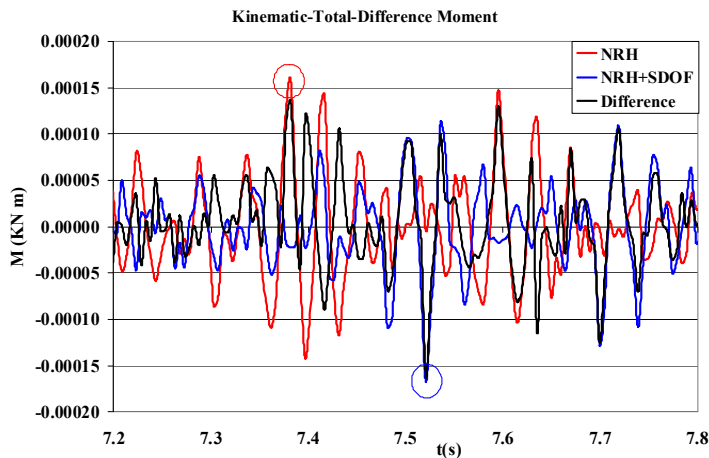


Figure 5.66 d) time history of kinematic, total and difference moment TMZ 12scale

First of all figure 5.66 a) shows the time histories of input motions for these two pile configuration for Tolmezzo 12 scale. As expected there are equal because we are considering the same input motion scaled 12 times. This plot is important to appreciate any anomalies.

In figure 5.66 b) a compare between the two different moment time histories at 100mm elevation from the top pile. They are very similar, they are in phase. There is a temporal delay between the two different bending moment time histories, but it is correlated with the time delay of input motion. To be sure about this, it is calculate in table 5.3, also in figure 5.66 c) it is shown a comparison between bending moment and input motion for NRH configuration.

The difference between the total bending moment and the kinematic one is very small in terms of amplitude. It has been noted that the peaks of the two bending moment do not occur in the same instant and they are not in phase. The kinematic bending arrives at 7.38 s, it is equal to $1.58 \cdot 10^{-4}$ KN m, instead the total bending moment arrives at 7.52 s, and the amplitude is $1.67 \cdot 10^{-4}$ KN m (Delay effective is 0,02 s). The difference in amplitude is around 6%, as explain in table 5.2.

Figure 5.67 a) shows the time histories of input motions for these two pile configuration for Tolmezzo 2 scale. The comparison between bending moment obtained from a no rotation pile head and a no rotation pile head with the oscillator are quite similar (Figure 5.67 b)). As in the previous case the temporal delay is duo to the input motion one. In particular, deleting this temporal delay from the moment time histories, it has been computed the real delay between the NRH moment and NRH+SDOF moment. As shown in figure 5.67 c) the peaks do not occur in the same instant. The kinematic bending arrives at 0.73 s, it is equal to $1.12 \cdot 10^{-3}$ KN m, instead the total bending moment arrives at 0.61 s, and the amplitude is $1.78 \cdot 10^{-3}$ KN m. The effective delay is 0.125 for the peaks. The difference in amplitude is around 51%, as explain in table 5.2. They are in phase.

The black line shown in figure 5.67 corresponds to absolute difference function between the kinematic and total moment, this function represents the effects of the oscillator on the bending moment in time.

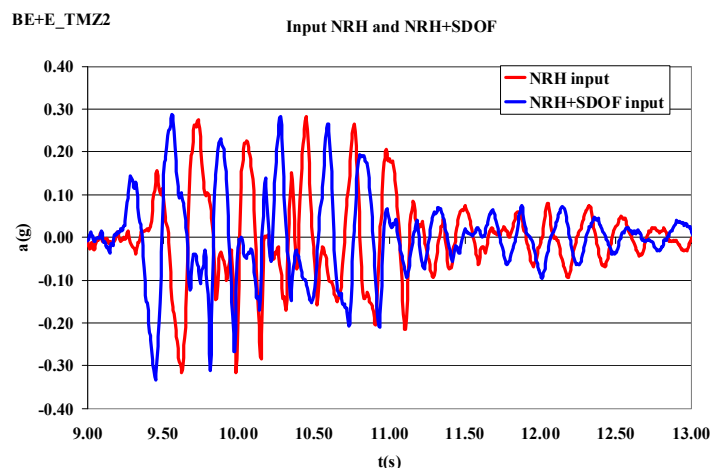


Figure 5.67 a) input motion on NRH-NRH+SDOF _TMZ2

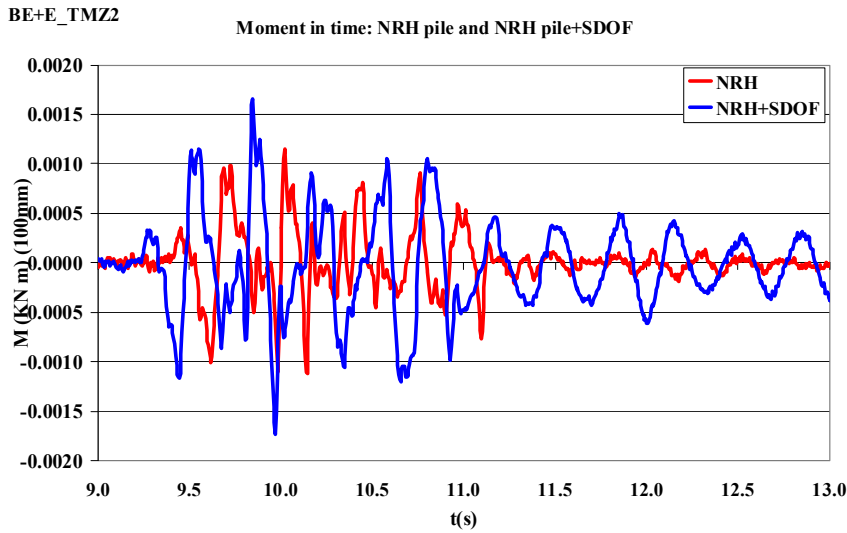


Figure 5.67 b) compared bending moment on the NRH- NRH+SDOF _TMZ 2scale

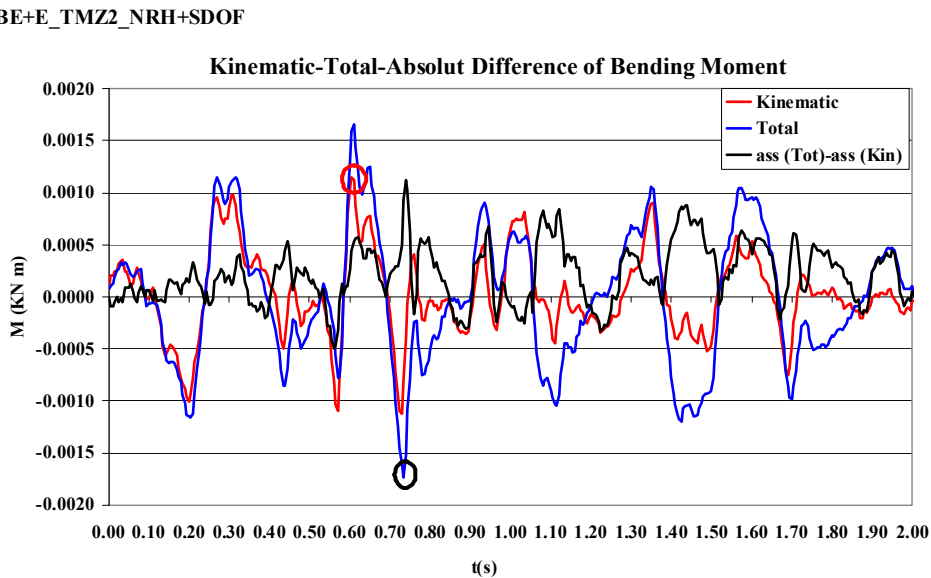


Figure 5.67 c) compared bending moment on the NRH- NRH+SD OF and absolute difference _TMZ 2scale

5.6.1.2 BE+E_STU 12 and 2 scale: simultaneous effects of inertial and kinematic interaction

As shown for Tolmezzo input motion also for Sturno input motion the comparison between bending moment obtained from a no rotation pile head and a no rotation pile head with the oscillator are quite similar. They are near strongly in phase. The time shift corresponds to the

time shift of each input motion. The present of oscillator increase the value of moment due to the increase of total weight on pile head.

Figure 5.68 a) shows the time histories of input motions for these two pile configuration for Sturno 12 scale. The comparison between bending moment obtained from a no rotation pile head and a no rotation pile head with the oscillator are quite similar (Figure 5.68 b)). As in the previous case the temporal delay is duo to the input motion one. In particular, deleting this temporal delay from the moment time histories, it has been computed the real delay between the NRH moment and NRH+SDOF moment. As shown in figure 5.68 c) the peaks do not occur in the same instant. The kinematic bending arrives at 1.45 s, it is equal to $2.08 \cdot 10^{-4}$ KN m, instead the total bending moment arrives at 1.20 s, and the amplitude is $2.78 \cdot 10^{-4}$ KN m. They are not in phase. The effective delay is 0.25 s for the peaks.

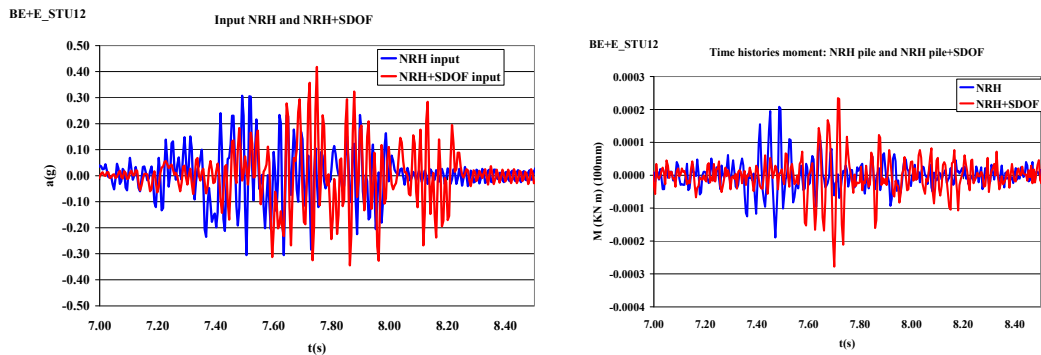


Figure 5.68 a) input motion on NRH-NRH+SDOF _STU 12 and b) bending moment on the NRH-NRH+SDOF _STU 12scale

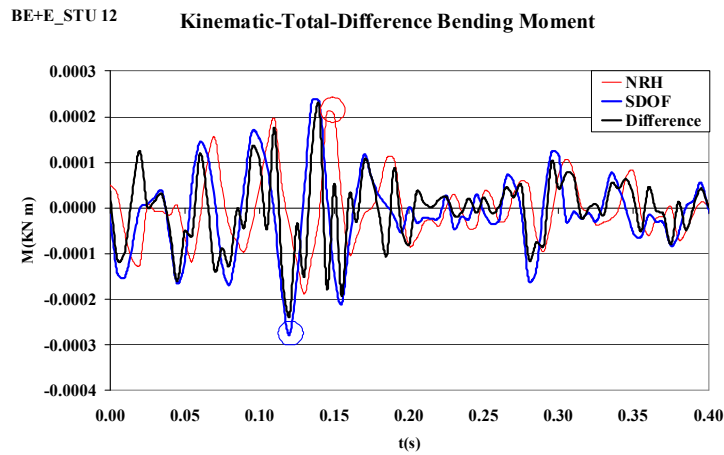


Figure 5.68 c) compared bending moment on the NRH-NRH+SDOF _STU 12scale

Figure 5.69 a) shows the time histories of input motions for the two pile configuration for Sturno 2 scale. Compared with the other cases they are practically the same.

In figure 5.69 b) a compare between the two different moment time histories at 100mm elevation from the top pile. They are very similar, they are in phase. In this case there temporal delay is small and negligible (0.02 s- table 5.3). To clarify Figure 5.66 c) shows a comparison between bending moment and input motion for NRH configuration, totally in agreement. The difference between the total bending moment and the kinematic one is very small in terms of amplitude. There is a temporal delay also in the peak values. It has been noted that the peaks of the two bending moment do not occur in the same instant and they are not in phase. The kinematic bending arrives at 9.08 s, it is equal to $8.17 \cdot 10^{-4}$ KN m, instead the total bending moment arrives at 9.57 s, and the amplitude is $7.22 \cdot 10^{-4}$ KN m (Delay effective is 0.49 s).

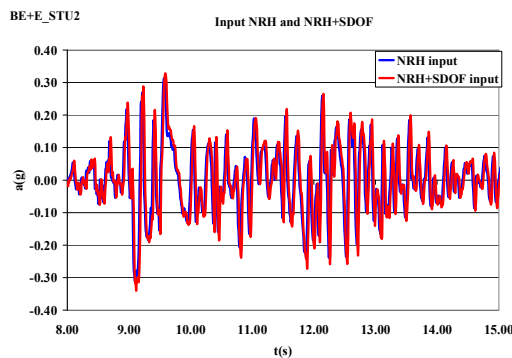


Figure 5.69 a) input motion on NRH-NRH+SDOF _STU 2

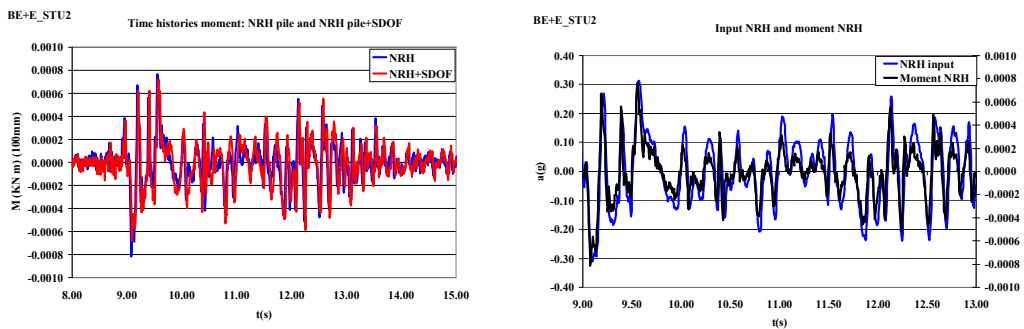


Figure 5.69 b) compared bending moment on the NRH-NRH+SDOF _STU 2scale and c) comparison with input motion NRH

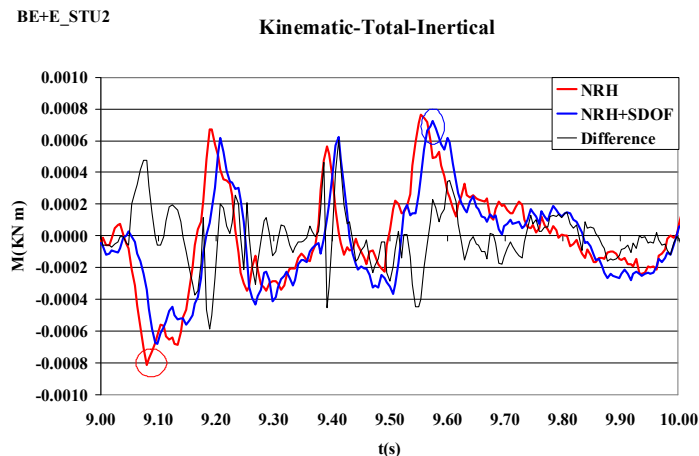


Figure 5.69 d) compared bending moment on the NRH-NRH+SDOF and difference _STU 2scale

5.6.1.3 Conclusion on simultaneous effects of inertial and kinematic interaction in layered soil BE+E

The crucial point is the time of occurrence of the peak of kinematic and total bending moments. In the different configurations the maximum bending moments do not happen in the same instant. In particular the moment time histories are not in phase and the delay between the peaks is quite random.

These evidences are consistent with the observation that the natural period of the tested SDOF systems is always different from that of the pile-ground system, which is always lower.

The experimental observations led to conclude that the maximum effects due to the single contributions of kinematic and inertial actions are not simultaneous, so that the total moment can not be simply determined as sum of the two maximum moments (computed, for example, by the *Substructuring* design approach).

Table 5.4: Time delay for NRH pile and NRH+SDOF pile: input motion and bending moment

BE+E					
Time delay					
TMZ 12 scale					
	Input	Input	Moment	Moment	Peak Moment
	s	s	s	s	
NRH	7.38	7.23	7.38	7.42	7.38
NRH+SDOF	7.52	7.35	7.52	7.54	7.52
Delay	0.14	0.12	0.14	0.12	0.14
TMZ 2 scale					
	Input	Input	Moment	Moment	Peak Moment
	s	s	s	s	s
NRH	9.89	9.74	9.69	9.73	0.735
NRH+SDOF	10.10	9.56	9.51	9.56	0.61
Delay	0.21	0.18	0.18	-0.17	0.125
STU 12 scale					
	Input	Input	Moment	Moment	Peak Moment
	s	s	s	s	s
NRH	7.52	7.49	7.52	7.49	1.45
NRH+SDOF	7.75	7.72	7.75	7.72	1.20
Delay	0.23	0.23	0.23	0.23	0.25
STU 2 scale					
	Input	Input	Moment	Moment	Peak Moment
	s	s	s	s	s
NRH	9.40	9.58	9.55	9.39	9.08
NRH+SDOF	9.42	9.60	9.57	9.41	9.57
Delay	0.02	0.02	0.02	0.02	0.49

Table 5.4 shows the peculiarity of the oscillator and of the soil deposit. Tokimatzu, 2009 puts in relation the natural period of the structure and soil deposit. He says that if the natural

period of the structure is greater than that of the ground, the kinematic and inertial forces tend to be out of phase, restraining the pile stress from increasing. In our test the total moment is always in phase with the kinematic one, the predominant period of the deposit (around 0.03 s) is always smaller than the oscillator period.

Table 5.4: Peculiarity of SDOFs

Input Motion	<i>SDOF</i>		
	Frequency	Period	Sa(g)
	Hz	s	g
STU 12	10.278	0.10	0.54
STU 5	7.15	0.14	0.645
STU 2	4.59	0.22	1.139
TMZ 12	7.32	0.14	0.02
TMZ 2	3	0.33	1.4

5.6.2 NRH+SDOF bending moment : layered soil E+R

To simulate the presence of the superstructure and investigate on the inertial effects an oscillator on the pile head is located. As explained in chapter 3, the weight of the oscillator has been chosen taking in account the frequency of input motion and the Young modulus of the first layer of the deposit.

As shown for BE+E soil configuration, it is used a no rotation pile head configuration on the top an oscillator. The values of weight of SDOF (height of superstructure e200 mm) are shown. In addition, the total weight on the pile head is specified (table 5.5)

The presence of superstructure induces an additional weight on the pile head. It should be noted that the values of weight is proportional to decrease of scaling factor.

Table 5.5: Total weight on pile head: NRH +SDOF configuration

Configuration E+R					
LB fraction E + Rubber					
Sturno 000		SDOF (h=200 mm)	Accelerometer	Pile head support	Total weight
ωp	$\omega m/\omega p$	Weight	Weight on pile		pile head
rad/sec		gr	gr	gr	gr
18.84	12	150	260	646	906
	5	400	510	646	1156
	2	800	910	646	1556
Tolmezzo 270		SDOF (h=200mm)	Accelerometer	Pile head support	Total weight
ωp	$\omega m/\omega p$	Weight	Weight on pile		pile head
rad/sec		gr	gr	gr	Gr
12.56	12	400	510	646	1156
Norcia 090		SDOF (h=200mm)	Accelerometer	Pile head support	Total weight
ωp	$\omega m/\omega p$	Weight	Weight on pile		pile head
rad/sec		gr	gr	gr	Gr
31.4	12	60	170	646	816
	5	150	260	646	906

In figure 5.78 the maximum bending moment along pile are shown for E+R soil configuration.

Also for soil configurations E+R, the magnitude of the top bending moment ($z = 0$ ordinate) increases when the superstructure is present. The maximum bending moment position migrates from the interface towards the top of the pile in FH conditions and reaches a maximum near at the top when the superstructure is present.

However, the bending moment diagrams found to display a similar pattern from NRH pile and NRH pile + SDOF, as shown in figures 5.71 a) and 5.71 b) for 2 scale factor, and 12 scale

factor. In this case the presence of superstructure is more incisive than the previous case. The particular soft stiffness of the first layer, reduce the restraint condition effects.

Only for Norcia 12 scale the NRH pile moment is bigger than NRH+SDOF pile configuration (figure 5.71c).

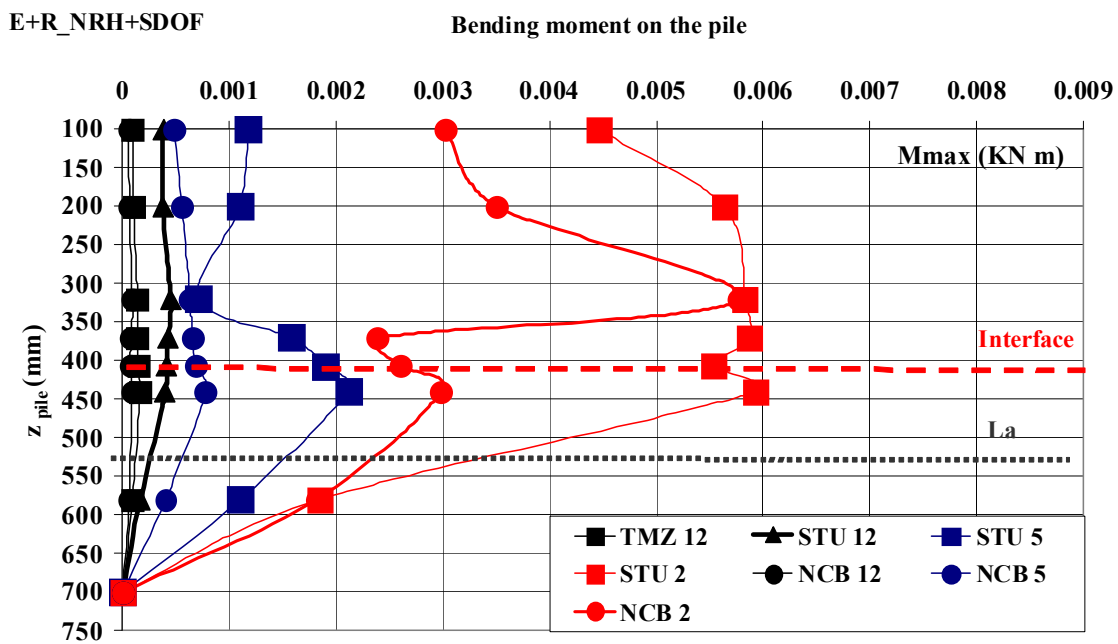
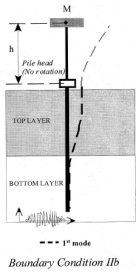


Figure 5.70: Envelop of maximum bending moment along the pile for all input motion (E+R_NRH+SDOF pile)

In table 5.6 the ratio between NRH and NRH +SDOF moment on the pile head and at interface.

Table 5.6: Percentual variation of moment between : NRH and NRH SDOF configuration

E+R	HEAD	INTERFACE
Input motion	SDOF/NRH	SDOF/NRH
STU12	55%	33%
STU 5	26%	96%
STU2	80%	33%
TMZ 12	17%	81%
NCB 12	-12%	67%
NCB 2	51%	67%

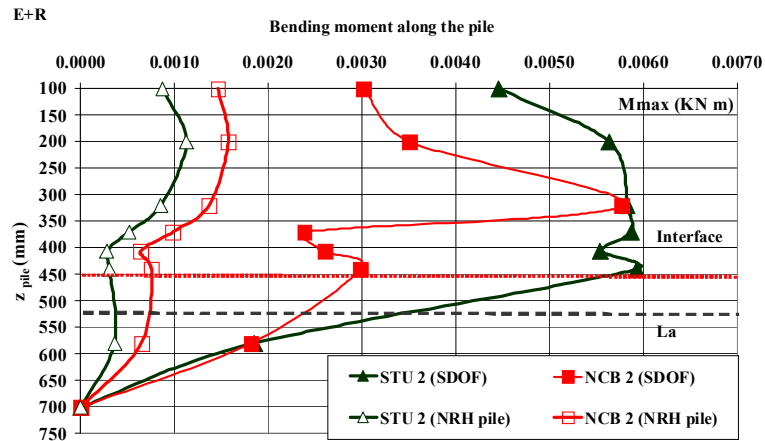


Figure 5.71a) E+R_ comparison between NRH and NRH +SDOF pile configuration 2 scale input motion

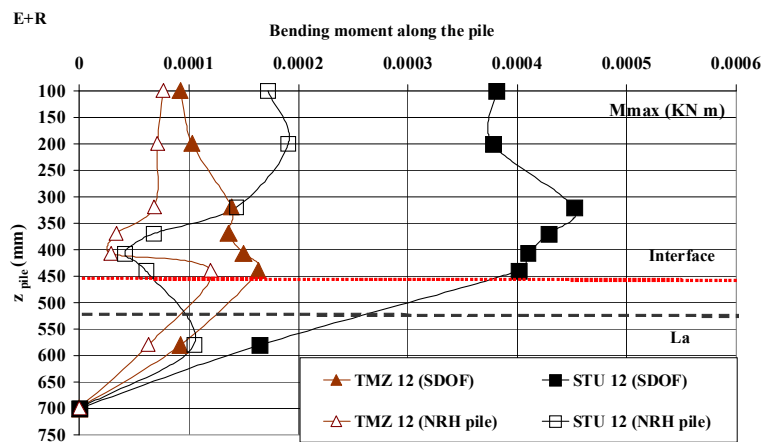


Figure 5.71 b) E+R_ comparison between NRH and NRH +SDOF pile configuration 12 scale TMZ and STU

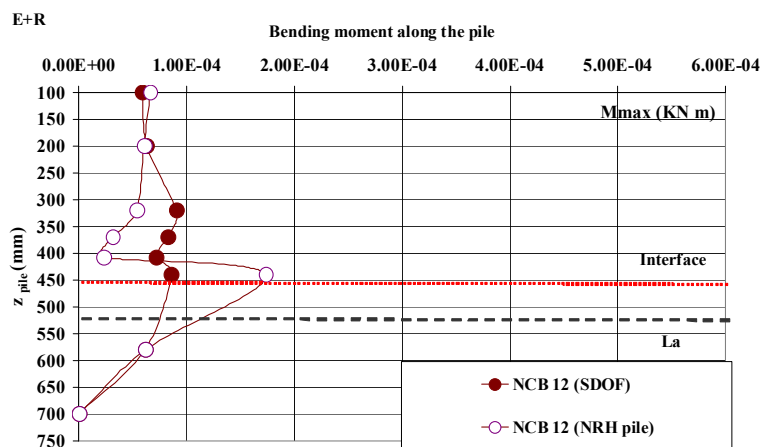


Figure 5.71 c) E+R_ comparison between NRH and NRH +SDOF pile configuration NCB 12

In figure 5.71 a) are shown the results for 2 scale input motion.

For case of STU2, figure 5.72 shows a compare between the time histories acceleration for four different point control: input motion, surface, pile head and SDOF position. The presence of oscillator, as an additional mass, produces an amplification of motion on the foundation level. From the input motion PGA (0.3g) to an increment of more than 50 % on the foundation (PGA=0.5 g).

In Figure5.73 the FFT of input motion, pile head and top of oscillator are shown.

For case of TMZ2, figure 5.75 shows a compare between the time histories acceleration for four different point control: input motion, surface, pile head and SDOF position.

The presence of oscillator, as an additional mass, produces an amplification of motion on the foundation level. From the input motion PGA (0.3g) to an increment of more than 30 % on the foundation (PGA=0.4 g).

In Figure5.76 the FFT of input motion, pile head and top of oscillator are shown.

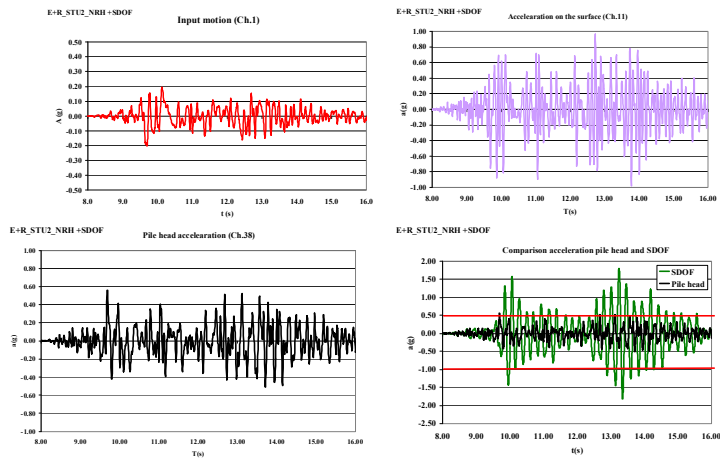


Figure 5.72) Input motion-surface-pile head-SDOF acceleration *_STU 2 scale (E+R)_NRH+SDOF*

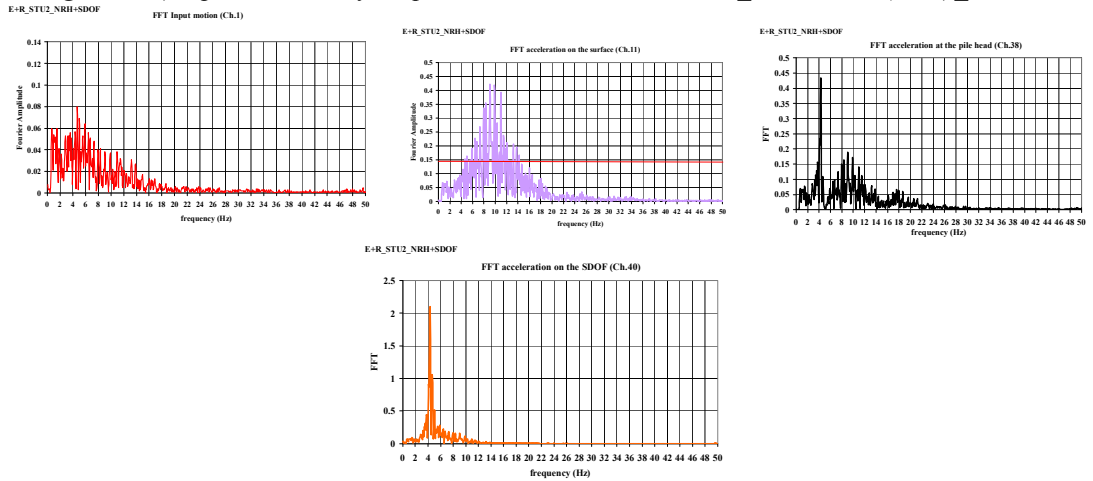


Figure 5.73) Input motion-surface-pile head-SDOF FFT *_STU 2 scale (E+R)_NRH+SDOF*

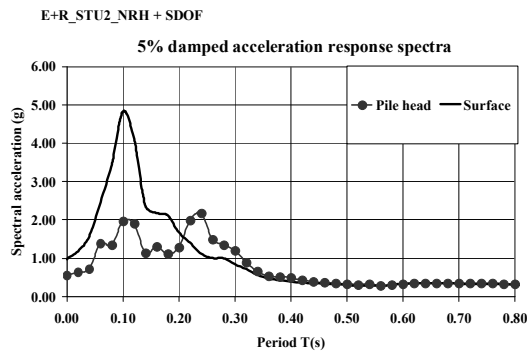


Figure 5.74) Input motion-surface-pile head-SDOF Response spectra *_STU 2 scale (E+R)_NRH+SDOF*

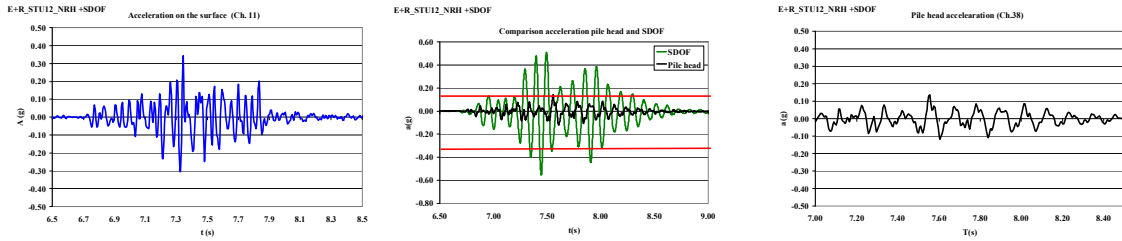


Figure 5.75) Input motion-pile head-on SDOF Acceleration_TMZ 2 scale (E+R)_NRH+SDOF

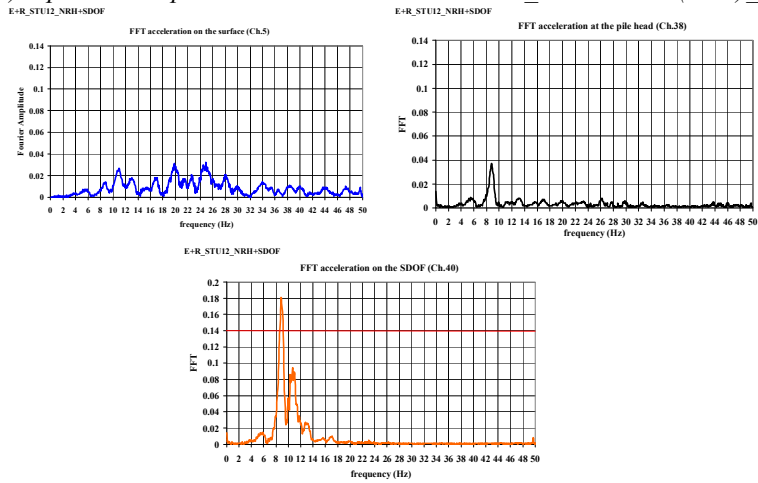


Figure 5.76) Input motion-pile head-on SDOF FFT_TMZ 2 scale (E+R)_NRH+SDOF

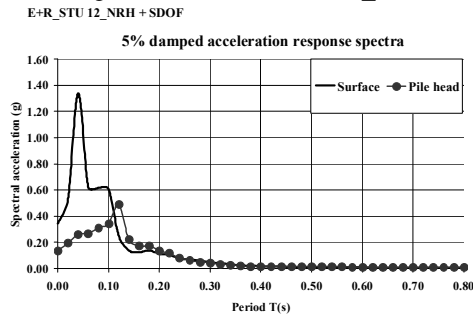


Figure 5.77) Input motion-pile head-on SDOF Spectral response_STU12 scale (E+R)_NRH+SDOF

5.6.2.1 E+R_STU 12 and 2 scale: simultaneous effects of inertial and kinematic interaction

In this section the chronological occur of inertial and kinematic moment is investigated. In the following figures the time histories of moment on pile head for NRH configuration (no rotation head) and NRH +SDOF pile configuration are compared. The NRH corresponds with the kinematic situation, in absence of superstructure.

The moments are computed at 100 mm elevation from the measurement of bending strain on pile.

Different from BE+E configuration, for E+R the presence of a very soft layer change the response in terms of bending moment. As shown for Tolmezzo input motion also for Sturno input motion the comparison between bending moment obtained from a no rotation pile head and a no rotation pile head with the oscillator are quite similar.

They are near strongly in phase. The time shift corresponds to the time shift of each input motion. The present of oscillator increase the value of moment due to the increase of total weight on pile head. The valuation of time delay is not easy to obtain.

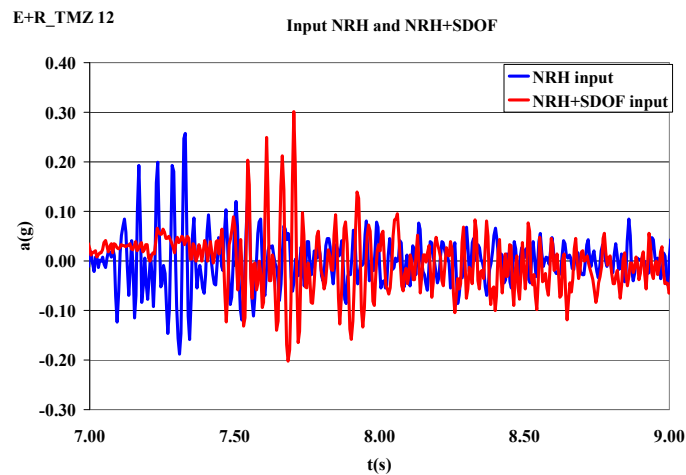


Figure 5.80(E+R)_NRH+SDOF

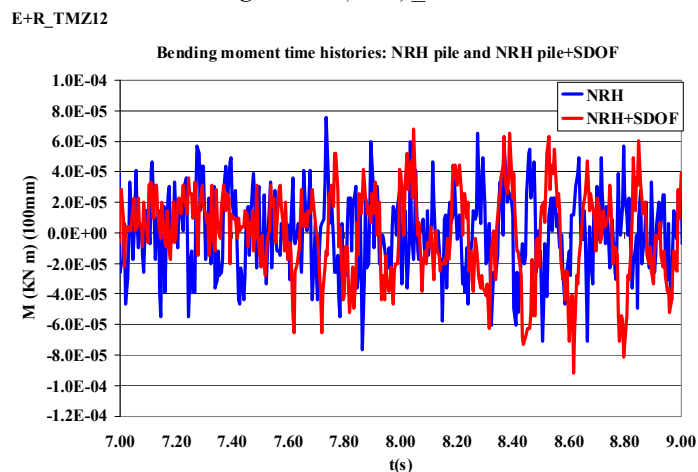


Figure 5.81(E+R)_NRH+SDOF

The time histories of bending moment near the pile head are shown, for STU2 (figure5.79). From the compare is evident that the value of mass affect the amplitude of moment. It should be noted that in the case of STU2 scale the time histories are practically equal.

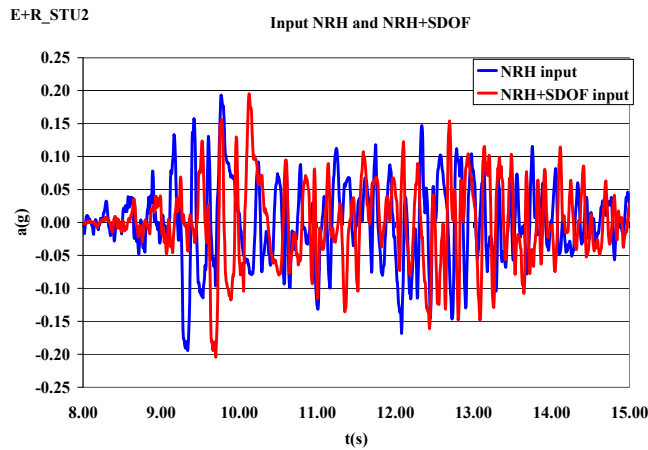


Figure 5.82) input motion (E+R)_NRH+SDOF

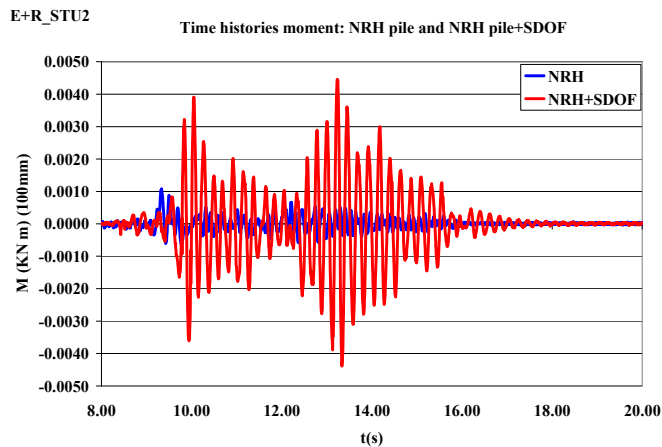


Figure 5.83) bending moment(E+R)_NRH+SDOF

5.7 Soil shear strain and bending strain on pile

From the original shear beam equation, shear stress τ at any depth z may be written as the integration of density ρ times acceleration u through higher levels.

$$\tau(z) = \int_0^z \rho a dz \quad [5.4]$$

The equation proposed by Zeghal and Elgamal (1994) for field measurements utilize acceleration measurement at the surface as they deal with site data.

If many accelerometers are present and significant amplification/attenuation is observed, a trapezoidal integration can be used to obtain shear stress.

Therefore shear stress is evaluated using Zeghal and Elgamal's expression with the interpolated surface acceleration obtained from trapezoidal integration, given surface acceleration and acceleration at depth d , first-order finite difference approximations for the shear stress τ'_{zy} and shear strain γ'_{zy} at time t are:

$$\tau'_{(d,t)} = \rho d \left(\frac{(a_d(t) + a_0(t))}{2} \right) \quad [5.5]$$

$$\gamma'_{(x,y)}(d,t) = \left(\frac{(u_d(t) - u_0(t))}{d} \right) \quad [5.6]$$

To evaluate the shear strain an idealized test soil response to base acceleration has been considered. Vertically propagating shear waves induce shear stresses within a test soil. Normal stresses are kept constant. Lateral deflection u of the soil column in the y -direction is caused by shear deformation. The shear stress at depth d is the product of the soil density ρ and the integral of lateral acceleration through the overlying soil (Brennan et al, 2005).

For these expressions to apply adjacent accelerometers must be within a half-wave length or “*spatial aliasing*” can occur. In all test the wave length of seismic signal (λ) is compared with the distance between the instrumentation positioned in the sand. The ratio between λ and d is always bigger than five, so that this procedure to calculate the signal gives a good approximation of the value of shear strain.

Hence to calculate shear strains, accelerations must be converted into displacements. Acceleration data are integrated with respect to time using the trapezoidal method to produce velocities. Integrated data are generally associated with a drift error. To compensate, the data are filtered using a high-pass Butterworth filter set at a suitably low value. 0.5 Hz is used. Phase distortion is negated by multiple application of the filter. After primary application, the filtered history is reversed in time and passed back through the filter. Subsequent reversal gives a filtered time history free from phase distortion. The MATLAB command *filt filt* is

used to eliminate phase distortion. Trapezoidal integration of the calculated velocities followed by forward reverse filter sequence is undertaken to produce displacements.

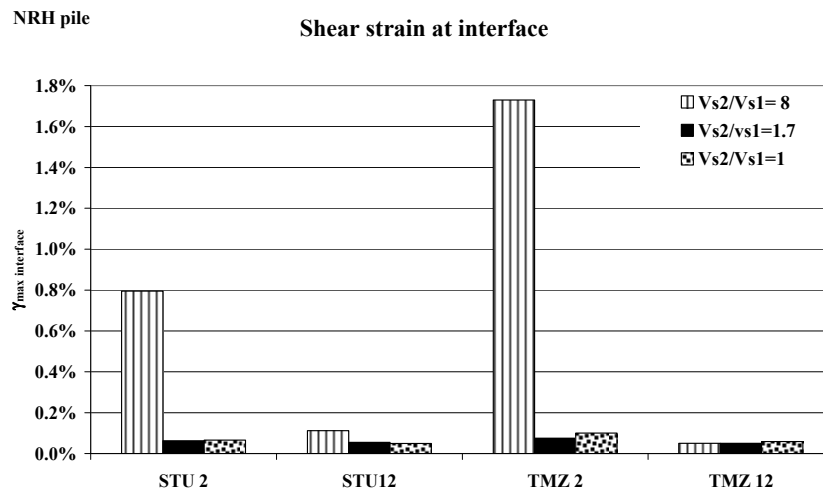


Figure 5.84: shear strain for all soil configurations

Relative displacement time histories are calculated by subtracting the table displacement history (derived from sensor a_0) from the time history in question. Equations 5.5 and 5.6 rely on the measurement of surface acceleration. In practice, this is difficult to achieve since an accelerometer needs to remain in good contact with the soil. Furthermore, reliable acceleration measurement within the shear stack sample's uppermost horizons is complicated by a large stiffness discontinuity between the lightly stressed sand and the embedded instrumentation. For these reasons, Brennan et al. (2005) linearly extrapolated the accelerations recorded deeper within a soil deposit to the surface.

In figures 5.76 the shear strain at interface for the three different soil configuration tested is reported, in case of no rotation pile head. The effects of very soft soil on the upper layer are evident. From the shear strain calculation, the dynamic tests induce a range of shear strain values from 10^{-2} to $10^{-1}\%$. The deposit is in non linear range. In figure 5.77 (red line, reported in figure 5.77). Experimental data are evaluated by comparison with two data sets. The first consists of the Seed & Idriss (1970) curves that chart the evolution of G/G_0 and D with strain level. These empirically derived curves for sands (solid lines) and their limits (dashed lines) are shown in Figure 6. The curves represent 'average' response since they are derived from a wide variety of test procedures and test soils. The second data set is taken from Cavallaro et al. (2001) who conducted a series of resonant column tests using LB 14- 25 as obtained from BLADE. Tests were conducted at stress levels spanning between 49kPa and 151kPa and between strains of 0.0002 and 0.055%, limits imposed by the test apparatus. The void ratio spanned between 0.563 and 0.660. Their data are summarized as dash-dot trend lines in Figure 5.57. The stiffness degradation recorded by Cavallaro et al. (2001) is akin to the Seed

& Idriss (1970) curve. In figure 5.85 the red lines are the experimental range of shear strain in the soil deposit.

In the following section are reported the time histories of shear strain and the bending strain at some instant coincident with the strong motion.

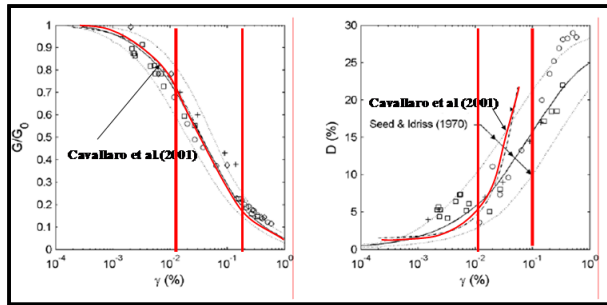


Figure 5.85: stiffness degradation recorded by Cavallaro et al. (2001) and Seed & Idriss (1970) curve

In the following section some examples of shear strain time histories; bending strain at particular instants are illustrated. Some examples are shown for Tolemezzo scaled 2 and 12 times for the two pile head configuration: no rotation head and no rotation head with oscillator.

5.7.1 TEST: BE+E_TMZ2_NRH

In figure 5.86 are plotted the free field acceleration in sand and outside and the input motion time histories.

In figure 5.87 a) the time histories of shear strain at three different elevations are plotted. In figure 5.79 b) the time histories of soil shear strain at interface for different instants with depths are shown.

In figure 5.88 a) the time histories of bending strain on pile for different instant with depth are shown. From the comparison between shear strain and bending strain on pile the two deformation are very different (figure 5.88 b), as following expressed by strain transmissibility.

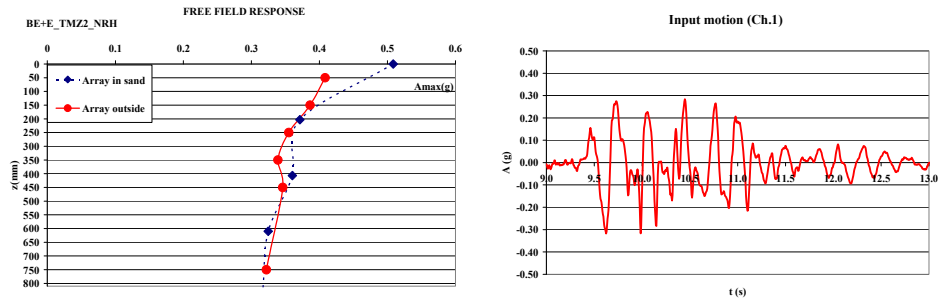


Figure 5.86 BE+E_TMZ2_NRH: a) free field and b) input motion

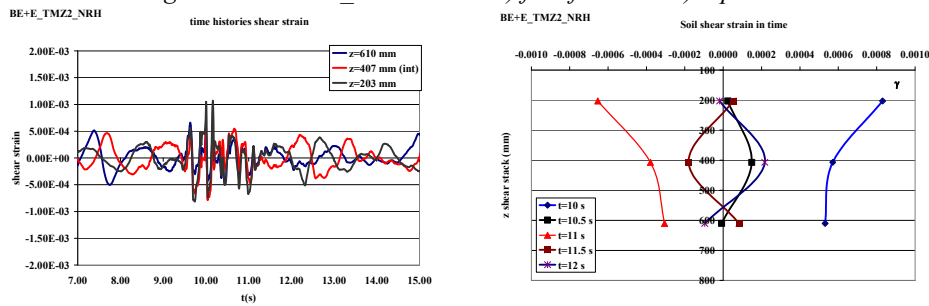


Figure 5.87 BE+E_TMZ2_NRH: a) shear strain time histories and b) shear strain with depth

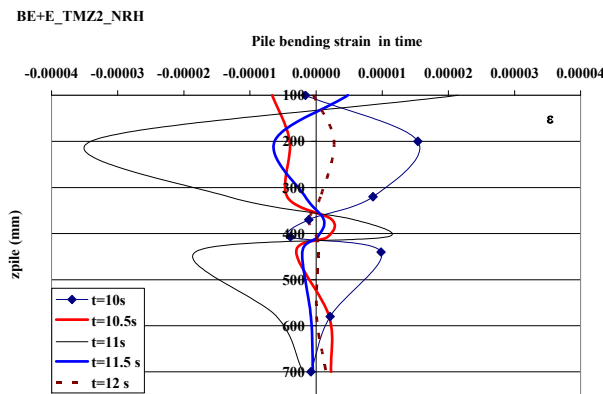
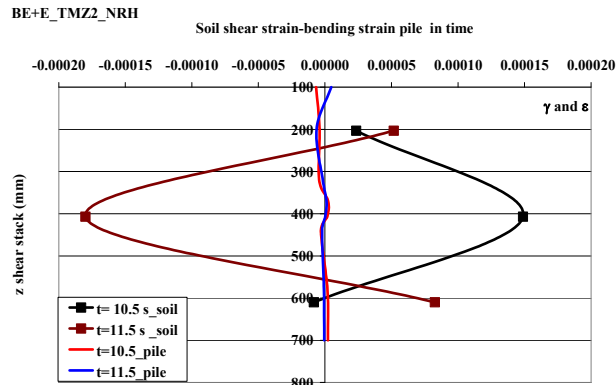


Figure 5.88 BE+E_TMZ2_NRH: a) bending strain along pile



and b) maximum shear strain with depth (strong motion analysis)

5.7.2 TEST: BE+E_TMZ2_NRH+SDOF

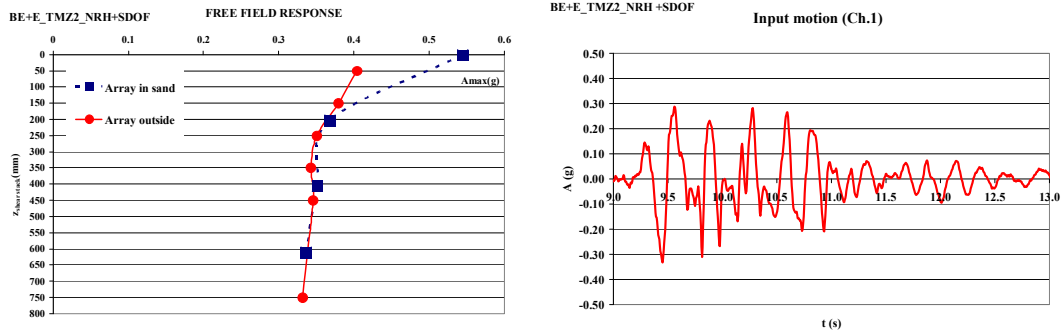


Figure 5.89 BE+E_TMZ2_NRH+SDOF: free field and input motion

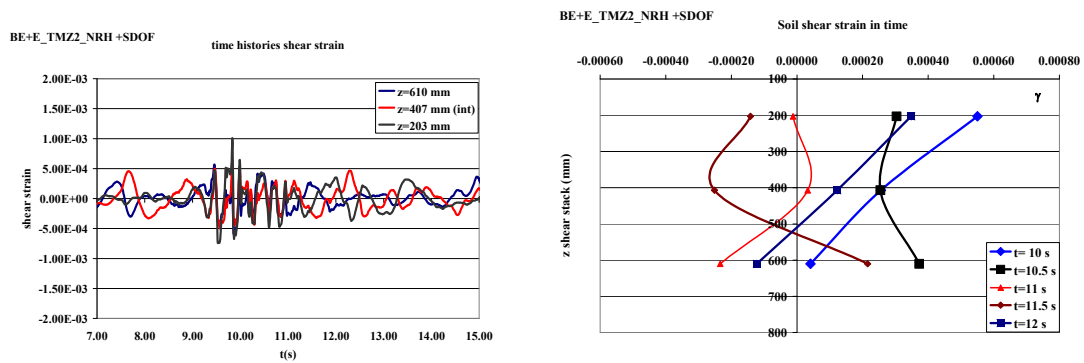


Figure 5.90 BE+E_TMZ2_NRH+SDOF: a) shear strain time histories and b) shear strain with depth

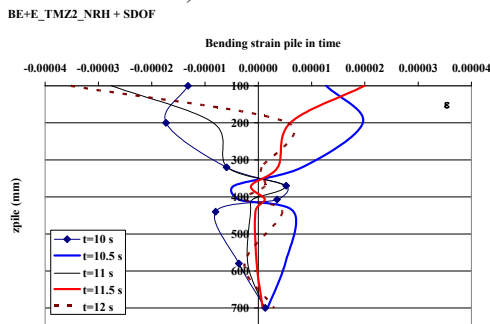
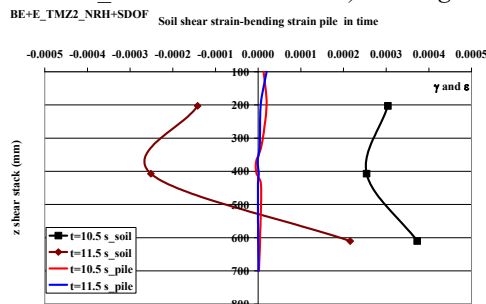


Figure 5.91a BE+E_TMZ2_NRH+SDOF: a) bending strain along pile



and b) maximum shear strain with depth (strong motion)

5.7.3 TEST: BE+E_TMZ12_NRH

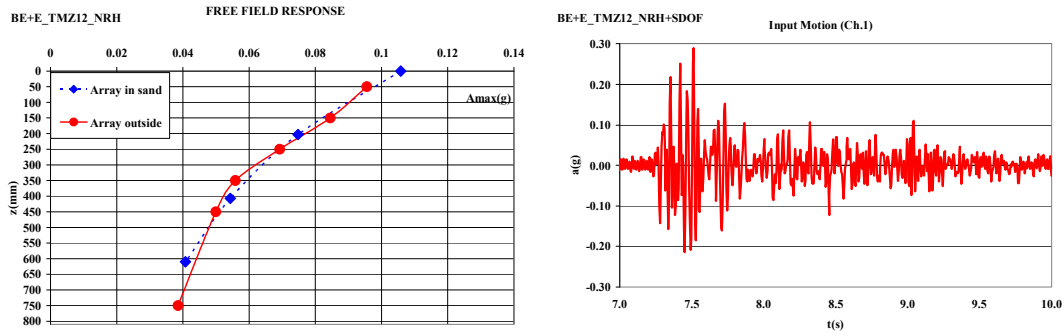


Figure 5.92 BE+E_TMZ 12NRH: free field and input motion

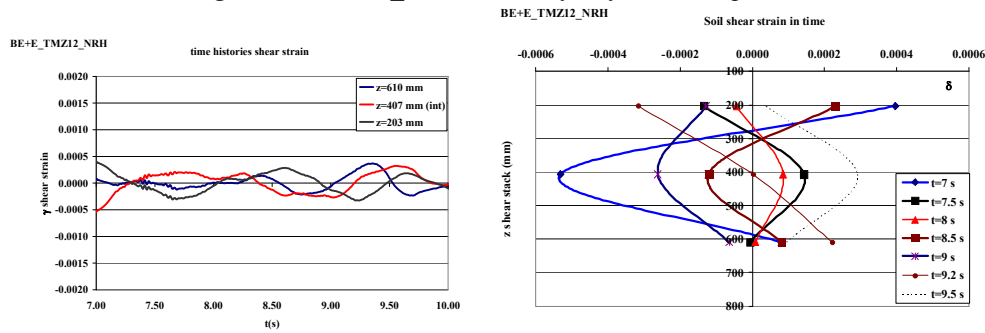


Figure 5.93 BE+E_TMZ 12NRH: a) shear strain time histories and b) shear strain with depth

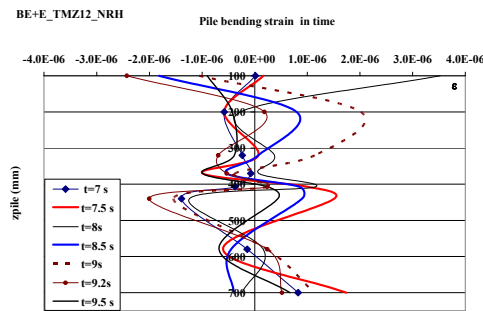
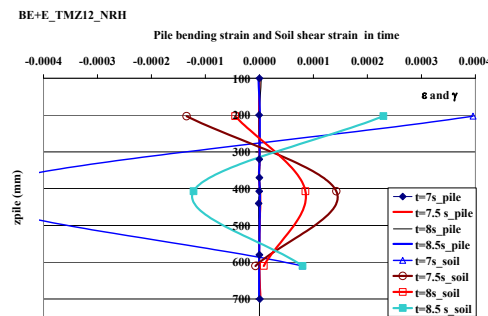


Figure 5.94a BE+E_TMZ 12NRH: a) bending strain along pile and



b) maximum shear strain with depth (strong motion)

5.7.4 TEST: BE+E_TMZ12_NRH and NRH+SDOF

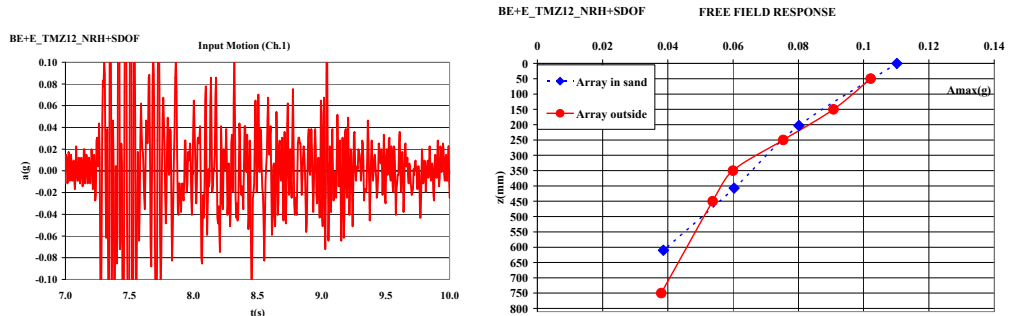


Figure 5.95 BE+E_TMZ12_NRH+SDOF: free field and input motion

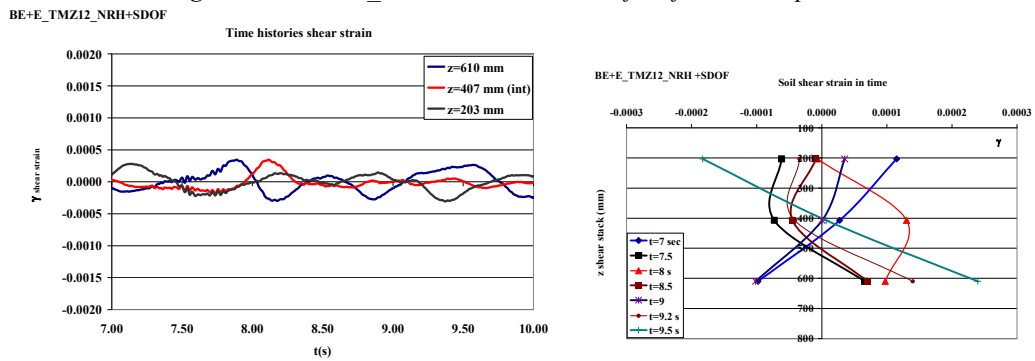


Figure 5.96 BE+E_TMZ12_NRH+SDOF: a) shear strain time histories and b) shear strain with depth

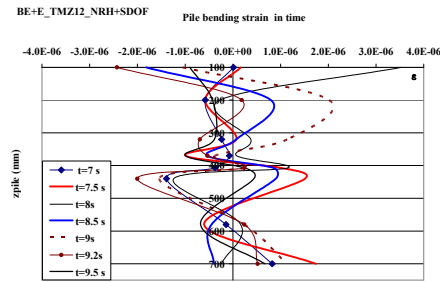
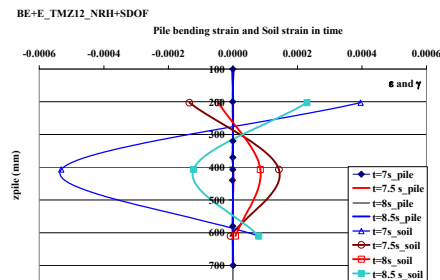


Figure 5.97 BE+E_TMZ12_NRH+SDOF: a) bending strain along pile



and b) maximum shear strain with depth (strong motion)

6. Analysis and discussion

6.1 Introduction

In the following chapter, the observed shaking table test results are compared with some performance predicted by numerical code and common analytical tools. First of all, the analyses are presented to examine free-field site response of the physical model. In order to prove the experimental results a comparison with analytical solution and numerical model (BDWF) has been presented. In accordance with the scale modelling guidelines introduced in Chapter 3, all analyses presented in this chapter have been performed at the model scale.

6.2 Free field analysis

Analytical reproduction of the observed site response serves to indicate that the model container is effective in minimizing boundary effects and that the potential soil column bending mode or motions are not distorting the site response.

Therefore an accurate free-field site response is a main component of the seismic soil pile interaction, it is a principal point to verify to reduce any mistake that could be transmitted in the numerical simulation analysis; this is true for all analysis techniques.

With the aim of reproducing the free-field site response analyses of model soil columns with pile in it, numerous simulation have been performed by using EERA code (Bardet, 2000).

The acceleration time histories and the spectra response of accelerometers located inside the shear stack (internal array) have been compared with the EERA values.

The EERA simulation have been carried out only for layered sand soil “BE+E” and for monolayer one “E”. Due to the high defromability of upper layer of layered soil configuration “E+R” (the rubber stiffness is around 0.1MPa), EERA code is unable to reproduce this stratigraphy.

The proprieties of the sub-layers of configuration BE+E have been shown in table 6.1. The total high of the deposit is 814 mm (total height of shear stack) and the interface between the

two different sands is located at 407 mm. The EERA code analysis are made in hypothesis of linear and linear equivalent behavior of soil. For the linear analysis the value of initial stiffness consider (G_0) for each material has been obtained from the modal test, done before the dynamic test (Chapter 4), the values of damping is hypothesized equal to 3%.

The wave propagation is “inside”, infinite rigid bedrock has been considered at bottom of the layered soil.

Table 6.1: Properties of soil configuration in (EERA code) for BE+E configuration

	Layer Number	Soil Material Type	Thickness of layer (m)	Maximum shear modulus G_{max} (MPa)	Initial critical damping ratio (%)	Total unit weight (kN/m^3)	Shear wave velocity (m/sec)
Surface	1	1	0.05	9	3	13.08	83
	2	1	0.05	9	3	13.08	83
	3	1	0.05	9	3	13.08	83
	4	1	0.05	9	3	13.08	83
	5	1	0.05	9	3	13.08	83
	6	1	0.05	9	3	13.08	83
	7	1	0.05	9	3	13.08	83
	8	1	0.03	9	3	13.08	83
	9	1	0.03	9	3	13.08	83
	10	1	0.02	37	3	18.86	137
	11	1	0.03	37	3	18.86	137
	12	1	0.05	37	3	18.86	137
	13	1	0.05	37	3	18.86	137
	14	1	0.05	37	3	18.86	137
	15	1	0.05	37	3	18.86	137
	16	1	0.10	37	3	18.86	137
	17	1	0.05	37	3	18.86	137
	18	1	0.01	37	3	18.86	139
bedrock	19.00	0.00	1.00	7266	0.00	22.00	1800

For the linear equivalent analysis, the degradation curve, $G(\gamma)$ and $D(\gamma)$ are used. The relevant Seed & Idriss (1970) $G-D-\gamma$ curves and Cavallaro et al.’s (2001) LB 14-25 resonant column test data are used to take in account the different value of stiffness with the soil degradation. In figure 6.0 Seed & Idriss (1970) $G-D-\gamma$ curves and Cavallaro et al.’s (2001) data are shown.

As mentioned in Chapter 5, (section 5.2) from the exhaustive analysis of experimental data, a discrepancy from the input motion on shaking table (Ch. 1) and the acceleration recorder in sand at 203 mm from the bottom of the shear stack (Ch.2) has been discovered. This divergence consists in a de-amplification of motion from the bottom of shear stack up to

203 mm from the bottom. This phenomena is most relevant for the input motion rich in high frequency (12 time scaled), as explained in Chapter 5.

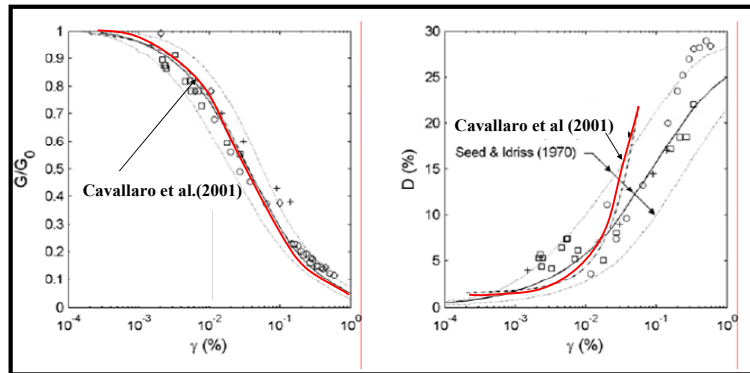


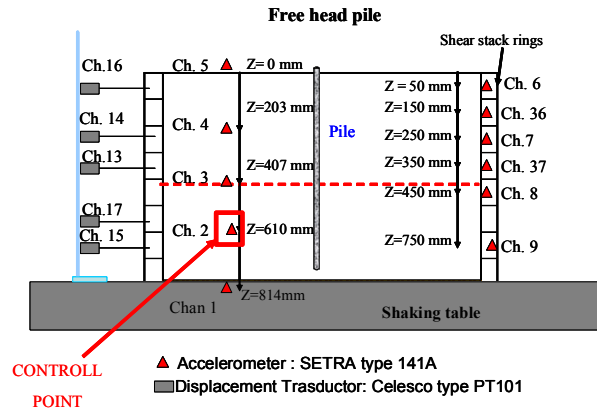
Figure 6.0: Seed & Idriss (1970) G-D- γ curves and Cavallaro et al.'s (2001) LB 14-25 resonant column test data

Preliminary analyses have been carried out to define the most appropriate input motion for EERA simulation. Therefore different analyses have been done considering: the acceleration recorded on shaking table (Ch. 1) and the acceleration recorded inside the shear stack (Ch. 2), at 203 mm from the bottom.

Figure 6.01 shows three different time histories acceleration at specifically elevation in sand, 610 mm (check point). In that figure the blue line is the experimental acceleration time history; the red line and the black line respectively refer to EERA acceleration time history using Ch. 1 and Ch.2 as input motion. As shown the EERA simulation obtained by Ch. 1 input motion is inappropriate to represent the experimental results.

With the intention to reproduce in EERA the real experimental soil column response in the shear stack, Channel 2 has been used in all analysis.

The simulations of the model free-field response with EERA code were fairly accurate, and the model soil-container system can be judged to have adequately reproduced free-field site response. The following paragraph will summarize the principal finding of these studies, for bilayer configuration BE+E.



Comparison different acceleration time histories : $z = 610$ mm

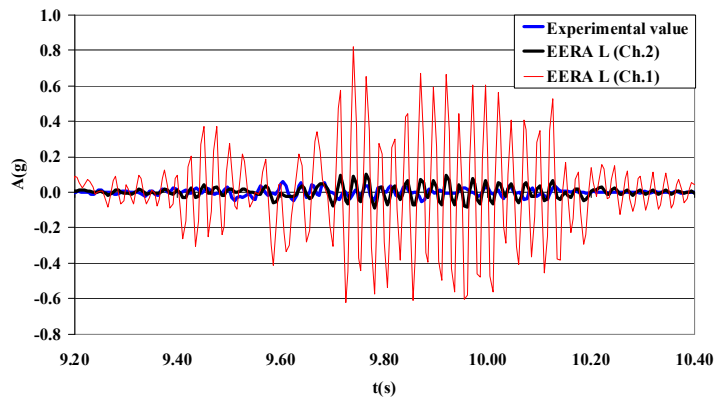


Figure 6.01: Acceleration time histories comparison between experimental-EERA L (Ch.1) and EERA L (Ch.2) at elevation $z=610$ mm in sand

6.2.1 EERA code analyses: earthquakes scaled 2 times

In figure 6.1 the surface acceleration time histories are shown for earthquake, Sturmo, 2 times scaled. The blue line represents the experimental time history on the surface (Ch.5), the black line and the red line represents respectively the acceleration time histories by EERA linear equivalent (LE) and linear (L)

In figure 6.2 the three spectra responses have been compared, and in figure 6.3 the three Fourier transform are shown.

In figure 6.4 the three free field responses have been compared, the peak acceleration is plotted with the depth.

The EERA linear simulation tends to overestimate the peak of the acceleration (0.36 g) compared with experimental values (0.31 g). It should be noted that in terms of elastic spectra response the simulation and the experimental value are quite similar. The high frequency

doesn't affect the spectra response. In case of EERA linear equivalent simulation, the peak acceleration on the surface is very close (0.30 g) to the experimental one (0.31 g). In this case the acceleration time histories are in agreement. Just a time delay has been noted. In the frequency domain the comparison is satisfactory.

In figure 6.5, 6.6, 6.7, 6.8 the same plots have been shown for Tolmezzo earthquake, 2 times scaled. The free field response between simulation and experimental values are quite close, there is a time delay. EERA linear produces an incremental value of PGA around of 7% (0.47 g) compared with experimental values (0.44 g). In this case the linear and the linear equivalent simulation the free field response is not so different from the experimental value, as shown in figure 6.8. It should be noted that the simulation and the experimental spectra response are very similar. From the Fourier transform comparison, an additional frequency compare for EERA simulation, as well known, the linear analysis usually amplify the high frequency content of the signal.

6.2.2 EERA code analyses: earthquakes scaled 12 times

In this section the EERA simulation have been carried out for the input motion scaled 12 times.

In figure 6.10 the acceleration time histories for Sturmo earthquake, 12 times scaled, are shown. The free field response between EERA linear simulation and experimental values is very dissimilar. The EERA linear analysis is unable to reproduce the real acceleration trend. The PGA on the surface obtained by EERA (0.40 g) is not comparable with experimental one (0.22 g). It is confirmed by the free field response shown in figure 6.13.

With respect to the linear equivalent EERA analysis, the values of acceleration are more close to the experimental one, but the trend of peak ground acceleration does not be satisfactory. In figure 6.11 and 6.12 the spectra response and the FFTs transforms are plotted.

In figure 6.13 the acceleration time histories for Tolmezzo earthquake, 12 times scale, are shown. The free field response obtained from numerical and experimental works are in good agreement. EERA linear and linear equivalent simulations make a value of PGA very close with experimental one (0.15 g). Also the trend of peak acceleration with depth, are very close to the experimental one, as shown in figure 6.16. In this case the linear and linear equivalent analyses are analogous.

In figure 6.14 and 6.15 the comparison has been done in the frequency domain. It has been noted that EERA simulation produces an additional high frequency content, as usually happens for linear analyses.

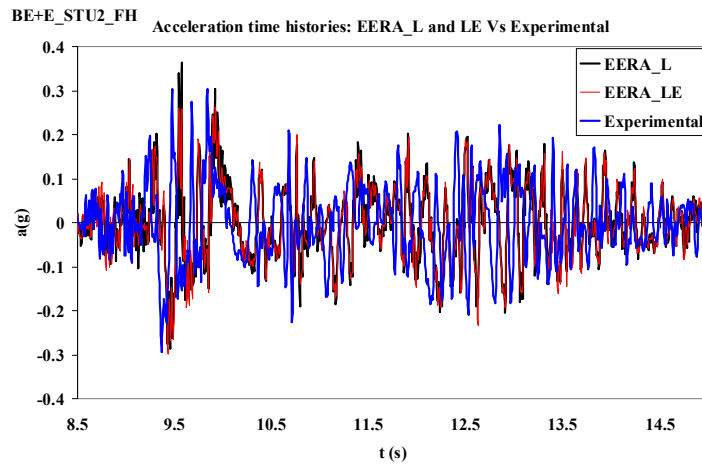
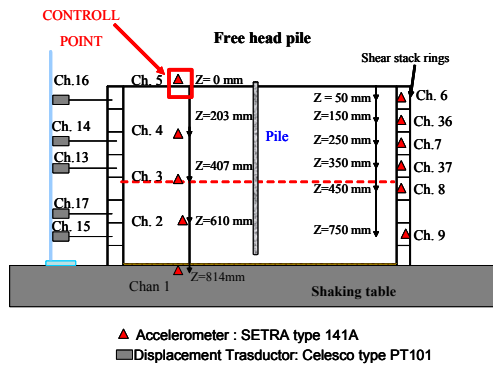


Figure 6.1: acceleration time histories comparison between EERA (linear and linear equivalent) and experimental (BE+E_STU2_FH)

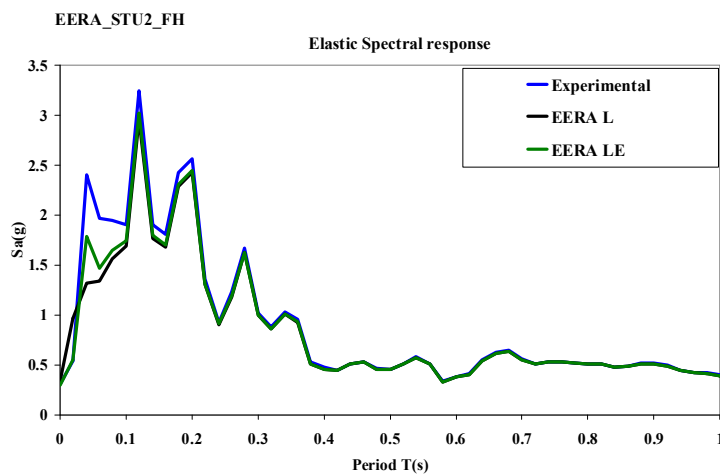


Figure 6.2: Elastic spectral response of surface acceleration (BE+E_TMZ2_FH)

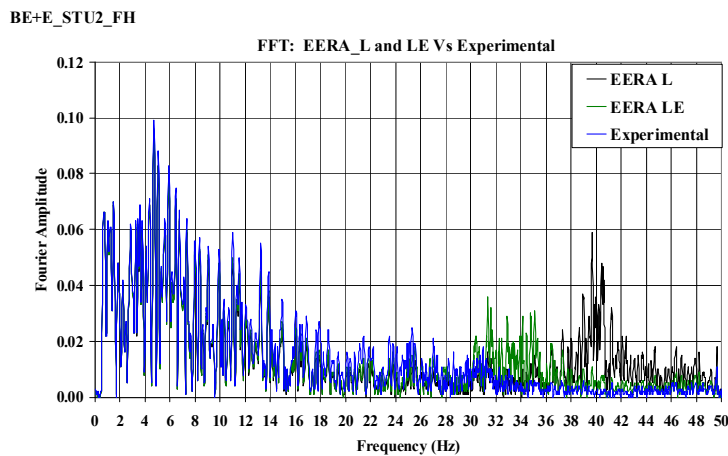


Figure 6.3 FFTs: EERA and experimental value on the surface (BE+E_STU2_FH)

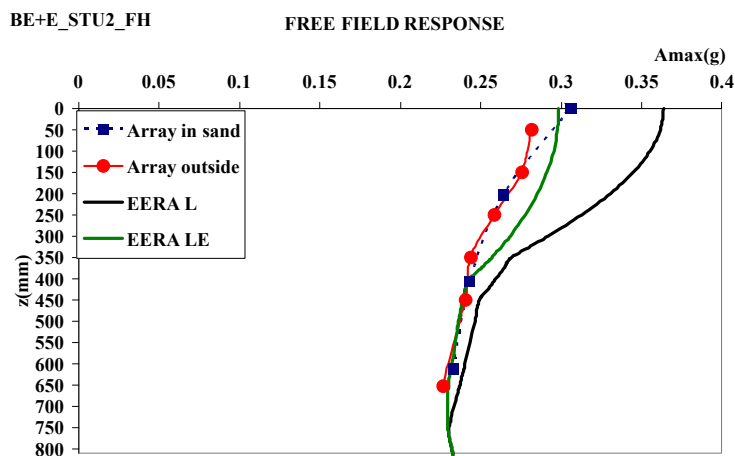


Figure 6.4: Free field response comparison EERA (L and LE) and experimental (BE+E_STU2_FH)

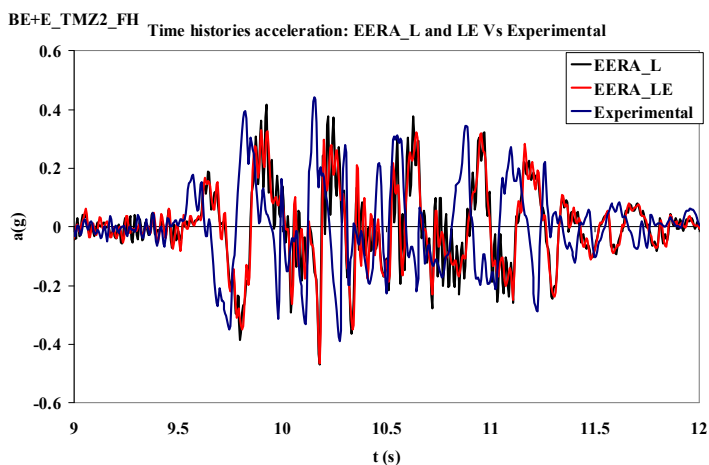


Figure 6.5: Acceleration time histories on the surface: comparison EERA (L and LE) and experimental (BE+E_TMZ2_FH)

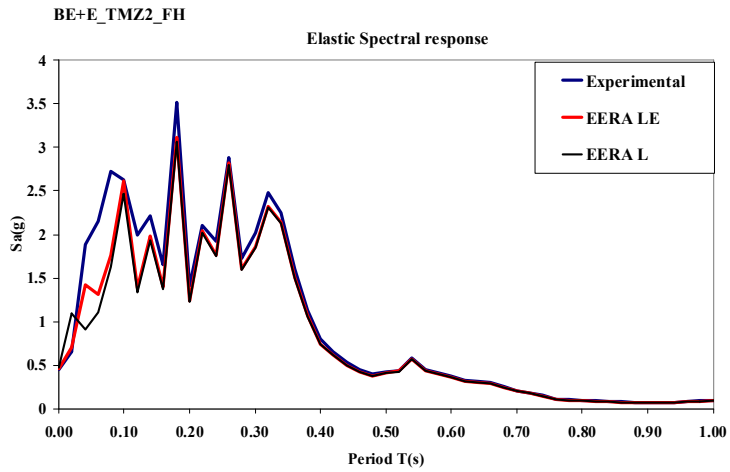


Figure 6.6: Elastic spectral response comparison EERA (L and LE) and experimental (BE+E_TMZ2_FH)

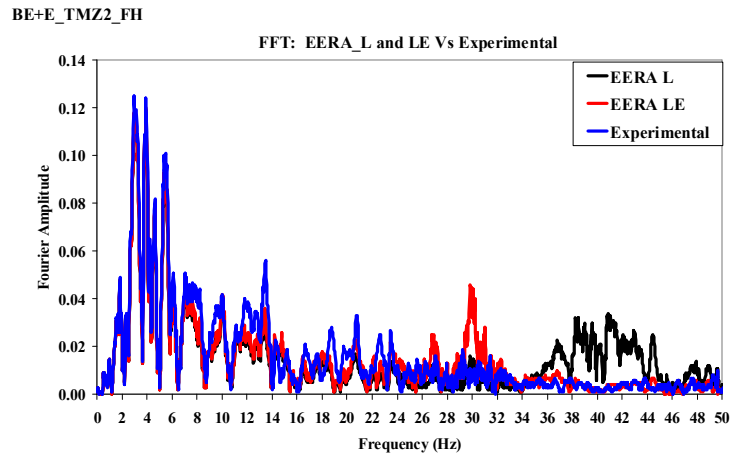


Figure 6.7: FFTs-EERA (L and LE) and experimental value on the surface (BE+E_TMZ2_FH)

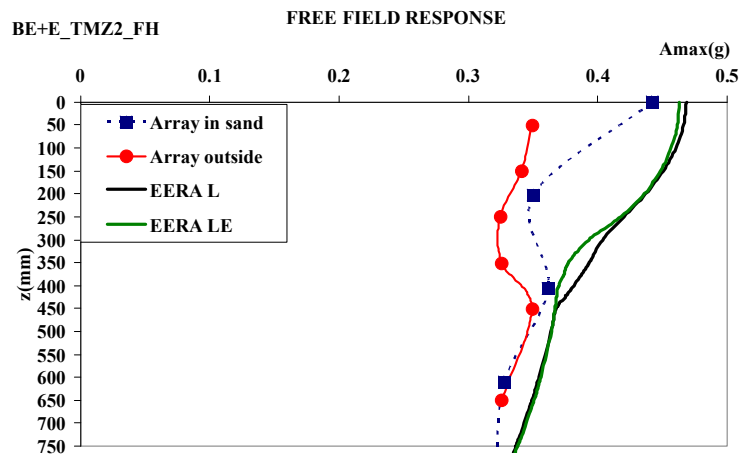


Figure 6.8: Free field response comparison EERA (L and LE) and experimental (BE+E_TMZ2_FH)

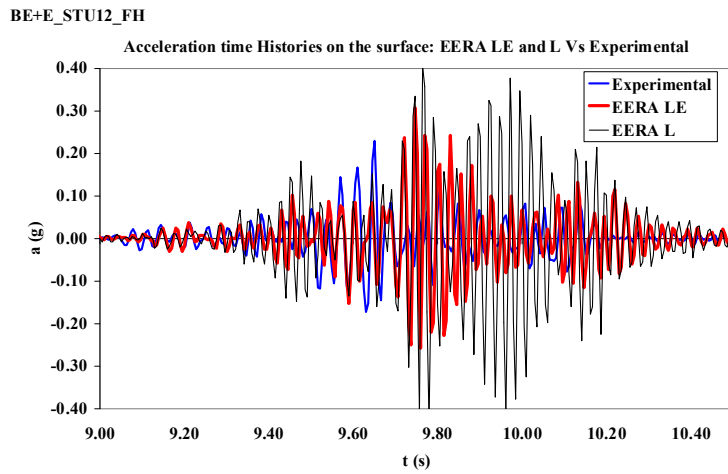


Figure 6.9: Acceleration time histories on the surface: EERA L-LE and experimental value (BE+E_STU12_FH)

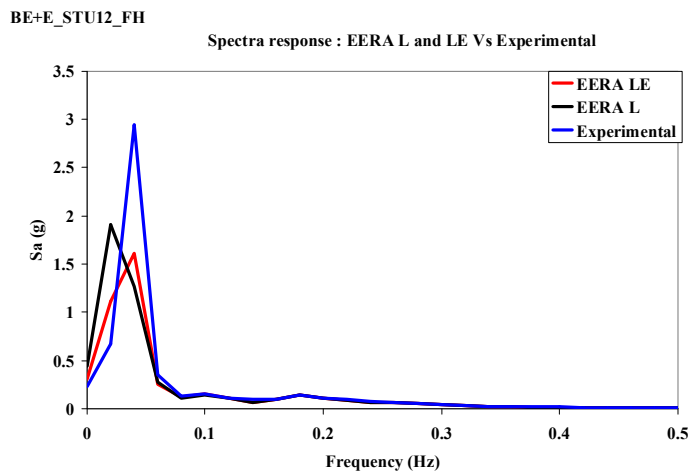


Figure 6.10: Spectra response acceleration on the surface:EERA (L and LE) and experimental ((BE+E_STU12_FH)

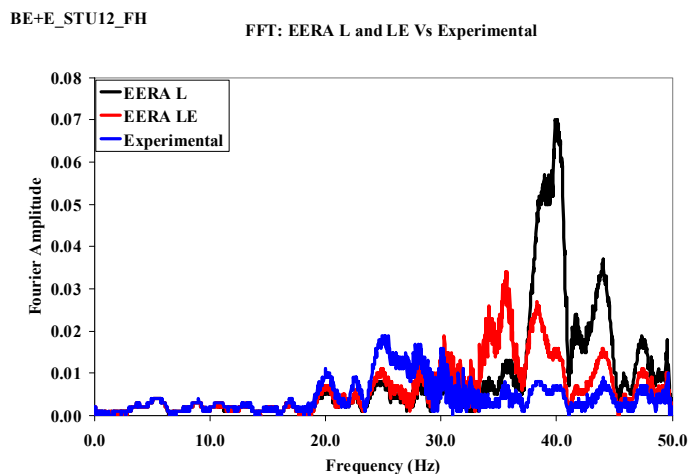


Figure 6.11: FFTs EERA (L and LE) and experimental value (BE+E STU12 FH)

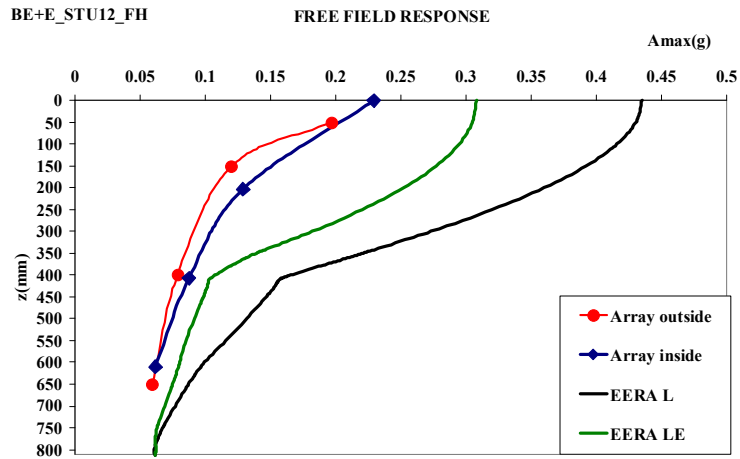


Figure 6.12: free field response: comparison EERA (LE and L) and experimental (BE+E_STU12_FH)

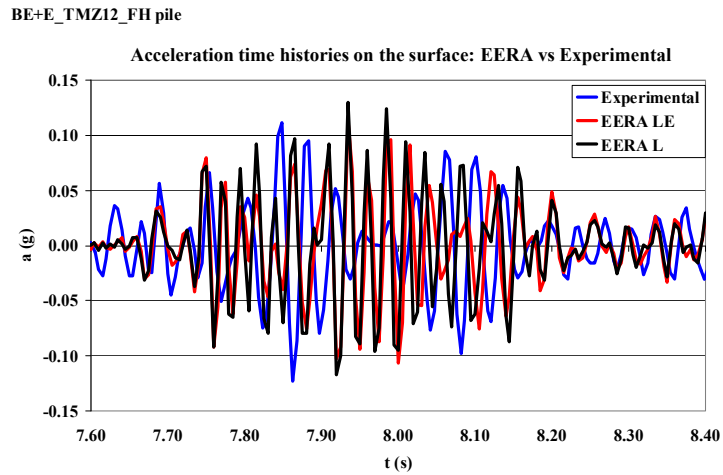


Figure 6.13: Acceleration time histories on the surface: comparison EERA (L and LE) and experimental (BE+E_TMZ12_NRH)

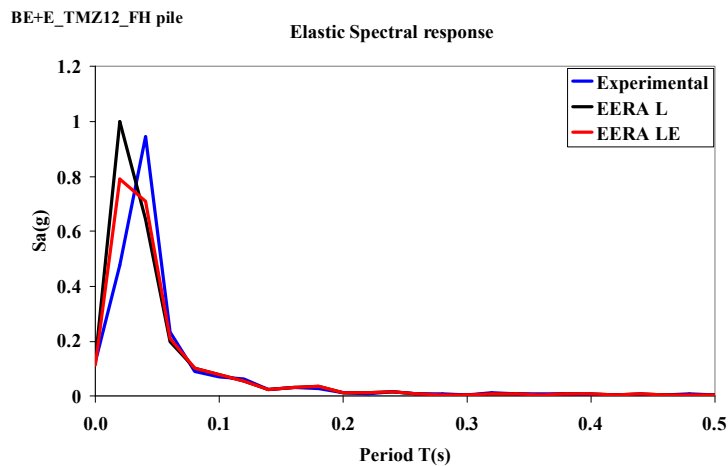


Figure 6.14: Elastic spectral response (BE+E_TMZ12_NRH)

BE+E_TMZ12_FH pile

FFT: EERA L and LE Vs Experimental

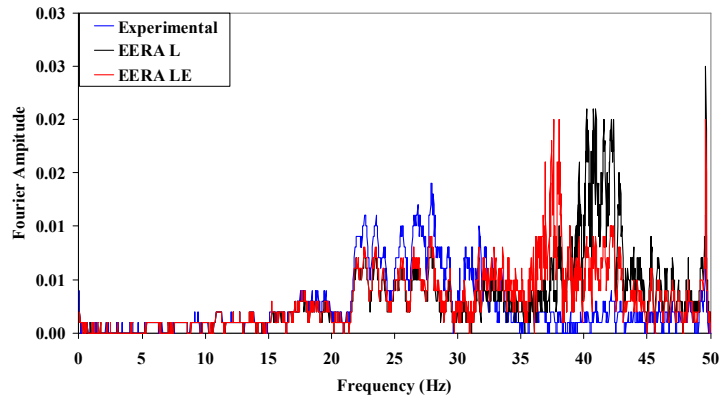


Figure 6.15: FFTs acceleration on the surface (BE+E_TMZ12_FH)

BE+E_TMZ12_FH

FREE FIELD RESPONSE

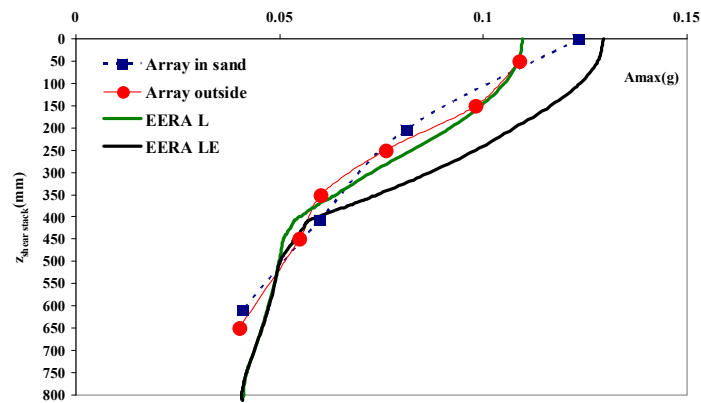


Figure 6.16: Free field response comparison EERA (L and LE) and experimental ((BE+E_TMZ12_FH)

6.2.3 Soil shear strain: EERA LE and experimental values

In this section for BE+E soil deposit, the soil shear strains at the bottom of the first layer γ provided by EERA linear equivalent analyses are compared with the experimental values. As explained in chapter 5, the experimental shear strains have been calculated by the acceleration integration using the trapezoidal method to produce velocities. Trapezoidal integration of the calculated velocities followed by forward reverse filter sequence is undertaken to produce displacements.

The shear strain is evaluated using Zeghal and Elgamal's expression with the interpolated surface displacement obtained from trapezoidal integration, and displacement at depth d , interface depth.

Table 6.2 shows shear strain values for four different earthquake: Sturmo and Tolmezzo scaled 12 and 2 times.

Table 6.2: Soil shear strain at interface from EERA code and experimental work

<i>Soil shear strain at interface</i>		
BE+E	EERA LE	Experimental
	γ	γ
FH pile		
STU 2	4.20E-04	7.95E-04
STU12	1.80E-04	6.80E-04
TMZ 2	5.60E-04	1.79E-03
TMZ 12	5.90E-05	3.34E-04

The shear strain obtained from EERA analysis are systematically smaller than the experimental measures.

It seems that EERA could underestimate the shear strain calculation, however some doubts are correlated on the effectiveness of shear strain evaluated using Zeghal and Elgamal's expression.

On this aspect an improvement on the methodology to calculate the shear strains will be done, in the future works.

In figure 6.17 the strain transmissibility obtained for by soil shear strains at the bottom of the first layer γ provided by EERA linear equivalent analyses and shaking table test have been provided, has been plotted. Obviously the strain transmissibility is smaller for the experimental values.

In figure 6.18 a comparison of shear strain transmissibility has been shown, by soil shear strains provided by EERA linear equivalent analyses.

In particular three different pile head conditions have been considered: free head pile, no rotation head pile and no rotation head pile with oscillator on the top.

From the comparison it seems that the kinematic bending on pile doesn't matter of the presence of mass on the pile head. A part of Tolmezzo earthquake 2 times scale, the values obtained for the three pile head configurations are quite close. The strain transmissibility does not affected by the presence of mass. The average range values are 5% to 10%, as might be expected (Mylonakis 2001).

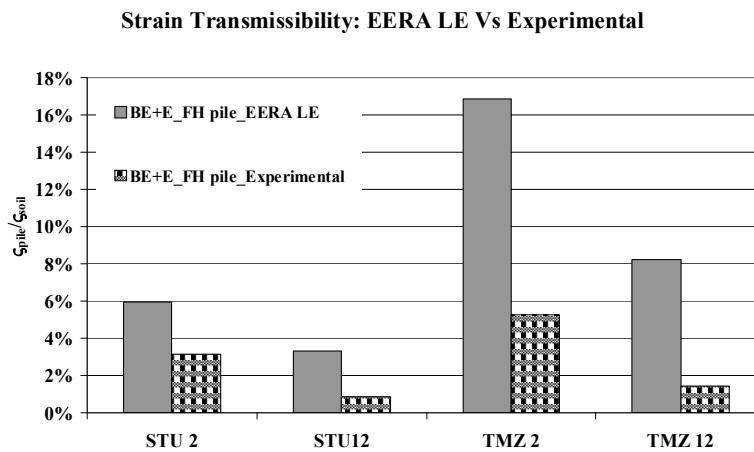


Figure 6.17: Comparison between strain transmissibility experimental value and EERA simulation

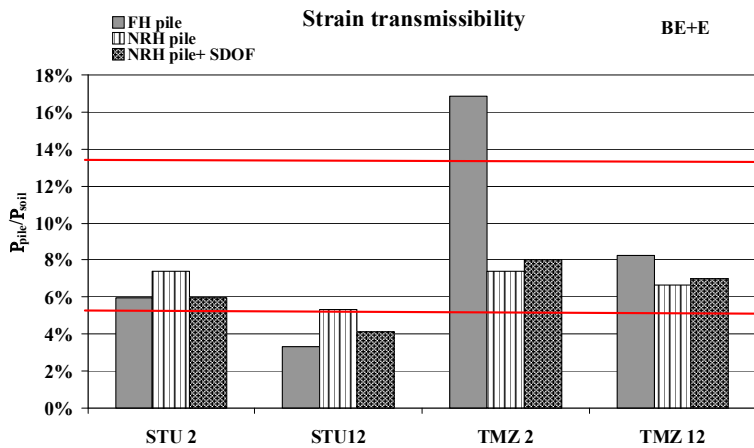


Figure 6.18: Strain transmissibility: comparison between three different pile head conditions

6.2.4 General observation on free field comparison with EERA code and experimental data

With the aim of checking accurate free-field site response some analyses of the model soil columns on analytical reproduction of the observed site response predicted by the program EERA. Some analyses have been carried out, in linear and linear equivalent range. Overall, the agreement is quite good. Some examples have been presented for layered sand soil “BE+E”. The following observations can be made about the EERA simulations of the test data:

1. the time histories of acceleration result shift in the period;
2. the amplitude of response in the high frequency range (12 times scaled input motion) was frequently under predicted. This may reflect the proximity of the accelerometer array to the model structures in test series 2.4 and 2.5, and feedback energy from the structures being recorded by the accelerometers. This phenomena was observed in several field case studies (Meymand, 1998). Another possible explanation for the under prediction of high frequency energy in the models was the strong twist motions imparted by the shaking table, which would not be accounted for in the EERA analyses, but cannot be isolated from the test data.
3. the linear analyses improve the high frequency response, and nonlinear analyses may offer the possibility of better estimates of response at the site period. Appropriately selected secant stiffness values provided more realistic descriptions of the observed soil-pile response. In general the linear equivalent analyses are more appropriated than linear simulation.
4. observed the spectra response of signal in EERA LE and experimental one, they are very close. So that the high frequency generated simulation, always present doesn't affected the spectral response, but only the acceleration time histories.
5. for input motion scaled 12 times, in particular for Sturno input motion, the simulation by EERA could be considered not reliable. The input motion have a very high frequency content and EERA is not able to simulated this king of input motion.

In conclusion, the EERA simulations of the observed model soil response were quite good, and the model soil-container system can be judged to adequately reproduce free-field site response. The small deviations between the observed and predicted behaviour may be acceptable for pure site response analyses, but the propagation of these errors into the SSPSI analysis requires further study (case 12 scaled input motion).

The use of more appropriate degradation curves, $G(\gamma)$ and $D(\gamma)$, obtained from specific laboratory test could improve the efficacy of numerical simulations.

6.3 Literature results Vs Experimental values

A wide application of the simplified literature formulas of Dobry & O'Rourke (1983), Nikolaou et al. (2001) have been carried out to compute the kinematic moments at the interface of the subsoil configurations investigated experimentally. The formulas of Dobry & O'Rourke (1983) have been applied by adopting both the shear strain at the bottom of the first layer γ provided by the simplified formula of Seed & Idriss (1982).

In the formula of Seed & Idriss (1982), the surface acceleration has been obtained from the experimental acceleration time histories (Ch. 5).

In the same way, the Nikolaou et al. (2001) equation has been applied by adopting both the shear stress at the interface provided by the authors ($\tau_{int} \sim a_s \rho_1 h_1$) and the value directly provided by experimental acceleration time histories. The formula of Nikolaou et al. (2001) has been applied without any corrective factor η .

In figure 6.19, 6.20, 6.21 the values of kinematic bending moments at interface normalized by yielding moment are shown for five earthquakes, for three different pile head condition.

From the comparison of the simplified formula and the experimental value, two tendencies could be underline:

- in the event of a seismic input having high frequency and short duration (12-scale), the formulas and the experimental values are comparable;
- in the event of a seismic input having high Arias energy and long duration (2-scale and 5 scale), the formulas and the experimental values are dissimilar.

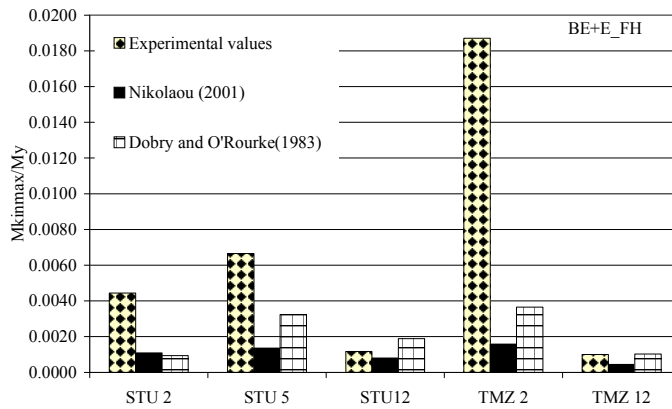


Figure6.19: Kinematic bending moment at interface: free head pile configuration

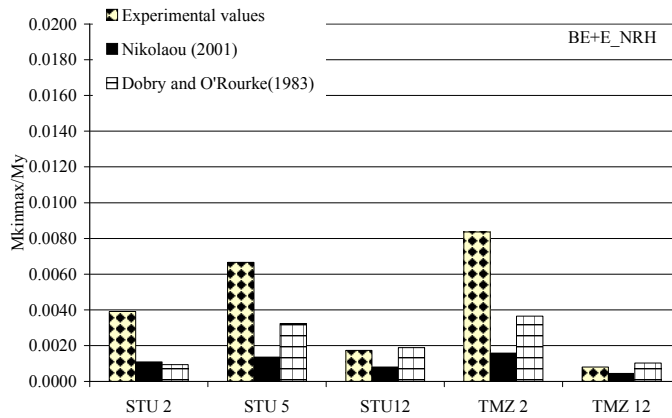


Figure6.20: Kinematic bending moment at interface: no rotation pile head configuration

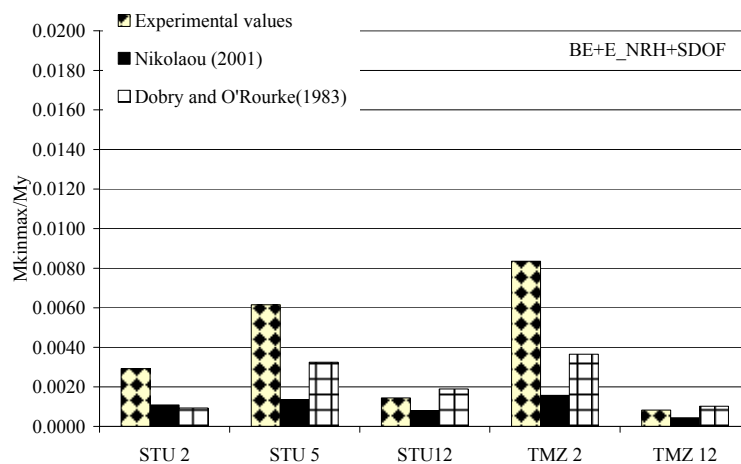


Figure6.21: Kinematic bending moment at interface: no rotation pile head +SDOF configuration

6.4 Numerical Analysis Vs Experimental results

An wide application of the simplified literature formulas of Dobry & O'Rourke (1983), Nikolaou et al. (2001) have been carried out to compute the kinematic moments at the interface of the subsoil configurations investigated experimentally and numerically by the BDWF approach of Mylonakis et al. (1997).

The analysis method adopted for the parameter study is the BDWF approach, proposed by Mylonakis et al. (1997). As the analytical aspects of the method are well known (Kavvadas & Gazetas 1993, Mylonakis et al., 1997; Nikolaou et al., 2001) only results will be discussed here. It is worth pointing out that the analyses are performed in the frequency domain, and the results are transformed in the time domain through standard Fourier transformations (DFT), as suggested by Veletsos & Ventura (1984). The reference soil profile consists of a soft surface layer, of thickness H_1 and shear wave velocity V_{s1} , underlain by a stiffer stratum, of thickness H_2 and shear wave velocity V_{s2} . An elastic bedrock with $V_{s\text{rock}}$ 1800 m/s has been considered at the bottom of the second layer To conform to most of the parameter studies presented in the literature (Nikolaou et al., 2001; Mylonakis, 2001), the pile has been modelled as a solid elastic cylinder. With the above-modified Young's modulus \bar{E}_p the "replacement" solid cylinder has flexural rigidity ($E_p I_p$) as the original hollow pile. (Mylonakis, 2001). The modified Young's modulus \bar{E}_p is equal to 16.244 MPa

The following parameters are constant in the analyses: pile length $L = 75$ cm m; pile diameter $d = 22$ mm; soil Poisson's ratio $\nu_1 = \nu_2 = 0.35$; soil mass density $\rho_1 = 1.3$ Mg/m³ $\rho_2 = 1.88$ Mg/m³. Five different earthquakes have been considered.

The kinematic moments induced on the pile soaked into stratified deposit BE+E have been analytically .

We performed linear analysis with ground parameters subject to small deformations.

For the linear analysis the value of initial stiffness consider (G_0) for each material has been obtained from the modal test, done before the dynamic test (Chapter 4), the values of damping is hypothesized equal to 3%.

Since under strong earthquakes soil no longer has a linear elastic response, analyses have been performed to evaluate how soil nonlinearity could affect predictions obtained by linear elastic analyses.

The non linear behaviour of the soil has been represented by the equivalent linear procedure, which provides soil stiffness and damping ratio consistent to the earthquake-induced level of shear strains.

This is still a crude representation of the actual soil response under earthquakes but certainly more realistic than the linear elastic model, widely adopted in the literature studies. To such a scope, equivalent linear site-response analyses of the subsoil depicted before have been firstly carried out. The "equivalent" parameters thus obtained (i.e., shear stiffness G_{eq}

and damping ratio D_{eq}) have been inserted in the BDWF formulation of Mylonakis et al. (1997) to investigate the seismic response of the pile. Soil nonlinearity has been represented by the curves of the normalized shear modulus G/G_0 and dampin ratio D versus the shear strain γ , provided by Cavallaro (2001) and Seed and Idriss (1970).

In figure 6.22 the values of kinematic bending moments at interface normalized by yielding moment are shown for five earthquakes, free head pile condition. Even if the analysis performed were linear, yet the results were comparable, in terms of magnitude, in the case of earthquake 12 times scaled.

The peculiarity of this input motions are that they are characterized by a high frequency and short duration (12-scale).

The BDWF model approximates better than formulas the behaviour of the pile at interface. The earthquakes scaled 12 times are in good relation between earthquake testing and the Winkler model results, which approximates the behaviour of the pile at interface better than the forecasts of the literature formulas, which result to be too succinct and less exhaustive. In case of earthquakes scaled 2 times and 5 times, a simple linear analysis is not able to reproduce the experimental evidence

In figure 6.23 the results by linear analyses (L) and by equivalent linear ones (L.E.) has been plotted. By effecting a linear analysis with a Winkler model, in which the stiffness parameters obtained by an equivalent linear EERA analysis are considered, the difference of the kinematc bending moment at interface obtained in an experimental way and the numeric one is lowered.

In case of earthquakes scaled 2 times and 5 times, the linear analysis does not allow to get the value of the experimental moment as expected due to the high energy associated to this kind of earthquakes. An improved forecast is obtained by way of recourse to a simple “equivalent linear model”.

Results are represented as envelopes of the maximum kinematic bending moments computed (in the time domain) along the pile for Sturmo earthquake scaled 12 times and for Tolmezzo earthquake scaled 2 times. (Figure 6.24 and 6.25).

Figure 6.24 shows that the maximum kinematic bending moment, generally verifies in correspondence to the soil layer interface, obtained by Spiab linear, is very close to the experimental value. For Tolmezzo earthquake 2 times scaled the Spiab LE analysis is more appropriate than the Linear one. The use of more appropriate degradation curves, $G(\gamma)$ and $D(\gamma)$, obtained from specific laboratory test could improve the efficacy of numerical simulations.

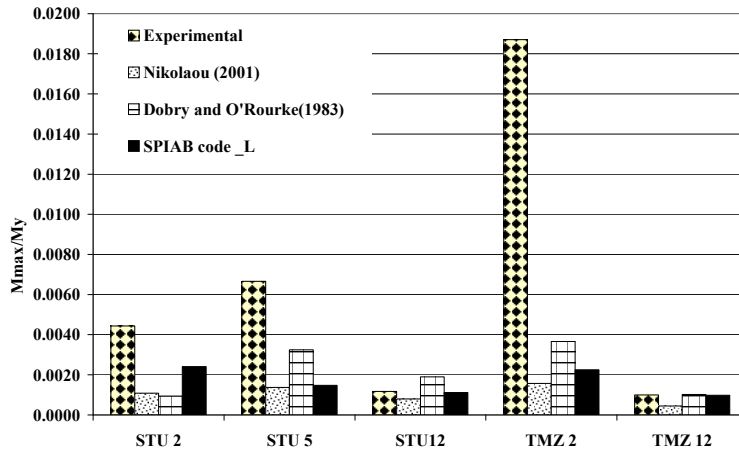


Figure 6.22: Comparison between Spiab Linear analysis, theoretical prediction, experimental values of kinematic bending moment at interface normalized by the yielding moment

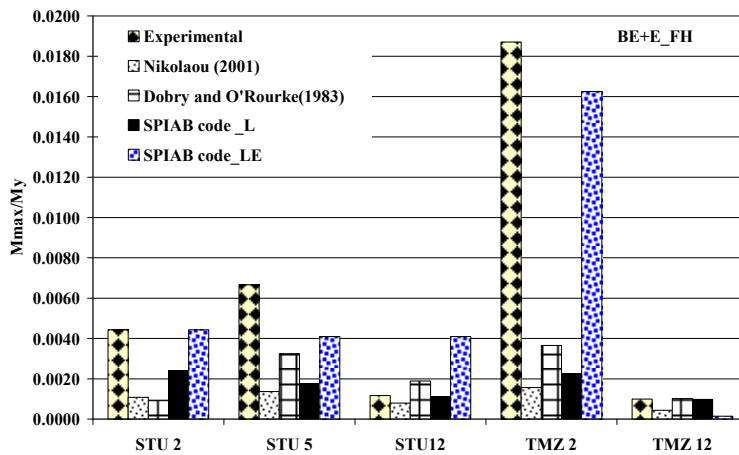


Figure 6.23 Comparison between Spiab Linear and Linear equivalent analysis, theoretical prediction and experimental values of kinematic bending moment at interface normalized by the yielding moment

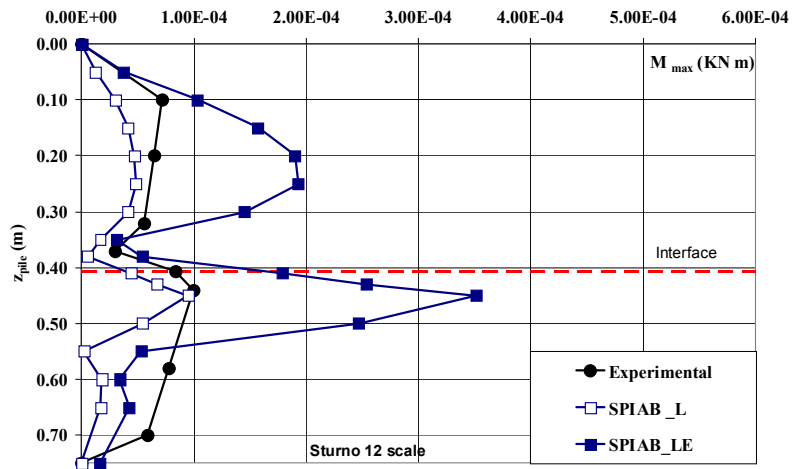


Figure 6.24: Bending moment along the pile, Sturno 12 scale

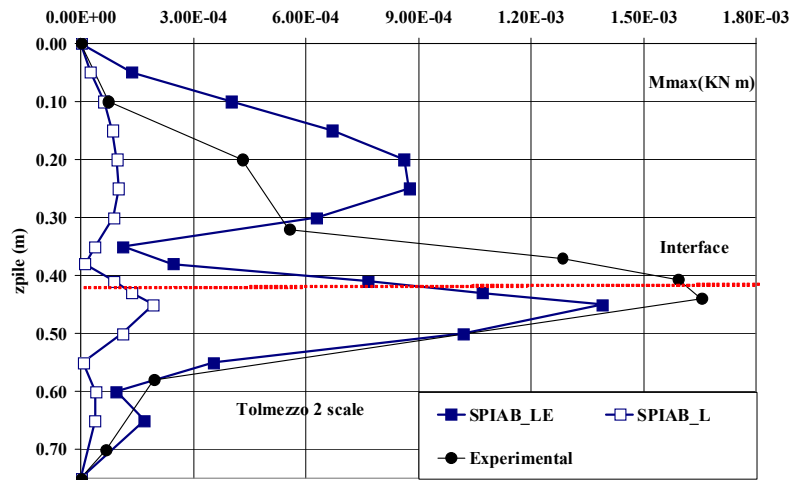


Figure 6.25: Bending moment along the pile Tolmezzo 2 scale

7. Summary and conclusion

The purpose of this work is an upgrading in the comprehension of the complex phenomenon of soil-pile-structure behaviour under seismic loading. In the past this topic has been generally studied by means of theoretical approaches. On the other hand the present study is mainly based on a huge experimental research on 1-g models. In particular the experimental activity described in this dissertation has been programmed in order to emphasize some crucial aspects of the kinematic interaction phenomenon: soil stiffness contrast; subsoil deformability; waveform input motion; pile head condition. Further the correlation between bending moments induced by kinematic and inertial actions has been investigated.

Around 400 shaking table tests were carried out on different soil, pile and structure configurations. Due to the great number of data, here only the most significant experimental results have been illustrated referring to free head and no rotation head pile conditions. The effect of the single degree of freedom structure (SDOF) located on pile head has been enhanced too. Three earthquakes have been utilised as input motion, properly scaled by three different factors (12, 5, 2 times). The model pile is realised by an alluminium alloy tube.

The physical model has been located in the laminar box called Shear Stack (specifically designed at BLADE in Bristol). Three different soil configurations have been pluviated inside the box: a monolayer subsoil and two deposits constituted by two soil layers, with stiffness increasing with depth. The shear wave velocity ratio at the interface V_{s2}/V_{s1} (between lower and upper layer) is equal to about 1.7 and 8 respectively.

Experimental results have then been compared with those by numerical back-analyses of the soil-pile-structure system.

In homogeneous soil the kinematic bending strain for a free-head pile increases with depth, reaching its maximum at approximately the mid-length of the pile (Gazetas et al.1992).

For layered deposits, the maximum kinematic bending moment is located near the interface between the two layers. The bending moments are characterized by a raise trend with the increase of stiffness contrast; the same results have been obtained by theoretical studies by Gazetas et al.,1993.

For all the three configurations it should be noted that as the input motion high frequency content reduces (going from 12 to 2 earthquake scaling factor) the kinematic bending moment along the pile amplifies. In these cases, with the increase of Arias Intensity, the seismic

motion recorded at the top of the pile increases, even though it is always smaller than the one recorded in free field condition.

Further it has been proved that the pile filters the high frequency components of the input motion (see Kanya and Kausel, 1991). It is interesting to note that the effects of stiffness contrast at the interface are significant both for the free head pile condition and the no rotation one.

The no rotation device on the pile head produces a change in the bending moment trend: for the monolayer configuration the maximum bending moment occurs at pile head (in a section very close to it); for the layered soil configurations the maximum bending moment happens at a deeper level. The migration of the maximum bending moment from the top to a lower section is more significant with the increase of the active length of the pile (because of the reduction of the stiffness of the top rubber layer).

The effects of scaling factors are more evident on the kinematic bending moment value than on the maximum bending moment at the pile head. The bending moment diagrams of free-head and no rotation head piles converge with depth and become similar beyond a certain distance from the surface. This depth is comparable with the classical “active pile length”, beyond which a head-loaded pile behaves as in infinitely long beam.

The comparison between monolayer and layered configurations put in evidence that the kinematic bending at the interface are bigger for the free than for the no rotation head pile.

In order to investigate on the correlation between kinematic and inertial effects, the bending moment time histories at pile head, in the two no rotation configurations without the mass and in presence of the SDOF system have been compared.

The crucial point is the time of occurrence of the peak of kinematic and total bending moments. In the different configurations the maximum bending moments do not happen in the same instant. In particular the moment time histories are not in phase and the delay between the peaks is quite random. These evidences are consistent with the observation that the natural period of the tested SDOF systems is always different from that of the pile-ground system, which is always lower. The experimental observations led to conclude that the maximum effects due to the single contributions of kinematic and inertial actions are not simultaneous, so that the total moment can not be simply determined as sum of the two maximum moments (computed, for example, by the substructuring design approach).

The free-field response of the soil deposit, measured by means of a vertical array of accelerometers located far from the pile, has been compared with the results obtained by 1-D analyses performed by the EERA code. The analyses have been carried out both assuming a linear behaviour of materials (small deformations) and exploring the non linear behaviour (at higher deformation) by the linear equivalent method. The agreement between experimental and numerical results is quite good. Response spectra of free-field motions obtained by equivalent linear EERA analyses are very close to those relative to measured free-field response. Actually numerical analyses usually generate additional high frequency contents

which are quite evident in the acceleration time histories, but do not significantly affect the spectral response.

In conclusion, EERA simulations of the observed model soil response were very successful; this result once again confirms that the soil container (Shear Stack) is well designed for not affecting the free-field soil response. Nevertheless the small deviations between the observed and predicted behaviour, acceptable for pure site response analyses, could have important effects into the SSPSI analysis, which need to be deeply studied (e.g. the case of 12 times scaled earthquakes).

Literature simplified formulas for predicting kinematic moments at the interface of the two-layered subsoil configurations (e.g. Dobry & O'Rourke, 1983, Nikolaou et al., 2001) have been widely applied and compared to both experimental data and numerical results by the BDWF approach of Mylonakis et al. (1997).

BDWF analyses have been performed first assuming small deformation behaviour of soils (linear analysis with initial value of soil properties); then the non linear soil behaviour has been explored by assuming soil properties derived by equivalent linear soil response analyses.

In the case of high frequency and short duration input motion (12-scale), BDWF linear analysis results well approximate the behaviour of the pile at the interface, because the earthquakes are characterized by low energy. On the other hand simplified formulas result to be too succinct and less exhaustive.

In the case of stronger input motion (5 and 2 scale), a simple linear analysis is not able to reproduce the experimental evidence, due to the high energy associated with this kind of earthquakes (especially for 2 scale input motion). On the other hand, as expected, BDWF equivalent linear analyses give kinematic bending moment at the interface close to those obtained by the the experimental data.

In conclusion it can be stated that experimental evidences generally confirm the main knowledge provided by theoretical studies, both regarding the free field behaviour of the soil and the foundation pile response. The investigation of the complete pile and SDOF system has provided very interesting indications about the correlation between kinematic and inertial effects.

The good quality of the tests and the huge amount of measurements acquired by this original experimental research represent a very precious data-bank for further understanding of complex SSPSI phenomenon.

References

- AGI, 2005 – Aspetti geotecnici della progettazione in zona sismica, Linee Guida – Edizione provvisoria, marzo 2005.
- Ahmad, S. & Mamoon, S. M. (1991). ‘Seismic response of piles to obliquely-incident waves’. Proc. 2nd Int. Conf Recent Advances Geotech. Earthq. Engng Soil Dyn., St Louis 1, 805-814.
- Ashour M., Pilling P., Norris G. (2004). Lateral behaviour of pile groups in layered soils. *Journal of Geotechnical and Geoenvironmental Engineering*, ASCE, 130, (6), 580-592.
- Bardet, J.P., Ichii, K., and Lin, C.H. 2000. EERA a Computer Program for Equivalent-linear Earthquake site Response Analyses of Layered Soil Deposits. Univ. of Southern California, Dep. of Civil Eng., 2000.
- Bathe, K.J. 1996 *Finite Element Procedures*. Prentice Hall
- Bentley, K.J., and El Naggar, M.H. 2000. Numerical analysis of kinematic response of single piles. *Canadian Geotechnical Journal*, 37: 1368–1382.
- Biondi G., Massimino M.R. 2002 Static and dynamic modelling of soil-shallow foundation-overstructure interaction. Research Report in the framework of an ECOLEADER Project. Pubblicata in proprio
- Blaney G. W., Kausel E., Roesset J.M., 1976. Dynamic stiffness of piles. Proc. 2nd int. Conf. Num. Methods geomech. Virginia Polytech. Inst. & State Un. Blacksburg VA II, pp. 1001-1012.
- Bradley Brendon A. et al, 2009 Intensity measures for the seismic response of pile foundations, *Soil Dynamics and Earthquake Engineering* 29 (2009) 1046–1058
- Brown D.A., Morrison C. e Reese L.C. (1988). Lateral load behaviour of pile group in sand. *Journal of Geotechnical and Geoenvironmental Engineering*, ASCE, 114, (11), 1261-1276.
- Brown D.A., Shie C.F. (1991). Modification of P-Y curves to account for group effects on laterally loaded piles. *ASCE Geotechnical Congress 1991*, 1, ASCE, Reston, Va., 479-490
- Cai, Y.X., Gould, P.L., and Desai, C.S. (2000). Nonlinear analysis of 3D seismic interaction of soil–pile–structure system and application. *Engineering Structures*, 22(2): 191–199.
- Cairo, R. Conte, E., Dente, G. (2005). Analysis of pile groups under vertical harmonic vibration. *Computers and Geotechnics*, 32, 7, 545-554.

Cairo, R., Conte, E., Dente, G. (2008). Nonlinear seismic response of single piles. 2008 Seismic Engineering Conference commemorating the 1908 Messina and Reggio Calabria Earthquake (MERCEA'08), Reggio Calabria, American Institute of Physics, Melville, New York, 1, 602-609.

Cairo, R., Dente, G. (2007a). Un metodo per l'analisi dell'interazione cinematica palo-terreno nei depositi orizzontalmente stratificati. XII Convegno ANIDIS, L'Ingegneria Sismica in Italia, Pisa, memoria n. 378.

Cairo, R., Dente, G. (2007b). Kinematic interaction analysis of piles in layered soils. XIV European Conference on Soil Mechanics and Geotechnical Engineering, ISSMGE-ERTC 12 Workshop "Geotechnical Aspects of EC8", Madrid, Pàtron Editore, Bologna, cd-rom, paper n. 13

Castelli F. (2006). Non-linear evaluation of pile groups lateral deflection. Proceedings International Conference on "Piling and Deep Foundations", Amsterdam, 31 May-2, June 2006, 127-134.

Castelli F., Maugeri M. (2007a). A pseudo-static analysis for the evaluation of the lateral behaviour of pile groups. Proceedings 4th International Conference on Earthquake Geotechnical Engineering, Thessaloniki, Greece, June 25-28, 2007, paper no.1399.

Castelli F., Maugeri M. (2007b). Numerical analysis for the dynamic response of a single pile. Proceedings XIV European Conference on Soil Mechanics and Geotechnical Engineering, ERCT 12 Workshop "Geotechnical Aspects of EC8", Madrid, September 25, 2007, 7 p.

Castelli F., Maugeri M., Mylonakis G. (2008). Numerical analysis of kinematic soil-pile interaction. Proceedings MERCEA 2008, 2008 Seismic Engineering International Conference Commemorating the 1908 Messina and Reggio Calabria Earthquake, Reggio Calabria and Messina, July 8-11, Vol.1, pp.618-625

Chau, K.L.; Shen, C.Y., Guo, X., 2009 Non linear seismic soil-pile-structure interactions: Shaking table test sand FEM analyses K Soil Dynamics and Earthquake Engineering 29 (2009) 300-310

Cloutoud D, Taherzadeh R, 2006 Soil, pile group and building interaction under seismic loading First European Conference on Earthquake Engineering and Seismology (Geneva, Switzerland, 3-8 September 2006 Paper Number:10

Conte, E., Dente, G. (1988). Effetti dissipativi nella risposta sismica del palo singolo. Deformazioni dei terreni ed interazione terreno-struttura in condizioni di esercizio, Monselice, 2, 19-38.

Conte, E., Dente, G. (1989). Il comportamento sismico del palo di fondazione in terreni eterogenei. XVII Convegno Nazionale di Geotecnica, Taormina, 1, 137-145.

Cox, W. R., Dixon, D. A., Murphy, B. S. (1984). Lateral load tests on 25.4-mm (1-in.) diameter piles in very soft clay in side-by-side and in-line groups. Laterally loaded deep foundations: analysis and performance, ASTM STP 835, J.A. Langer, E.T. Mosley, and C.D. Thompson (ed), American Society for Testing and Materials, 122-139.

Crewe A.J., Lings, M.L., Taylor, C.A., Yeung, A.K. & Andrighetto. 1995. Development of a large flexible shear stack for testing dry sand and simple direct foundations on a shaking table' European seismic design practice, Elnashai (ed), Balkema, Rotterdam.

D.M. 14/01/2008 del Ministero delle Infrastrutture. Norme Tecniche per le Costruzioni. Gazzetta Ufficiale n. 29 del 4/02/2008

De Sanctis, L., Maiorano, R., 2007. Effetti della costituzione del sottosuolo sui momenti dell'interazione cinematica di pali in gruppo e di pali isolati. IARG 2007. Salerno, 4-6 luglio 2007.

Dennehy, K. & Gazetas, G. (1985). Seismic vulnerability analysis and design of anchored bulkheads, chapters 5 and 6, research report. Troy, NY: Rensselaer Polytechnic Institute.

Dente G. (1999) La risposta sismica dei pali di fondazione. Hevelius Edizioni, 1999

Dente G. (2005) Fondazioni su pali – Linee guida sugli aspetti geotecnici della progettazione in zona sismica Patron Editore Bologna – Edizione Provvisoria Marzo 2005- p.p. 147-160

Dente, G. (1983). La risposta dinamica dello strato eterogeneo attraversato da onde di taglio. Atti XV Convegno Nazionale di Geotecnica, Spoleto, pp. 153-161.

Dezi F., Dall'Asta A., Leoni G., Scarpelli G. 2007, Influence of the soil-structure interaction on seismic response of railway bridge in 4th Int. Conf. on Earthquake Engineering, Thessaloniki

Dihoru L., Bhattacharya S., Taylor C.A., Wood D.M., Moccia F., Simonelli A.L., Mylonakis G. 2009. Experimental modelling of kinematic bending moments of piles in layered soils, International Conference on Performance Based Design in Earthquake Geotechnical Engineering, IS-Tokyo, Tsukuba, Japan, in print

Dobry R. and O'Rourke M.J., 1983, Discussion on 'Seismic response of end-bearing piles' by Flores-Berrones R., Whitman R.V.', J. Geotech. Engng. Div., ASCE, 109, 778-781.

Dobry R., Gazetas G. (1988). Simple method for dynamic and damping of floating pile groups. Géotechnique, Vol.38, no.4, pp 557-574.

Dobry R., Vicente E., O'Rourke E., Roesset J. (1982). Horizontal stiffness and damping of single piles. Journal of Geotechnical Engineering Division, ASCE, Vol.108, no.GT3

Dungca J.R., Kuwano J., Takahashi A., Saruwatari T., Izawa J., Suzuki H., Tokimatsu K., 2006 Shaking table tests on the lateral response of a pile buried in liquefied sand. Soil Dynamics and Earthquake Engineering 26 (2006) 287–295

EC8-1. 2004. General rules, seismic actions and rules for buildings. CEN European Committee for Standardization, Bruxelles, Belgium, January 2004, Final Draft.

EC8-5. 2003. Foundations, retaining structures and geotechnical aspects. CEN European Committee for Standardization, Bruxelles, Belgium, December 2003, Final Draft.

Fan, K., Gazetas, G., Kaynia, A., Kausel, E., Ahmad, S. 1991. Kinematic response of single piles and pile groups. Journal of Geotechnical Engineering, ASCE, 117, 12, 1860-1879.

Finn W.D.L., Fujita N. "Piles in liquefiable soils: seismic analysis and design issues", Soil Dynamics and Earthquake Engineering, n.22, 731-742, 2002

Finn. 2005. A Study of Piles during Earthquakes: Issues of Design and Analysis. Bulletin of Earthquake Engineering, 3: 141-234, Springer

Flores-Berrones, R. & Whitman, R. V. (1982). Seismic response of end-bearing piles. J. Geotech. Engng Div. Am. Soc. Civ. Engrs 108, No. 4, 554-569.

Gazetas G. (1984). Seismic response of end-bearing single piles. Soil Dynamics and Earthquake Engineering, 3, (2), 82-93.

Gazetas G. (1991). Foundation vibrations. Foundation engineering handbook, 2nd ed. Y. Fang ed., Van Nostrand Reinhold, New York, 553-593.

Gazetas G., Dobry R. (1984). Horizontal response of piles in layered soils. *Journal of Geotechnical Engineering*, ASCE, Vol.110, no.1, pp 20-40.

Gazetas G. Seismic response of end-bearing single piles. *Soil Dyn Earthquake Engng* 1984;3(2):82-93.

Gazetas G., Mylonakis G., 1998. Seismic soil-structure interaction: new evidence and emerging issue. Proc. 3rd Conf Geotechnical Earthquake Engineering and Soil Dynamics, ASCE, Seattle, pp.1119-1174.

Gazetas, G., Dobry, R. (1984). Simple radiation damping model for piles and footings. *Journal of Engng. Mech.*, ASCE, 110, 6, 937-956.

Gazetas, G., Fan, K., Tazoh, T., Shimizu, K., Kavvadas, M., Makris, N. (1992). Seismic pile-group-structure interaction. Piles under dynamic loads, *Geotech. Spec. Publ. No. 34*, ASCE, 56-93.

Gazetas, G., Tazoh, T., Shimizu, K., and Fan, K. 1993. Seismic response of the pile foundation of the Ohba-Ohashi Bridge. In *Proceedings of the 3rd International Conference on Case Histories in Geotechnical Engineering*, 1803-1809.

German,R.,1989, Particle Packing Characteristics, Metal Powder Industries Federation, New Jersey.

A. H. Hadjian, 2002 The fundamental period and modal shape of layered soil profiles *Soil Dynamics and Earthquake Engineering* Volume 22, Issues 9-12, October-December 2002, Pages 885-891

Hajjalilue-Bonab M., Levacher D., Chazelas J.L. (2007). Experimental evaluation of static and dynamic p-y curves in dense sand. Proc. 4th International Conf. on Earthquake Geotechnical Engineering, paper no.1696, Thessaloniki, Greece, 2007.

Juirmarongrit T., Ashford S.A. (2006). Soil-Pile response to blast-induced lateral spreading. II: analysis and assessment of the p-y method. *Journal Geotechnical and Geoenvironmental Engineering*, ASCE, Vol.132, no.2, pp 163-172.

Guin J, Banerjee PK. Coupled soil-pile-structure interaction analysis under seismic excitation. *J Struct Engng* ASCE 1998;124(4):434-44.

Kagawa T., Kraft L.M. (1980). Lateral load-deflection relationships of piles subjected to dynamic loadings. *Soils and Foundations*, Vol.20, no.4, 1980, pp 19-36.

Kagawa, T. & Kraft, L. M. (1981). Lateral pile response during earthquakes. *J. Geotech. Engng Div. Am. Sot. Ciu. Enars* 107. No. 12. 1713-1731.

Kanya, A. 1997. Earthquake-induced forces in piles in layered media. *Geotechnical Special Publication 70*, ASCE 75-95.

Kausel, E., Roësset, J.M. (1981). Stiffness matrices for layered soils. *Bull. Seism. Soc. Amer.*, 71, 6, 1743-1761.

Kavvadas M, and Gazetas G. 1993. Kinematic seismic response and bending of free-head piles in layered soil. *Geotechnique*, Vol.43, no.2, 1993, pp 207-222.

Kaynia A., Kausel E., 1982. Dynamic Stiffness and Seismic Response of Pile Groups. Res. Rep. R82-03, MIT, Cambridge, MA.

Kaynia AM, Kausel E. Dynamic behavior of pile groups. In: Proceedings of 2nd International Conference on Numerical Methods in Offshore Piling, Austin, Texas; 1982. p. 509–532.

Kaynia A.M. & Mahzooni. S. 1996. Forces in pile foundations under seismic loading, *J. Engng. Mech. ASCE*, 122, 1, 46-53.

Kaynia A.M. 1997. Earthquake-induced forces in piles in layered media, *Geotechnical Special publication 70*, ASCE, pp. 75-95

Kaynia A.M., Kausel E. (1991). Dynamics of piles and pile groups in layered soil media. *Soil Dynamics and Earthquake Engineering*, 10, pp 386-401.

Kaynia, A.M., Novak, M., 1992. Response of pile foundations to Rayleigh waves and obliquely incident body waves. *Earthq. Engng. Struct. Dyn.*, 21, 303-318.

Kimura M. & Zhang F. 2000 “Seismic evaluation of pile foundations with three different methods based on three-dimensional elasto-plastic finite element analysis”, *Soils and Foundations*, 40, 5, 113-132

Kobori, T., Minai, R. & Baba, K. (1981). Dynamic behaviour of a pile under earthquake-type loading. *Proceedings of 1st international conference on recent advances in geotechnical earthquake engineering and soil dynamics*, Rolla 2, 795-800.

K. K. Koo, K. T. Chau* ; †, X. Yang, S. S. Lam and Y. L. Wong “Soil–pile–structure interaction under SH wave excitation *Earthquake Engng Struct. Dyn.* 2003; 32:395–415 (DOI: 10.1002/eqe.230)

Kramer, S.L. 1996. *Geotechnical Earthquake Engineering*. Prentice-Hall, Upper Saddle River, NJ.

Liam Finn W.D, 2009, Some emerging issues in performance based design *Int. Conf. on Performance-Based Design in Earthquake Geotechnical Engineering*, IS-Tokyo 2009

Lysmer, J., and Kuhlemeyer R.L. 1969. Finite dynamic model for infinite media. *ASCE EM 90*: 859-877.

Lu,X, Li P, Chen B, Chen Y,2005 Computer simulation of the dynamic layered soil– pile–structure interaction system, *Can. Geotech. J.* 42: 742–751 (2005)

Maheshwari B.K., Truma K.Z., El Naggar M.H. Gould P.L. 2004 “Three-dimensional finite element non linear dynamic analysis of pile groups for lateral transient and seismic excitations”, *Canadian Geotechnical Journal* , 41, 118-133

Maheshwari, B.K., Truman, K.Z., Gould, P.L., and El Naggar, M. H. 2005. Three-dimensional nonlinear seismic analysis of single piles using finite element model: effect of plasticity of soil. *International Journal of Geomechanics ASCE* , vol. 5 (1), 35-44.

Makris N, Badoni D, Delis E, Gazetas G. Prediction of observed bridge response with soil–pile-structure interaction. *J Struct Engng ASCE* 1994;120(10):2992–3011.

Maiorano, R.M.S, Aversa, S. 2006. Importanza relativa di interazione cinematica ed inerziale nell’analisi dei pali di fondazione sotto azioni sismiche. In *Atti del V Convegno Nazionale dei Ricercatori di Geotecnica*, (Bari, Italy) . Hevelius ed., Benevento (Italy).

Maiorano, R.M.S., Aversa S., 2006. Importanza relativa di interazione cinematica ed inerziale nell’analisi dei pali di fondazione sotto azioni sismiche- *Atti del V Convegno Nazionale dei Ricercatori di ingegneria geotecnica*, Bari, 15-16 settembre 2006.

Maiorano, R.M.S., Aversa, S., and Wu, G. 2007. Effects of soil non-linearity on bending moments in piles due to seismic kinematic interaction. In *Proceedings of the 4th International*

Conference on Earthquake Geotechnical Engineering, paper N° 1574, Thessaloniki, Greece, June.

Maiorano, R.M.S., de Sanctis, L., Aversa, S., Mandolini, A. 2008. Kinematic response analysis of piled foundations under seismic excitation. *Canadian Geotechnical Journal*, (in print)

Makris N., Gazetas G. (1992). Dynamic pile-soil-pile interaction. Part II: lateral and seismic response. *Earthquake Engineering and Structural Dynamics*, Vol.21, 1992, pp 145-162.

Mamoon, S.M., Ahmad, S. (1990). Seismic response of piles to obliquely incident SH, SV and P waves. *Journal of Geotechnical Engineering*, ASCE, 117, 186-204.

Mamoon, S.M., Banerjee, P.K., 1990. Response of piles and pile groups to travelling SH waves. *Earthq. Engng. Struct. Dyn.*, 19 (4), 597-610.

Margason, E. "Pile Bending During Earthquakes", Lecture March 6, 1975, ASCE/UC-Berkeley seminar on design construction & performance of deep foundations, 1975

Margason, E. and Holloway, D.M. 1977. Pile design during earthquakes. In *Proceedings of the 6th World Conference on Earthquake Engineering*. New Delhi, 237-243.

Masayuki, H. & Shoichi, N. (1991). A study on pile forces of a pile group in layered soil under seismic loading. *Proc. 2nd Int. Conf Recent Advances Geotech. Earthq. Engng Soil Dyn.*, St Louis 3.

Massimino M.R., 2005 Experimental and numerical modelling of a cslaed soil-structure system. In: Maugeri M., Editor. *Seismic Prevention of Damage for Meditterrean Cities, a case History: the City of Catania (Italy)*. (pp. 227-241). Southampton: Wit Press (UK), ISBN: 88-555-2755-X/ ISSN: 1361-617X

Meymand P. J.1998, Shaking Table Scale Model Tests of Nonlinear Soil-Pile-Superstructure Interaction In Soft Clay. PhD Thesis, University of California, Berkeley

Mineiro, A.J.C. "Simplified Procedure for Evaluating Earthquake Loading on Piles", *De Mello Volume*, Lisbon, 1990

Mizuno H. (1987). Pile damage during earthquake in Japan (1923-1983). *Dynamic response of pile foundations: Experiments, observation and analysis*. T. Nogami, ed., ASCE, New York, 53-78.

Muir Wood, D., Crewe, A., Taylor, C.A., 2002, Shaking Table Testing of Geotechnical Models, *UPMG- International Journal of Physical Modelling in Geotechnics*, 2,1-13.

Muir Wood, D., 2004, *Geotechnical Modelling*, Spon Press, Oxfordshire.

Mylonakis G., Nikolaou A., Gazetas G. (1997). Soil-pile-bridge seismic interaction: kinematic and inertial effects. Part I: soft soil. *Earthquake Engineering Structural Dynamics*, 27, (3), 337-359.

Mylonakis, G. (2001). Simplified model for seismic pile bending at soil layer interfaces. *Soils and Foundations*, vol. 41, n. 4, 47-58.

Mylonakis, G., 1999. *Seismic Pile Bending at Deep Interfaces*. Report GEL-99-01, Geotechnical Laboratory, City College of New York.

National Cooperative Highway Research Program. (NCHRP 2001). *Static and dynamic lateral loading of pile groups*. Report 461.

NEHRP "Recommended Provisions for Seismic Regulations for New Buildings and other Structures", Building Seismic Safety Council, Washington, D.C., 1997

NEHRP-2003. Recommended provisions for seismic regulations for new buildings and other structures. Building Seismic Safety Council, Washington D.C.

Ng C.W., Zhang L., Nip D.C. (2001). Response of laterally loaded large-diameter bored pile groups. *Journal of Geotechnical and Geo-environmental Engineering*, Am. Soc. Civ. Engrs 127, no. 8, 658-669.

Nikolaou A. S., Mylonakis G., Gazetas G., 1995. Kinematic bending moments in seismically stressed piles. Report NCEER-95-0022, National Center for Earthquake Engineering Research. Buffalo: State University of New York.

Nikolaou S., Mylonakis G., Gazetas G., Tazoh T. 2001. Kinematic pile bending during earthquakes: analysis and field measurements. *Géotechnique*, 51 (5), 425-440

Nikolaou, A., Gazetas, G. (1997). Seismic design procedure for kinematically stressed piles. *Seismic behaviour of ground and geotechnical structures*, Seco & Pinto (eds): 253-260. Rotterdam: Balkema.

Nikolaou, A.S., and Gazetas, G. 1997. Seismic design procedure for kinematically loaded piles. In *Proceedings of the 14th International Conference Soil Mechanics and Foundation Engineering*. Hamburg, Special volume, ISSMFE TC4 Earthquake geotechnical engineering, pp.253-260.

Nogami. T., Jones. H. W., Mosher. R. L. (1991). Seismic response of pile-supported structures: assessment of commonly used approximations. *Proc. 2nd Int. Conf Recent Advances Geotech. Earthq. Engng Soil Dyn.*, St Louis 1,931-940.

Novak M. (1974). Dynamic stiffness and damping of piles. *Canadian Geotechnical Journal*, 11, 574-598.

Novak M. "Dynamic stiffness and damping of piles" *Canadian Geotechnical Journal*, 11, 574-591, 1974

Novak M., Sheta M. (1982). Dynamic response of piles and pile groups. *Proceedings 2nd International Conference on Numerical Methods in Offshore Piling*, Austin, 489-507.

Novak M. Piles under dynamic loads. In: *State of the art paper. Second international conference on recent advances in geotechnical earthquake engineering and soil dynamics*, vol. III. Missouri: University of Missouri-Rolla; 1991. p.250–73.

Novak, M. (1991). Piles under dynamic loads. *Proc. 2nd Int. Conf Recent Advances Geotech. Earthq. Engng Soil Dyn.*, St Louis 3, 2433-2455.

OPCM 3274. 2003. Primi elementi in materia di criteri generali per la classificazione sismica del territorio nazionale e di normative tecniche per le costruzioni in zona sismica. *Gazzetta Ufficiale della Repubblica Italiana*, n. 105-8/5/03.

Pender, M. 1993. Aseismic pile foundation design analysis. *Bullettin NZ National Society of Earthquake Engineering*. 26 (1), 49-160.

Penzien, J. (1970). Soil-pile foundation interaction. *Earthquake engineering* (ed. R. L. Wiegel), chapter 14. New York: Prentice-Hall.

Poulos, H.G., Tabesh, A. (1996). Seismic response of pile foundations – Some important factors. *Proc. 11th WCEE, Acapulco*, Paper No. 2085.

Randolph, M.F. 1981. Response of flexible piles to lateral loading. *Géotechnique*, 31(2), 247-259.

Rathje .M., Abrahamson N.A., Bray J.D., 1998. Simplified frequency content estimates of earthquake ground motions. *J. Geotech. Geoenv. Eng.*, vol. 124, n. 2, pp.150-159

Reese L.C., Cox W.R., Koop F.D. (1974). Analysis of laterally loaded piles in sand. Proc. VI OTC, Houston, Texas, pp 473-483.

Reese L.C., Van Impe W.F. (2001). Single piles and pile groups under lateral loading. Balkema, Rotterdam, The Netherlands.

Reese L.C., Welch R.C. (1975). Lateral loading of deep foundations in stiff clay. *Geotechnical Testing Journal*, GTJODJ, Vol.XII, no.1, pp 30-38.

References

ReLUIS, 2007. Report on the II year of activity on the research Theme 6.4 “Deep Foundation” (<http://www.reluis.it>)

ReLUIS, 2008. Report on the III year of activity on the research Theme 6.4 “Deep Foundation” (<http://www.reluis.it>)

Rollins K.M., Peterson K.T., Weaver T.J., 1998. Lateral load behavior of full-scale pile group in clay. *Journal of Geotechnical and Geoenvironmental Engineering*, ASCE, 124, (6), 468-478.

Rovithis E., Kirtas E., Pitilakis K. (2007a). Utilization of p-y curves for estimating soil-pile interaction under seismic loading. Proc. 2nd Japan-Greece Workshop on Seismic Design, Observation and Retrofit of Foundations. Vol.1, pp 357-368.

Rovithis E., Kirtas E., Pitilakis K. 2007a. Effect of the frequencies of the coupled Soil-Pile-Structure System on pile dynamic response. The 2nd Japan-Greece Workshop on Seismic Design, Observation, and Retrofit of Foundation. Tokyo, 3-4 April 2007.

Saitoh, M. 2005. Fixed-head pile bending by kinematic interaction and criteria for its minimization at optimal pile radius. *Journal of Geotechnical and Geoenvironmental Engineering*, ASCE, 131, 10, 1243-1251

Scassera G., Lanzo G., Mollaioli F., Stewart J.P., Bazzurro P., Decanini L.D., 2006. Preliminary comparison of ground motions from earthquakes in Italy with ground motion prediction equations for active tectonic regions. Proc. 8th US Nat. Conf. on Earthquake Eng., San Francisco, Paper No. 1824

Scasserra G., Lanzo G., Stewart J.P., D'Elia B. 2008. SISMA (Site of Italian Strong Motion Accelerograms): a web-database of ground motion recordings for engineering applications. Proceedings of the 2008 Seismic Engineering Conference commemorating the 1908 Messina and Reggio Calabria Earthquake, MERCEA'08, Santini & Moraci Editors, July 8-11, Reggio Calabria, Italy, Vol. 2, 1649-1656.

Seed, H.B., Idriss, I.M. 1982. Ground motions and soil liquefaction during earthquakes. *Earthquake Engineering Research Institute Monograph*. University of California, Berkeley, 1982.

Seed, H.B., Wong, R.T., Idriss, I.M., and Tokimatsu, K.1986. Moduli and damping factors for dynamic analyses of cohesionless soils. *J. of Geotechnical Engineering*, ASCE, 112:1016-1032.

Sen R, Davis TG, Banerjee PK. Dynamic analysis of piles and pile groups embedded in homogenous soils. *Earthquake Engng Struct Dyn* 1985;13(1):53–65.

Sheppard, D. A. “Seismic Design of Concrete Piling”, *PCI Journal* (March/April), 1983

-
- Smith, I.M., Griffiths, D.V. (1988). Programming the finite element method. 2nd ed. J. Wiley and Sons, New York.
- Sica, S., Mylonakis, G., Simonelli, A.L., 2007. Kinematic bending of piles: analysis vs. code provisions, in 4th Int. Conf. on Earthquake Engineering, Thessaloniki
- Sica, S., Mylonakis, G., Simonelli, A.L., 2009. Kinematic pile bending in layered soils: linear vs. equivalent-linear analysis, in Int. Conf. on Performance-Based Design in Earthquake Geotechnical Engineering, IS-Tokyo 2009
- Simonelli A.L., Sica S. 2007. Interazione cinematica palo-terreno: analisi ed indicazioni di normativa, XII Convegno Nazionale L'ingegneria sismica in Italia, ANIDIS, Pisa
- Simonelli A.L., Sica S. 2008. Soil-pile kinematic interaction. Panel paper. In Proc. of the 2008 Seismic Eng. Conference commemorating the 1908 Messina and Reggio Calabria Earthquake, MERCEA'08, Reggio Calabria, Italy (in print)
- Stewart, J.P., Fenves, G.L., Seed, R.B. (1999). Seismic soil-structure interaction in buildings. I: analytical methods. Journal of Geotechnical and Geoenvironmental Engineering, ASCE, 125, 1, 26-37.
- Tajimi, H. (1969). Dynamic analysis of structure embedded in elastic stratum. Proc. 4th Wld Conf. Earthq. Engng, Santiago, 53-69.
- Tajimi, H. (1977). Seismic effects on piles. Proc. 2nd. Conf: Soil Mech., Tokyo, state-of-the-art report 2, Specialty Session 10, 15-26.
- Tan, F.S.C., 1990, Centrifuge and theoretical modelling of conical footings on sand, PhD Thesis, University of Cambridge, U.K..
- Tazoh, T., Shimizu, K., Wakahara, T. "Seismic observations and analysis of grouped piles. Dynamic response of pile foundations: experiment, analysis and observation", Geotech. Spec. Publ. ASCE, 11, 1-20, 1987
- Tazoh, T., Wakahara, T., Shimizu, K. & Matsuzaki, M. (1988). Effective motion of group pile foundations. Proc. 9th Wld Conf. Earthq. Engng, Tokyo 3, 587-592.
- Tokimatsu K, Suzuki H., Sato M, 2005, Effects of inertial and kinematic interaction on seismic behaviour of pile with embedded foundation, Soil Dynamics and Earthquake Engineering 25 (2005) 753-762
- Tokimatsu K, Suzuki H. 2009, Seismic soil-pile-structure interaction based on large shaking table tests. in Int. Conf. on Performance-Based Design in Earthquake Geotechnical Engineering, IS-Tokyo
- Tomisawa K, and Muira S, 2007 A study on seismic response of single pile in improved ground through dynamic centrifuge model tests, Thessaloniki 4th International Conference on Earthquake Geotechnical Engineering June 25-28, 2007
- Towhata I, Vargas-Monge W., Orense R.P., Yao M. Shaking table tests on subgrade reaction of pipe embedded in sandy liquefied subsoil. Soil Dynamics and Earthquake Engineering 18 (1999) 347-361
- Velestos A.S. & Ventura C.E. 1984 "Efficient analysis of dynamic response of linear system". Earthquake Engineering and Structural Analysis, 12, 521-536
- Vucetic M., Dobry R. 1991. Effect of soil plasticity on cyclic response. J. Geotech. Engrg., Vol. 117 (1), pp. 89-107
- Whitman R.V., Bielak J. (1980). Foundations. Design of earthquake resistant structures, Ed. E. Rosenblueth, Pentech Press, Plymouth, pp. 223-260.

Wolf, J. P. & Von Arx, G. A. (1982). Horizontally traveling waves in a group of piles taking pile-soil-pile interaction into account. *Earthq. Engng Struct. Dyn.* 10,225-237.

Wolf, J.P., von Arx, G.A., de Barros, F.C.P., Kakubo, M., 1981. Seismic analysis of the pile foundation of the reactor building of the NPP Angra 2. *Nucl. Eng. Des.*, 65, 329-341.

Wu, G. 2006. VERSAT-P3D: Quasi-3D dynamic finite element analysis of single piles and pile groups. Version 2006. 2000-2006 Wutec Geotechnical International, Canada, 2006.

Wu, G., and Finn, W.D.L. 1997a. Dynamic elastic analysis of pile foundations using finite element method in the frequency domain. *Canadian Geotechnical Journal*, 34:34-43.

Wu, G., and Finn, W.D.L. 1997b. Dynamic nonlinear analysis of pile foundations using finite element method in the time domain. *Canadian Geotechnical Journal*, 34:44-52.

J. Yang & X.R. Yan, 2009-11-24 Nonlinearity in seismic soil-structure interaction, in *Int. Conf. on Performance-Based Design in Earthquake Geotechnical Engineering*, IS-Tokyo 2009,

Yao S., Kobayashi K., Yoshida N., Matsuo H., Interactive behavior of soil-pile superstructure system in transient state to liquefaction by means of large shake table tests. *Soil Dynamics and Earthquake Engineering* 24 (2004) 397-409

Zhang F. & Kimura M. 2002 “Numerical prediction of the dynamic behaviour of a RC group-pile foundation”, *Soils and Foundations*, 42, 3, 77-92

Zhang F., Kimura M., Nakai T., Hoshikawa T. 2000 “Mechanical behaviour of pile foundations subjected to cyclic lateral loading up to the ultimate state”, *Soils and Foundations*, 40, 5, 1-17

Acknowledgments

This work was the result of a joint research on soil-pile interaction among the University of Sannio (Italy), the University of Bristol (United Kingdom) and the University of Patras (Greece).

My most sincere thanks to Prof. A.L. Simonelli for his precious mentorship and inquisitiveness. They will always be valued, and I greatly appreciate the opportunity that Prof. Simonelli gave me to work with him and become involved with other aspects of his work.

I wish to extend my best thanks to all the members of the University of Sannio, in particular Prof. S. Sica, who provided me with precious guidance, support and encouragement throughout all the period of my PhD work.

I also would like to thank Prof. G. Mylonakis from the University of Patras and Prof. C. Taylor from the University of Bristol, who also provided a wealth of ideas on the experimental work.

I would particularly like to thank Dr. L. Dighoru for her assistance with all aspects of the testing program: she provided valuable input on the experimental components of the project, especially as regards the tests on the shaking table at Bristol University. I also wish to thank for their friendly help the technicians of Bristol Laboratory, Dave and Edd, as well as Eleonora and Domenico for their valuable contribution. A honest recognition to Prof. S. Bhattacharya for his helpful and continuous assistance during the researches in Bristol and his fruitful suggestions for the experimental analysis.

Finally, this research would have not been possible without the support of RELUIS (Rete dei Laboratori Universitari di Ingegneria Sismica), funded by the Dipartimento della Protezione Civile. The support from RELUIS is gratefully acknowledged.

APPENDIX I list of the tests

Soil Configuration	Pile head condition	N° test	Input motion
E	free	16	All 3 scale; all 3 input motion
	fix: no rotation head	16	All 3 scale; all 3 input motion
	fix + mass: no rotation head+ oscillator	0	
	guide: free head+ mass	16	All 3 scale; all 3 input motion
	mass: free head+ mass + oscillator (L=400mm)	16	All 3 scale; all 3 input motion
	mass: free head+ mass + oscillator (L=200mm)	18	All 3 scale; all 3 input motion
	PULSE TEST	30	
	Push test	1	
Soil Configuration	Pile head condition	N° test	Input motion
BE+ E	free	14	A-STU000:all 3 scale; A-TMZ270: 12 scale;2 scale
	fix: no rotation head	10	A-STU000:all 3 scale; A-TMZ270: 12 scale;2 scale
	fix +mass: no rotation head+ oscillator (L=200mm)	12	A-STU000:all 3 scale; A-TMZ270: 12 scale;2 scale
	guide: free head+ mass	14	A-STU000:all 3 scale; A-TMZ270: 12 scale;2 scale
	mass: free head+ mass + oscillator (L=400mm)	0	
	mass: free head+ mass + oscillator (L=200mm)	18	A-STU000:5 scale;2 scale A-TMZ270: 12 scale;2 scale
	PULSE TEST	38	
	Hammer test from the top	6	
Soil Configuration	Pile head condition	N° test	Input motion
E+R	free	22	All 3 scale; all 3 input motion
	fix: no rotation head	18	All 3 scale; all 3 input motion
	fix+mass: no rotation head+ oscillator (L =200 mm)	12	A-STU000:12 scale; 5 scale,2 scale; A-TMZ270: 12 scale; R-NCB 090:12 scale,5 scale
	guide: free head+ mass	12	All 3 scale; all 3 input motion
	mass: free head+ mass + oscillator (L=400mm)	17	All A-STU000; all ATMZ 270; R-NCB 090: 5 scale, 2 scale
	mass: free head+ mass + oscillator (L=200mm)	2	A-TMZ270: 2 scale; R-NCB 090:2 scale
	PULSE TEST	9	
	LVDT Calibration	1	

APPENDIX II: mass of the oscillator

H = 200 mm	Configuration I : LB fraction E			Configuration II: LB fraction E + LB fraction B+E			Configuration III : Rubber + LB fraction E			
	Sturno 000		Effective Mass	Sturno 000		Effective Mass	Sturno 000		Effective Mass	
	ω p	$\omega m/\omega p$	Mass	ω p	$\omega m/\omega p$	Mass	ω p	$\omega m/\omega p$	Mass	
	rad/sec		gr	rad/sec		gr	rad/sec		gr	
	18.84	12	160	18.84	12	150	18.84	12	150	
		5	400		5	400		5	400	
		2	1000		2	1000		2	800	
	Tolmezzo 270		Effective Mass	Tolmezzo 270		Effective Mass	Tolmezzo 270		Effective Mass	
	ω p	$\omega m/\omega p$	Mass	ω p	$\omega m/\omega p$	Mass	ω p	$\omega m/\omega p$	Mass	
	rad/sec		g	rad/sec		gr	rad/sec		gr	
	12.56	12	380	12.56	12	400	12.56	12	400	
		2	2200		2	2200		2	2200	
	Norcia 090		Effective Mass				Norcia 090		Effective Mass	
	ω p	$\omega m/\omega p$	Mass				ω p	$\omega m/\omega p$	Mass	
	rad/sec		gr				rad/sec		gr	
	31.4	12	60				31.4	12	60	
		5	140					5	150	
		2	350					2	350	
H = 400 mm	Configuration I : LB fraction E			Configuration II : LB fraction E + LB fraction B+E			Configuration III : Rubber + LB fraction E			
	Sturno 000		Effective Mass	Sturno 000		Effective Mass	Sturno 000		Effective Mass	
	ω p	$\omega m/\omega p$	Mass	ω p	$\omega m/\omega p$	Mass	ω p	$\omega m/\omega p$	Mass	
	rad/sec		gr	rad/sec		gr	rad/sec		gr	
		18.84	12	20	18.84	12	20	18.84	12	20
			5	50		5	50		5	50
			2	120		2	120		2	120
		Tolmezzo 270		Effective Mass	Tolmezzo 270		Effective Mass	Tolmezzo 270		Effective Mass
		ω p	$\omega m/\omega p$	Mass	ω p	$\omega m/\omega p$	Mass	ω p	$\omega m/\omega p$	Mass
		rad/sec		gr	rad/sec		gr	rad/sec		gr
	12.56	12	50	12.56	12	50	12.56	12	50	
		2	300		2	300		2	300	
	Norcia 090		Effective Mass				Norcia 090		Effective Mass	
	ω p	$\omega m/\omega p$	Mass				ω p	$\omega m/\omega p$	Mass	
	rad/sec		gr				rad/sec		gr	
	31.4	12	7				31.4	12	7	
		5	20					5	20	
		2	50					2	50	

APPENDIX III: Raw data

1 INTRODUCTION

In this Appendix the raw data of all tests discussed in Chapter 5 are plotted. In particular the plots are relative to:

- time histories of acceleration in sand; on the external wall of the shear stack; on the top of pile; on the top of SDOF;
- the time histories of displacement of the shear stack;
- the time histories of strain gauges located at the different elevations along the pile (for each elevation there are two strain gauges).

Table 1 shows the legend of instrumentation, it has been defined the correspondence between channels and instruments. In figure A the layout of instrumentation inside and outside shear stack is illustrated. In figure B a schema of all strain gauges along the pile is shown.

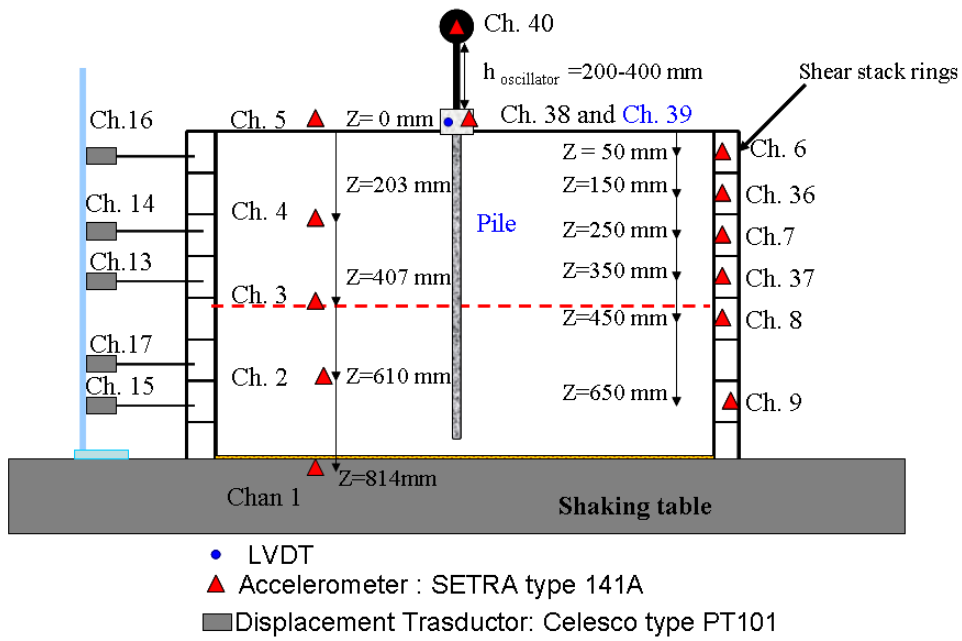


Figure A: Layout of instrumentations

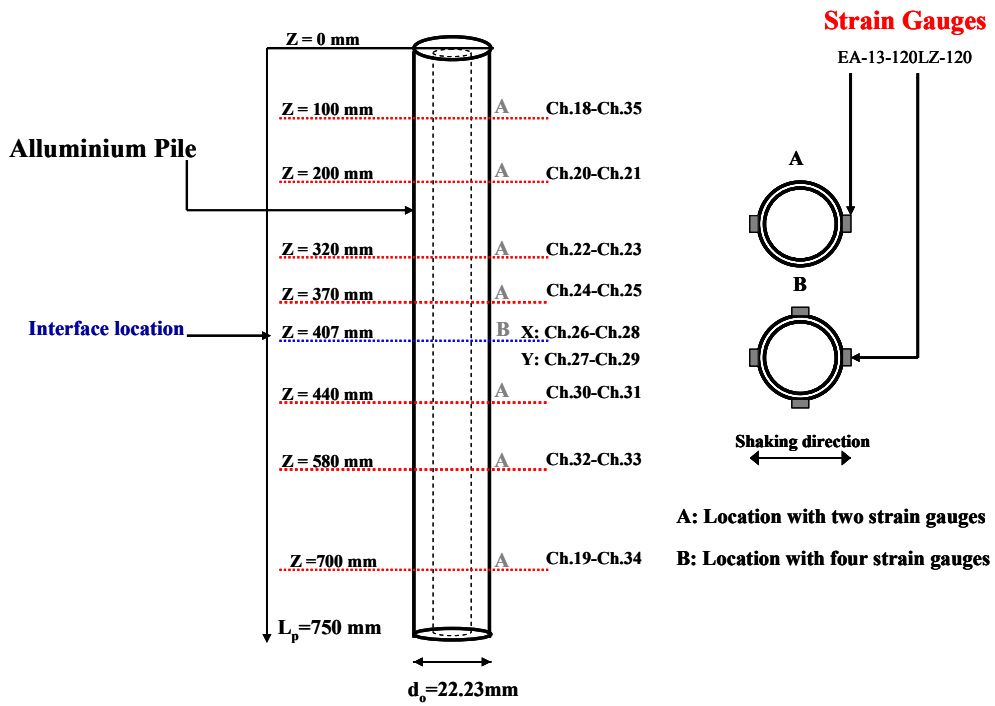


Figure B: strain gauges along the pile

Table 1: Test instrumentation record

TIRFRM.DOC		Test Ref:				Date / Time: 14/07/08				
TEST INSTRUMENTATION RECORD										
Channel	Instrument Data		Position (x,y,z)		Instrumentation to Amplifier cable no.	Amplifier Data		Filter Data		Filter to A/D cable no.
ch.	type	location		calibration		type	ch.	type	ch.	-3dB
1	Setra 1407	Shaking table	(0,0,810)	1 V /g	A050	Fylde	10548	Fern	2	80 Hz
2	Setra 6982	In sand, bottom quarter	(270,490,610)	1 V/g	A051	Fylde	1523	Fern	15	80 Hz
3	Setra 6983	In sand, half depth	(270,490,407)	1 V/g	A052	Fylde	1524	Fern	16	80 Hz
4	Setra 6985	In sand,	(270,490, 203)	1 V/g	A053	Fylde	1526	Fern	20	80 Hz
5	Setra 6984	Sand surface	(270,490,0)	1 V/g	A054	Fylde	1525	Fern	21	80 Hz
6	Setra 1406	Outside,Ring1		1 V/g	A055	Fylde	10559	Fern	13	80 Hz
7	Setra 1408	Outside,Ring3		1 V/g	A020	Fylde	10549	Fern	3	80 Hz
8	Setra 1402	Outside,Ring5		1 V/g	A056	Fylde	10547	Fern	1	80 Hz
9	Setra 1412	Outside,Ring7		1 V/g	A010	Fylde	10560	Fern	14	80 Hz
10	Setra 6985	Sand surface Y	(270,800,255)	1 V/g	A024	Fylde	10557	Fern	11	80 Hz
11	Setra 1409	Sand surface Y	(270,260,255)	1 V/g	A025	Fylde	10550	Fern	4	80 Hz
12	Setra 1410	Sand surface Z	(270,260,255)	1 V/g	A026	Fylde	10551	Fern	5	80 Hz
13	CEL 1728	Ring 4	(-, -,350)	55.55mm/V	A004			Fern	25	80 Hz
14	CEL 1730	Ring 3	(-, -,250)	55.55mm/V	A006			Fern	26	80 Hz
15	CEL 1727	Ring 7	(-, -,650)	55.55mm/V	A005			Fern	28	80 Hz
16	CEL 1729	Ring 1	(-, -,50)	55.55mm/V	A007			Fern	29	80 Hz
17	CEL 1722	Ring 5	(-, -,450)	41.67 mm/V	A008			Fern	30	80 Hz
36	Setra 6407	Outside, Ring2	(-, -,150)	1V/g	A016	Fylde	10555	Fern	9	
37	Setra 6409	Outside,Ring4	(-, -,340)	0.65 V/g	A011	Fylde	1529	Fern	12	
38	Setra 6981	Y-direction PILE HEAD		1 V/g	A015	Fylde	1522	Fern	17	
39	LVDT	Y-direction PILE HEAD	Excitation 15 V	4.352 mm/V	A003	RDP 611		Fern	22	

40	Setra 6980	Y-Mass SDOF		1 V/g	A014	Fylde	1521		31	
18	SG 27	100-Y-left		1000 $\mu\epsilon/V$	BNC A01			Fern	6	80 Hz
19	SG 26	700-Y-right		1000 $\mu\epsilon/V$	BNC A02					
20	SG 22	200-Y-right		1000 $\mu\epsilon/V$	BNC A03					
21	SG 23	200-Y-left		1000 $\mu\epsilon/V$	BNC A04					
22	SG 21	320-Y-right		1000 $\mu\epsilon/V$	BNC A05					
23	SG 20	320-Y-left		1000 $\mu\epsilon/V$	BNC A06				22	
24	SG 7	370-Y-left		1000 $\mu\epsilon/V$	BNC A07				23	
25	SG 8	370-Y-right		1000 $\mu\epsilon/V$	BNC A08				24	
26	SG 4	407-X- Hole		1000 $\mu\epsilon/V$	BNC A09					
27	SG 5	407-Y-right		1000 $\mu\epsilon/V$	BNC A010				32	
28	SG 6	407-X		1000 $\mu\epsilon/V$	BNC A011					
29	SG 9	407-Y-left		1000 $\mu\epsilon/V$	BNC A012				31	
30	SG 2	440-Y-left		1000 $\mu\epsilon/V$	BNC B01					
31	SG 3	440-Y-right		1000 $\mu\epsilon/V$	BNC B02					
32	SG 25	580-Y-left		1000 $\mu\epsilon/V$	BNC B03					
33	SG 24	580-Y-right		1000 $\mu\epsilon/V$	BNC B04					
34	SG 0	100-Y-left		1000 $\mu\epsilon/V$	BNC B05					
35	SG 28	700-Y-right		1000 $\mu\epsilon/V$	BNC B06					

2 SOIL CONFIGURATION: E_LEIGHTON BUZZARD FRACTION E

2.1 E_STU12_FH

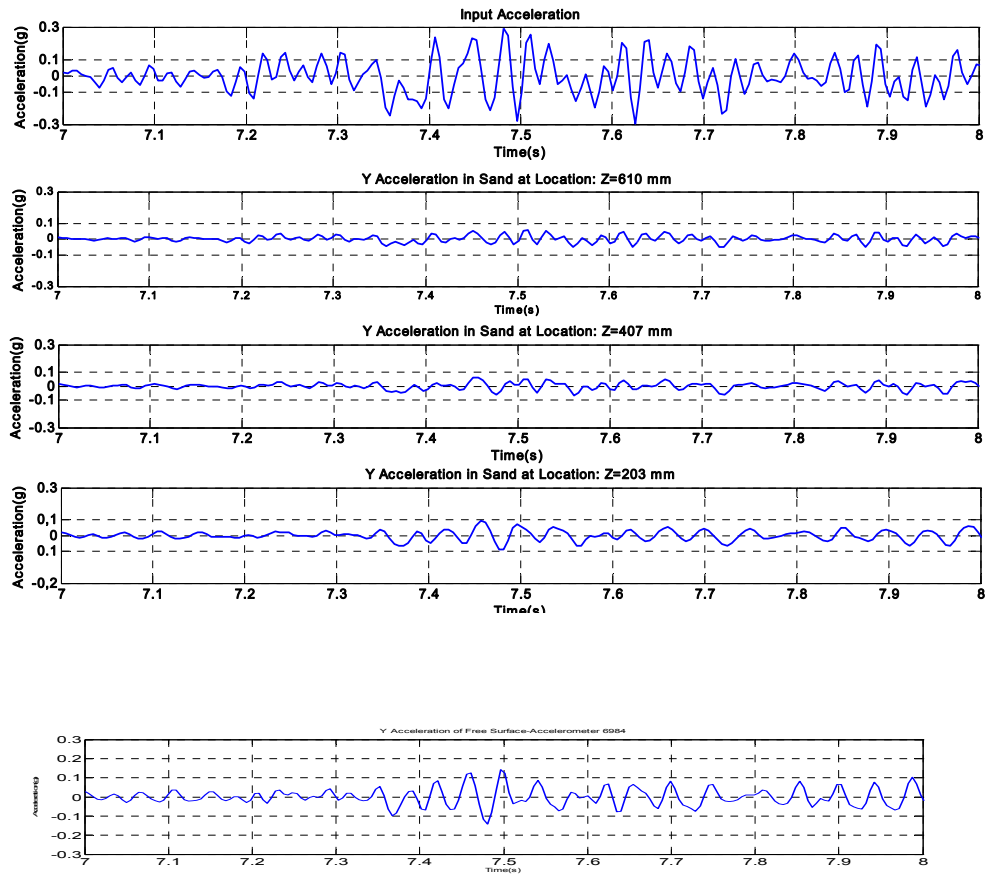


Figure 2: time histories acceleration in sand

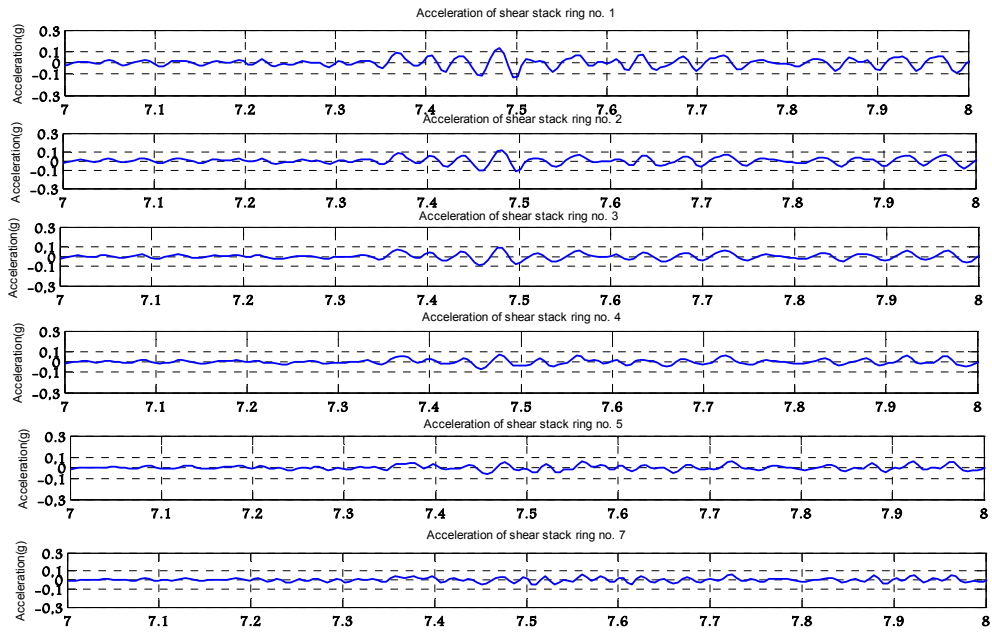


Figure 1.2 : time histories Acceleration on the shear stack external wall

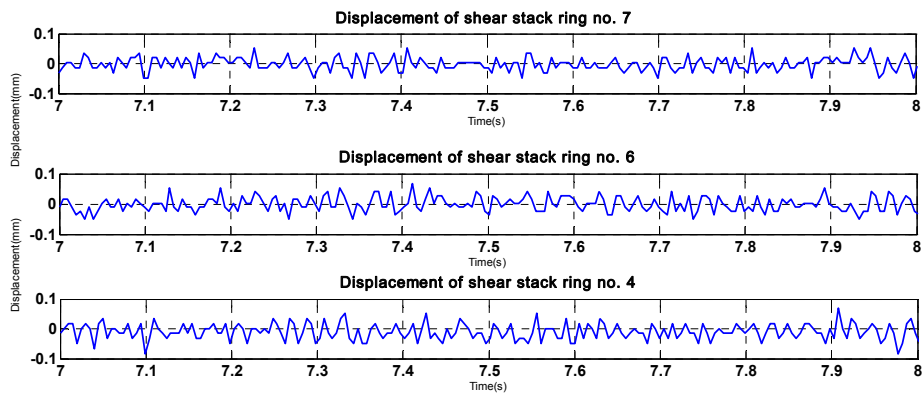


Figure 1.3: Displacement_Celesco Trasductor measurement

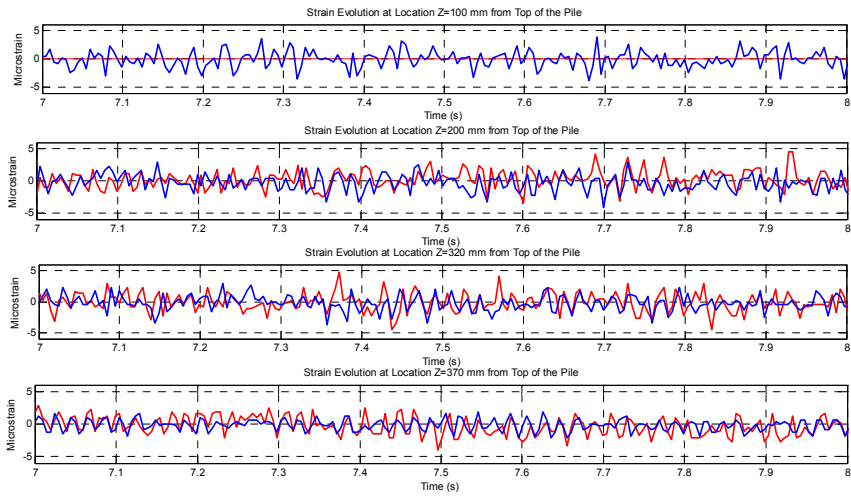


Figure 1.3: Raw strain gauges data from 100 mm to 370 mm from the pile head

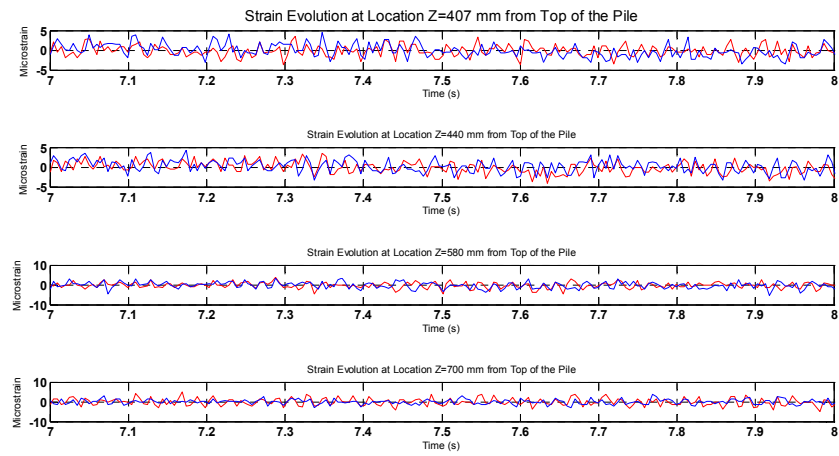


Figure 1.4: Raw strain gauges data from 407mm to 700 mm from the pile head

2.2

E_STU5_FH

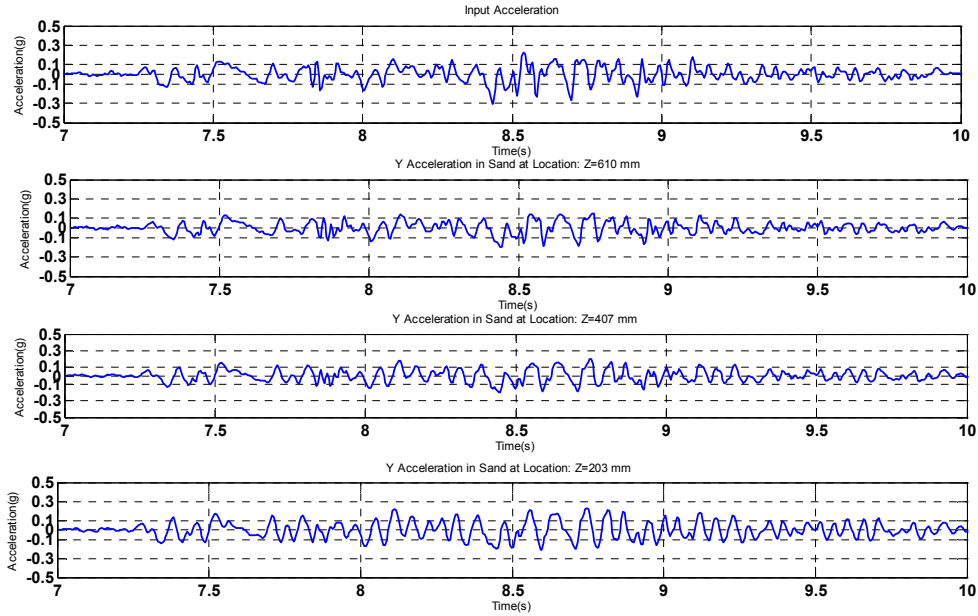


Figure 1.5: time histories acceleration in sand

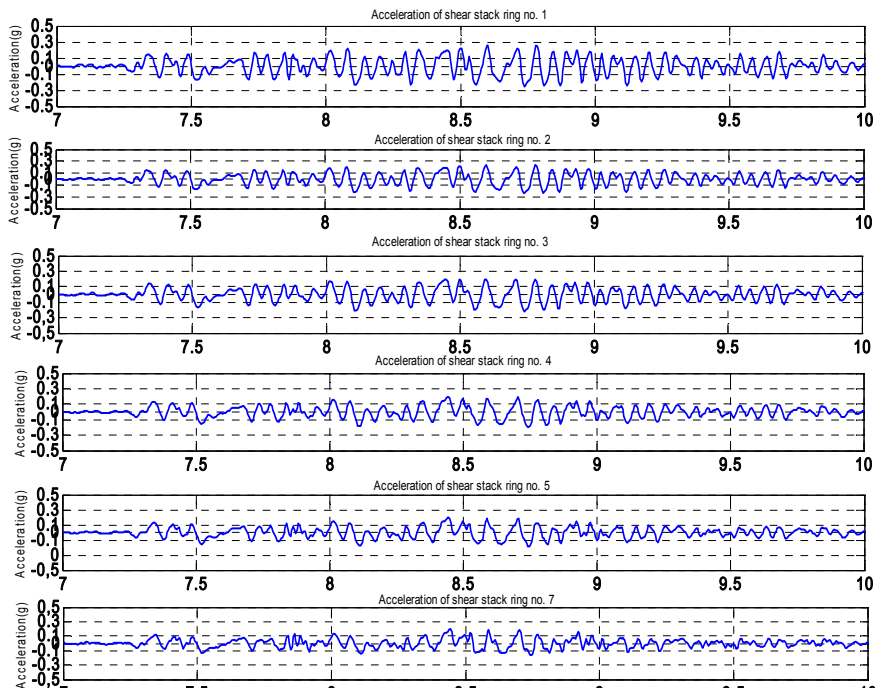


Figure 1.6: Time histories acceleration_external array

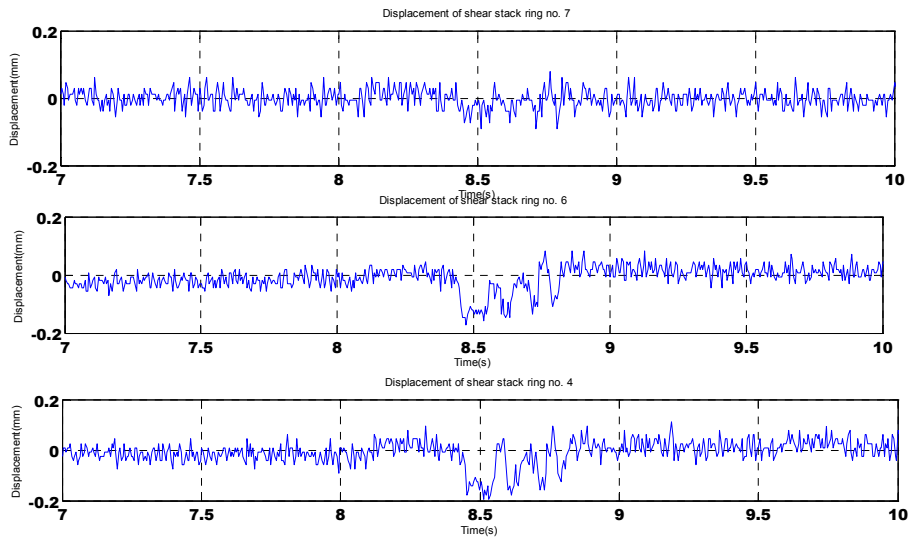


Figure 1.7: Displacement of shear stack

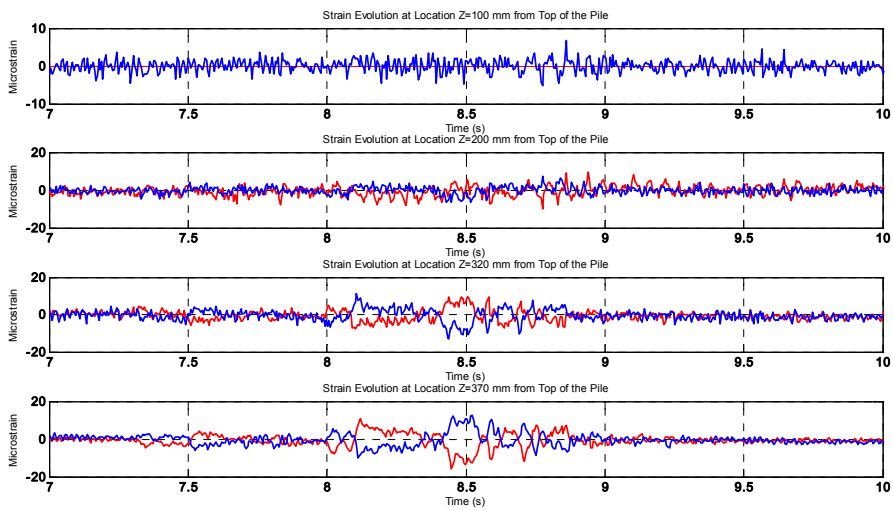


Figure 1.8: strain gauges 100-407 mm

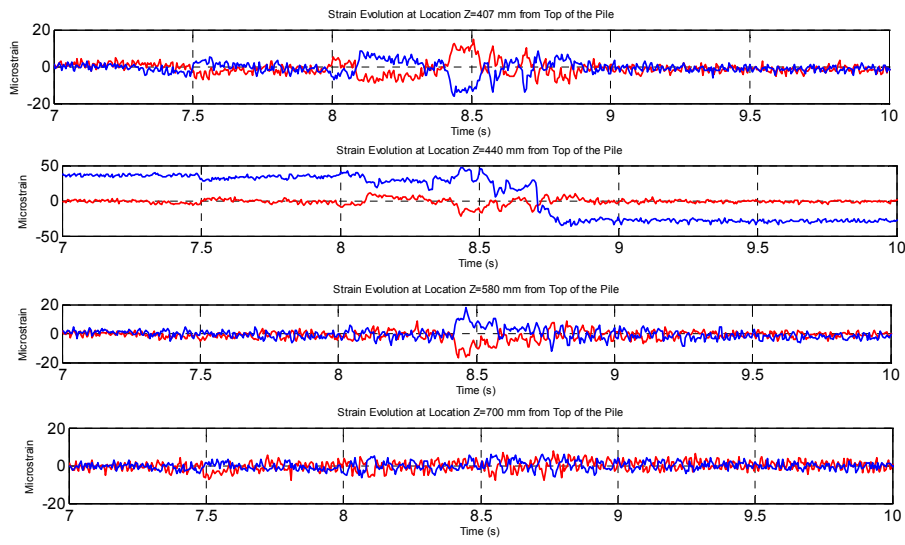


Figure 1.9: Strain gauges 440-700 mm

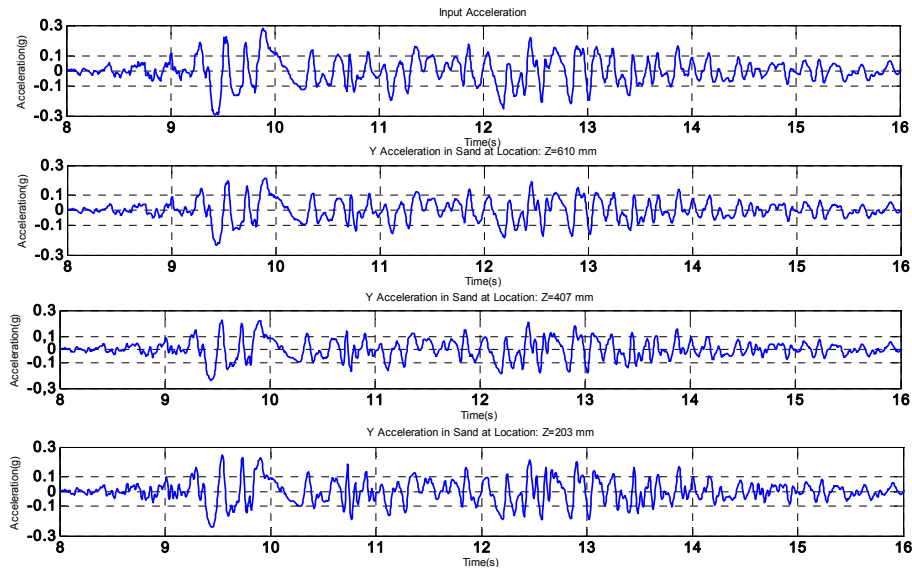


Figure 20: acceleration time histories: inside array

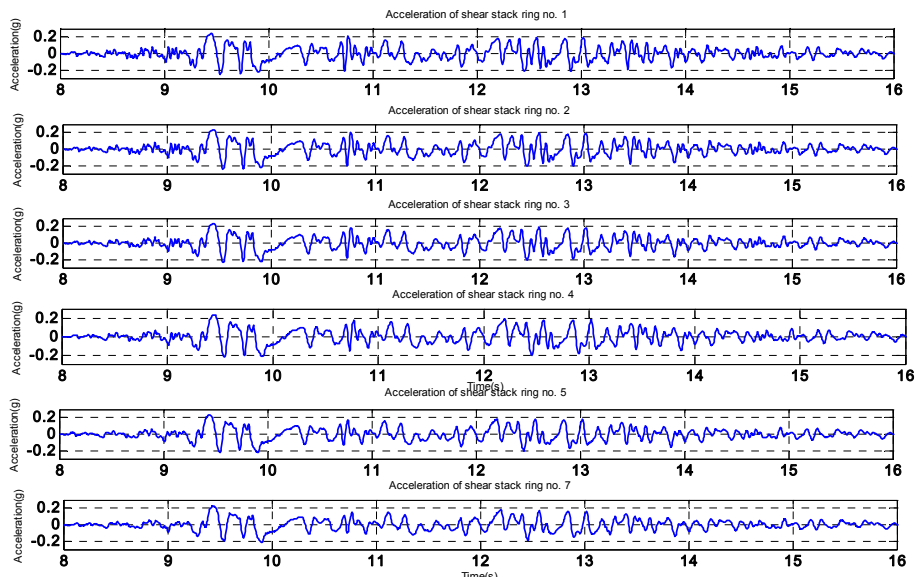


Figure 21: acceleration time histories: outside array

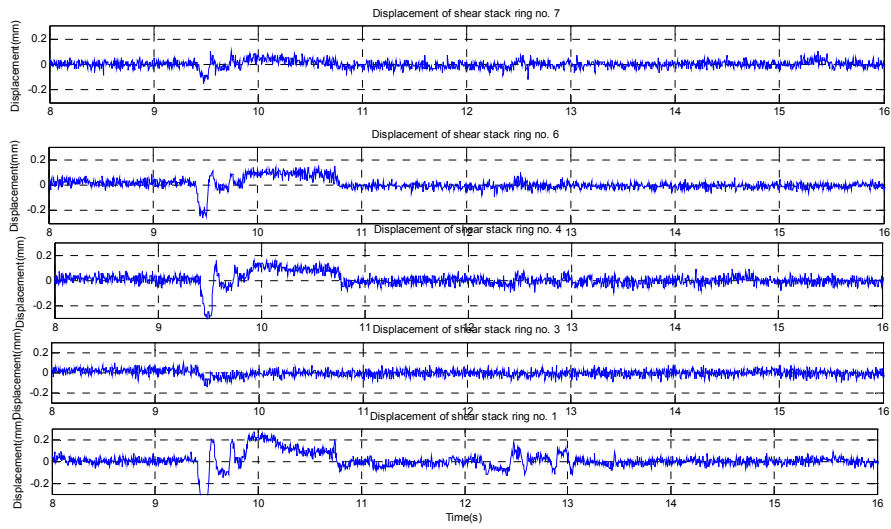


Figure 22: displacement of shear stack

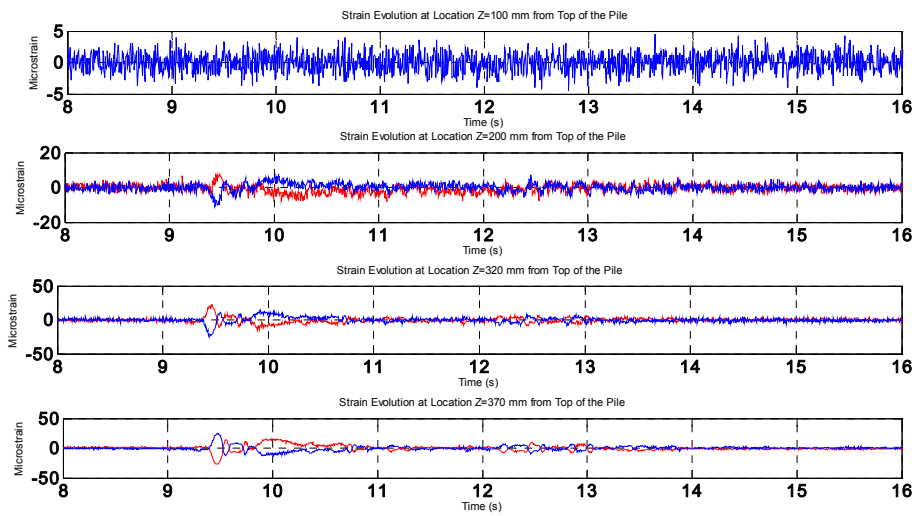


Figure 23: strain gauges 100-407 mm

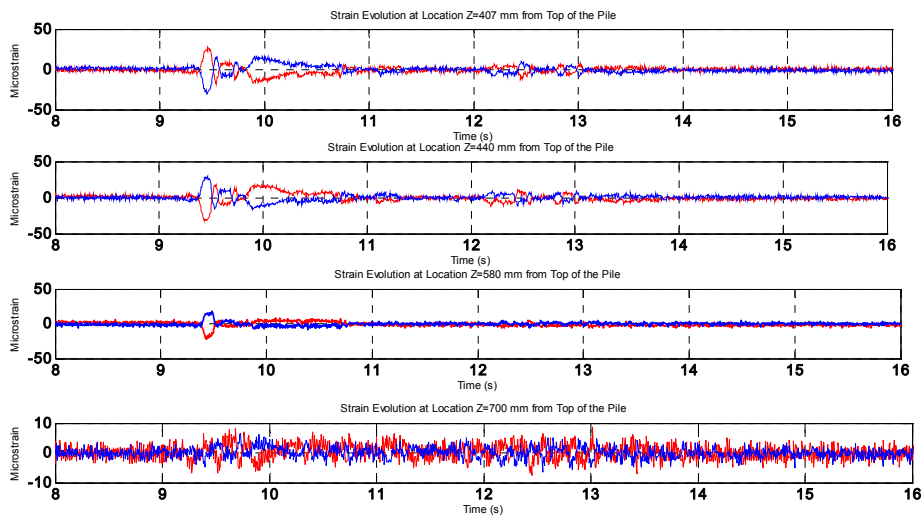


Figure 1.14: strain gauges 440-700 mm

2.4 E_TMZ 12_FH

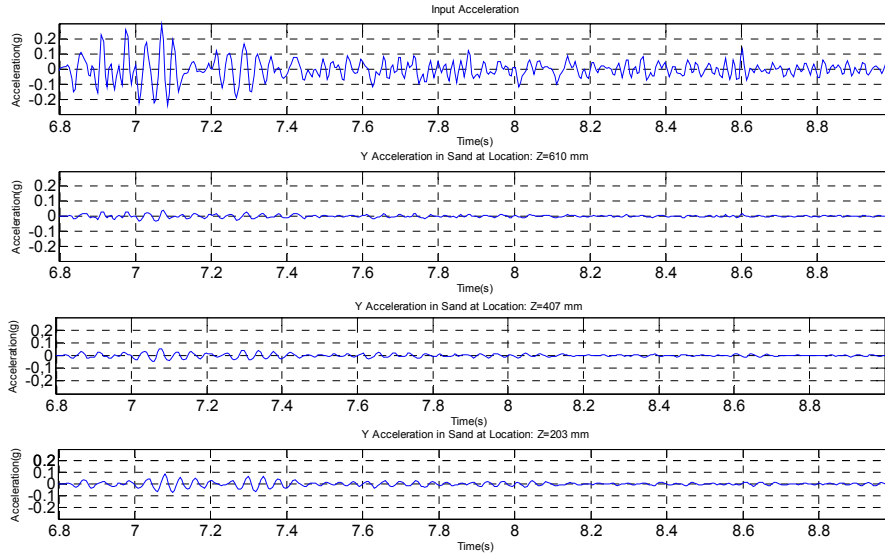


Figure 25: time histories acceleration: array inside

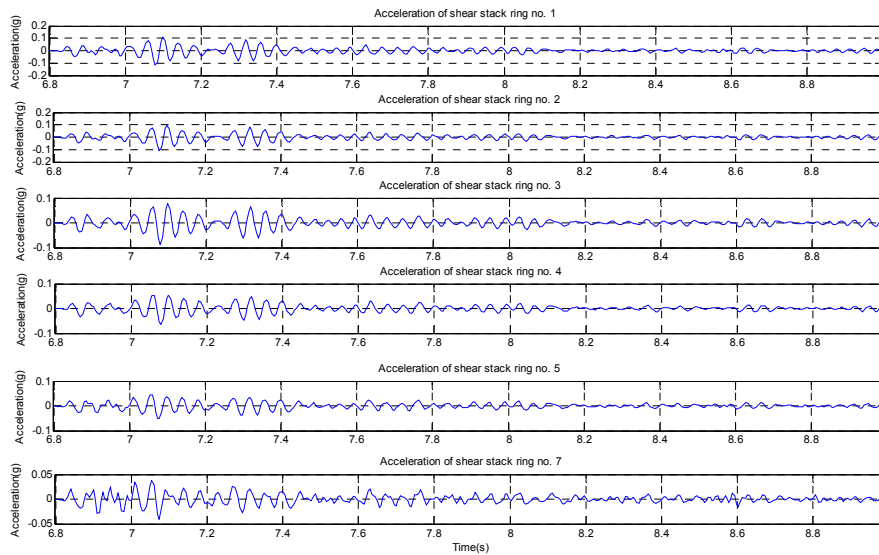


Figure 1.16: time histories acceleration: array outside

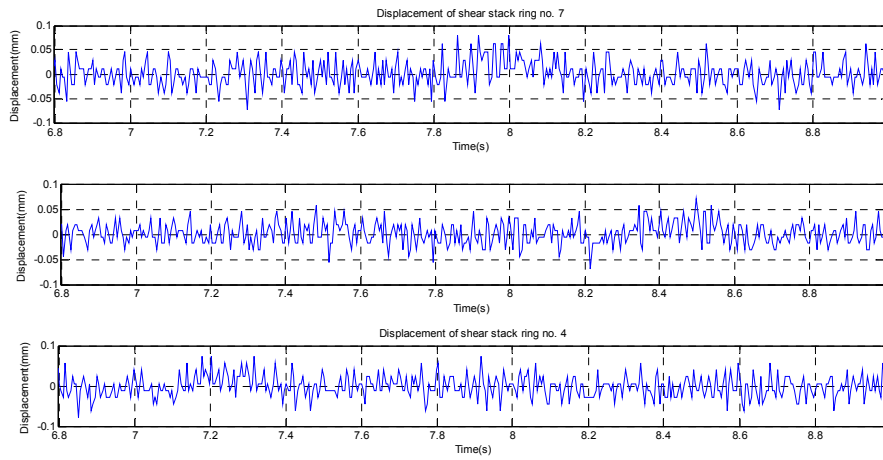


Figure 27: displacement of shear stack

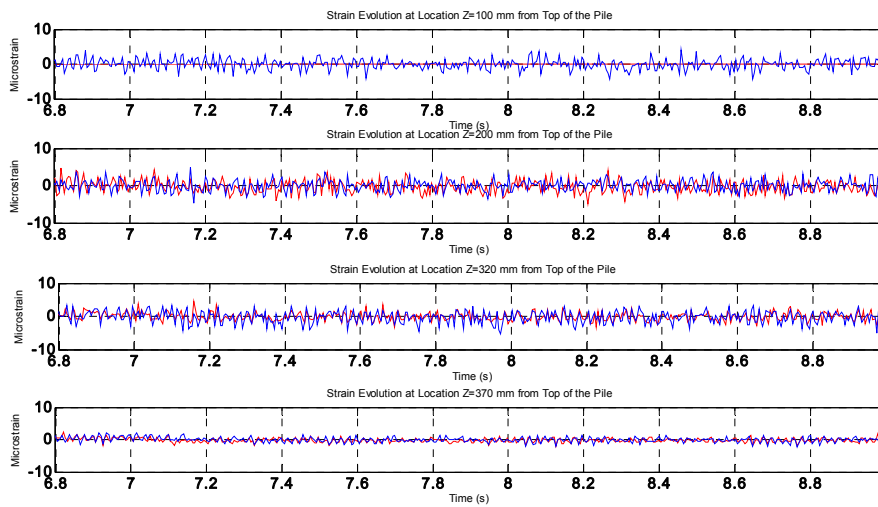


Figure 28: strain gauges 100-407 mm

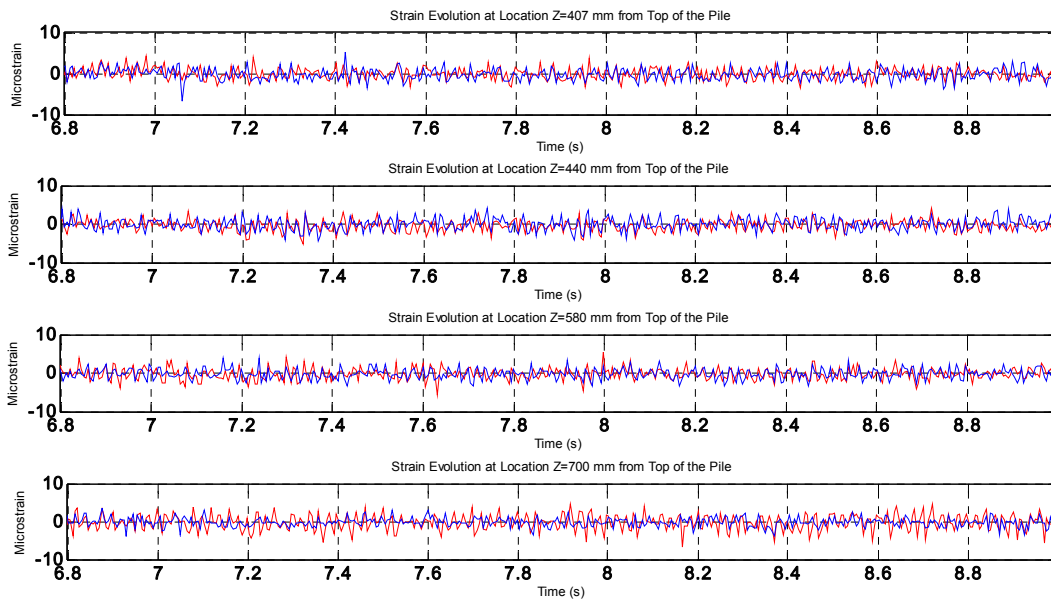


Figure 29: strain gauges 440-700 mm

2.5 *E_TMZ 2_FH*

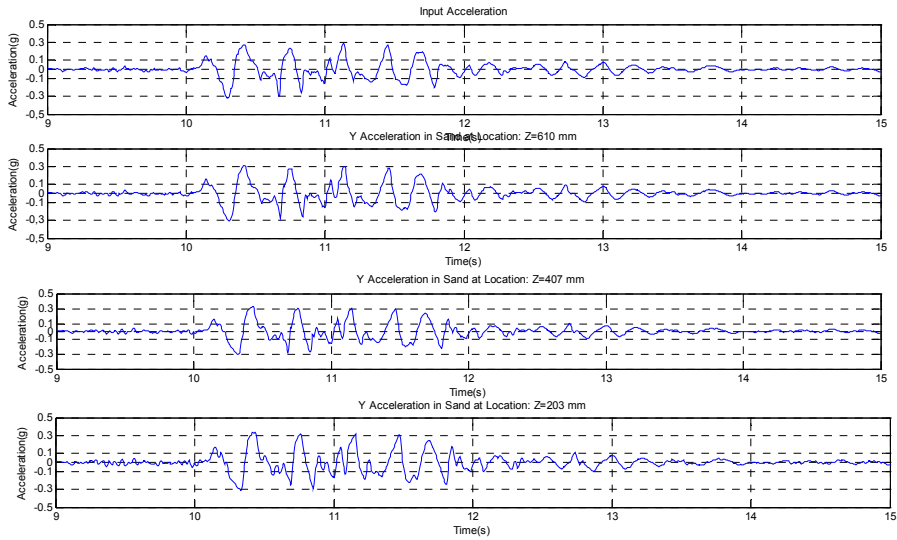


Figure 2.20: Acceleration : array inside

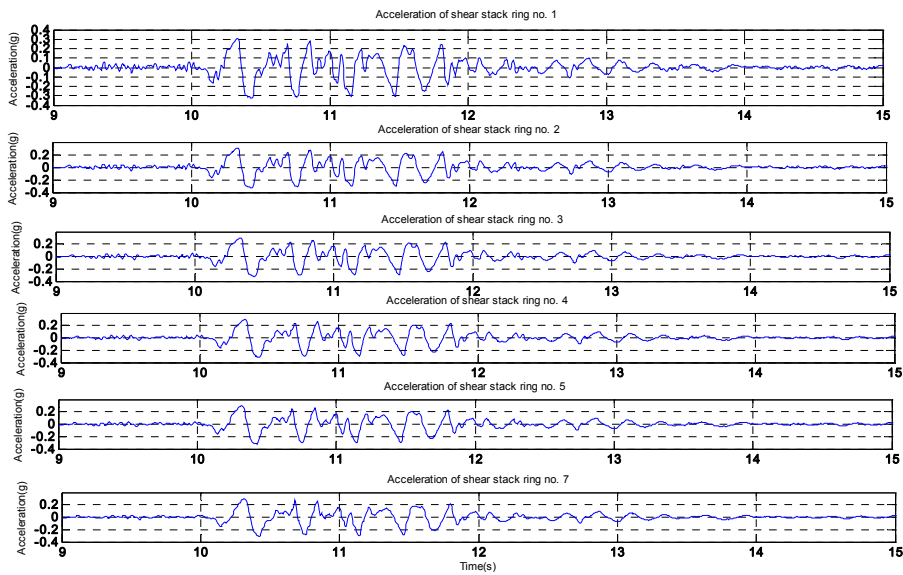


Figure 1.21: Acceleration: array outside

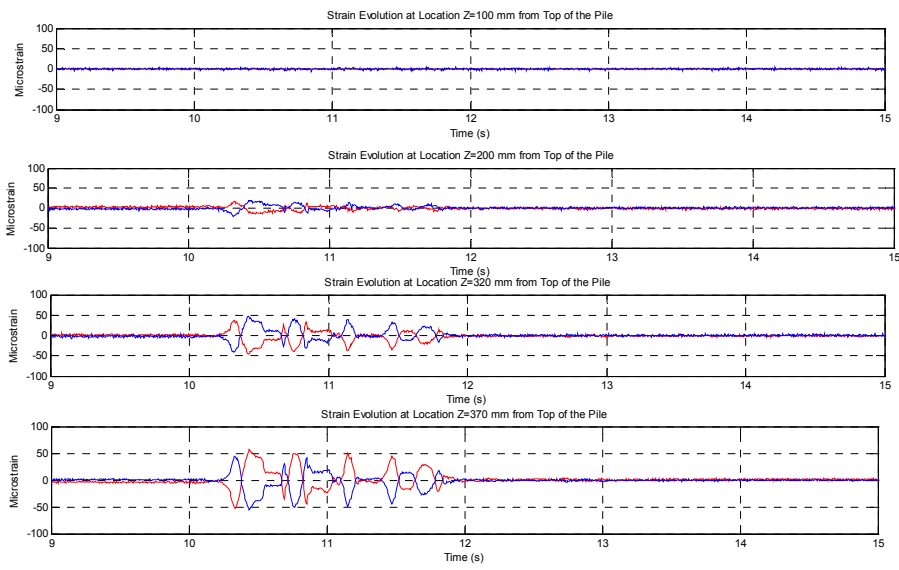


Figure 1.22: strain gauges 100-407 mm

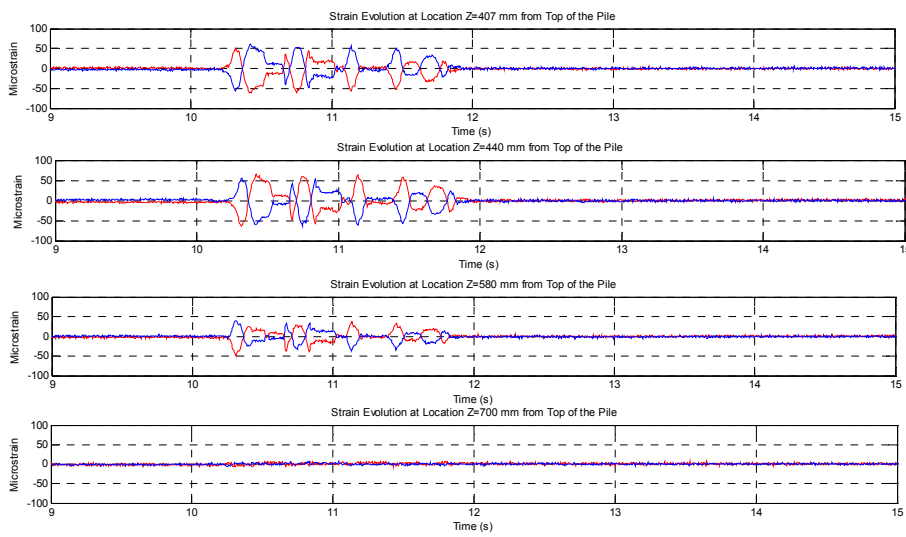


Figure 1.23: strain gauges 440-700 mm

2.6 *E_NCB 12_FH*

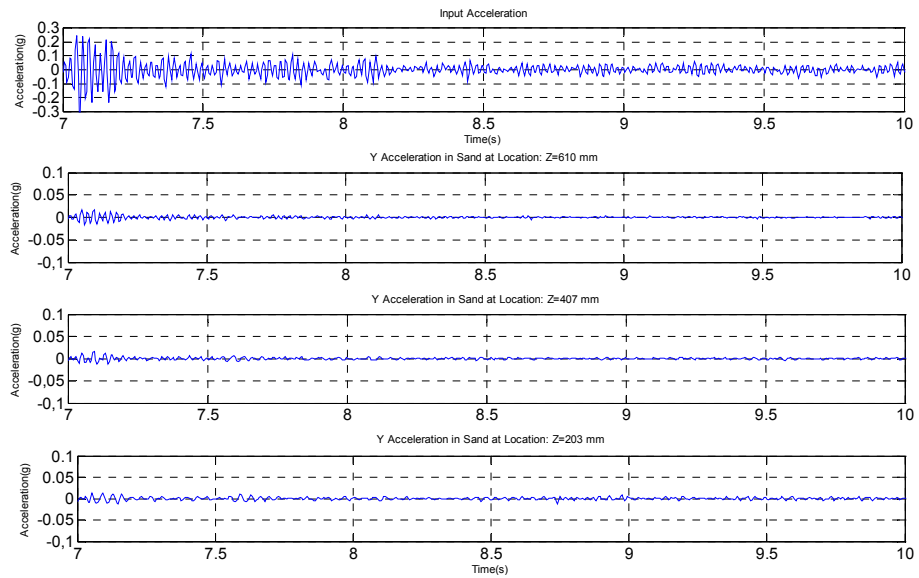


Figure 1.24: Acceleration in sand

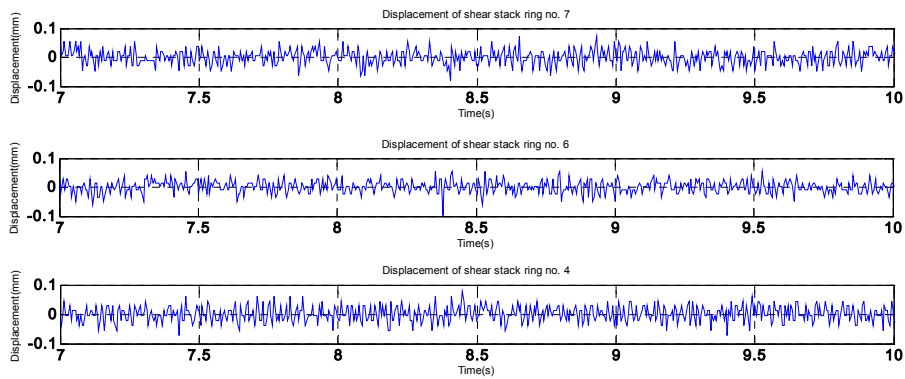


Figure 1.25: Displacement of shear stack

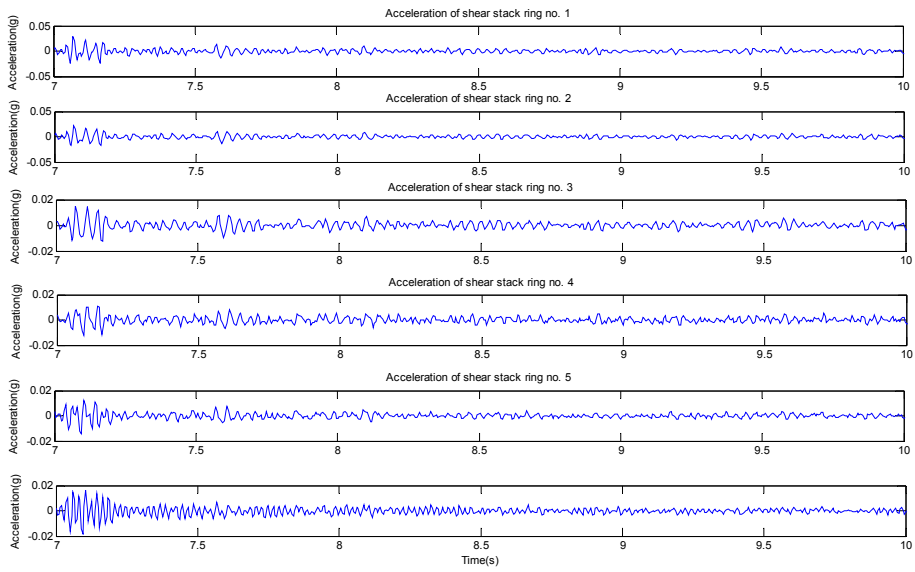


Figure 1.26 accelerations: array external

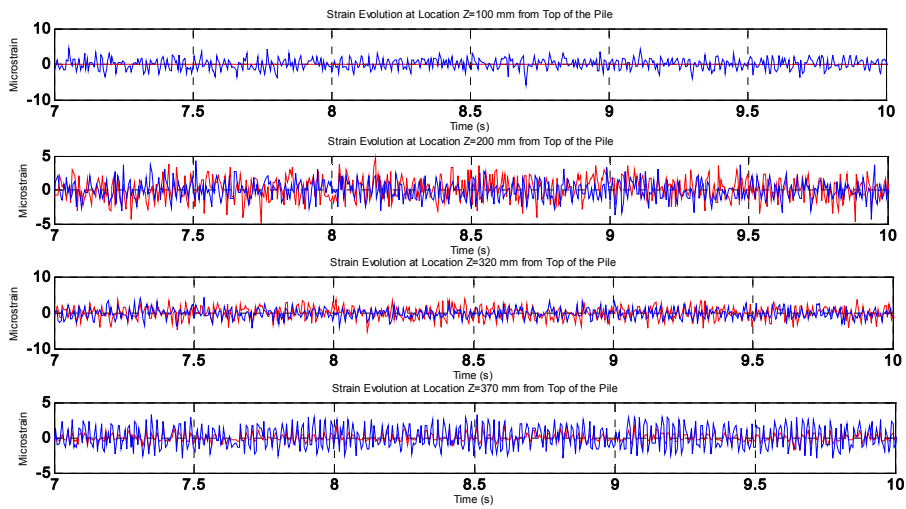


Figure 1.27: Strain gauge 100-370 mm

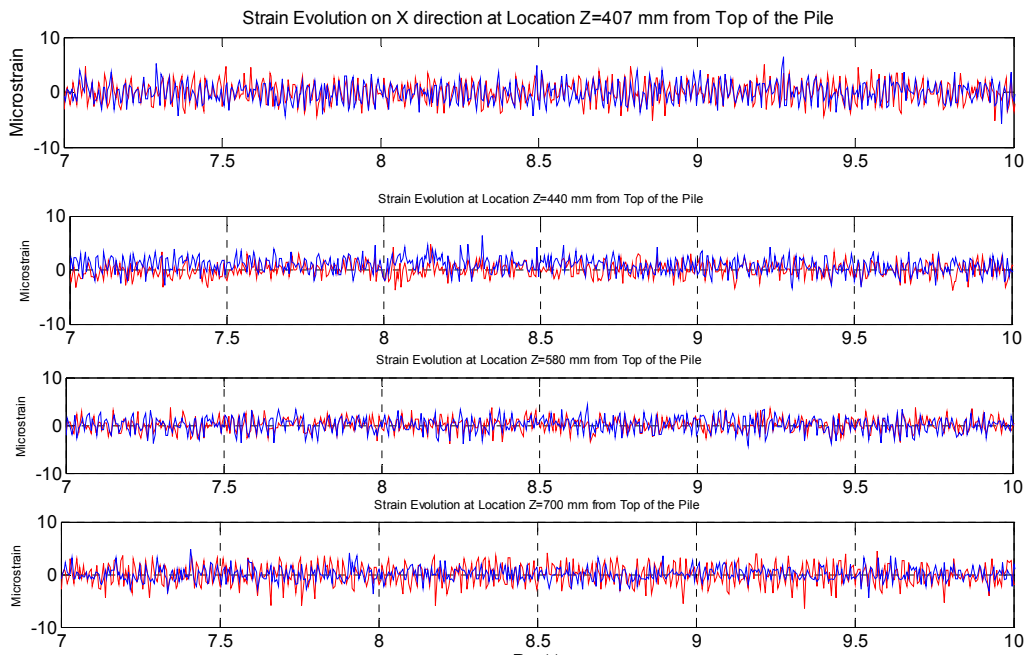


Figure 1.28: Strain gauges 407-700 mm

2.7 *E_NCB 5_FH*

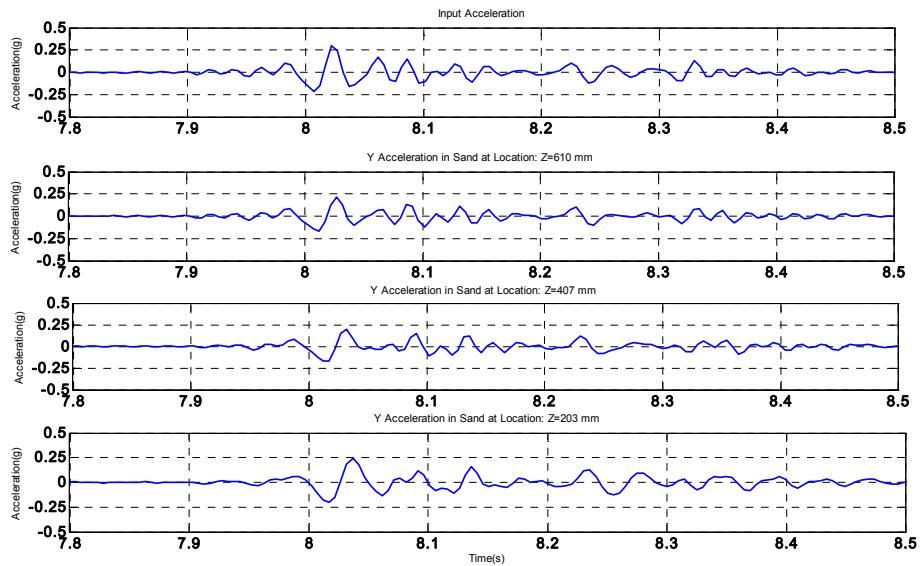


Figure 1.29: acceleration inside

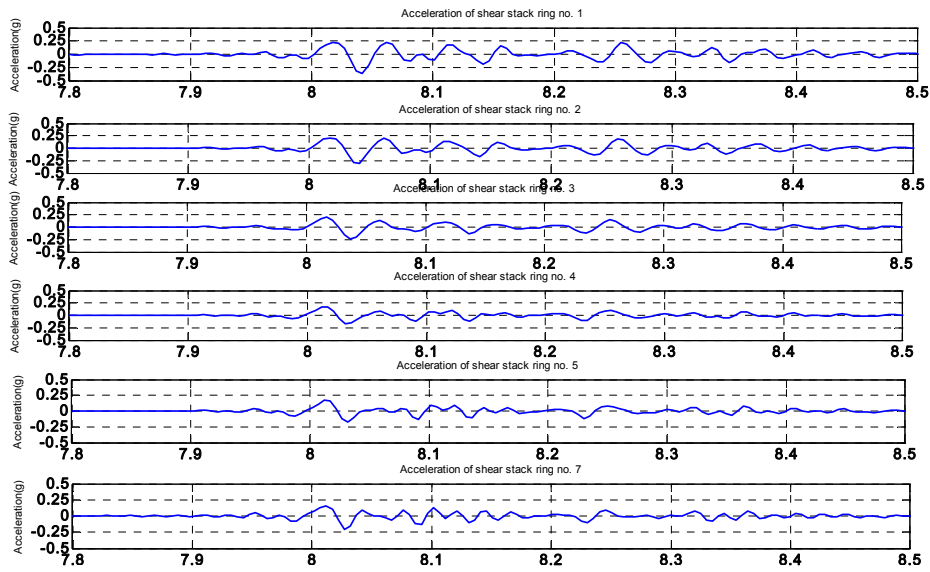


Figure 1.30: acceleration outside

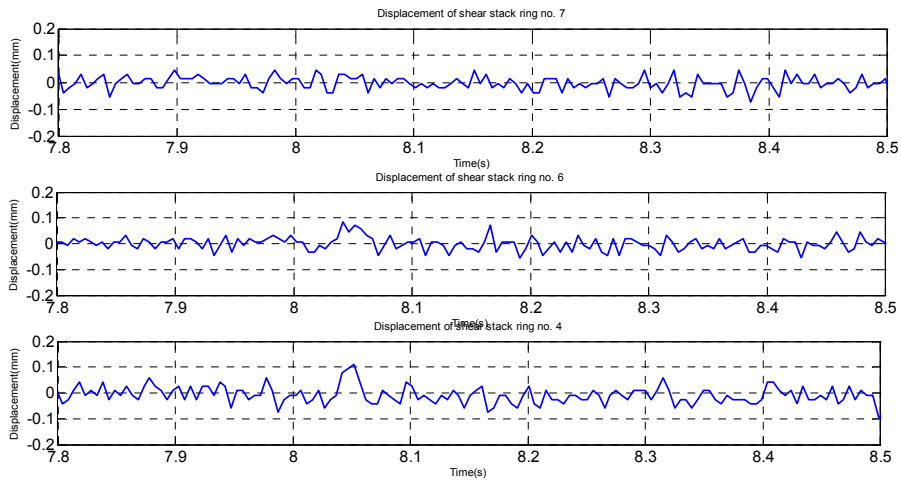


Figure 1.31: displacement of shear stack

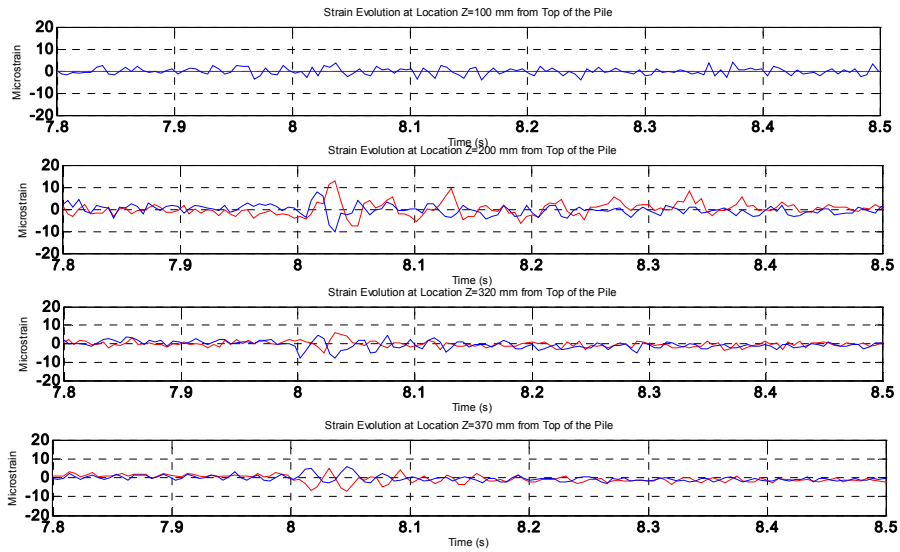


Figure 1.32: Strain gauges 100-370

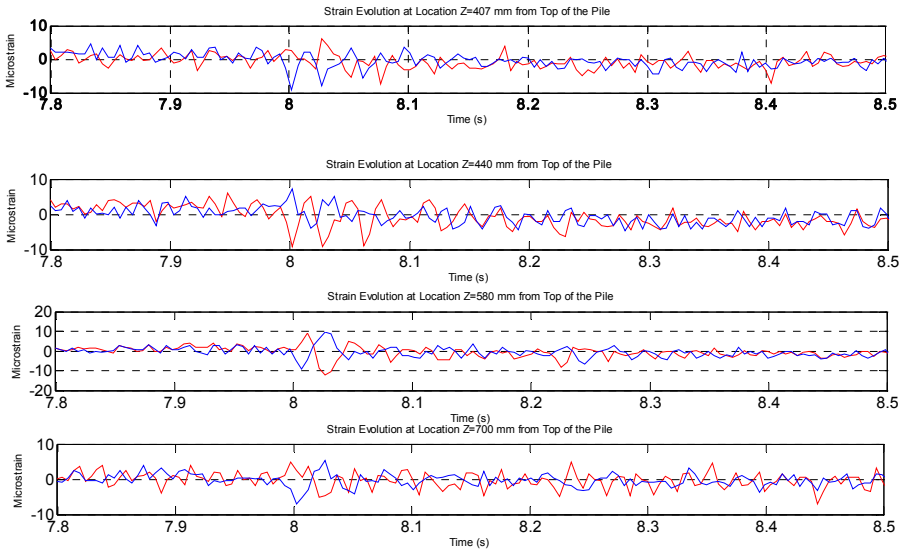


Figure 1.33: Strain gauges 407-700 mm

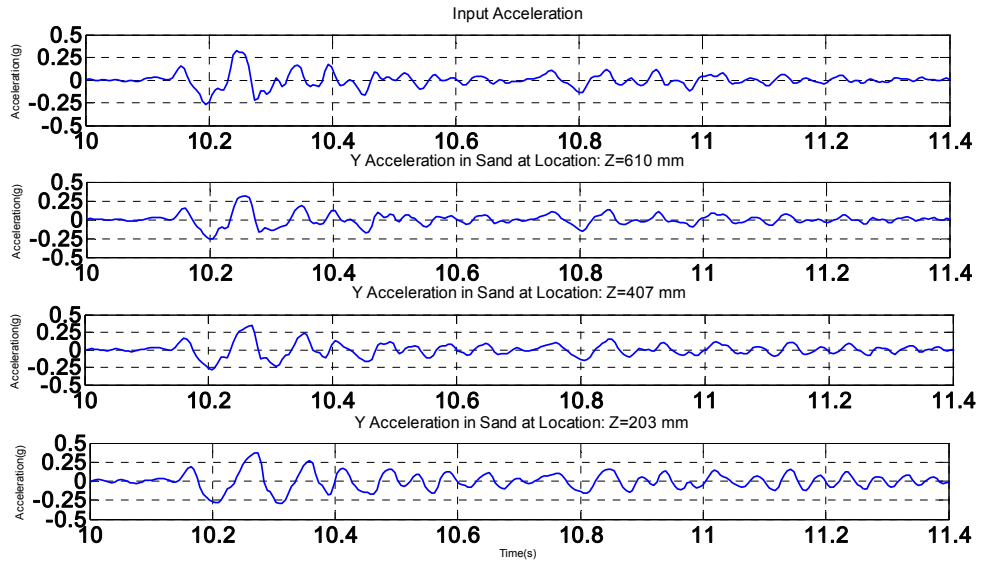


Figure 1.34: acceleration in sand

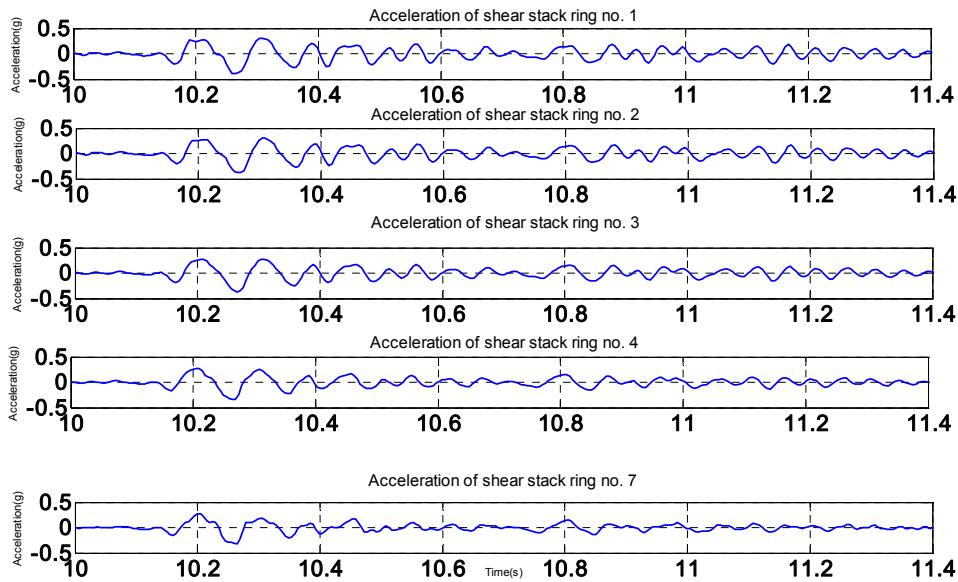


Figure 1.35: acceleration outside

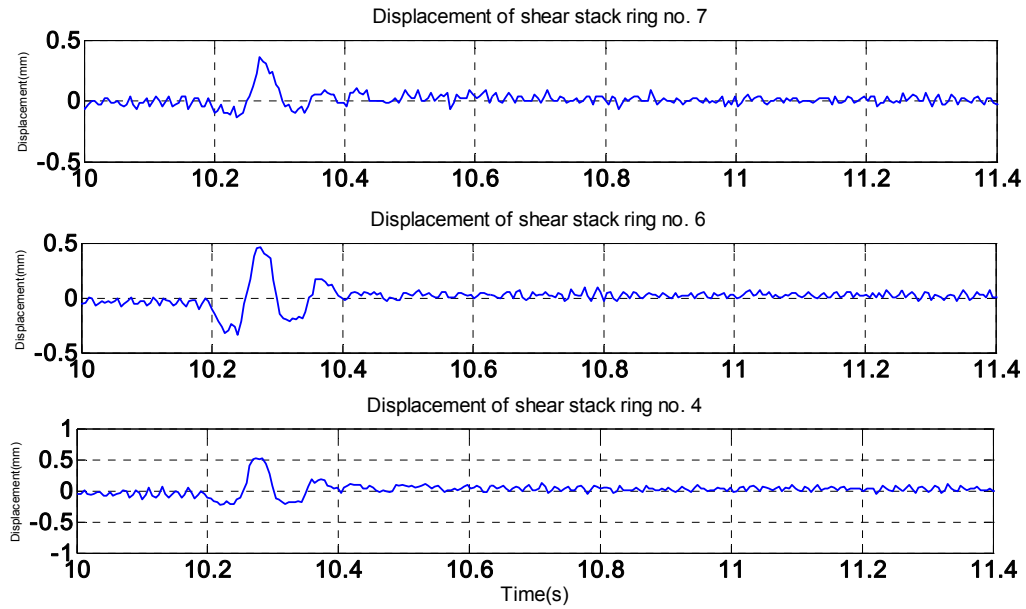


Figure 1.36: displacement of the shear stack

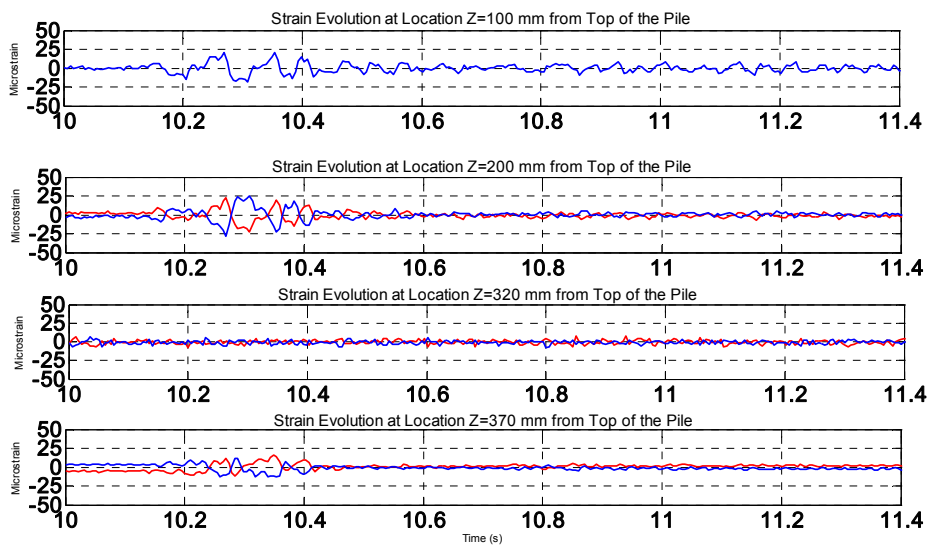


Figure 1.37: strain gauges 100-370 mm

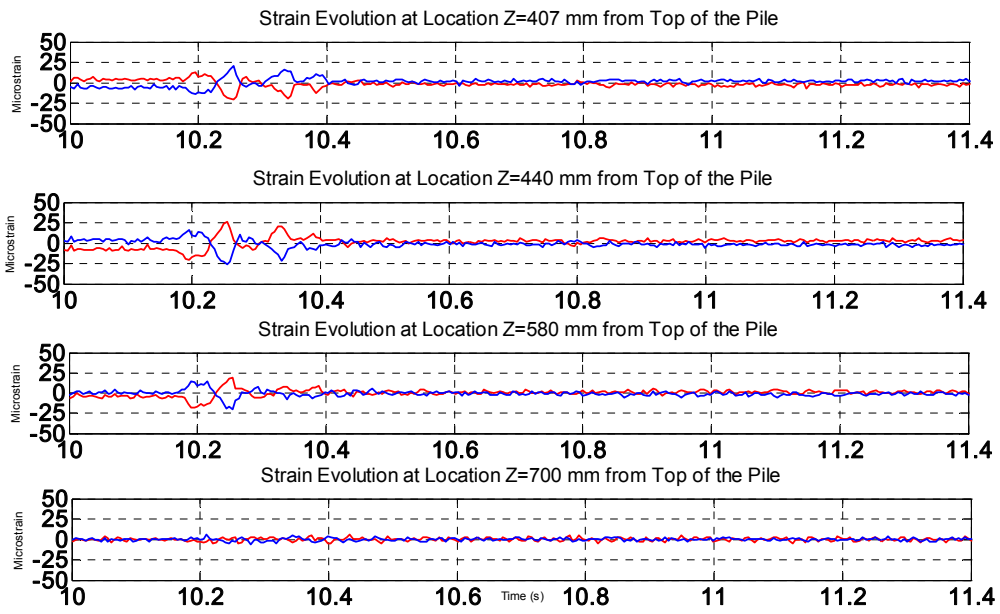


Figure 1.38: strain gauges 407-700 mm

2.9 *E_STU 12_NRH*

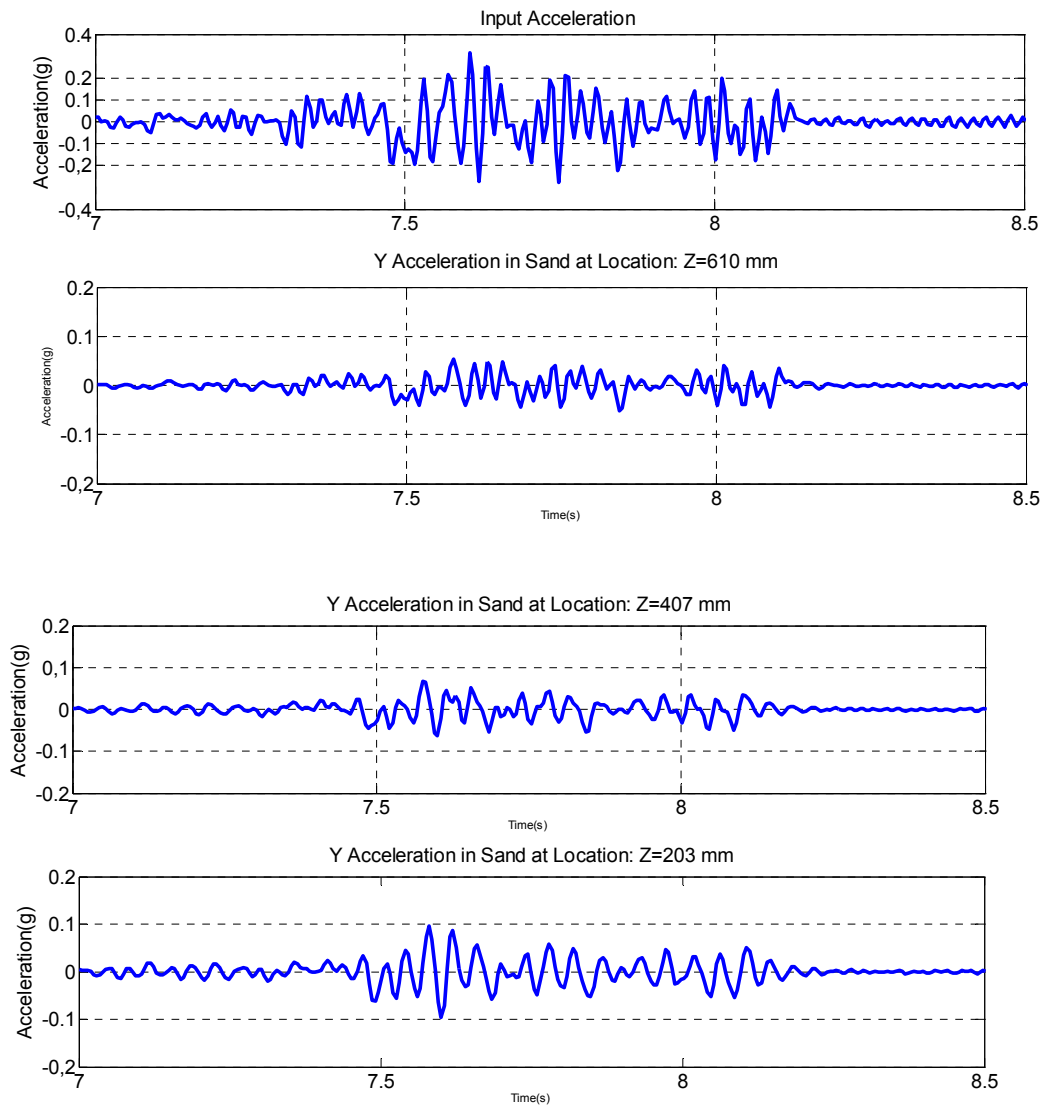


Figure 1.39: acceleration- array inside

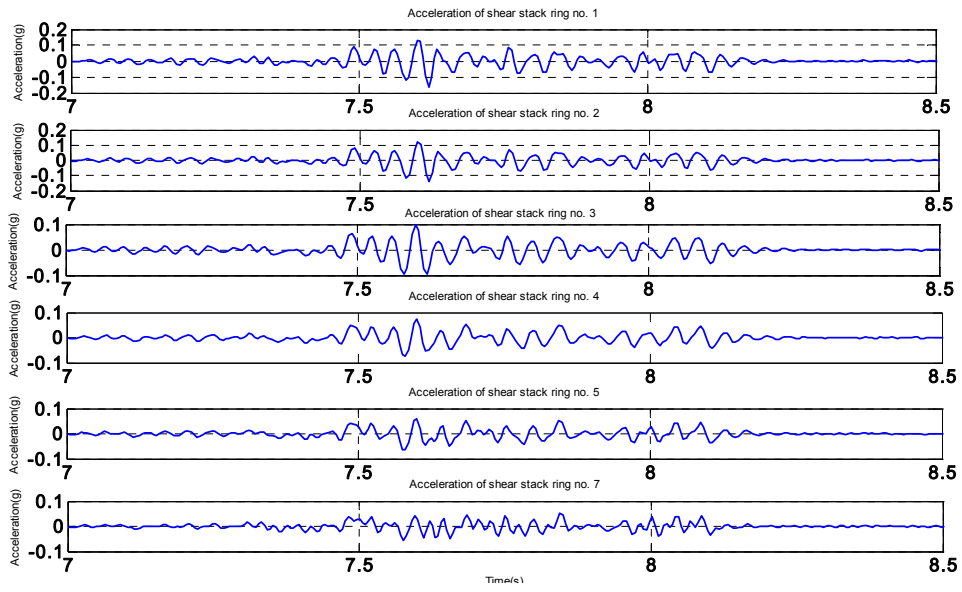


Figure 1.40: accelerations array outside

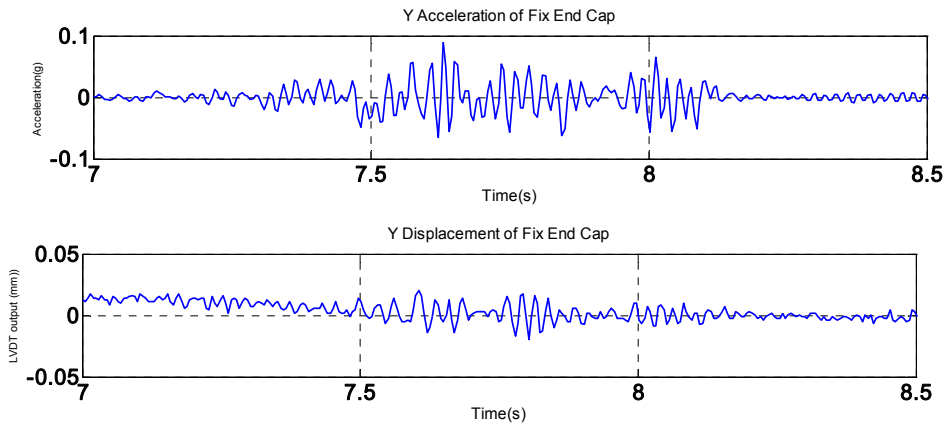


Figure 1.41: top pile: acceleration and LVDT measurement

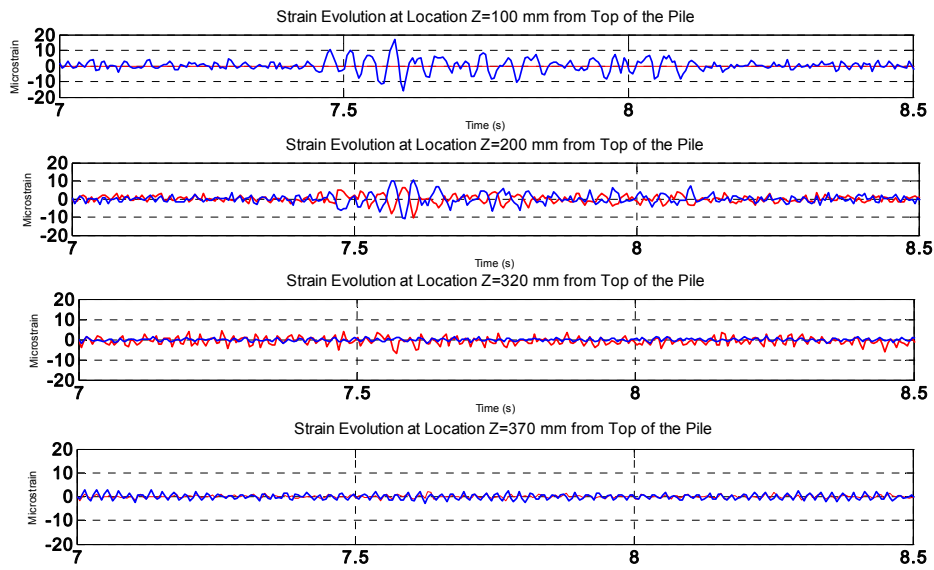


Figure 1.42: strain gauges 100-370 mm

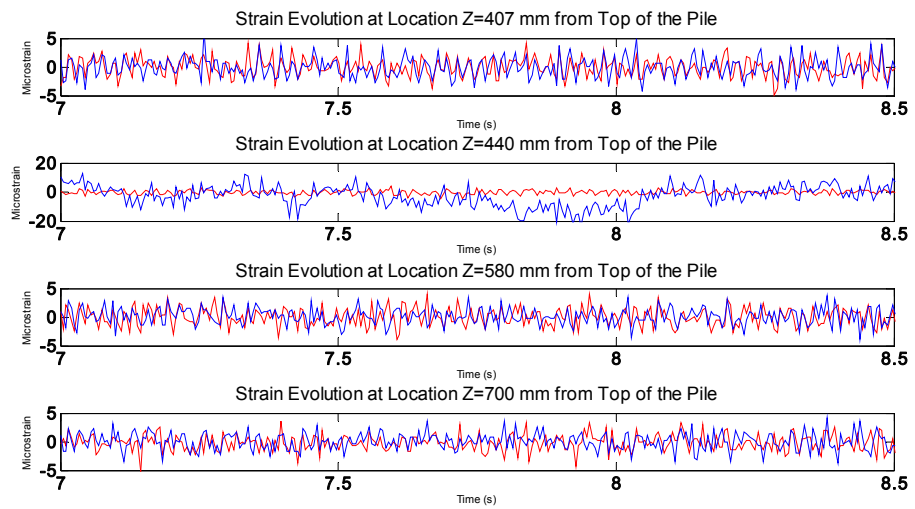


Figure 1.42: strain gauges 407-700 mm

2.10 *E_STU 5_NRH*

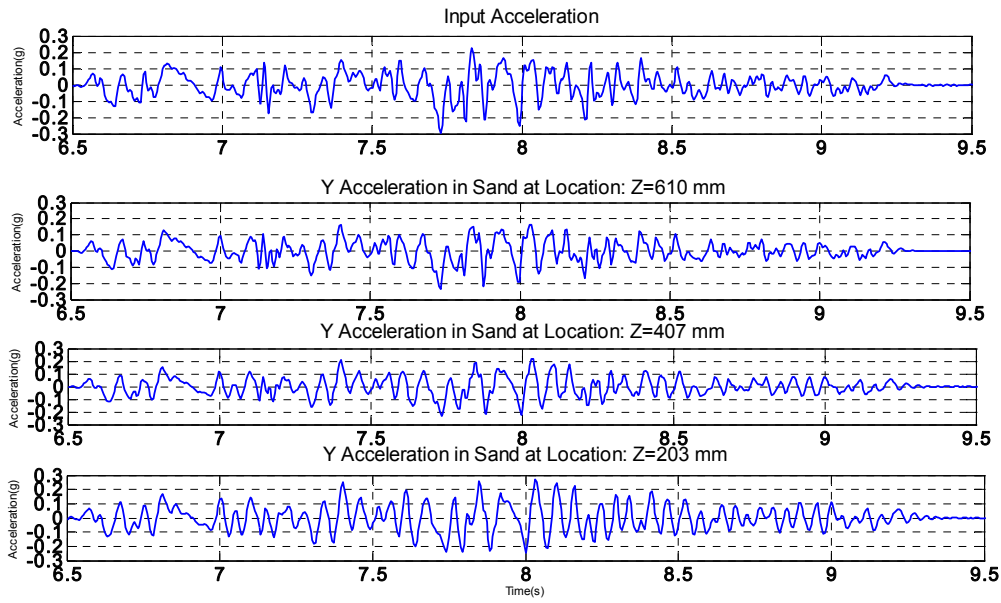


Figure 1.43: acceleration in sand

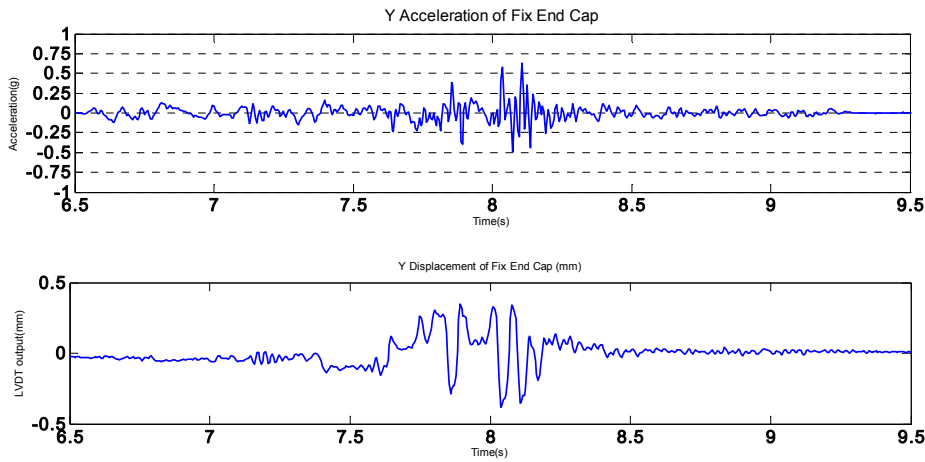


Figure 1.45: pile head: acceleration and LVD measurement

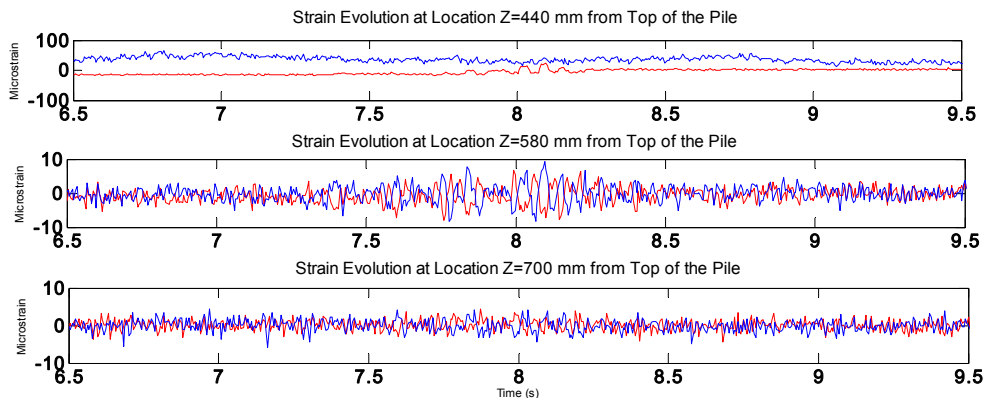


Figure 1.47: Strain gauges 440-700 mm

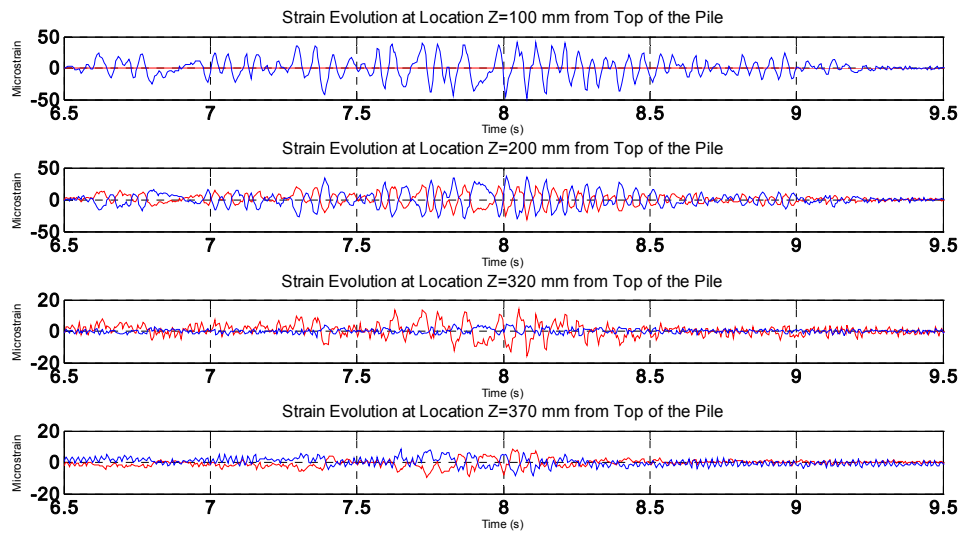


Figure 1.46: Strain gauges 100-370 mm

2.11 E_STU 2_NRH

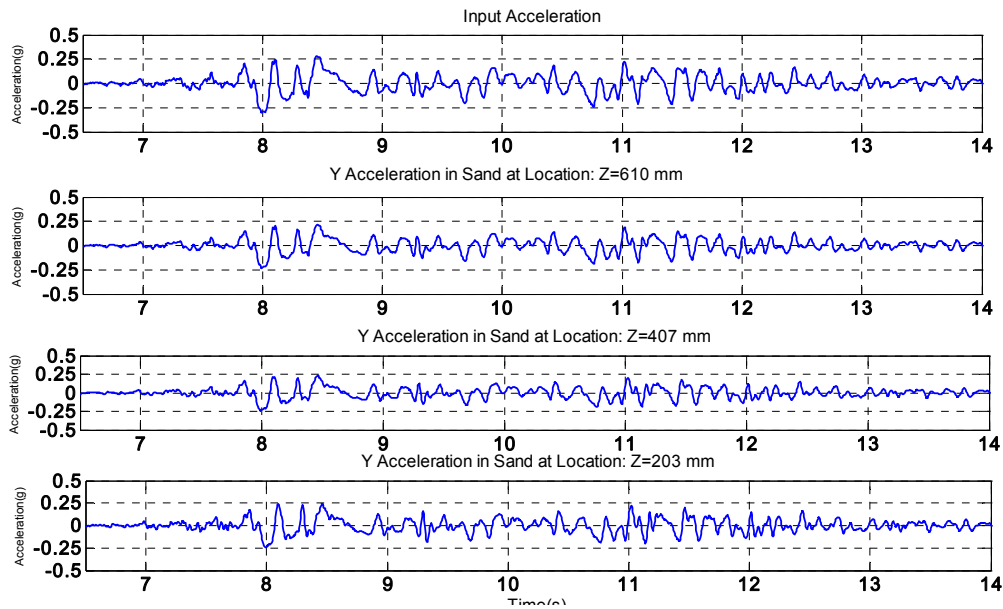


Figure 1.48:acceleration: array inside

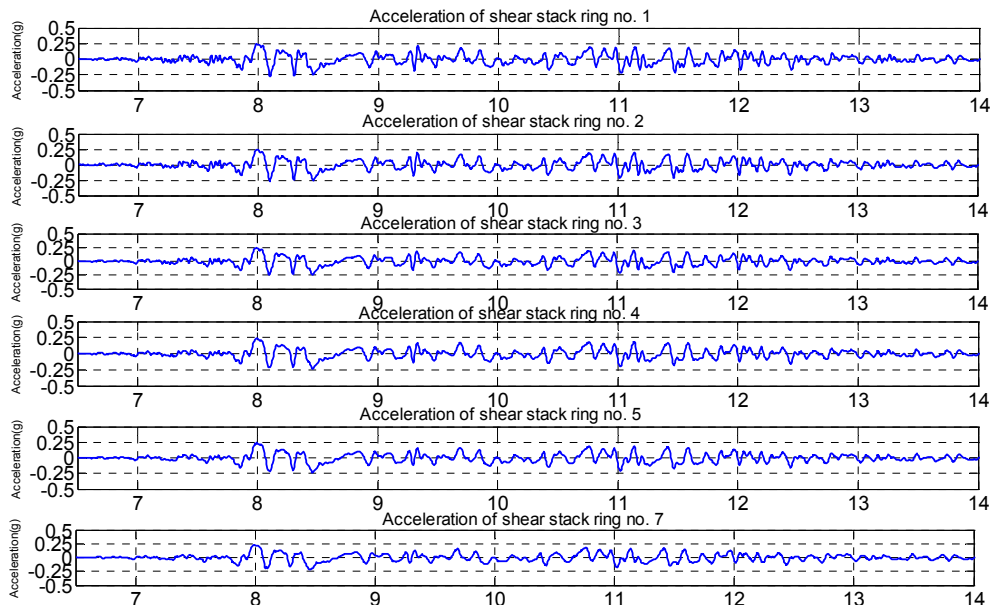


Figure 1.49:acceleration : array external

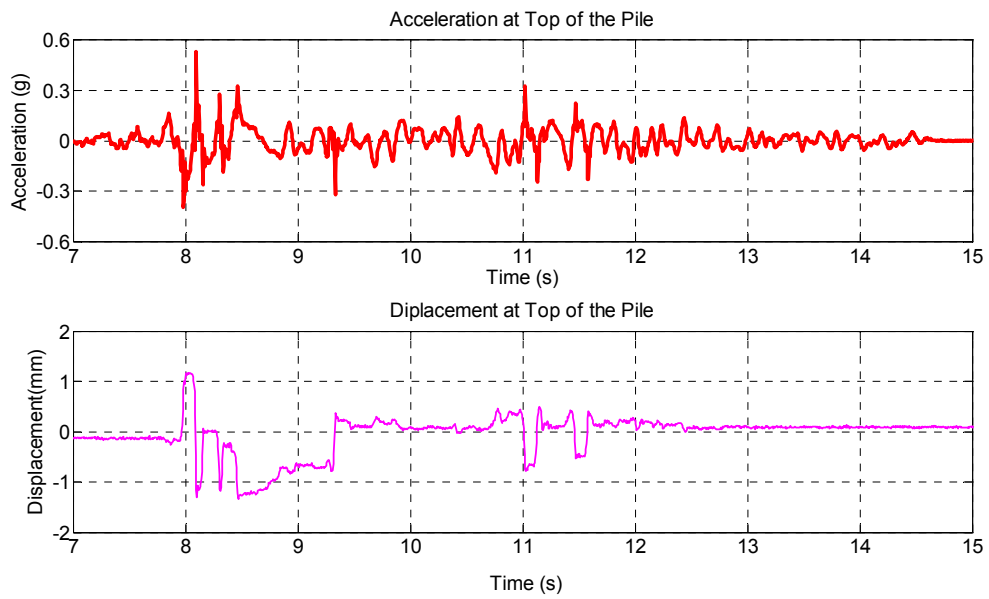


Figure 1.50: pile head- acceleration and LVDT

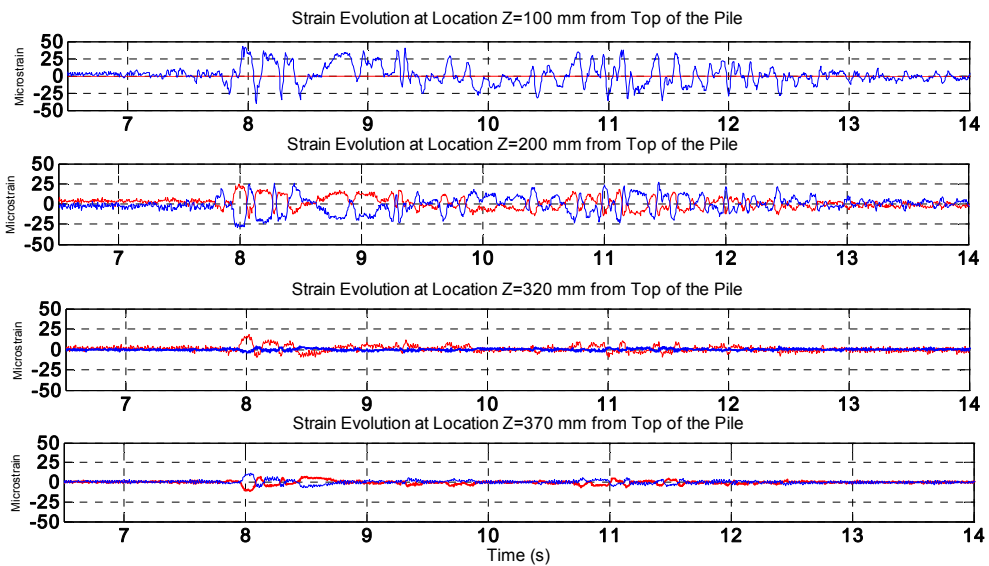


Figure 1.51: strain gauges 100-370 mm

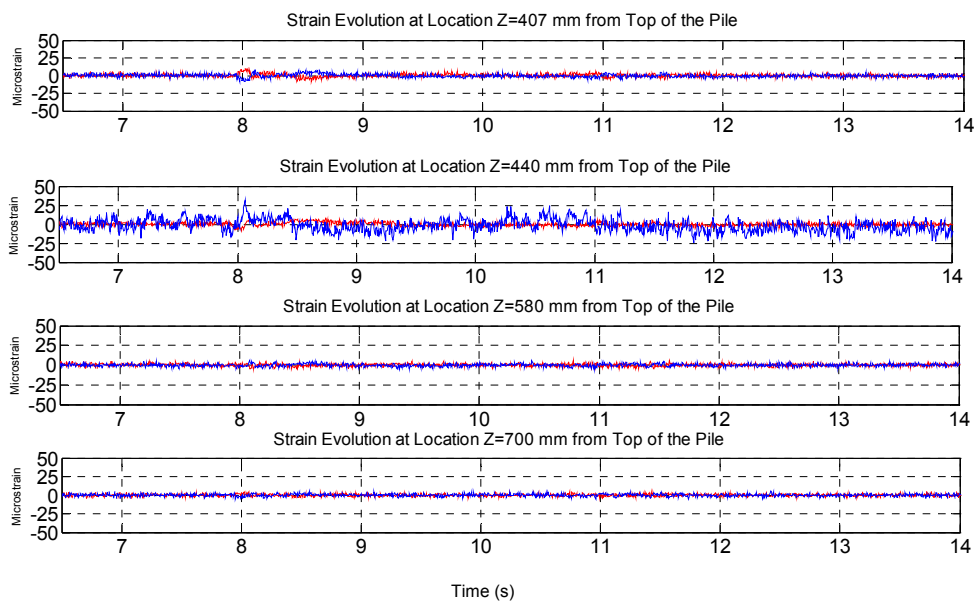


Figure 1.52: strain gauges 40-7700 mm

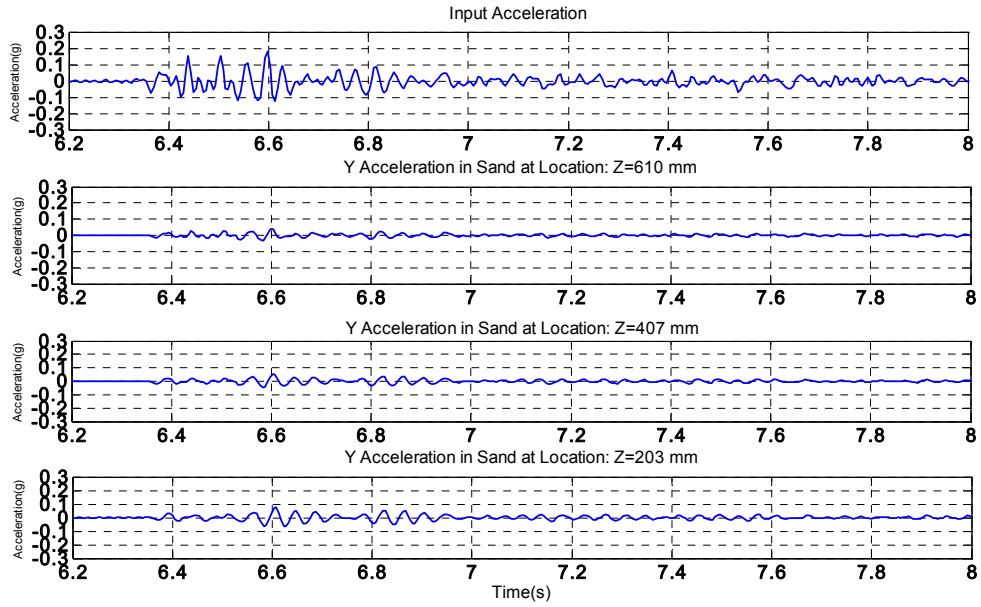


Figure 1.53: acceleration- array inside

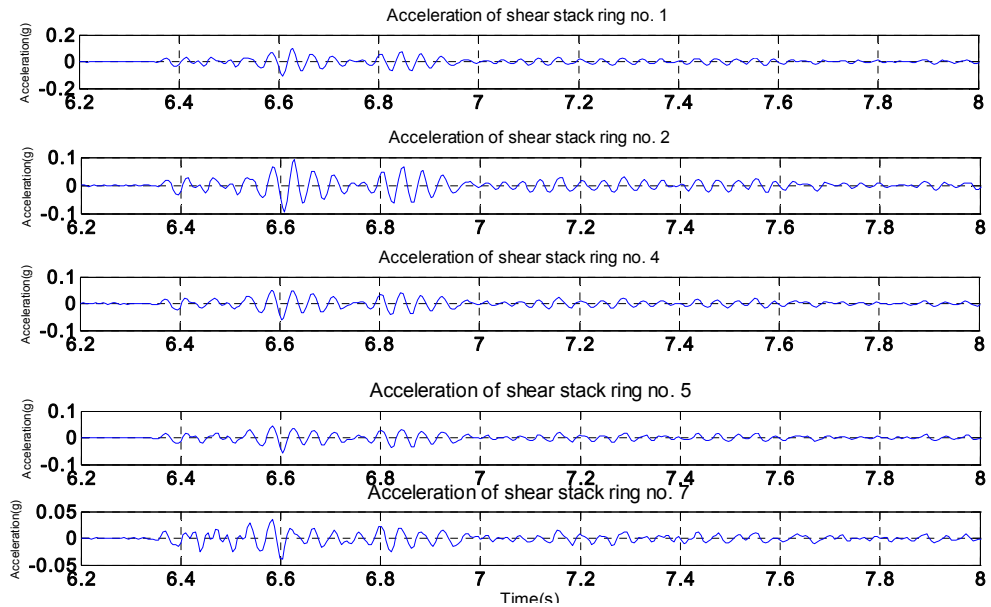


Figure 1.54: acceleration – array external

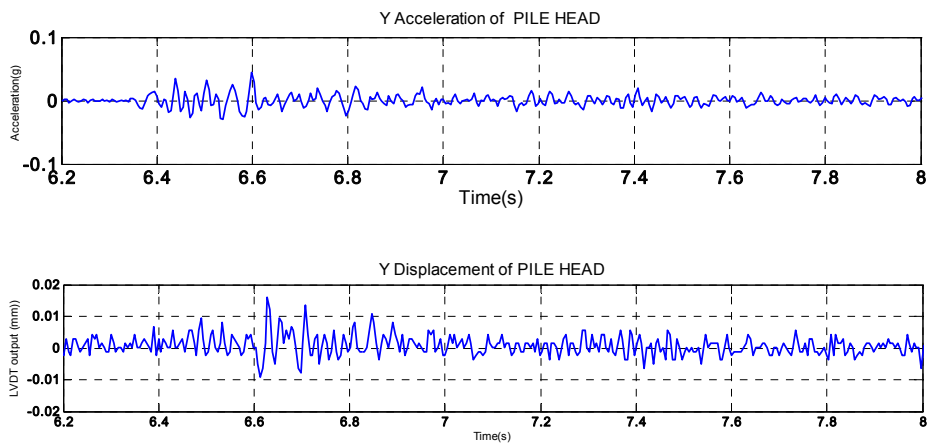


Figure 1.55: pile head: acceleration and LVDT measurement

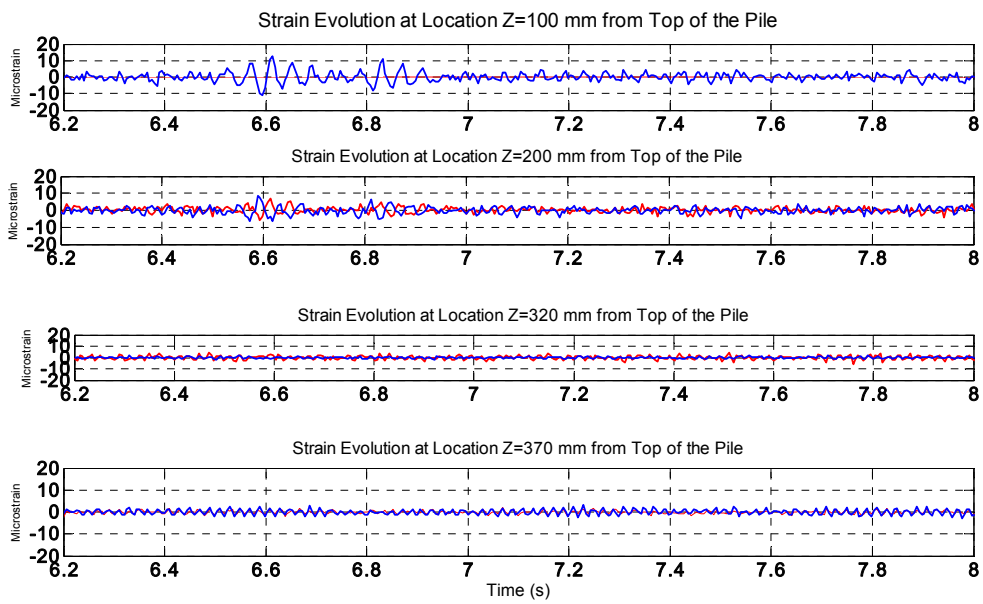


Figure 1.56 strain gauges 100-370 mm

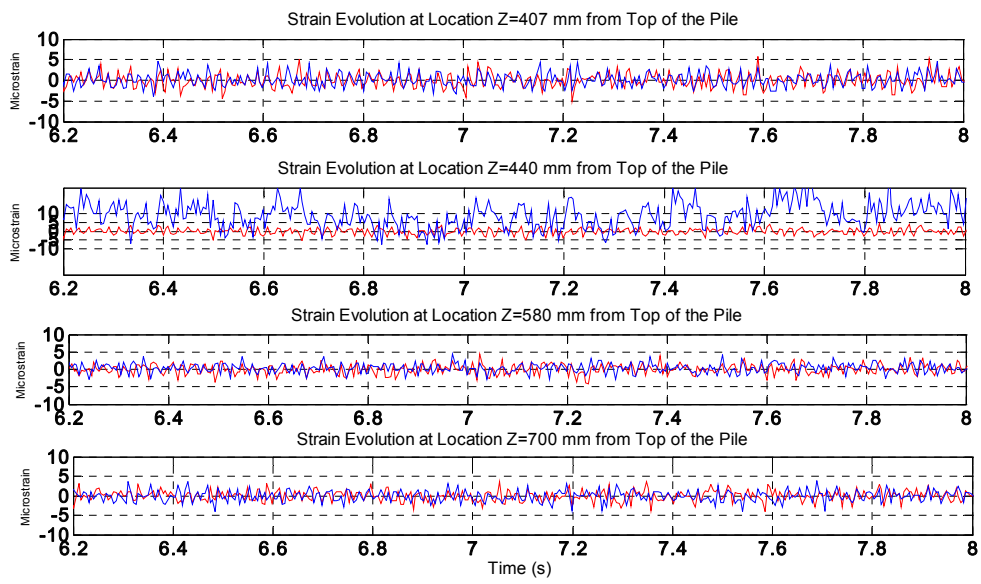


Figure 1.57 strain gauges 407-700 mm

2.12 E_TMZ 2_NRH

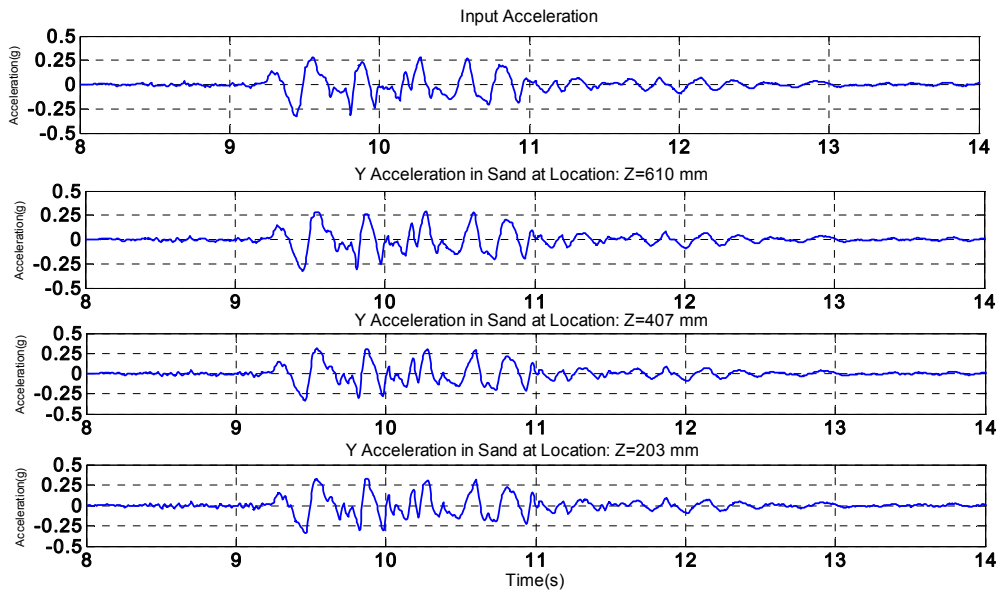


Figure 1.58: acceleration array inside

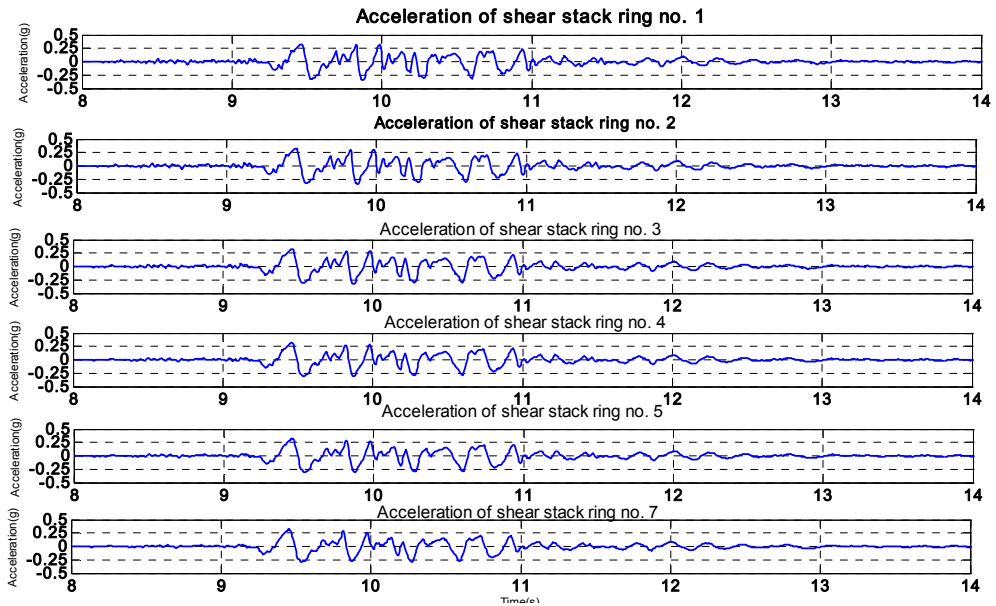


Figure 1.59: acceleration array outside

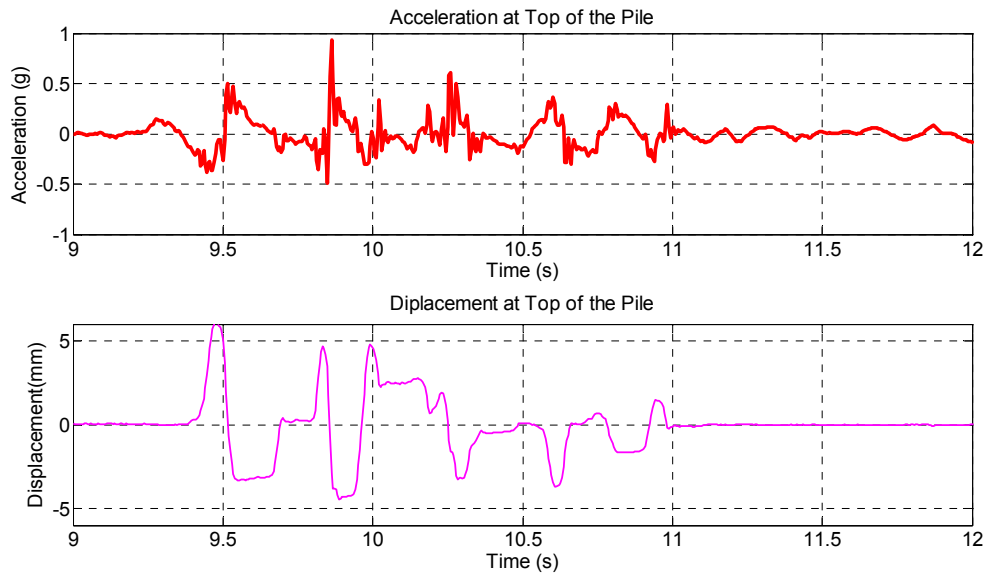


Figure 1.60:top of pile

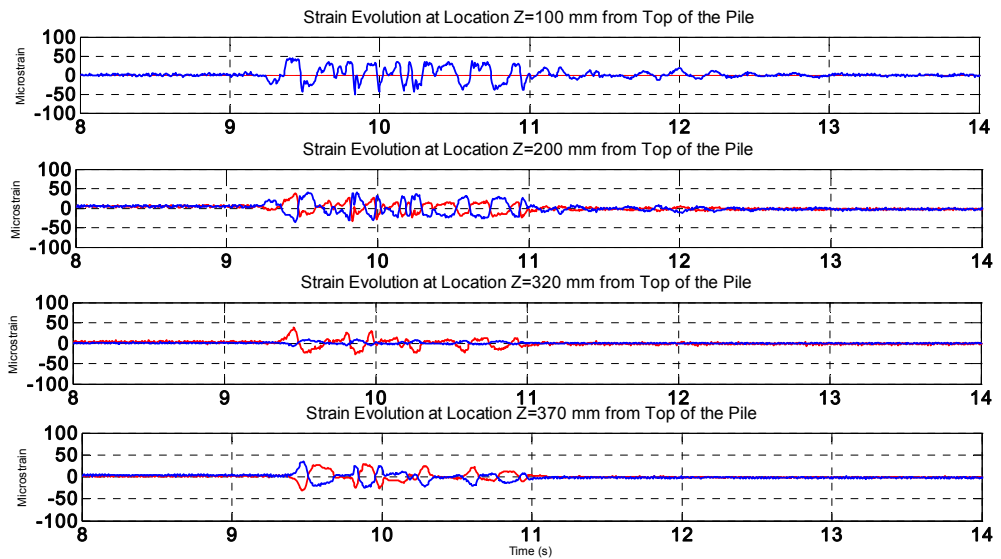


Figure 2: strain gauges 100-370 mm

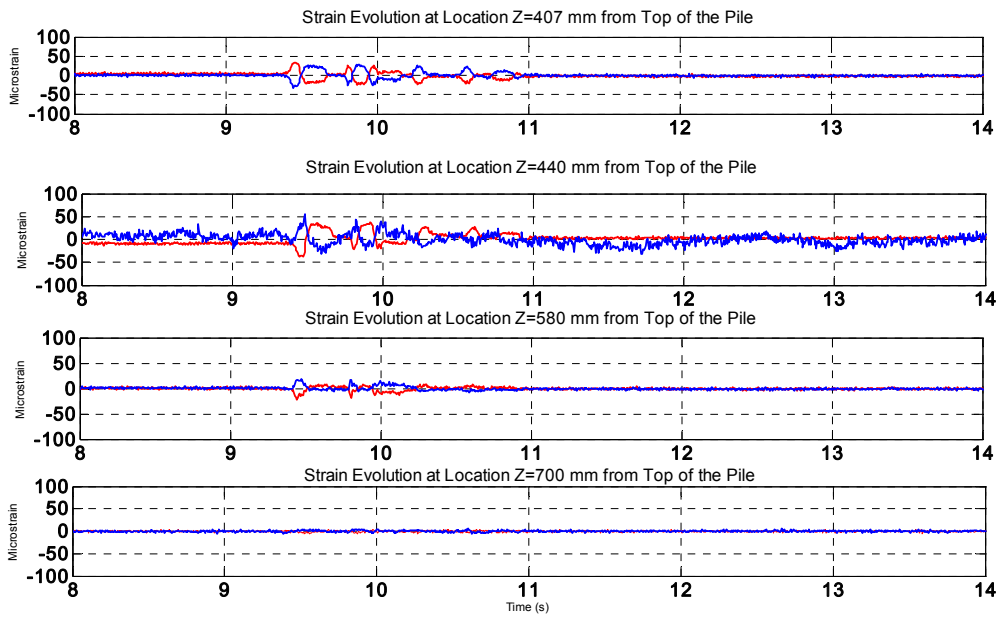


Figure 1.62: strain gauges 407-700mm

2.13 *E_NCB 12_NRH*

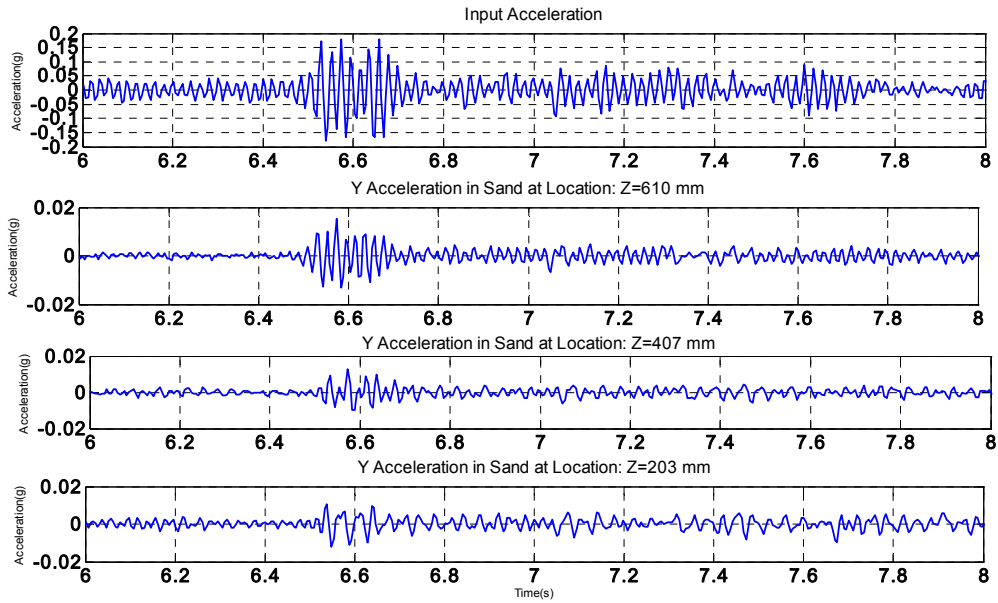


Figure 1.63: acceleration: array inside

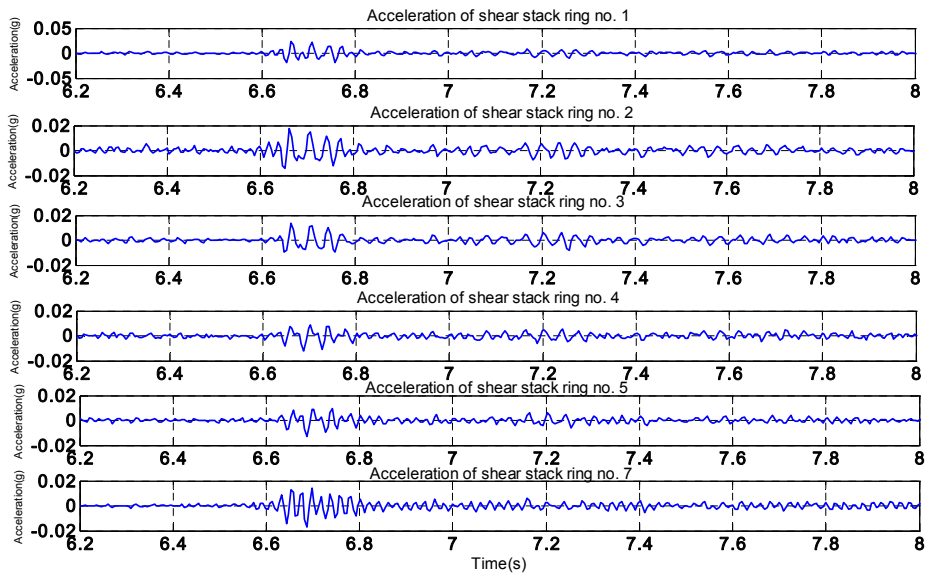


Figure 1.64: acceleration array external

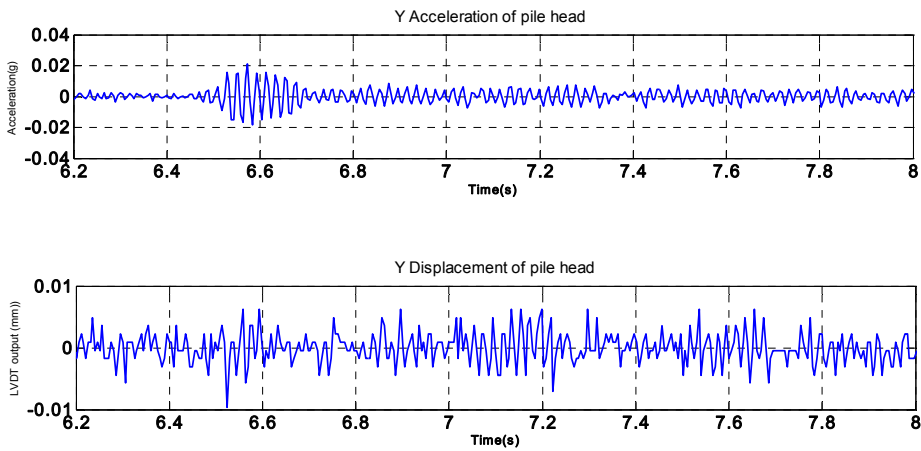


Figure 1.65: pile head – acceleration and displacement

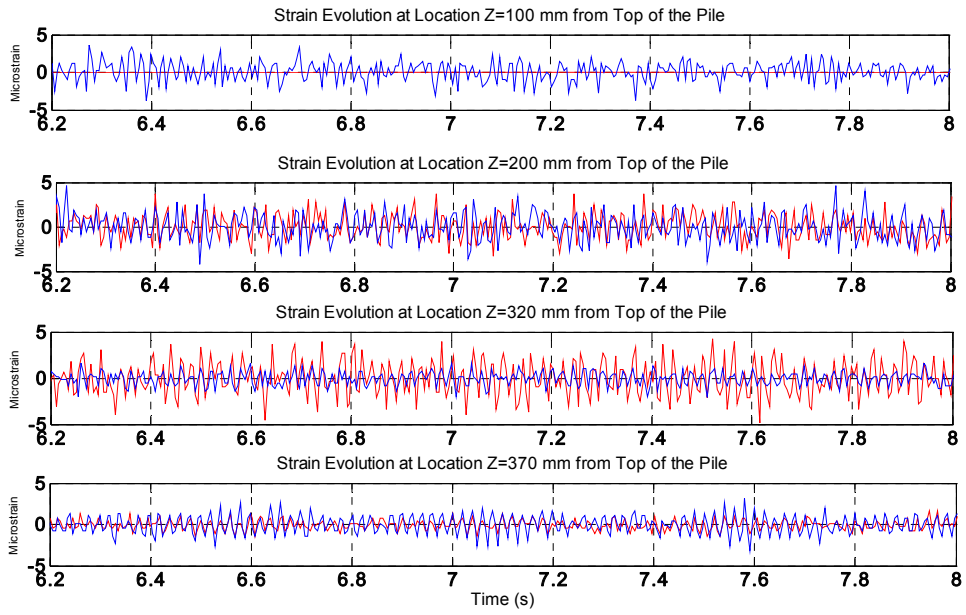


Figure 1.66: strain gauges 100-370 mm

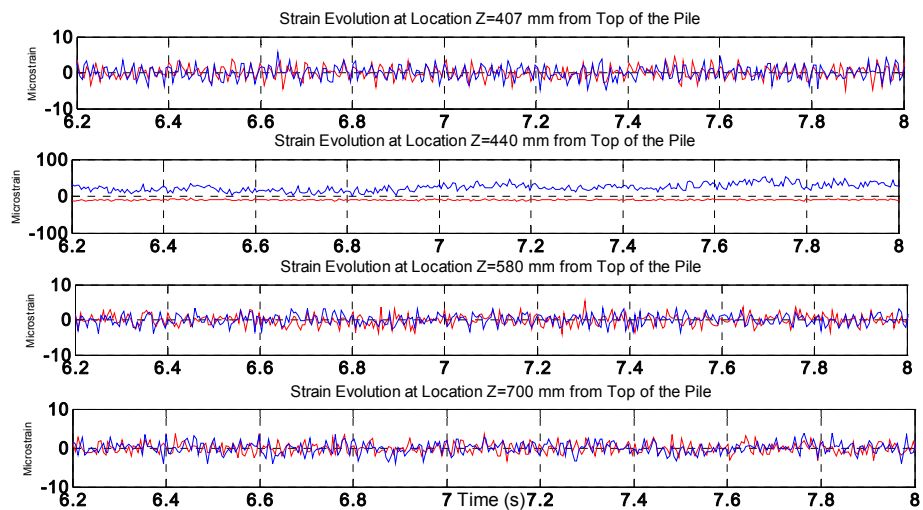


Figure 1.67: strain gauges 407-700 mm

2.14 E_NCB5_NRH

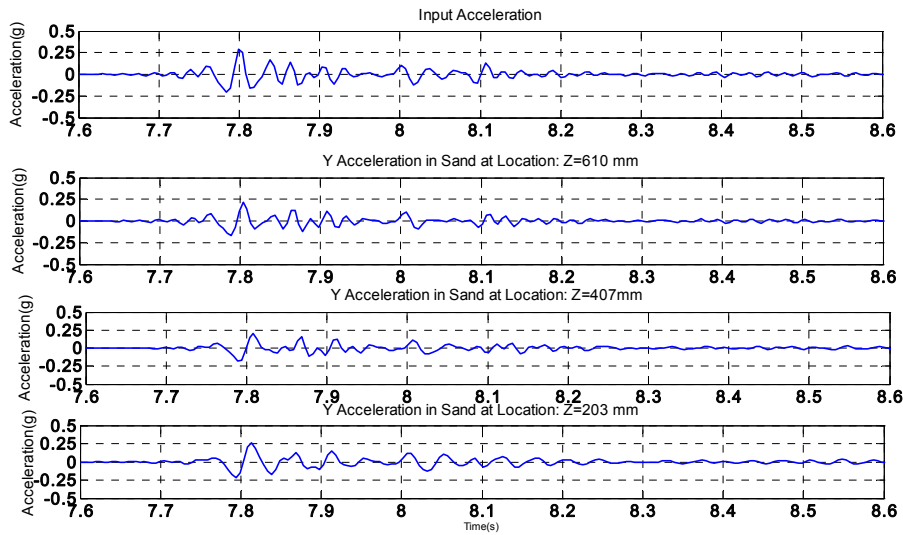


Figure 1.68: acceleration array inside

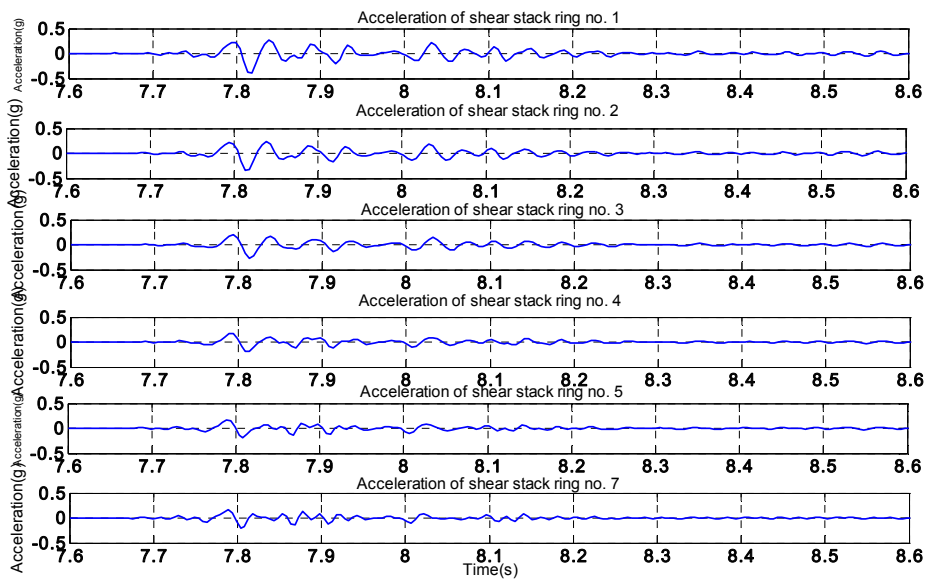


Figure 1.69: Layout instrumentation

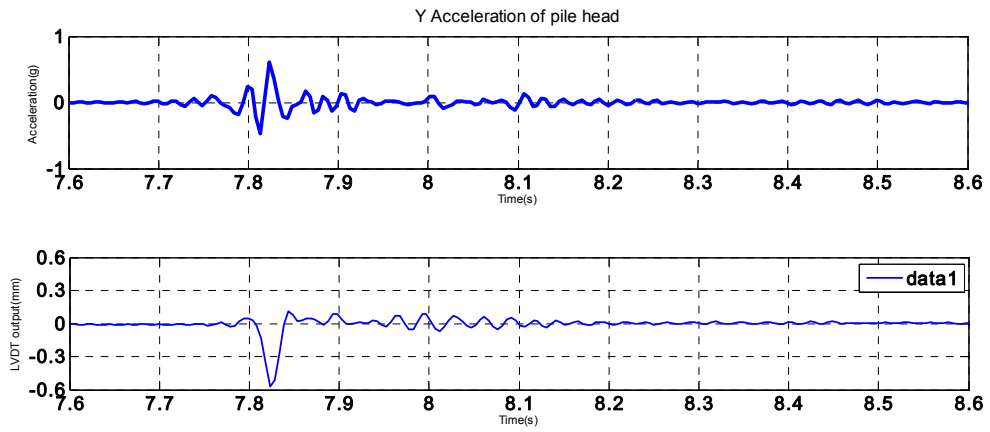


Figure 1.70: pile head: acceleration and LVDT measurement

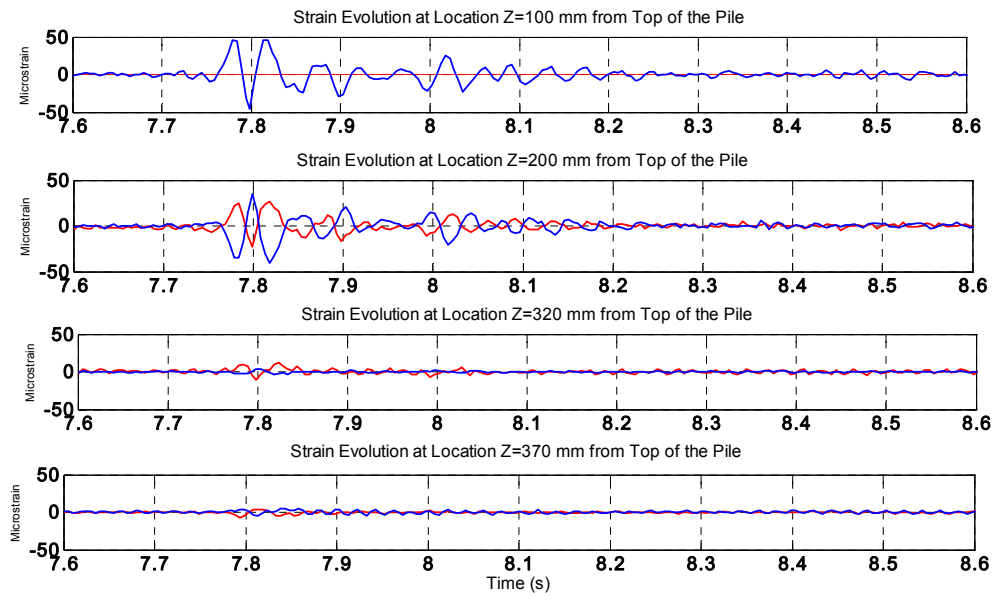


Figure 2: strain gauges 100-370 mm

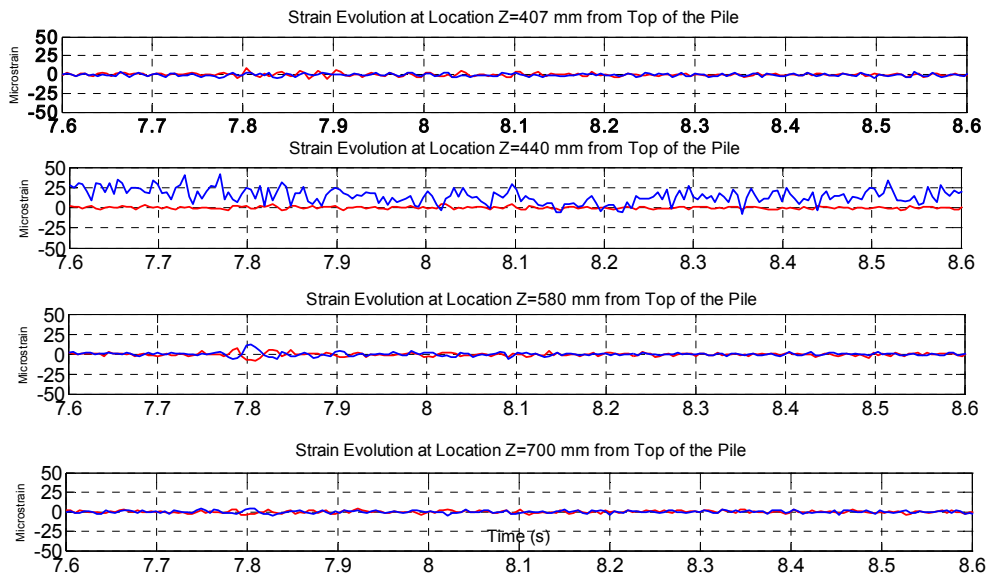


Figure 1.72: strain gauges 407-700mm

2.15 E_NCB2_NRH

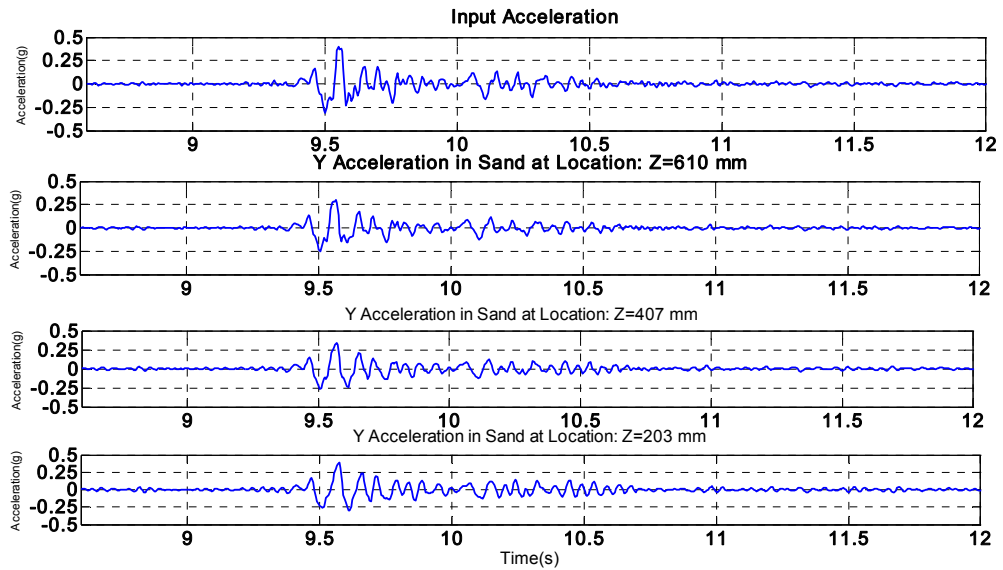


Figure 1.73: acceleration in sand

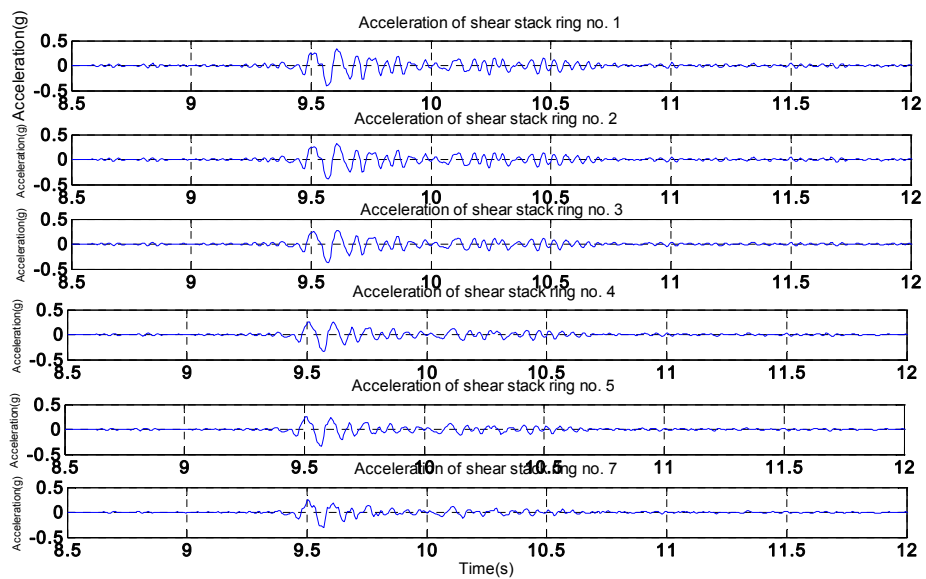


Figure 1.74: acceleration external array

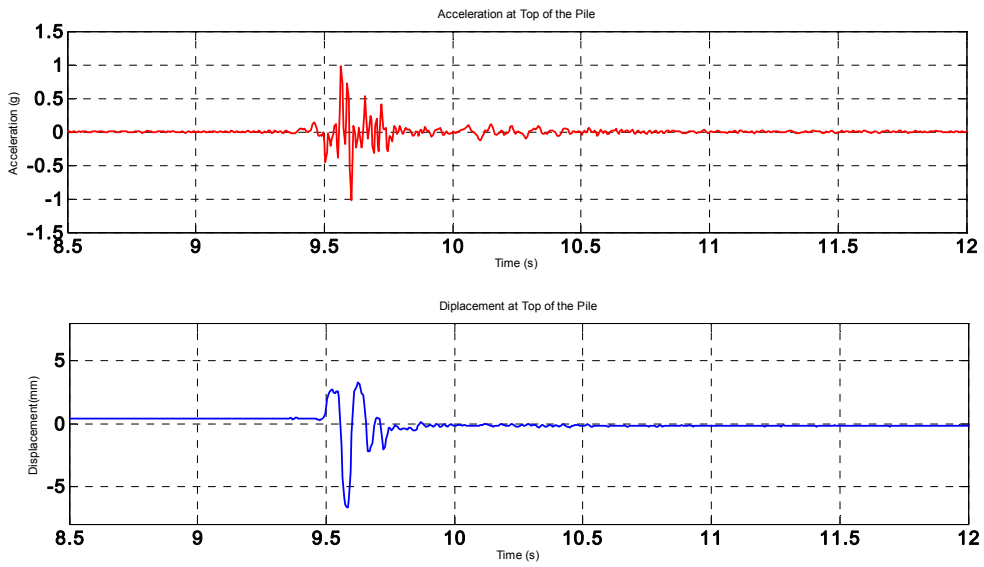


Figure 1.75: pile head

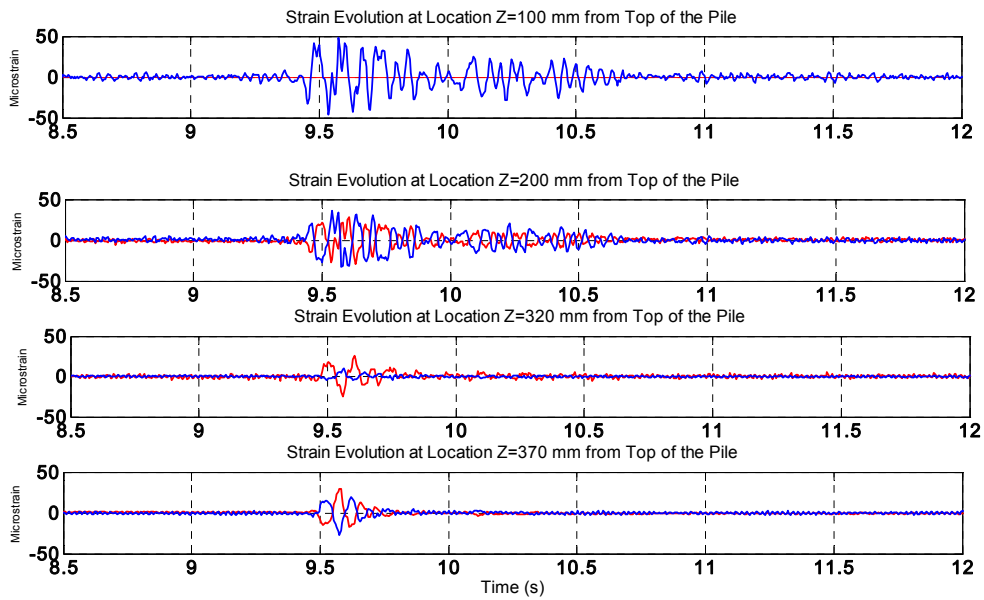


Figure 1.76: Strain gauges 100-370 mm

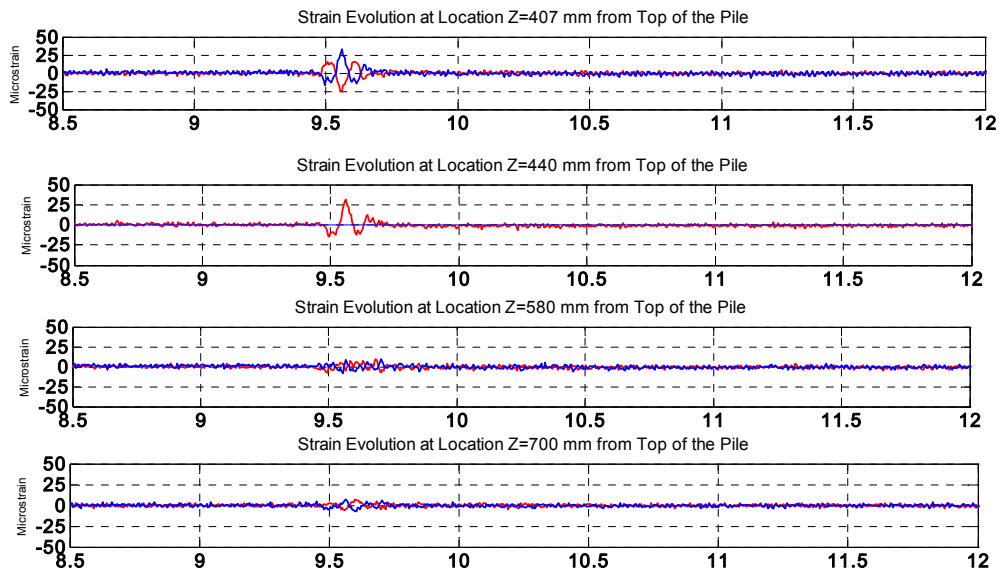


Figure 1.77: Strain gauges 407-700 mm

3 SOIL CONFIGURATION: LAYERED (BE+E)

3.1 BE+E_STU 12_FH

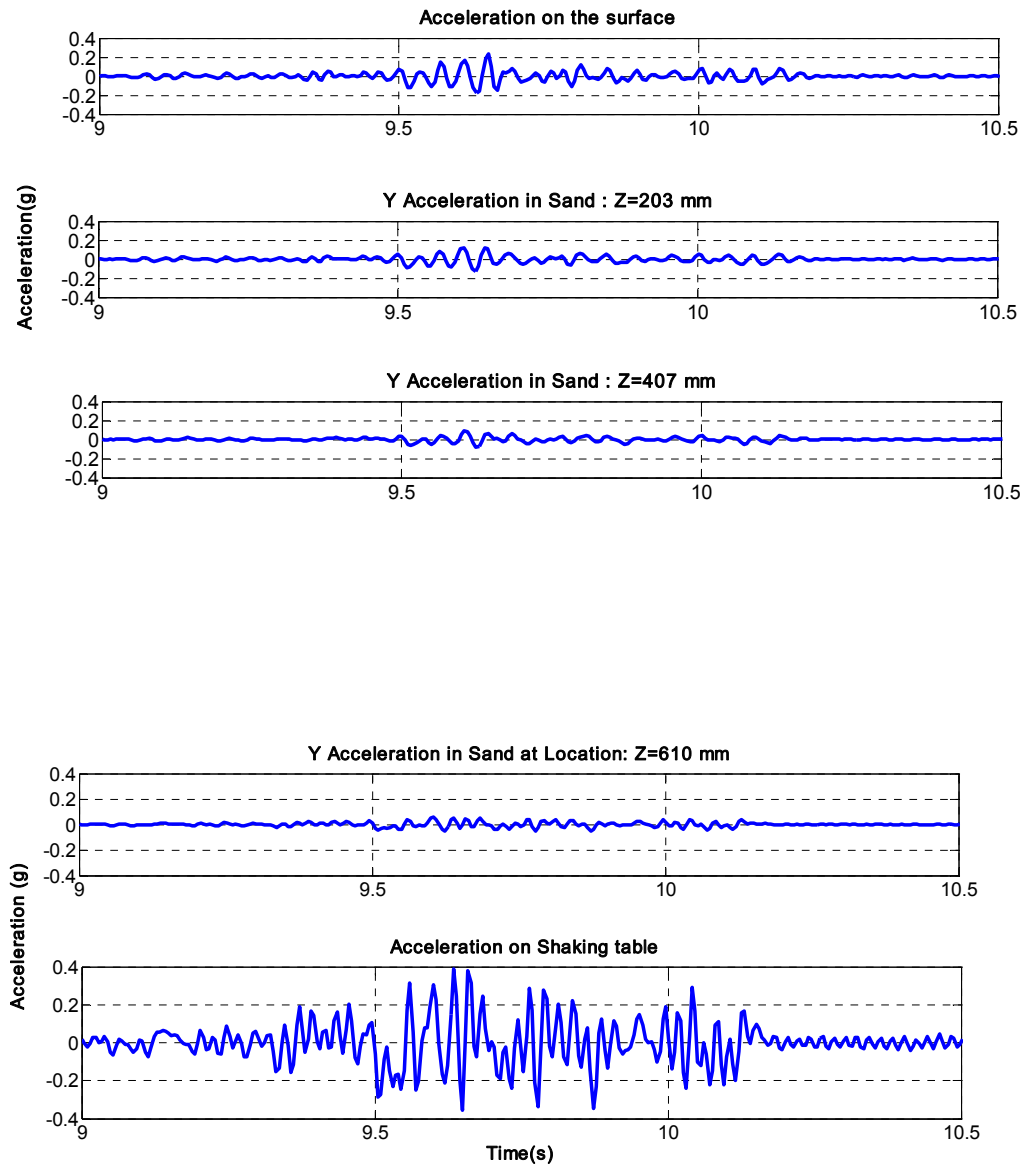


Figure 1.78: acceleration_array inside

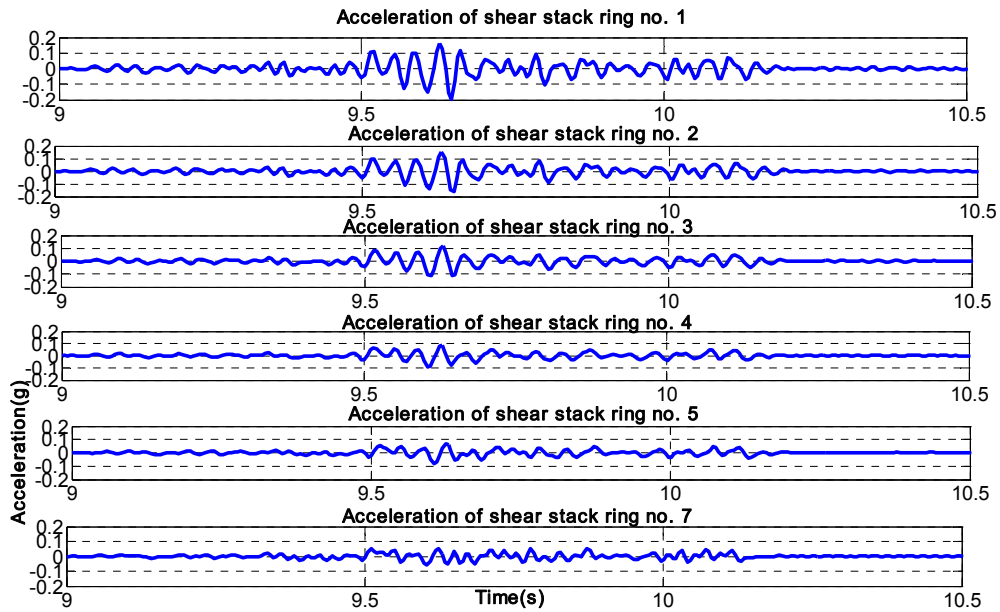


Figure 1.79: acceleration_array outside

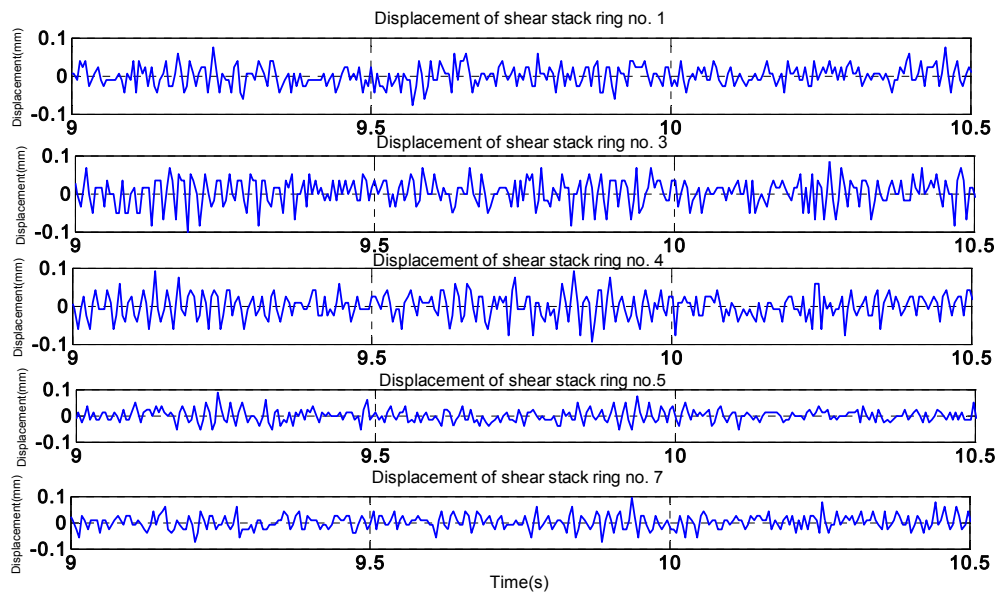


Figure 1.80: displacement of shear stack

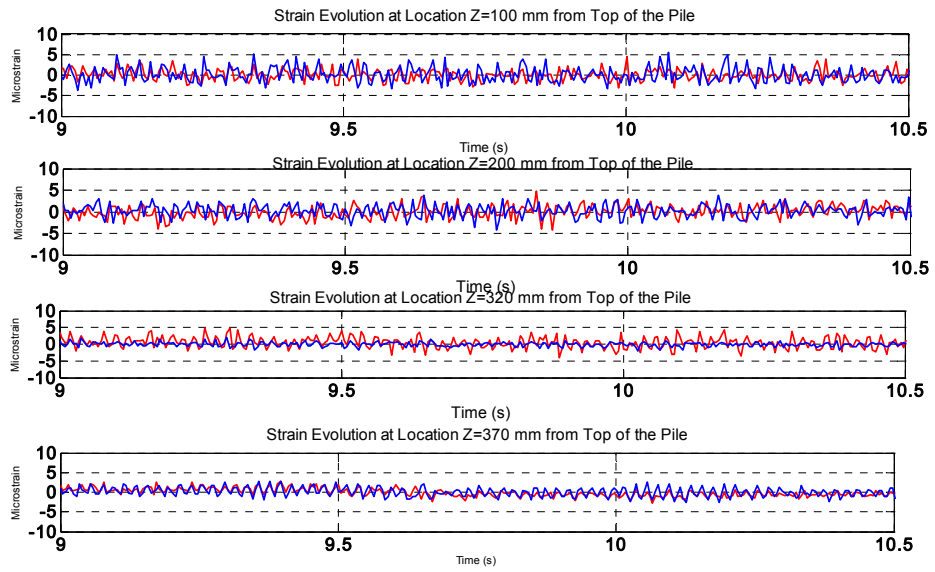


Figure 1.81: strain gauges 100-370 mm

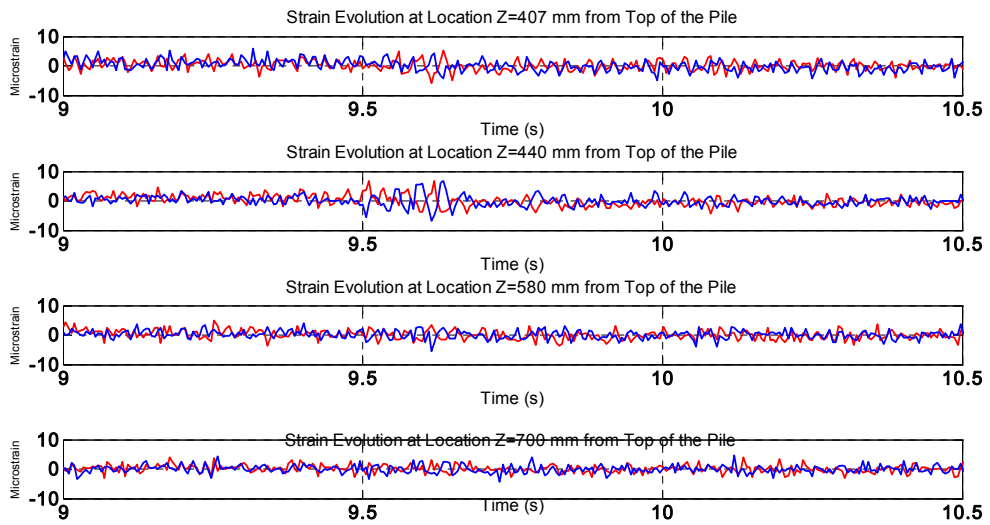


Figure 1.82: strain gauges 407-700 mm

3.2 BE+E_STU 5_FH

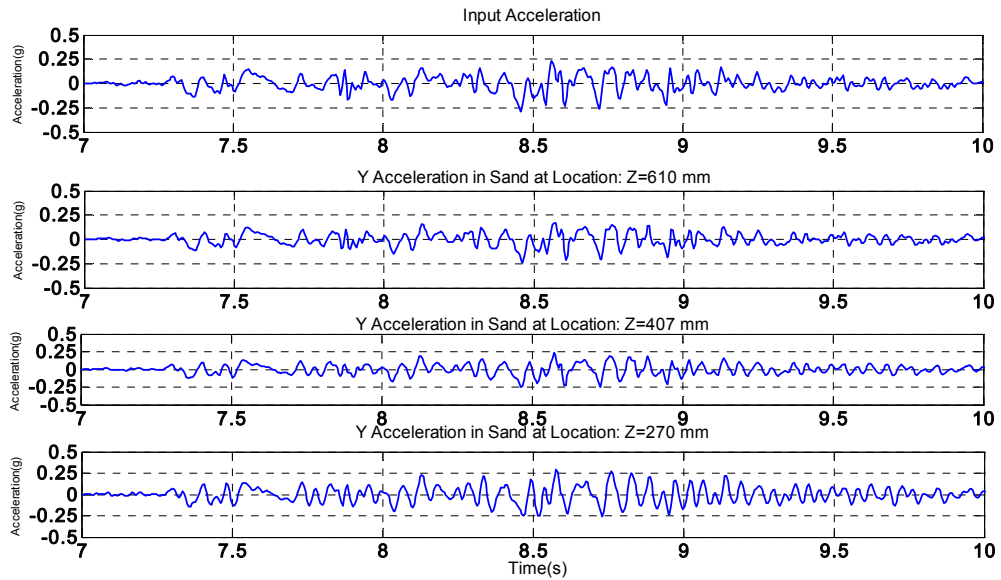


Figure 1.83: acceleration_array insideside

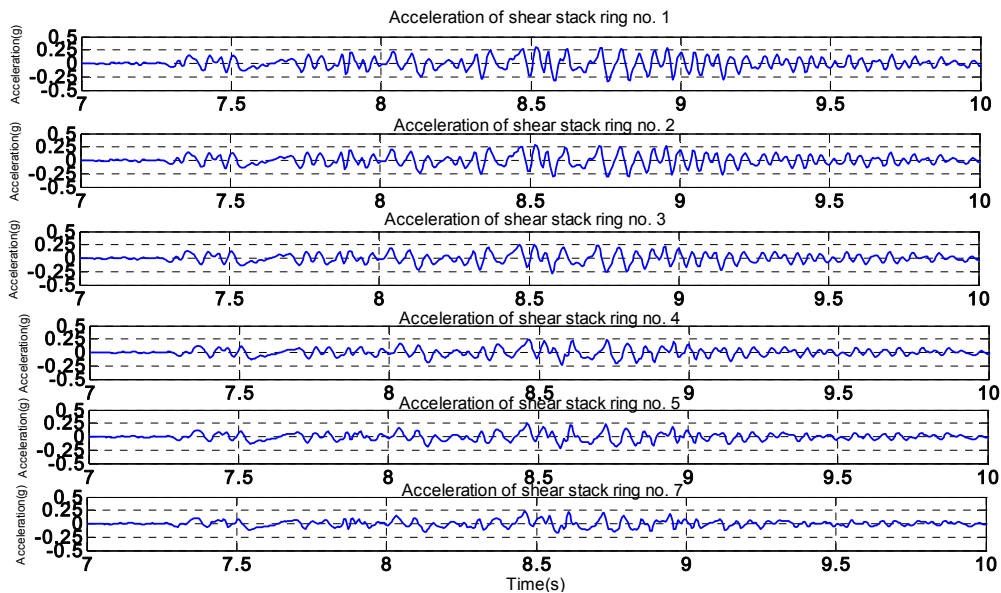


Figure 1.84: acceleration_array outside

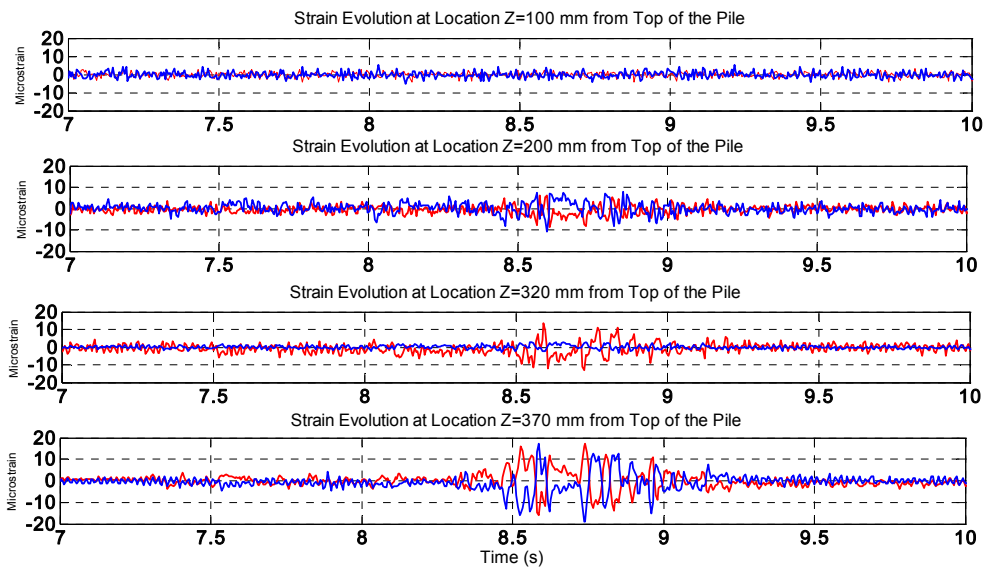


Figure 1.85: strain gauges 100-370 mm

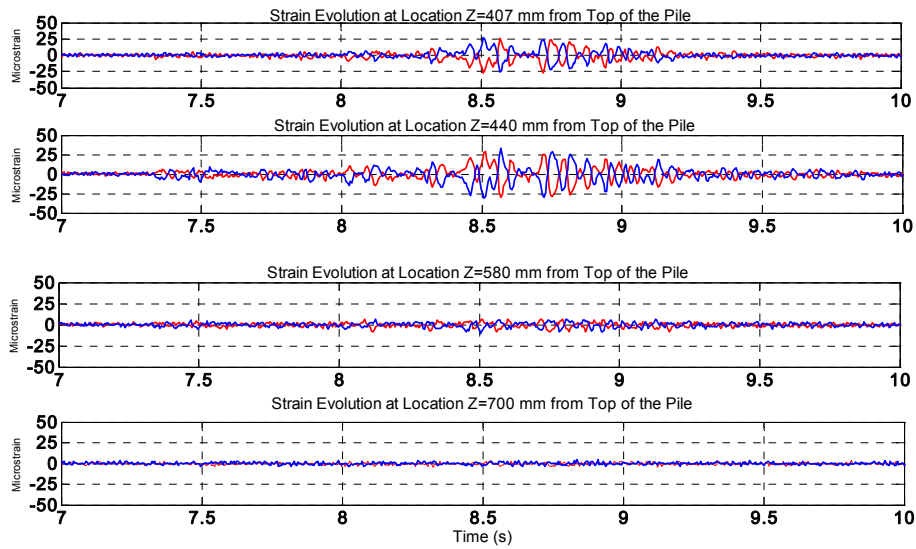


Figure 1.86: strain gauges 407-700 mm

3.3 BE+E_STU 2_FH

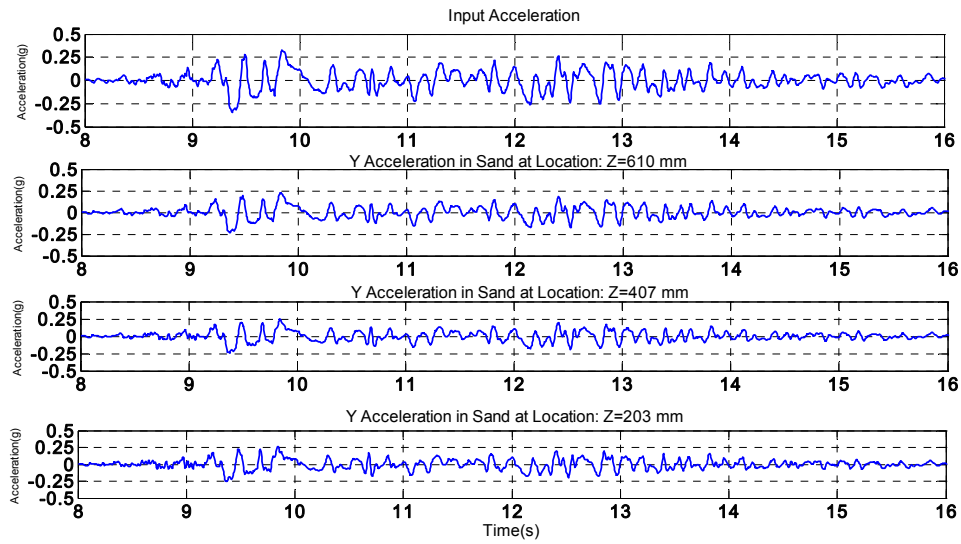


Figure 1.87: acceleration_array inside

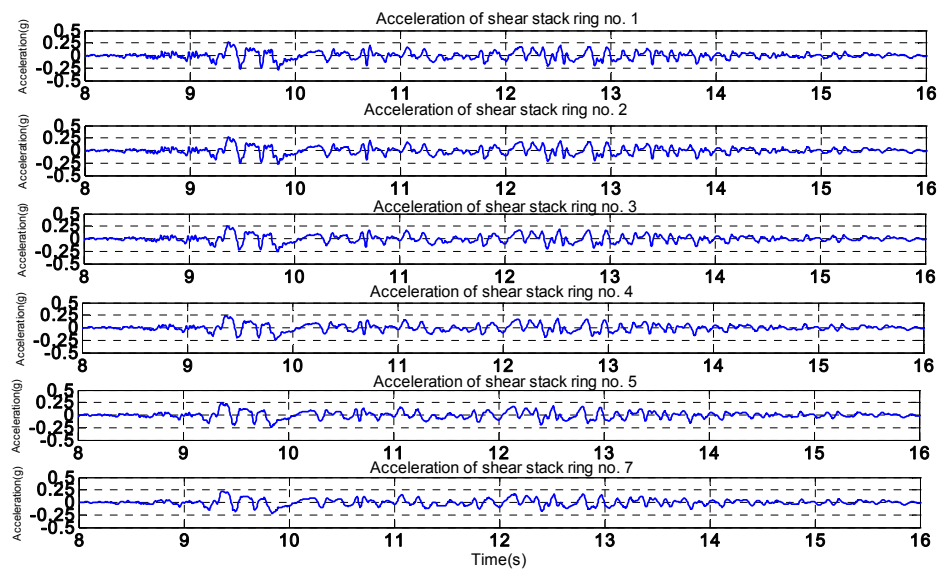


Figure 1.88: acceleration array outside

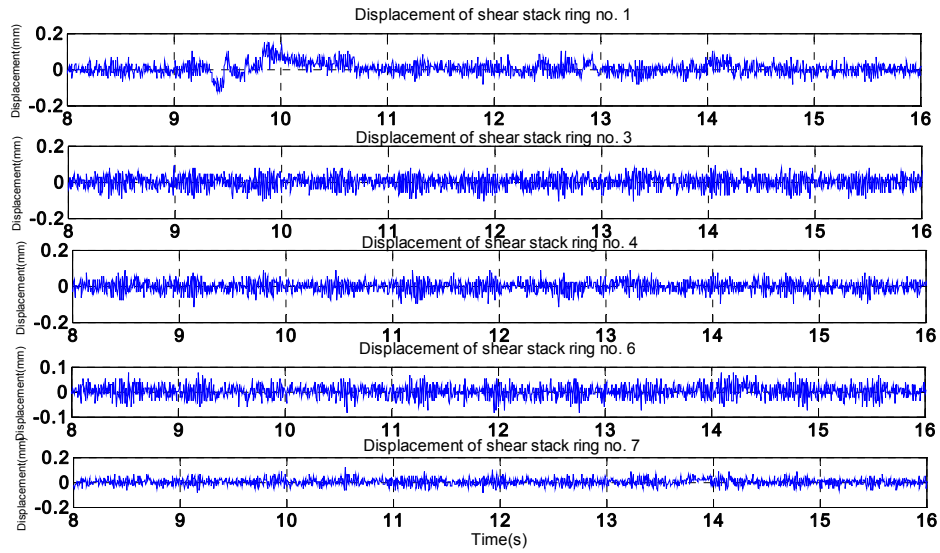


Figure 1.89: displacement of the shear stack

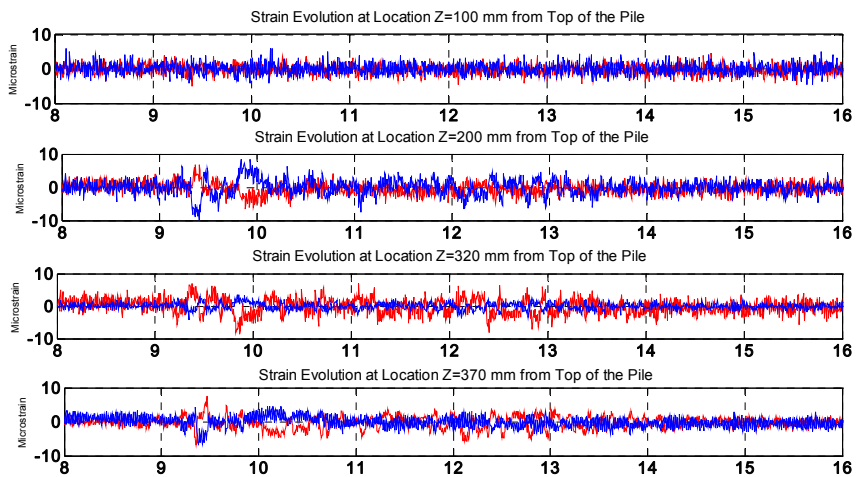


Figure 1.90: strain gauges 100-370 mm

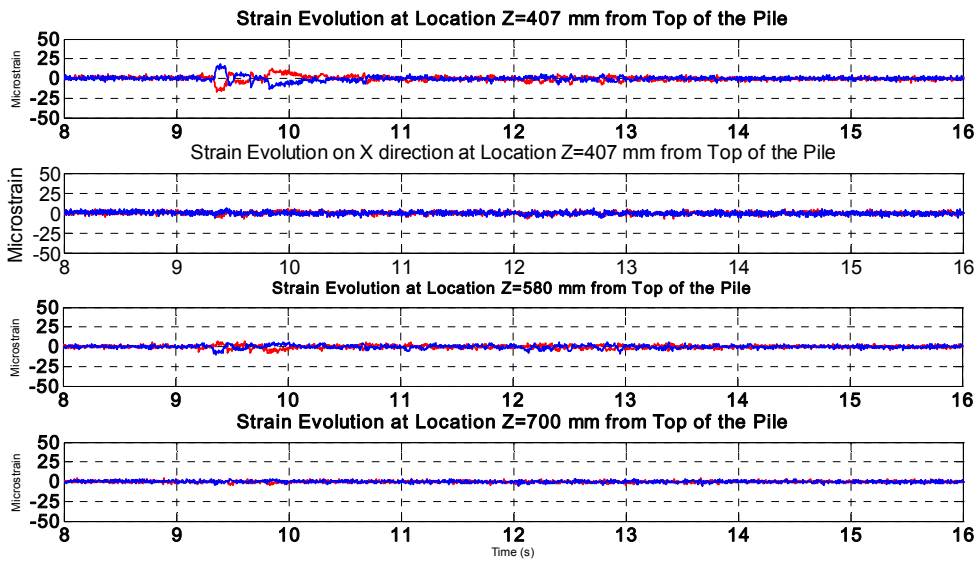


Figure 3: strain gauges 407-700 mm

3.4 BE+E_TMZ 12_FH

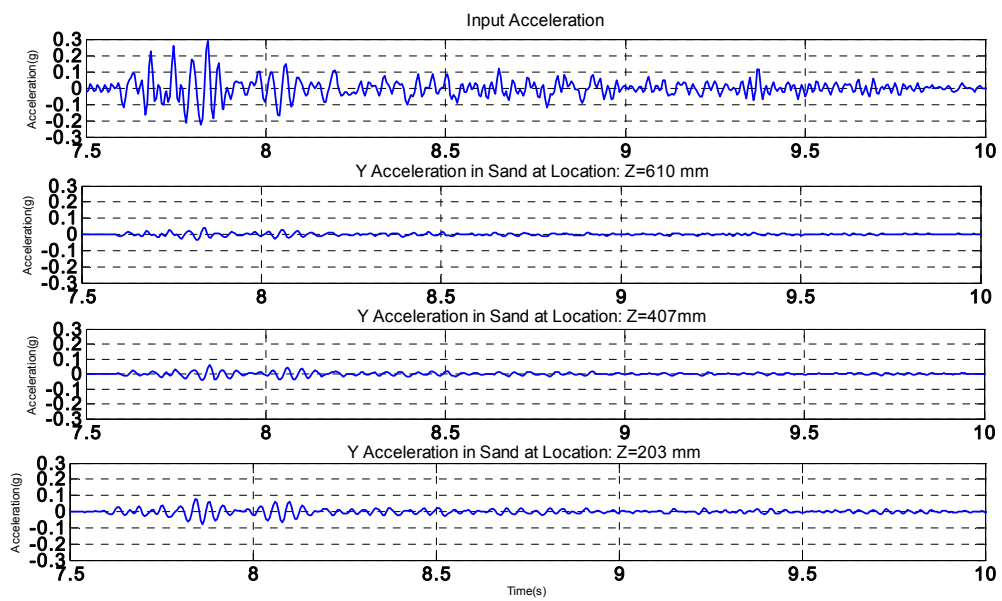


Figure 1.92: acceleration in sand

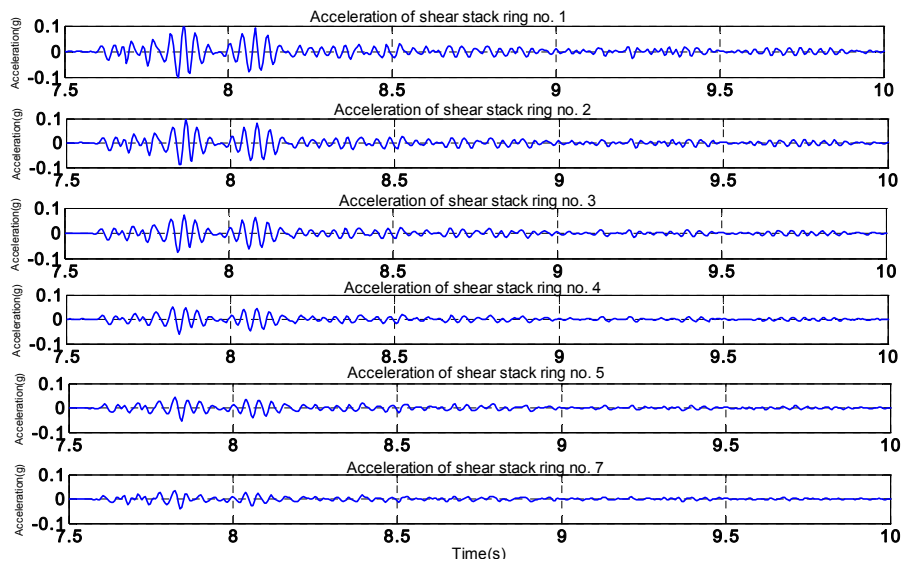


Figure 1.93: acceleration external array

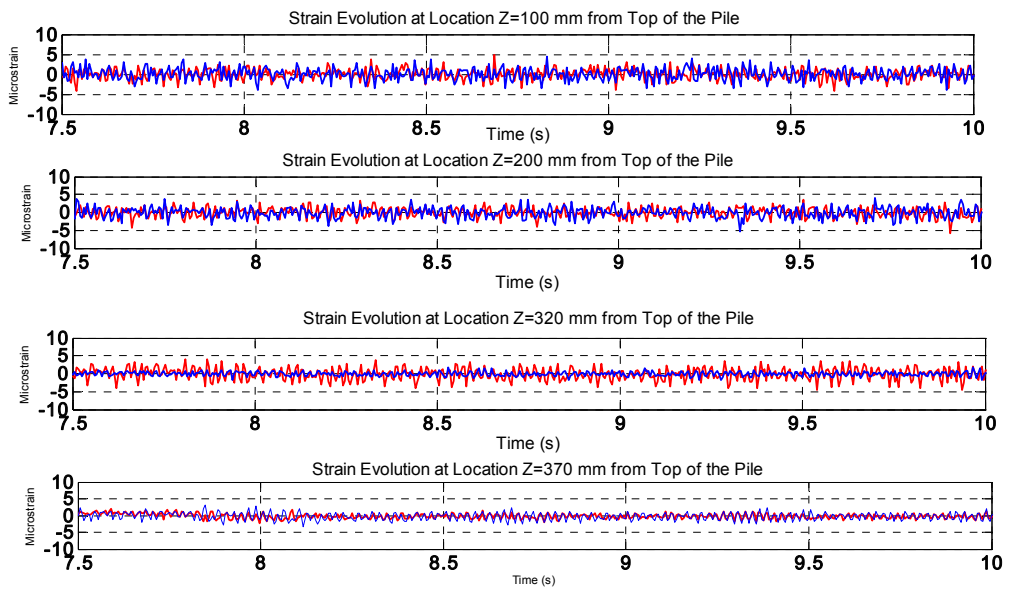


Figure 1.94: strain gauges 100-370 mm

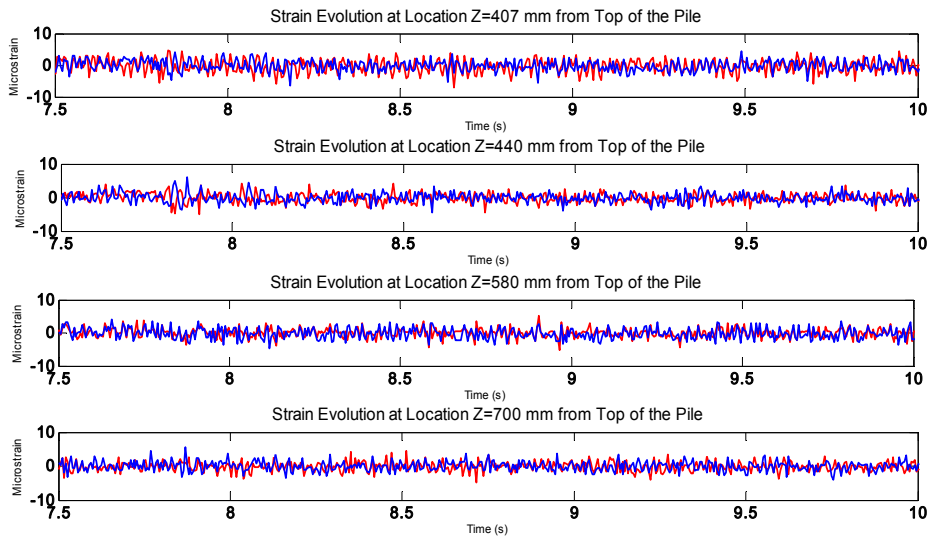


Figure 3.95: strain gauges 407-700 mm

3.5 BE+E_TMZ 2_FH

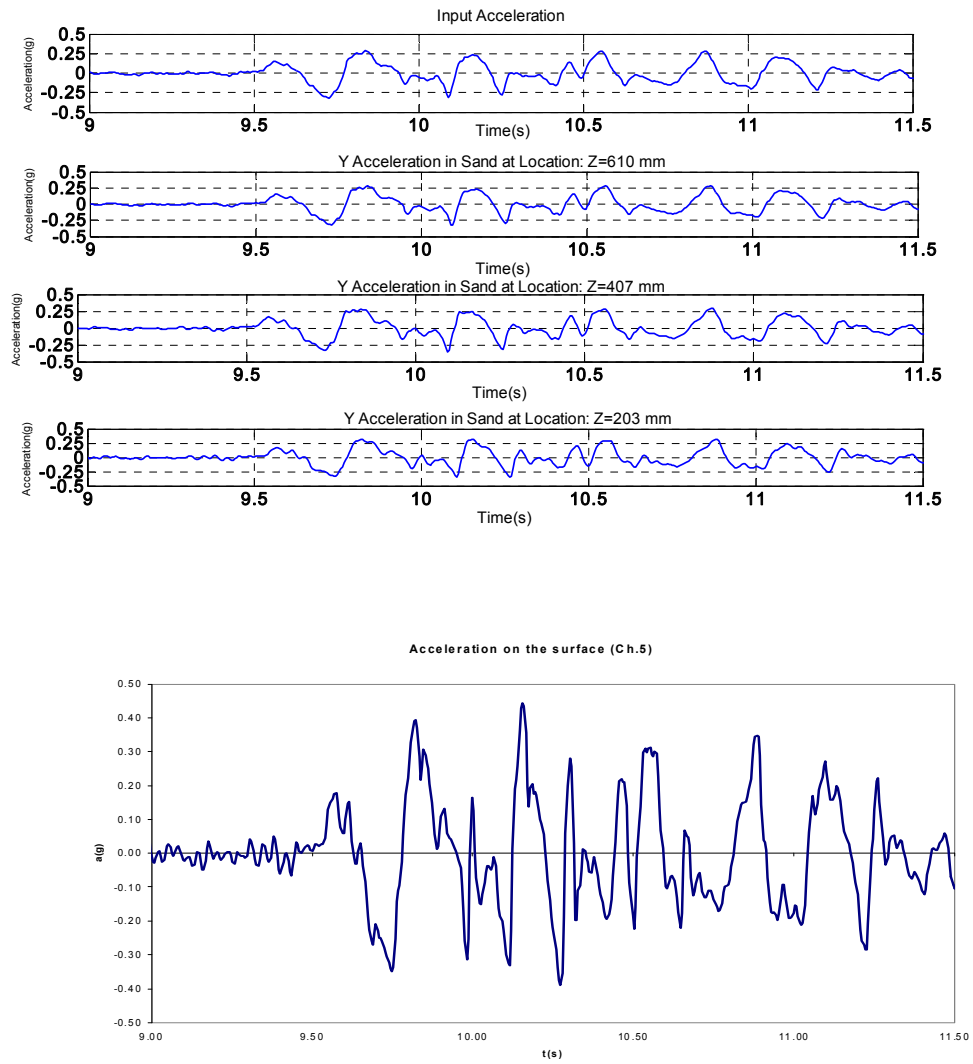


Figure 1.94: acceleration array inside

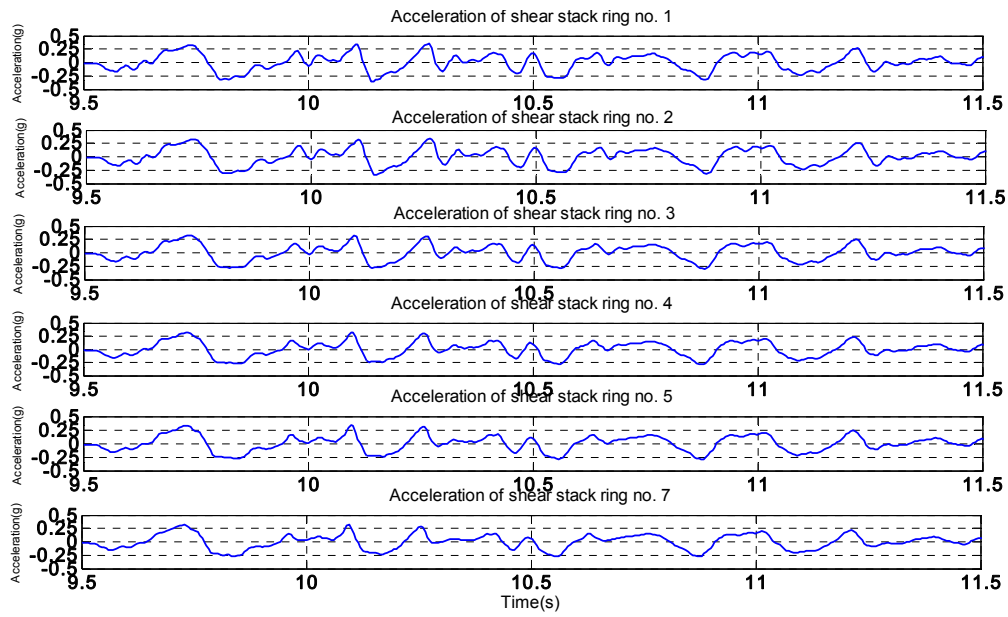


Figure 1.95 acceleration array outside

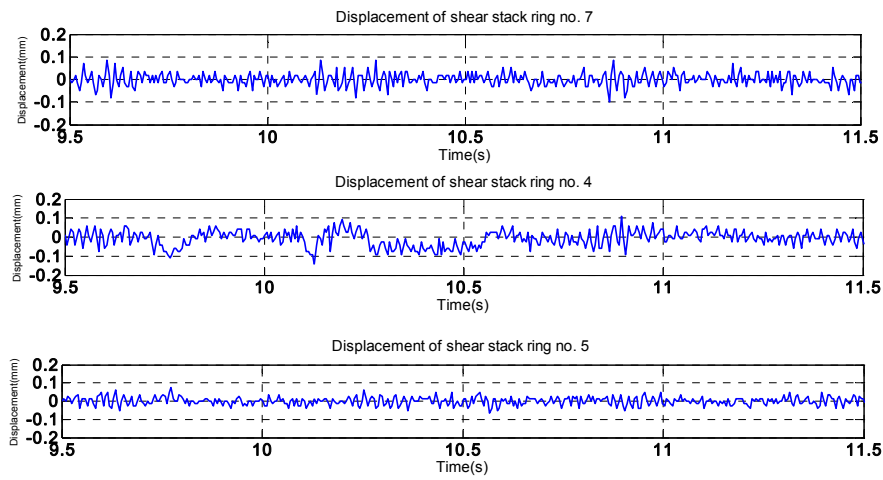


Figure 1.96 displacement

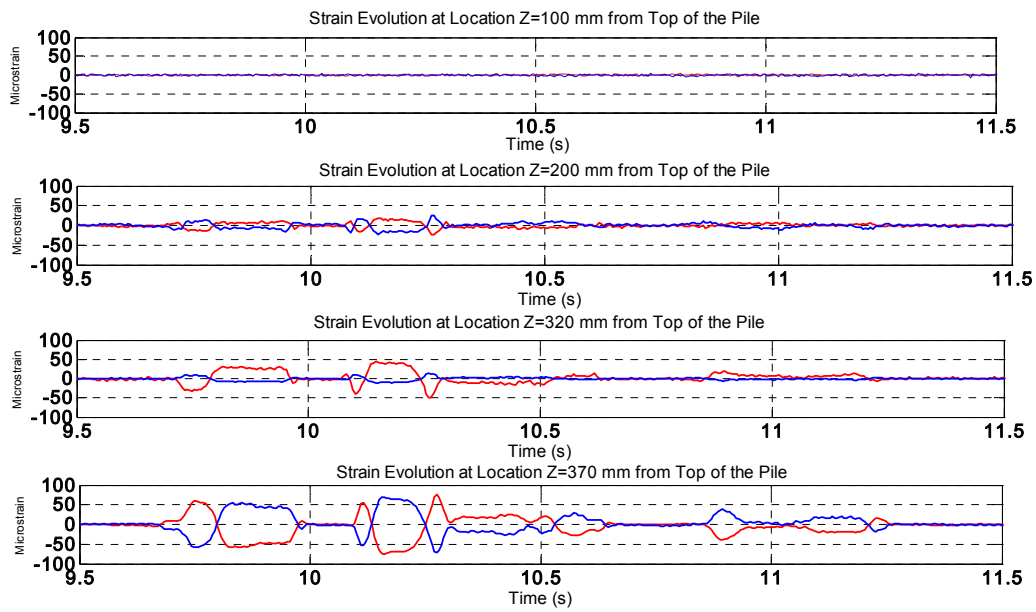


Figure 1.97 strain gauges 100-370

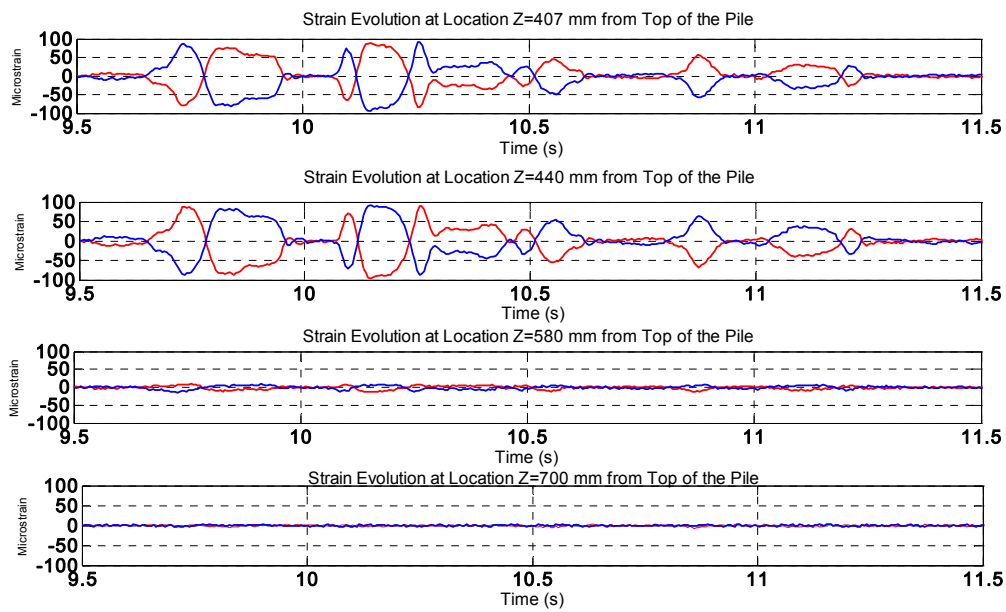


Figure 1.98 strain gauges 407-700

NO ROTATION HEAD (NRH)

3.6 BE+E_STU12_NRH

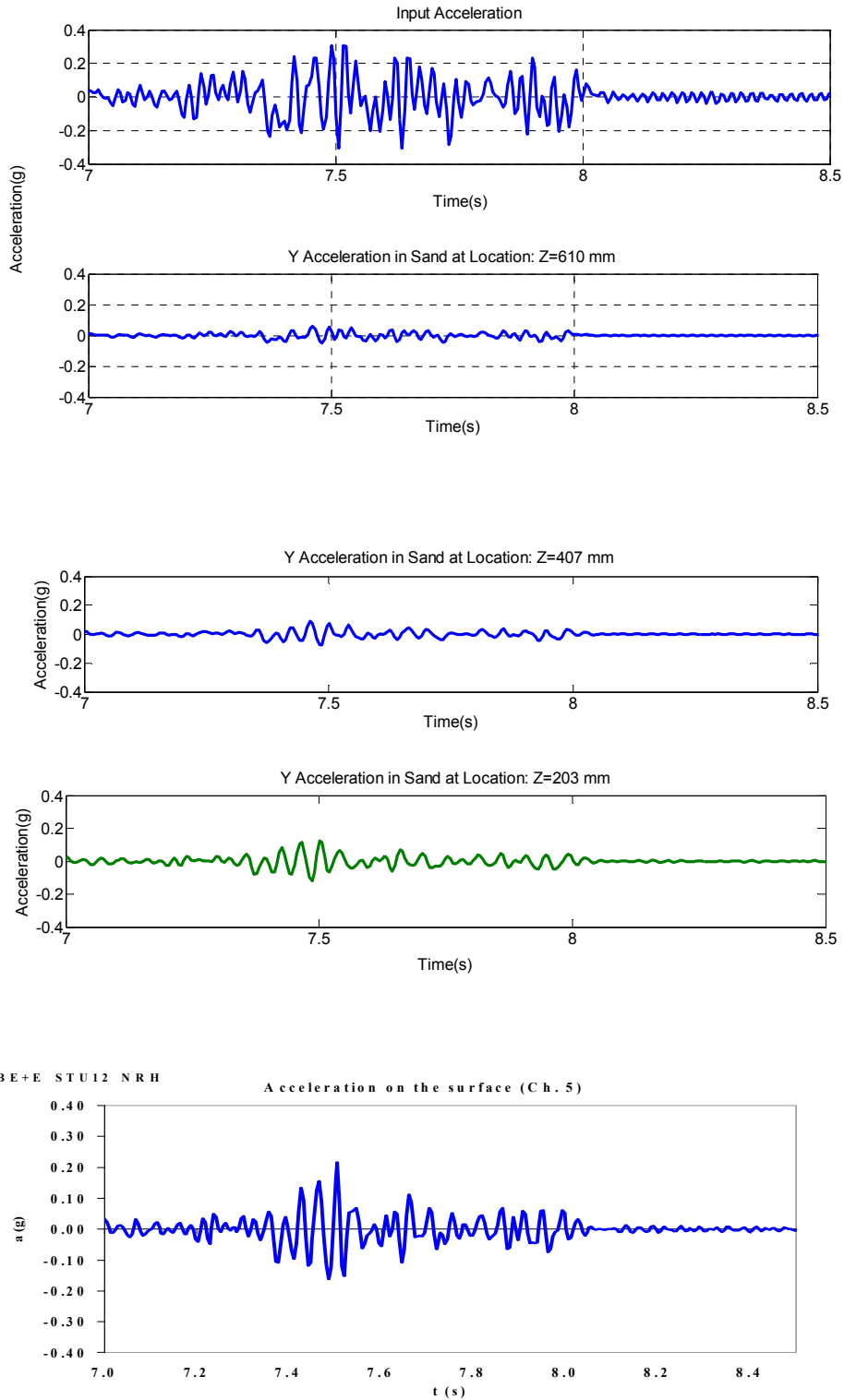


Figure 1.99: acceleration array inside

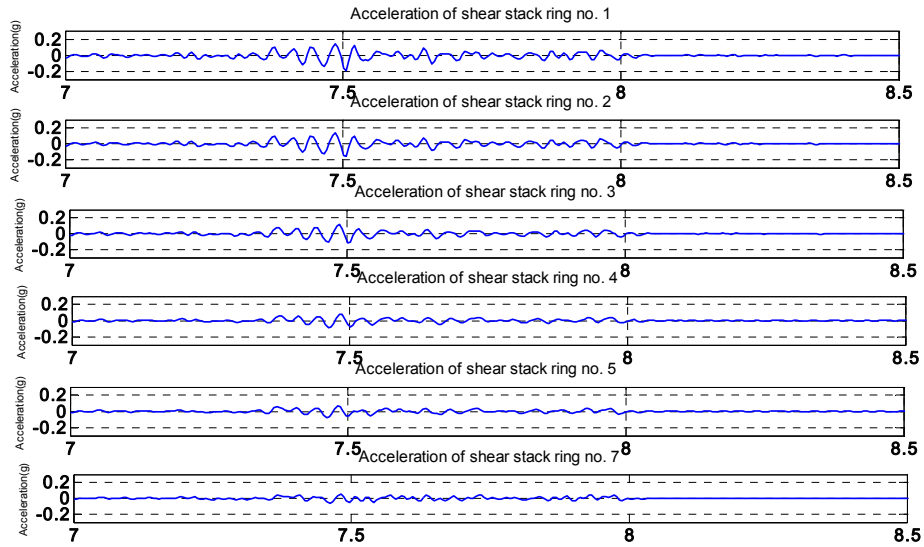


Figure 1.100: acceleration array outside

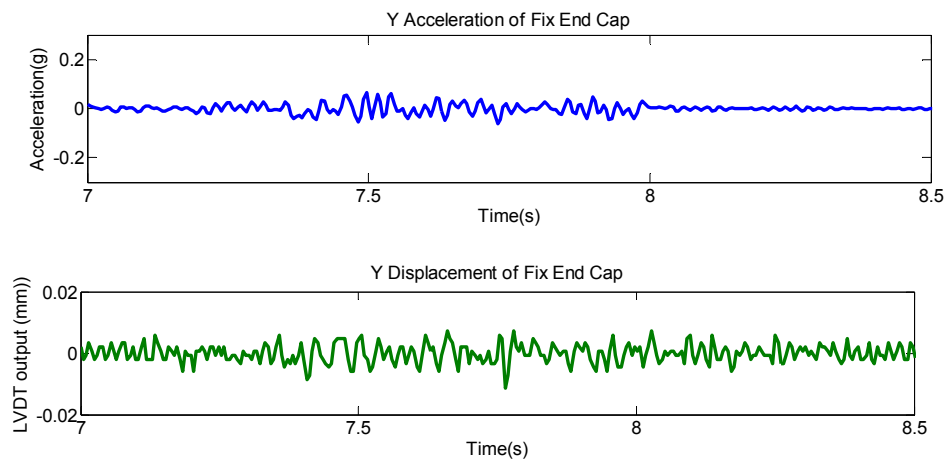


Figure 1.101: top pile

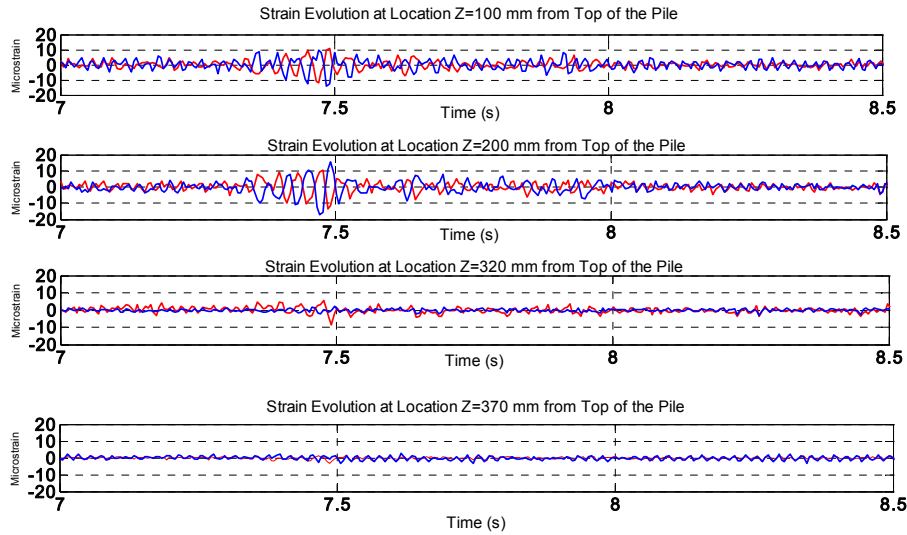


Figure 1.102: strain gauges 100-370 mm

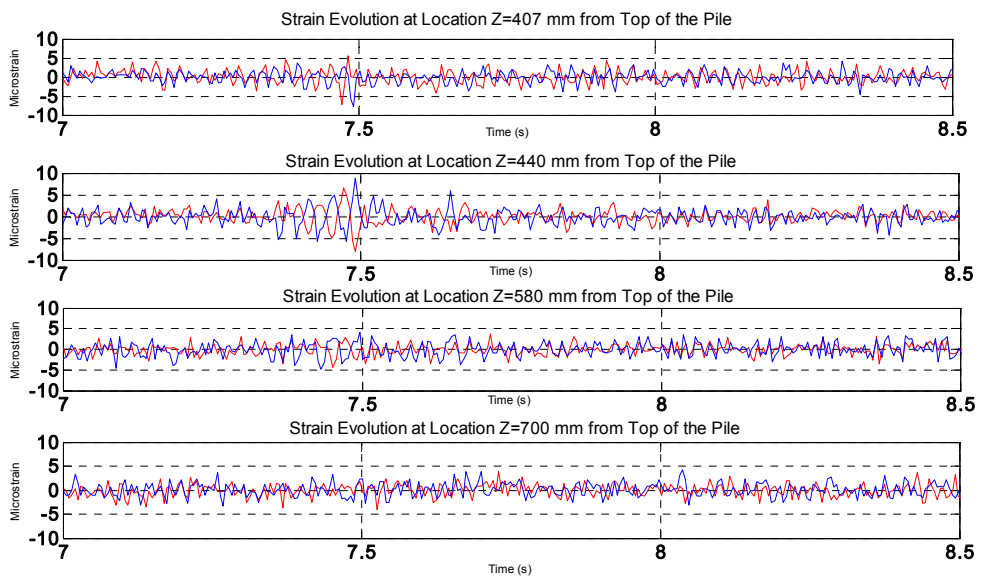


Figure 1.103: strain gauges 407-700 mm

3.7 BE+E_STU5_NRH

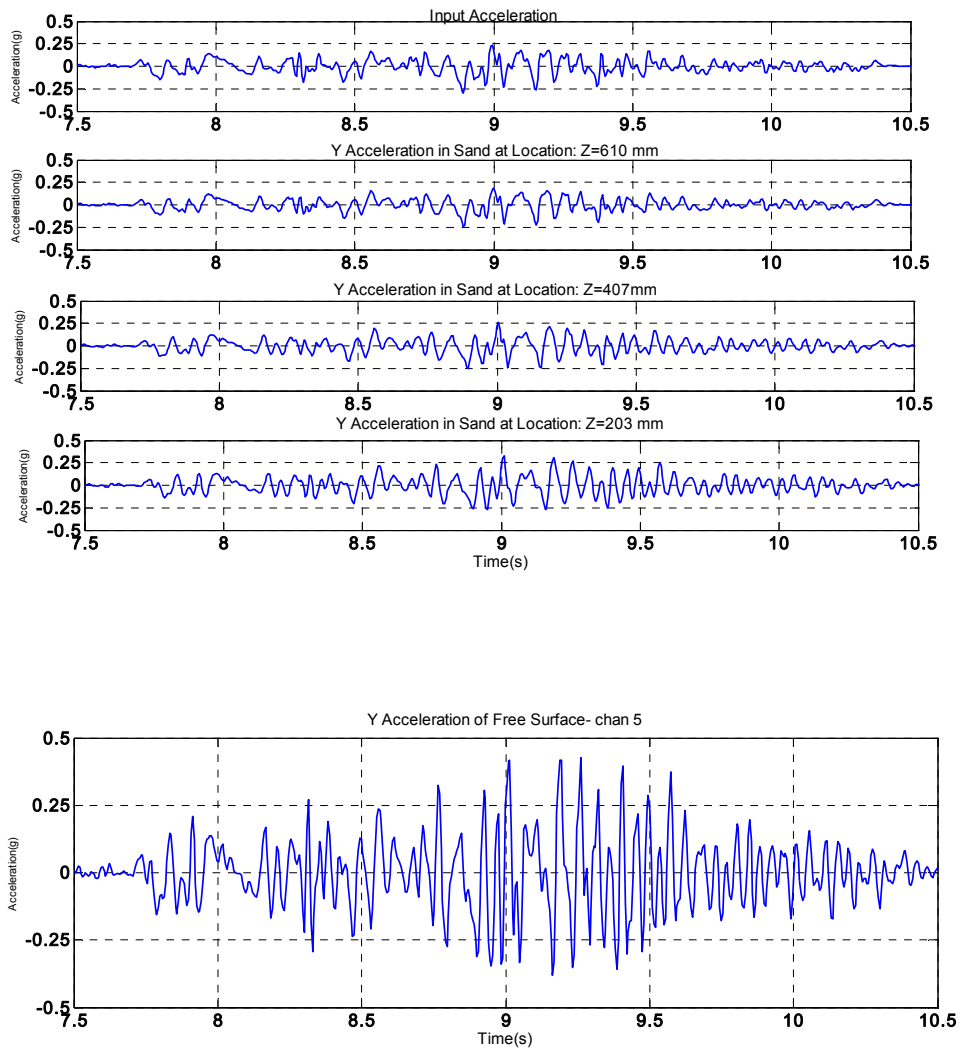


Figure 1.104: acceleration: array inside

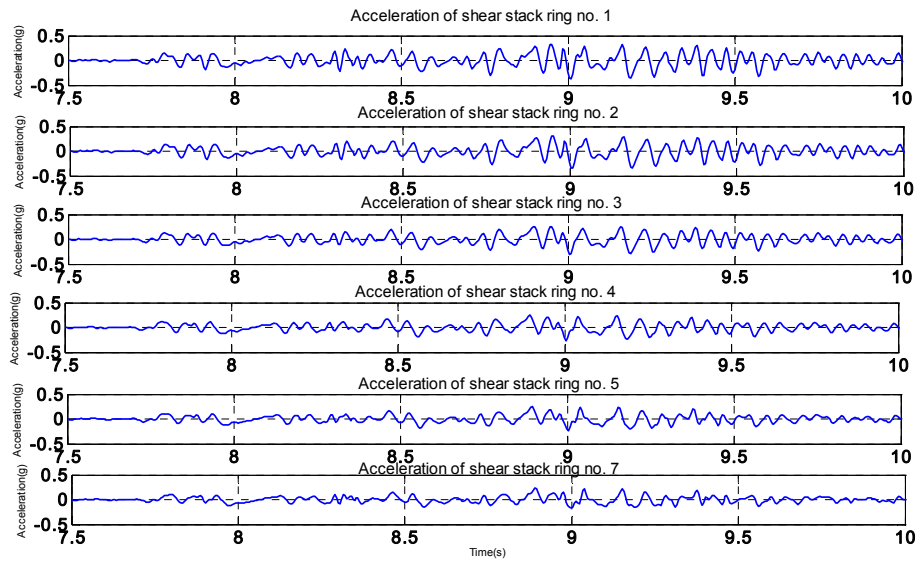


Figure 1.105: acceleration: array outside

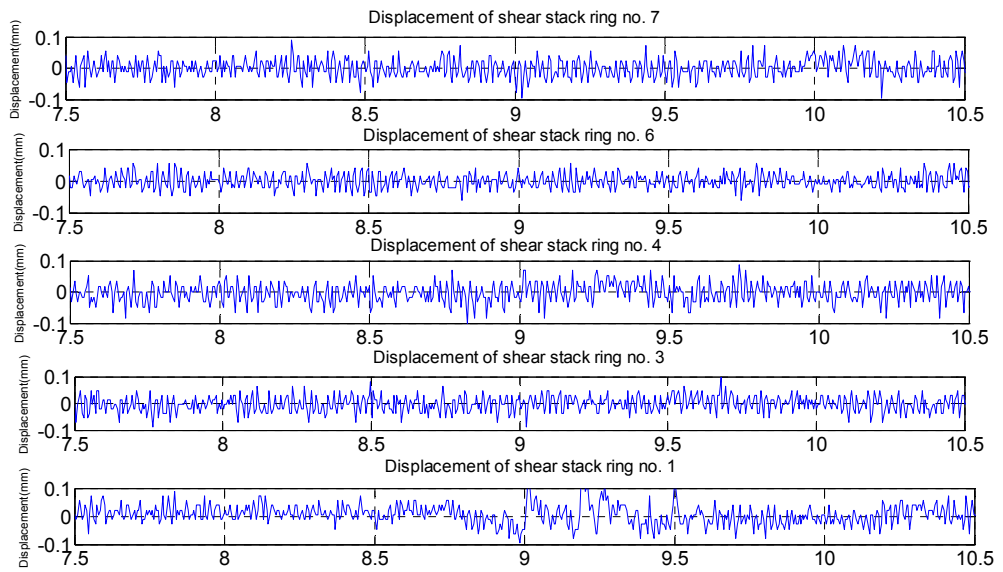


Figure 1.106: acceleration: array outside

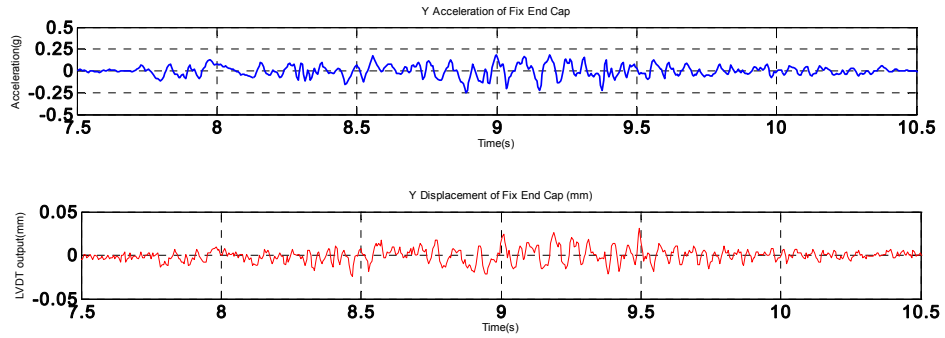


Figure 1.107: top pile

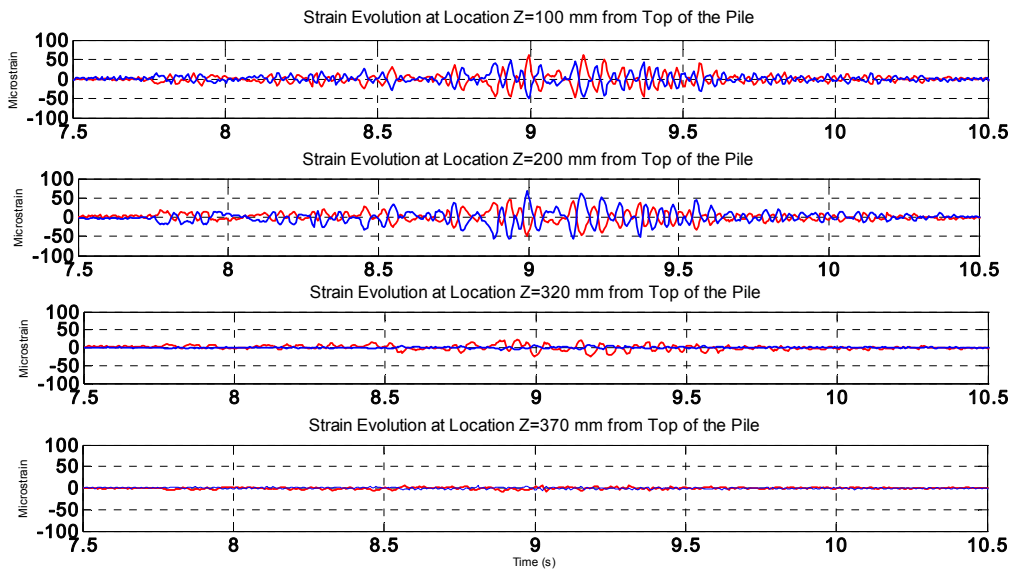


Figure 1.108: strain gauges 100-370 mm

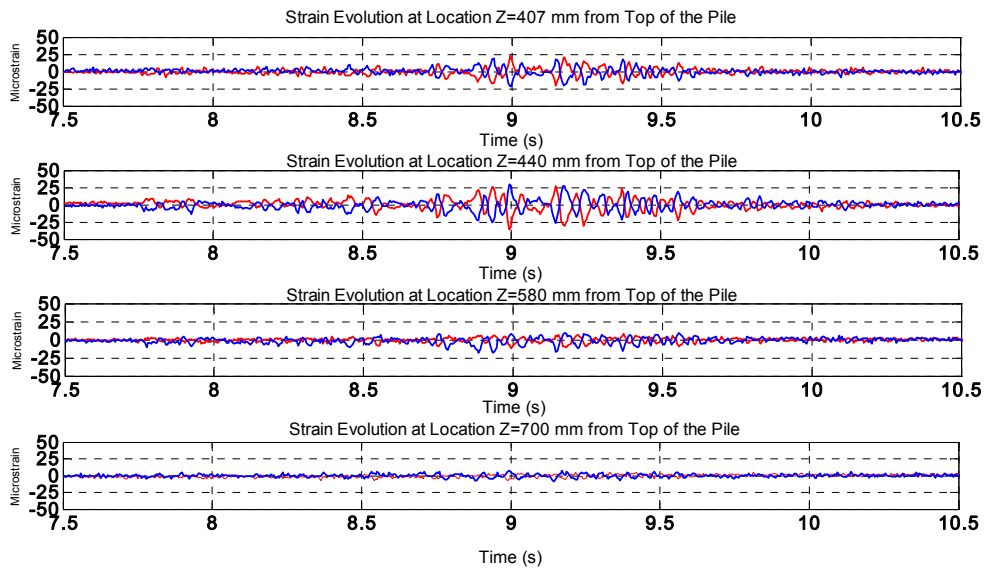


Figure 1.109: strain gauges 407-700 mm

3.8 BE+E_STU2_NRH

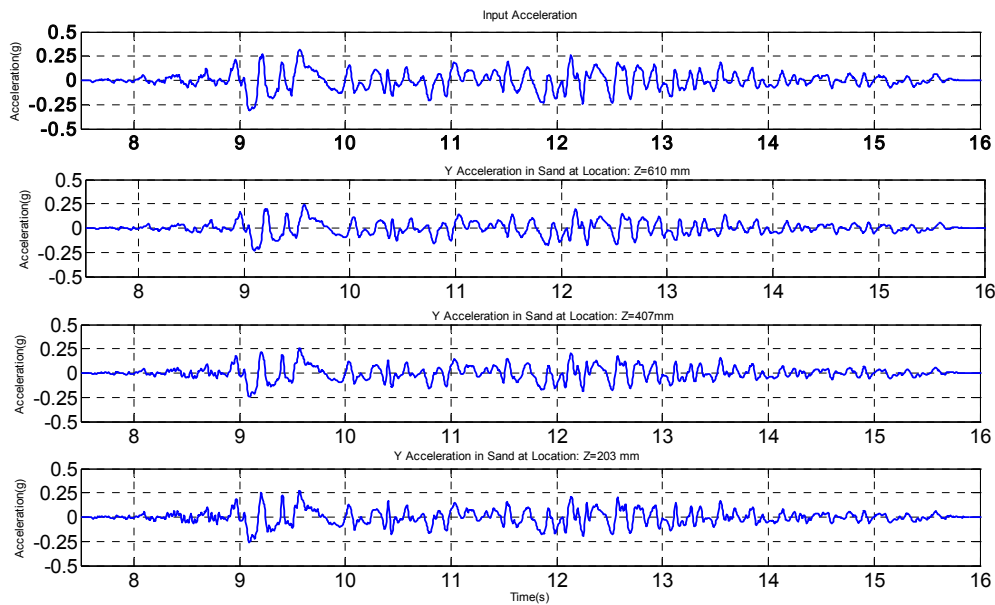


Figure 1.110: acceleration_array inside

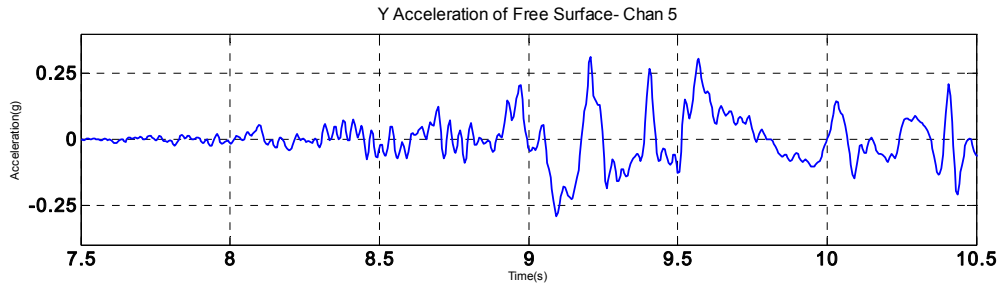


Figure 1.111 acceleration_surface

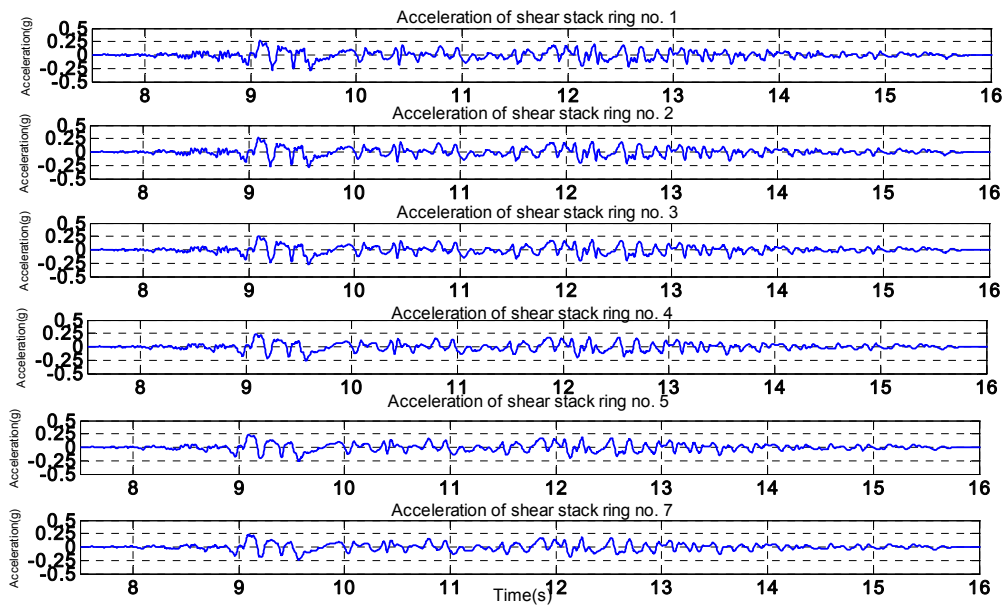


Figure 1.112 acceleration_outside

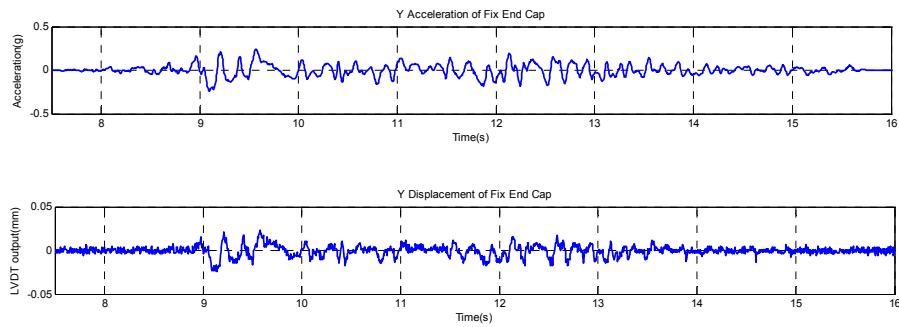


Figure 1.113 pile head

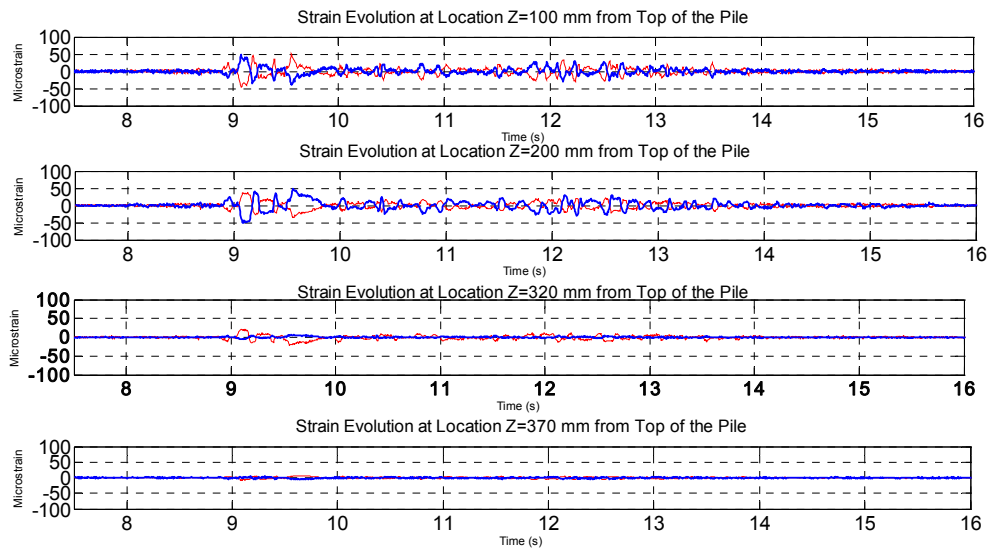


Figure 1.114 strain gauges 100-370

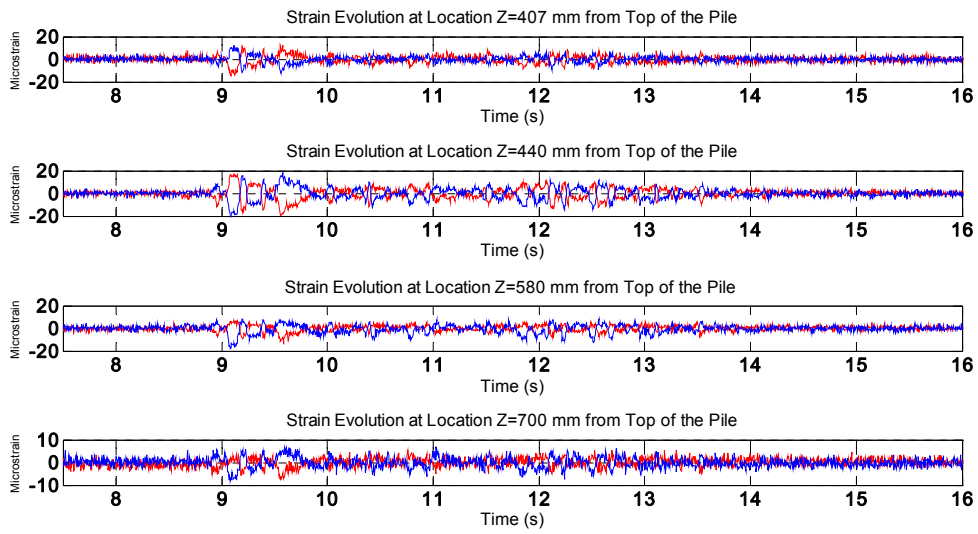


Figure 1.115 strain gauges 407-700

3.9 BE+E_TMZ12_NRH

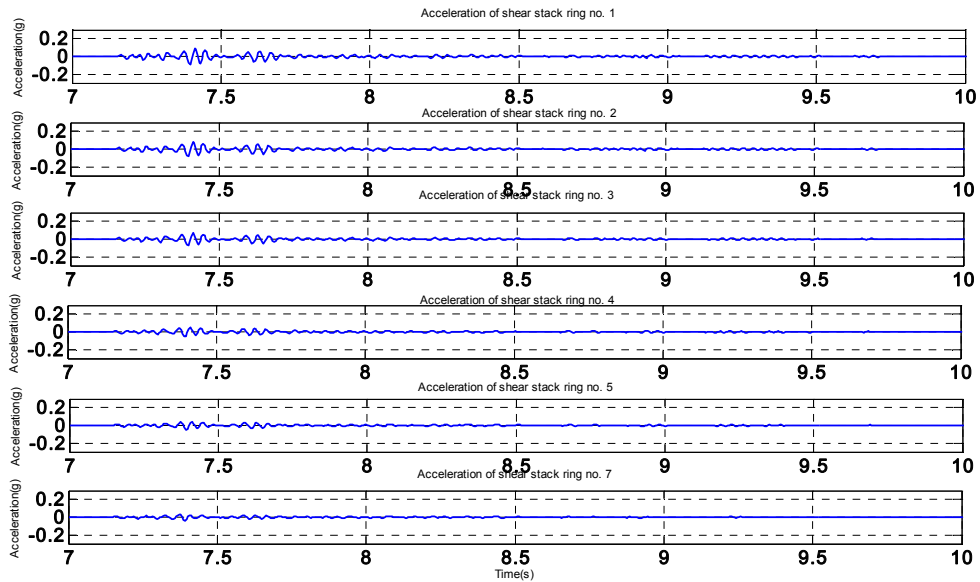
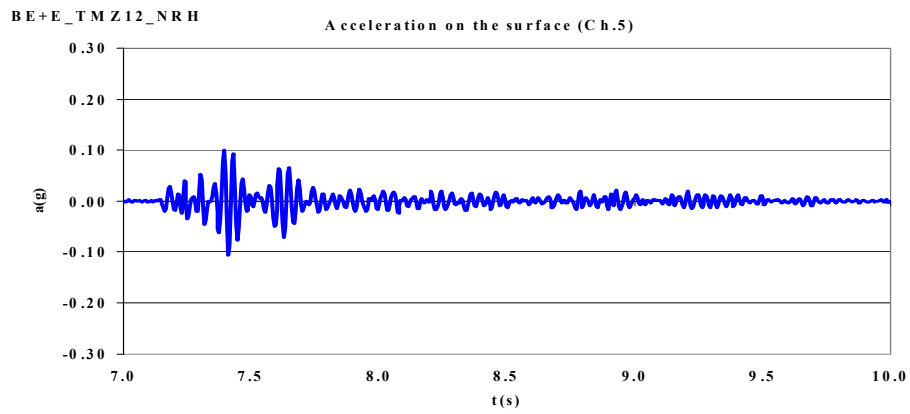
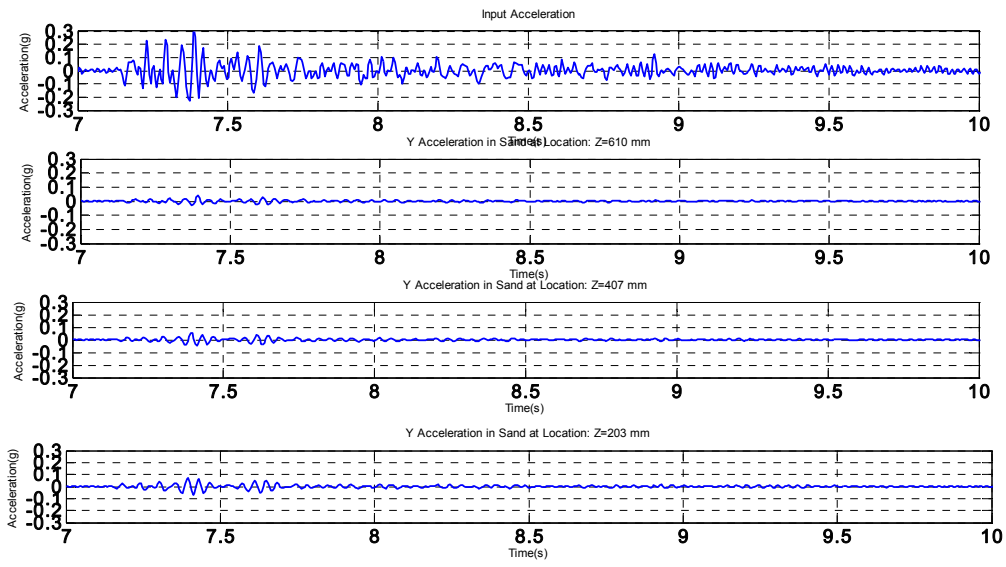


Figure 1.116 acceleration: array outside



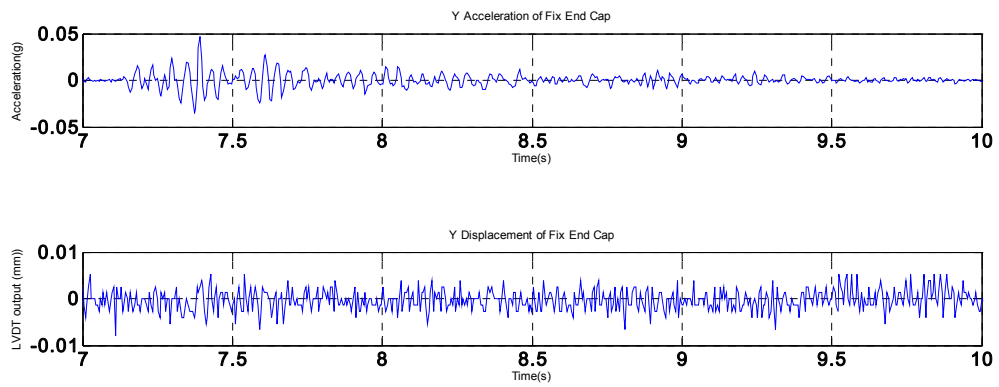


Figure 1.118 top pile : acceleration and LVDT

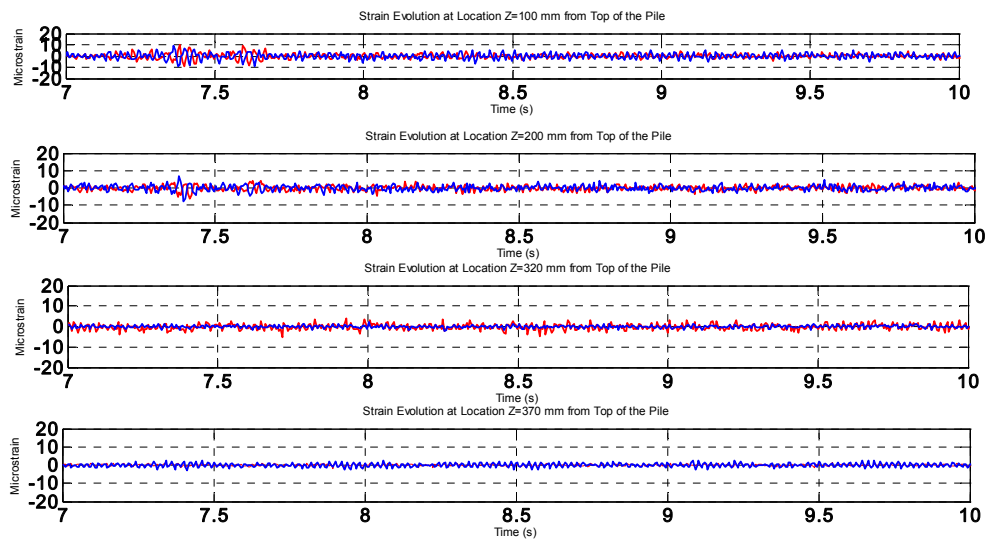


Figure 1.119 strain gauges: 100-370 mm

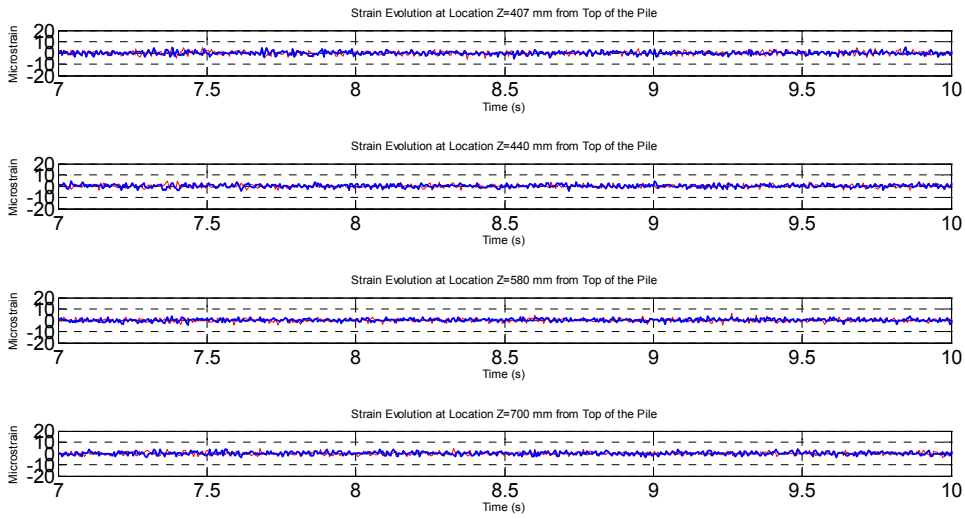


Figure 1.120 strain gauges: 407-700 mm

3.10 BE+E_TMZ2_NRH

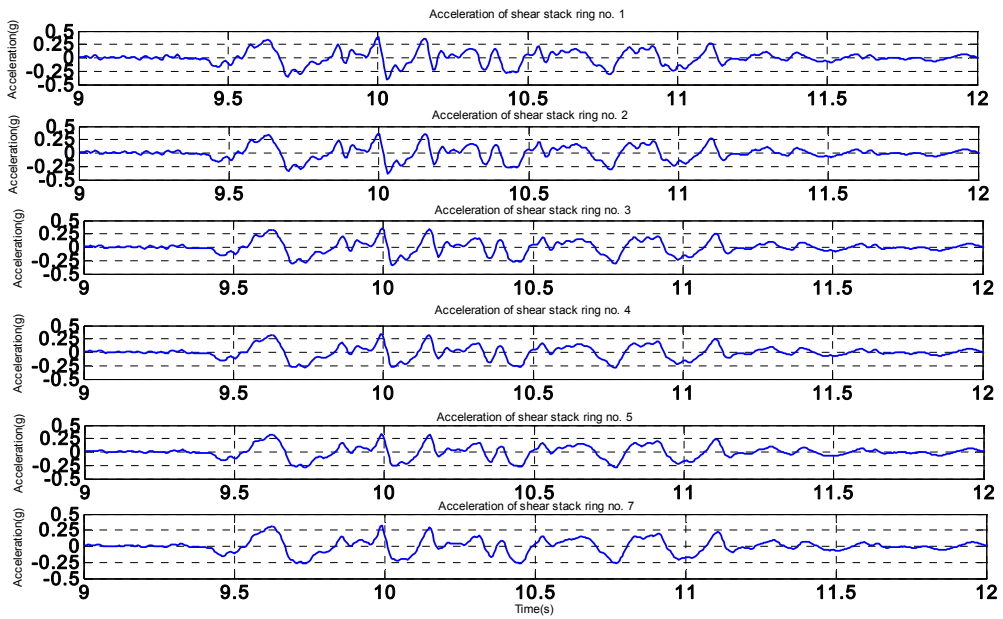


Figure 1.121 acceleration: array outside

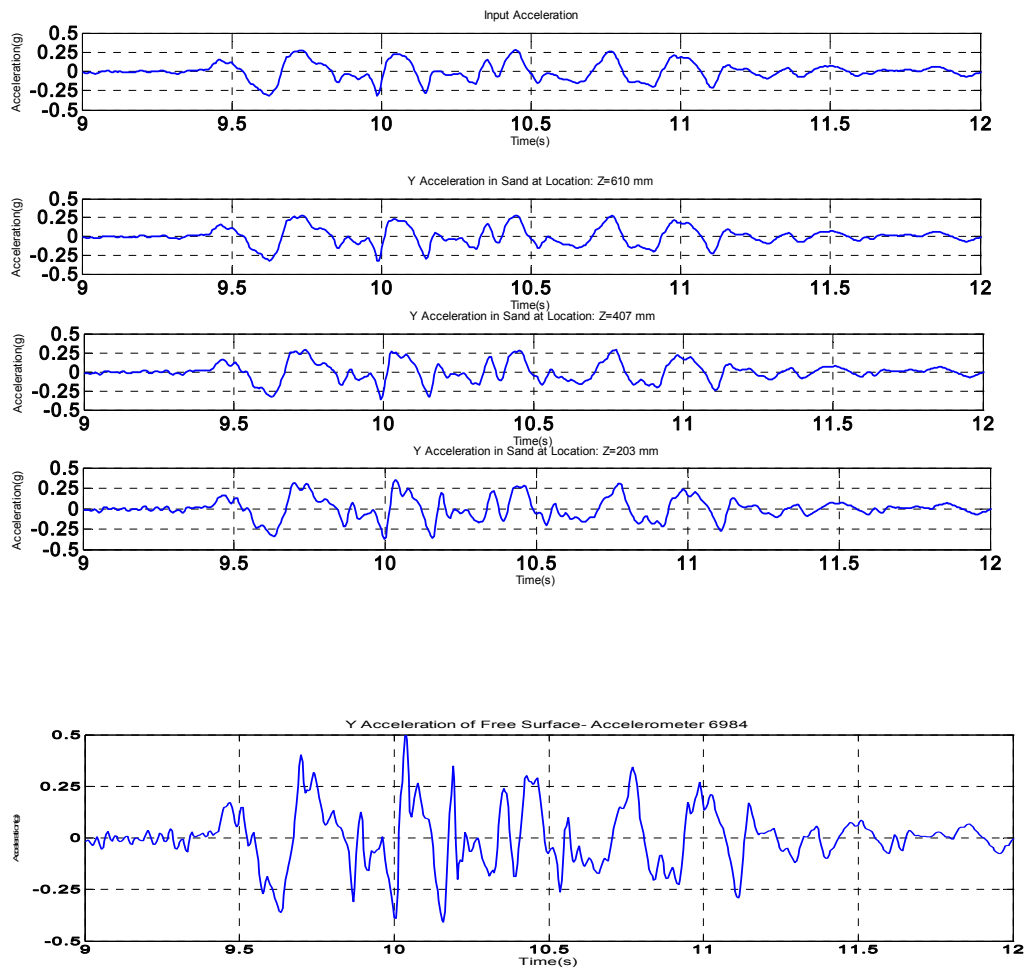


Figure 1.122 acceleration: array inside

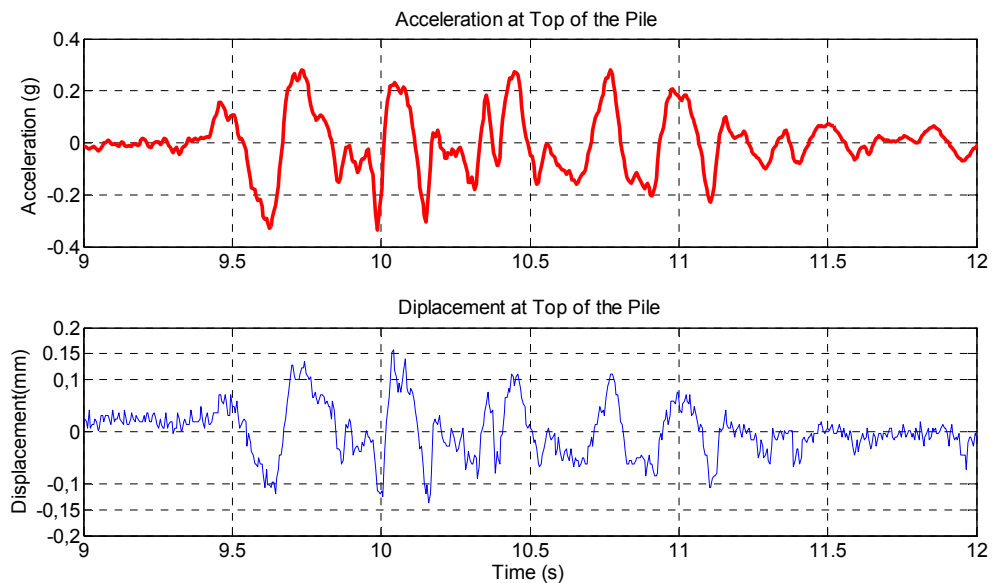


Figure 1.123 top pile: acceleration and LVDT

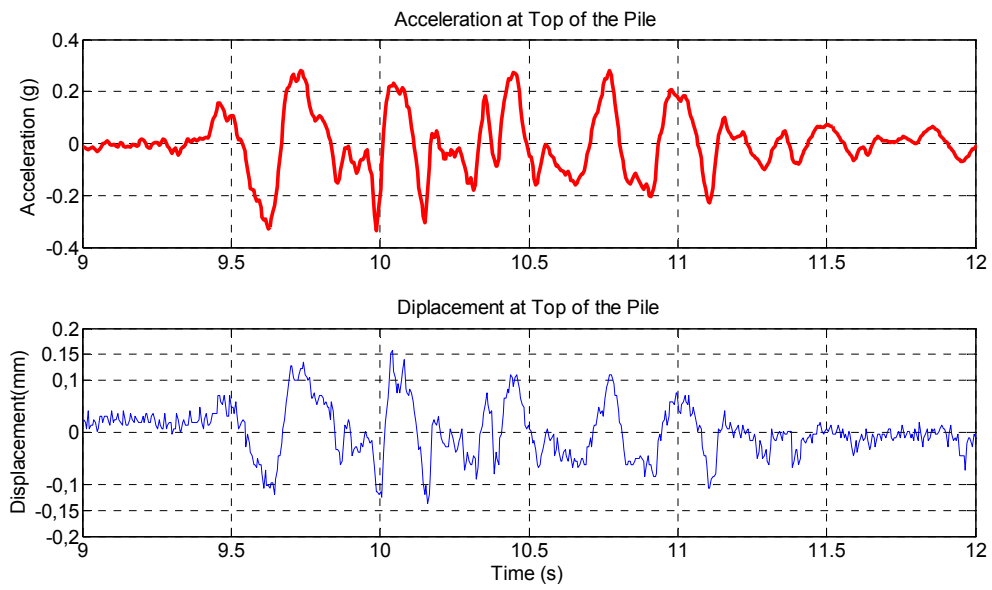


Figure 1.123 top pile: acceleration and LVDT

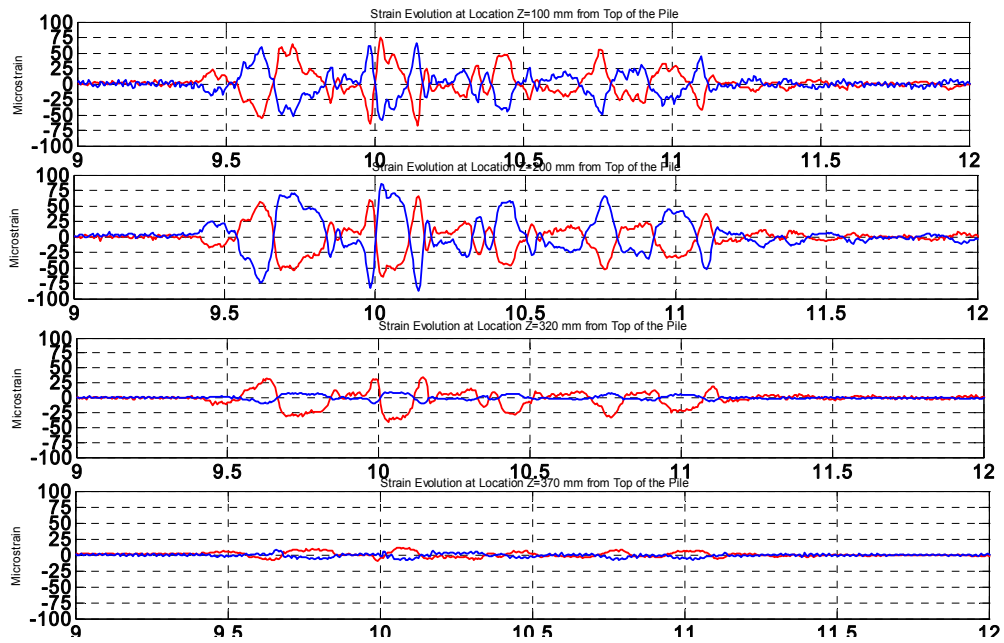
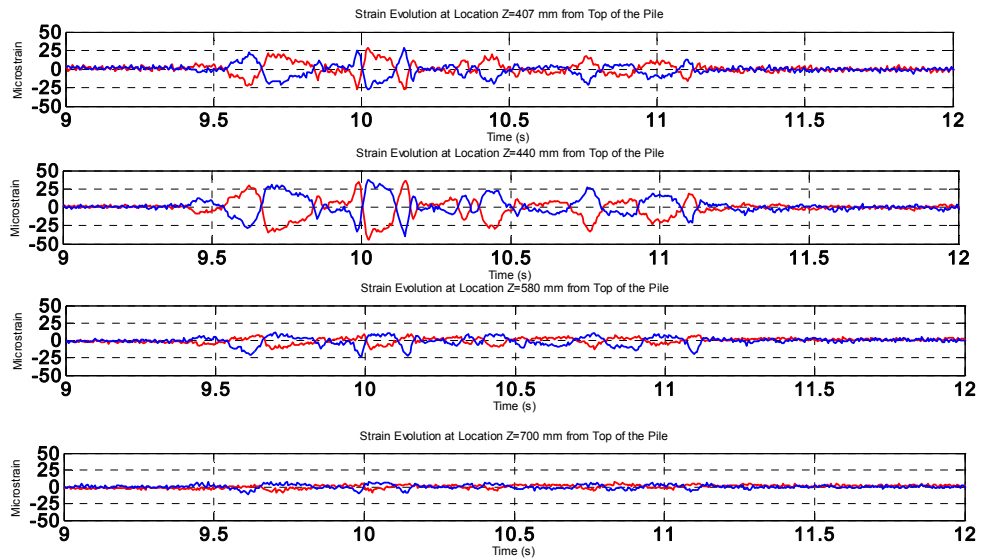


Figure 1.124 strain gauges 100-370 mm



NO ROTATION HEAD +SDOF (NRH+SDOF)

3.11 BE+E_STU12_NRH+SDOF

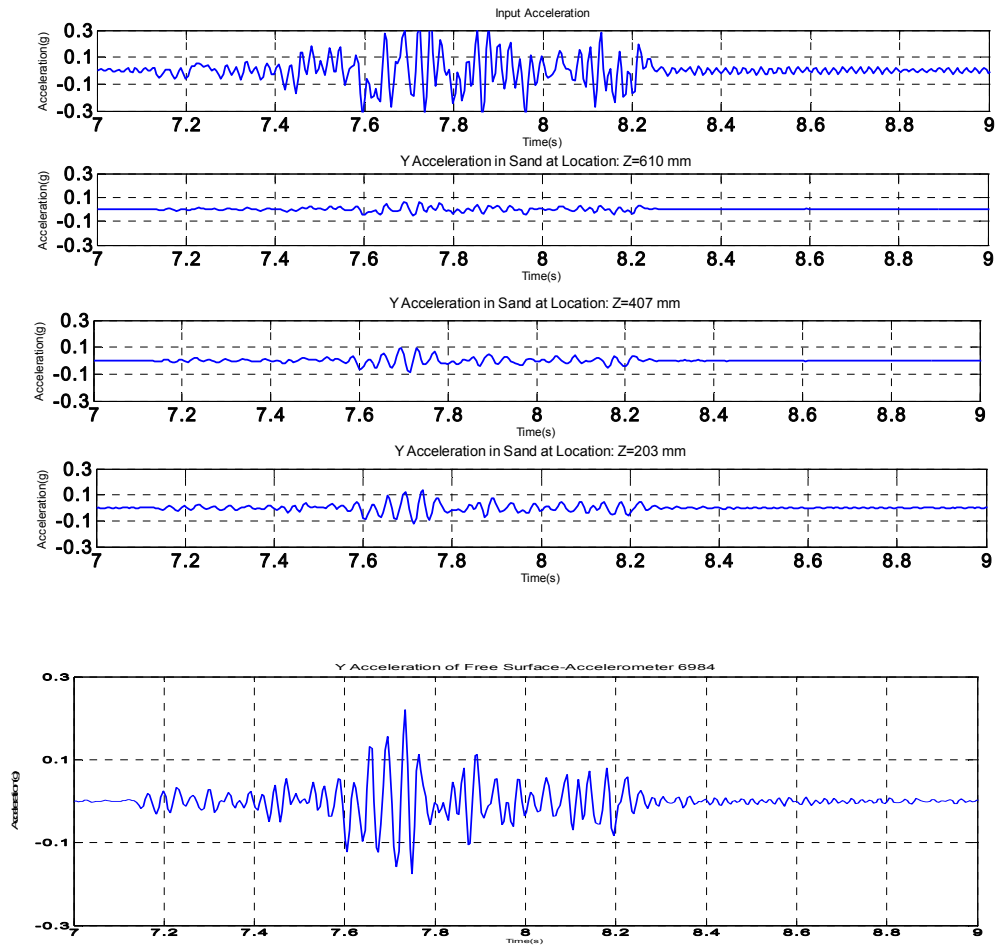


Figure 1.126 acceleration: array inside

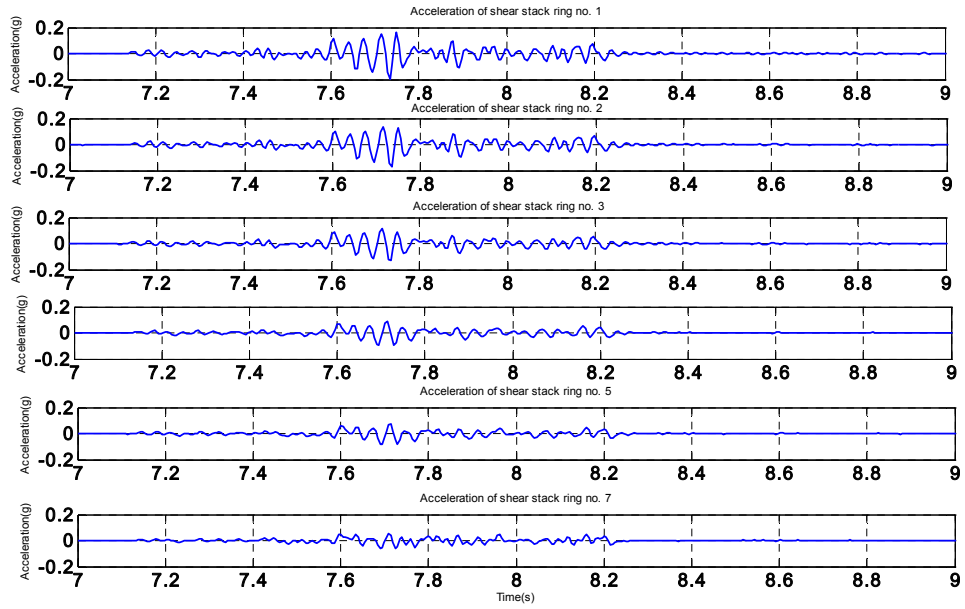


Figure 1.127 acceleration : array outside

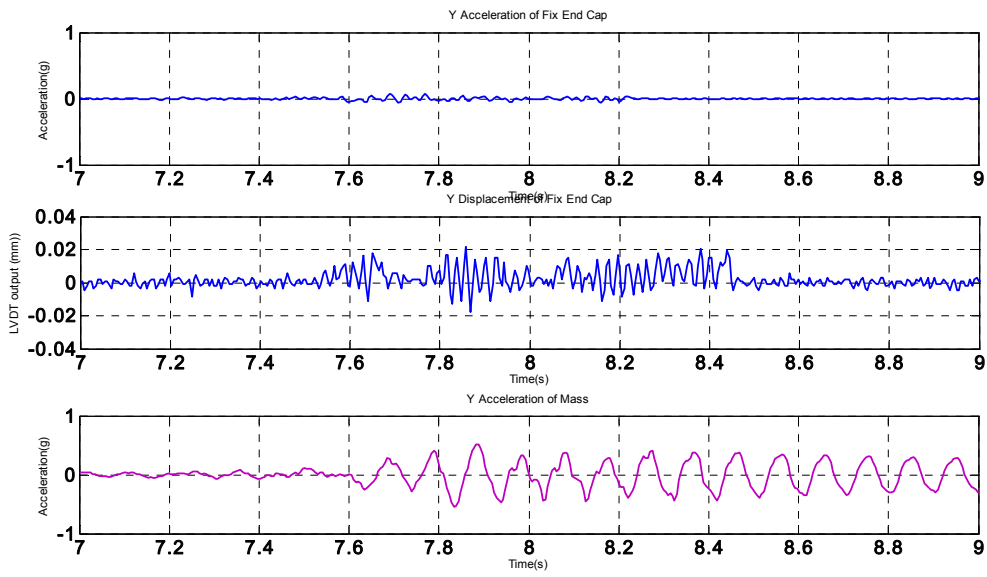


Figure 1.128 top pile: acceleration-LVD-acceleration SDOF

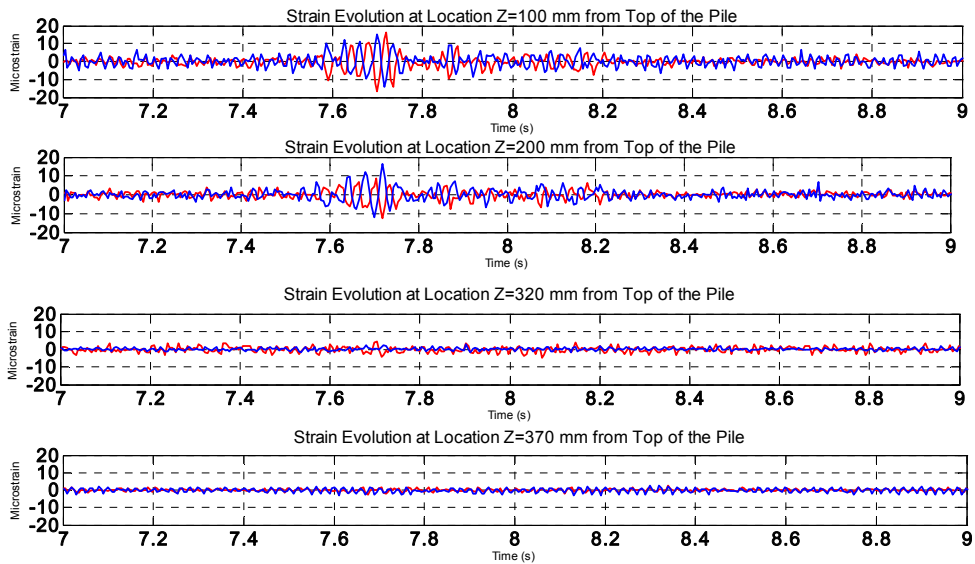


Figure 1.129 strain gauges: 100-370 mm

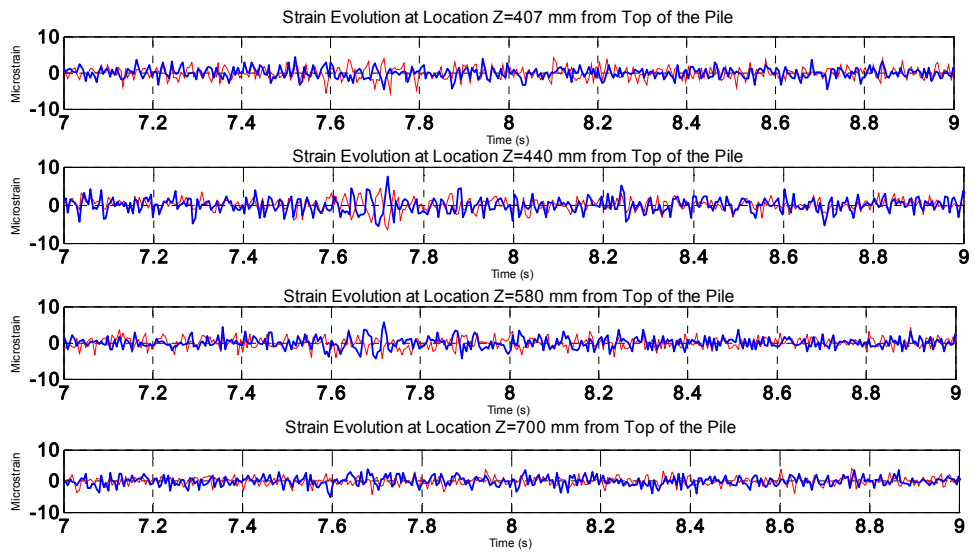


Figure 1.130 strain gauges: 407-700 mm

3.12 BE+E_STU5_NRH+SDOF

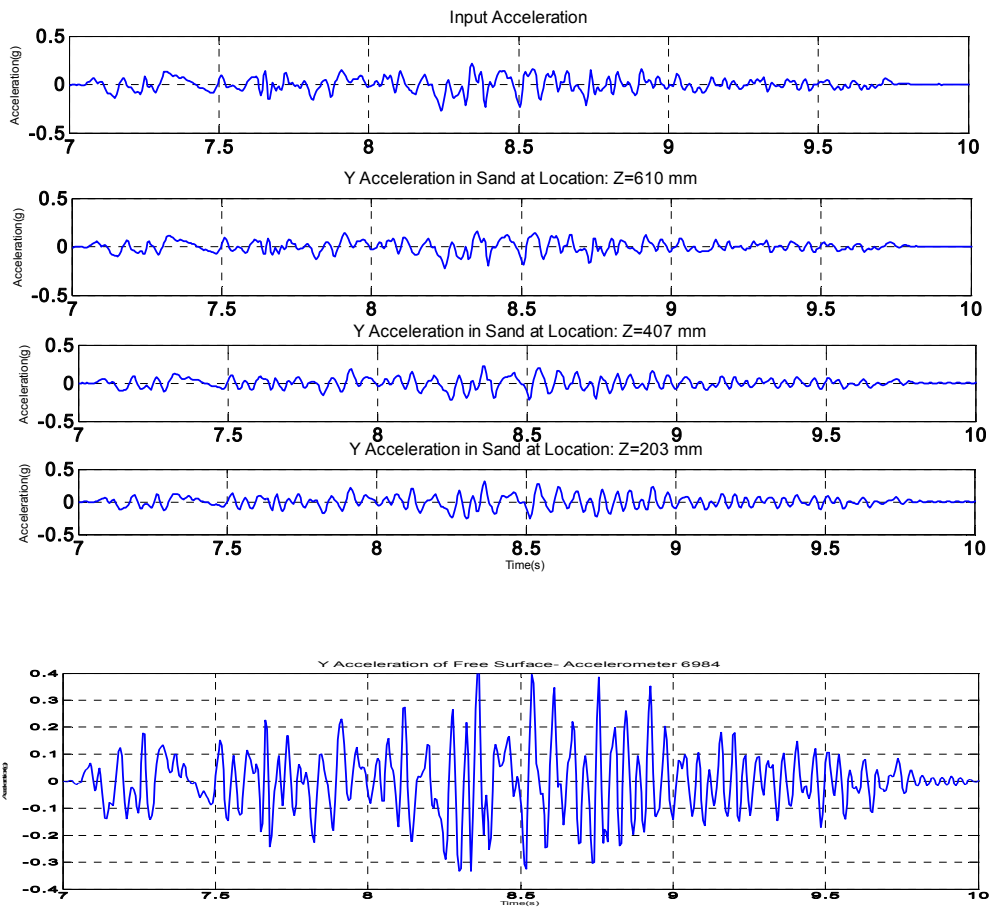


Figure 1.131 acceleration: array inside

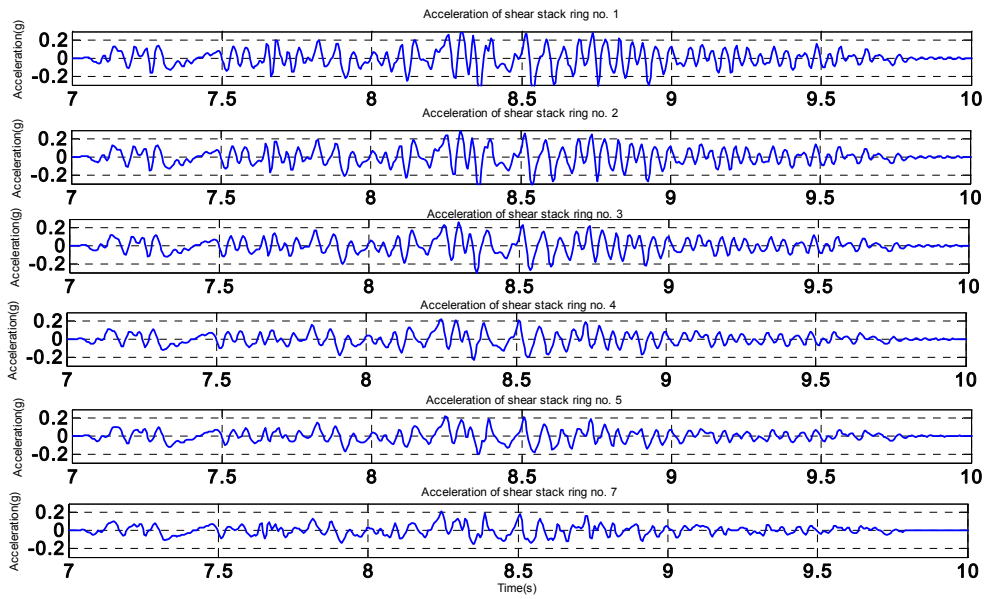


Figure 1.132 acceleration: array outside

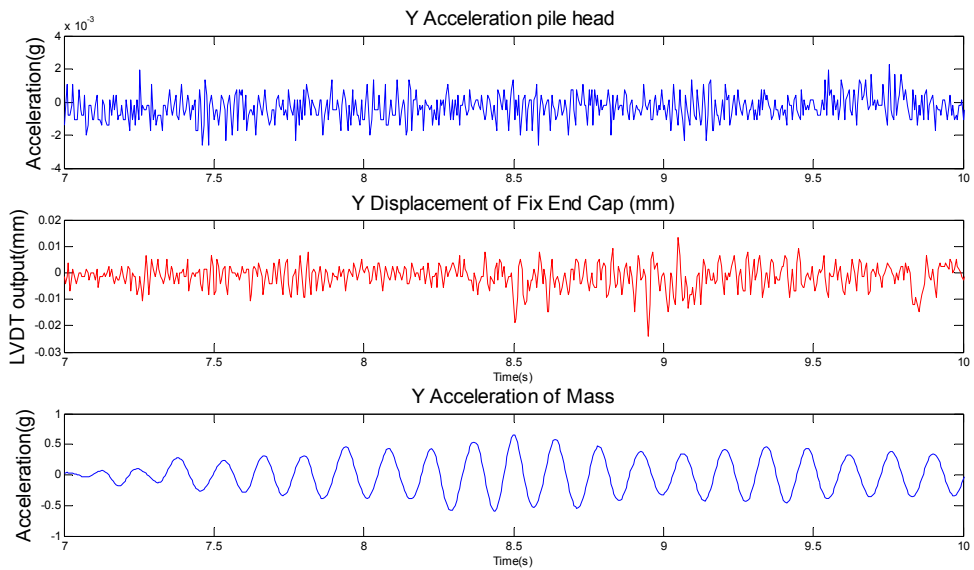


Figure 1.133 top pile: acceleration-LVDT-acceleration SDOF

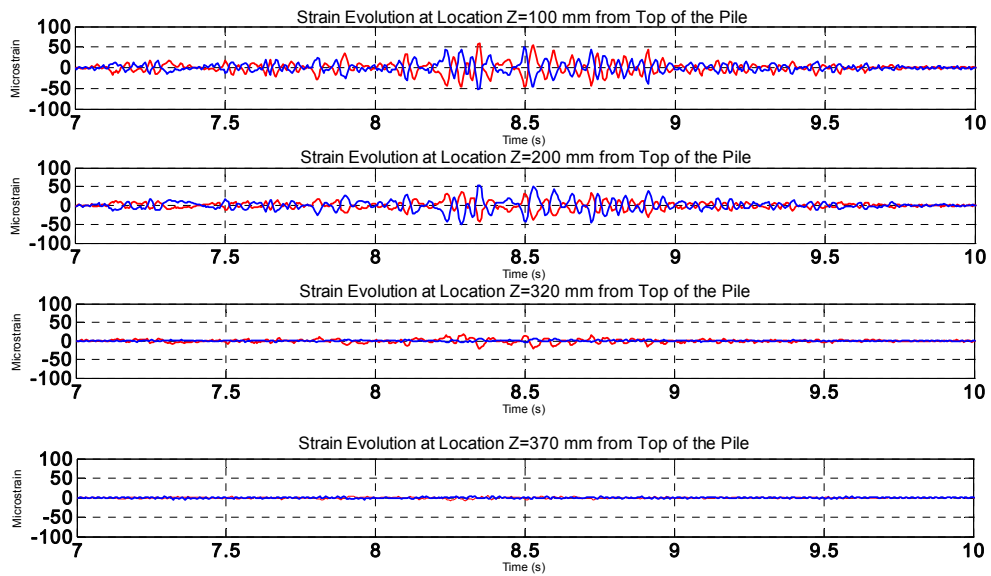


Figure 1.134 strain gauges 100-370 mm

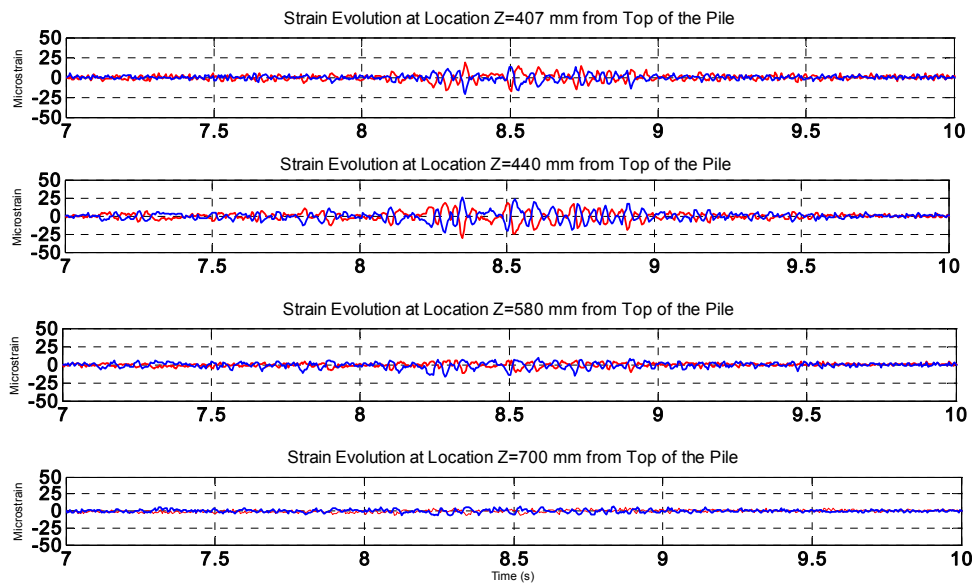


Figure 1.135 strain gauges 407-700 mm

3.13 BE+E_STU2_NRH+SDOF

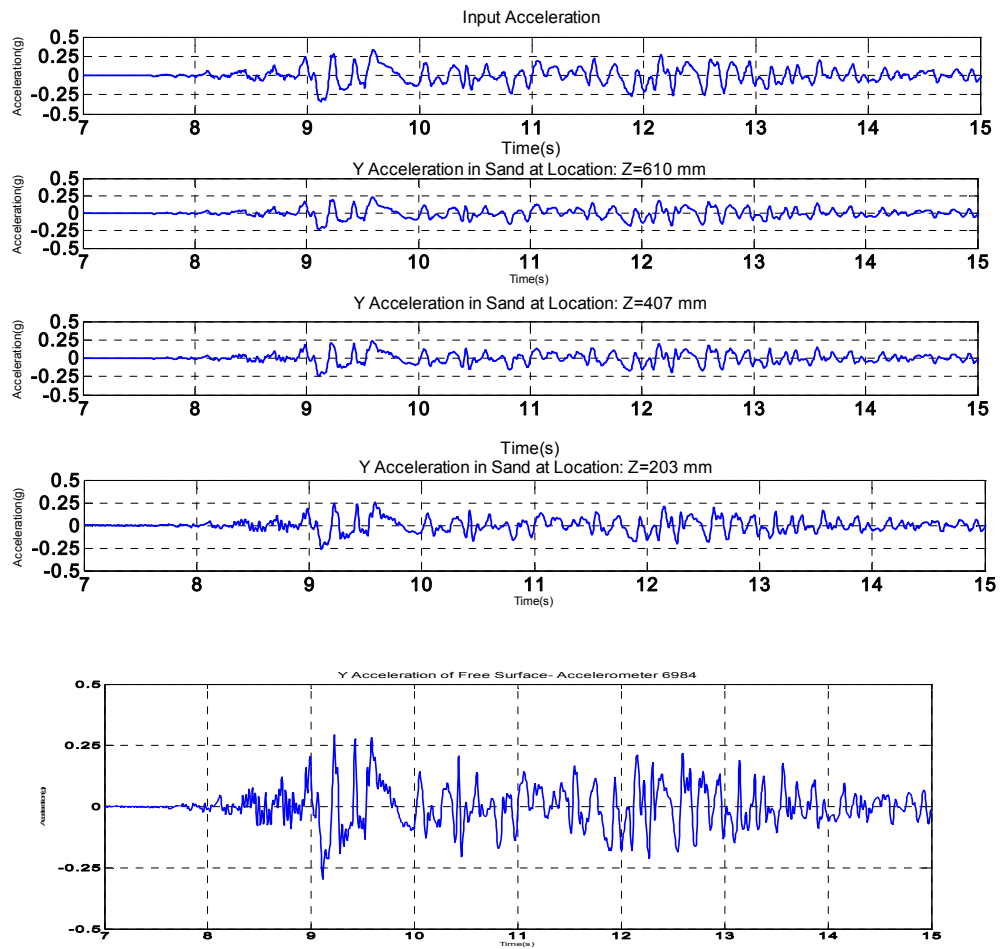


Figure 1.136 acceleration: array inside

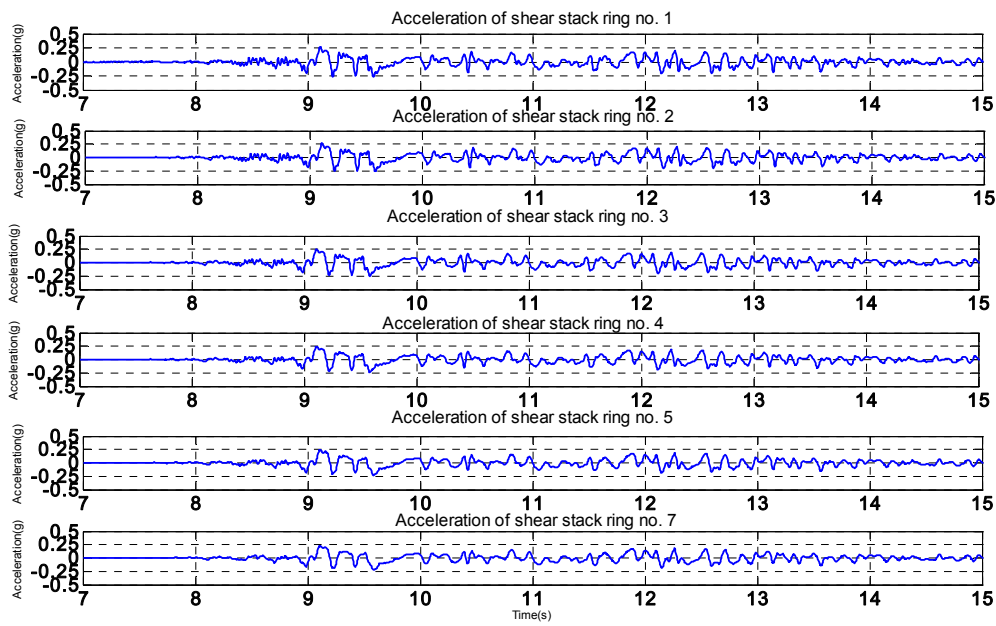


Figure 1.138 acceleration: array outside

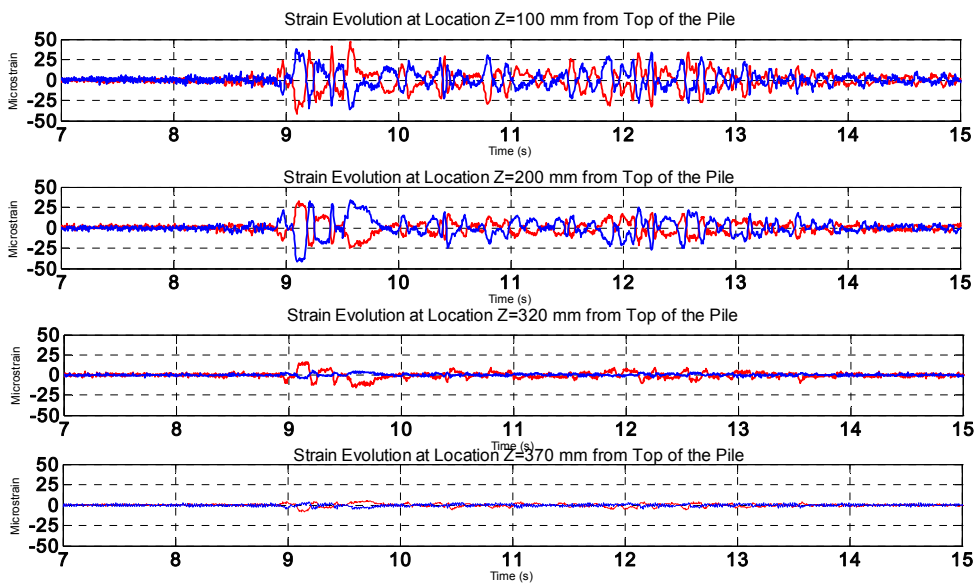


Figure 1.140 strain gauges: 100-370 mm

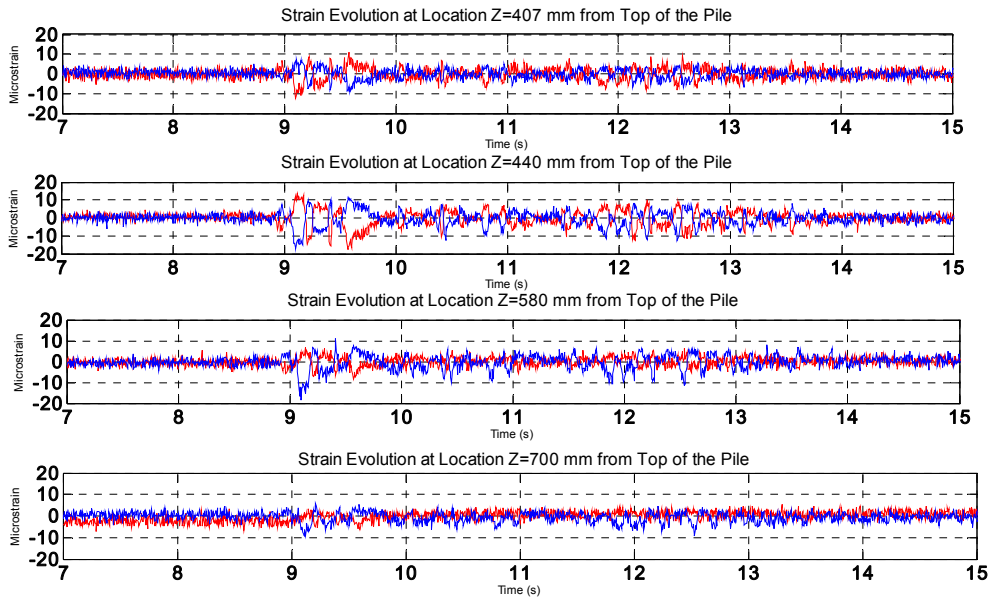


Figure 1.141 strain gauges: 407-700 mm

3.14 BE+E_TMZ12_NRH+SDOF

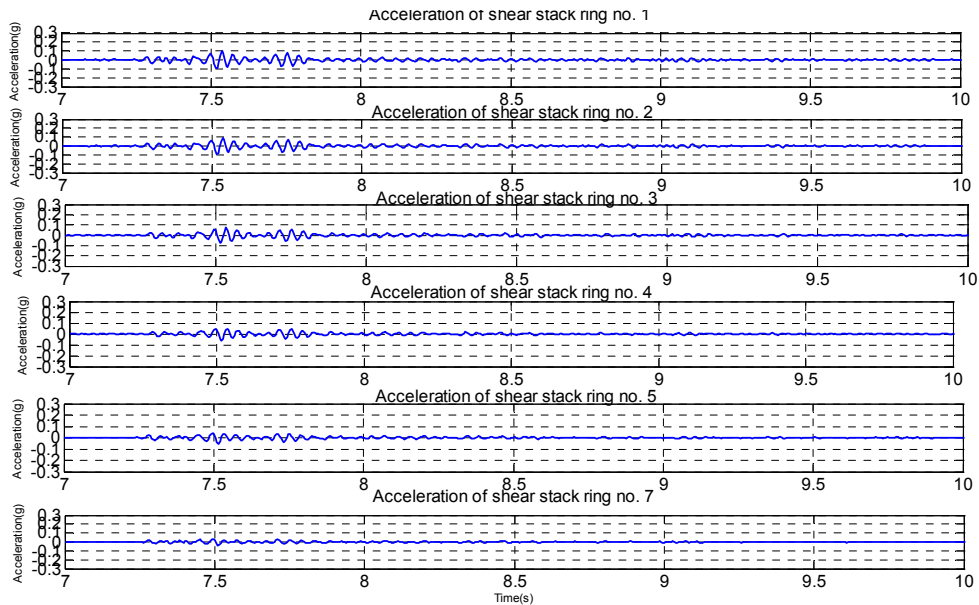


Figure 1.142 acceleration: array outside

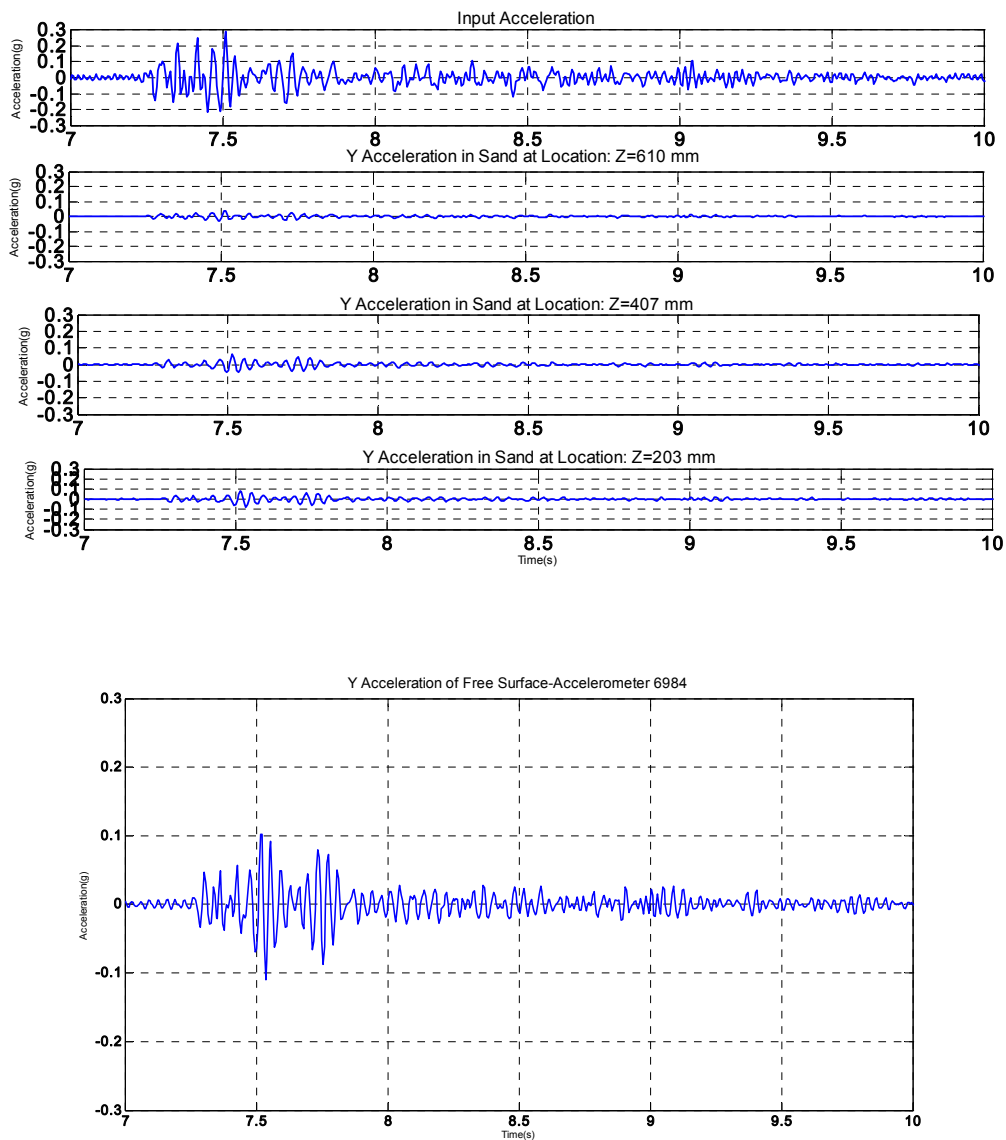


Figure 1.143 acceleration: array inside

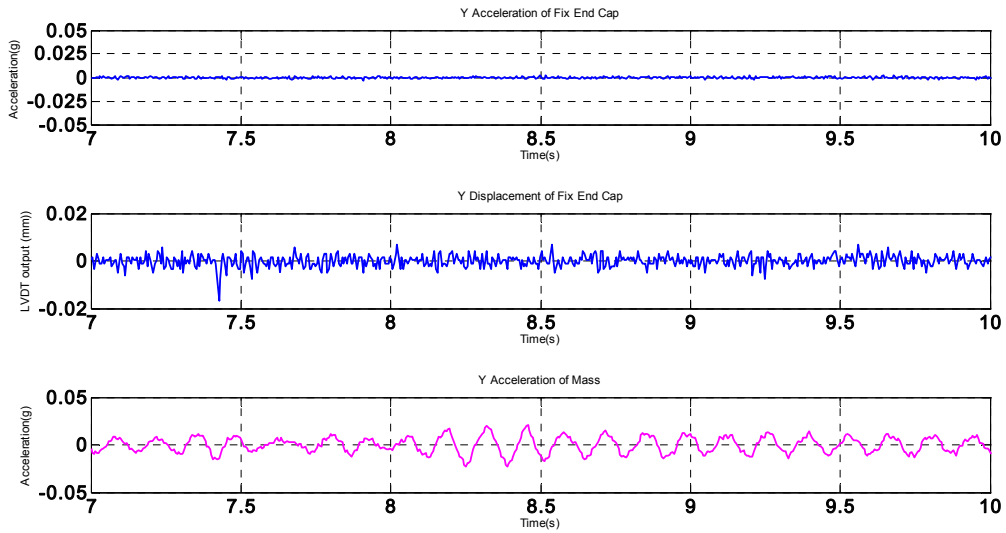


Figure 1.144 top pile: acceleration-LVDT-acceleration SDOF

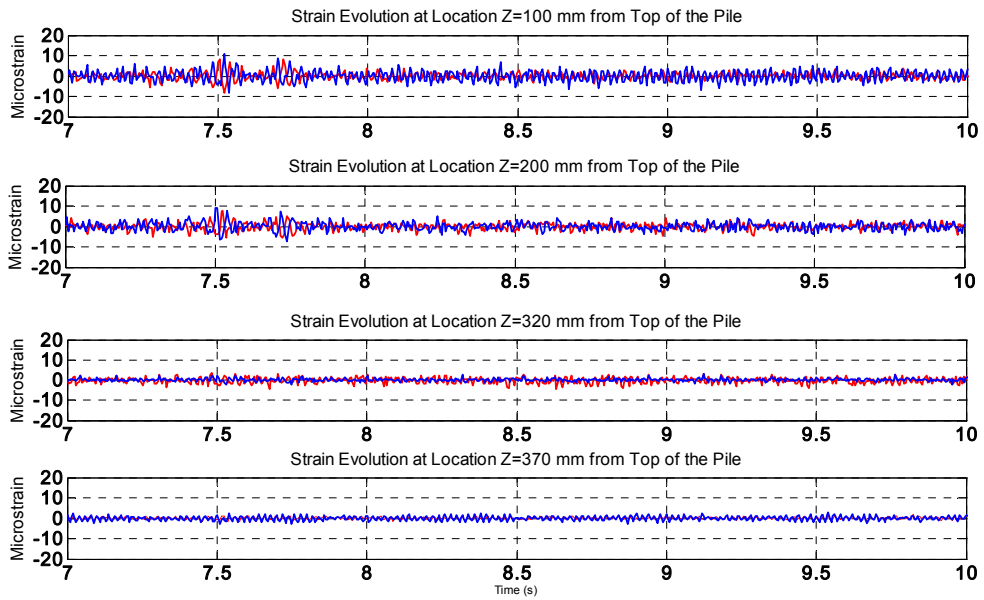


Figure 1.145 : strain gauges 100-370 mm

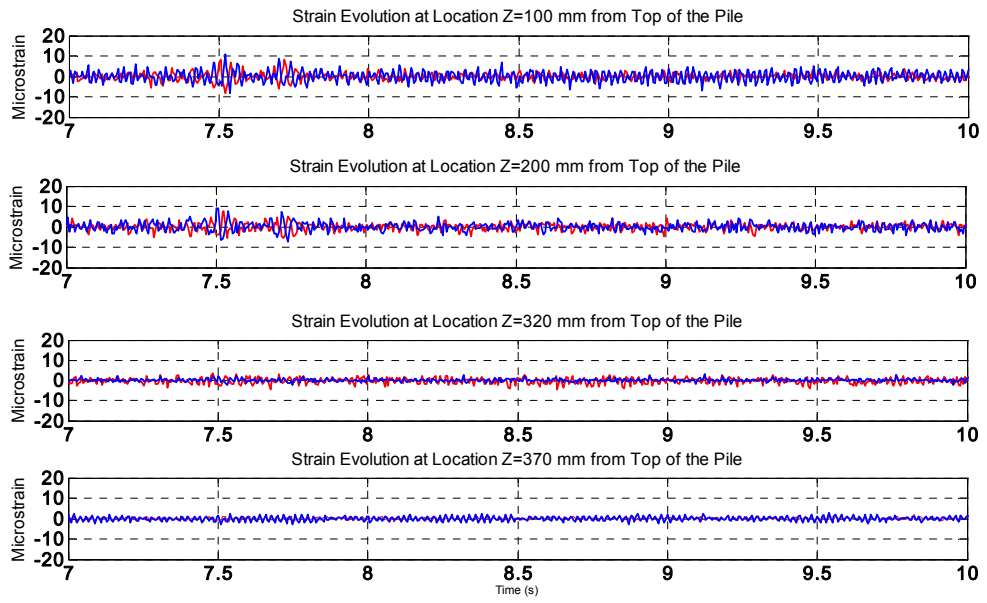


Figure 1.146 : strain gauges 407-700 mm

3.15 BE+E_TMZ2_NRH+SDOF

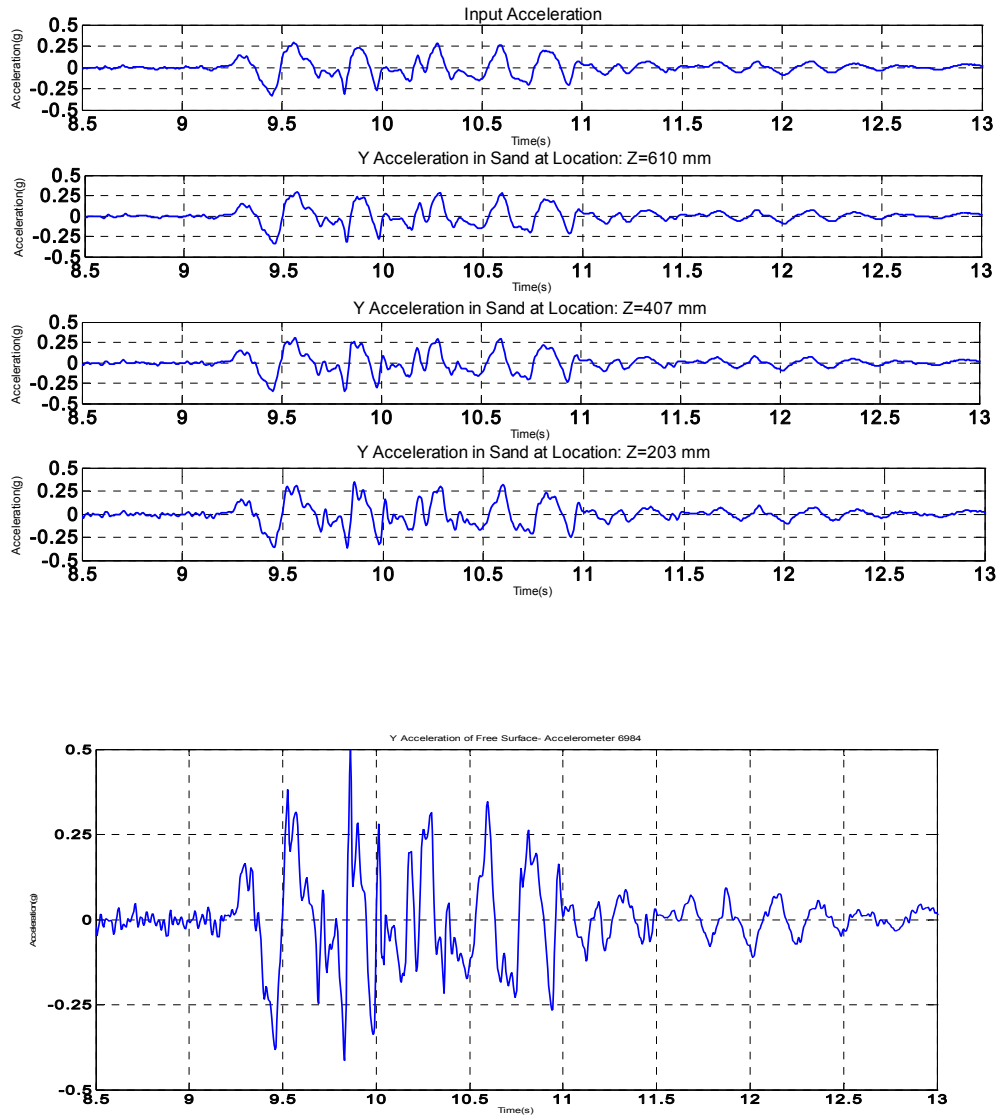


Figure 1.147 : acceleration : array inside

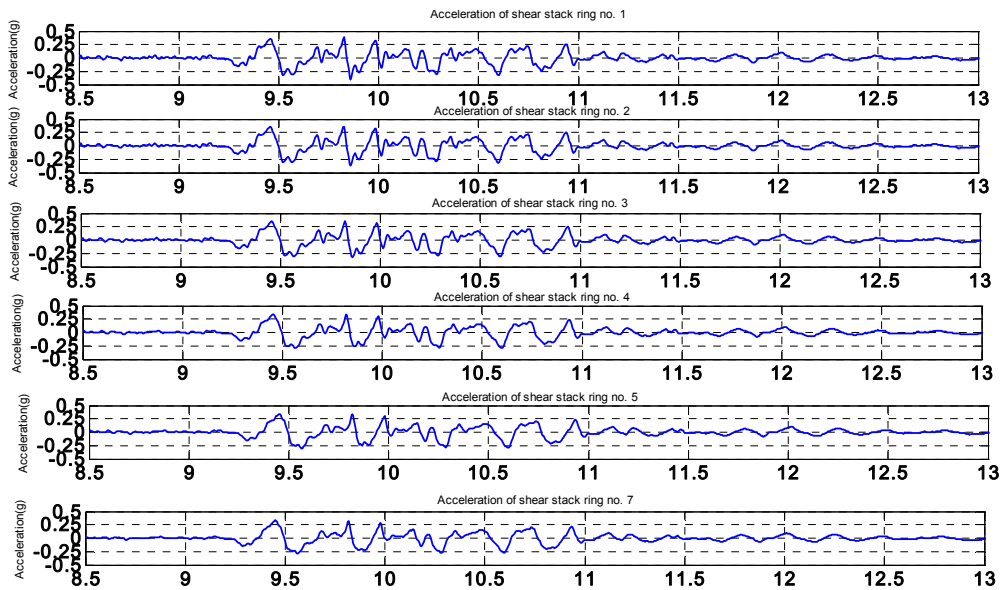


Figure 1.148 : acceleration : array outside

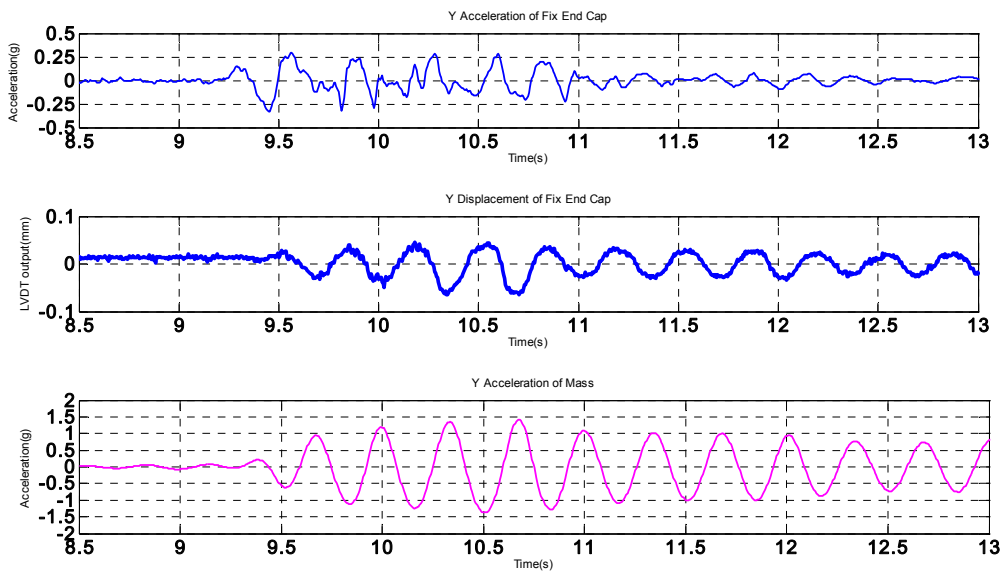


Figure 1.149 : top pile acceleration-LVDt-acceleration SDOF

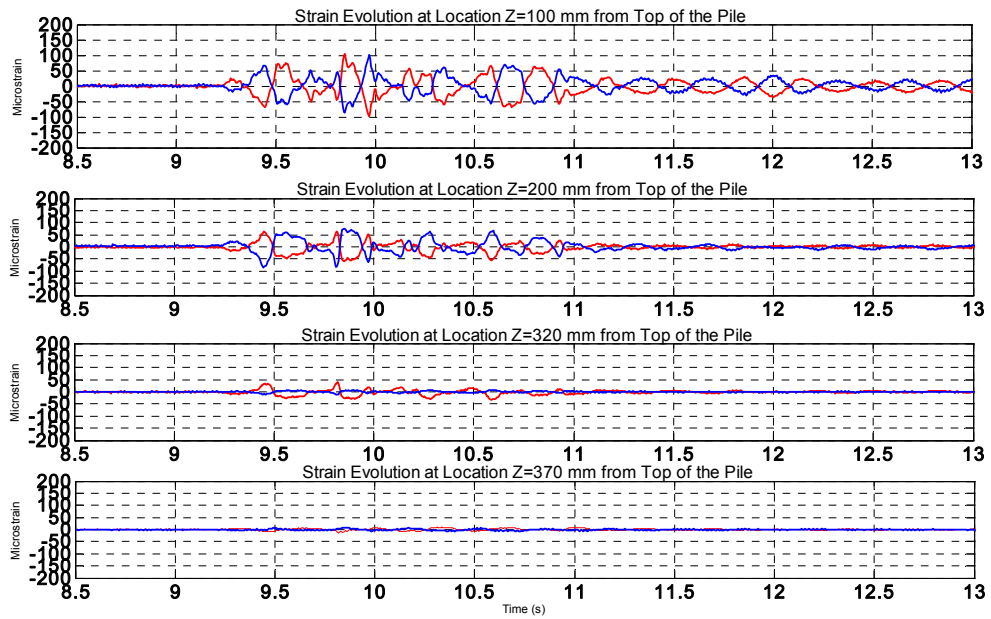


Figure 1.150: strain gauges 100-370 mm

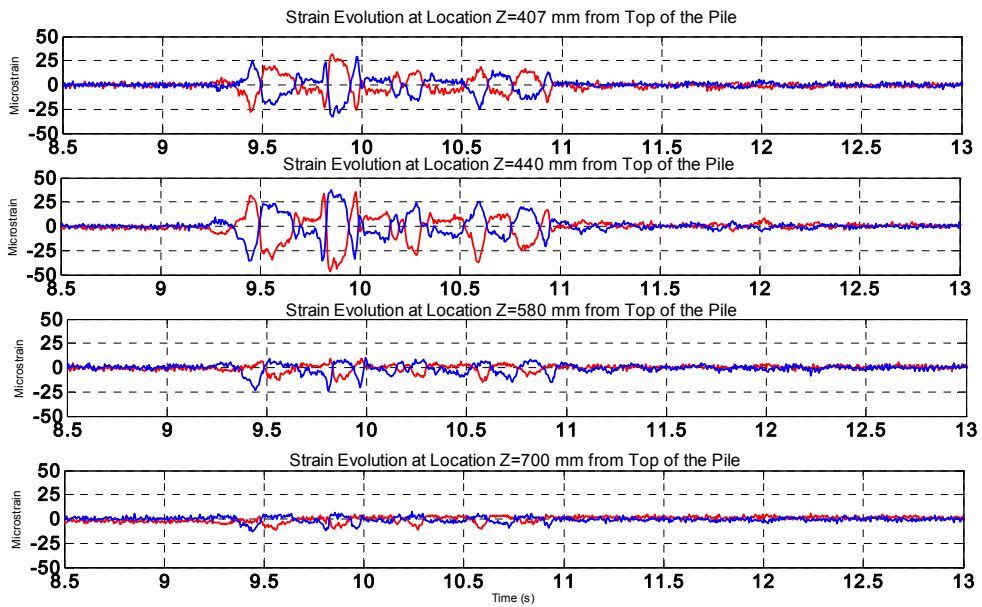


Figure 1.151 : strain gauges 100-370 mm

4 SOIL CONFIGURATION: LAYERED (E+R)

4.1 E+R_STU12_FH

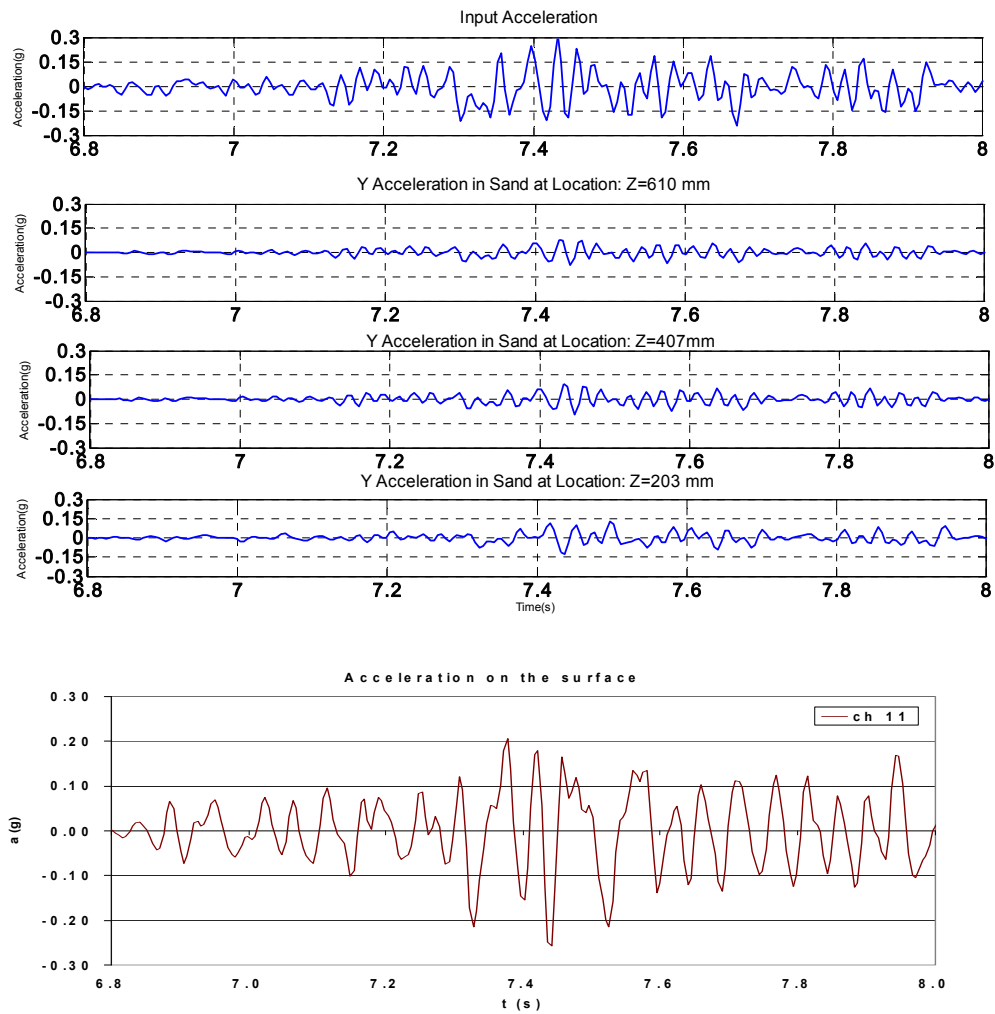


Figure 1.152: acceleration : array inside

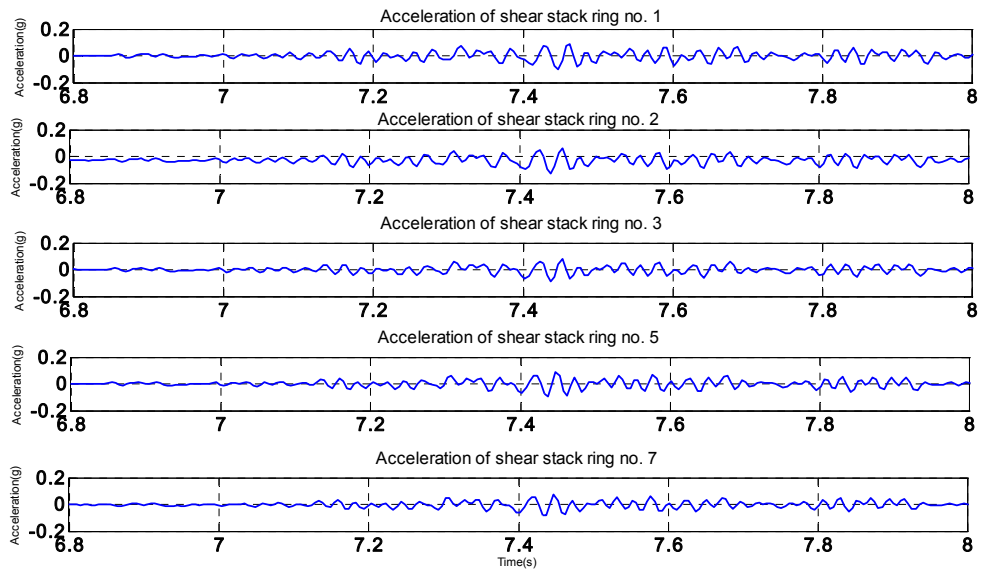


Figure 1.153: acceleration : array outside

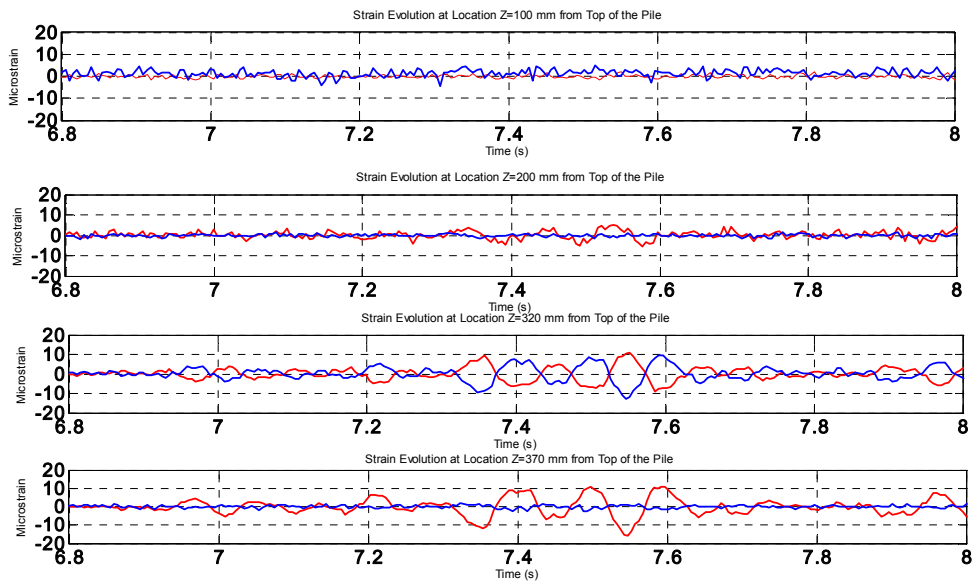


Figure 1.154: strain gauges 100-370 mm

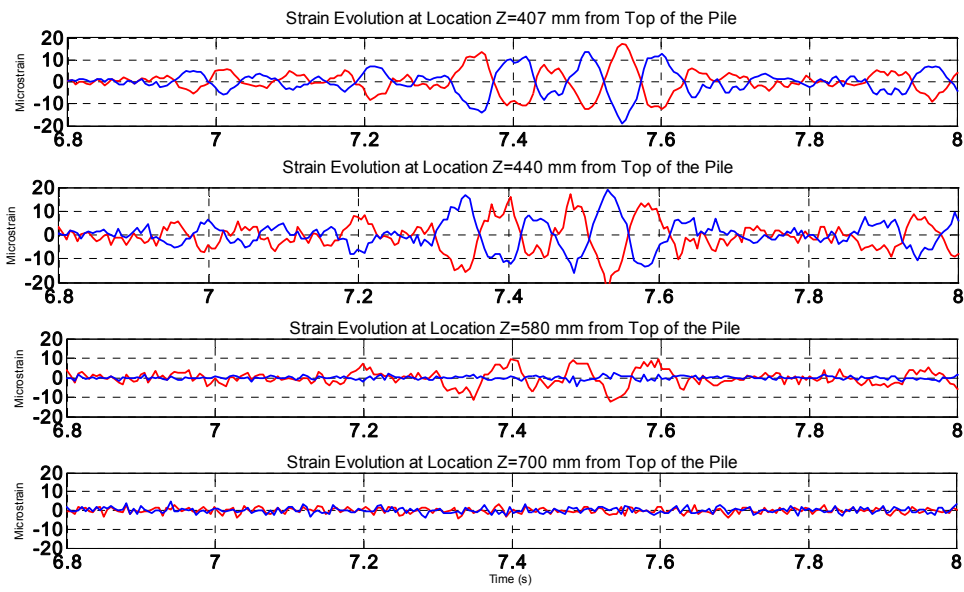


Figure 1.155: strain gauges 407-700 mm

4.2 E+R_STU2_FH

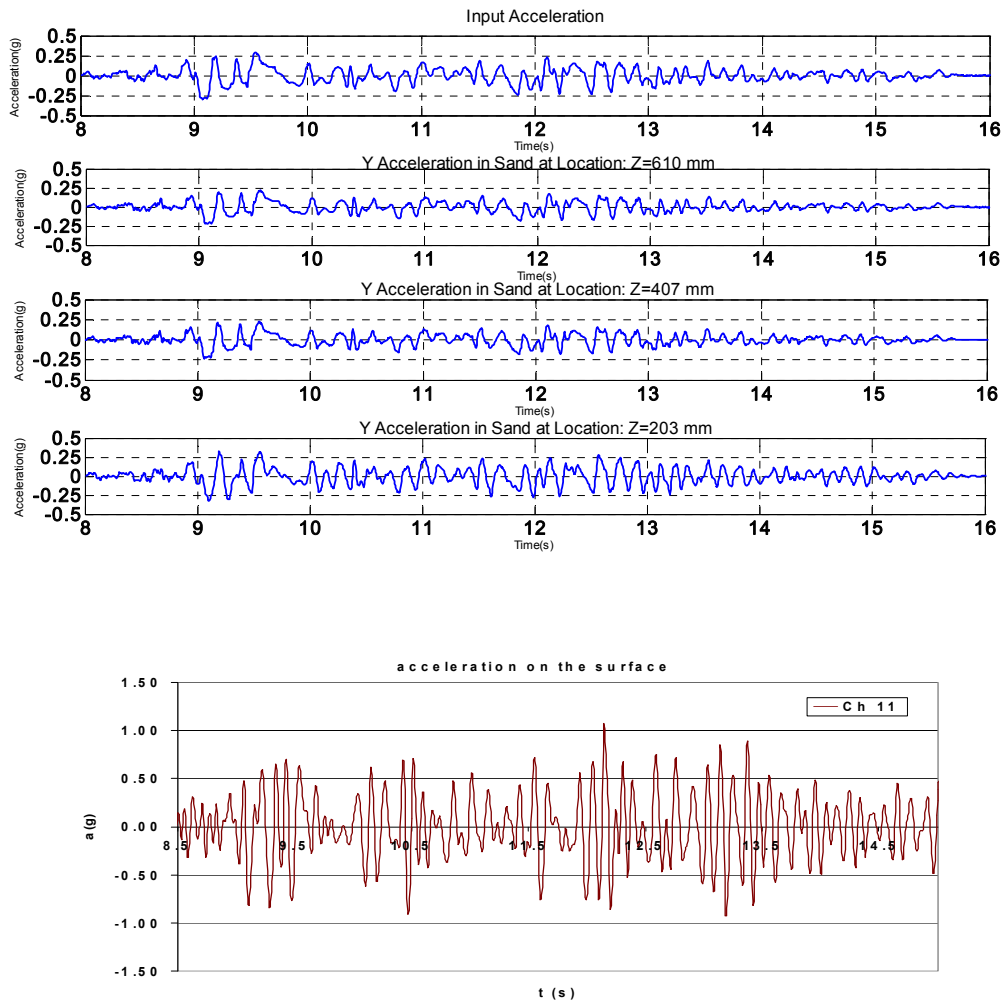


Figure 1.156: acceleration : array inside

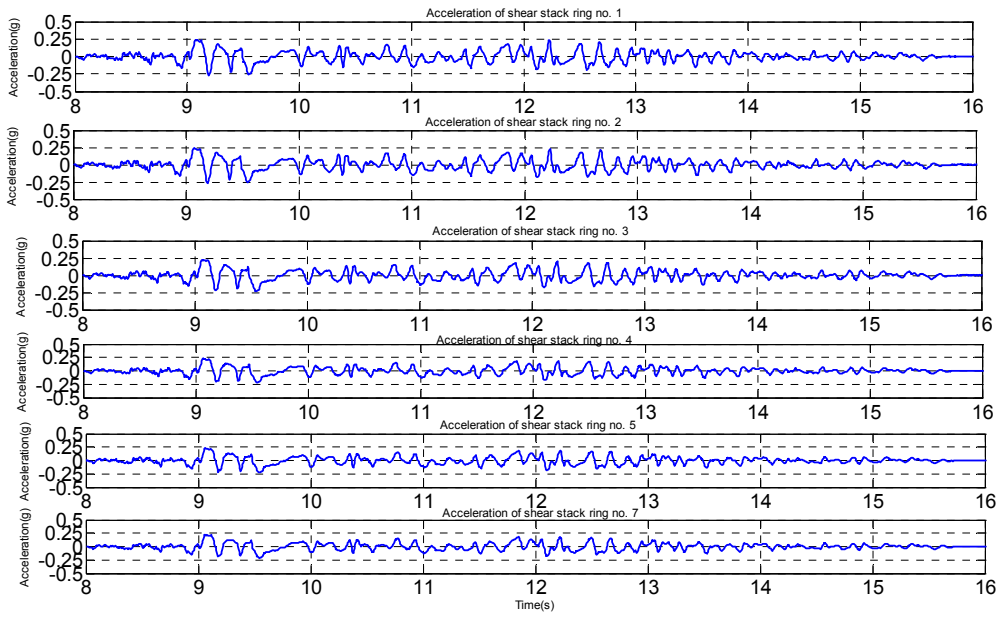


Figure 1.157: acceleration : array outside

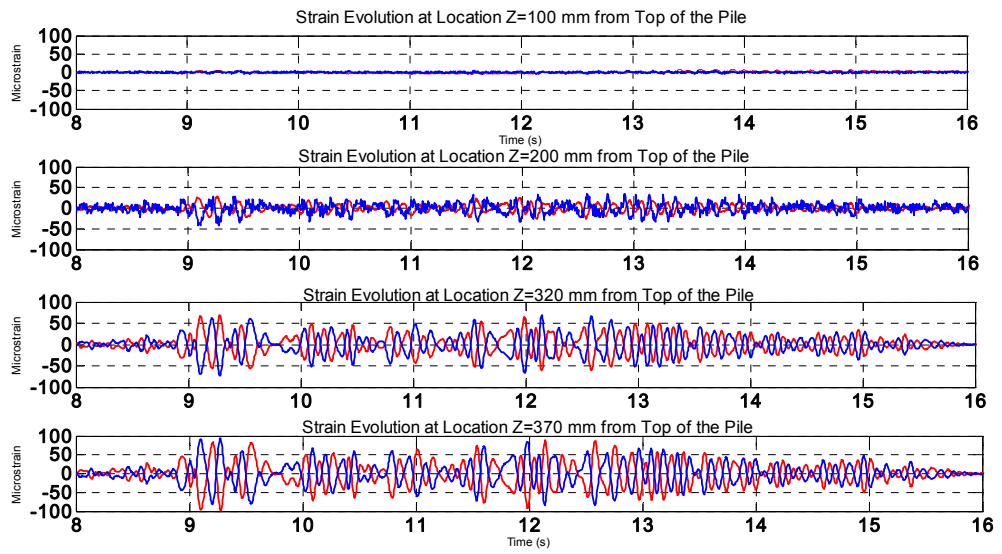


Figure 1.158 strain gauges 100-370 mm

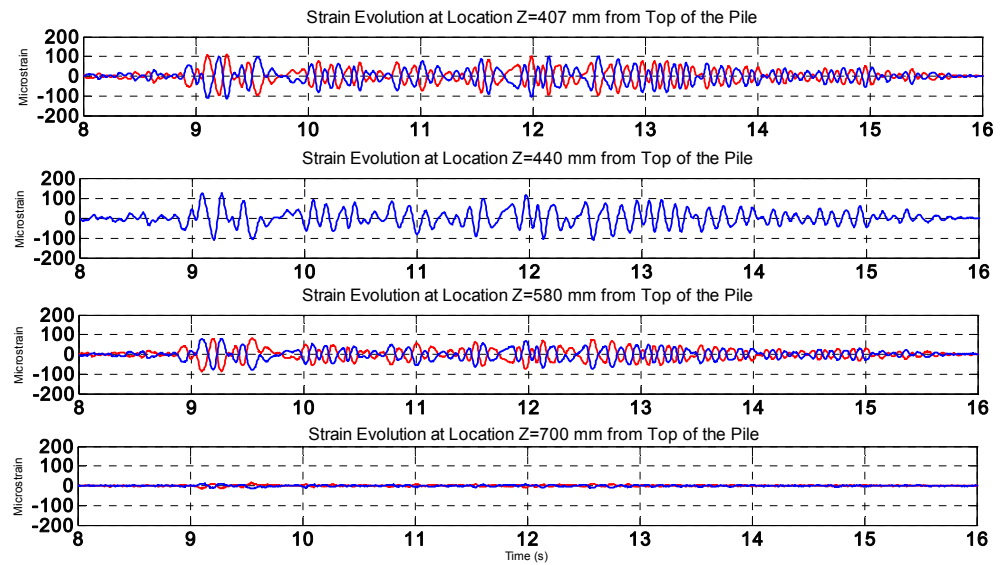


Figure 1.159 strain gauges 407-700 mm

4.3 E+R_TMZ12_FH

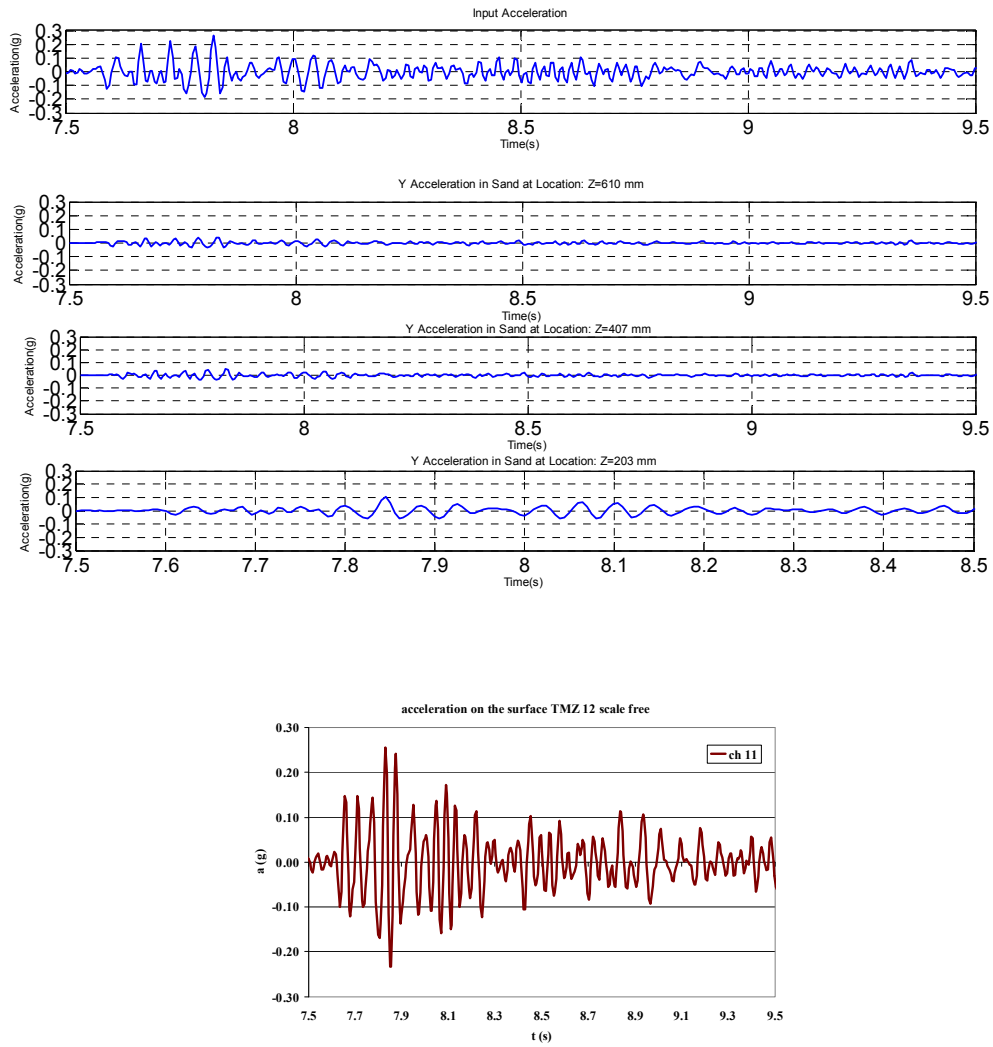


Figure 1.160: acceleration : array inside

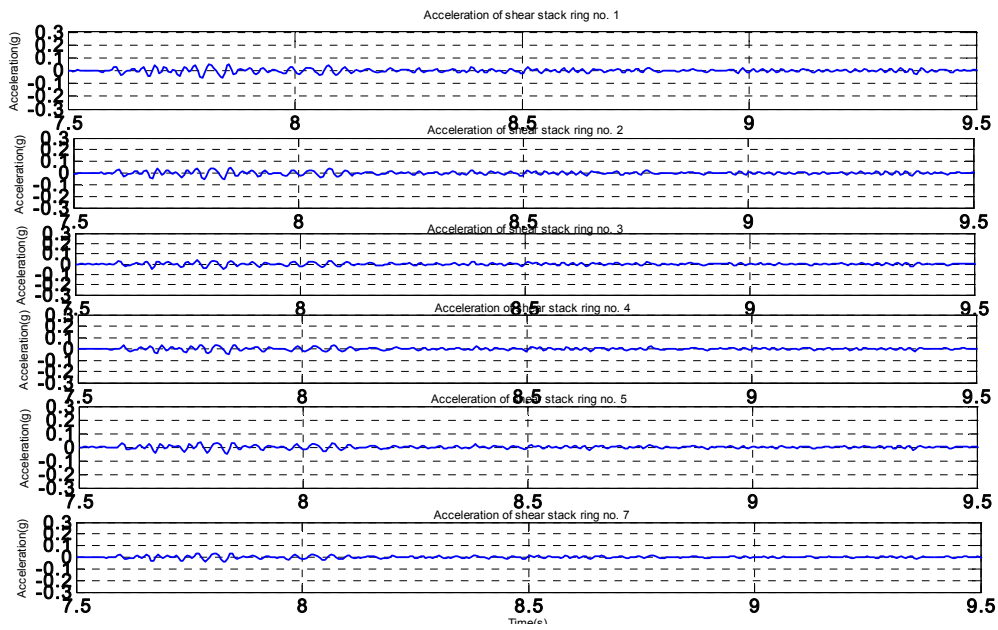


Figure 1.161: acceleration : array outside

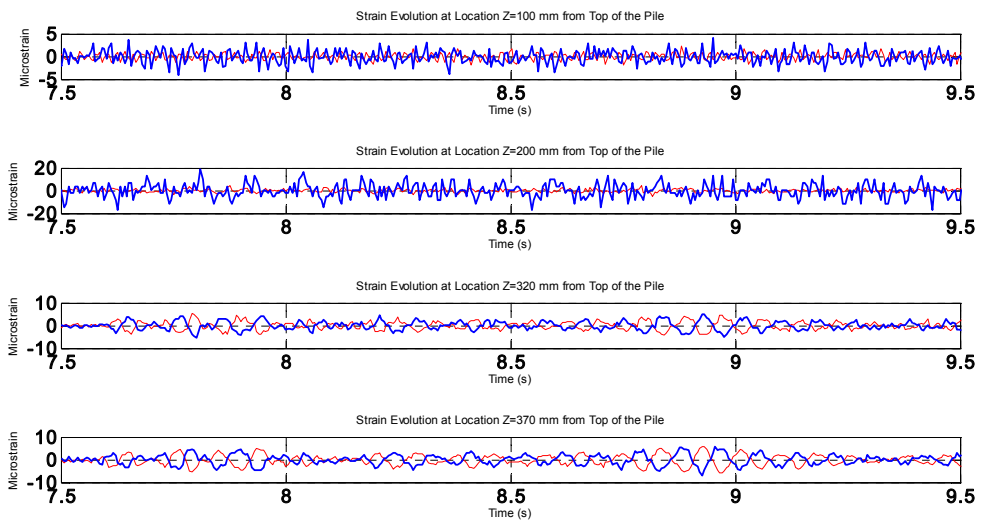


Figure 1.162: strain 100-370

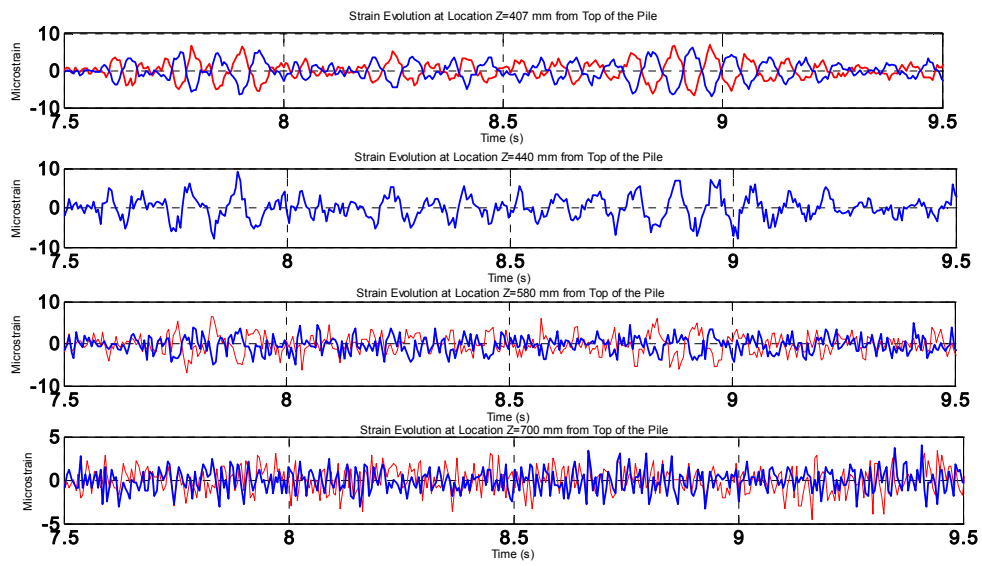


Figure 1.163: strain407-700

4.4 E+R_TMZ2_FH

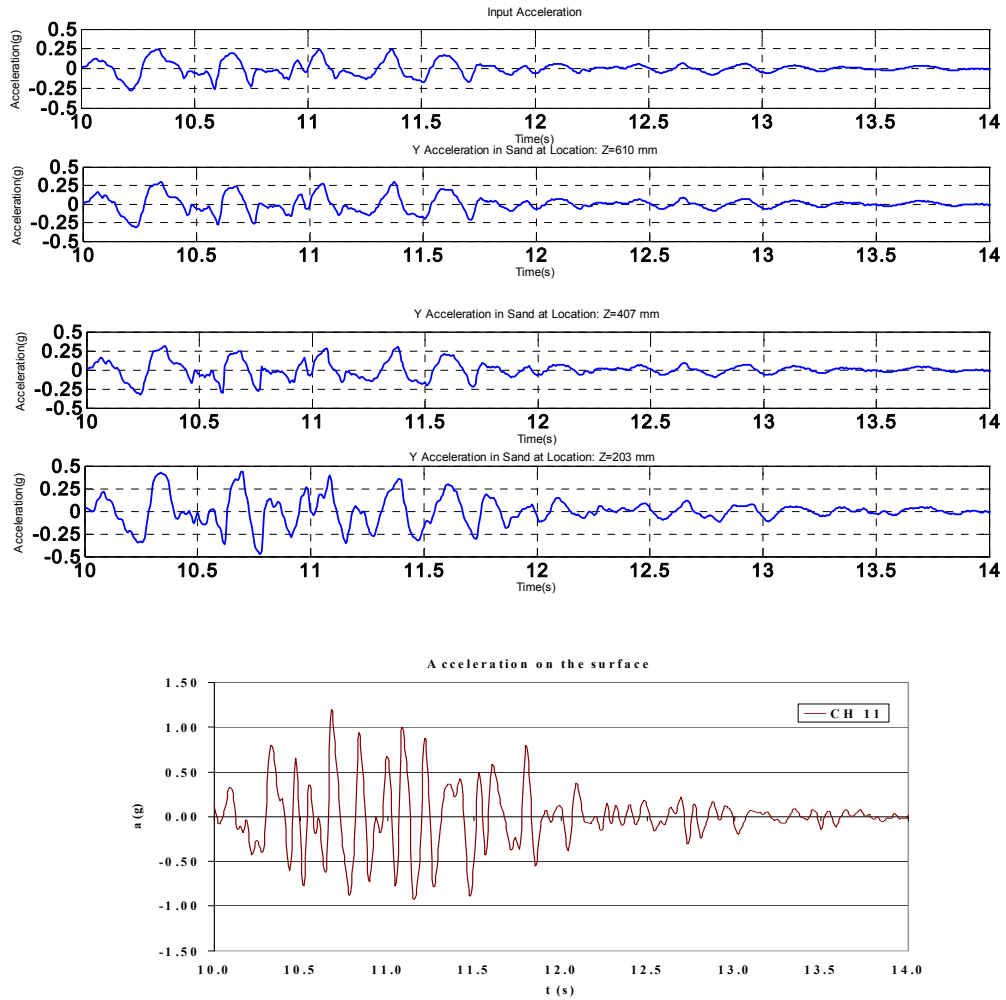


Figure 1.164: acceleration : array inside

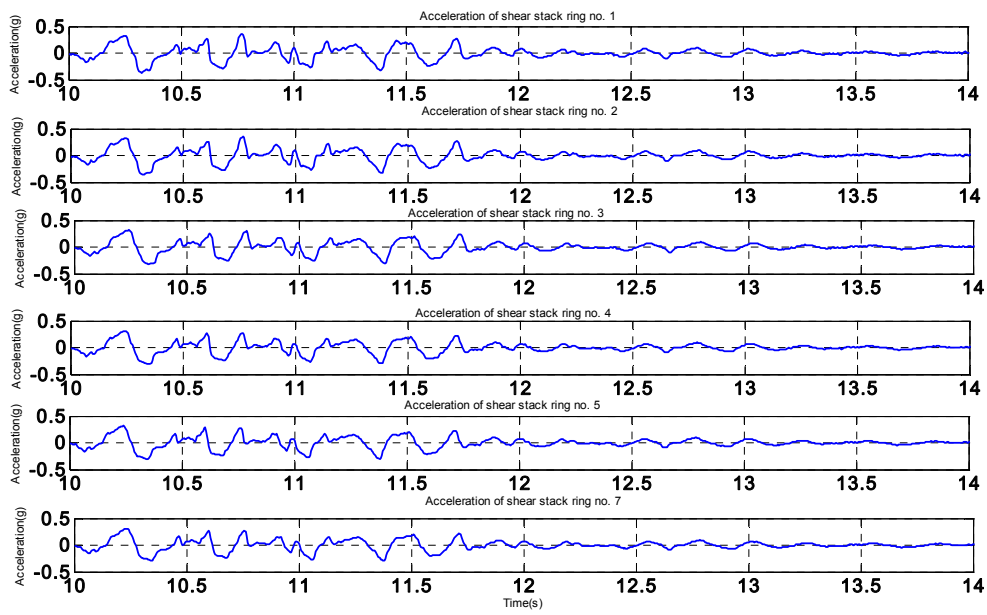


Figure 1.165: acceleration : array outside

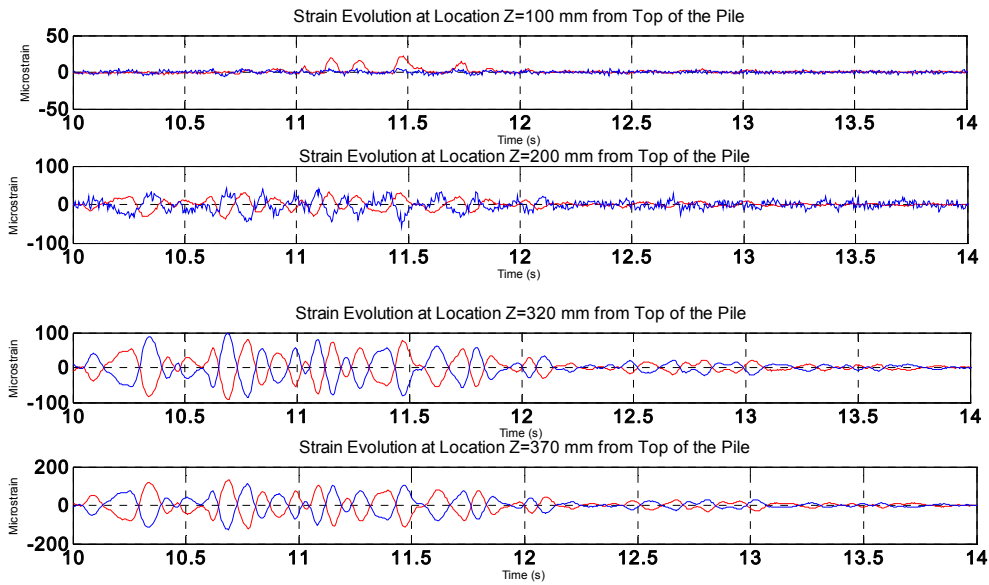


Figure 1.166: strain gauges 100-370

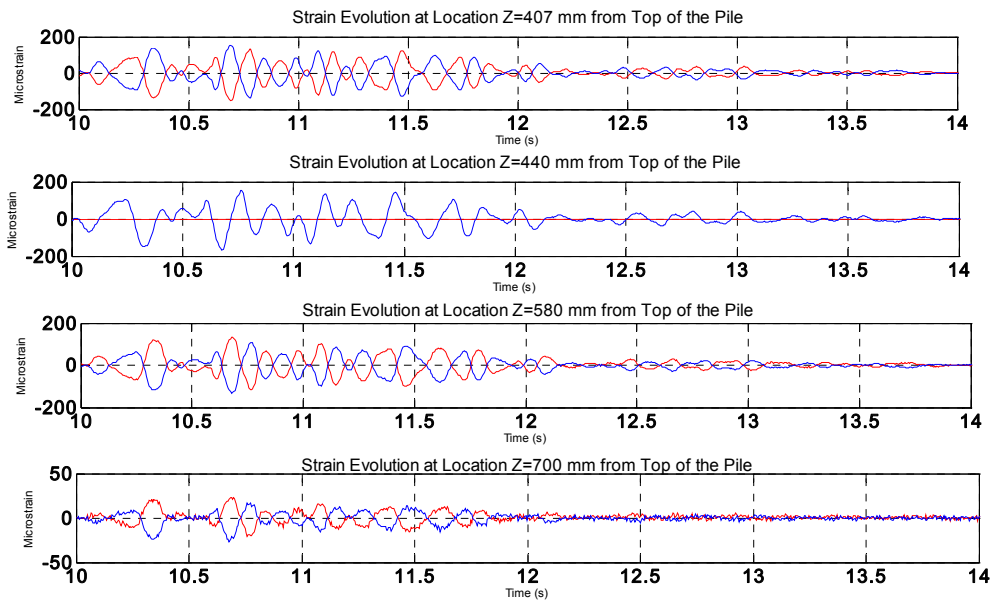


Figure 1.167: strain gauges 407-700

4.5 E+R_STU 12_NRH

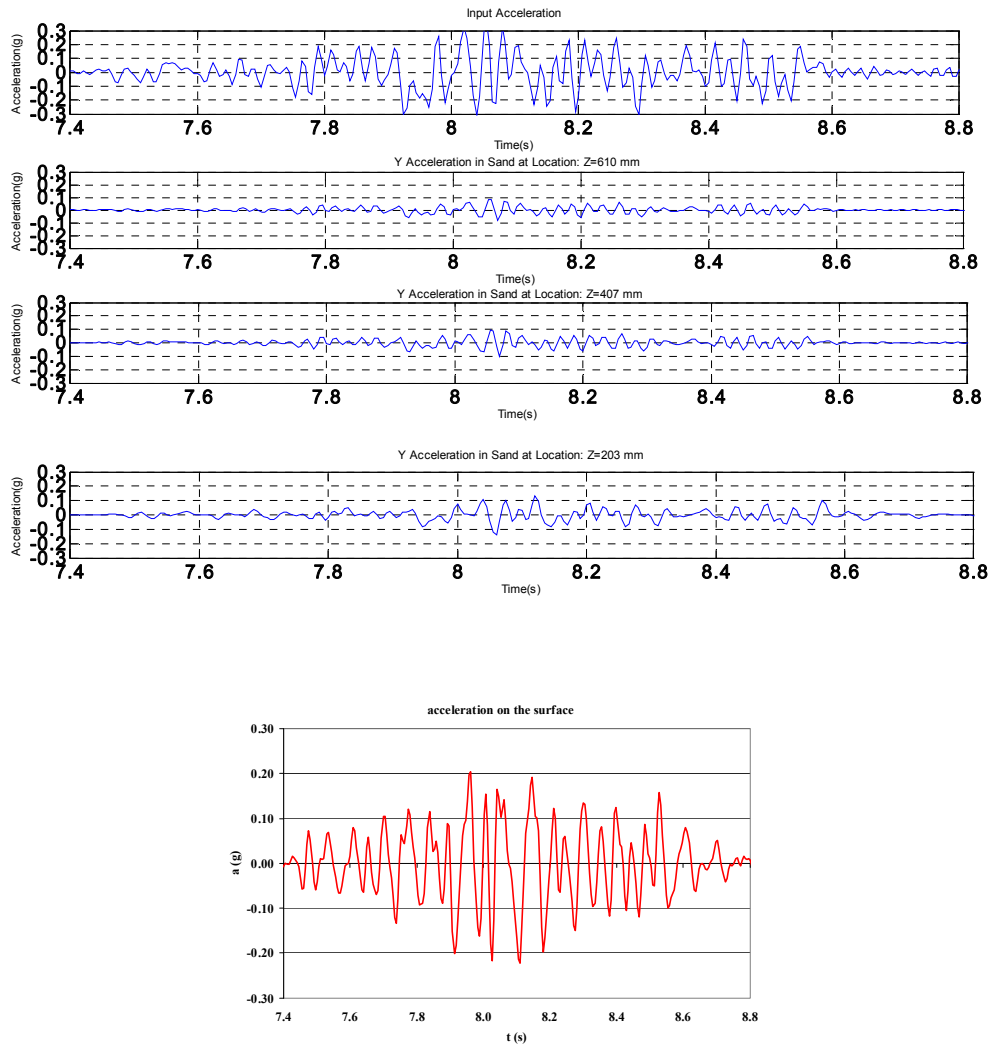


Figure 1.168: acceleration : array inside

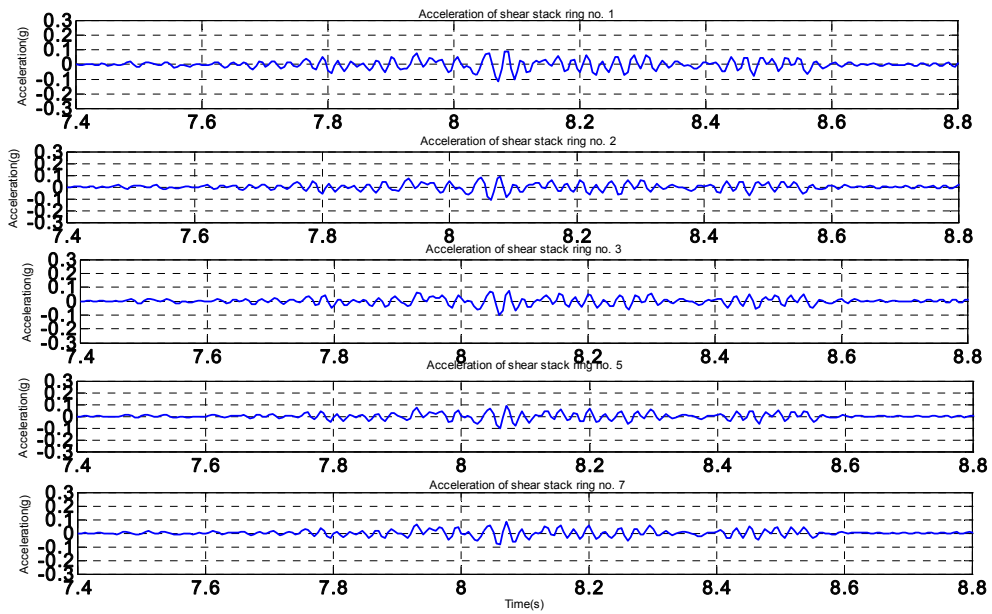


Figure 1.169: acceleration: array outside

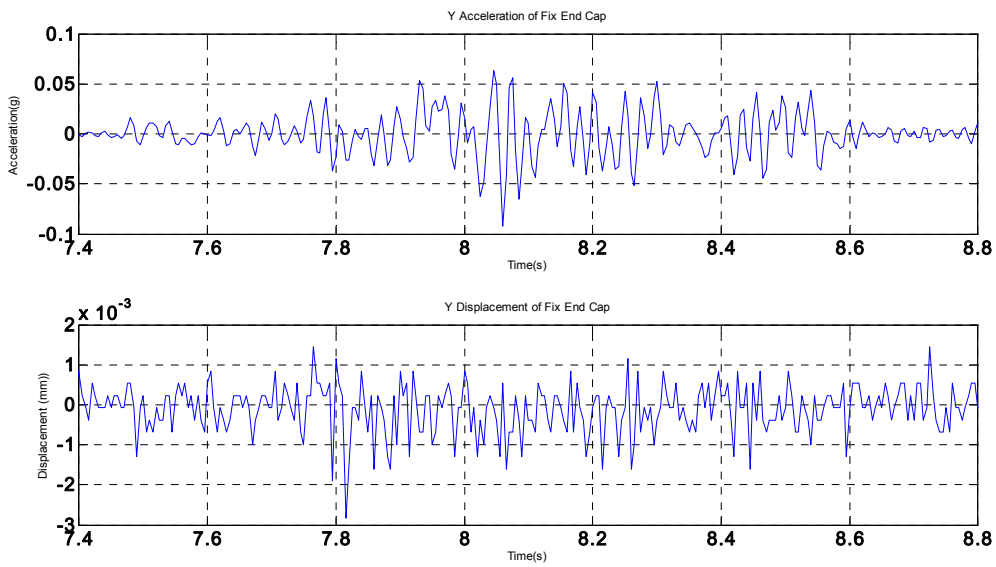


Figure 1.170: pile head

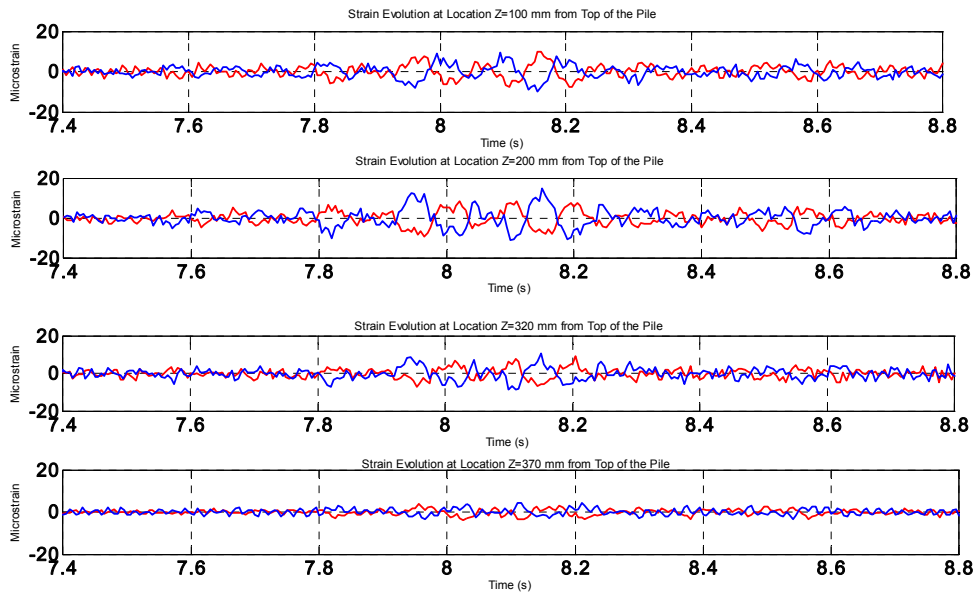


Figure 1.171: acceleration: array outside

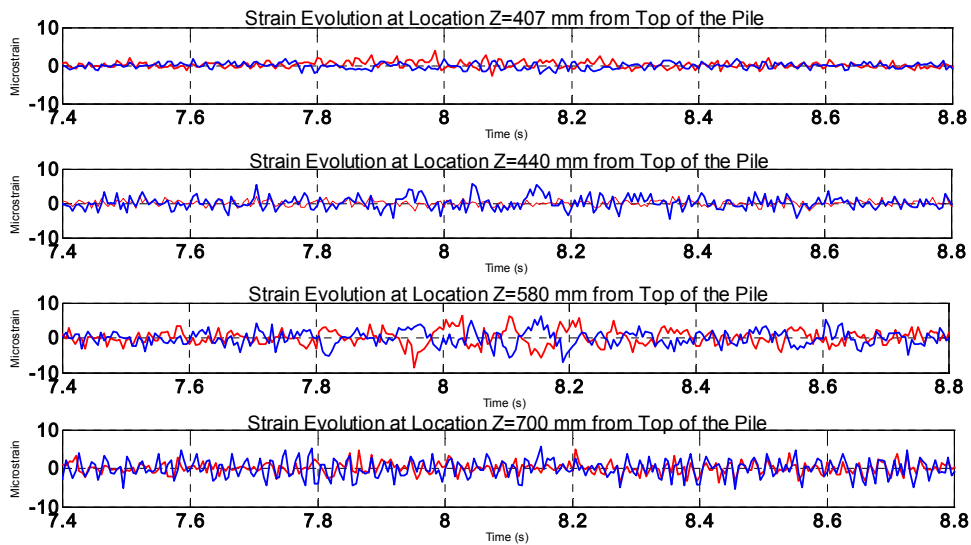


Figure 1.172: pile head

4.6 E+R_STU 2_NRH

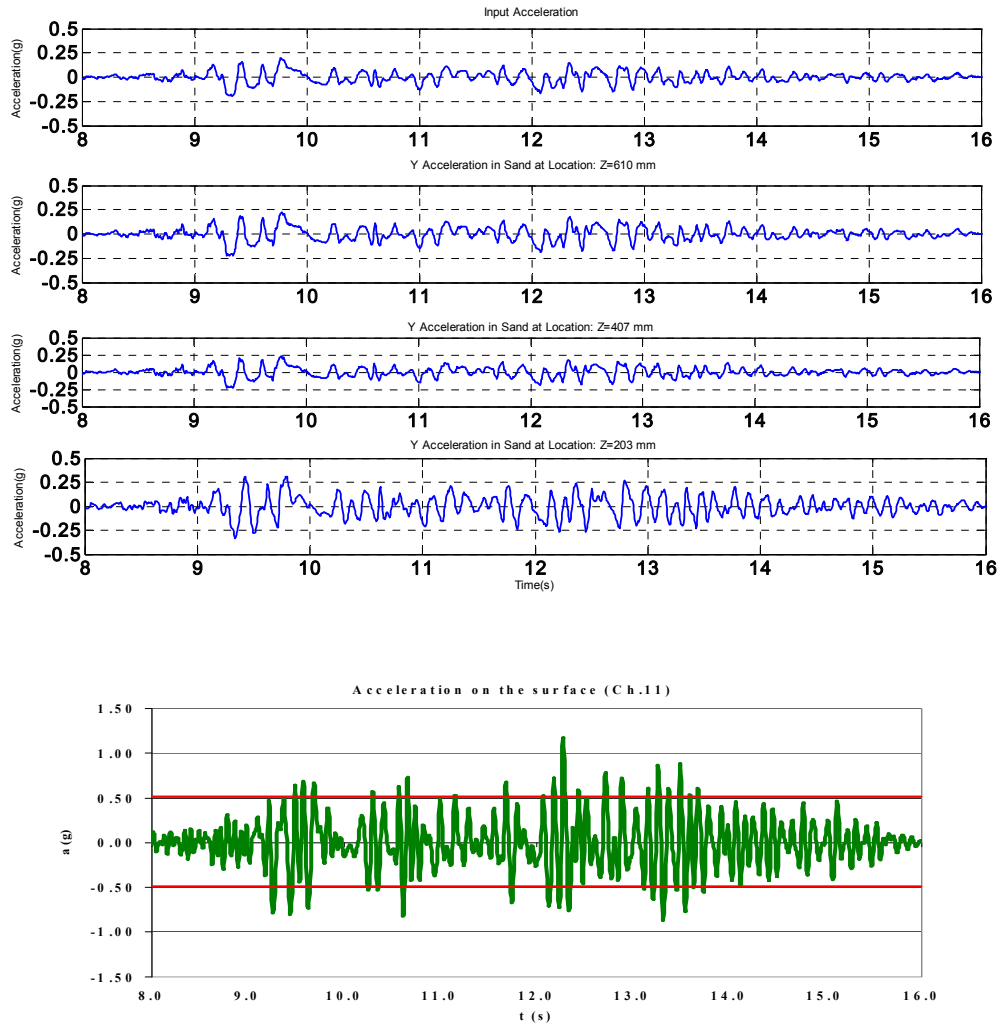


Figure 1.173 acceleration : array inside

Figure 1.174 acceleration : array outside

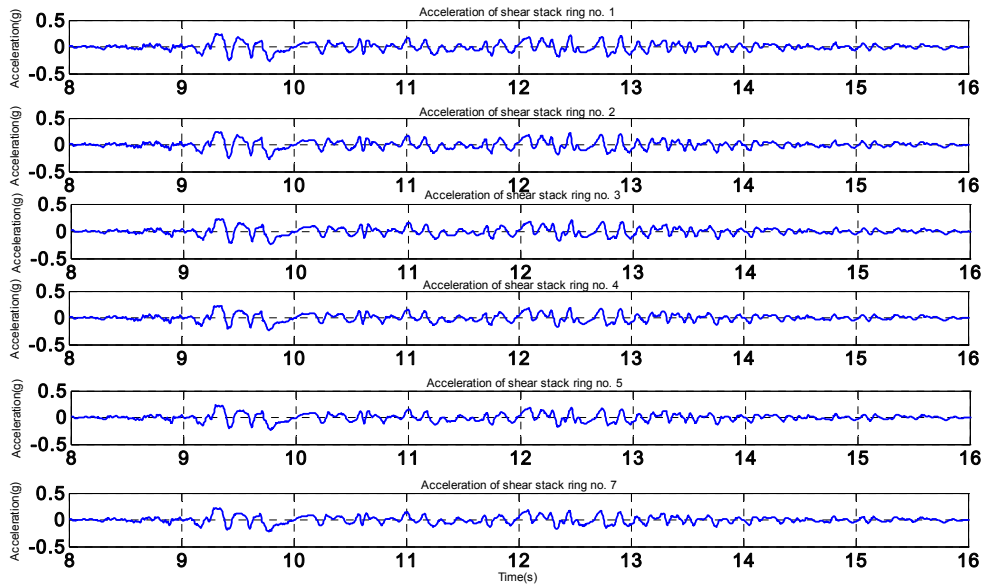


Figure 1.174 acceleration : array outside

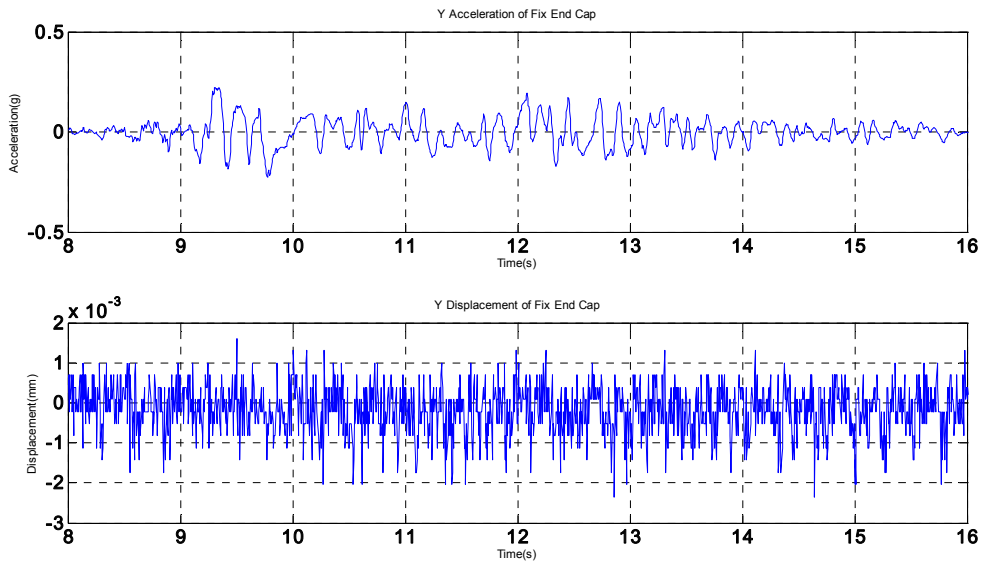


Figure 1.176 top pile

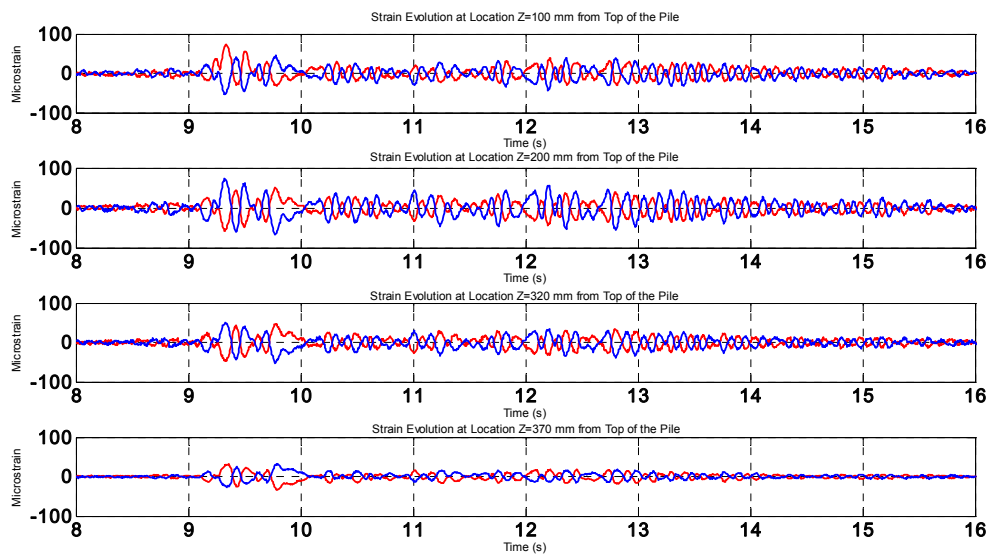


Figure 1.177 strain gauges 100-370

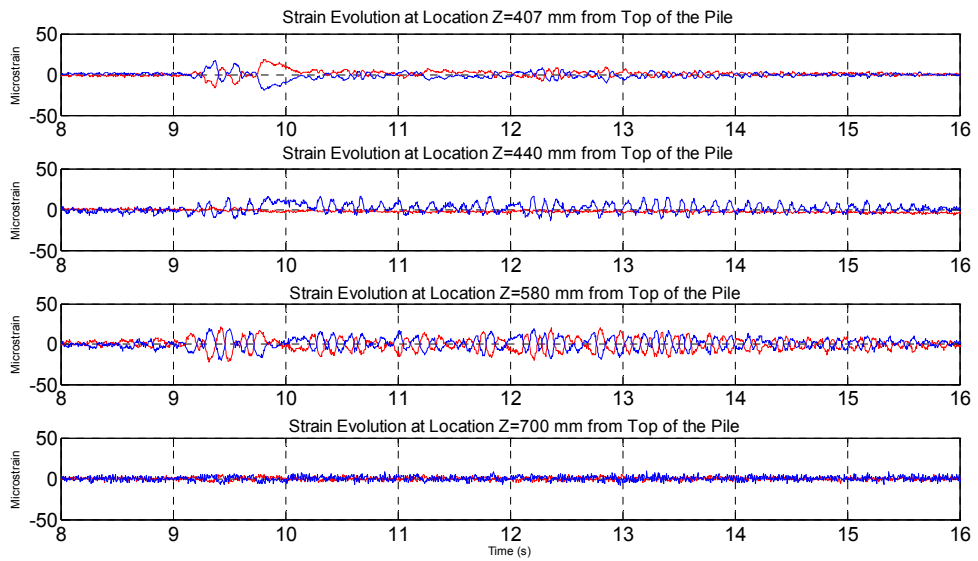


Figure 1.178 strain gauges 407-700

4.7 E+R_TMZ 12_NRH

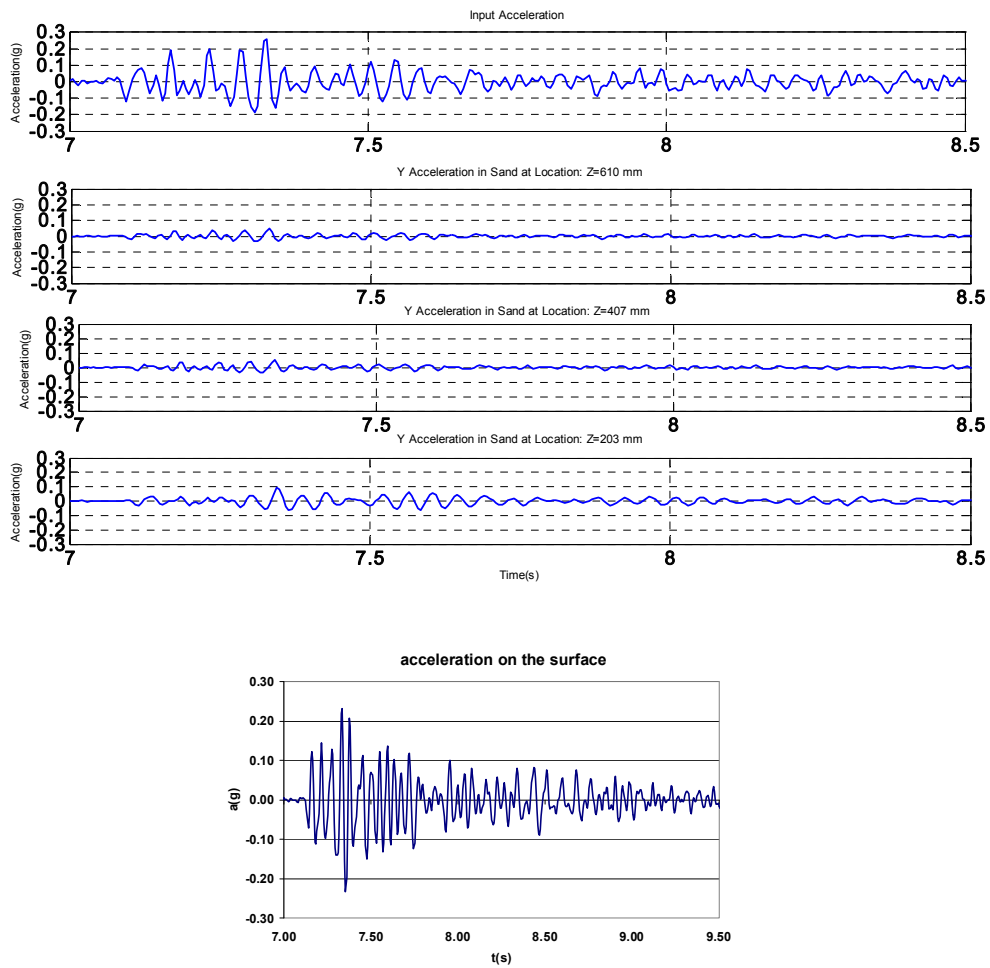


Figure 1.180 acceleration : array inside

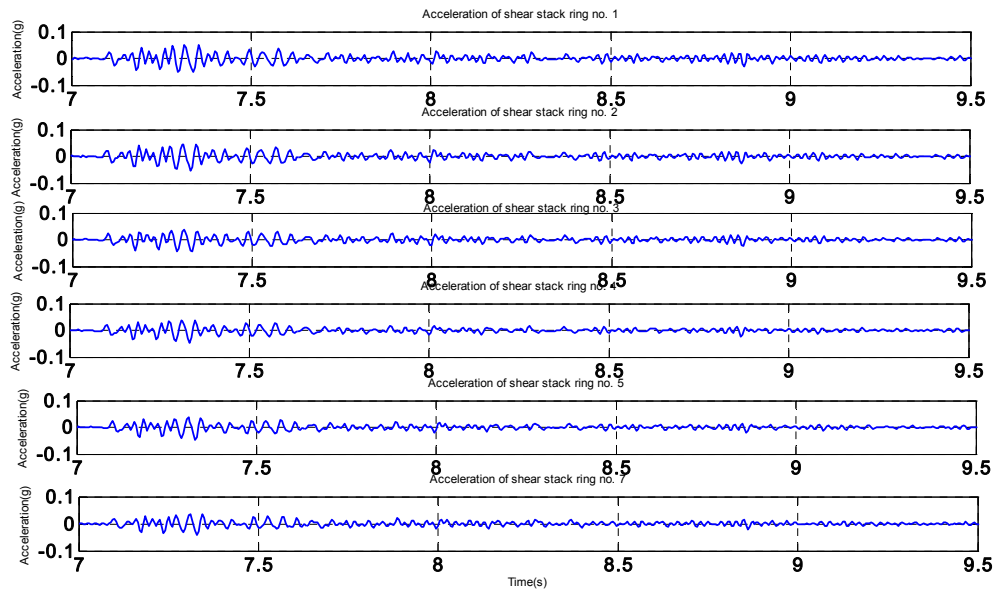
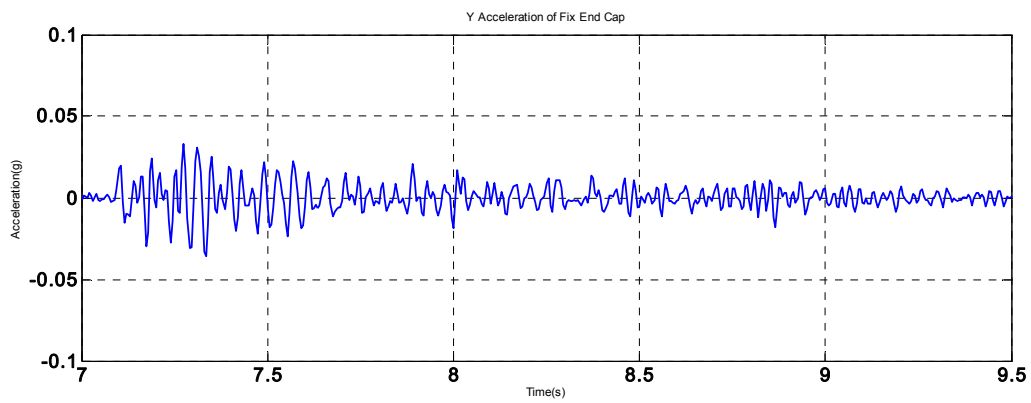


Figure 1.181 acceleration : array outside



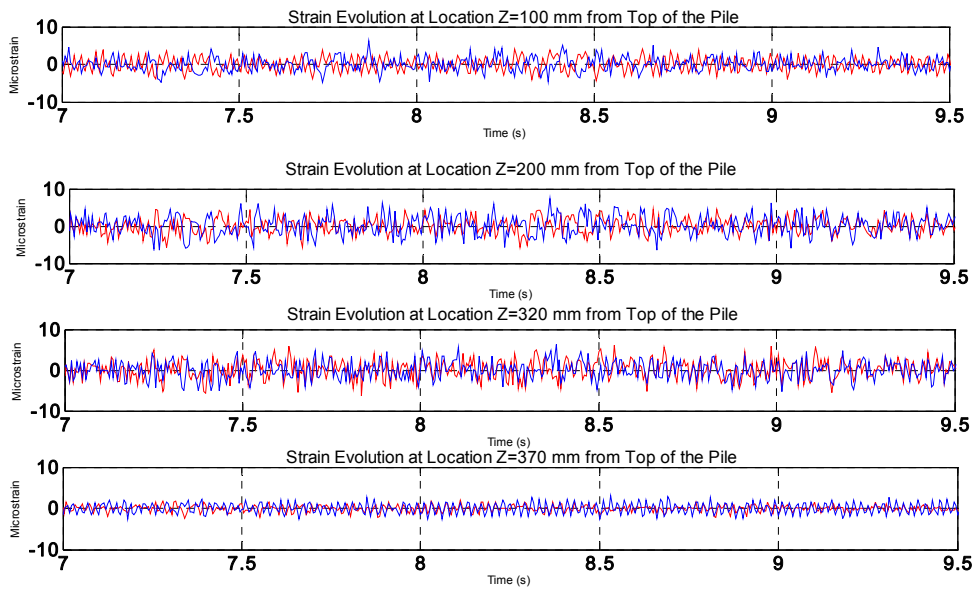


Figure 1.182 strain gauges 100-370 mm

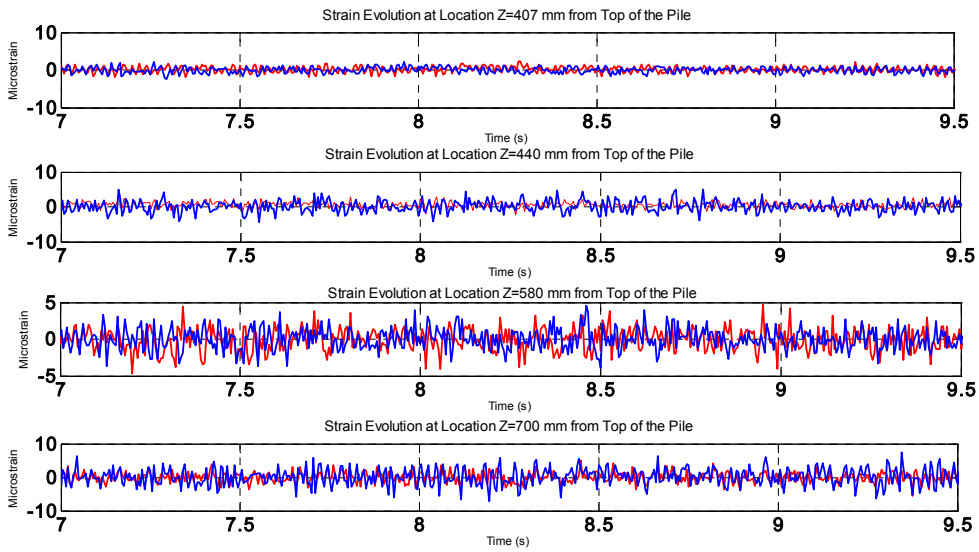


Figure 1.183 strain gauges 407-700 mm

4.8 E+R_TMZ 2_NRH

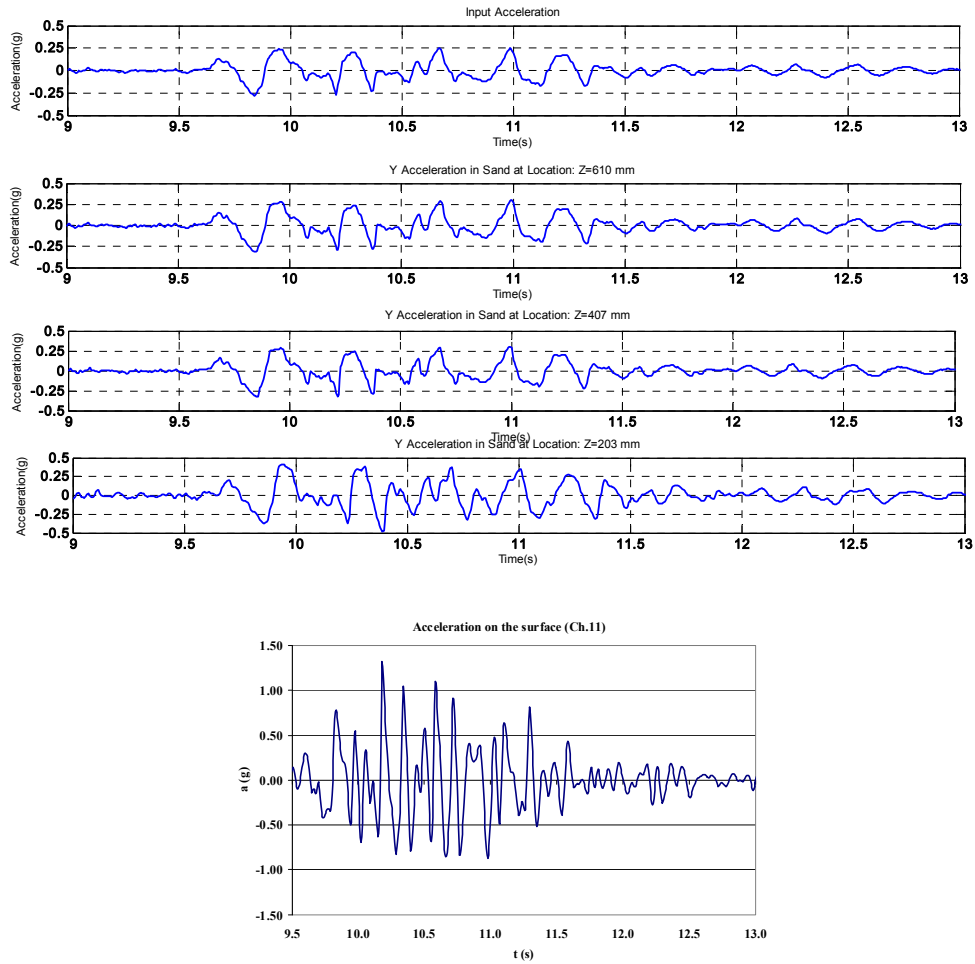


Figure 1.184 acceleration: array inside

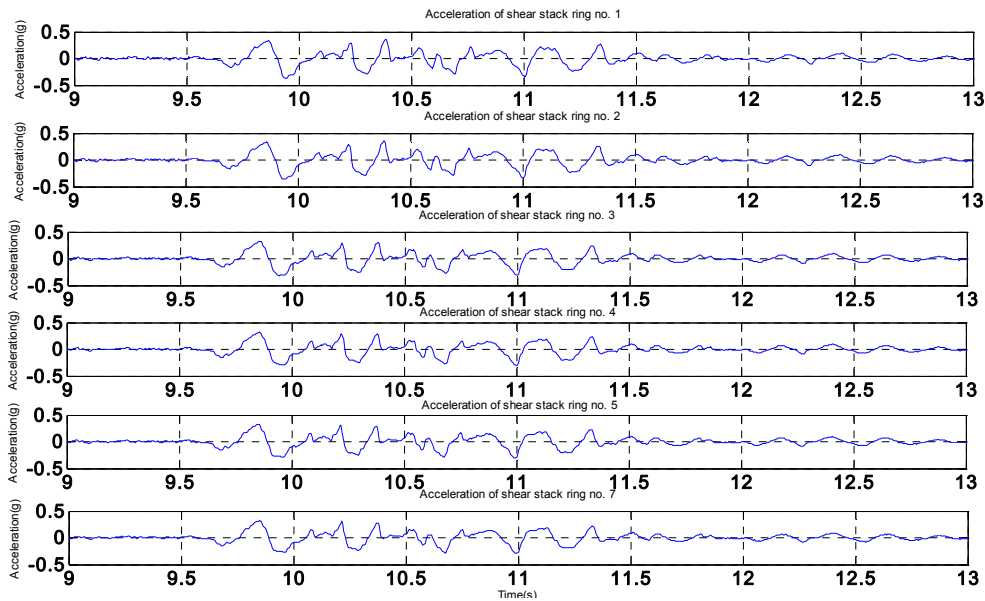


Figure 1.185 acceleration: array outside

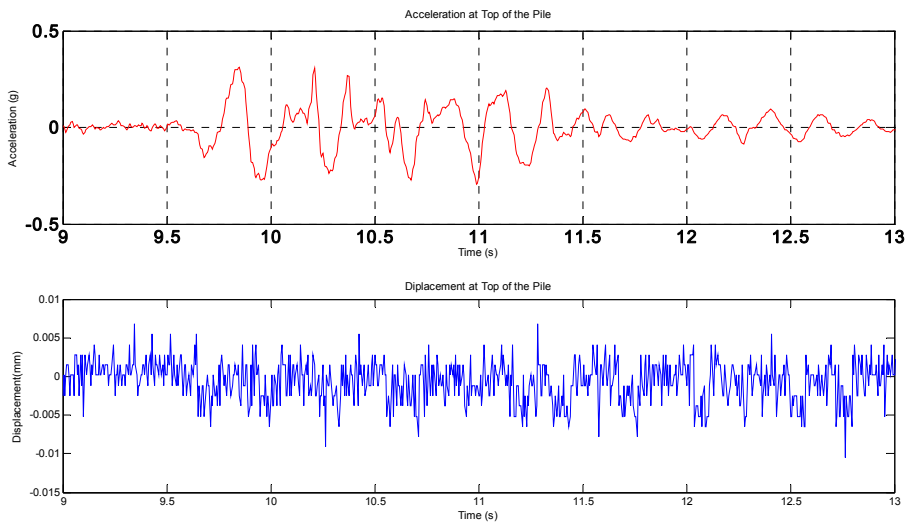


Figure 1.186: top pile: acceleration and LVDT

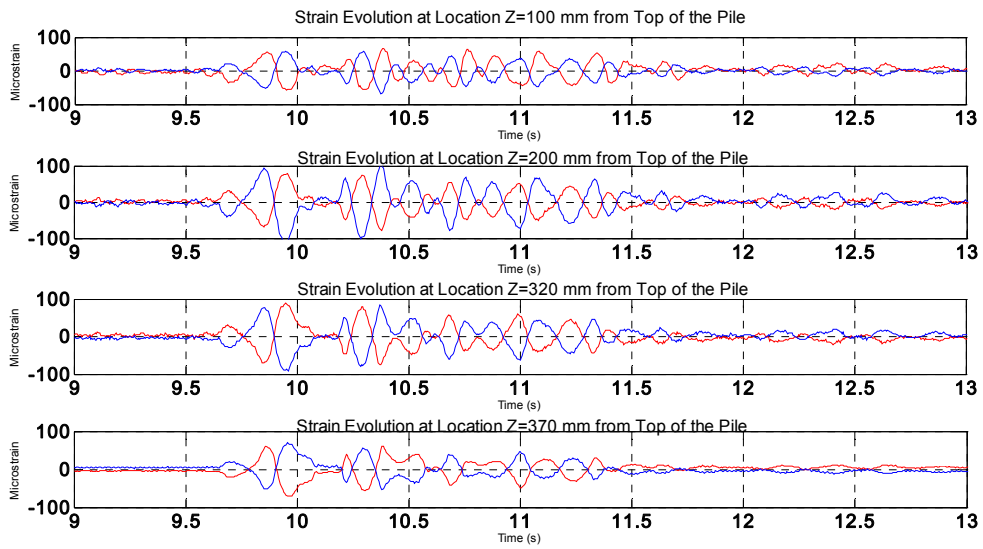


Figure 1.187 strain gauges 100-370 mm

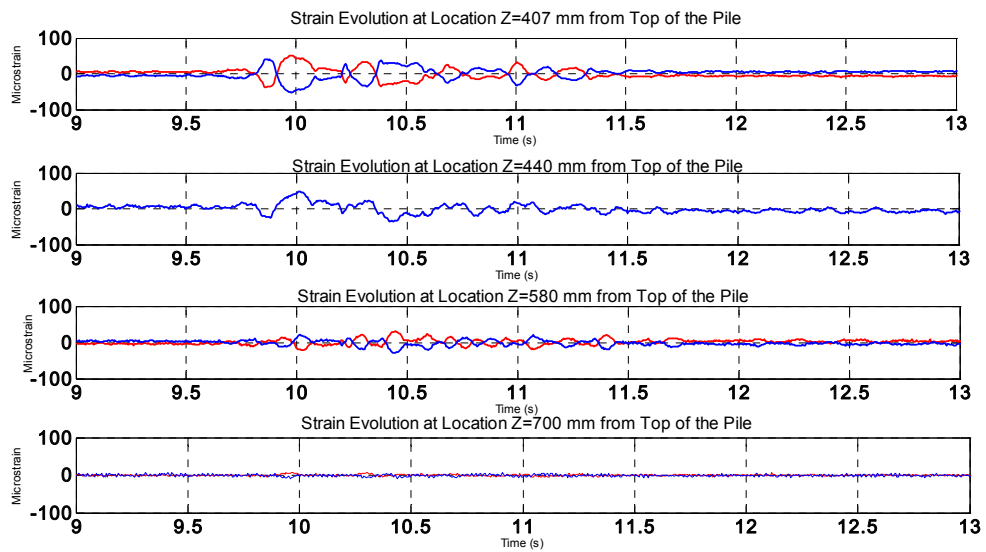


Figure 1.188: strain gauges 407-700 mm

4.9 E+R_STU12_NRH+SDOF

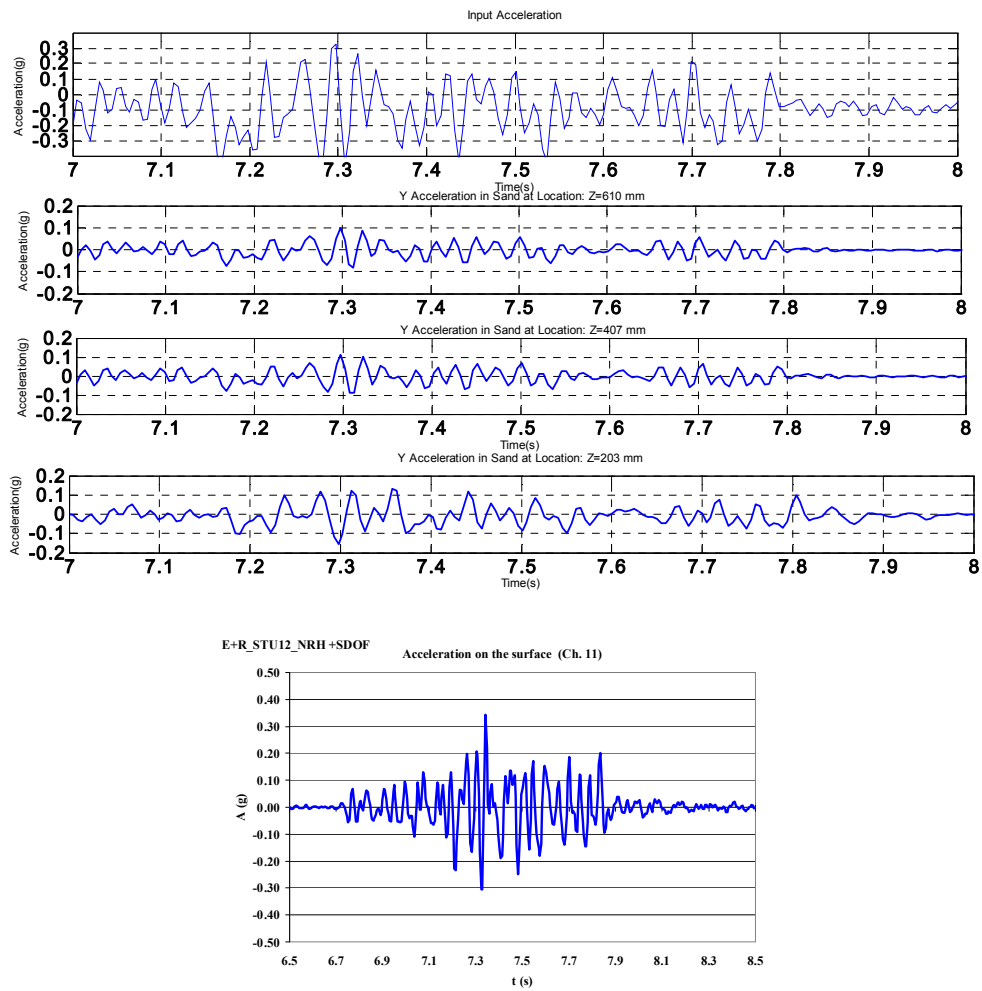


Figure 1.189 acceleration : array inside

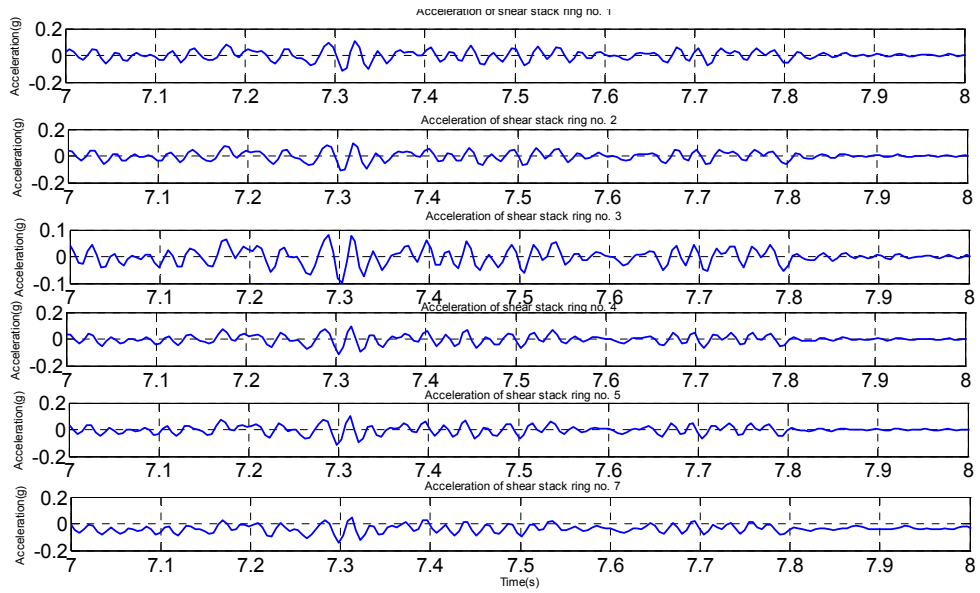


Figure 1.190 acceleration : array outside

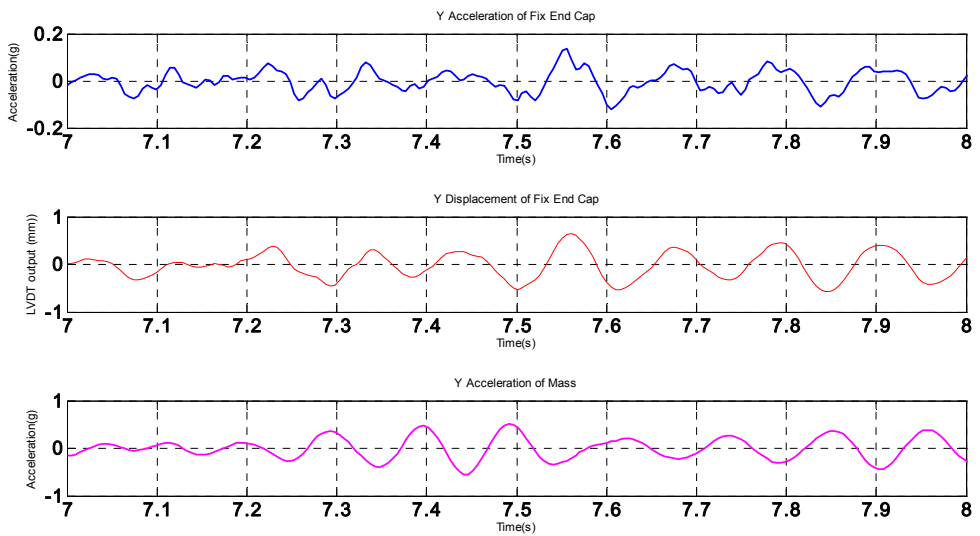


Figure 1.191 top pile : acceleration and LVDT; SDOF acceleration

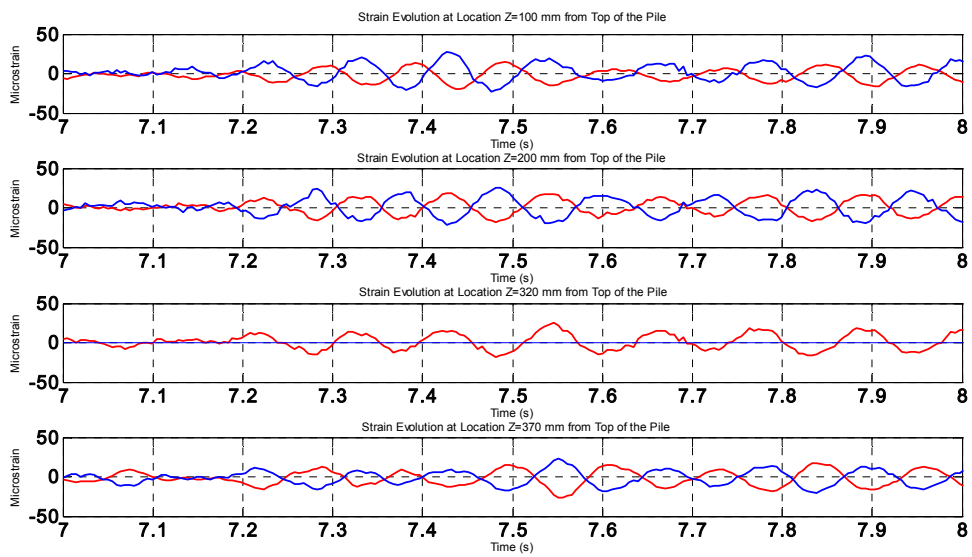


Figure 1.192 strain gauges 100-370 mm

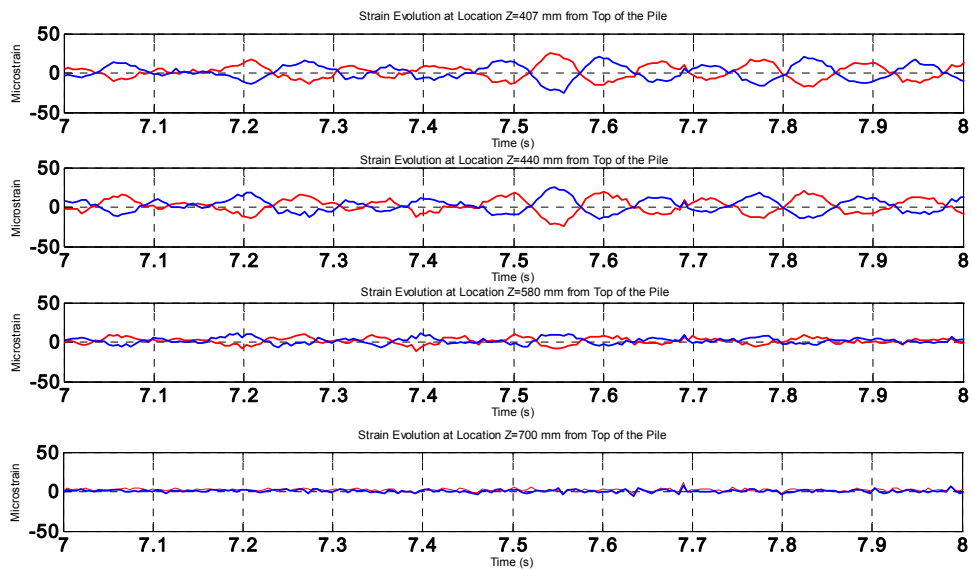


Figure 1.193 strain gauges 407-700 mm

4.10 E+R_STU2_NRH+SDOF

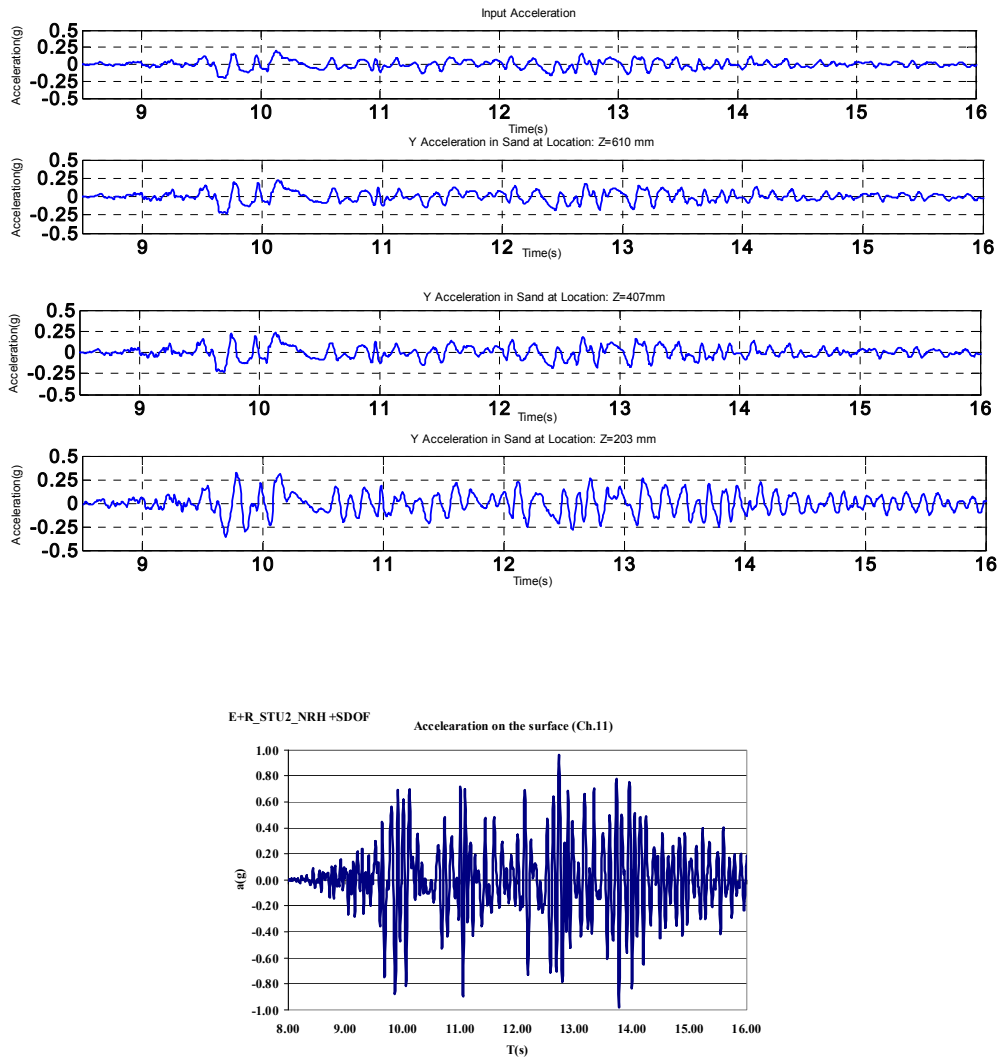


Figure 1.194 acceleration: array inside

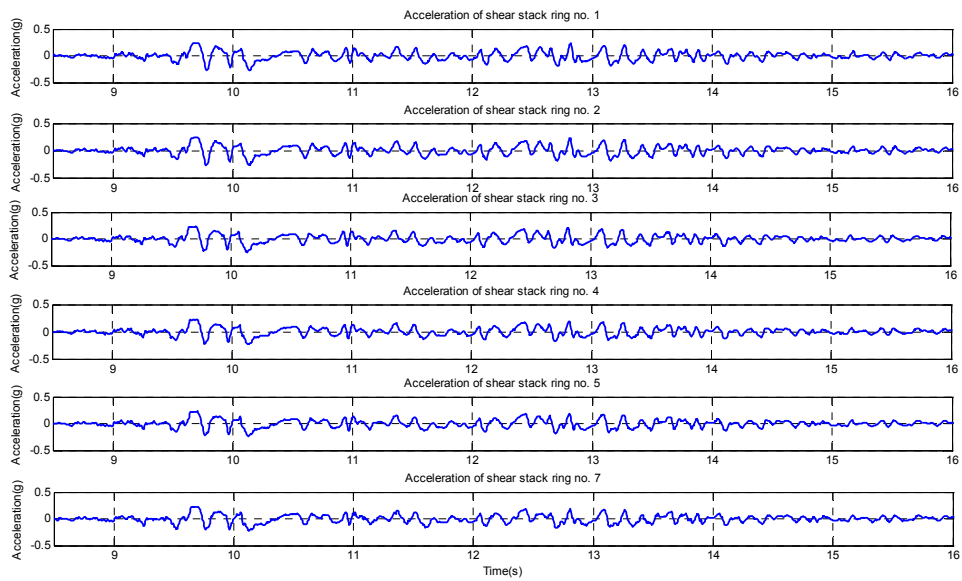


Figure 1.195 acceleration: array outside

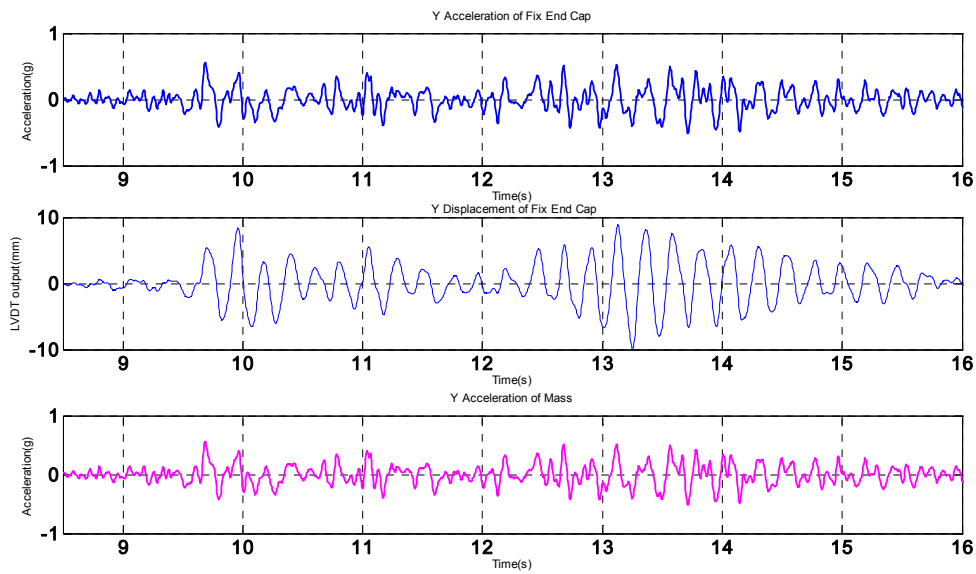


Figure 1.196 top pile acceleration and LVD and SDOF acceleration

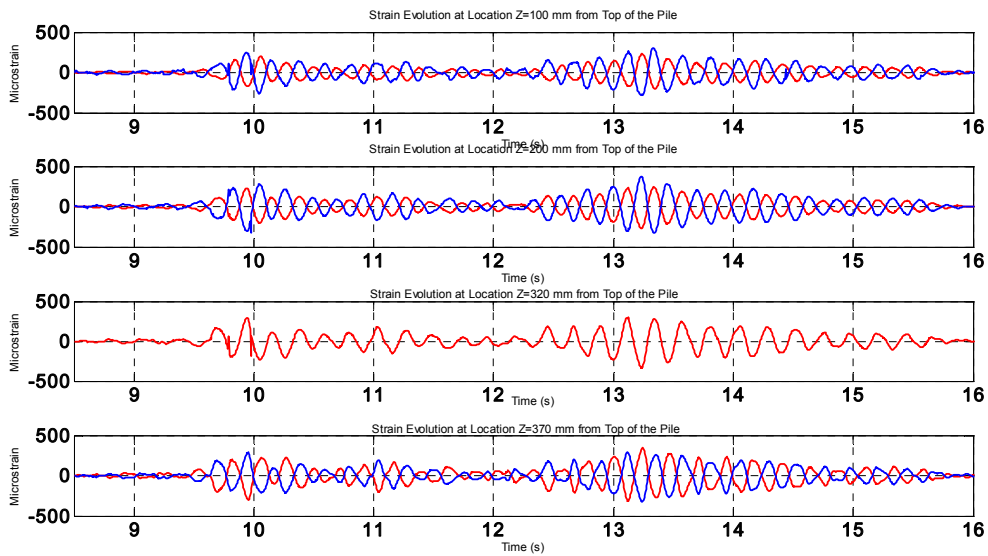


Figure 1.197 strain gauges 100-370 mm

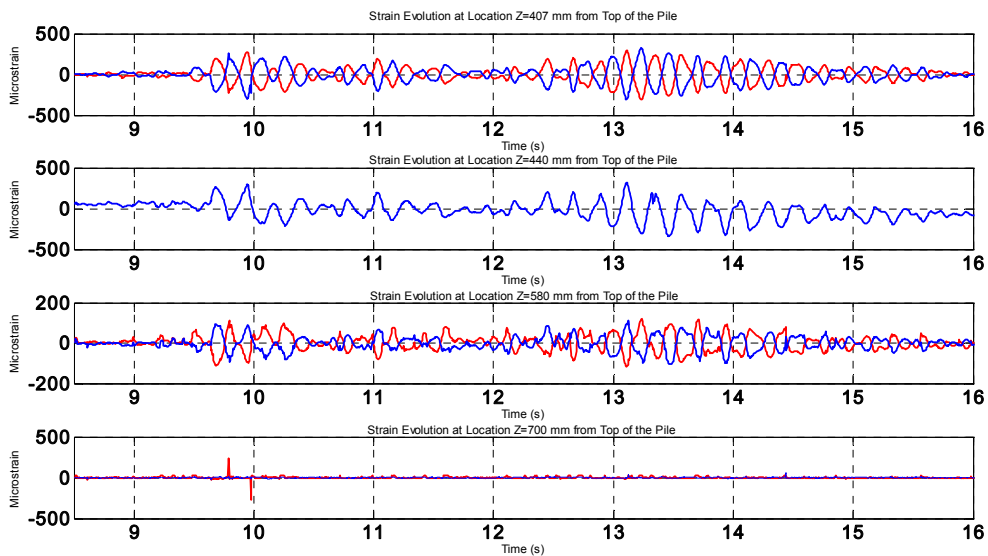


Figure 1.198 strain gauges 407-700 mm

4.11 E+R_TMZ12_NRH+SDOF

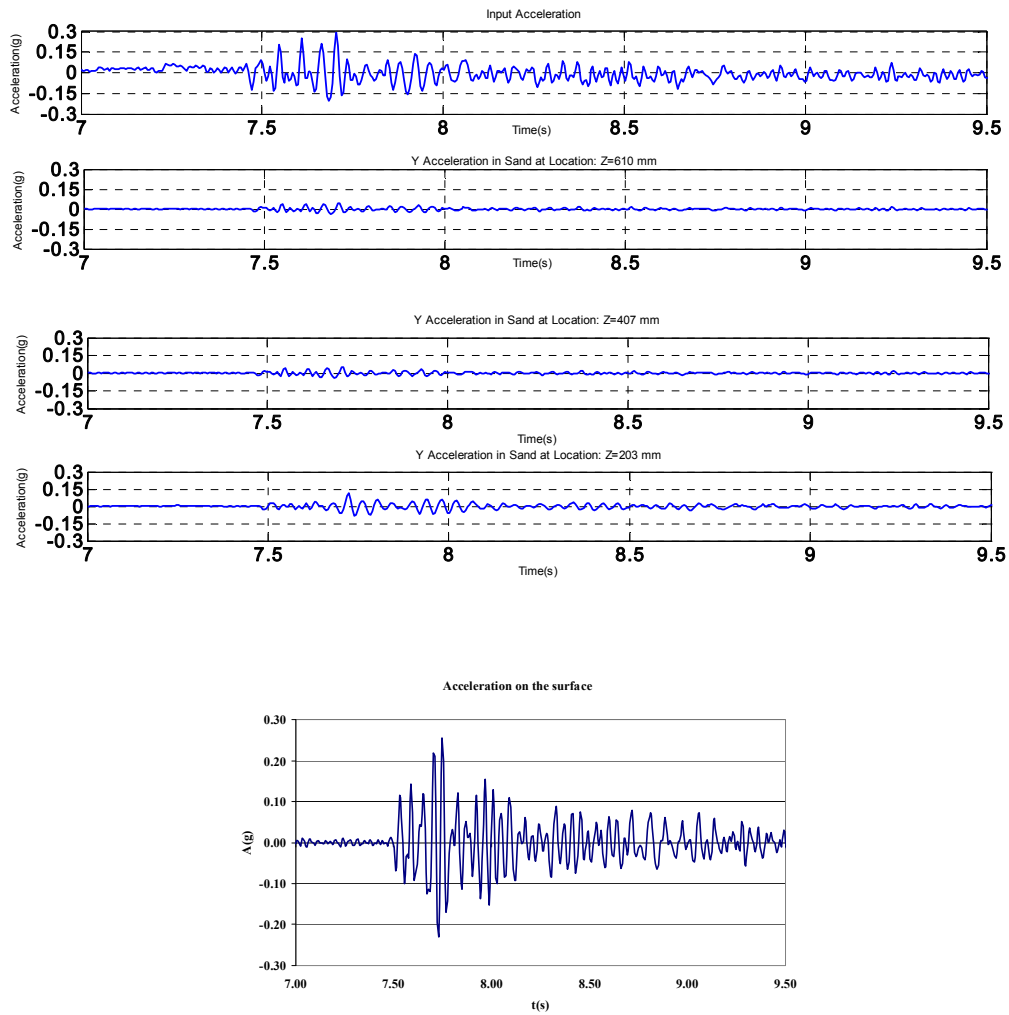


Figure 1.199 acceleration: array inside

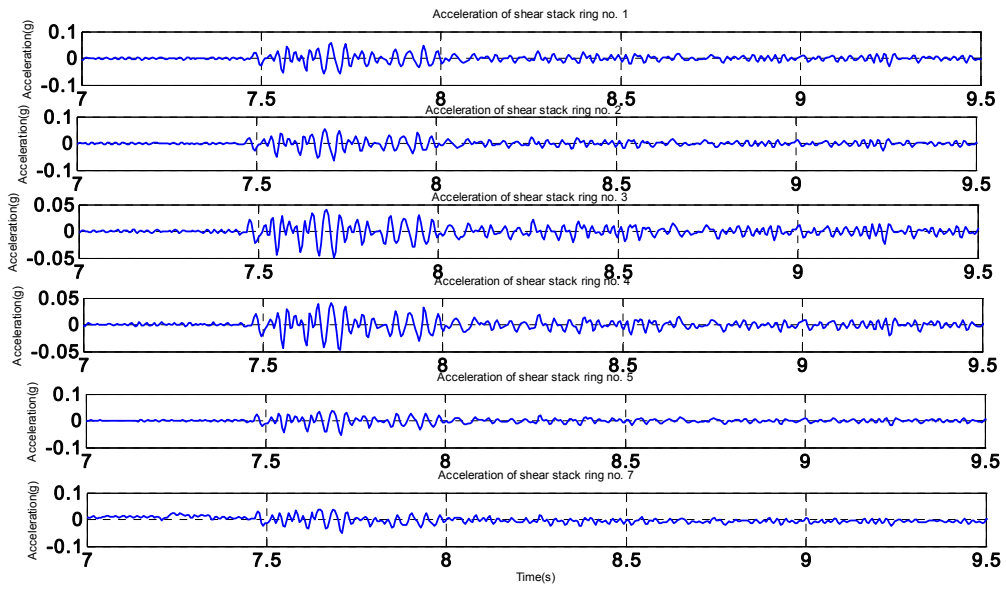


Figure 1.200 acceleration array outside

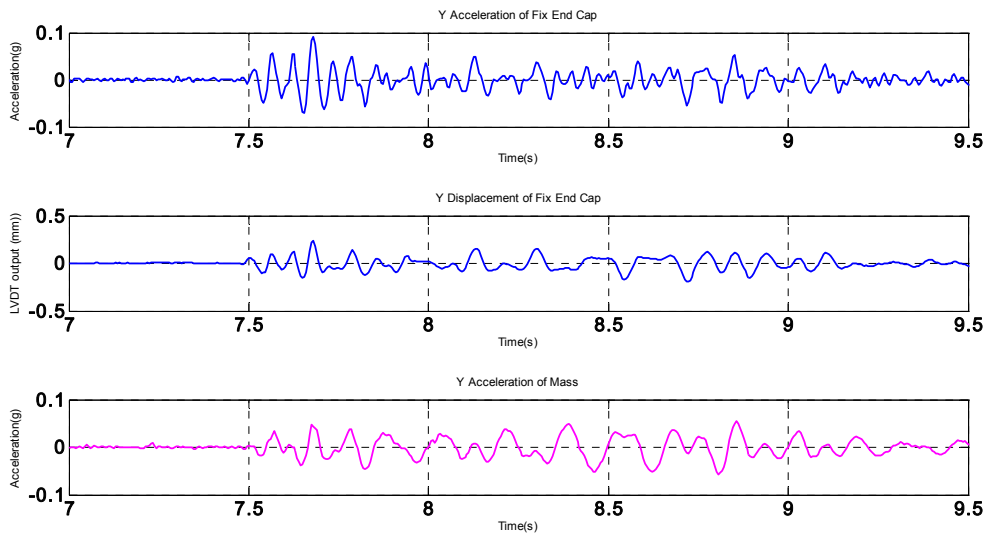


Figure 1.201: top pile acceleration and LVDT; SDOF acceleration

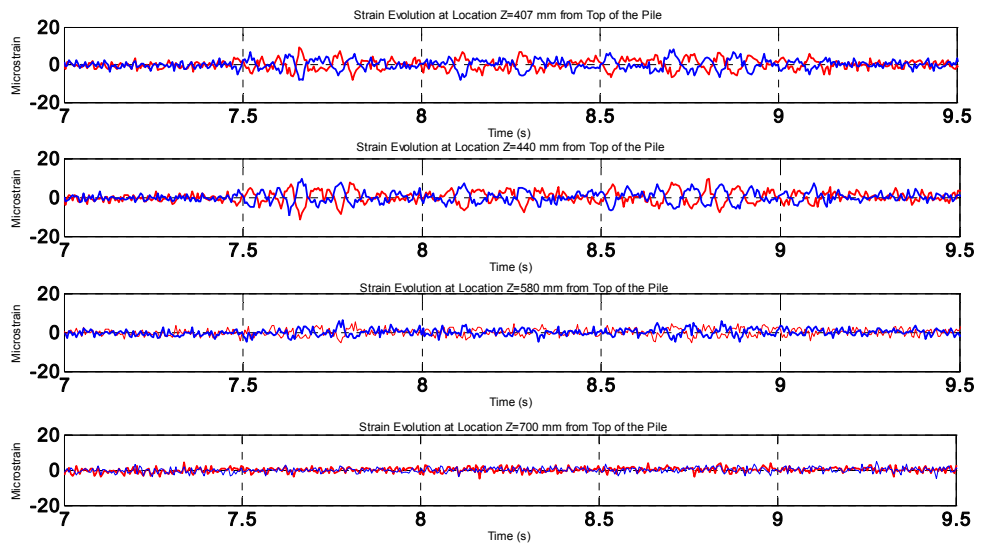


Figure 1.202 strain gauges 407-700mm

4.12 E+R_NCB5_NRH+SDOF

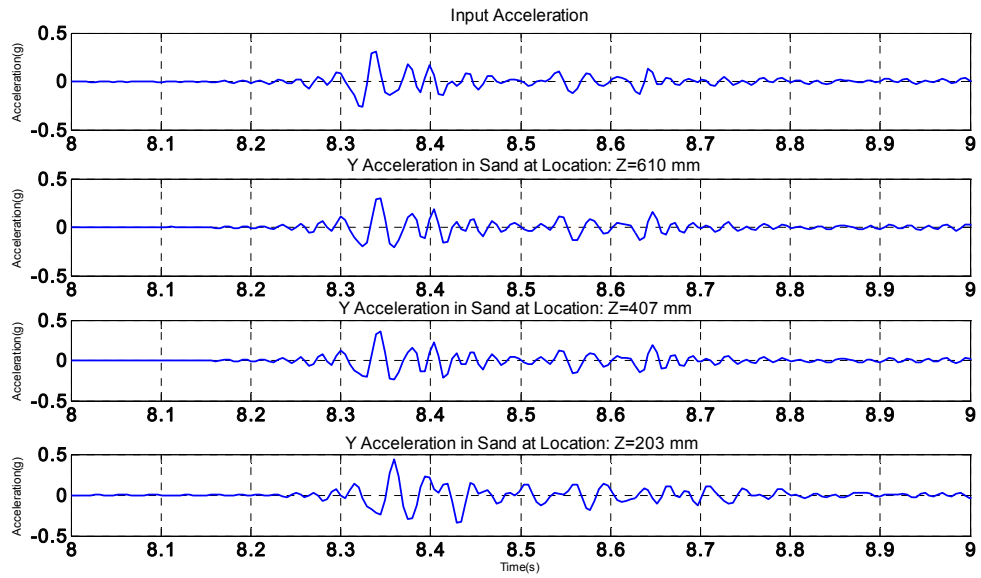


Figure 1.203 acceleration: array inside

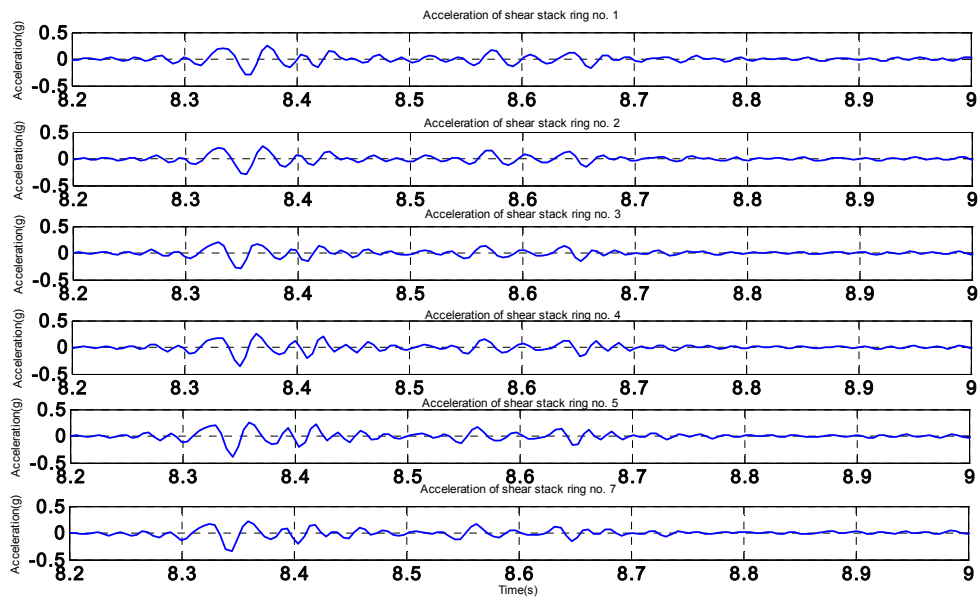


Figure 1.204 acceleration: array inside

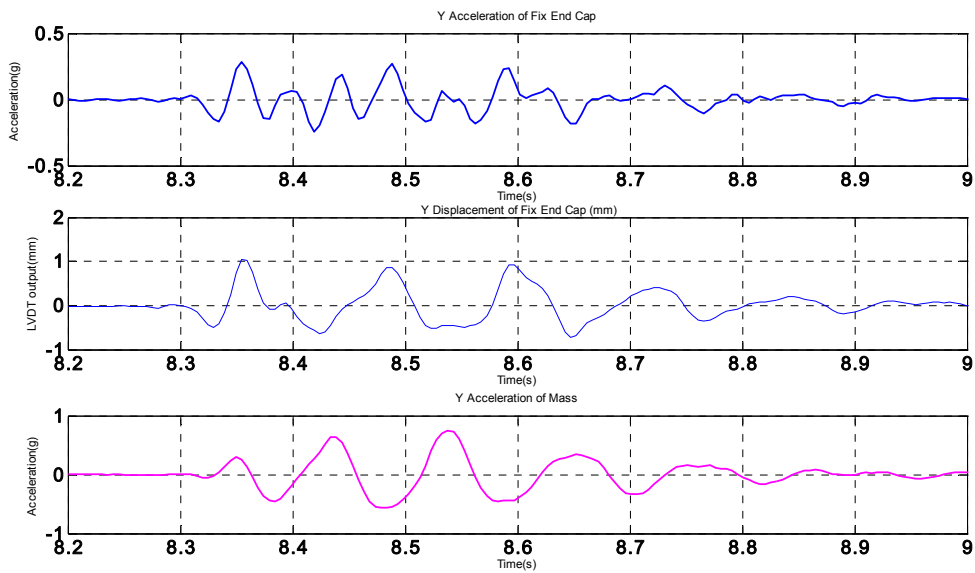


Figure 1.205 top pile acceleration and LVDT; SDOF acceleration

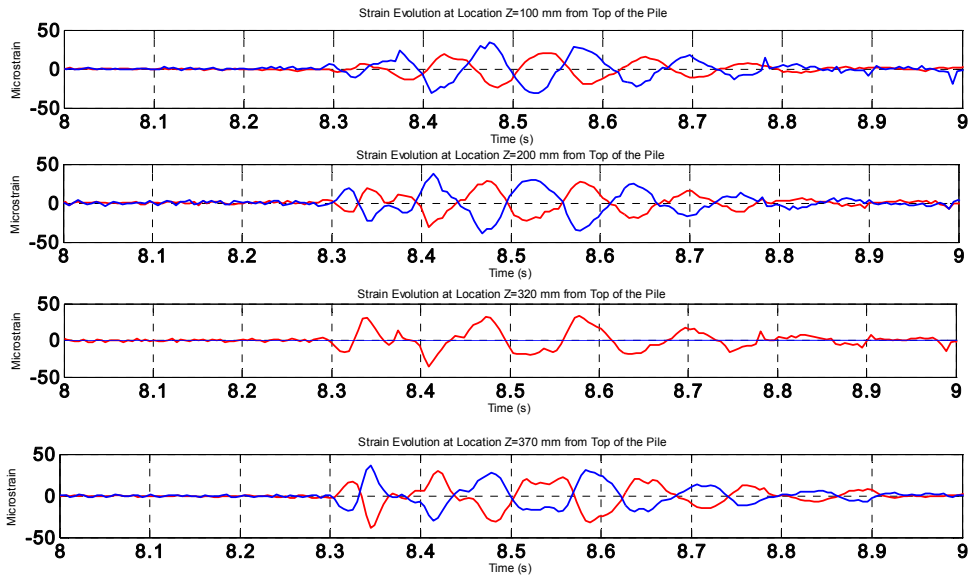


Figure 1.206 strain gauges 100-370 mm

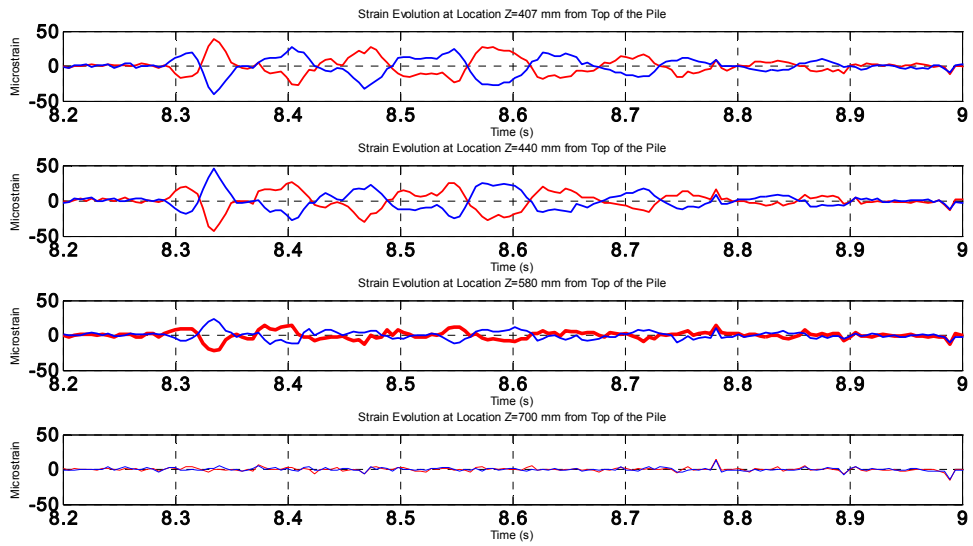


Figure 1.207 strain gauges 407-700 mm

